



Exploring the primordial universe, inflation and primordial gravitational waves with QUBIC, the Q & U Bolometric Interferometer for Cosmology.

Louise Mousset

► To cite this version:

Louise Mousset. Exploring the primordial universe, inflation and primordial gravitational waves with QUBIC, the Q & U Bolometric Interferometer for Cosmology.. Instrumentation and Methods for Astrophysic [astro-ph.IM]. Université Paris Cité, 2021. English. NNT : 2021UNIP7133 . tel-03783687

HAL Id: tel-03783687

<https://theses.hal.science/tel-03783687>

Submitted on 22 Sep 2022

HAL is a multi-disciplinary open access archive for the deposit and dissemination of scientific research documents, whether they are published or not. The documents may come from teaching and research institutions in France or abroad, or from public or private research centers.

L'archive ouverte pluridisciplinaire **HAL**, est destinée au dépôt et à la diffusion de documents scientifiques de niveau recherche, publiés ou non, émanant des établissements d'enseignement et de recherche français ou étrangers, des laboratoires publics ou privés.

Exploring the primordial Universe, inflation and primordial gravitational waves with QUBIC, the Q&U Bolometric Interferometer for Cosmology.

Par Louise MOUSSET

Thèse de doctorat de Physique de l'Univers

Dirigée par Jean-Christophe HAMILTON

*Présentée et soutenue publiquement le 15 octobre 2021
devant un jury composé de :*

<i>Présidente</i>	Simona MEI	PU, Université de Paris
<i>Rapporteurs</i>	Marian DOUSPIS	Astronome, Université Paris-Saclay
	Jean-Loup PUGET	DR émérite, École Normale Supérieure
<i>Examineurs</i>	Jonathan AUMONT	CR, Université Toulouse III-Paul Sabatier
	Véronique VAN ELEWYCK	MCU, Université de Paris
	Matias ZALDARRIAGA	Professor, Institute for Advanced Study
<i>Directeur de thèse</i>	Jean-Christophe HAMILTON	DR, Université de Paris

Résumé

La détection des modes B primordiaux de polarisation du fond diffus cosmologique est aujourd'hui l'un des défis majeurs de la cosmologie observationnelle. Leur mesure permettrait de contraindre les modèles d'inflation cosmique, cette phase d'expansion accélérée aux tout premiers instants de l'univers. Le projet QUBIC a terminé la campagne de tests et de validation en France et l'instrument a été envoyé en Argentine. L'observation du ciel débutera après une nouvelle courte campagne de tests en laboratoire. Cet instrument s'appuie sur une technologie particulièrement innovante, l'interférométrie bolométrique dont le principe optique sera décrit en détail. La mesure d'un signal aussi ténu que celui des modes B exige un contrôle des effets systématiques irréprochable. C'est justement ce à quoi QUBIC entend répondre grâce à la possibilité de *self-calibration* propre à l'interférométrie et à un design optique assurant une cross-polarisation minimale. Un deuxième enjeu majeur pour cette mesure est le traitement des avant-plans astrophysiques qui viennent contaminer le signal de l'univers primordial. Pour cela, l'interférométrie bolométrique offre la possibilité de faire de l'imagerie spectrale, c'est-à-dire de reconstruire, en *post-processing*, des cartes du ciel dans plusieurs sous-bandes de fréquence alors même que l'instrument intègre le signal dans une large bande. Sachant que les avant-plans se distinguent par leur spectre d'émission, l'imagerie spectrale est la clé pour s'affranchir de ces contaminations.

Cette thèse fait le pont entre l'instrument QUBIC et l'estimation des paramètres cosmologiques à partir du signal mesuré. J'ai tout d'abord participé activement à l'assemblage de l'instrument et à son étalonnage, notamment au travers de la vérification optique de l'alignement des miroirs. Aussi, une partie importante de ma thèse a été dédiée à la prise et à l'analyse des données d'étalonnage, notamment à la mesure des franges d'interférence et du lobe du télescope, toujours mises en regard avec des simulations optiques. Ces mesures sont un premier pas vers la *self-calibration* complète de l'instrument. Cependant, le coeur de ma thèse a été de démontrer la faisabilité de l'imagerie spectrale au travers de simulations complètes de la chaîne d'analyse, allant de la simulation d'une observation du ciel, jusqu'à l'estimation des paramètres cosmologiques, en passant par la reconstruction des cartes du ciel en sous-bandes de fréquence.

Mots clés : Cosmologie, Fond diffus cosmologique, Inflation, Interférométrie bolométrique, Imagerie spectrale, Analyse de données

Abstract

The detection of primordial B -mode polarization in the cosmic microwave background is one of the main targets for observational cosmology today. Their detection would constrain cosmic inflation models, an accelerating expansion phase occurring at the very beginning of the universe. The QUBIC project recently completed the calibration and the validation of the instrument and it has been sent to Argentina. Observation of the sky will begin after another short calibration phase in the laboratory. This instrument relies on an innovative technology, bolometric interferometry, which will be described in detail. Measurement of the extremely weak B -mode signal requires exquisite control of systematic effects. This is an important advantage of QUBIC thanks to self-calibration, a technique coming from interferometry, and to a specific optical design ensuring minimal cross-polarization. A second challenge for this measurement is the mitigation of astrophysical foregrounds which contaminate the signal of the primordial universe. For this purpose, bolometric interferometry makes spectral imaging possible, i.e. the reconstruction, in post-processing, of sky maps in several frequency sub-bands even though the instrument integrates the signal in a wide band. Knowing that foregrounds have distinct emission spectra, spectral imaging is the key to eliminate these contaminants.

This thesis describes a detailed analysis going from the QUBIC instrument through to the estimation of cosmological parameters. I contributed to the assembling and calibration of the instrument, especially in the optical verification of the mirror alignment. An important part of my thesis is dedicated to calibration data taking and data analysis, especially the measurement of interference fringes and the telescope beam, which are compared to optical simulations. Those measurements are a first step for the full self-calibration of the instrument. However, the heart of my thesis is the demonstration that spectral imaging is feasible. This is done through end-to-end simulations covering the simulation of a sky observation with QUBIC to the estimation of cosmological parameters, including the reconstruction of frequency sub-band maps.

Keywords: Cosmology, Cosmic Microwave Background, Inflation, Bolometric interferometry, Spectral imaging, Data analysis

Remerciements

Je tiens tout d'abord à remercier l'ensemble des membres de mon jury de thèse.

Bien sûr un grand merci à mes deux directeurs Jean-Christophe et Steve pour ces trois ans que nous avons passé ensemble. Jean-Christophe, merci pour tes conseils avisés, le temps que tu trouvais toujours à m'accorder quand je débarquais dans ton bureau à l'improviste, ton sens de l'humour et ton optimisme à toute épreuve. Steve, merci pour ton calme, ta patience, ton aide sur les problèmes informatiques divers et variés et les nombreuses relectures de textes en anglais.

Aussi, je tiens à remercier l'ensemble de l'équipe à l'APC : Michel, Jean-Pierre, Damien, Laurent, Fabrice, Jean, Claude... Merci pour l'ambiance chaleureuse, les rigolades autour de l'instrument et toute la physique que j'ai pu glaner au détour de conversations. Merci pour votre bienveillance qui se résumerait sûrement par "Il n'y a que ceux qui ne font rien qui ne cassent rien". Merci aussi à l'ensemble du groupe Cosmologie de l'APC et au laboratoire en général.

Un grand merci à tous les doctorants, parfois compagnons de galère mais aussi de rigolades et de succès ! En particulier merci à Bastien, Thomas, Calum, Guillaume et Raphaël d'avoir rendu le bureau si agréable, peut-être grâce aux nombreux cafés.

Ensuite je voudrais remercier mes collègues argentins et en particulier Martín et Manu. Era siempre un placer trabajar con ellos, especialmente en La Plata y Barichelo. Gracias por todo lo que aprendimos juntos y gracias por enseñarme español y mostrarme la cultura argentina !

Mes remerciements vont maintenant à ma famille, en particulier Léo et Rémi, Mousse, mes cousins, ma soeur et bien évidemment mes parents. Merci de m'avoir toujours encouragée sur la longue voie des études. Merci aussi de m'avoir transmis ce goût pour le bricolage et cette curiosité envers le monde.

Puisque cette thèse n'aurait pu être menée à bien sans le soutien de nombreux amis, merci à vous tous ! Merci à mes colloques formidables, Cécile, Yvan et Coco. Merci à Blandine, Joséphine parce que c'est toujours un plaisir de se revoir. Un grand merci à tous les musiciens, les Planches à Musique, l'Orchestre Impromptu, l'Association Baroque sur Diège, parce qu'un peu de musique fait beaucoup de bien au milieu de toute cette physique. Merci Florent, Mathilde, Kévin pour tous ces bons moments ! Merci Grégoire même s'il y a quelque chose que je ne comprends pas... Merci aux Sciences et Musico, Louis, Suzanne, Elsa, Tristan, Elia, Tim, Noé parce que vous êtes un groupe d'amis formidables. Merci à Aurélien pour tous ces chouettes moments et ton aide en physique à Cachan. Merci à Pierre-François et Brooke pour les encouragements, les conseils précieux et la piscine ! Merci au groupe des matelots pour avoir bravé la tempête avec autant de sérénité.

Enfin, je conclurai ces remerciements avec Jérémy parce que cette thèse te doit beaucoup. Merci de m'avoir autant accompagnée et soutenue, merci pour toutes ces discussions à base de schémas rocambolesques et merci pour la vie en général !

Contents

Introduction	9
1 The Q&U Bolometric Interferometer for Cosmology (QUBIC)	13
1.1 A general description of QUBIC	14
1.1.1 The project	14
1.1.2 A general description of the instrument	14
1.1.3 Brief description of each part	15
1.2 A synthetic imager	20
1.2.1 Observing the sky through an instrument	21
1.2.2 A more general definition for the PSF	26
1.2.3 A bolometric interferometer seen as a synthetic imager	26
1.2.4 Expression of the QUBIC Point Spread Function	28
1.2.5 QUBIC synthesized beam	29
1.2.6 QUBIC as an interferometer	32
1.3 A polarimeter	34
1.3.1 The Stokes parameters	34
1.3.2 Measuring a linear polarization	35
1.4 Optical combiner alignment	37
1.4.1 Experimental setup	37
1.4.2 Comparison to a model	38
1.4.3 Analysis by detecting the center of each spot	38
1.4.4 Analysis by doing the product of images	39
1.4.5 Conclusion of the optical alignment	41
2 First steps towards self-calibration	43
2.1 Optimization of the polarimeter design	44
2.1.1 Limiting the cross-polarization	44
2.1.2 Systematic effect modeling	46
2.1.3 Limiting the leakage from intensity to polarization	47
2.2 Self-calibration principle	50
2.2.1 Redundant baseline comparison	50
2.2.2 Number of baselines	50
2.3 Synthesized beam analysis	51
2.3.1 Synthesized beam maps	51
2.3.2 Appropriate peak numbering	51
2.3.3 Determination of the focal length of the optical combiner	55
2.3.4 Prospective for this work	58
2.4 Simulate interference fringes on the focal plane	58
2.4.1 QUBIC soft simulations	59
2.4.2 Analytical model	62
2.4.3 Maynooth simulations	62
2.5 Measurement and data analysis to obtain fringe images	64

2.5.1	Combination of images	64
2.5.2	Data taking process	65
2.5.3	Detecting “bad” detectors	67
2.5.4	Data analysis process	69
2.5.5	Verification of the horn-array orientation with fringe measurements	74
2.6	Bolometer inter-calibration using the fringes	76
2.6.1	Theoretical principle	76
2.6.2	Illustration on a simulation	77
2.6.3	First trial on real data	82
2.6.4	Prospective for this work	85
3	The Cosmic Microwave Background	87
3.1	Our vision of the universe before 1920	88
3.1.1	Few words about general relativity	88
3.1.2	A static and perpetual universe	88
3.2	From a perpetual universe to an expanding universe	89
3.2.1	Questioning the vision of the universe	89
3.2.2	The Hubble-Lemaître law	90
3.2.3	The standard model of cosmology	91
3.2.4	Proper and comoving distances	92
3.2.5	Relation between the scale factor and the redshift	93
3.2.6	Measurable distances in cosmology	94
3.2.7	The Hot Big Bang model	95
3.3	Thermal history of the Universe	95
3.3.1	Prediction and first observation of the CMB	95
3.3.2	Big Bang nucleosynthesis	97
3.3.3	Recombination	97
3.4	The CMB black-body spectrum	100
3.4.1	A black-body at 2.7 K today	100
3.4.2	Sunyaev Zel’dovich (SZ) effect	101
3.4.3	The CMB dipole	102
3.4.4	CMB thermodynamic units	103
4	Spatial anisotropies in the CMB map	105
4.1	Temperature anisotropies	105
4.1.1	Sound waves in the primordial plasma	106
4.1.2	Physical processes that create temperature anisotropies	107
4.1.3	Processes that attenuate the anisotropies	108
4.1.4	Angular power spectrum	110
4.1.5	Observed power spectrum	113
4.2	Polarization anisotropies	115
4.2.1	Thomson scattering	115
4.2.2	Thomson scattering as a source of linear polarization in the CMB	116
4.2.3	E and B -mode introduction	117
4.2.4	Origin of quadrupole anisotropies	119
4.2.5	Polarization statistics	122
4.2.6	Perturbations on the way	123
5	Observing and measuring the CMB	125
5.1	Projects targeting B -modes	126
5.1.1	Ground based telescopes	126
5.1.2	Balloons	127
5.1.3	LiteBIRD space mission	127
5.1.4	Summary and discussion	127

5.2	Making sky maps	129
5.2.1	Why scanning?	129
5.2.2	Data model	130
5.2.3	Map-making solution	130
5.2.4	Numerical implementation	131
5.2.5	QUBIC monochromatic map-making	132
5.2.6	HWP angle spacing	135
5.2.7	Spatial correlations	138
5.3	Power spectrum estimation with real data	139
5.3.1	Interest of doing cross spectra	139
5.3.2	Pixel and beam window correction	140
5.3.3	Partial coverage and pseudo spectra	141
5.3.4	E and B leakage and pure decomposition	141
5.3.5	Theoretical error bars on the reconstructed power spectrum	142
5.3.6	Namaster	142
5.3.7	Maximum likelihood solution	143
5.4	Foreground contamination of the CMB signal	144
5.4.1	Astrophysical foregrounds	144
5.4.2	Atmospheric opacity	145
5.5	QUBIC on a TOAST	147
6	Spectral imaging	149
6.1	Spectral dependence	150
6.1.1	The polychromatic synthesized beam	150
6.1.2	Spectral imaging capabilities	152
6.2	Testing spectral imaging on simple cases	153
6.2.1	Extended source reconstruction	153
6.2.2	Angular resolution	154
6.2.3	Frequency Point Spread Function (FPSF) characterization	155
6.2.4	Galactic dust	158
6.3	Noise characterization	163
6.3.1	Noise behavior in the sub-bands at map level	163
6.3.2	Fast noise simulator	163
6.3.3	Noise analysis using the power spectrum	166
6.4	Spectral imaging on real data	168
7	Constraining Cosmology from CMB observation	171
7.1	First doubts and questions	172
7.1.1	Missing matter	172
7.1.2	Horizon problem	173
7.1.3	Flatness problem	173
7.1.4	Absence of magnetic monopoles	174
7.2	Saving the Big Bang model with cosmic inflation	174
7.2.1	Hubble radius	174
7.2.2	Definition of inflation	174
7.2.3	A scalar field: the inflaton	176
7.2.4	The slow-roll approximation	177
7.2.5	How inflation ends?	177
7.3	Primordial perturbations from inflation	178
7.3.1	From microscopic physics to macroscopic observables	178
7.3.2	Connection with CMB observations	180
7.4	Experimental evidences for inflation	181
7.4.1	Scale invariance	181
7.4.2	Tensor modes	182

7.4.3	Coherence	183
7.4.4	Gaussian	183
7.4.5	Adiabatic	183
7.4.6	Discussion	183
7.5	New surprise, the expansion is accelerating	184
7.6	Constraints on the cosmological parameters	184
7.6.1	The success of the Λ CDM model	184
7.6.2	From CMB observation to cosmological parameters	186
7.6.3	Others cosmological probes	189
7.7	Constraining r with QUBIC	190
7.7.1	Description of the simulations	190
7.7.2	QUBIC Full Instrument expected performance	191
7.7.3	Spectral imaging and constraints on r	192
7.7.4	Ability to recognize the presence of dust residuals	194
General conclusion		197
Annexes		201
A.1	Demonstration of the Huygens-Fresnel principle	201
A.2	Cosmic variance and some statistics for a normal distribution	202
A.3	Fringe data taking	203
A.4	Rigorous expression of the focal length	205
A.5	Spectral imaging paper	207
Résumé en français		239
B.1	Introduction	239
B.2	Contexte scientifique	239
B.3	L'interféromètre bolométrique QUBIC	240
B.4	Vérification de l'alignement des miroirs	240
B.5	Premiers pas vers la self-calibration	241
B.6	Imagerie spectrale	242
B.7	Conclusion	244
Bibliography		245

Introduction

The Q&U Bolometric Interferometer for Cosmology (QUBIC) was designed to measure the Cosmic Microwave Background (CMB) polarization [1]. The quest for B -mode polarization of the CMB is among the major challenges of observational cosmology. It would reveal primordial gravitational waves, validating inflation theory, with consequences in particle physics. Characterization and calibration of the QUBIC instrument started in 2018 at Astroparticle Physics & Cosmology (APC) laboratory. Now, it has been sent to Salta, in Argentina, and re-assembled there. New calibration tests will be made before installing it on the observation site near San Antonio de los Cobres.

The assembling of the instrument started right at the beginning of my PhD. I had the opportunity to participate in the calibration of the instrument which was a crucial step for the project. Thus, my work combined instrumentation, calibration, data analysis and simulations. The structure of this manuscript is based on the idea of making the connection from the QUBIC instrument and the cosmological parameters we want to constrain. Figure 1 illustrates the organization that I will detail below.

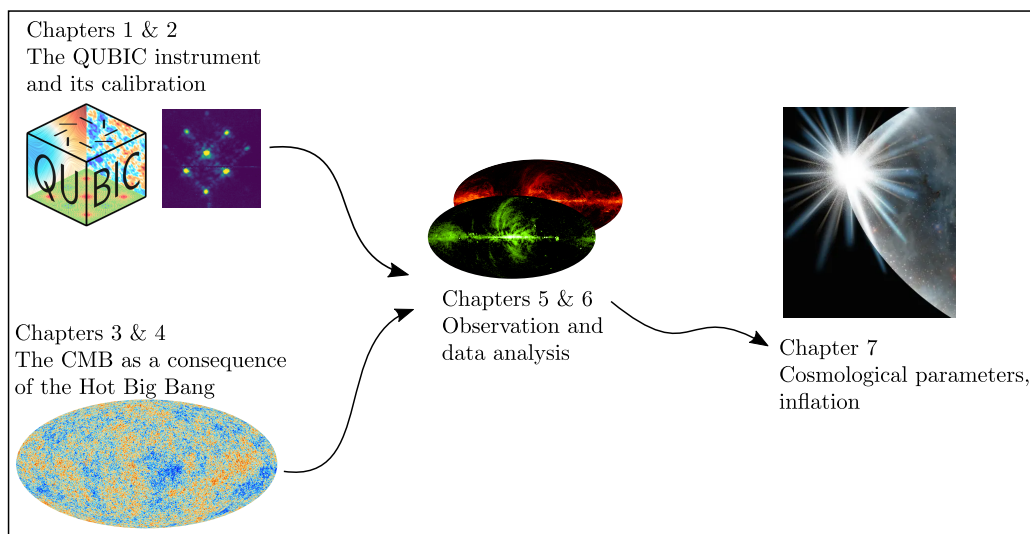


Figure 1: Illustration of the manuscript organization.

The first chapter is dedicated to a presentation of the instrument, focusing on the optical design which is completely unusual in the CMB field. Indeed, QUBIC has a horn array placed before the optical combiner so that the image on the focal plane is an interference pattern. Here I chose to describe QUBIC as a synthetic imager, i.e. an imager having a very peculiar point spread function, and not as an interferometer which was the approach chosen when the design was made.

As a bolometric interferometer, QUBIC combines the advantages of interferometry in terms of control of instrumental systematic effects with those of bolometric detectors in terms of wide-band, background-limited sensitivity. The precise control of systematic effects was the main objective for building such a new instrument. It has been shown that thanks to redundant baselines, a baseline being a pair of horns, the instrument can be self-calibrated. The second chapter aim at showing the advantage of QUBIC in terms of systematic effects. I first review the concept of self-calibration and

I adapt the formalism developed for it, mainly during the PhD of Marie-Anne Bigot-Sazy (2013), to the current instrument design. Then, I focus on optics calibration measurements and data analysis which are an essential step for self-calibration, especially the measurement of interference fringes for individual baselines. Measurements are always compared with optical simulations developed for that purpose.

Now it is time to get closer with cosmology! What will QUBIC measure? In chapter 3, I first review how our understanding of the universe evolved, roughly between 1920 and 1970 when the Hot Big Bang model started to be considered as the dominant one in Cosmology. One of its major success is the prediction of a relic thermal radiation around 3 K today, the CMB. It is a partially polarized photon field released 380 000 years after the Big Bang when neutral hydrogen was formed. It was first detected by Penzias and Wilson [107] in 1965 many years after its prediction [18].

Despite its apparent homogeneity, the CMB radiation has spatial temperature and polarization anisotropies which will be discussed in chapter 4. They are the direct imprint of fluctuations occurring in the primordial plasma. What is really remarkable is that the angular power spectrum of the anisotropies was predicted much before the first detection [108]! The polarization field can be decomposed into scalar and tensor modes respectively called E and B -modes. Anisotropies are an incredible source of information about the physics of the primordial universe. Indeed, density perturbations in the primordial plasma create E -modes, which have already been detected. On the contrary, gravitational waves propagating in the primordial plasma create E and B -modes, and the primordial B -mode signature has not been detected yet.

At this stage, we have an instrument designed to measure the CMB. Chapter 5 presents the CMB from the point of view of people who analyze the data. I review the usual data analysis techniques for map-making and power spectrum estimation in the CMB field. It will be illustrated with the QUBIC case, sometime pointing out specificities of this instrument. In addition, observers have to deal with the contamination of the CMB signal by astrophysical foreground emissions and with atmosphere opacity for ground-based instruments. In polarization, the two dominant astrophysical foregrounds are the synchrotron radiation and the thermal dust emission from the Milky Way, both producing non-primordial B -mode polarization.

CMB and foregrounds can be distinguished thanks to their distinct spectral behavior. This is why the key of any foreground mitigation technique is to have measurements in multiple frequency channels. Several years after the QUBIC instrument was designed, it was realized that bolometric interferometry allows to do spectral imaging thanks to the frequency-dependent shape of the QUBIC synthesized beam. This results in the ability to produce sky maps in multiple frequency sub-bands while our detectors integrate the signal in a single wide frequency band, all being done in post-processing. Chapter 6 is dedicated to the characterization of this technique using end-to-end simulations which is the heart of my thesis. Spectral imaging was also successfully tested on calibration data for the first time.

Finally, how can we better constrain our model of the universe using CMB observation? In chapter 7, we will start by reviewing our current vision of the universe which has changed a lot since the first observation of the CMB. A phase of cosmic inflation, has been added to the Hot Big Bang model. We will describe the observational motivations for it and the experimental evidences. Inflation necessarily creates primordial gravitational waves (in some cases with very low amplitude). This is why the quest for a B -mode signature in the CMB is among the major challenges of observational cosmology. The B -mode intensity is characterized by the tensor-to-scalar ratio r . I will end this manuscript with forecasts on the ability that QUBIC has to constrain this parameter.

Back on the structure: As described above, this manuscript follows the path from an instrument to the cosmological parameters we aim at constraining. This structure could give the impression that a project goes step by step: making an instrument, observing, analyzing the data and finally see by chance what cosmological parameter can be constrained. Of course, it is not the case as an instrument is always designed for a specific purpose, aiming at measuring given quantities. For example, QUBIC has been developed in order to measure the tiny B -mode signature which requires a very high control of instrumental systematic effects. However, when I started my PhD, the design of the instrument was

already finalized and this is certainly why this structure well reflects my path along these three years.

Moreover, this structure allows me to introduce the theoretical concepts, either related to the cosmology or to the QUBIC instrument, when they are needed to contextualize my work. Indeed, in order to be as pedagogical as I can, I feel more comfortable with this structure that distills the theory along the manuscript than with the classical one which consists in a huge theoretical part at the beginning followed by the personal contributions.

Reading guideline: As the plan is not standard, it may be difficult for the reader to understand what my personal contributions are. This is why one can find a brief summary at the beginning of each chapter saying explicitly, what my personal work is. In summary, chapters [2](#) and [6](#) contain the majority of my work but additional contributions are presented in chapters [1](#), [5](#) and [7](#).

Chapter 1

The Q&U Bolometric Interferometer for Cosmology (QUBIC)

Contents

1.1	A general description of QUBIC	14
1.1.1	The project	14
1.1.2	A general description of the instrument	14
1.1.3	Brief description of each part	15
1.2	A synthetic imager	20
1.2.1	Observing the sky through an instrument	21
1.2.2	A more general definition for the PSF	26
1.2.3	A bolometric interferometer seen as a synthetic imager	26
1.2.4	Expression of the QUBIC Point Spread Function	28
1.2.5	QUBIC synthesized beam	29
1.2.6	QUBIC as an interferometer	32
1.3	A polarimeter	34
1.3.1	The Stokes parameters	34
1.3.2	Measuring a linear polarization	35
1.4	Optical combiner alignment	37
1.4.1	Experimental setup	37
1.4.2	Comparison to a model	38
1.4.3	Analysis by detecting the center of each spot	38
1.4.4	Analysis by doing the product of images	39
1.4.5	Conclusion of the optical alignment	41

This chapter is dedicated to the description of the QUBIC instrument and to a presentation of bolometric interferometry. In the first section, I briefly present the project and I give an overview of the instrument which combines optical, cryogenic and electronic technologies. When QUBIC was designed, the understanding of the instrument was based on the concepts developed for interferometry. However, the possibility of seeing QUBIC as an imager more than an interferometer was already considered in the last chapter of the thesis by Romain Charlassier in 2010 [2]. In section 2, I focus on the optics and I made the choice to present QUBIC as a synthetic imager, i.e. a classic telescope having a very particular point spread function. The crucial concept of synthesized beam is also introduced. In section 3, I explain the way we measure the polarization with the rotating Half-Wave-Plate (HWP). Finally, section 4 is dedicated to the verification of the mirror alignment using a laser which was done at the beginning of the QUBIC assembling, in 2018.

Personal contributions: I was responsible for the optical combiner alignment presented in section 1.4, in collaboration with people in Roma. Simulations used in section 1.2 for pedagogical purpose, especially Figures 1.15 and 1.19 are part of my work and I will detail it in chapter 2. I also realized myself the illustrations shown in Figures 1.14, 1.16 and 1.21 using a green laser. Finally, the approach I chose in section 1.2 to describe the optics of the instrument is quite different from what has been done in the past.

1.1 A general description of QUBIC

1.1.1 The project

QUBIC is an international collaboration, involving several universities and laboratories in France, Argentina, Italy, Ireland and the U.K. The instrument will be installed in Argentina, at Alto Chorillo, near San Antonio de los Cobres. It is a telescope observing the sky in the millimeter wavelength range, aiming at measuring the Cosmic Microwave Background (CMB) polarization, specifically the signature of the cosmological inflation era with the elusive *B*-modes CMB polarization. The assembling and calibration started at APC around April 2018.



Figure 1.1: The QUBIC collaboration.

1.1.2 A general description of the instrument

QUBIC is a telescope entirely enclosed in a cryostat with the particularity that it is neither a standard imager nor a classical interferometer but a novel combination of both: a bolometric interferometer. A picture and a sketch of the instrument design is shown in Figure 1.2. The signal from the sky directly enters the cryostat through a 56 cm diameter window and a series of filters designed to cut high-frequency radiation that would bring background power in the cryostat [3]. The signal polarization is immediately modulated by a rotating Half-Wave-Plate (HWP) maintained at 4 K [4]. A polarizer is placed right after so that a single, modulated, polarization is transmitted to the array of 400 back-to-back horns [5] which directly illuminate an optical setup consisting of two mirrors cooled down to 1 K. This optical system [6] focuses the radiation from the horns onto two focal planes (one for each frequency 150 and 220 GHz, split by a dichroic filter), assuring an observation at infinity. The signals

from individual horns are superimposed on the focal plane in order to form an interference pattern¹. These images are sampled by an array of 1024 NbSi Transition-Edge-Sensors (TES) cooled down to 300 mK [7] in each focal plane.

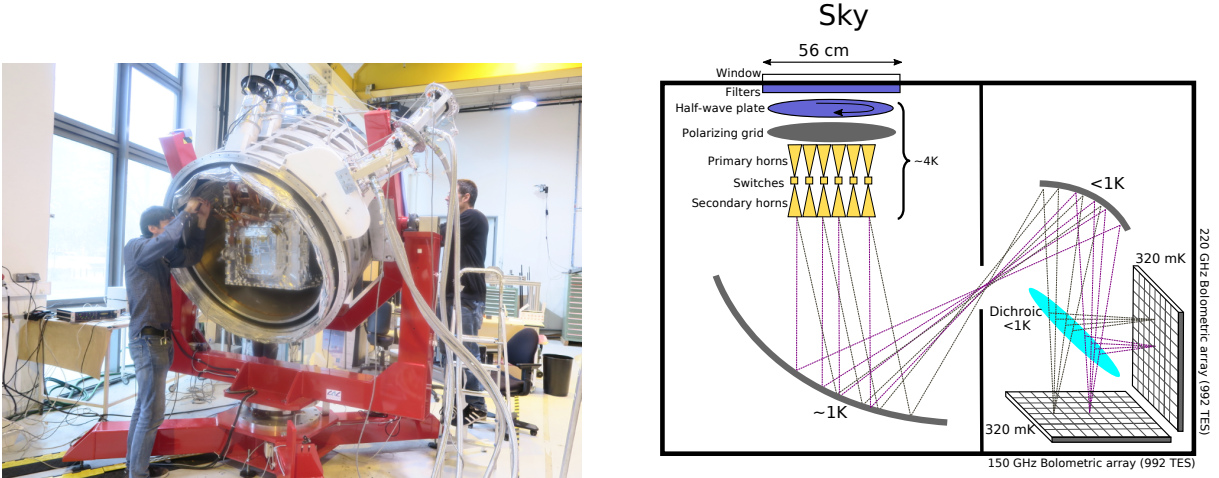


Figure 1.2: QUBIC instrument at APC during assembling and a sketch showing the design of the instrument.

The QUBIC Technical Demonstrator (TD)

The QUBIC TD was built to test and validate the QUBIC design and all its sub-systems (optics, cryogenics, detectors, read-out electronics, scan strategy and calibration). It differs from the Full Instrument (FI) in that it has a reduced number of detector pixels (only one quarter of one focal plane), a reduced number of feedhorns (the central 8×8 horns of the full array with 400 horns), reduced primary and secondary mirror size (400 mm in diameter rather than 600 mm), reduced filter sizes (up to 280 mm in diameter) and a neutral density filter, instead of a dichroic, to manage the radiative loading inside a laboratory on the single focal plane. In all other respects the TD is the same as the FI, especially cryogenics, the most technically challenging part.

1.1.3 Brief description of each part

Window and filters

The sky signal enters the cryostat through a 56 cm diameter window made from high-density polyethylene, a material transparent at millimeter wavelengths. After the window there is a series of thermal (infrared) and low-pass blocking filters. The goal is to select only the interesting frequency band in order to avoid heating load in the cryostat. Picture of the window is shown in Figure 1.3 on the left. With Manuel Gonzalez, we were responsible for the assembling of the 300 K filters right after the window shown on the right picture. They are made with ten stacked insulating layers spaced with washers [16].

Half-Wave-Plate (HWP) and polarizer

HWP design and performance are described in detail in [4]. The QUBIC HWP rotates step by step and not continuously. It is operated at 4 K in order to reduce its thermal emission. To reduce the thermal load at the cryogenic stage where the HWP stays, the motor is placed outside the cryostat, at room temperature. Two magnetic joints are used to transfer the rotation from the motor to a fiberglass tube and the HWP rotates thanks to a belt surrounding it and several pulleys. A model of the HWP rotating system is shown in Figure 1.4 together with a picture of the device. A polarizer is placed right after the HWP. This will be justified in detail in section 2.1.

¹As we will see in section 1.2, this is actually similar to classical imager.

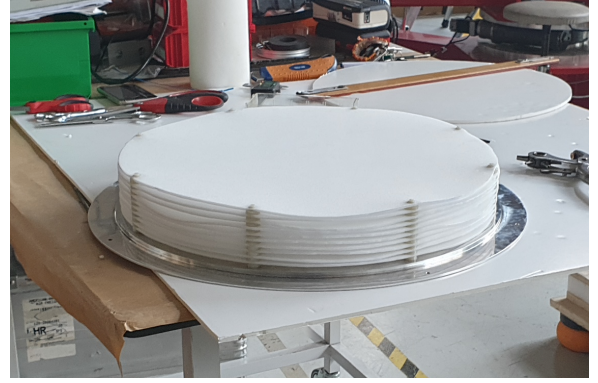
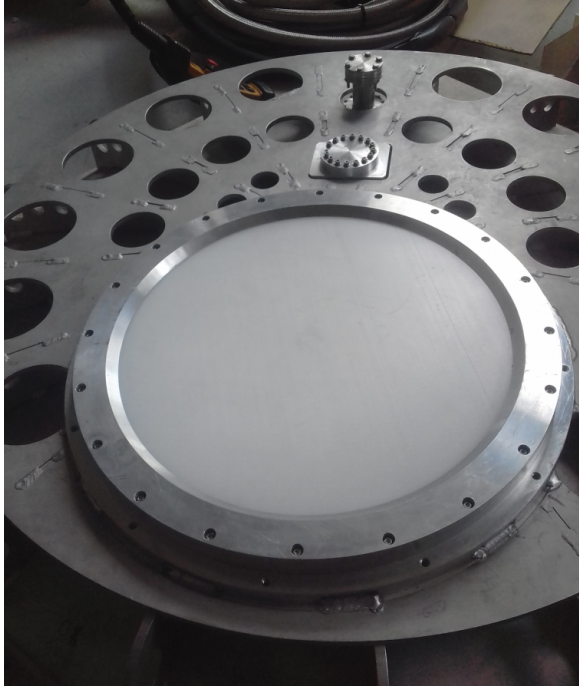


Figure 1.3: *Left*: 56 cm diameter window made from high-density polyethylene. *Right*: Infrared filters mounting on the instrument.

The choice of putting the HWP and the polarizer before the optics was made in order to reduce the impact of cross-polarization. Indeed, once the polarizer has selected a polarization, any cross polarization generated after (at the horns, mirrors, or other optical components) becomes irrelevant. However, the price to pay is a complex cryogenic system as all optical components must be cooled down in addition to the detectors.

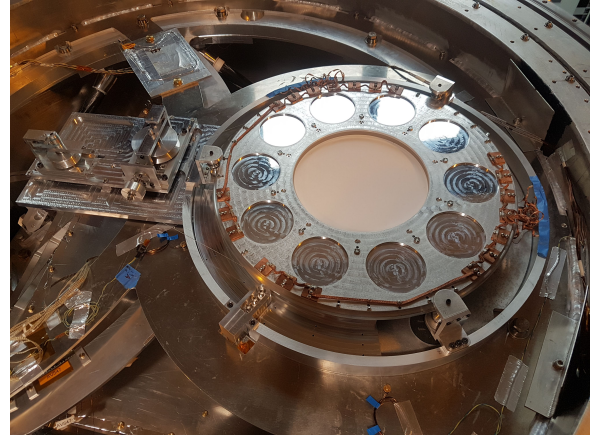
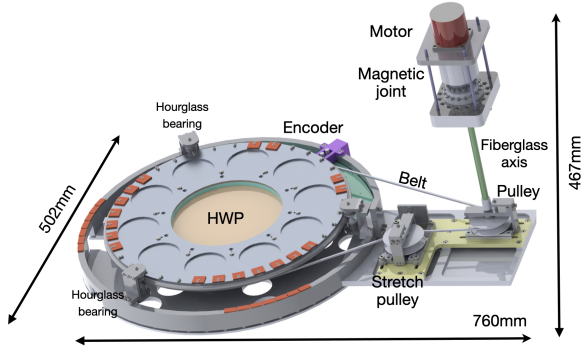


Figure 1.4: Model of the HWP rotating system and a picture once installed in the cryostat. Taken from [4].

Horns

The QUBIC input aperture consists of an array of 400 back-to-back conical corrugated horn pairs, spaced by 14 mm, laid out square grid within a circular area as shown in Figure 1.5. The back-to-back horn array has two objectives: the front (sky) horns define the field of view of the instrument, while the back horns illuminate the optical combiner. The right panel of Figure 1.5 shows a single element of the horn array. The sky-facing and detector-facing feedhorns are identical and were designed to have a FWHM of 12.9° at 150 GHz.

A shutter, or switch, is placed in the waveguide section joining each back-to-back horn pair so signals can be switched on and off in the calibration procedure. In its rest position the switch is open. To close it, there is a small coil and when it is biased, a small ferrite is attracted inside. The ferrite is connected to a hook which pulls a steel blade across the waveguide.

Detail on this system and performance can be found in [5]. Figure 1.6 shows pictures of the TD horn array and of the switches.

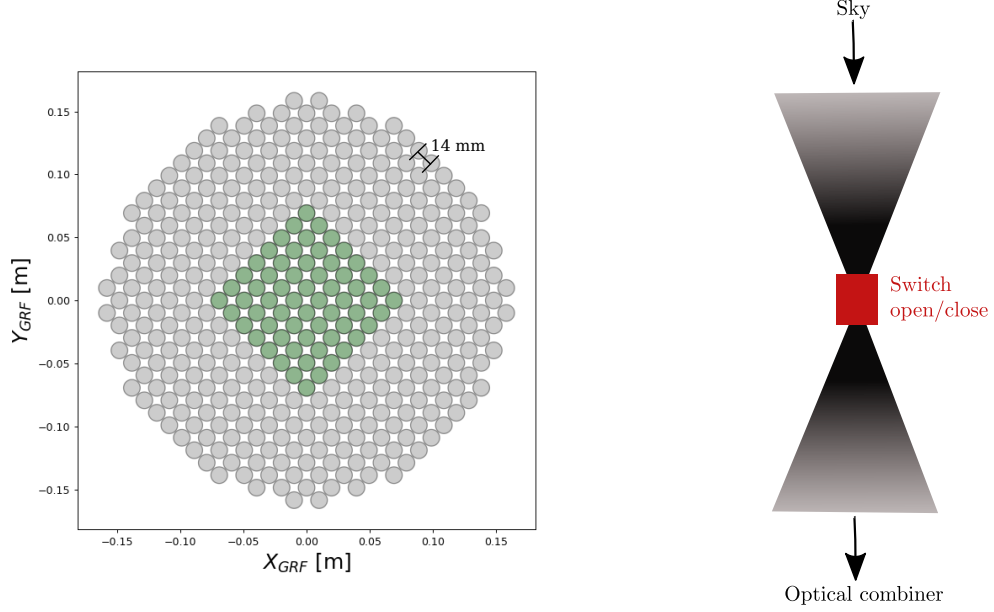


Figure 1.5: *Left:* Horn array for the FI. The TD horn array is highlighted in green. *Right:* Sketch of a single back-to-back horn (see papers [5], [6] for details).

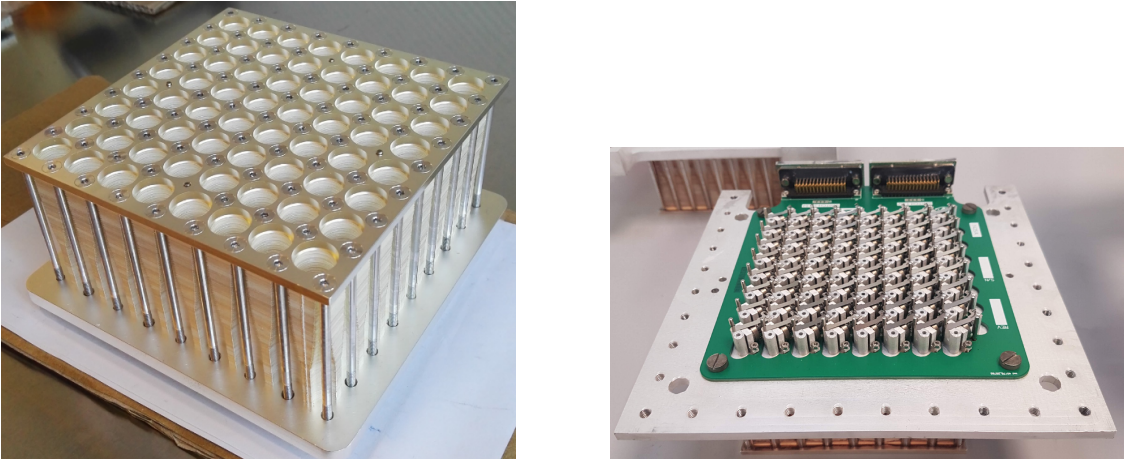


Figure 1.6: *Left:* One side of the 8×8 TD horn array, a similar system is placed after the shutters. *Right:* TD switches placed in the waveguide section joining each back-to-back horn pair. See [5] for detail.

Mirrors

The combination of the light onto the focal plane is done by an off-axis Gregorian telescope: a primary parabolic mirror and a secondary elliptic mirror. For the TD, the two mirrors have a diameter of 400 mm while for the FI, it will be extended to 600 mm. The focal length of the optical combiner is 30 cm, see [6] for detail. A picture of a TD mirror when it was mounted on its support is shown in Figure 1.7.



Figure 1.7: TD primary mirror being mounted on its adjustable support (hexapode).

Bolometers

A bolometer is a device for measuring the power of incident radiation via the heating of a material. The temperature is known by measuring the electric resistance of the absorber material which can be a metal, a semiconductor or a superconductor. The bolometer is connected to a thermal reservoir, a body of constant temperature, through a thermal link. Figure 1.8 shows the principle of operation. The QUBIC detectors are Transition-Edge Sensors (TES) [7], chosen for their high sensitivity and

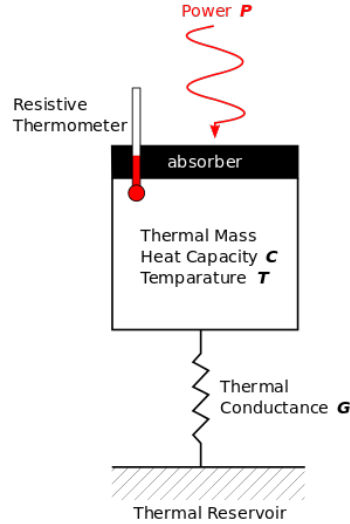


Figure 1.8: Operating principle of a bolometer.

their low noise. A quarter focal plane is a 256 pixel array, each pixel being a TES, see left panel in Figure 1.9. The superconducting phase transition of four TES among the 256 is shown in the right panel. The array currently used has a critical temperature of about 410 mK.

The TES is a feedback system in which the power from the absorption of a photon is removed by negative electrothermal feedback, so that the temperature is kept constant. The TES is voltage-biased by driving a current source I_{bias} through a load resistor R_{sh} (see left part of Figure 1.10). When a photon is absorbed by the TES, its resistance increases causing a drop of the TES current. So the Joule dissipation decreases, cooling back the temperature of the TES. Another effect of electrothermal feedback is to reduce the response time of the TES by several orders of magnitude [17], reaching ~ 20 ms in the case of QUBIC [7].

Detection chain architecture

The TES is operated in series with a coil, see Figure 1.10 (left), which is inductively coupled to a SQUID (Superconducting QUantum Interference Device). A SQUID measures extremely small magnetic fields. The drop of current is detected through a drop of magnetic flux to the SQUID which is converted into an output voltage.

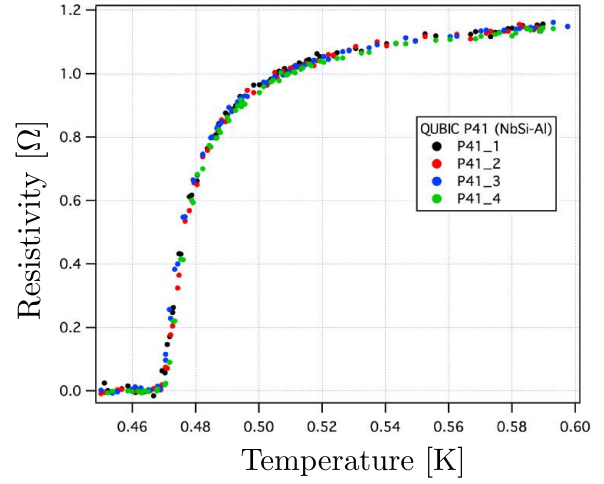
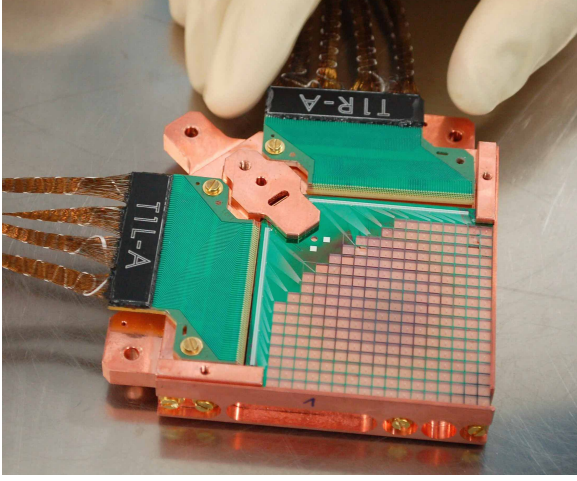


Figure 1.9: *Left*: Picture of a quarter of the focal plane made with 256 TES. *Right*: Superconducting transition phase of four $\text{Nb}_{0.15}\text{Si}_{0.85}$ TESs. Taken from [7].

As shown on Figure 1.10 (right), the 256-pixels array, corresponding to a quarter of a focal plane, is divided in two parts, leading to two blocks of 128 SQUIDS each. The SQUIDS are maintained at a temperature of 1 K. Each block is controlled and amplified by an ASIC (Application Specific Integrated Circuit) cooled to 40 K. Finally, a warm FPGA (Field Programmable Gate Array) controls the acquisition of the signal to a computer. This design allows time domain multiplexing with a factor equal to 128.

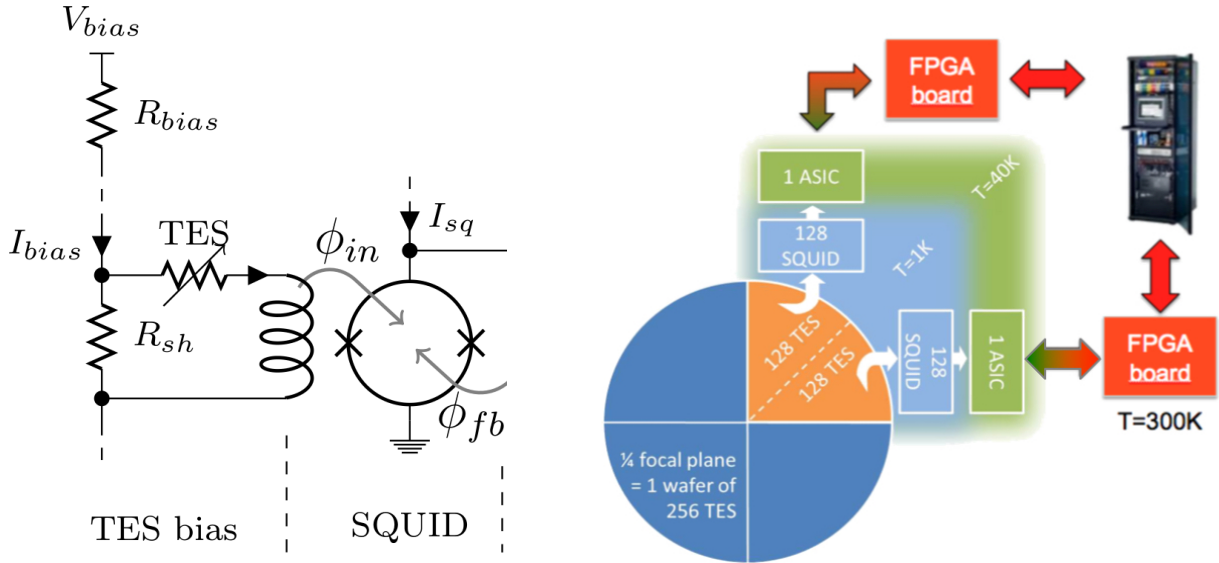


Figure 1.10: *Left*: Layout of a TES coupled to a SQUID. *Right*: Architecture of the QUBIC detection chain for one quarter of the focal plane. Taken from [7].

Output signal: The output signal consists of Time-Ordered Data (TOD) from each TES. The number of points is determined by the sampling period during the acquisition. To get an image of the sky, one needs to scan the observed region and then by a map-making process, we can solve a linear system to build an image of the sky. This will be detailed in chapter 5.

Cryogenic system

Cryogenic design and performance are described in [3]. The cryogenic system cools the detector arrays to 0.32 K, the beam combiner optics at 1 K, and the rotating HWP, the polarizing analyzer, the horn

array, and the switches to 4 K. The outer vacuum shell of the cryostat allows operation under high-vacuum conditions, it must withstand a pressure difference of ~ 100 kPa. It has a diameter of 1.4 m and a height of 1.55 m (see Figure 1.2).

The cool down to 4 K is ensured by two pulse-tube refrigerators working in parallel. A pulse-tube refrigerator extracts heat using a compression cycle of helium gas. One potential drawback of the use of pulse-tube refrigerators is the presence of vibrations, synchronous with the periodic ($\nu \sim 1.7$ Hz) aperture of the rotary valve.

Then, the cool down to 1 K and 0.3 K requires two sorption coolers also called evaporation refrigerators. The operating principle is the following: the refrigerator is filled with helium under high pressure. Below 4 K, the helium is liquid and falls by gravity to the bottom part called the evaporator. An equilibrium between liquid and gas at the equilibrium vapor pressure is achieved. A cryopump, made with activated charcoal, placed at the top of the refrigerator, absorbs the helium gas until all the liquid has been converted to gas. Evaporation is an endothermic process so it cools down the part of the instrument connected to the refrigerator. When all the liquid helium has been consumed, the part to cool down is disconnected from the refrigerator (using a gas switch) and the refrigerator can be cycled. For that purpose, it is warmed up using an electric resistance, so helium desorbs from the activated charcoal and is re-condensed when reaching the part below 4 K. Once all liquid helium has been recovered, the refrigerator is usable again.

In the case of QUBIC, a ^4He sorption cooler (see Figure 1.11, left) cools down the entire optics box (around 150 kg) from 4 K to 1 K. The cool down from 1 K to 0.3 K of the detector arrays is done by a double stage $^3\text{He}/^4\text{He}$ sorption cooler (see Figure 1.11, right), with an operating principle similar to the one described above.

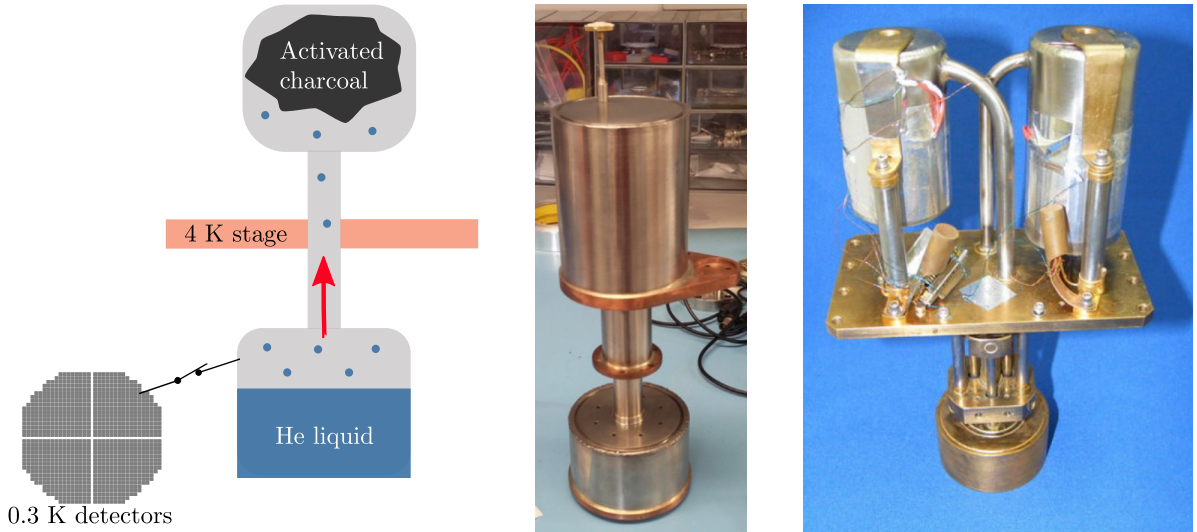


Figure 1.11: Sketch of a sorption cooler with activated charcoal. Pictures of the QUBIC 1 K ^4He sorption cooler and of the 0.3 K $^3\text{He}/^4\text{He}$ evaporation refrigerator.

1.2 A synthetic imager

When presenting QUBIC, we usually focus on its specificity of doing interferometry. Of course this is true but in this section, I would like to show that QUBIC can perfectly be described as a classical imager having a particular aperture. For that purpose I will start by introducing some formalism, starting from basic optical concepts. The beginning will certainly seem far from QUBIC but the approach should be clear at the end of the section. As far as I know, it is the first time that the optical working principle of QUBIC is derived from first principles.

1.2.1 Observing the sky through an instrument

An important concept in optics is that the image formed by an optical system is the convolution of the object by the Point Spread Function (PSF) of the system. The PSF is proportional to the Fourier transform of the instrument pupil. A precise description of Fourier optics can be found, for example, in Pellat-Finet [230] and this part is widely inspired by the lecture of Eric Aristidi which can be found at <http://sites.unice.fr/site/aristidi/>.

Signal coming from the sky

The light coming from a direction \hat{k} on the sky and that enters into an optical system is assumed to be a plane wave (true if the source is at infinity). The corresponding electric field at time t , in \mathbf{r} can be written as

$$\mathbf{E}(\mathbf{r}, t) = \mathbf{E}_0 e^{i(\mathbf{k} \cdot \mathbf{r} - \omega t)} \quad (1.1)$$

where ω is the pulsation, $\mathbf{k} = \frac{2\pi}{\lambda} \hat{k}$ is the wave vector associated with wavelength λ and \mathbf{E}_0 is the amplitude. The magnetic field \mathbf{B} can be written in a similar way. \mathbf{E} and \mathbf{B} are orthogonal to each other and both are orthogonal to the direction of propagation \hat{k} .

If we are not interested in the polarization, a scalar field is sufficient to describe the plane wave:

$$U(\mathbf{r}, t) = \psi_0 e^{i(\mathbf{k} \cdot \mathbf{r} - \omega t)} \quad (1.2)$$

where ψ_0 could be E_0 or B_0 . The space part of $U(\mathbf{r}, t)$ is called the complex amplitude and is written as

$$\psi(\mathbf{r}) = \psi_0 e^{i\mathbf{k} \cdot \mathbf{r}}. \quad (1.3)$$

The intensity is $I = |\psi(\mathbf{r})|^2$.

We will note (α, β, γ) the components of the unit vector \hat{k} , so $\alpha^2 + \beta^2 + \gamma^2 = 1$. The complex amplitude of the plane wave becomes:

$$\psi(x, y, z) = \psi_0 e^{\frac{2i\pi}{\lambda}(\alpha x + \beta y + \gamma z)}. \quad (1.4)$$

α , β and γ can be written as a function of two angles (θ_x, θ_y) as shown in Figure 1.12 (left):

$$\begin{cases} \alpha = \sin \theta_x \\ \beta = \cos \theta_x \sin \theta_y \\ \gamma = \cos \theta_x \cos \theta_y = \sqrt{1 - \alpha^2 - \beta^2} \end{cases} \quad (1.5)$$

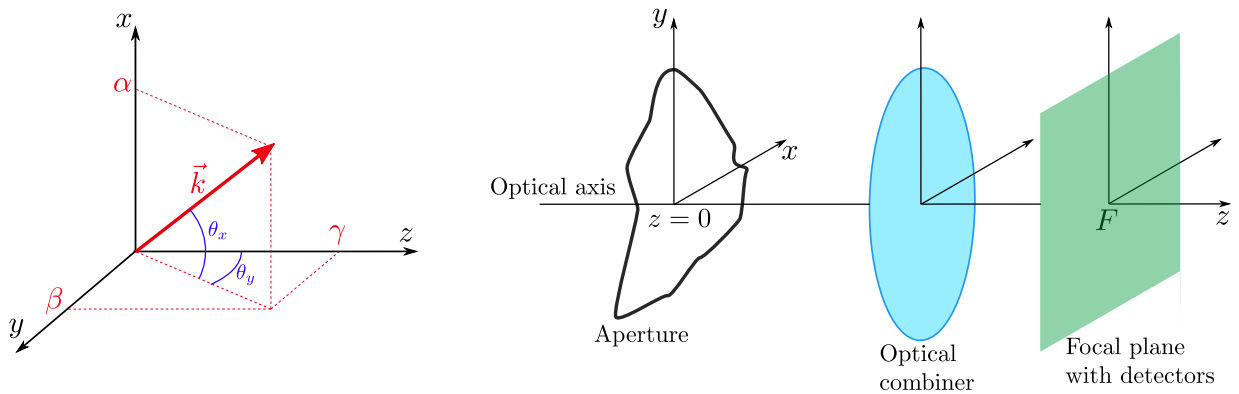


Figure 1.12: *Left*: Projection of the wave vector \mathbf{k} using θ_x and θ_y angles. *Right*: Sketch of a classic imager.

Propagation through a telescope

The optical axis of the instrument is z and we want to understand how the light transforms when it propagates through the instrument. We consider a very simple imager as shown in Figure 1.12 (right) composed of an aperture that could have any shape and a lens. The detectors are placed in the focal plane of the lens. The light goes through optical elements which are orthogonal to the optical axis.

We will note $f_{z_1}(x, y) = \psi(x, y, z_1)$ the amplitude in the plane with abscissa $z = z_1$. The transformation that allows to compute the amplitude in a plane $z = z_2$, knowing the amplitude in a previous plane $z = z_1$, is the Fresnel transform defined in the following.

Propagation of a plane wave

For a plane wave $f_z(x, y) = \psi_0 e^{\frac{2i\pi}{\lambda}(\alpha x + \beta y + \gamma z)}$, it follows that:

$$f_{z_2}(x, y) = f_{z_1}(x, y) e^{\frac{2i\pi}{\lambda}\gamma(z_2 - z_1)} \quad (1.6)$$

So a plane wave propagating from a plane in z_1 to a plane in z_2 is simply phase shifted. For other types of waves, we will see that the transformation is more complex.

Transmission factor of an optical element

The coefficient in transmission of an optical element (aperture, lens, filter...) is defined as:

$$t(x, y) = \frac{\psi(x, y, 0^+)}{\psi(x, y, 0^-)} \quad (1.7)$$

where $z = 0^+$ and $z = 0^-$ are the planes at the entrance and at the output of the element. We can give two examples. In case of a rectangular aperture of width a and length b , we have:

$$t(x, y) = \Pi\left(\frac{x}{a}\right) \Pi\left(\frac{y}{b}\right) \quad (1.8)$$

where Π is the rectangular function. In case of a circular aperture with diameter d , it will be:

$$t(x, y) = \Pi\left[\frac{\sqrt{x^2 + y^2}}{d}\right]. \quad (1.9)$$

Angular spectrum

We note $f_0(x, y)$ the amplitude of a monochromatic wave in the plane $z = 0$. It can be any type of wave, not especially a plane wave. $f_0(x, y)$ can be expanded in a Fourier series:

$$f_0(x, y) = \int_{-\infty}^{\infty} \int_{-\infty}^{\infty} \hat{f}_0(u, v) e^{2i\pi(ux + vy)} du dv \quad (1.10)$$

$\hat{f}_0(u, v)$ is the Fourier transform in space of $f_0(x, y)$. We make the substitution $\alpha = \lambda u$, $\beta = \lambda v$ where λ is the wavelength so

$$f_0(x, y) = \int_{-\infty}^{\infty} \int_{-\infty}^{\infty} \frac{1}{\lambda^2} \hat{f}_0\left(\frac{\alpha}{\lambda}, \frac{\beta}{\lambda}\right) e^{\frac{2i\pi}{\lambda}(\alpha x + \beta y)} d\alpha d\beta \quad (1.11)$$

$\hat{f}_0\left(\frac{\alpha}{\lambda}, \frac{\beta}{\lambda}\right)$ is called the angular spectrum of $f_0(x, y)$ associated with angular frequencies $\frac{\alpha}{\lambda}$ and $\frac{\beta}{\lambda}$.

Huygens-Fresnel principle

It states that every point on a wave front is itself the source of spherical wavelets. The amplitude at a point on a plane z is the sum of all the amplitudes of these spherical wavelets. We call it *principle* for historical reason but it can be demonstrated using the Maxwell equations. A demonstration is done in annex A.1 in the case of paraxial optics but it is generally valid for off-axis optics as well, and a general demonstration can be done using the Green functions [231], [232].

A convolution is well adapted to describe an operation acting on every point of the wave front so the Huygens-Fresnel principle can be written as:

$$f_z(x, y) = f_0(x, y) \otimes \frac{e^{ikr}}{i\lambda r} \quad (1.12)$$

with $r = \sqrt{x^2 + y^2 + z^2}$. In the paraxial approximation we have $|x|, |y| \ll z$ so

$$r = \sqrt{\rho^2 + z^2} \simeq z \left(1 + \frac{\rho^2}{2z^2} \right) \quad \text{with} \quad \rho^2 = x^2 + y^2. \quad (1.13)$$

So expression 1.12 becomes:

$$f_z(x, y) \simeq e^{ikz} f_0(x, y) \otimes \frac{1}{i\lambda z} e^{\frac{i\pi}{\lambda z}(x^2+y^2)}. \quad (1.14)$$

Let us write the principle in a different way using a Fourier transform. We start by making the convolution product explicit:

$$f_z(x, y) = \frac{e^{ikz}}{i\lambda z} \int \int f_0(x', y') e^{\frac{i\pi}{\lambda z}((x-x')^2 + (y-y')^2)} dx' dy' \quad (1.15)$$

$$= \frac{e^{ikz}}{i\lambda z} e^{\frac{i\pi}{\lambda z}(x^2+y^2)} \int \int f_0(x', y') e^{\frac{i\pi}{\lambda z}(x'^2+y'^2)} e^{\frac{2i\pi}{\lambda z}(xx' + yy')} dx' dy' \quad (1.16)$$

So finally, this is a Fourier transform with spatial frequencies $\left(\frac{x}{\lambda z}, \frac{y}{\lambda z}\right)$:

$$f_z(x, y) = \frac{e^{ikz}}{i\lambda z} e^{\frac{i\pi}{\lambda z}(x^2+y^2)} \mathcal{F}_{\frac{x}{\lambda z}, \frac{y}{\lambda z}} \left[f_0(x', y') e^{\frac{i\pi}{\lambda z}(x'^2+y'^2)} \right] \quad (1.17)$$

where we used the notation $\hat{f}(u, v) = \mathcal{F}_{u,v}[f(x, y)]$ for the Fourier transform.

Diffraction at infinity

In the far field, when $z \rightarrow \infty$, at first order in $(x^2 + y^2)$, we have

$$e^{\frac{i\pi}{\lambda z}(x^2+y^2)} \simeq 1 + \frac{i\pi}{\lambda z}(x^2 + y^2). \quad (1.18)$$

Considering an aperture of diameter d , we always have $x^2 + y^2 \leq d^2$. The Fraunhofer limit consists in neglecting the second term which is justified if

$$\frac{d^2}{\lambda z} \ll 1 \quad \Rightarrow \quad z \gg \frac{d^2}{\lambda}. \quad (1.19)$$

Thus, in the Fraunhofer approximation, expression 1.17 reduces to:

$$f_\infty(x, y) = \frac{e^{ikz}}{i\lambda z} \hat{f}_0\left(\frac{x}{\lambda z}, \frac{y}{\lambda z}\right). \quad (1.20)$$

This is a major result, the diffracted amplitude of a wave at infinity in a point (x, y) is equal to the Fourier transform of this wave taken in the plane $z = 0$.

We can also write the diffracted amplitude in a direction of propagation (α, β) with $\alpha \simeq \frac{x}{z}$, $\beta \simeq \frac{y}{z}$:

$$f_\infty(\alpha, \beta) = \frac{e^{ikr}}{i\lambda r} \hat{f}_0 \left(\frac{\alpha}{\lambda}, \frac{\beta}{\lambda} \right) \quad (1.21)$$

Let us take the example of a plane wave $f_0(x, y) = \psi_0 e^{\frac{2i\pi}{\lambda}(\alpha_0 x + \beta_0 y)}$. The diffracted amplitude at infinity is:

$$f_\infty(\alpha, \beta) = \frac{e^{ikr}}{i\lambda r} \psi_0 \delta(\alpha - \alpha_0, \beta - \beta_0) \quad (1.22)$$

where δ is the Dirac distribution. This means that the intensity will be zero except in the direction (α_0, β_0) .

Observation in the far field using a lens

A lens can be modeled by a transmission factor that modifies the phase of the incident wave. In the case of a plane-convex lens, it will be

$$t(x, y) = \exp \frac{-i\pi(x^2 + y^2)}{\lambda R} (n - 1) \quad (1.23)$$

where n is the optical index of the glass and R is the radius of curvature for the convex side of the lens.

We consider a plane wave at normal incidence on the lens with amplitude ψ_0 . The lens is at $z = 0$. Using the Fresnel transform, we can compute the amplitude in a plane $z > 0$. The general expression is complicated but in the plane $z = \frac{R}{n-1}$ it reduces to:

$$f_z(x, y) = -i\psi_0 \lambda z e^{ikz} \delta(x, y) \quad (1.24)$$

This leads to a bright point on the optical axis at $z = \frac{R}{n-1}$ which defines the focal length of the lens. So a lens converts a plane wave into a spherical wave centered on its focal plane as represented in Figure 1.13. Each direction on the sky, associated with a wave vector \mathbf{k} corresponds to a single point \mathbf{x} on the focal plane. This would be similar for any optical combiner, for instance using a primary and a secondary mirror.

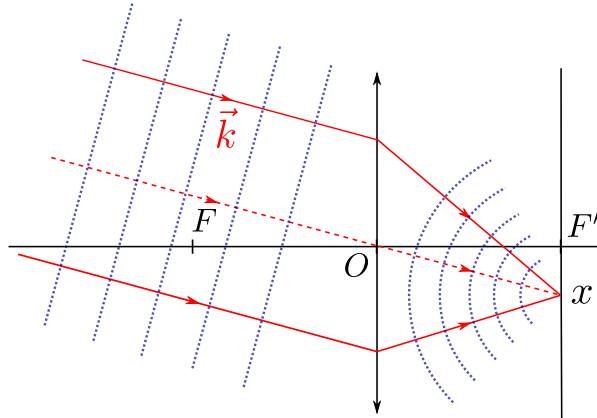


Figure 1.13: A lens converts a plane wave into a spherical wave whose center is in the focal plane of the lens.

This expression is similar to equation 1.22, where we looked at the propagation of a plane wave at infinity. That is why observing in the focal plane of a lens is equivalent to observing at infinity. It gives the possibility to build a very compact optical system observing in the far field where the Fraunhofer approximation is valid. It is also a good way to observe at infinity without losing too much intensity as the power decreases with the square of the distance. Note that if the focal plane is covered with sensors, such as a CCD, the image is sampled by the sensors.

Point Spread Function of a telescope

We go back to the example of a basic imager as described in Figure 1.12 with a pupil and an optical combiner like lens or mirrors.

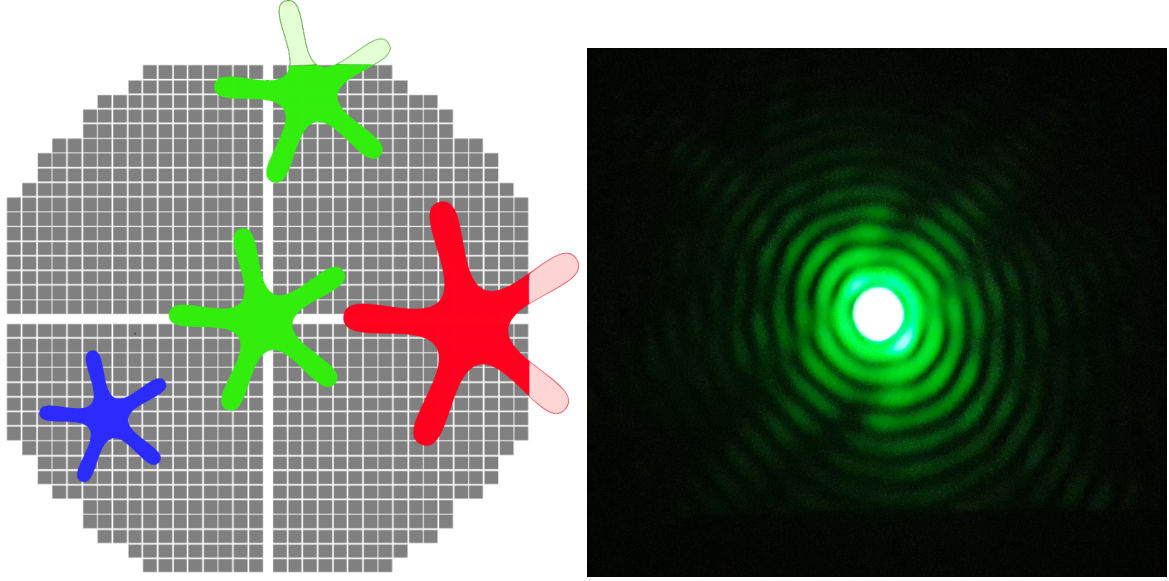


Figure 1.14: *Left:* Sketch to illustrate the concept of the PSF. We show PSF at different wavelengths (blue, green and red) for different directions on the sky on a focal plane. *Right:* Airy disk obtained at infinity by illuminating a circular aperture with a laser.

We refer to the focal plane pattern resulting from a far field point source in a direction \mathbf{k} as the Point Spread Function (PSF). This is illustrated in Figure 1.14 (left). A point source in the far field leads to an incoming plane wave, $f_{0-}(x, y) = \psi_0 e^{ik(\alpha_0 x + \beta_0 y)}$ where $z = 0^-$ is the plane right before the aperture. Right after the aperture, in the plane $z = 0^+$, the amplitude becomes:

$$f_{0+}(x, y) = f_{0-}(x, y)t(x, y) \quad (1.25)$$

where $t(x, y)$ is the transmission of the aperture. To write the amplitude in the focal plane of the lens, we propagate $f_{0+}(x, y)$ at infinity, using the Fraunhofer approximation:

$$f_F(\alpha, \beta) = \frac{e^{ikr}}{i\lambda r} \hat{f}_{0+} \left(\frac{\alpha}{\lambda}, \frac{\beta}{\lambda} \right) \quad (1.26)$$

$$= \frac{e^{ikr}}{i\lambda r} \hat{t} \left(\frac{\alpha}{\lambda}, \frac{\beta}{\lambda} \right) \otimes \hat{f}_{0-} \left(\frac{\alpha}{\lambda}, \frac{\beta}{\lambda} \right) \quad (1.27)$$

$$= \frac{e^{ikr}}{i\lambda r} \hat{t} \left(\frac{\alpha}{\lambda}, \frac{\beta}{\lambda} \right) \otimes \psi_0 \delta(\alpha - \alpha_0, \beta - \beta_0) \quad (1.28)$$

$$= \frac{e^{ikr}}{i\lambda r} \hat{t} \left(\frac{\alpha - \alpha_0}{\lambda}, \frac{\beta - \beta_0}{\lambda} \right) \psi_0 \quad (1.29)$$

In terms of intensity, we have:

$$I_F(\alpha, \beta) = \frac{1}{\lambda^2 r^2} |\psi_0|^2 \left| \hat{t} \left(\frac{\alpha - \alpha_0}{\lambda}, \frac{\beta - \beta_0}{\lambda} \right) \right|^2 \quad (1.30)$$

This shows that the PSF is proportional to the Fourier transform of the pupil:

$$\text{PSF}_{\mathbf{k}}(\alpha, \beta) \propto \left| \hat{t} \left(\frac{\alpha - \alpha_0}{\lambda}, \frac{\beta - \beta_0}{\lambda} \right) \right|^2. \quad (1.31)$$

The signal on the focal plane is the convolution of the incoming signal with the PSF of the instrument. The PSF can be as complicated as needed. It includes optical element transmissions, propagation

inside the telescope, possible reflections and any other possible optical effect. The position of the figure on the focal plane depends on the incident angle of the incoming light, an inclination angle leads to a translation of the figure on the focal plane. The image is centered on the point conjugated to the incident direction according to optical geometry.

We have seen that diffraction and propagation can be represented with a convolution. This shows that they are linear filters in the spatial frequency domain. For instance, in case of a circular aperture, the PSF is the well known Airy disk as shown in Figure 1.14 (right). The first extinction in the Airy disk is for $\theta \simeq 1.22 \frac{\lambda}{d}$, with λ the wavelength and d the aperture diameter. That is why the resolution is not infinite, it is of the order of magnitude of $\frac{\lambda}{d}$. To have access to a better resolution, so to higher spatial frequencies, the diameter must be increased or the wavelength decreased (see Figure 1.14, left).

1.2.2 A more general definition for the PSF

A convolution in real space

A signal S is observed through a system that can be modeled by a mathematical operator A . The observed signal is $AS(\vec{x})$. Assuming that A is Linear and Invariant by Translation (LIT), we will show that this operation is equivalent to a convolution. By definition of the Dirac distribution, we have:

$$S(\mathbf{x}) = \int S(\mathbf{y})\delta(\mathbf{x} - \mathbf{y})d\mathbf{y}, \quad (1.32)$$

and because A is linear, we can write:

$$AS(\mathbf{x}) = \int S(\mathbf{y})A\delta(\mathbf{x} - \mathbf{y})d\mathbf{y}. \quad (1.33)$$

We define $h(\mathbf{x}) = A\delta(\mathbf{x})$, so

$$AS(\mathbf{x}) = \int S(\mathbf{y})h(\mathbf{x} - \mathbf{y})d\mathbf{y} \equiv (h \otimes S)(\mathbf{x}) \quad (1.34)$$

This shows that any LIT operator convolves the incoming signal by a function $h(\mathbf{x})$. In optics, this function is the Point Spread Function (PSF) of the instrument. It is the analogue in space to the impulse response in time used for example in electronics.

A product in Fourier space

The Fourier transform offers a description in terms of frequencies and not in position \mathbf{x} . It is well adapted for a signal not localised in space such as a sine wave. Another advantage is that convolution in real space becomes a simple product in Fourier space:

$$\mathcal{F}_{\mathbf{k}}[h \otimes S] = \mathcal{F}_{\mathbf{k}}[h] \times \mathcal{F}_{\mathbf{k}}[S] \quad (1.35)$$

The Fourier transform of the PSF is called the transfer function $H(\mathbf{k}) = \mathcal{F}_{\mathbf{k}}[h]$.

1.2.3 A bolometric interferometer seen as a synthetic imager

We now have all the concepts and the mathematical formalism needed to describe the QUBIC optics. As briefly mentioned in section 1.1.3 the specificity of QUBIC is to have a horn array at the entrance of the telescope.

The horn-array is responsible for the QUBIC PSF shown in Figure 1.15, for different horn array configurations, considering a point source in the far field, emitting at 150 GHz, aligned with the optical axis. In case of only one horn open, we are back to classical imager with a Gaussian PSF. When two horns are open, the PSF is made with fringes whose orientation and spacing depend on the baseline chosen as in the Young experiment. When the number of open horns increases, the PSF becomes more complex. It is the result of constructive interferences between all re-emitted radiation from the open horns. Finally, when all horns are open, the PSF has a central peak and four secondary peaks contained

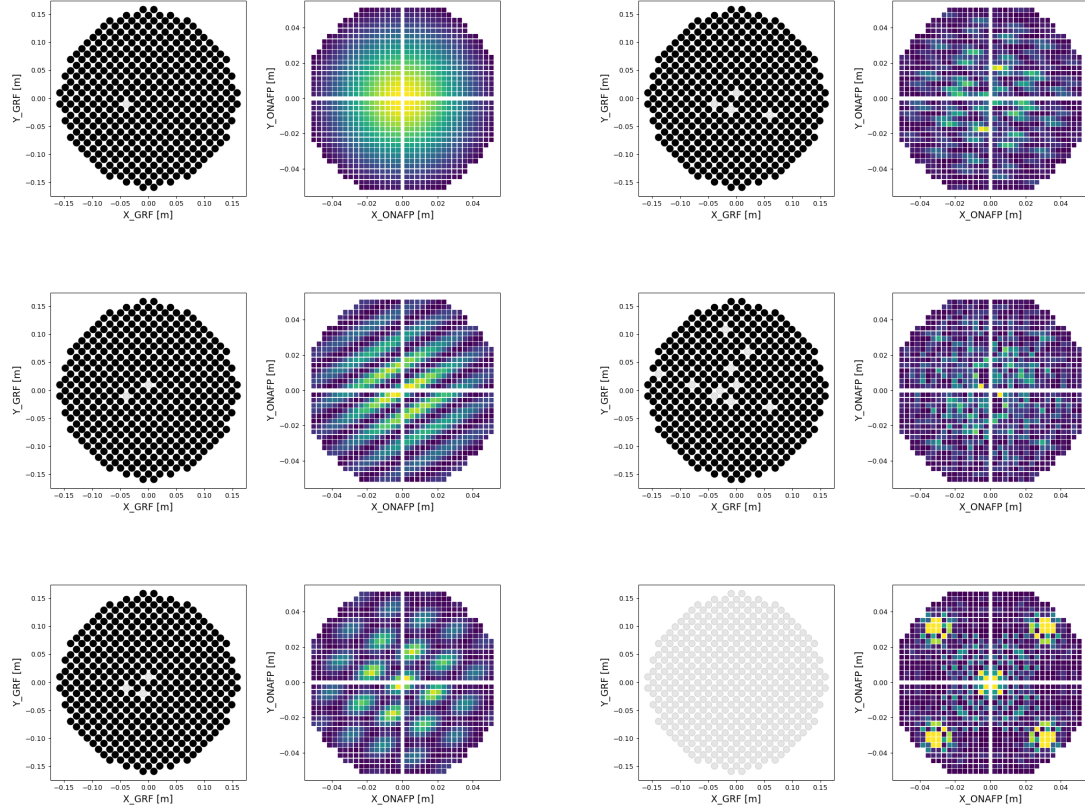


Figure 1.15: Pattern obtained on the focal plane (PSF) when opening 1, 2, 3, 4, 10 and 400 horns. The horn array is shown on the left. These images are obtained considering an on-axis point source in the far field, emitting at 150 GHz.

on the focal plane. This is valid for this configuration with a given wavelength and a given point source direction. The horn-array is similar to a diffracting grid. Figure 1.16 is a picture of diffraction of a laser by a child's toy glasses made with a double axis diffracting grid (~ 530 lines per millimeter). I made this optical setup myself in order to better understand the QUBIC optics using an equivalence in the visible domain. We will come back on this setup in chapter 6, section 6.1.1.

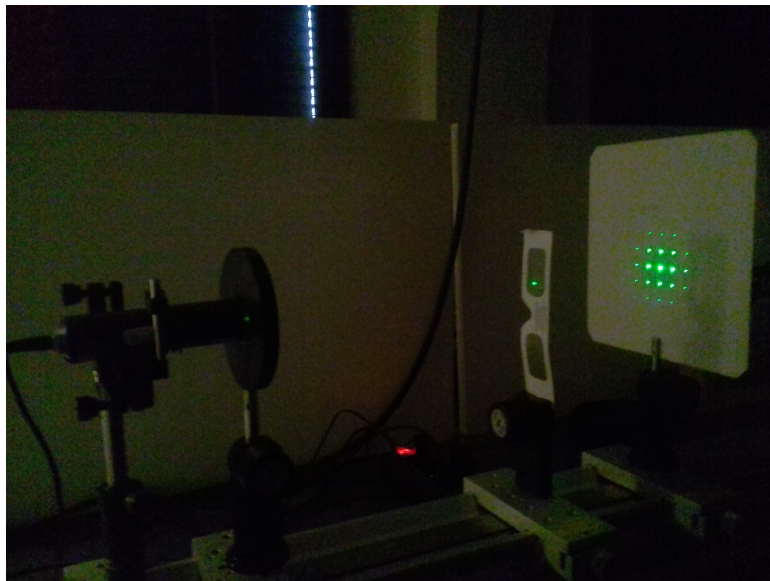


Figure 1.16: Diffraction of a laser by a double axis diffracting grid (~ 530 lines per millimeter).

Thus, QUBIC can be seen as an imager with a very peculiar PSF caused by the horn-array. If the horns were infinitely small, the secondary peaks in the PSF would be sent to infinity outside the focal plane and we would be back to a standard imager with a square aperture.

It is also possible to consider QUBIC as an interferometer, and actually, any imager is an interferometer in the sense that each point of its aperture can be seen as a source re-emitting the radiation, equivalent to the horns. This is precisely the Huygens-Fresnel principle mentioned in section 1.2.1. In this way, the formation of an image on the focal plane can be seen as the result of constructive interference between all re-emitted radiation.

I think this summarizes the most important concept I wanted to present in this chapter.

1.2.4 Expression of the QUBIC Point Spread Function

We just saw how the QUBIC PSF looks like and now we will derive the mathematical expression of the PSF for an instrument like QUBIC. We note $\mathbf{x}_h(x_h, y_h, 0)$ the position vector of horn h . We consider an incoming plane wave with a wave vector $\mathbf{k} = \frac{2\pi}{\lambda}(\alpha_0, \beta_0, \gamma_0)$. We note $\mathbf{r}(x, y, z)$ a point on the focal plane with corresponding angles $\alpha \simeq \frac{x}{f}$, $\beta \simeq \frac{y}{f}$ where f is the focal length. We will refer to Figure 1.17 for the notation.

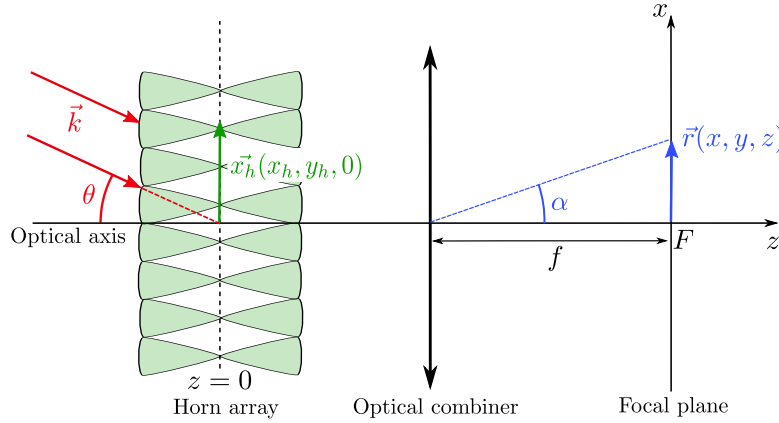


Figure 1.17: Optical sketch for an instrument like QUBIC.

$A_{\mathbf{k}}(x, y)$ is the transmission of a single horn for an incident direction \mathbf{k} . We make the hypothesis that every horn has the same transmission. The transmission of the horn array in case of N horns can be written as:

$$t_{\mathbf{k}}(x, y) = \sum_{h=1}^N A_{\mathbf{k}}(x - x_h, y - y_h) \quad (1.36)$$

To write the Fourier transform of the transmission expressed in $\left(\frac{\alpha - \alpha_0}{\lambda}, \frac{\beta - \beta_0}{\lambda}\right)$ we use the property of translation for a Fourier transform. This gives:

$$\hat{t}_{\mathbf{k}}\left(\frac{\alpha - \alpha_0}{\lambda}, \frac{\beta - \beta_0}{\lambda}\right) = \hat{A}_{\mathbf{k}}\left(\frac{\alpha - \alpha_0}{\lambda}, \frac{\beta - \beta_0}{\lambda}\right) \sum_{h=1}^N e^{-2i\pi \frac{\alpha - \alpha_0}{\lambda} x_h} e^{-2i\pi \frac{\beta - \beta_0}{\lambda} y_h} \quad (1.37)$$

$$= \hat{A}_{\mathbf{k}}\left(\frac{\alpha - \alpha_0}{\lambda}, \frac{\beta - \beta_0}{\lambda}\right) \sum_{h=1}^N \exp\left\{-i\left(\frac{\mathbf{r}}{f} - \mathbf{k}\right) \cdot \mathbf{x}_h\right\}. \quad (1.38)$$

Finally, by taking the square modulus, we obtain the PSF:

$$\text{PSF}_{\mathbf{k}}(\mathbf{r}, \lambda) = \text{PSF}_{\mathbf{k}}^{\text{horn}} \sum_{h, h'=1}^N \exp\left\{-i\left(\frac{\mathbf{r}}{f} - \mathbf{k}\right) \cdot (\mathbf{x}_h - \mathbf{x}_{h'})\right\} \quad (1.39)$$

where $\text{PSF}_{\mathbf{k}}^{\text{horn}} = \left|\hat{A}_{\mathbf{k}}\left(\frac{\alpha - \alpha_0}{\lambda}, \frac{\beta - \beta_0}{\lambda}\right)\right|^2$ is the PSF of a single horn. In case of a square array of horns with P horns on each side, separated by Δ_h , it is possible to compute an analytical expression of the

PSF. Indeed, the transmission can be written:

$$t_{\mathbf{k}}(x, y) = \sum_{h=1}^P \sum_{h'=1}^P A_{\mathbf{k}} [x - (h-1)\Delta_h, y - (h'-1)\Delta_h] \quad (1.40)$$

and using the formula $\sum_{n=0}^{N-1} x^n = \frac{1-x^N}{1-x}$, we can simplify the terms in equation 1.37. If we note $C_\alpha = \pi\Delta_h \frac{\alpha-\alpha_0}{\lambda}$, we have:

$$\sum_{h=1}^P e^{-2iC_\alpha(h-1)} = \frac{1 - e^{-2iC_\alpha P}}{1 - e^{-2iC_\alpha}} \quad (1.41)$$

$$= \frac{e^{-iC_\alpha P} (e^{iC_\alpha P} - e^{-iC_\alpha P})}{e^{-iC_\alpha} (e^{iC_\alpha} - e^{-iC_\alpha})} \quad (1.42)$$

$$= \frac{e^{-iC_\alpha P} \sin(C_\alpha P)}{e^{-iC_\alpha} \sin(C_\alpha)}. \quad (1.43)$$

So the PSF of a square array of horns can be written:

$$\text{PSF}_{\mathbf{k}}(\mathbf{r}, \lambda) = \text{PSF}_{\mathbf{k}}^{\text{horn}} \frac{\sin^2(C_\alpha P)}{\sin^2(C_\alpha)} \times \frac{\sin^2(C_\beta P)}{\sin^2(C_\beta)} \quad (1.44)$$

$$= \text{PSF}_{\mathbf{k}}^{\text{horn}} \frac{\sin^2(P \frac{\pi}{\lambda} \Delta_h (\frac{x}{f} - \alpha_0))}{\sin^2(\frac{\pi}{\lambda} \Delta_h (\frac{x}{f} - \alpha_0))} \times \frac{\sin^2(P \frac{\pi}{\lambda} \Delta_h (\frac{y}{f} - \beta_0))}{\sin^2(\frac{\pi}{\lambda} \Delta_h (\frac{y}{f} - \beta_0))} \quad (1.45)$$

where we replaced (α, β) by $(\frac{x}{f}, \frac{y}{f})$.

1.2.5 QUBIC synthesized beam

In this section, we introduce the notion of the instrument beam which is similar to the radiation pattern of an antenna. Previously, we defined the PSF which, in summary, is the response of the instrument on the detectors for one direction on the sky and one wavelength. On the contrary, the beam is the response of one detector for all the directions on the sky at one wavelength. It basically gives the field of view of the detector.

We consider a point source in the far field of the instrument. The image on the focal plane is the PSF centered on the image given by optical geometry. Now, we consider a single detector on the focal plane. This detector sees a sample of the PSF, depending where it is placed on the focal plane. If we scan the field of view with the instrument, which is equivalent to move the point source, the PSF moves on the focal plane. In this way, the detector will sample the PSF as long as the scan. So, knowing the scanning strategy, the signal seen by the detector can be used to make an image of the full PSF with high resolution (not limited by the pixel size on the focal plane). A sketch of this method for a scan in azimuth and elevation is shown in Figure 1.18 (left).

So in this way, you measure the response of the detector for all directions on the sky and this is precisely the definition of the detector beam. So it is very clear why the detector beam will have the same expression as the PSF. This could also be justified by the principle of reversibility of light: considering a source at the detector place, the beam would be the PSF projected on the sky.

Detector beam measurement

For this measurement, the QUBIC instrument scans in azimuth and elevation a calibration source placed on the wall in the laboratory [8]. The source can be consider in the far field, we also use a flat mirror to increase the path length. The signal emitted by the source is modulated by a sine wave with frequency around 1 Hz in order to improve the accuracy of the measurement. Indeed, it is always easier to detect a signal which varies in time at a known frequency than a constant signal. Because of the modulation, we have to scan slowly and a complete scan (30×30 degrees) takes approximately 24 hours. In this way, by ordering the TOD on an image, we get a map for each detector that shows its beam. One example is shown in Figure 1.19. The calibration source is tunable in frequency, so we have measured the beams at 130, 140, 150, 160 and 170 GHz.

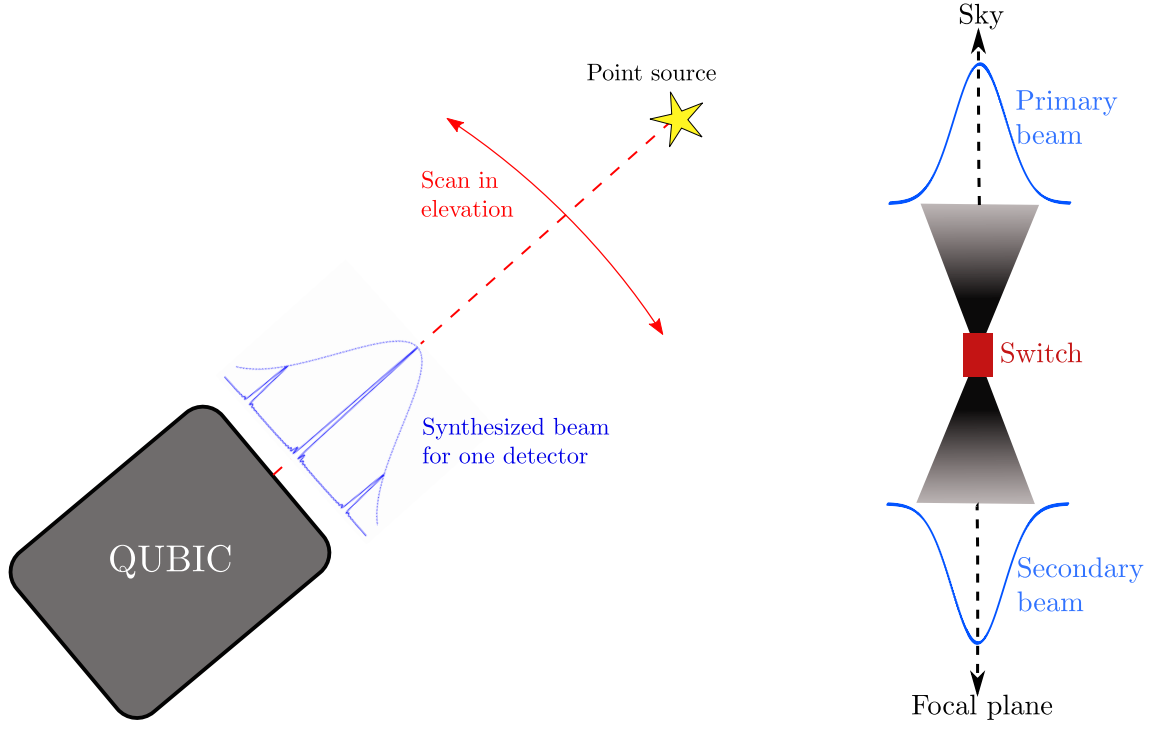


Figure 1.18: *Left*: Sketch of the beam measurement by scanning a point source. *Right*: Sketch of the primary and secondary beams for a single horn.

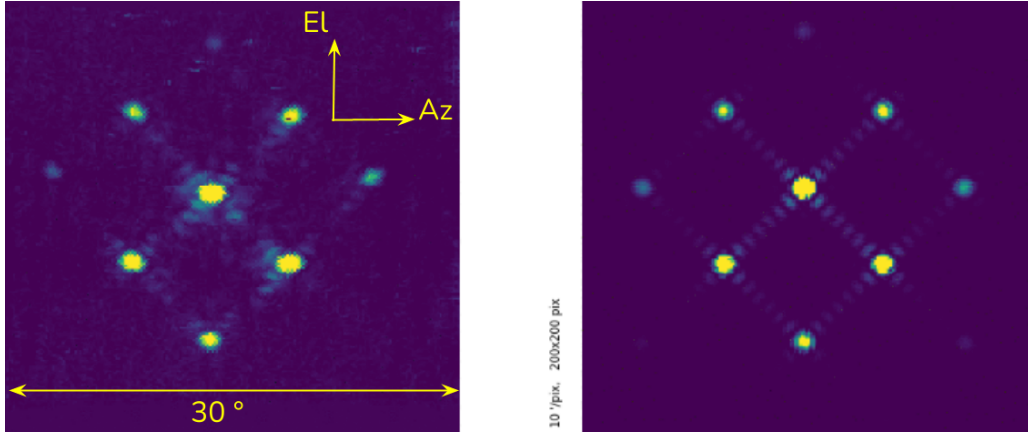


Figure 1.19: Beam for one detector at 150 GHz. Comparison between measurement (left) and simulation (right). Taken from [8].

Synthesized beam expression

QUBIC observes the sky through the horns. Before defining the beam for a detector on the focal plane, we need to define the beam of a single back-to-back horn. The beam looking at the sky, $B_{\text{prim}}(\mathbf{k}, \lambda)$, is called the primary beam and is a Gaussian with a Full Width at Half Maximum (FWHM) of 13° [6]. The beam looking toward the focal plane, $B_{\text{sec}}(\mathbf{r}, \lambda)$, is called the secondary beam and is identical to the primary one. Figure 1.18 (right) is a sketch showing the two beams.

The beam of one detector q on the focal plane centered in \mathbf{r}_q is called synthesized beam $B_{\mathbf{r}_q}(\mathbf{k}, \lambda)$. As explained previously, it is identical to the PSF (considering a focal plane with infinity resolution and no spatial limit):

$$B_{\mathbf{r}_q}(\mathbf{k}, \lambda) = \text{PSF}_{\mathbf{k}}(\mathbf{r}_q, \lambda). \quad (1.46)$$

The detector sees the sky through the horns so the synthesized beam can be written as a function of

the primary and secondary beams:

$$B_{\mathbf{r}_q}(\mathbf{k}, \lambda) = B_{\text{prim}}(\mathbf{k}, \lambda) B_{\text{sec}}(\mathbf{r}_q, \lambda) \sum_{h, h'=1}^N \exp \left\{ -i \left(\frac{\mathbf{r}_q}{f} - \mathbf{k} \right) \cdot (\mathbf{x}_h - \mathbf{x}_{h'}) \right\}. \quad (1.47)$$

The PSF of a single horn is identical to the product of the primary and secondary beams:

$$B_{\text{prim}}(\mathbf{k}, \lambda) B_{\text{sec}}(\mathbf{r}_q, \lambda) = \text{PSF}_{\mathbf{k}}^{\text{horn}}(\mathbf{r}_q, \lambda) \quad (1.48)$$

Note that in this expression, f is the focal length of the optical combiner, not the frequency. A cut of the synthesized beam, considering a square horn array is shown in Figure 1.20, for two detectors, one placed at the center of the focal plane and another $r = 12$ mm apart. The beam is shifted by $r/f \simeq 2.3^\circ$. This shift will be used in section 2.3.3 to measure the focal length from the synthesized beam maps.

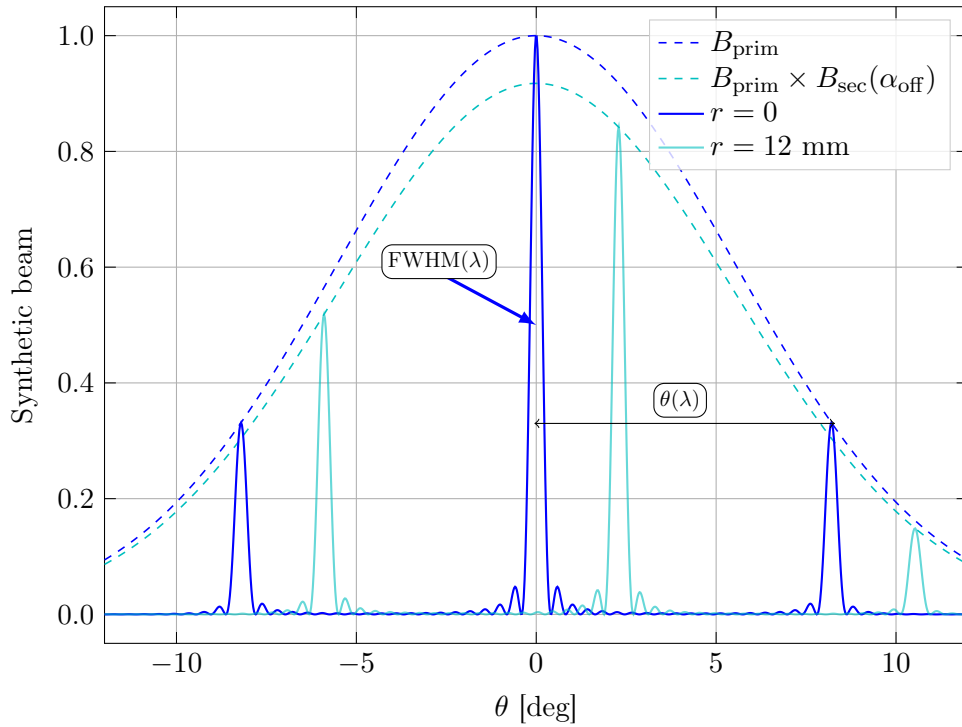


Figure 1.20: Cut of the synthesized beam as a function of θ (off-axis angle of the source) for a square array of 20×20 pupils separated by $\Delta_h = 14$ mm for a source emitting at 150 GHz (2 mm wavelength) for a detector located at the center of the focal plane ($r = 0$) and 12 mm apart. Dashed lines represent the primary beam of the pupils (Gaussian). Resolution and peak separation depend linearly on the wavelength λ [9].

Synthesized beam in terms of amplitude

We defined the instrument beam in terms of intensity, i.e. the PSF was defined in equation 1.39 by taking the square modulus of the transmission. We may need a definition of the instrument beam in terms of amplitude of the electric field. From equation 1.47, we write

$$A_{\mathbf{r}_q}(\mathbf{k}, \lambda) = A_{\text{prim}}(\mathbf{k}, \lambda) A_{\text{sec}}(\mathbf{r}_q, \lambda) \sum_{h=1}^N \exp \left\{ i \left(\frac{\mathbf{r}_q}{f} - \mathbf{k} \right) \cdot \mathbf{x}_h \right\} \quad (1.49)$$

where the instrument beams in terms of amplitude are defined such as $|A|^2 = B$.

Mean intensity received by a detector

We can compute the mean intensity received by a detector. Signals coming from two lines of sight \mathbf{k} and \mathbf{k}' are not coherent (sources are at infinity) so they will not interfere and we can sum the intensities over all the directions. So far we have only considered monochromatic waves. Actually, the signal must be integrated over the wavelength range defined by filters with band-pass $F(\lambda)$. Signals at different wavelengths do not interfere with each other so we can sum the intensities. Finally, for a detector centered at \mathbf{r}_q , the signal must be integrated over its surface a and averaged over its integration time τ . Therefore, the mean intensity received by a detector is:

$$I(\mathbf{r}_q) = \int_{\mathbf{k}} \int_a \int_{\lambda} \langle |S(\mathbf{k}, \lambda, t)|^2 \rangle_{\tau} B_{\text{synth}}(\mathbf{r}_q, \lambda) d\mathbf{k} da F(\lambda) d\lambda. \quad (1.50)$$

where $S(\mathbf{k}, \lambda, t)$ is the amplitude of the incoming signal at time t .

Angular resolution

Similarly to the case of a simple aperture, the resolution, given by the FWHM of the peaks in the synthesized beam is inversely proportional to the diameter D of the aperture, the largest baseline in the case of QUBIC:

$$r = \frac{\lambda}{D}. \quad (1.51)$$

So, for the FI, the largest baseline is made with 22 horns spaced with $\Delta_h = 14$ mm leading to a resolution of 0.39° at 150 GHz while for the TD, with a 8×8 horn array, it is 0.83° .

The angular separation between peaks is $\frac{\lambda}{\Delta_h}$ so it linearly depends on the wavelength λ . Chapter 6 is dedicated to spectral imaging, a technique entirely based on this wavelength dependence.

Making imagery with a single detector

The measurement of the synthesized beam is a good illustration of the possibility to get an image with a single detector by scanning the field of view. An analogy would be to look at a painting on a wall through a very small hole. By changing the sighting direction, you can reconstruct the entire painting. This is similar to the principle of a camera obscura known since a very long time.

1.2.6 QUBIC as an interferometer

So far, we have shown that QUBIC can be treated as an imager with a very specific PSF. Is-it possible to consider it as an interferometer and to apply the techniques developed in radio astronomy? In radio astronomy, because wavelengths are large, the resolution of a classical (single dish) imager ($\sim \frac{\lambda}{D}$) is poor. However a much better resolution can be achieved with interferometry.

Interferometry means a recombination of light coming from the same direction on the sky but which traveled on different paths. In radio astronomy, the electric field $E(t)$ (amplitude and phase) is registered with several antennas and the combination is done analogically or numerically, adding a phase shift on signals. This is possible because the frequency is low. On the contrary, in the visible domain, the signal is the average intensity $\langle E(t)E^*(t) \rangle_{\tau}$ where τ is the integration time of the detector.

We will use the Young experiment to introduce the concept of visibility, which is the usual observable in radio astronomy. The Young experiment, consists in observing a point source in the far field through 2 circular apertures T_1 and T_2 separated by a distance $\|\vec{T_1 T_2}\| = d$. We define $\mathbf{b} = \frac{\vec{T_1 T_2}}{\lambda}$ the baseline vector in wavelength unit, a baseline being composed by two apertures. The interference pattern obtained is shown in Figure 1.21. This is again a very simple setup I made, using a laser illuminating two holes perforated in an aluminum sheet. We recognize the Airy disk seen in Figure 1.14, for the case of one aperture, but with fringes inside.

We consider an extended source in direction \mathbf{k} at infinity, emitting at frequency ν . We note $B(\mathbf{k})$ the brightness distribution of the source observed with the instrument beam and B_{tot} the total observed

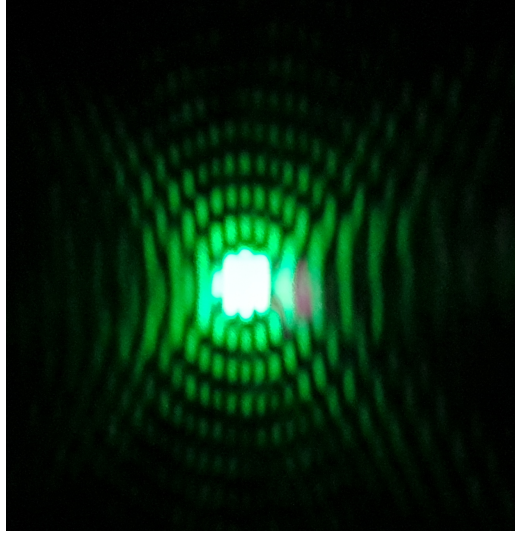


Figure 1.21: Interference pattern obtained with the Young experiment, two holes lighted by a laser observed at infinity. The Airy disk contains vertical fringes.

brightness. The intensity in \mathbf{r} on the focal plane, at time t is:

$$\begin{aligned} I(\mathbf{r}, t) &= \int B(\mathbf{k}) [1 + \cos(2\pi \mathbf{k} \cdot \mathbf{b} - \varphi_{\mathbf{r}})] d\mathbf{k} \\ &= B_{\text{tot}} + \int B(\mathbf{k}) \cos(2\pi \mathbf{k} \cdot \mathbf{b} - \varphi_{\mathbf{r}}) d\mathbf{k} \end{aligned}$$

with $\varphi_{\mathbf{r}}$ the phase shift occurring after the apertures, it is 0 in the center of the focal plane. We can integrate over the source because it is spatially incoherent. From the previous expression, we can say that observing the sky through two apertures is equivalent to have a spatial filter in front of the source (at infinity) with a sinusoidal transfer function:

$$F_{\mathbf{b}}(\mathbf{k}, \mathbf{r}) = \cos(2\pi \mathbf{k} \cdot \mathbf{b} - \varphi_{\mathbf{r}}). \quad (1.52)$$

Using trigonometry, intensity writes in a different form:

$$\begin{aligned} I(\mathbf{r}) &= B_{\text{tot}} + \int B(\mathbf{k}) [\cos(2\pi \mathbf{k} \cdot \mathbf{b}) \cos \varphi_{\mathbf{r}} + \sin(2\pi \mathbf{k} \cdot \mathbf{b}) \sin \varphi_{\mathbf{r}}] d\mathbf{k} \\ &= B_{\text{tot}} + I_1 \cos \varphi_{\mathbf{r}} + I_2 \sin \varphi_{\mathbf{r}} \end{aligned}$$

where we introduced the two observables I_1 and I_2 . They contain all the spatial information that can be obtained from the two apertures. The measurement of the intensity at different points with specific phase shift as $\varphi_{\mathbf{r}} = 0$ and $\varphi_{\mathbf{r}} = \pi/2$ give access to I_1 and I_2 .

By convention, the complex visibility V is:

$$V = I_1 + iI_2 = |V| e^{i\phi} = |V| (\cos \phi + i \sin \phi)$$

where, by definition, $\cos \phi = \frac{I_1}{|V|}$ and $\sin \phi = \frac{I_2}{|V|}$. The couple $(|V|, \phi)$ is equivalent to (I_1, I_2) . We have

$$I(\mathbf{r}) = B_{\text{tot}} + |V| \cos \phi \cos \varphi_{\mathbf{r}} + |V| \sin \phi \sin \varphi_{\mathbf{r}} \quad (1.53)$$

$$= B_{\text{tot}} + |V| \cos(\varphi_{\mathbf{r}} - \phi). \quad (1.54)$$

Thus, the meaning of $(|V|, \phi)$ is the following: $|V|$ is the maximum intensity that the filter can transmit and the intensity is maximum when $\varphi = \phi(2\pi)$. So ϕ is the phase shift of the filter which gives the maximum intensity.

Imagery from the visibility

The measurement of a single visibility from a given pair of apertures corresponds to an observation through a given filter. As we selected a single spatial frequency we lost many information and it is not sufficient to reconstruct an image. However, by measuring a set of visibilities, varying the orientation and the space between the two apertures, we will see that the reconstruction of an image becomes feasible. This is equivalent to varying the orientation and the spatial frequencies of the filter. From the expressions of I_1 and I_2 , we can write:

$$V(\mathbf{b}) = \int_{\mathbf{k}} B(\mathbf{k}) e^{2i\pi \mathbf{k} \cdot \mathbf{b}} d\mathbf{k}. \quad (1.55)$$

We define (u, v) as the two components of the aperture vector \mathbf{b} projected on the plane perpendicular to the source direction: the uv-plane. By measuring the visibility for different baselines, we can sample the visibility $V(u, v)$ on the uv-plane:

$$V(u, v) = \int_{\mathbf{k}} B(l, m) e^{2i\pi(ul+vm)} dl dm = \mathcal{F}[B(l, m)] \quad (1.56)$$

where $(l, m) = \mathbf{k}$. This is the Van-Cittert Zernicke theorem [233]: the complex visibility is the Fourier transform of the observed field (beam multiplied by the intensity of the source). So an interferometer measures the Fourier modes of the observed sky, the spatial frequency of the mode is given by the length of the baseline.

We see that, if V is known for any (u, v) then the intensity of the source, knowing the beam of the instrument, is known at any point on the sky (l, m) . Actually, it is possible to show that a finite number of samples would be sufficient for the reconstruction of the image of the source. The technique that allows to make an image by sampling the complex visibility is called aperture synthesis and it is a wide field in radio astronomy.

In radio astronomy, the synthesized beam called “dirty” beam can also be computed, it is the Fourier transform of the set of visibilities.

Treating QUBIC as an interferometer

For QUBIC, the direct observable is the dirty image and it is possible to retrieve a set of complex visibilities from it. This was developed during the thesis of Romain Charlassier [2], [10]. Then, visibilities could be used to produce images as in radio astronomy. It is also convenient to get power spectra. However, this possibility was not followed because of its heavy hardware complexity. Indeed, it involves an individual phase shifter for each aperture and specific phase shifting schemes in order to demultiplex each individual visibility from the global measurement.

1.3 A polarimeter

1.3.1 The Stokes parameters

The polarisation of an electromagnetic wave is described by the orientation of the electromagnetic field $\underline{\mathbf{E}}(\mathbf{r}, t)$ orthogonal to the direction of propagation \mathbf{k} . We can decompose $\underline{\mathbf{E}}(\mathbf{r}, t)$ on a basis $(\mathbf{e}_x, \mathbf{e}_y)$ orthogonal to \mathbf{k} :

$$\underline{\mathbf{E}}(\mathbf{r}, t) = \underline{\mathbf{E}}_0 e^{i(\mathbf{k}\mathbf{r} - \omega t)} \quad \text{with} \quad \underline{\mathbf{E}}_0 = A_x \mathbf{e}_x + A_y e^{-i\varphi} \mathbf{e}_y \quad (1.57)$$

where ω is the angular frequency in radians per second, φ a phase and A_x, A_y the amplitudes. When $\varphi = 0$, the wave is linearly polarized. When $\varphi = \frac{\pi}{2}$ and $A_x = A_y$, it is circularly polarized. The electromagnetic radiation can be described by the four Stokes parameters [19]. The first one is the intensity:

$$I = |\underline{\mathbf{E}}_x|^2 + |\underline{\mathbf{E}}_y|^2. \quad (1.58)$$

It can be measured by a detector not sensitive to the polarization such as a bolometer. At high frequencies, an instrument does not measure $I(t)$ but $\langle I(t) \rangle_\tau$ where the average is done over the

integration time τ of the detector, much longer than the electromagnetic oscillation period $\frac{2\pi}{\omega}$. The second Stokes parameter is defined as the difference of intensities between two orthogonal axes:

$$Q = |\underline{E}_x|^2 - |\underline{E}_y|^2. \quad (1.59)$$

We see that for a linear polarization oriented at 45° of x and y , Q is zero. So we need a second parameter to fully describe the linear polarization. This is the parameter U which is the parameter Q' measured in a frame $(\mathbf{e}'_x, \mathbf{e}'_y)$ rotated of 45° from the frame $(\mathbf{e}_x, \mathbf{e}_y)$. In this frame, the electric field components are: $E_{x'} = (E_x + E_y)/\sqrt{2}$ and $E_{y'} = (E_y - E_x)/\sqrt{2}$. So,

$$U = Q' = |\underline{E}_{x'}|^2 - |\underline{E}_{y'}|^2 = \underline{E}_x \underline{E}_y^* + \underline{E}_y \underline{E}_x^* = 2 \operatorname{Re}(\underline{E}_x \underline{E}_y^*). \quad (1.60)$$

Finally, we need a last parameter to describe the circular polarization, it is the Stokes parameter V . To measure a circular polarization, we can use a quarter-wave plate which introduces a $\pi/2$ phase shift on E_x : $E_{x'} = e^{i\frac{\pi}{2}} E_x$ and $E_{y'} = E_y$. The field E_x and E_y that were in phase quadrature become in phase so the polarization is linear, at 45° of $(\mathbf{e}'_x, \mathbf{e}'_y)$. Thus, Q' is zero and it is U' that characterizes the circular polarization:

$$V = U' = \underline{E}_{x'} \underline{E}_{y'}^* + \underline{E}_{y'} \underline{E}_{x'}^* = i (\underline{E}_x \underline{E}_y^* - \underline{E}_y \underline{E}_x^*) = -2 \operatorname{Im}(\underline{E}_x \underline{E}_y^*). \quad (1.61)$$

The I and V parameters do not depend on the reference frame contrary to Q and U . In a basis $(\mathbf{e}'_x, \mathbf{e}'_y)$ rotated from $(\mathbf{e}_x, \mathbf{e}_y)$ by an angle α around \mathbf{e}_z , the electric field becomes:

$$\begin{pmatrix} \underline{E}'_x \\ \underline{E}'_y \end{pmatrix} = J_{\text{rot}} \begin{pmatrix} \underline{E}_x \\ \underline{E}_y \end{pmatrix} \quad \text{with the rotation matrix} \quad J_{\text{rot}} = \begin{pmatrix} \cos \alpha & \sin \alpha \\ -\sin \alpha & \cos \alpha \end{pmatrix}. \quad (1.62)$$

It follows that

$$Q' = Q \cos(2\alpha) + U \sin(2\alpha) \quad (1.63)$$

$$U' = -Q \sin(2\alpha) + U \cos(2\alpha) \quad (1.64)$$

which can be condensed in:

$$(Q' \pm iU') = e^{\mp 2i\alpha} (Q \pm iU). \quad (1.65)$$

Note that this is the definition of a spin-2 quantity and we will come back on this point in section 4.2.5. In the case of $\alpha = \frac{\pi}{4}$, we have $Q' = U$. So, as said previously, we verify that U is equivalent to Q in a referential frame rotated by 45° .

1.3.2 Measuring a linear polarization

QUBIC bolometers are full power detectors, they are not polarization sensitive. The measurement of the polarization is achieved by modulating the incoming radiation with a rotating HWP and a polarizing grid as shown in Figure 1.22. The choice of this design will be discussed in section 2.1. As we will see, this allows QUBIC to measure the Stokes parameters I , Q and U .

We use the formalism introduced by Jones in 1942 [234], [235]. This is a method to describe the behavior of polarized light crossing optical elements. Each optical element is associated with a 2×2 matrix acting on the electric field. The matrix terms may be complex in order to include the phase shifts. The electric field after the optical element \mathbf{E}_{out} is

$$\begin{pmatrix} E_x^{\text{out}} \\ E_y^{\text{out}} \end{pmatrix} = J \begin{pmatrix} E_x^{\text{in}} \\ E_y^{\text{in}} \end{pmatrix} \quad (1.66)$$

where J is the Jones matrix and \mathbf{E}_{in} the incident electric field.

We consider an on-axis point source in the far field. The incident electric field is $\underline{\mathbf{E}}(\mathbf{r}, t) = \underline{E}_x \mathbf{e}_x + \underline{E}_y \mathbf{e}_y$. The instrument frame $(\mathbf{e}_x, \mathbf{e}_y, \mathbf{e}_z)$ is defined such that \mathbf{e}_z is the optical axis of the instrument (see Figure 1.22).

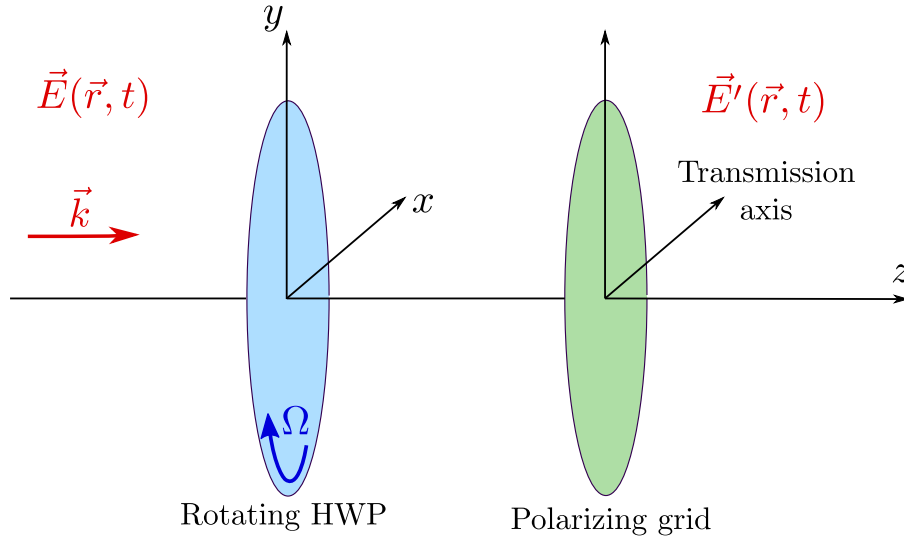


Figure 1.22: Rotating half wave plate (HWP) and polarizing grid to modulate the polarization of the radiation.

The Jones matrix associated with the HWP is:

$$J_{\text{hwp}} = \begin{pmatrix} 1 & 0 \\ 0 & -1 \end{pmatrix} \quad (1.67)$$

so that the rotating HWP is

$$J_{\text{rot}}^T J_{\text{hwp}} J_{\text{rot}} = \begin{pmatrix} \cos(\Omega t) & -\sin(\Omega t) \\ \sin(\Omega t) & \cos(\Omega t) \end{pmatrix} \begin{pmatrix} 1 & 0 \\ 0 & -1 \end{pmatrix} \begin{pmatrix} \cos(\Omega t) & \sin(\Omega t) \\ -\sin(\Omega t) & \cos(\Omega t) \end{pmatrix} \quad (1.68)$$

$$= \begin{pmatrix} \cos(2\Omega t) & \sin(2\Omega t) \\ \sin(2\Omega t) & -\cos(2\Omega t) \end{pmatrix}, \quad (1.69)$$

Ω being the HWP angular speed and t the time. The polarizing grid is placed such that its transmission axis is aligned with \mathbf{e}_x so its Jones matrix is:

$$J_{\text{pol}} = \begin{pmatrix} 1 & 0 \\ 0 & 0 \end{pmatrix}. \quad (1.70)$$

Thus, the electric field coming out of the polarizing grid and entering the horn array is

$$\underline{\mathbf{E}}_h(\mathbf{r}, t) = J_{\text{pol}} J_{\text{rot}}^T J_{\text{hwp}} J_{\text{rot}} \underline{\mathbf{E}}(\mathbf{r}, t) = [\underline{E}_x \cos(2\Omega t) + \underline{E}_y \sin(2\Omega t)] \mathbf{e}_x \quad (1.71)$$

where the h index stands for the horn array. The corresponding intensity is therefore

$$S(t) = [\underline{E}_x \cos(2\Omega t) + \underline{E}_y \sin(2\Omega t)]^2. \quad (1.72)$$

Using the definition of the Stokes parameters given in section 1.3.1, we can write $S(t)$ as the following:

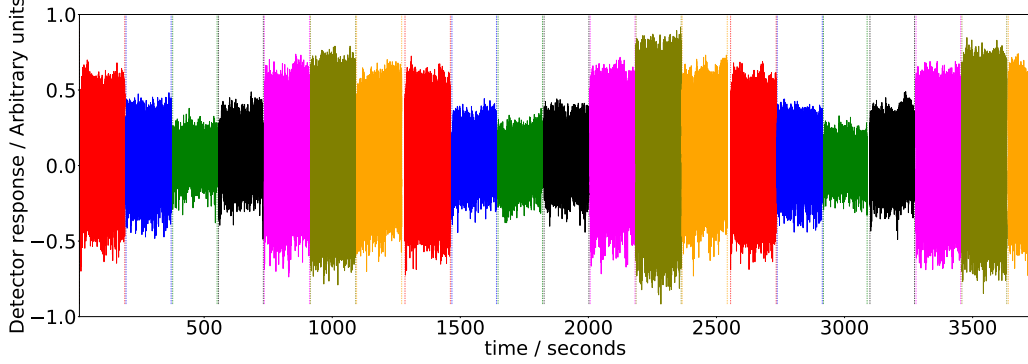
$$S(t) = \frac{I+Q}{2} \cos^2(2\Omega t) + \frac{I-Q}{2} \sin^2(2\Omega t) + \frac{U}{2} \sin(4\Omega t) \quad (1.73)$$

$$= \frac{1}{2} [I + Q \cos(4\Omega t) + U \sin(4\Omega t)] \quad (1.74)$$

where we see that the three Stokes parameters are modulated four times faster than the angular speed of the HWP. For QUBIC, the HWP can move step by step on eight positions regularly spaced between 0 and $\pi/2$ ². The intensity corresponding to each position $\alpha = \Omega t$ is a linear combination of I , Q and U as shown in Table 1.1. Figure 1.23 shows the peak-to-peak amplitude of the detected calibration source for different HWP positions as measured with a TES near the center of the focal plane. Thus, by measuring $S(t)$ at least three times with different HWP positions, we can measure the three Stokes parameters in direction z on the sky. We simply have to solve a linear system. Some detail will be given in section 5.2.6.

²The eight positions are well identified by an encoder but we can have access to all positions through counting the number of motor steps.

Position	0	1	2	3	4	5	6	7
α [rad]	0	$\frac{\pi}{16}$	$\frac{\pi}{8}$	$\frac{3\pi}{16}$	$\frac{\pi}{4}$	$\frac{5\pi}{16}$	$\frac{3\pi}{8}$	$\frac{7\pi}{16}$
$2S$	$I + Q$	$I + \frac{Q+U}{\sqrt{2}}$	$I + U$	$I - \frac{Q-U}{\sqrt{2}}$	$I - Q$	$I - \frac{Q+U}{\sqrt{2}}$	$I - U$	$I + \frac{Q-U}{\sqrt{2}}$

Table 1.1: Intensity measured as function of I , Q , U for the eight HWP steps of QUBIC.Figure 1.23: Peak-to-peak amplitude of the detected calibration source for different HWP positions as measured with a TES near the center of the focal plane. The 7 positions, each associated with a given color, are spaced by 15° in order to span 90° between position 1 and position 7. Taken from [8].

1.4 Optical combiner alignment

The QUBIC mirrors are placed on hexapods in order to adjust their position. They were first aligned using a mechanical FARO arm to measure the position of their surfaces in three dimensions. Then, the measured positions were compared to a mechanical model and the hexapods were adjusted until reaching the requirements.

An optical alignment using a laser was done as a check for the mechanical procedure. In this section, we will summarize the optical alignment method described in paper [6]. This work was realized in May 2018, I was responsible for the data taking and data analysis in collaboration with people in Roma. Here I show the analysis for data taken on May, 17 and 22.

1.4.1 Experimental setup

The optical alignment of the combiner was done with a He-Ne laser moved along (x, y) axis over the 64 positions of the 8×8 feed-horn array, see Figures 1.24 and 1.25. The method relies on the fact that

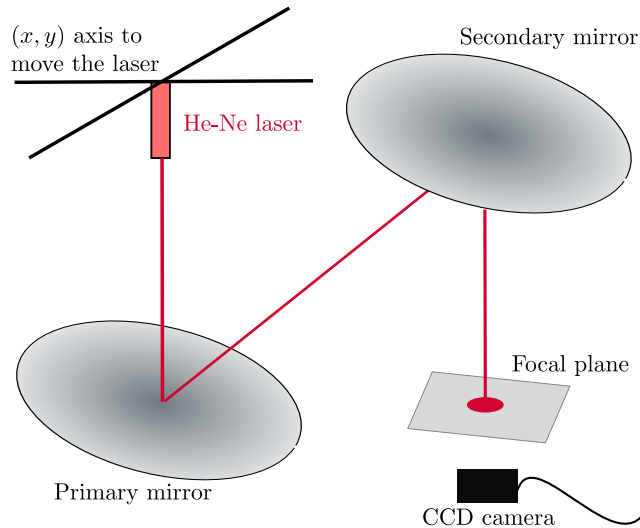


Figure 1.24: Sketch of the experimental setup.

while translating the laser along x and y axes, the spot on the focal plane should not change place. A mechanical support allowed to tilt the laser from the nominal direction 0.0° along x and y directions. For each horn position the illumination map on a fake focal plane has been acquired by a CCD camera. We will look at six data sets, two for which the laser is at 0.0° and the four others for which it is tilted at $\pm 6.5^\circ$ in the x and y directions.

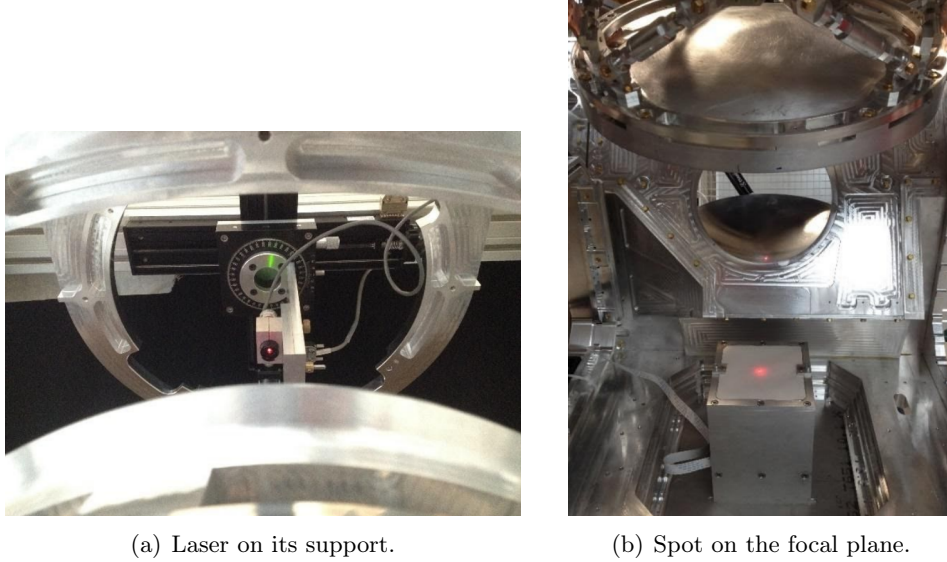


Figure 1.25: Pictures taken during the optical alignment.

1.4.2 Comparison to a model

We generated optical models of the combiner at ambient temperature with Zemax software, using the real measured surfaces of both TD mirrors. Measurements are compared to a model considering nominal laser directions, referred as “Nominal Zemax model” and listed in Table 1.2. We also compared

Laser inclination along (x, y) [deg]	Zemax centroid positions (X, Y) [mm]
(0, 0)	(0.463, -0.647)
(0, +6.5)	(0.167, -40.158)
(0, -6.5)	(0.568, 30.226)
(+6.5, 0)	(-34.862, -5.189)
(-6.5, 0)	(35.426, -4.478)

Table 1.2: Nominal Zemax model centroid positions.

to a model with measured tilt angle of the laser, referred as “Zemax model” in the plots. We made the hypothesis that the tilt of the laser support was constant during the six measurements, so we assumed the same tilt for the on-axis positions and for the off-axis positions. However this assumption does not seem to be correct because nominal inclinations are more consistent with data as shown in the following plots.

1.4.3 Analysis by detecting the center of each spot

The center of each laser spot is detected as in the example shown in Figure 1.26, left. I did it for the 64 horn positions and for the five inclinations. The result is shown in Figure 1.26, right, where we show the ellipses at 1, 2 and 3 sigma. The positions obtained with Zemax software are shown with

errorbars assuming a $\pm 0.5^\circ$ laser direction error. The two on-axis measurements superimpose in the middle of the plot. The dispersion is large, due to the difficulty of detecting the laser spot center. This is because of a poor reflectivity of the mirrors in the visible range. Indeed in the microwave domain, a rough surface is sufficient to reflect the light. A similar analysis was performed in Roma and the

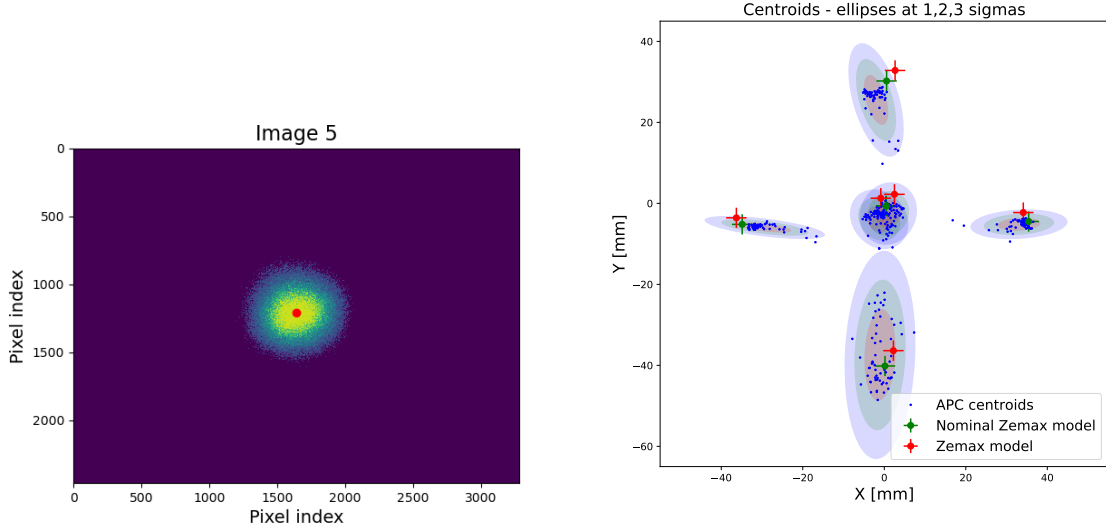


Figure 1.26: Analysis by detecting the centers of each spot. *Left*: Detection of the spot center on one image. *Right*: Centers detected with the APC pipeline compared to Zemax models with nominal laser inclinations (green) and with measured tilt angles.

comparison is shown in Figure 1.27.

1.4.4 Analysis by doing the product of images

I have performed a second type of analysis. An image can be seen as the probability distribution of light in the focal plane. Doing the product gives the probability distribution of the mean. Then, it is possible to draw contours at 1, 2 and 3 sigma on the product image. Figure 1.28, left, is an example of the product image with the 3 contours. One advantage of this method is that we do not do any assumption concerning the shape of the distribution which is clearly not a Gaussian. Figure 1.28, right, shows the results obtained with this analysis for the five laser inclinations still compared with the two Zemax models (nominal and measured laser tilts).

17 and 22/05/18

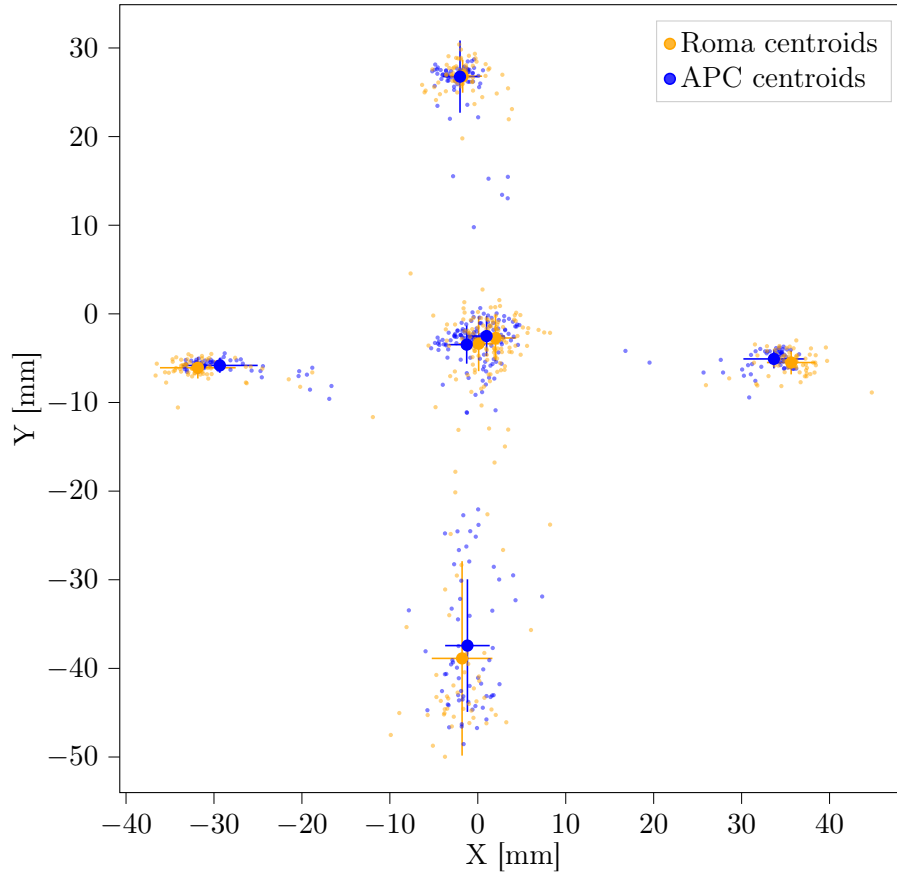
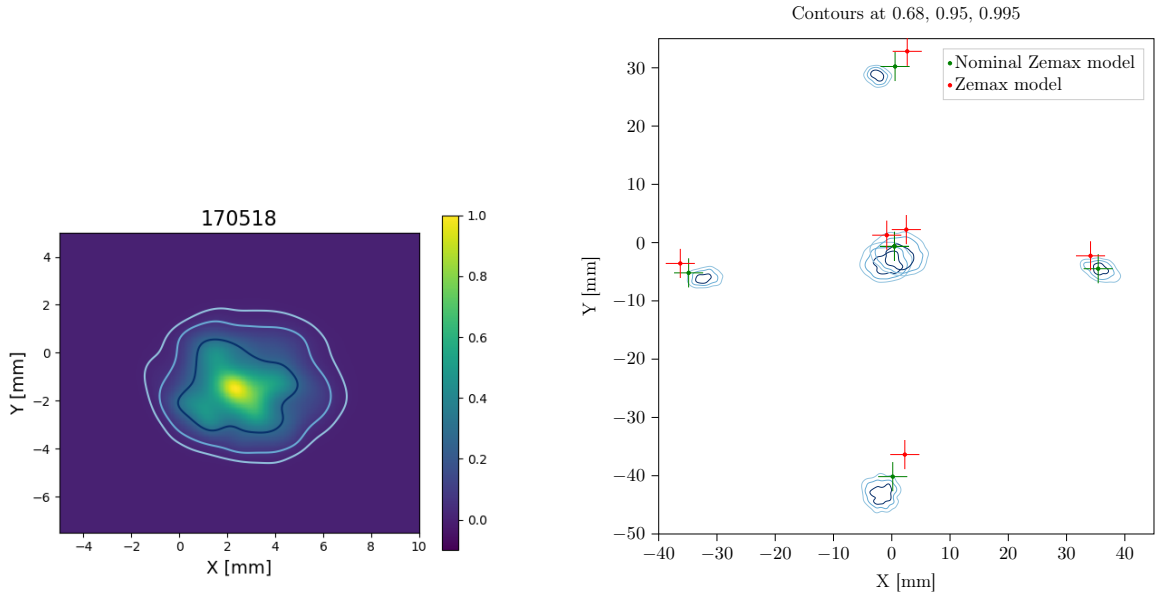


Figure 1.27: Comparison between APC and Roma pipelines.

Figure 1.28: *Left*: Product image for the data set of the 17/05/18 at 0.0° inclination. Contours at 1, 2 and 3 sigma are shown. *Right*: Contours for each data set compared to the Zemax models with nominal laser inclinations (green) and with measured laser tilt (red).

1.4.5 Conclusion of the optical alignment

The results of the procedure showed that we were able to recover consistent centroid positions with three different analysis and assuming nominal laser directions. However, we were not able to satisfy the tightest constraints of the Zemax model, the current accuracy can not constrain the alignment within the expected tolerances. For this reason we have to rely on the FARO arm 3D measurement. However, since the FI mirrors will have a much better surface roughness, the optical alignment for the FI will have a much better accuracy. It is expected to be more precise than with the mechanical process. So this work is an important step for FI mirror alignment as we have developed all the hardware and data analysis tools needed for it.

Conclusion

In this chapter we have presented the concept of bolometric interferometry, focusing on the optical design. I made the choice to present QUBIC as a classical imager with a very peculiar PSF caused by the horn array. The crucial concept of synthesized beam has been defined too. We have also seen how QUBIC can measure the polarization, thanks to the rotating HWP and the polarizing grid. Finally, I presented the optical alignment procedure and data analysis of the two mirrors.

In the next chapter we will focus on the instrument calibration and we will see how this particular design is an advantage regarding the control of instrumental systematic effects.

Chapter 2

First steps towards self-calibration

Contents

2.1	Optimization of the polarimeter design	44
2.1.1	Limiting the cross-polarization	44
2.1.2	Systematic effect modeling	46
2.1.3	Limiting the leakage from intensity to polarization	47
2.2	Self-calibration principle	50
2.2.1	Redundant baseline comparison	50
2.2.2	Number of baselines	50
2.3	Synthesized beam analysis	51
2.3.1	Synthesized beam maps	51
2.3.2	Appropriate peak numbering	51
2.3.3	Determination of the focal length of the optical combiner	55
2.3.4	Prospective for this work	58
2.4	Simulate interference fringes on the focal plane	58
2.4.1	QUBIC soft simulations	59
2.4.2	Analytical model	62
2.4.3	Maynooth simulations	62
2.5	Measurement and data analysis to obtain fringe images	64
2.5.1	Combination of images	64
2.5.2	Data taking process	65
2.5.3	Detecting “bad” detectors	67
2.5.4	Data analysis process	69
2.5.5	Verification of the horn-array orientation with fringe measurements	74
2.6	Bolometer inter-calibration using the fringes	76
2.6.1	Theoretical principle	76
2.6.2	Illustration on a simulation	77
2.6.3	First trial on real data	82
2.6.4	Prospective for this work	85

QUBIC was initially mainly designed for a precise control of systematic effects thanks to interferometry. The capability of self-calibration of the instrument has been studied in detail in the thesis by Marie-Anne Bigot-Sazy [11]. This chapter gives an overview of the optical calibration of the instrument. In the first section, I present work, based on the formalism developed by Marie-Anne but adapted to the current instrument configuration in order to justify the design of the QUBIC polarimeter. Then, in the second section, I describe the principle of self-calibration based on the comparison between redundant baselines.

The rest of the chapter presents two analysis I performed with calibration data in order to explore the self-calibration ability. In section 2.3, I present an analysis of the detector synthesized beam maps obtained by scanning a calibration source in the laboratory. The displacement of the multiple peak beam on the sky from one detector to another is used to measure the focal length of the optical combiner. Note that determining the focal length is not needed, it is more one exercise to explore self-calibration. Sections 2.4 and 2.5 treat the interference fringes measured from individual baselines: simulations, data taking and data analysis. This is a key step for self-calibration. Finally, section 2.6 describes a method to inter-calibrate bolometers by fitting the fringe images. Here again, the focal length is measured from the data as an exercise to test self-calibration. Those analyses can be seen as a first step toward a complete self-calibration procedure which is not yet developed.

Personal contributions: This chapter is mainly personal work, realized in collaboration with many people, especially Jean-Christophe, Steve, Michel, Jean, James and Cr  idhe.

2.1 Optimization of the polarimeter design

The control of systematic effects is fundamental for experiments targeting the B -mode signal. As we will see in this section, the design of the QUBIC polarimeter has been optimized to limit two major systematic effects: cross-polarization and intensity to polarization leakage.

As we have seen in section 1.3.2, the modulation of the polarization is done with a rotating HWP followed by a polarizing grid. They are placed at the entrance of the instrument, between the window and the horn-array.

Historically, the design of QUBIC was different [12]. The HWP was placed between the horn-array and the primary mirror and the polarizing grid was placed between the secondary mirror and the two focal planes. In this way, both polarization directions could be observed at the same time, on two focal planes, one in transmission and the other in reflection. In 2014, the BICEP experiment claimed a primordial B -modes detection [152] but it was quickly shown through a joint analysis using the Planck data that the observed B -modes were due to polarized emission from galactic dust [153]. It was then realized by the CMB community how measurements in several frequency bands are crucial to disentangle CMB with foregrounds (see section 5.4). This is why the QUBIC design was updated in order to have two focal planes centered on 150 and 220 GHz instead of two focal planes with the two polarization directions but both at 150 GHz.

In addition of adding a frequency band, this new design is also robust to cross-polarization. This will be explained in the next section. Moreover, it was optimized to limit the leakage from intensity to polarization. However, it has the inconvenient of losing half of the photons but through a twice wider bandwidth with respect to before.

2.1.1 Limiting the cross-polarization

QUBIC bolometers are full power detectors. As seen in section 1.3.2, the measurement of the polarization is only done by modulating the signal amplitude with the rotating HWP and the polarizing grid.

Every optical element has its own systematic effects which could induce cross-polarization. This means that the two polarization directions (x, y) of the signal can be mixed when interacting with the instrument. Knowing that QUBIC is a polarimeter aiming at measuring the tiny B -mode signal, cross-polarization is a major issue. The x -axis is defined as the transmission axis of the polarizing grid. As sketched in Figure 2.1, by putting the HWP and the polarizing grid right after the window, the x polarization is selected as early as possible. In this way, any cross-polarization occurring after the polarizing grid, for example generated by the horn-array, the mirrors or any reflection in the instrument, has no impact. The modulation of the polarization was tested during the calibration phase and a very low cross-polarization was indeed detected. Those measurements are presented in [8] and [4]. As shown

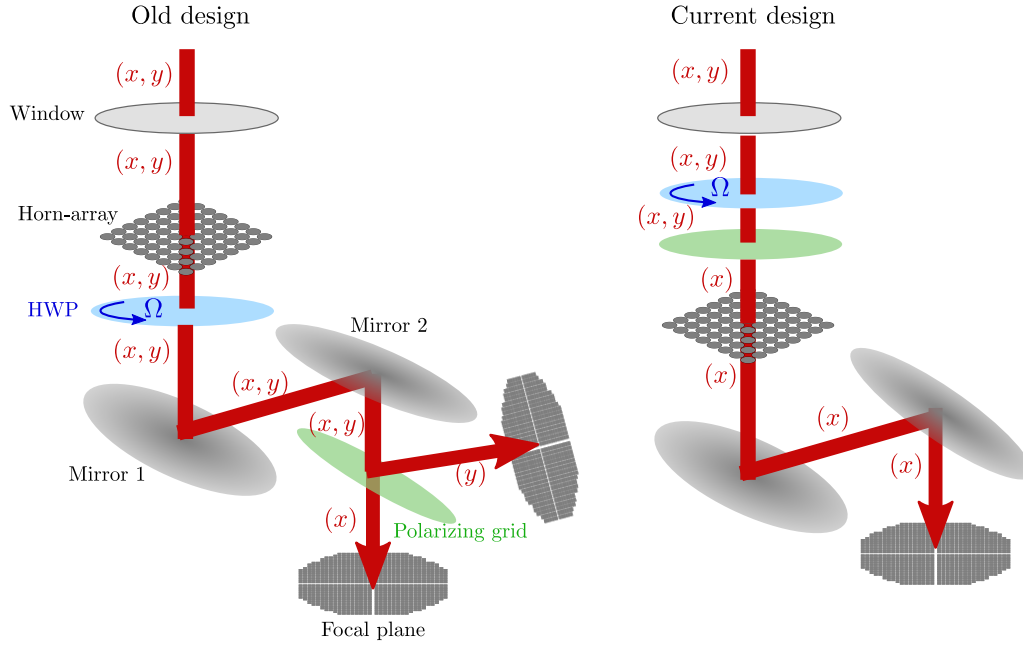


Figure 2.1: Comparison of the two designs in terms of cross-polarization. (x, y) represent the two directions of polarization.

in Figure 2.2, the cross-polarization contamination at 150 GHz is compatible with zero to within 0.4%.

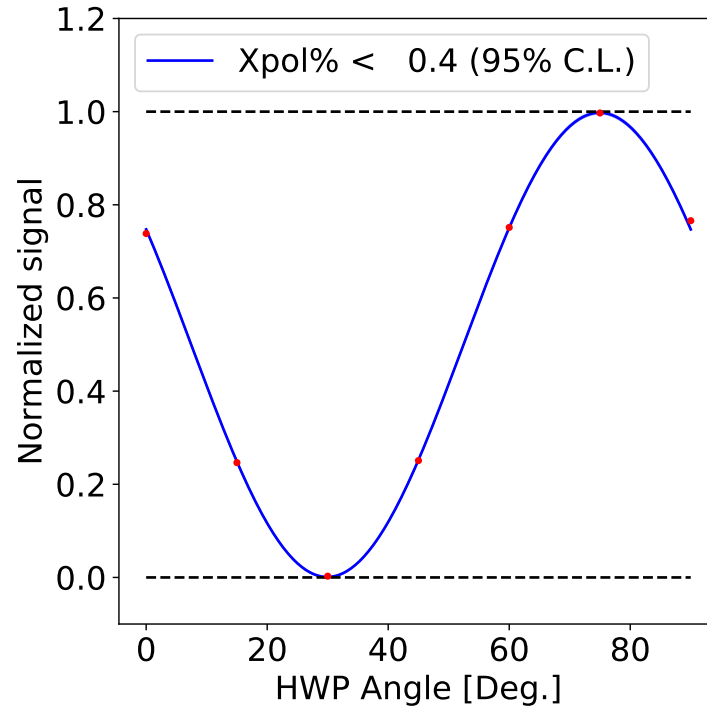


Figure 2.2: Amplitude of the detected calibration source at 150 GHz as measured with a TES near the center of the focal plane for the HWP in the different positions and fitted to a sine curve. Taken from [8].

2.1.2 Systematic effect modeling

In this section, we copy the formalism developed by Marie-Anne Bigot-Sazy in her thesis [11] and in the corresponding paper [13]. However her work was based on the old design so I adapted it to the current one.

In order to model systematic effects, we introduce gain and coupling terms in the Jones matrices defined in section 1.3.2. A generic Jones matrix to model systematic effects is

$$J = \begin{pmatrix} 1 - g_x & e_x \\ e_y & 1 - g_y \end{pmatrix} \quad (2.1)$$

where g_x, g_y are the gain parameters and e_x, e_y the coupling parameters associated with the polarization directions x and y . The terms may be complex if they introduce a phase shift. The HWP and the polarizing grid are modeled by the following matrices

$$J_{\text{hwp}} = \begin{pmatrix} 1 - h_x & \xi_x \\ \xi_y & -1 - h_y \end{pmatrix} \quad \text{and} \quad J_{\text{pol}} = \begin{pmatrix} 1 - \varepsilon_x & \rho_x \\ \rho_y & \varepsilon_y \end{pmatrix}. \quad (2.2)$$

Still following [13], we write the propagation of electric field \mathbf{E} through horn i up to bolometer q as

$$\begin{pmatrix} E_{iq}^x \\ E_{iq}^y \end{pmatrix} = \alpha_{iq} \beta_i(\mathbf{k}) \begin{pmatrix} E_x \\ E_y \end{pmatrix} = \begin{pmatrix} \alpha_{iq}^x & 0 \\ 0 & \alpha_{iq}^y \end{pmatrix} \begin{pmatrix} \beta_i^x(\mathbf{k}) & 0 \\ 0 & \beta_i^y(\mathbf{k}) \end{pmatrix} \begin{pmatrix} E_x \\ E_y \end{pmatrix}. \quad (2.3)$$

The matrices α_{iq}, β_{iq} fully characterize the instrument. Their terms can be defined from equation 1.49. β_{iq} includes the primary beam in terms of amplitude A_{prim} , the incident direction \mathbf{k} and the horn position \mathbf{x}_i . We have

$$\beta_i^x(\mathbf{k}) = A_{\text{prim},i}^x(\mathbf{k}, \lambda) \exp \left\{ \frac{i2\pi}{\lambda} \mathbf{x}_i \cdot \mathbf{k} \right\} \quad \text{and} \quad \beta_i^y(\mathbf{k}) = A_{\text{prim},i}^y(\mathbf{k}, \lambda) \exp \left\{ \frac{i2\pi}{\lambda} \mathbf{x}_i \cdot \mathbf{k} \right\}. \quad (2.4)$$

α_{iq} includes the secondary beam in terms of amplitude A_{sec} and the phase induced by the optical combiner:

$$\alpha_{iq}^x = A_{\text{sec},i}^x(\mathbf{r}_q, \lambda) \exp \left\{ \frac{i2\pi}{\lambda} \mathbf{x}_i \cdot \frac{\mathbf{r}_q}{f} \right\} \quad \text{and} \quad \alpha_{iq}^y = A_{\text{sec},i}^y(\mathbf{r}_q, \lambda) \exp \left\{ \frac{i2\pi}{\lambda} \mathbf{x}_i \cdot \frac{\mathbf{r}_q}{f} \right\}. \quad (2.5)$$

where f is the focal length of the optical combiner and \mathbf{r}_q the position of the bolometer¹.

The definition above assumes ideal horns. The propagation through a horn i , taking into account systematic effects, is modeled by the matrix

$$J_{\text{horn},i} = \begin{pmatrix} 1 - g_{x,i} & e_{x,i} \\ e_{y,i} & 1 - g_{y,i} \end{pmatrix}. \quad (2.6)$$

Finally, the complex electric field \mathbf{E} propagating through the HWP, the polarizing grid and the horn i is

$$\mathbf{E}_i = \alpha_{iq} \beta_i(\mathbf{k}) J_{\text{horn},i} J_{\text{pol}} J_{\text{rot}}^T J_{\text{hwp}} J_{\text{rot}} \mathbf{E} \quad (2.7)$$

where J_{rot} is the rotation matrix defined in section 1.3.2.

¹To be complete, α_{iq} should also include the gain of the bolometer, the integration over its surface and the integration over the frequency bandwidth.

2.1.3 Limiting the leakage from intensity to polarization

In this section, we want to justify the choice of using a rotating HWP followed by a polarizing grid. At the time of the current polarimeter design was made, three possibilities were considered:

1. the current one, a rotating HWP followed by a fixed polarizing grid so that the electric field entering the horn array is

$$\underline{E}_h = J_{\text{pol}} J_{\text{rot}}^T J_{\text{hwp}} J_{\text{rot}} \underline{E}. \quad (2.8)$$

As we have seen in section 1.3.2, this leads to a modulation of the intensity $S(t)$ at four times the HWP angular speed:

$$S(t) = |\underline{E}_h|^2 = \frac{1}{2} [I + Q \cos(4\Omega t) + U \sin(4\Omega t)]. \quad (2.9)$$

2. The second configuration that was studied is to use a rotating polarizing grid and no HWP so that the electric field entering the horn array is

$$\underline{E}_h = J_{\text{rot}}^T J_{\text{pol}} J_{\text{rot}} \underline{E}. \quad (2.10)$$

This leads to a modulation with a frequency twice higher than the angular speed

$$S(t) = \frac{1}{2} [I + Q \cos(2\Omega t) + U \sin(2\Omega t)]. \quad (2.11)$$

3. Finally, the third possibility is a fixed HWP followed by a rotating polarizing grid so that the electric field entering the horn array is

$$\underline{E}_h = J_{\text{rot}}^T J_{\text{pol}} J_{\text{rot}} J_{\text{hwp}} \underline{E}. \quad (2.12)$$

This leads to

$$S(t) = \frac{1}{2} [I + Q \cos(2\Omega t) - U \sin(2\Omega t)]. \quad (2.13)$$

The second possibility is the simplest one from the point of view of hardware. However, the first one was selected in order to limit the impact of systematic effects. This study was first performed around 2014 by Jean-Christophe Hamilton, using the *Mathematica* software for analytical calculation. I decided to reproduce it in the context of a project for L3 students I was supervising: Mustapha Aknine and Ludovic Goetz. We decided to use the *SageMath* free and open software which, as *Mathematica*, is made for analytical calculations.

We still follow the formalism developed by Marie-Anne. She actually realized a very similar study in order to decide between putting the HWP above or below the horn array (section 5.4.2 in her thesis [11]).

Considering systematic effects, the signal $S(t)$ can always be written as

$$S(t) = T_0 + T_{c4} \cos(4\Omega t) + T_{s4} \sin(4\Omega t) + T_{c2} \cos(2\Omega t) + T_{s2} \sin(2\Omega t) \quad (2.14)$$

where the terms T_i are linear combinations of the Stokes parameters I, Q, U . The aim is to measure Q and U . In the first configuration, Q is associated with T_{c4} and U to T_{s4} while in the two other cases, Q is associated with T_{c2} and U to T_{s2} . The goal is to avoid leakage of intensity I in the terms associated with polarization Q or U . Leakage between Q and U is less problematic because the two polarization components are of the same order of magnitude while the intensity is much higher. This will be justified in chapter 3. To give an example, in the case of the first configuration, we want to avoid terms of the type $T_{c4} = Q + \epsilon I$ where ϵ is a small error term but because $I \gg Q$, the effect is dramatic.

The terms T_i can be isolated after having performed a demodulation of the signal. Thus, we obtain a linear system which can be written in a matrix form

$$\begin{pmatrix} T_0 \\ T_{c4} \\ T_{s4} \\ T_{c2} \\ T_{s2} \end{pmatrix} = \begin{pmatrix} \square & \square & \square \\ \times & \times & \times \\ \times & \times & \times \\ \circ & \circ & \circ \\ \circ & \circ & \circ \end{pmatrix} \cdot \begin{pmatrix} I \\ Q \\ U \end{pmatrix} \quad (2.15)$$

where the $[5 \times 3]$ matrix contains the coefficients of the linear I, Q, U combinations. In the following, this matrix will be called M . The “ \square ” correspond to the T_0 term which gives the intensity, the “ \times ” are the terms which give Q and U in the case of the first configuration and the “ \circ ” give Q and U for the two other configurations. The problematic terms leading to leakage from I to Q or U are shown in red. The leakage between Q and U is shown in green.

Signal entering the horn array

We start by looking at the signal entering the horn array: $S(t) = |\underline{E}_h|^2$. In the ideal case, without any systematic error, the matrices of the three configurations are

$$M_1 = \begin{pmatrix} \frac{1}{2} & 0 & 0 \\ 0 & \frac{1}{2} & 0 \\ 0 & 0 & \frac{1}{2} \\ 0 & 0 & 0 \\ 0 & 0 & 0 \end{pmatrix}, \quad M_2 = \begin{pmatrix} \frac{1}{2} & 0 & 0 \\ 0 & 0 & 0 \\ 0 & 0 & 0 \\ 0 & \frac{1}{2} & 0 \\ 0 & 0 & \frac{1}{2} \end{pmatrix} \text{ and } M_3 = \begin{pmatrix} \frac{1}{2} & 0 & 0 \\ 0 & 0 & 0 \\ 0 & 0 & 0 \\ 0 & \frac{1}{2} & 0 \\ 0 & 0 & -\frac{1}{2} \end{pmatrix}. \quad (2.16)$$

Now we add systematic effects by considering the HWP and polarizer Jones matrices defined in 2.2. For each term of the matrix M we only keep the first order term by doing a Taylor expansion. The matrices of each configuration become

$$M_1 = \begin{pmatrix} U & 0 & 0 \\ 0 & U & -V \\ 0 & V & U \\ W & W & X \\ X & -X & W \end{pmatrix}, \quad M_2 = \begin{pmatrix} Y & 0 & 0 \\ 0 & 0 & 0 \\ 0 & 0 & 0 \\ 0 & Y & Z \\ 0 & -Z & Y \end{pmatrix} \text{ and } M_3 = \begin{pmatrix} U & -W & -X \\ 0 & 0 & 0 \\ 0 & 0 & 0 \\ W & U & -V \\ -X & -V & -U \end{pmatrix}. \quad (2.17)$$

with

$$\begin{aligned} U &= -\varepsilon_x - \frac{1}{2}h_x + \frac{1}{2}h_y + \frac{1}{2} & V &= \rho_x - \frac{1}{2}\xi_x - \frac{1}{2}\xi_y \\ W &= -\frac{1}{2}h_x - \frac{1}{2}h_y & X &= \frac{1}{2}\xi_x - \frac{1}{2}\xi_y \\ Y &= -\varepsilon_x + \frac{1}{2} & Z &= \rho_x. \end{aligned} \quad (2.18)$$

We already see that the third configuration is not adapted because the M_3 matrix presents leakage from I in Q and U , shown in red. However, it is not possible to select between 1 and 2 on this criteria. For that purpose, we need to push the calculation further, taking into account the propagation through the horns.

Signal arriving on a bolometer for a given baseline

We express analytically the signal arriving on a bolometer coming from one baseline (horn i , horn j). For that purpose, we compute

$$S(t) = |\mathbf{E}_i + \mathbf{E}_j|^2 \quad (2.19)$$

where \mathbf{E}_i and \mathbf{E}_j are the electric fields from horns i and j arriving on the bolometer.

For simplification, we assume that the beam is identical in the two directions x and y so that $\alpha_{iq}^x = \alpha_{iq}^y \equiv \alpha_{iq}$ and $\beta_i^x(\mathbf{k}) = \beta_i^y(\mathbf{k}) \equiv \beta_i(\mathbf{k})$. In order to simplify the expressions, we define three coefficients called A_i , A_j and A_{ij} such as

$$A_i = \frac{1}{2} |\alpha_{iq} \beta_i(\mathbf{k})|^2 \quad (2.20)$$

$$A_j = \frac{1}{2} |\alpha_{jq} \beta_j(\mathbf{k})|^2 \quad (2.21)$$

$$A_{ij} = \frac{1}{2} |\alpha_{iq} \beta_i(\mathbf{k}) + \alpha_{jq} \beta_j(\mathbf{k})|^2 = A_i + A_j + \text{Re}(\alpha_{iq} \beta_i(\mathbf{k}) \alpha_{jq}^* \beta_j^*(\mathbf{k})). \quad (2.22)$$

Thus, in the ideal case, with no systematic errors, when the two horns are open, the three matrices are

$$M_1 = \begin{pmatrix} A_{ij} & 0 & 0 \\ 0 & A_{ij} & 0 \\ 0 & 0 & A_{ij} \\ 0 & 0 & 0 \\ 0 & 0 & 0 \end{pmatrix}, \quad M_2 = \begin{pmatrix} A_{ij} & 0 & 0 \\ 0 & 0 & 0 \\ 0 & 0 & 0 \\ 0 & A_{ij} & 0 \\ 0 & 0 & A_{ij} \end{pmatrix} \quad \text{and} \quad M_3 = \begin{pmatrix} A_{ij} & 0 & 0 \\ 0 & 0 & 0 \\ 0 & 0 & 0 \\ 0 & A_{ij} & 0 \\ 0 & 0 & -A_{ij} \end{pmatrix}. \quad (2.23)$$

To include systematic errors, we decide not to make the difference between x and y components, i.e. $h_x = h_y = h$, $\xi_x = \xi_y = \xi, \dots$ so that the computing time is reasonable. Thus we obtain

$$M_1 = \begin{pmatrix} U & 0 & 0 \\ 0 & U & -V \\ 0 & V & U \\ -W & -W & 0 \\ 0 & 0 & -W \end{pmatrix}, \quad M_2 = \begin{pmatrix} U & 0 & X \\ 0 & 0 & -X \\ 0 & X & 0 \\ 0 & U & Z \\ 2X & -Z & U \end{pmatrix} \quad \text{and} \quad M_3 = \begin{pmatrix} U & -W & -X \\ 0 & 0 & X \\ 0 & X & 0 \\ -W & U & -V \\ 2X & -V & -U \end{pmatrix}. \quad (2.24)$$

with

$$U = -A_{ij}(2\epsilon + g_i + g_j - 1) - A_i(g_i - g_j) + A_j(g_i - g_j) \quad (2.25)$$

$$V = 2A_{ij}(\rho - \xi) \quad (2.26)$$

$$W = 2A_{ij}h \quad (2.27)$$

$$X = \frac{1}{2} A_{ij}(e_i + e_j) + \frac{1}{2} A_i(e_i - e_j) - \frac{1}{2} A_j(e_i - e_j) \quad (2.28)$$

$$Z = 2A_{ij}\rho. \quad (2.29)$$

This result justifies the choice of the first configuration which is the only one avoiding leakage from I to Q, U at first order (red terms). The leakage between Q, U at first order is present in any configuration (green terms).

Thus, we have seen how the QUBIC polarimeter has been optimized in order to limit systematic effects. Actually, the entire concept of bolometric interferometry was motivated by the control of systematics. Historically, the idea was to combine the sensibility of bolometers with the advantage of interferometry for the calibration of systematics. This is what we will see in the following.

2.2 Self-calibration principle

The control of systematic effects is a major issue for experiments targeting B -modes. The QUBIC interferometer was designed precisely with this objective in mind [10]. Interferometry offers the possibility to self-calibrate the instrument systematic effects. This technique has been used for a long time in radio astronomy, see for example [188].

2.2.1 Redundant baseline comparison

Self-calibration relies on the concept of equivalent (or redundant) baselines. One baseline b is formed with two horns: $b = [i, j]$. The number of baselines is $N_b = N_h(N_h - 1)/2$ where N_h is the number of horns. We consider radiation coming from direction \mathbf{n} and the horn positions are written \mathbf{d}_i . The phase difference between the electric fields emitted by horn i and horn j is such that

$$E_j(\mathbf{n}) = E_i(\mathbf{n}) \exp(2i\pi \mathbf{u}_b \cdot \mathbf{n}) \quad \text{where} \quad \mathbf{u}_b \equiv (\mathbf{d}_j - \mathbf{d}_i)/\lambda. \quad (2.30)$$

Two baselines b and b' are redundant if $\mathbf{u}_b = \mathbf{u}_{b'}$. An example is shown in Figure 2.3. The self-

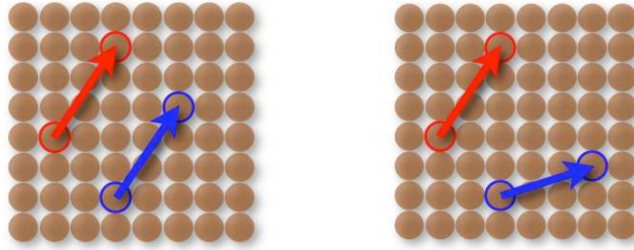


Figure 2.3: Illustration showing two equivalent baselines on the left and two non equivalent on the right for the TD 8×8 horn-array. Taken from [2].

calibration technique relies on the fact that in case of an ideal instrument without any systematic effect, equivalent baselines produce the same interference pattern on the focal plane, for an observation at infinity, in the Fraunhofer regime. Thus, by measuring the differences, one can calibrate the systematics of the instrument. The demonstration of this technique for QUBIC was the topic of the thesis by Marie-Anne Bigot-Sazy [13].

2.2.2 Number of baselines

As shown in [2], the baselines can be grouped into equivalence classes called β_i for which $\forall b, b' \in \beta, \mathbf{u}_b = \mathbf{u}_{b'} \equiv \mathbf{u}_\beta$. Considering a square array of horns, the number of classes is given by

$$N_{\neq} = 2\sqrt{N_h}(\sqrt{N_h} - 1) \quad (2.31)$$

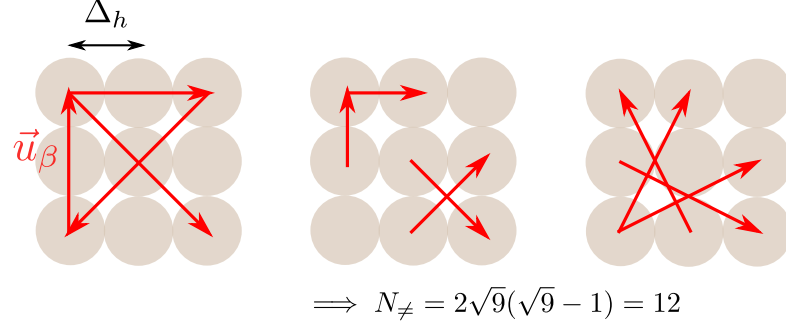
and the number of baselines contained in a given class is

$$N_{\text{eq}}(\beta_i) = \left(\sqrt{N_h} - \left| \frac{\mathbf{u}_\beta \cdot \mathbf{e}_x}{\Delta_h} \right| \right) \times \left(\sqrt{N_h} - \left| \frac{\mathbf{u}_\beta \cdot \mathbf{e}_y}{\Delta_h} \right| \right) \quad (2.32)$$

where Δ_h is the separation between horns. Those formula are illustrated in Figure 2.4 in the case of $N_h = 9$.

The full data analysis framework for self-calibration is not yet developed. However, in the following of this chapter I will present two analyses I performed using calibration data, one concerning the detector synthesized beam and the other concerning the interference fringes observed on the focal plane. Besides obtaining the detector inter-calibrations, we will see that we can also constrain the focal length of the optical combiner. This is a pedagogical illustration to show how QUBIC can observe itself thanks to interferometry. Thus, those two analyses can be seen as a first step toward a complete self-calibration.

All equivalence classes for $N_h = 9$:



Number of baselines in two classes β_1 and β_2 :

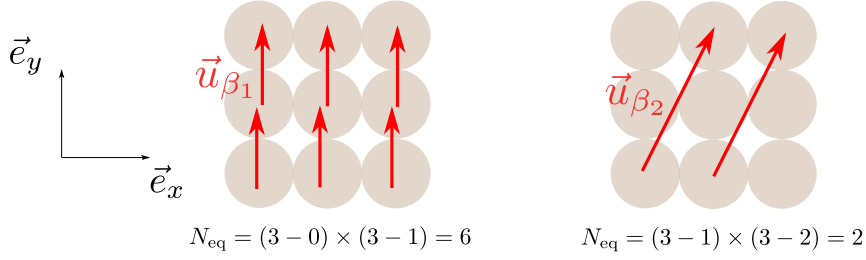


Figure 2.4: Illustration of the classes of equivalence in the case of $N_h = 9$.

2.3 Synthesized beam analysis

In section 1.2.5 we described the measurement of the full detector synthesized beams by scanning the calibration point source in the lab. Here, I present an analysis using the detector synthesized maps. This work is still in progress but I explain the method and I show the first results.

2.3.1 Synthesized beam maps

The QUBIC simulation software called `qubicsoft`² can be used to simulate the synthesized beam maps for each detector. Figure 2.5 shows the comparison between measurement and simulation for three detectors at 150 GHz, using the data set from April 2019. The position of the peaks is fit on each detector map assuming that they are positioned on a 3×3 square centered on the most intense peak. An example is shown in Figure 2.6. This model is far of being optimal especially because we do not always expect to see nine peaks. Depending on the detector, we may only see six or even four peaks, see for example TES 9 in Figure 2.6. This will certainly be improved in the next future.

2.3.2 Appropriate peak numbering

One difficulty is that the numbering shown in Figure 2.6 is not well defined. This is because the beam shifts on the sky from one detector to another and at some point the “central peak”, number 4, is not ever the same as in the previous detector maps. Figure 2.7 illustrates this phenomenon. We consider two detectors, TES 87 and 96 from ASIC 1, shown by a red point on the focal plane. The corresponding simulated synthesized beam is shown on the right. The 7×7 numbering grid moves with the synthesized beam and we see that the visible peaks are different between the two TES. For the first one, the central peak is number 24 while for the second one, it is 23. The colored zones on the focal plane split the detectors according to their most visible central peak which can be either 23, 24, 16 or 30. Thus, we need to identify each peak on the measured maps by the correct index using this 7×7 grid numbering.

Figure 2.8, shows the superposition of the nine peak positions detected by the fit for the 137 best synthesized beam maps. This data set comes from one of the first cool down and this is why many maps

²<https://github.com/qubicsoft/qubic>

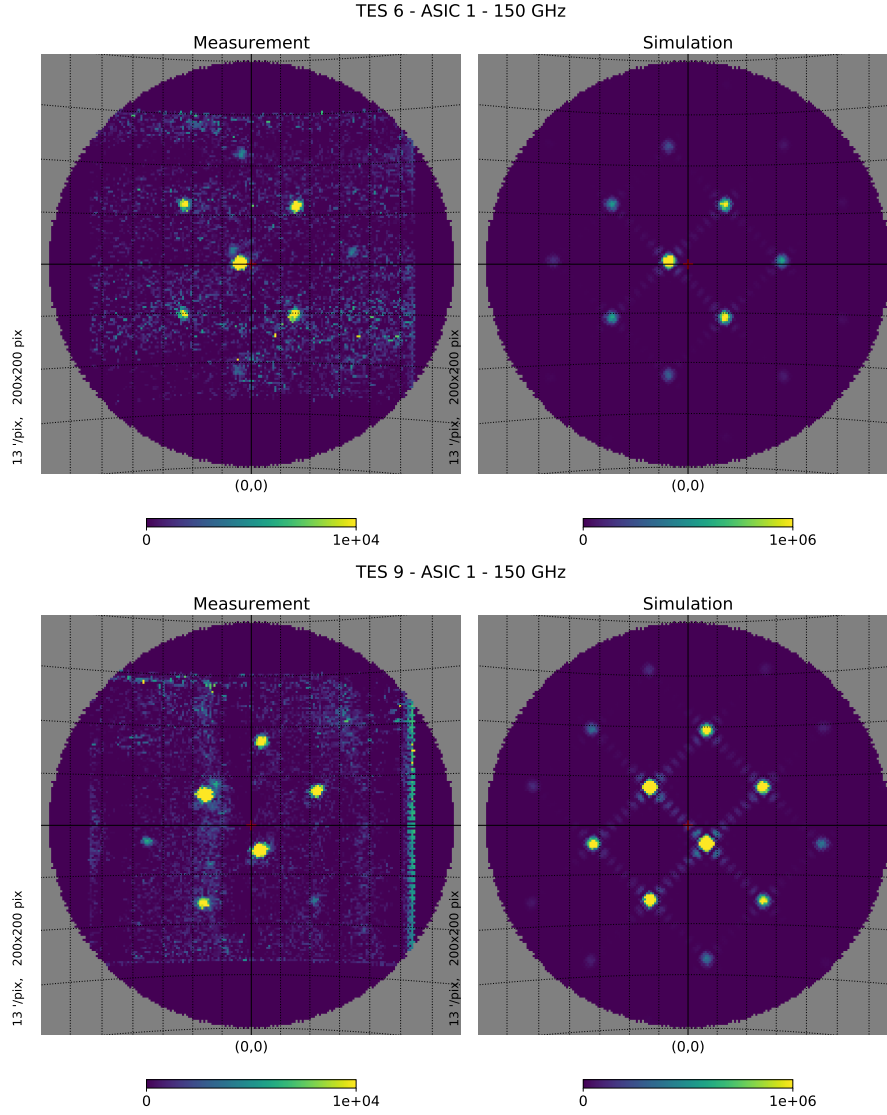


Figure 2.5: Comparison between measurement (left) and simulation (right) of the synthesized beam maps for two detectors at 150 GHz, using the data set from April 2019.

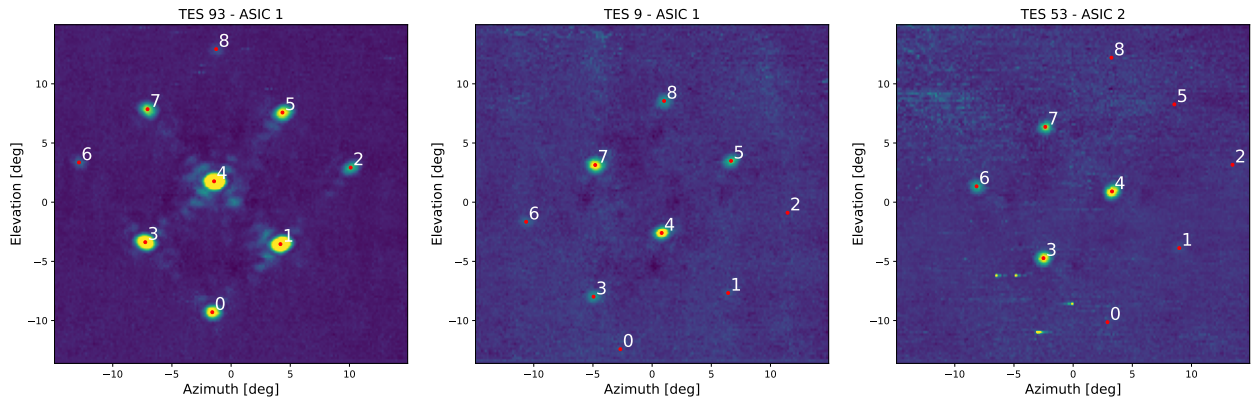


Figure 2.6: Fit of the synthesized beam peak positions for three detectors: TES 93 and 9 from ASIC 1 and TES 53 from ASIC 2 using the data set from April 2019 with the calibration source emitting at 150 GHz. Red points show the fit positions, numbered from 0 to 8.

are very noisy so I decided to remove them in the analysis because the fit is meaningless. The detector sensitivity was improved for the next cool downs. The peak numbering follows the one previously shown in Figure 2.6. As we can see, this numbering is not good.

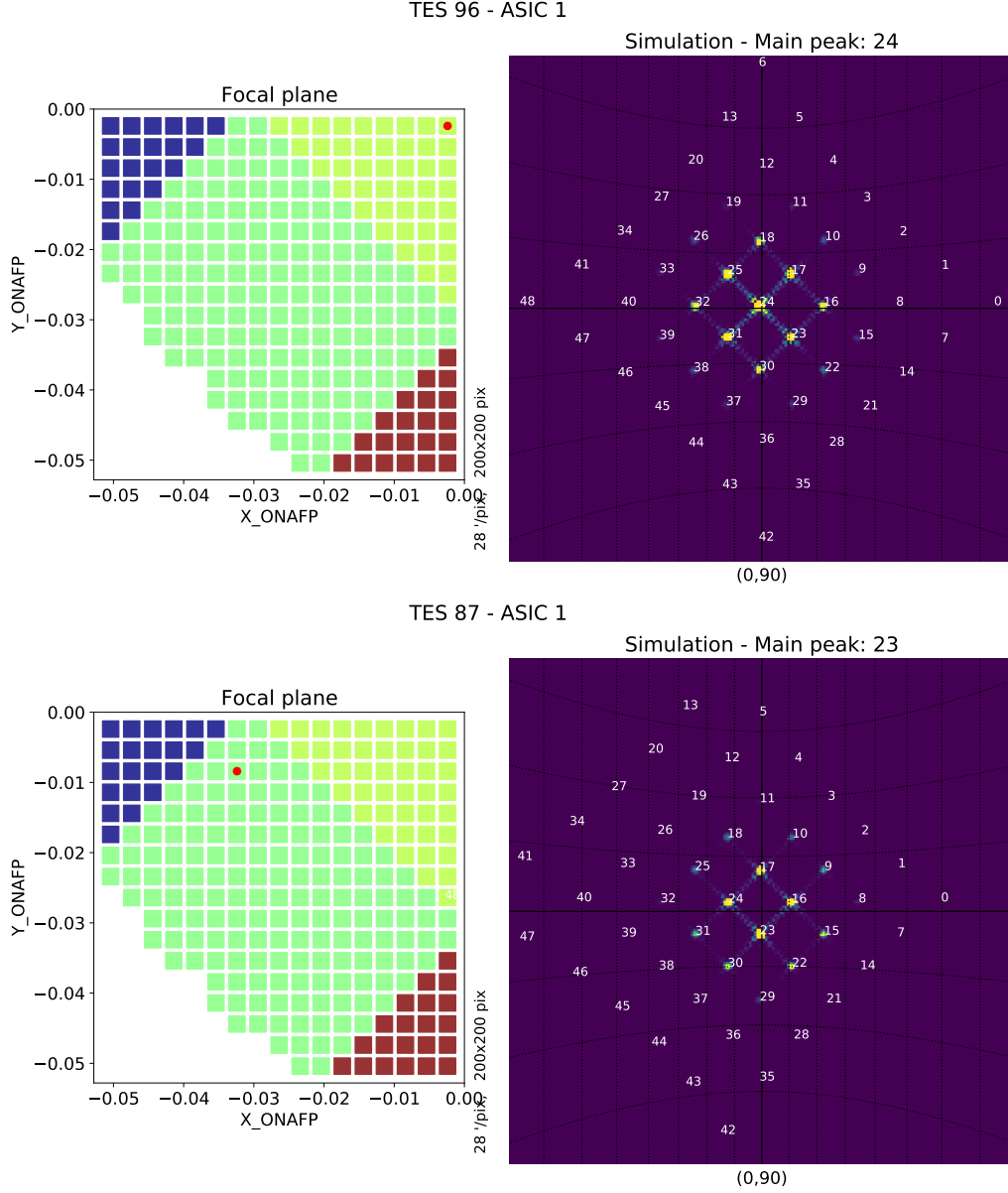


Figure 2.7: Absolute peak numbering. We consider two detectors, TES 87 and 96 from ASIC 1, shown by a red point on the focal plane. The corresponding simulated synthesized beam is shown on the right. The 7×7 numbering grid moves with the synthesized beam and we see that the visible peaks are different between the two TES. For the first one, the “central peak” is number 24 while for the second one, it is 23. The colored zones on the focal plane split the detectors according to their visible central peak which can be 23, 24, 16 or 30.

However, by identifying each detector peak with the correct number from the 7×7 grid, as shown in Figure 2.7, we obtain something which makes much more sense. This is shown in Figure 2.9, where the real data are compared with the simulation. Note that the points are at the same position as in Figure 2.8, we only changed the colors associated with the peak index. In this way, as expected, we clearly see the detector array shape projected on the sky for each peak of the synthesized beam.

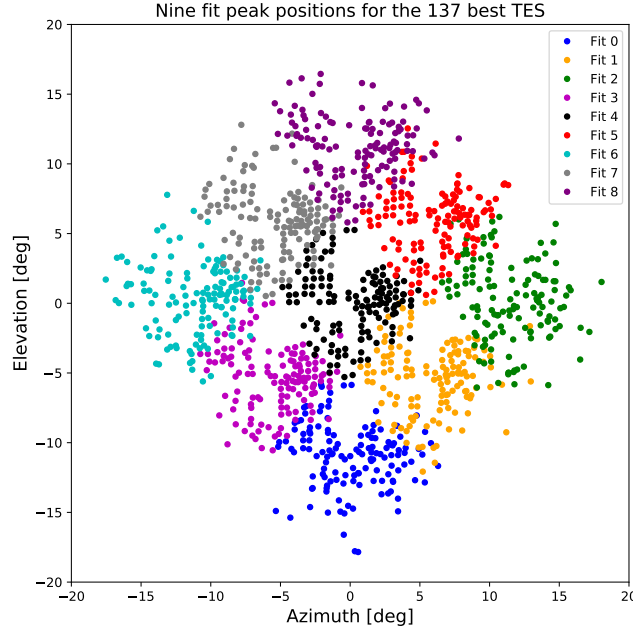


Figure 2.8: Superposition of the nine peak positions detected by the fit for the 137 best synthesized beam maps. The peak numbers from 0 to 8 follow the one previously shown in Figure 2.6.

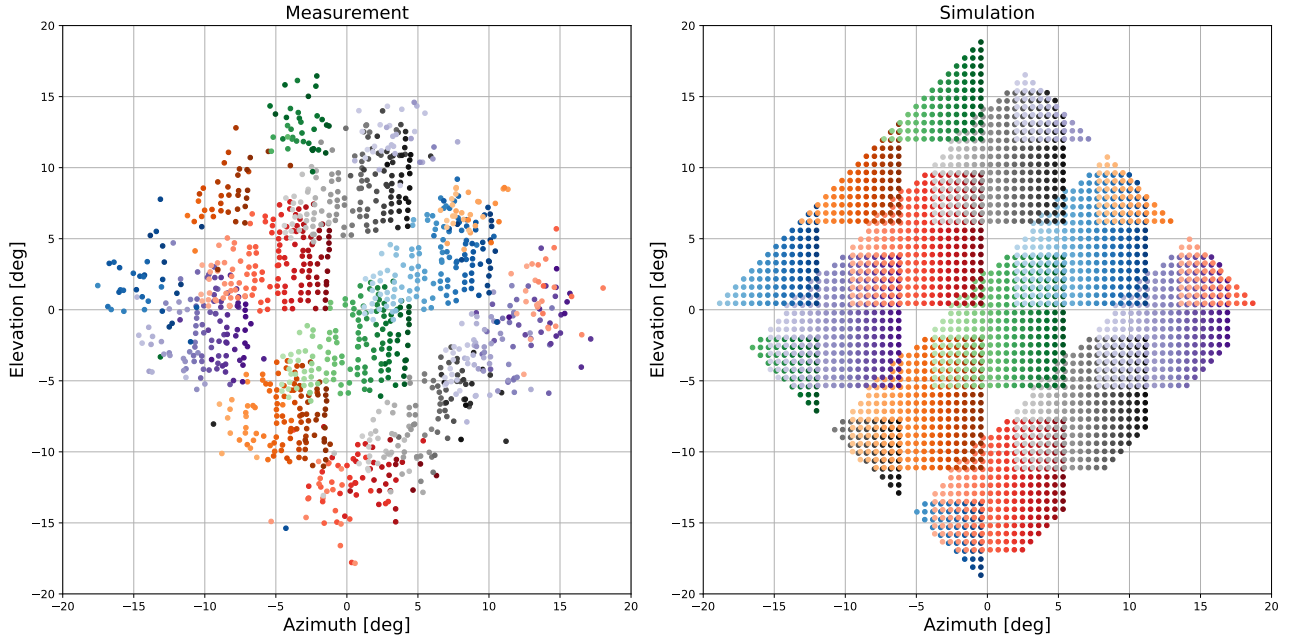


Figure 2.9: Measurement (left) compared to simulation (right) of the peak positions using the 7×7 numbering. The simulation considers a point source emitting at 150 GHz. The focal length of the optical combiner is equal to 30 cm.

2.3.3 Determination of the focal length of the optical combiner

First of all, determining the focal length of the optical combiner is not needed. It is more one exercise to explore the capabilities of bolometric interferometry. We know it is 30 cm but this analysis is a pretext to test how QUBIC can observe itself thanks to self-calibration.

We consider a given peak of the synthesized beam. This peak is shifted from one detector to another by an angle $\alpha \sim r/f$ where r is the distance between the two detectors and f is the focal length of the combiner. This was shown in chapter 1, section 1.2.5. This formula is rigorous only if one of the two detectors is placed at the center of the focal plane. If not, it is still possible to write an analytical formula and this is presented in annex A.4.

The effect of changing the focal length must not be confounded with that of changing the emission wavelength which modifies the space between the peaks of a given detector. Those two effects are illustrated in Figure 2.10 where on the top left, we show a simulation for $f = 40$ cm, $\nu = 150$ GHz and on the top right $f = 30$ cm, $\nu = 135$ GHz that must be compared to the bottom simulation for $f = 30$ cm, $\nu = 150$ GHz.

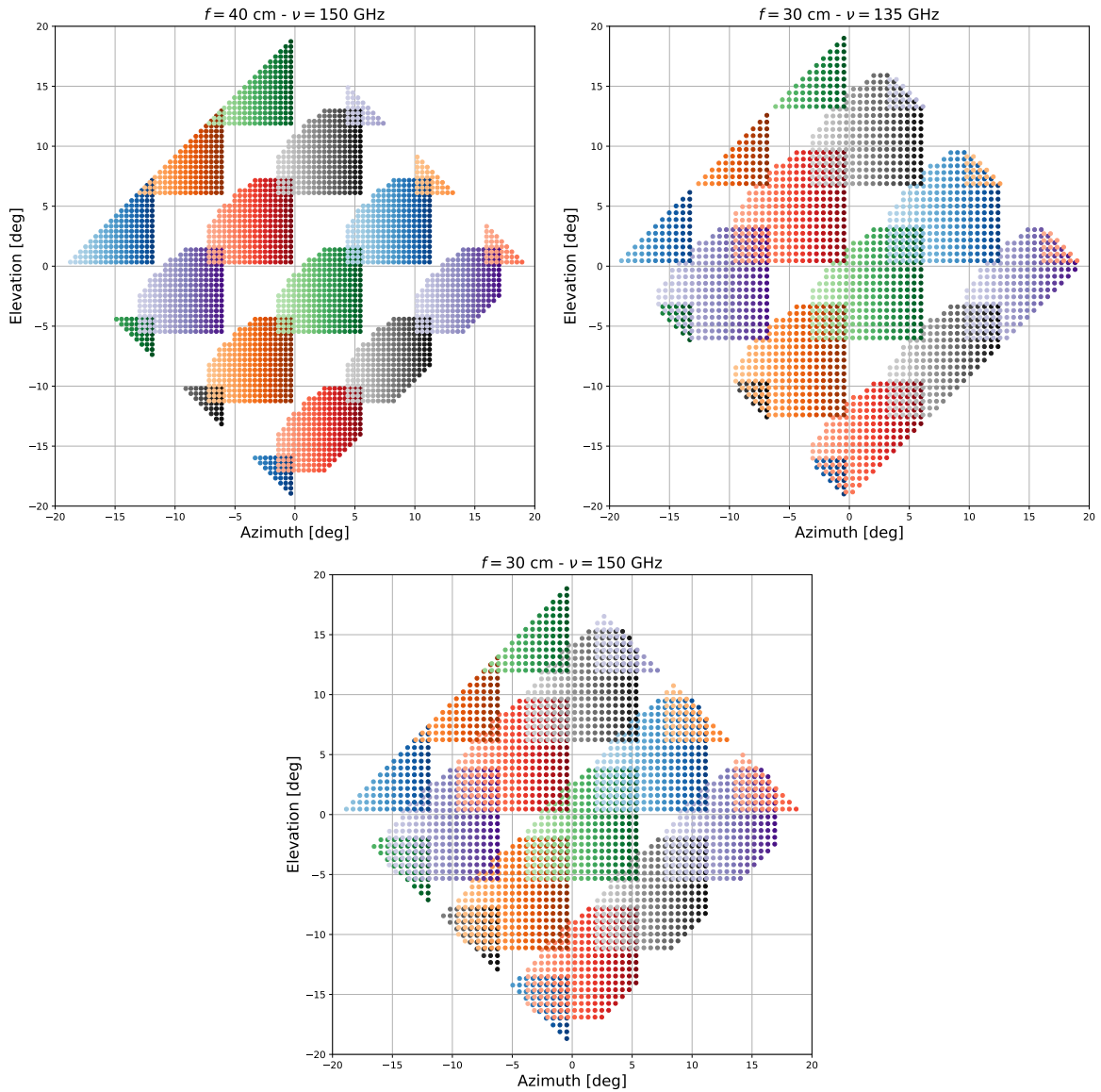


Figure 2.10: On the bottom I reproduce the simulation shown in Figure 2.9 at 150 GHz with a focal length equal to 30 cm. On the top left plot, I show the effect of changing the focal length, $f = 40$ cm keeping the frequency fixed. On the top right plot, I show the effect of varying the frequency of the calibration source, $\nu = 135$ GHz, keeping the focal length fixed.

In this section, we use the QUBIC software model to fit the focal length which is expected to be

$f = 30$ cm. For that purpose, each peak position (az, el) is translated in a unit vector \mathbf{u} , both for the theoretical and the experimental value. Then, the focal length is estimated by minimizing the χ^2

$$\chi^2(f) = \sum_{d,p} \frac{\theta_{d,p}^2}{\sigma_{d,p}^2} \quad (2.33)$$

where θ is the angle between the theoretical and the experimental unit vector ($\cos \theta = \mathbf{u}_{th} \cdot \mathbf{u}_{exp}$) and σ is the error associated with the experimental value. The sum is done over detectors d and peaks p . Note that the number of detectors which have a given peak vary. In this case, the number of degrees of freedom is equal to 1230. In Figure 2.11, we show the χ^2 as a function of the focal length between 20 and 47 cm. The minimum is obtained by interpolating the χ^2 values and then minimizing the interpolation function, using the `scipy` python library [212]. The errors on the fitted peak positions

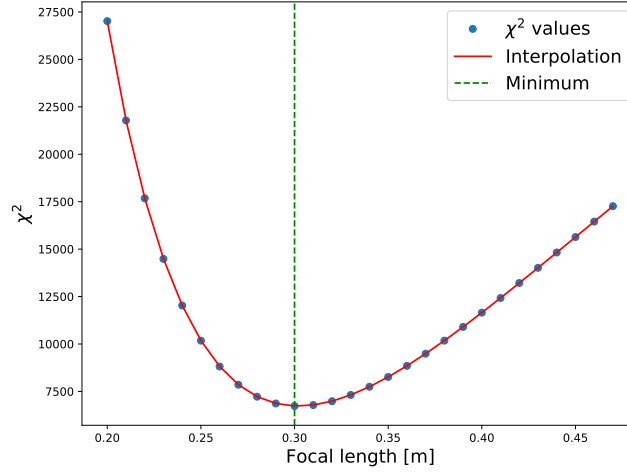


Figure 2.11: χ^2 value as a function of the focal length. The red line is an interpolation with a minimum shown by the green vertical line.

are actually unknown. This will be improved in the future. For now, we approximate the errors by the peak FWHM which is equal to 0.83° , which is probably over-estimated. Error on the focal length is estimated by looking at the values of the focal length such that $\chi^2(f) = \chi_{min}^2 + 1$ [48]. Finally, the focal length, assuming this model, is found to be

$$f = 30.00^{+0.02}_{-0.01} \text{ cm}. \quad (2.34)$$

However, this result must be taken with caution, especially because of the bad estimation of the errors. Moreover, this model with a single parameter is certainly too simple and this is why I decided to redo the fit assuming a more complex model.

As we can see in Figure 2.9, the measured positions look shifted, especially in azimuth compared to the simulation. This can be due to a shift of the calibration source with respect to the optical axis of the instrument. This shift can easily be fitted together with the focal length. The χ^2 is the same as 2.33 except that it now depends on three parameters: the focal length f and the two shifts in azimuth and elevation, δ_{az} and δ_{el} . To minimize the χ^2 , I used the `iminuit` python package [213], [214] which provides a powerful minimizer. I also compared with a minimization by a Monte-Carlo Markov Chain (MCMC), see the end of this section for a brief explanation about MCMC working principle. The `iminuit` minimization leads to

$$f = 32.7 \pm 0.2 \text{ cm}, \quad \delta_{az} = -1.34^\circ \pm 0.04^\circ \quad \text{and} \quad \delta_{el} = -0.53^\circ \pm 0.04^\circ. \quad (2.35)$$

The probability distributions obtained with the MCMC are presented in the corner plot, Figure 2.12. The values obtained with the `iminuit` minimization are superimposed with gray dashed lines on the plot. We see that the two methods, `iminuit` and the MCMC give compatible results. The reduced

χ^2 is 2.8 which is about two times smaller than in the case where only the focal length was fitted. However, again because of the bad estimation of the errors, this value must be taken with caution. The focal length is found to be around 32.7 cm which is much higher than the theoretical value of

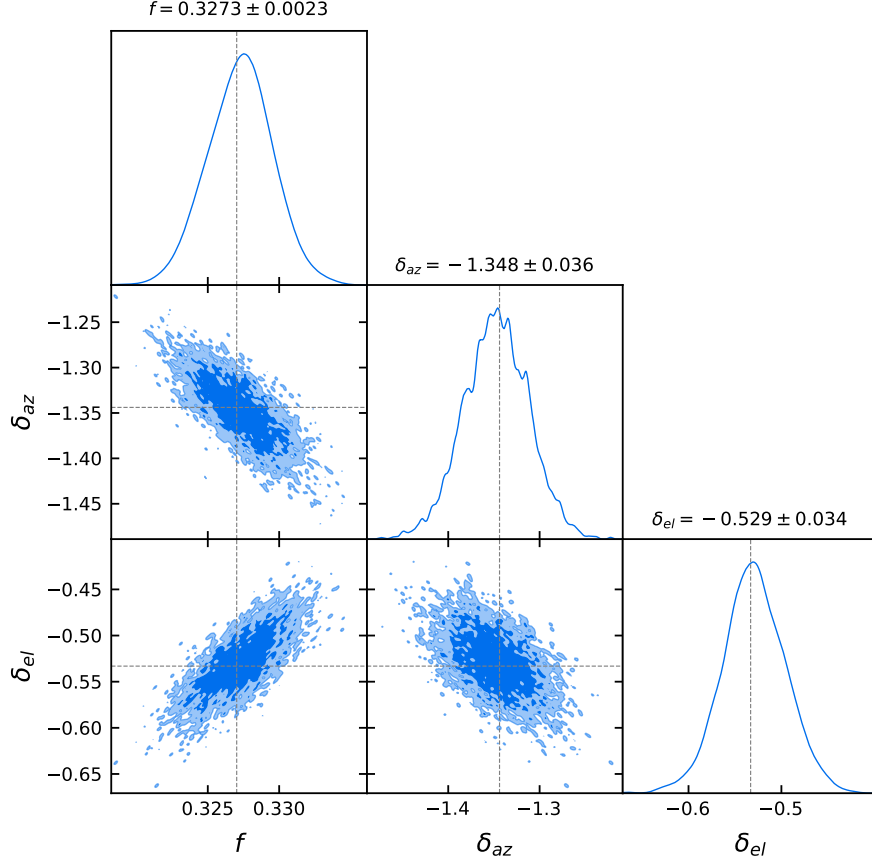


Figure 2.12: Probability distributions of the focal length f and the two shifts in azimuth and elevation, δ_{az} and δ_{el} , after running a MCMC. Results obtained with the `iminuit` minimization are shown with gray dashed lines.

30 cm from the optical design. I find the difference too high compared to the mechanical precision. This is why this result must be taken with caution and needs to be confirmed on others data sets. I see two effects that may induce such a shift in the analysis. The first one is that the fit of the peak positions was done on flat maps. It would be much better to use the spherical `Healpix` representation to avoid any distortion due to a projection effect. The second one is that the `qubicsoft` model does not take into account optical aberrations which may distort the peak positions. It would be better to use the optical model developed in Maynooth that I will describe in section 2.4.3. This may explain the difference between the measured and the expected value of the focal length.

Monte-Carlo Markov Chain working principle

A possibility to minimize the χ^2 is to sample the distribution using a MCMC. This is also a good way to get errors on the estimated parameters. This method was first presented in 1949 by Metropolis [215]. A Markov chain is a sequence of random variables $\{x_t\}$ for which the probability to obtain the state x_t only depends on the previous state x_{t-1} . It is defined by the initial state and the transition kernel which gives the rule to go from a step to the next one. Let us recall the Metropolis algorithm in one dimension (1D parameter space). We first choose a probability distribution $q(y|x)$, called candidate, which must be symmetric (i.e. $q(y|x) = q(x|y)$) and easily computed, for example a Gaussian or uniform distribution. Then, we do

1. Initialization: start from x_0

2. At iteration t , do:

- Propose the next point \tilde{x} using the candidate law $q(x_{t+1}|x_t)$.
- Compute the acceptance rate

$$\alpha(\tilde{x}, x_t) = \frac{f(\tilde{x})}{f(x_t)}. \quad (2.36)$$

where f is a function proportional to the distribution we want to sample. Then there are two possibilities:

- If $\alpha \geq 1$ then \tilde{x} is accepted and $x_{t+1} = \tilde{x}$.
- However, if $\alpha < 1$ there is still a chance to accept \tilde{x} : a number u is generated following a uniform distribution between 0 and 1 and \tilde{x} is accepted only if $u \leq \alpha$. If not, \tilde{x} is rejected and $x_{t+1} = x_t$.

3. Go to step $t + 1$

4. Stop after N iterations, once the chain has converged.

2.3.4 Prospective for this work

This analysis must be seen as a first step. Indeed, we only recently understood the peak numbering issue. This first analysis looks very promising and will be pursued in different ways:

- The fit of the peak positions can be improved a lot: including directly the correct peak numbering and performing the fit on spherical maps instead of flat projections. Moreover, realistic errors on the fitted peak positions must be estimated.
- We will use the optical instrument model developed in Maynooth which provides much more realistic simulations, especially to take into account optical aberrations.
- We will apply it to data sets acquired at various calibration source frequencies.
- We will study the distortions of the peak positions due to optical aberrations and see how they evolve with the detector position on the focal plane.
- So far, I only worked with the positions of the synthesized beam peaks. However, the amplitudes are an important source of information too. For example, they could be used to inter-calibrate the gains of the bolometers. In the next section, I propose a way of doing that using interference fringes but I finally wonder if the synthesized beam maps would not be better for that purpose...

In conclusion, this work is a major step for the calibration of the instrument. As we will see in chapter 5, map-making requires to know the synthesized beam with accuracy so this work will be crucial to build the sky maps from the timeline data.

In the following, I will focus on the measurement of the interference fringes on the focal plane, i.e. the Point Spread Function of the telescope when only two horns are open. This measurement is fundamental because self-calibration is based on the comparison of redundant baselines. I will start by presenting optical simulations that I developed in order to compare with calibration data. Then I will describe the data taking and data analysis procedure to get the fringes. Finally, I will present a method to inter-calibrate the detectors by fitting the data with simulations.

2.4 Simulate interference fringes on the focal plane

I built a library, called `selfcal_lib`, which is part of the `qubicsoft` package in order to simulate the intensity, and especially the interference fringes, on the focal plane. This library was developed with the goal of making comparisons between simulations and real calibration data.

2.4.1 QUBIC soft simulations

The first possibility for simulating fringes is to use the `qubicsoft` package which calculates the interference at infinity using geometric optics. This is computed as if the horn plane and the focal plane were parallel which is not the case on the real instrument. The Global Reference Frame (GRF) and ON-Axis Focal Plane (ONAFP) reference frames are defined on Figure 2.13 under the `qubicsoft` approximation that the two planes are parallel. Thus, in the `qubicsoft` a simple $\pi/2$ rotation is needed to pass from the GRF to the ONAFP frame which is not the case on the real instrument. Originally,

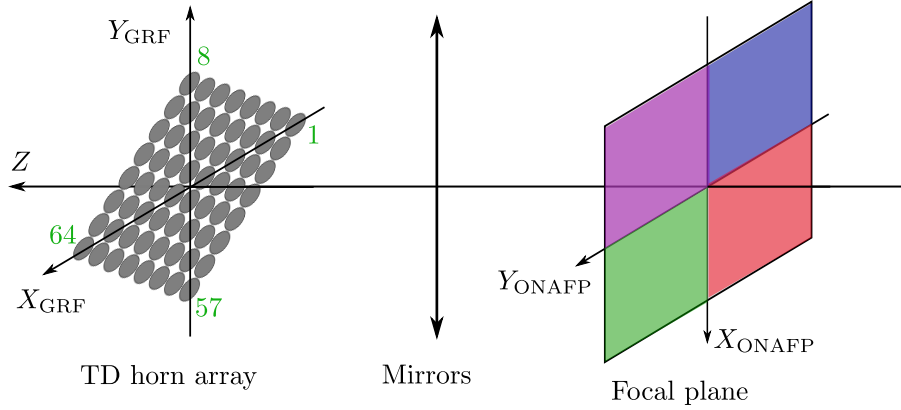


Figure 2.13: GRF and ONAFP frames as defined in the `qubicsoft` package. Green numbers indicates the TD horn array orientation. On the focal plane, the four colors corresponds to the four quadrants.

everything in `qubicsoft` was defined in the GRF frame. However, when comparing between simulations and calibration data, we realized it was convenient to work in the ONAFP frame, which is the intuitive frame for the detector plane. Indeed, on the real instrument, it does not make sense to work with the GRF frame only.

Another tricky point to match simulations with calibration data is the horn and TES numbering.

Horn numbering: The `qubicsoft` package is usable for the TD and FI instruments. The TD horn array, corresponding to the center of the FI horn array, only has 64 horns while the FI horn array has 400 horns. The `qubicsoft` horn calibration files are defined in the GRF frame. The calibration file uses the instrument numbering, the one used for example to command the optical switches. Horns are indexed from 1 to 64 for the TD and 1 to 400 for the FI. This is shown in Figure 2.14 (left). On the contrary, the indices defined in the `qubicsoft` package consider that the FI horn array is placed on a squared grid 22×22 , numbered from 0 to 483. This is shown in Figure 2.14 (right). In the following, I will define TD baselines by the red indices and FI baselines by the blue indices.

Detector numbering: On the focal plane, detectors are grouped in four quadrants, and each quadrant contains two ASICs. This is shown in Figure 2.15. The TD only has quadrant 3 with ASIC 1 and 2. Each ASIC has 128 detectors, numbered by the TES index going from 1 to 128. However, among the 128 detectors, they are four thermometers with indices 4, 36, 68 and 100 which are treated like TES during data taking.

Regarding the `qubicsoft` detector numbering, the detector calibration file is defined in the ONAFP frame. It uses a natural ordering, shown in Figure 2.16 (left) so that the first quadrant is placed on the upper right quadrant and the position of the other arrays is obtained by rotating the first array by 90, 180 and 270 degrees. Moreover, a second indexing is used in `qubicsoft`: the focal plane is placed on a square array with dimension 34×34 and TES are numbered on a grid going from 0 to 1155 as shown in Figure 2.16 (right). Tools have been developed to convert indices from one numbering to another,

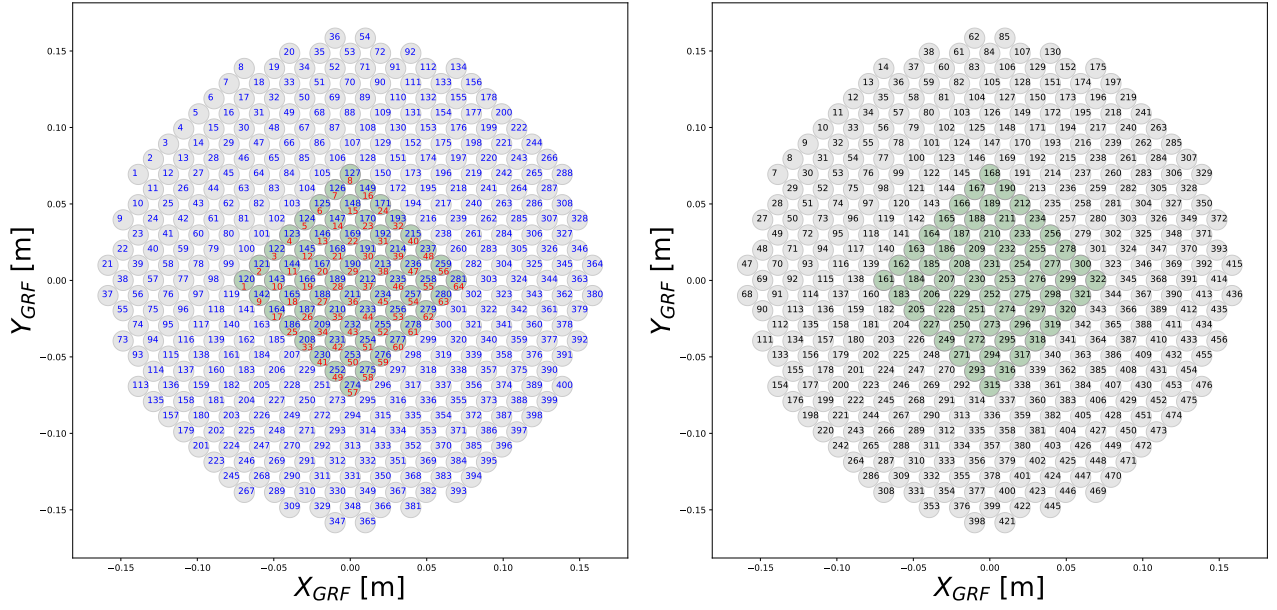


Figure 2.14: *Left*: Horns indices going from 1 to 400 for the FI and from 1 to 64 for the TD. *Right*: Horn indices defined in the `qubicsoft` package considering that the FI horn array is placed on a squared grid 22×22 , numbered from 0 to 483.

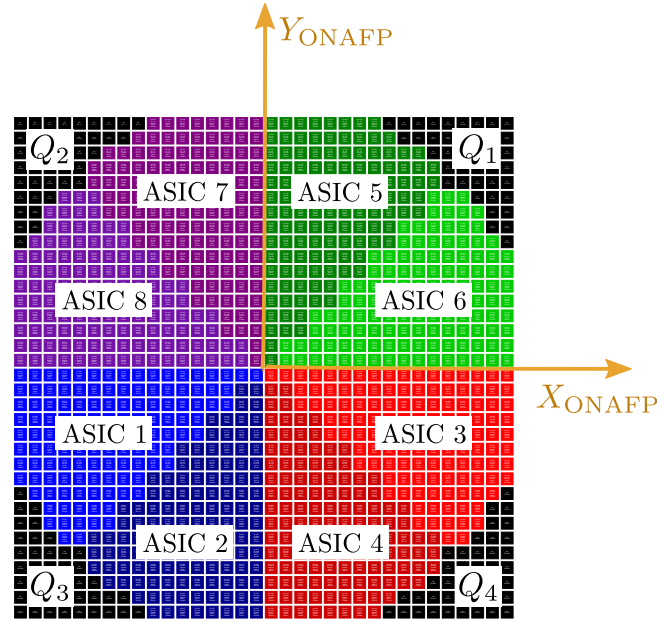


Figure 2.15: Quadrants and ASIC numbering on the focal plane, defined in the ONAFP frame.

especially in the `qubicpack` package³ developed for data reading, visualization and analysis.

An example of a `qubicsoft` fringe simulation is shown in Figure 2.17, considering the TD [49-51] baseline. The absolute power is arbitrary, it is fixed by the spectral radiance of the source. Only relative differences are significant.

³<https://github.com/satorchi/qubicpack>

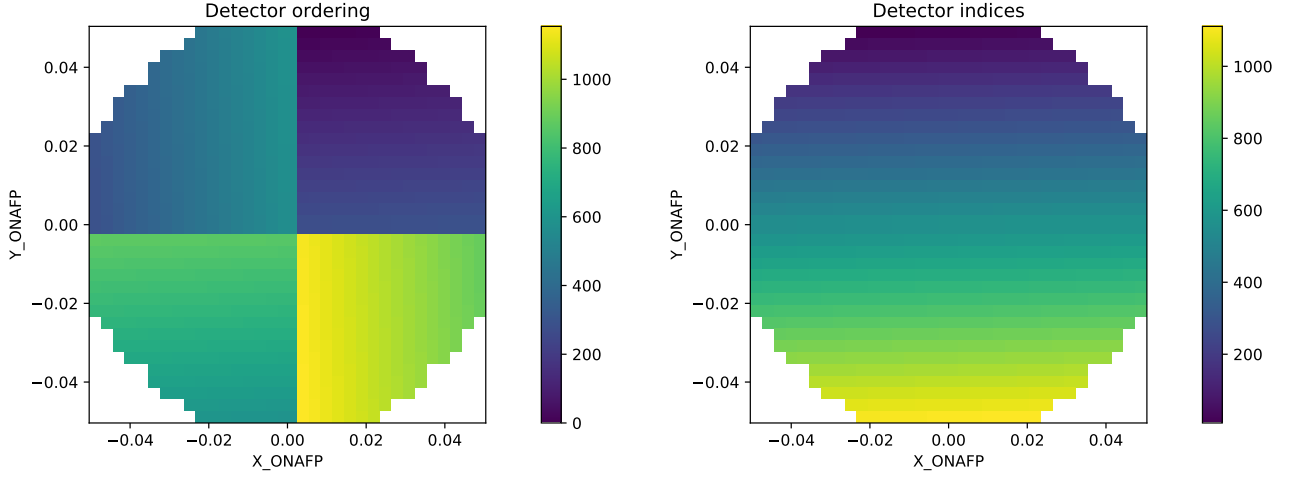


Figure 2.16: *Left*: TES ordering defined in the `qubicsoft` calibration detector file. *Right*: `qubicsoft` detector indexing.

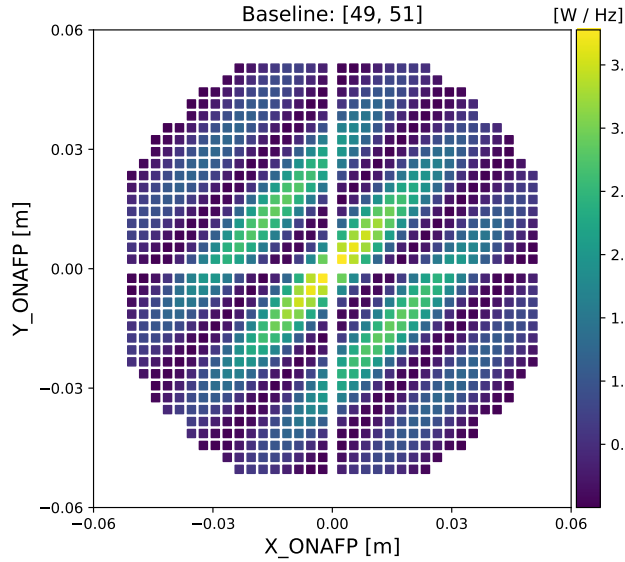


Figure 2.17: Fringes obtained on the focal plane with the `qubicsoft` model for TD [49-51] baseline, considering an on-axis point source. The FI entire focal plane is shown although the TD only has one quarter of the focal plane. The absolute power is arbitrary, only relative differences are significant.

2.4.2 Analytical model

The second possibility to simulate fringes is an analytical model with a two dimension sine function. We consider a point source in the far field with zenith angle θ and azimuth angle φ in the GRF frame. The fringe signal F at position (x, y) on the focal plane is

$$F(x, y) = A \cos \left(\frac{2\pi}{i_f} (x \cos \alpha + y \sin \alpha) + \phi \right) \times G \quad (2.37)$$

where

- A is the amplitude.
- i_f is the inter-fringe distance: $i_f = \lambda f / L$ where λ is the light wavelength, f the focal length and L the baseline length (distance between the two horns).
- α is the baseline orientation angle with respect to the x axis so that $(x \cos \alpha + y \sin \alpha)$ defines the baseline direction, perpendicular to the fringes.
- ϕ is a phase given by $\phi = \frac{2\pi}{\lambda} r \sin \theta$ where r is the radial distance of the baseline center (middle point between the two horns).
- Finally, G is a 2D Gaussian that models the primary beam. It is centered at the geometrical image of the source ($x_c = f \tan \theta \cos \varphi$, $y_c = f \tan \theta \sin \varphi$). The code has an option to include or not the Gaussian.

An example is shown in Figure 2.18 for baseline [49-51] with an on-axis point source ($\theta = \varphi = 0$).

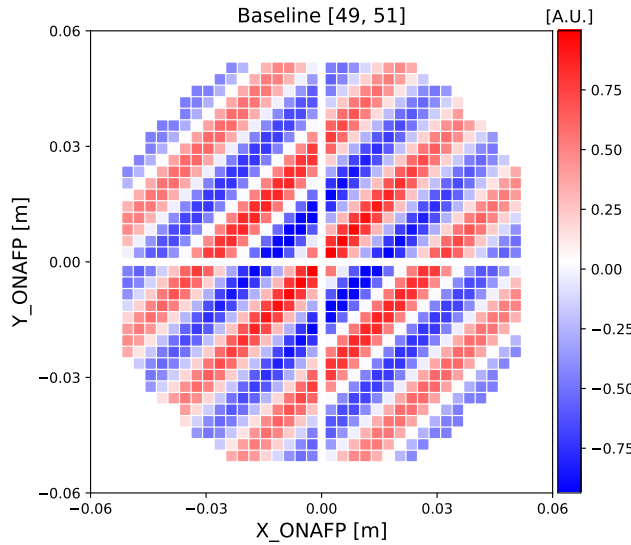


Figure 2.18: Fringes obtained on the focal plane with the analytical model for TD [49-51] baseline, considering an on-axis point source. The FI entire focal plane is shown but the TD instrument only has the x and y negative quarter in the ONAFP frame. The negative signal is not relevant, only relative difference are significant.

2.4.3 Maynooth simulations

Finally, a third type of optical simulations, far more realistic, is developed in Maynooth University. Simulations are performed using GRASP (a commercial optical modeling software) and MODAL (Maynooth University). Details of the QUBIC optics modeling are given in [6]. While both software packages model systems using the technique of physical optics, there are differences in how systems are implemented which make them complementary. MODAL can calculate the coupling of beams from free-space to

feedhorns, while **GRASP** considers feedhorns to be point sources. However, **GRASP** can describe surfaces using a grid of points which permits the modeling of real measured mirror surfaces, and then using the physical theory of diffraction, **GRASP** can model mirror edge effects. The two packages can exchange data through common file formats which permits the analysis of a complete optical system, using the best package for each subsystem and then combining the results. They can also be used independently and compared as a verification of modeling results. A model was created in **GRASP** to match the **MODAL** model. This model provides the electric field (amplitude and phase) on the focal plane for each horn separately.

In the **qubicsoft** package, I implemented a way to plot the intensity on the focal plane for any configuration of the horn array using the output files from the **MODAL** simulations. The **MODAL** simulations compute the electric field on a circular region slightly larger than the real FI focal plane and with a much higher resolution (241×241 pixels) than the one provided by the bolometer array (992 detectors placed on a 34×34 square grid). The full resolution image can be set at the instrument resolution by two methods: either by interpolating the image and then integrating in each detector area or simply by averaging the pixels in each detector area. The first method is more rigorous but takes much more computation time and because the **MODAL** resolution is very high, it makes very small difference. An example is shown in Figure 2.19. Contrary to the analytical or the **qubicsoft** model, the Maynooth simulations take into account optical aberrations mainly caused by the off-axis optical combiner [6]. This is visible in Figure 2.19 where the fringes are curved. This breaks the symmetry between opposite quadrants, for example upper-left and bottom-right.

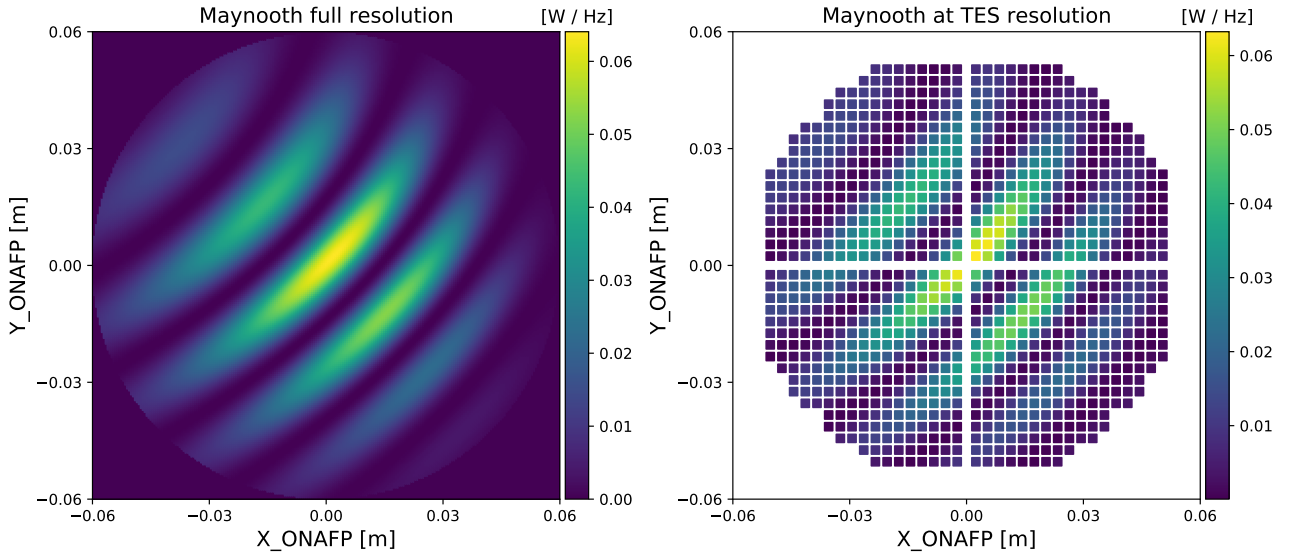


Figure 2.19: Fringes obtained on the focal plane with the output files from **MODAL** simulation model plotting with the **qubicsoft** package. We show fringes for TD [49-51] baseline, considering an on-axis point source. *Left*: A region slightly higher than the FI focal plane at high resolution is shown. *Right*: The FI focal plane is shown even if the simulation considers the TD optics (8×8 horn array, smaller mirrors...). Remember that on the TD, we only have the third quadrant, placed at the bottom left. The signal has been integrated in each detector.

The comparison of the output of the models for a given baseline is presented in [8]. This is one of my contributions to this paper and it is a good verification to validate the different simulation methods.

We now have three independent models to simulate the fringes on the focal plane. In the next section I will describe the procedure to measure the fringes in the laboratory.

2.5 Measurement and data analysis to obtain fringe images

2.5.1 Combination of images

In order to measure interference fringes, the simplest way would be to close all the horns except one baseline. The mechanical switches for the horns, shown in Figure 1.6 can be activated independently. However, in case of the TD instrument, only two horns can be closed at the same time. It is because a current is required to keep the shutter closed, and this generates heat so we can not activate more than two at a time in order to keep the cryogenics stable. The system and performance are described in [5]⁴.

In this section, we will see that it is nevertheless possible to measure fringes by doing a combination of images acquired by closing two horns at maximum. This calculation was already presented in [13] (Appendix A) but an error was noticed by Cr  idhe O’Sullivan after publication. Here I give the correct version.

We note E_i the complex field coming from horn i at a particular bolometer and the associated power $C_i = |E_i|^2$. We want to measure the power when one baseline [horn i - horn j] is open:

$$S_{ij} = C_i + C_j + 2 \operatorname{Re}(E_i E_j^*). \quad (2.38)$$

This corresponds to a fringe pattern on the focal plane. However, as said before, this measurement is not directly feasible as we can not open only one baseline.

We note S_{tot} the power when all horns are open, C_{-i} when all horns are open except i and S_{-ij} when all horns are open except i and j . Figure 2.20 shows the different configurations for the FI.

The total power for all horns open is

$$S_{\text{tot}} = \left| \sum_{m=1}^{N_h} E_m \right|^2 = \sum_{m=1}^{N_h} |E_m|^2 + \sum_{m \neq l} 2 \operatorname{Re}(E_m E_l^*), \quad (2.39)$$

where N_h is the total number of horns (64 in the case of the TD). The second sum groups the interference terms between each horn pair. The power for all horns open except horn i is

$$C_{-i} = \left| \sum_{m \neq i}^{N_h-1} E_m \right|^2 = S_{\text{tot}} - C_i - \sum_{k \neq i} 2 \operatorname{Re}(E_i E_k^*), \quad (2.40)$$

where the sum is the interference term between horn i and all the others. Finally, the power for all horns open except horns i and j is

$$S_{-ij} = S_{\text{tot}} - C_i - C_j - \sum_{k \neq i} 2 \operatorname{Re}(E_i E_k^*) - \sum_{k \neq j} 2 \operatorname{Re}(E_j E_k^*) + 2 \operatorname{Re}(E_i E_j^*). \quad (2.41)$$

Note that the last term must be added not to remove twice the $[i, j]$ baseline with the two sums. Using equation 2.40, we obtain

$$\begin{aligned} S_{-ij} &= S_{\text{tot}} + C_{-i} - S_{\text{tot}} + C_{-j} - S_{\text{tot}} + 2 \operatorname{Re}(E_i E_j^*) \\ &\Rightarrow 2 \operatorname{Re}(E_i E_j^*) = S_{-ij} - C_{-i} - C_{-j} + S_{\text{tot}}, \end{aligned}$$

and by replacing in equation 2.38, we finally get

$$S_{ij} = C_i + C_j + S_{-ij} - C_{-i} - C_{-j} + S_{\text{tot}}. \quad (2.42)$$

This expression differs from the result presented in Appendix A of [13] where by combining equations (A2) and (A8) one can find a similar expression but the term S_{tot} is missing.

⁴The FI switch system is different and it will be possible to close simultaneously any number of switches. However, closing all the horns except two changes significantly the thermal load arriving on the detectors. So even in the case of the FI, it is not clear that we will use this new feature for calibration.

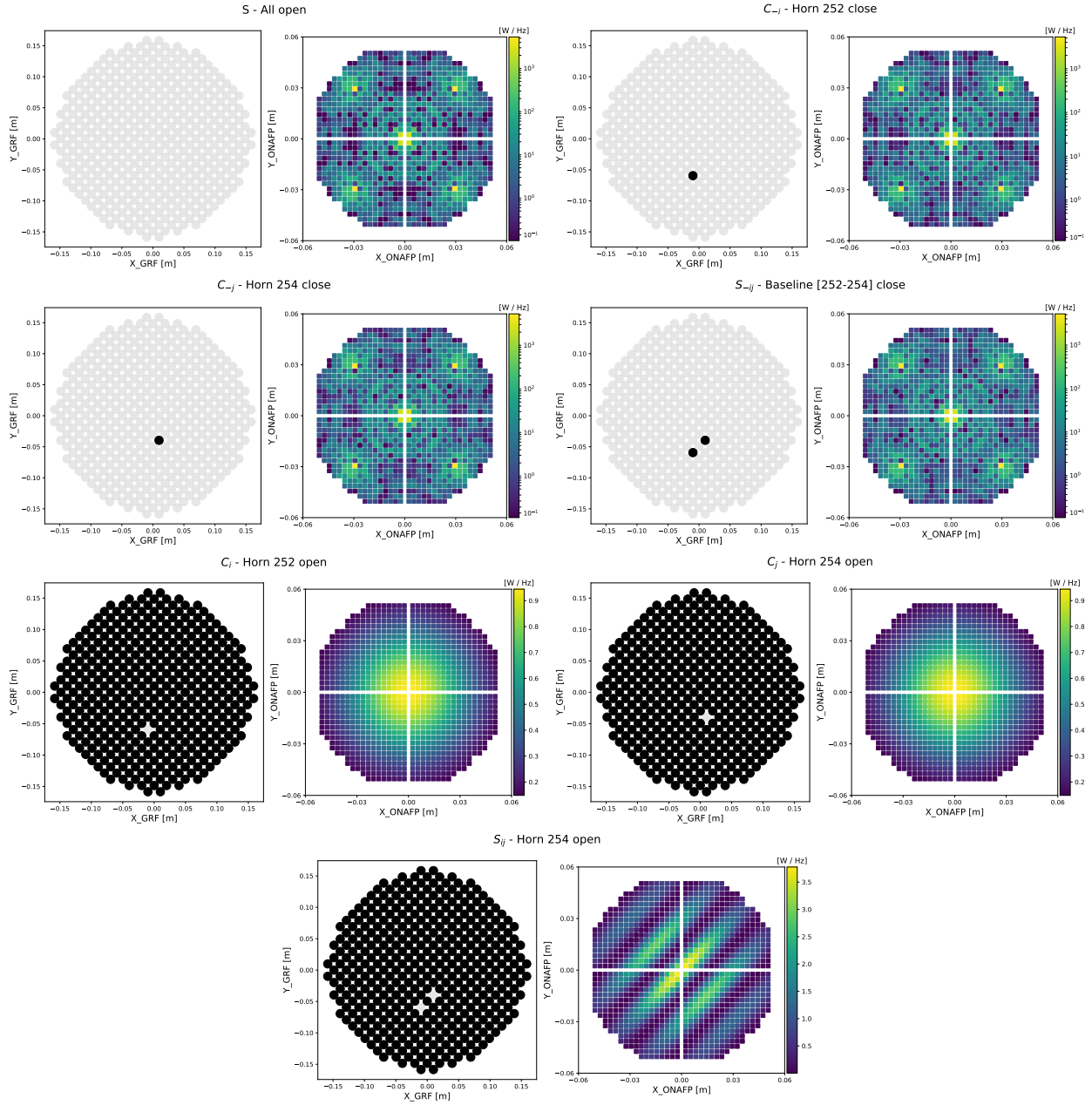


Figure 2.20: Horn array and image on the focal plane for each configuration: S_{tot} , C_{-i} , C_{-j} , S_{ij} , C_i , C_j and S_{ij} for the FI baseline [252, 254].

Thus, by observing C_i , C_j , S_{-ij} , C_{-i} , C_{-j} and S_{tot} separately and by making the linear combination given by 2.42, one can reconstruct S_{ij} . The problem is that we can not observe C_i and C_j as we would have to close all horns except one. However, C_i and C_j correspond to the secondary beam of one horn so they will not change the interference image (see Figure 2.21). So finally, to get the fringe pattern, one can make the “reduced” combination:

$$S_{ij} \sim S_{-ij} - C_{-i} - C_{-j} + S_{\text{tot}}. \quad (2.43)$$

Note that the reduced measurable configuration has negative values contrary to the complete one.

2.5.2 Data taking process

We describe the measurement of fringes on the focal plane for a given baseline $[i, j]$. The calibration source emits at 150 GHz with no modulation (Direct Current mode). The instrument is fixed with respect to the calibration source (no scan). The two horns are closed one by one following the six steps:

TD baseline: [49, 51]

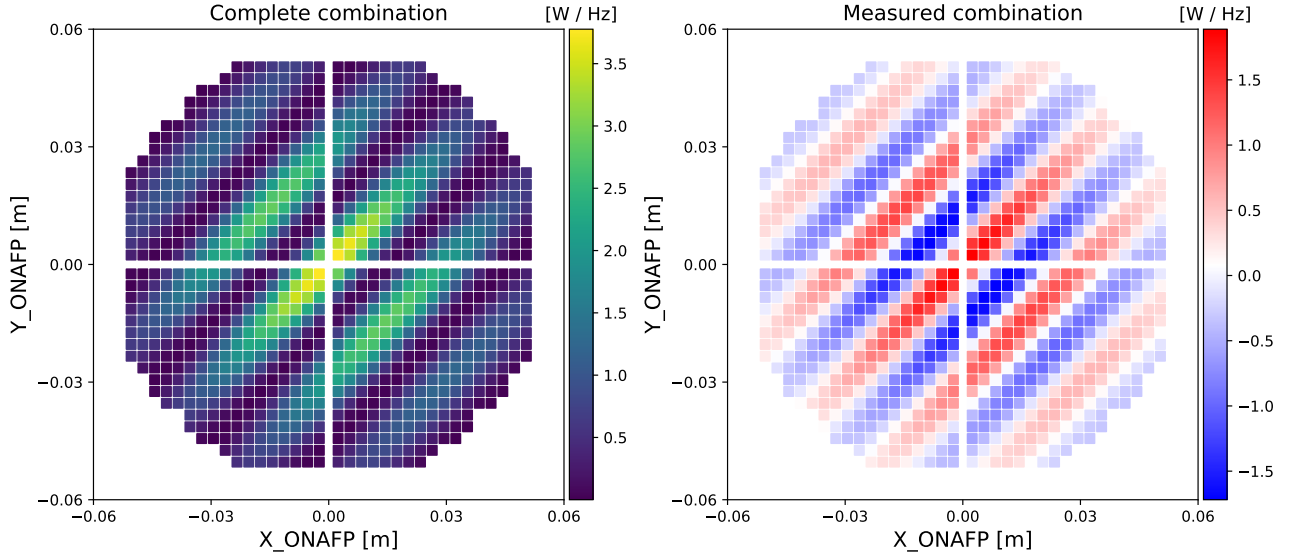


Figure 2.21: The complete combination $S_{-ij} - C_{-i} - C_{-j} + S_{\text{tot}} + C_i + C_j$ compared to the reduced measurable one: $S_{-ij} - C_{-i} - C_{-j} + S_{\text{tot}}$. The fringe pattern is the same in both cases. However the measured combination has negative values, highlighted by the red and blue color map.

1. All open $\Rightarrow S_{\text{tot}1}$
2. Close horn $i \Rightarrow C_{-i}$
3. Close horn j (so i and j are closed) $\Rightarrow S_{-ij}$
4. All open $\Rightarrow S_{\text{tot}4}$
5. Close horn $j \Rightarrow C_{-j}$
6. All open $\Rightarrow S_{\text{tot}6}$

The index 1, 4 or 6 added to S_{tot} corresponds to the step number. The duration of each step, called waiting time, is a few seconds (1, 3 or 5 s depending on the data set), and the cycle is repeated many times (from 10 to 1000 times). Figure 2.22 shows a simulation of the expected TOD for two detectors. As we can see, the shape of the cycle is not intuitive and differs a lot from one TES to another. This is due to changes in the interference pattern when closing one or two horns. The focal plane of the

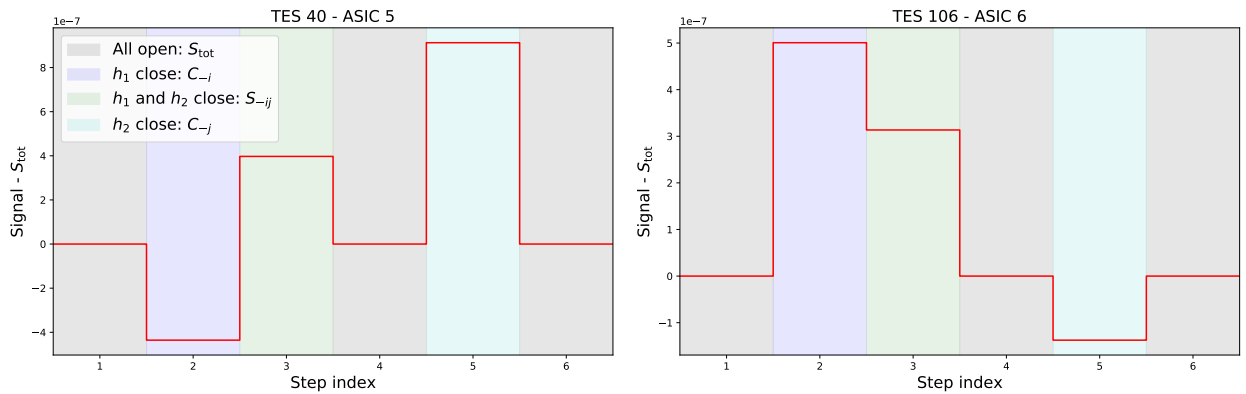


Figure 2.22: Simulation of the expected TOD signal for two arbitrary TES on one cycle. We subtract S_{tot} so that the all open configuration is centered on zero.

TD instrument has 248 bolometers. Thus, the data consist of 248 TOD signals. One of them is shown

in Figure 2.23. This is a raw TES signal without applying any filtering. As we can see, the system is rather stable, with no significant $1/f$ drift over 180 seconds. This method was developed in order

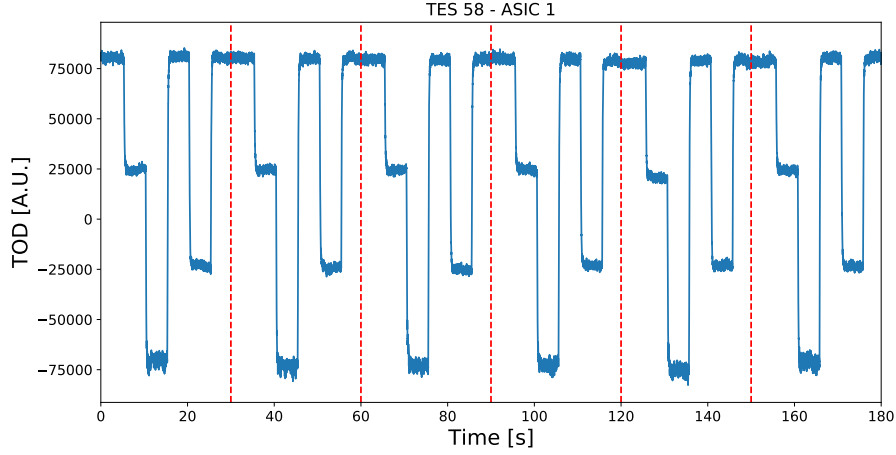


Figure 2.23: TOD obtained with data set from 2020-10-27, with baseline [18-22] for TES 58, ASIC 1. We show the six first cycles, delimited by red dashed lines.

to avoid long integration time during which the mean of the noise can drift to higher or lower value. Indeed, as the fringes are obtained through the linear combination of images given by expression 2.43 variation of the background signal from one image to another is very problematic.

Data sets are listed in annex A.3 with the setting parameters. In this section, I will focus on the 2020-10-27 data set for which I took the data and developed the analysis with the help of Jean-Christophe and Michel.

2.5.3 Detecting “bad” detectors

I wrote a code to detect the “bad” detectors which have a non correct TOD signal. “Bad” does not necessary mean that the detector is not working properly, it may be that for this particular horn baseline, at 150 GHz, for this particular orientation with respect to the point source, the detector does not see any power fluctuation along the cycle. An example of “bad” TOD is shown in Figure 2.24. In order to detect the bad detectors, I first fold the signal by superimposing the cycles and I fit the

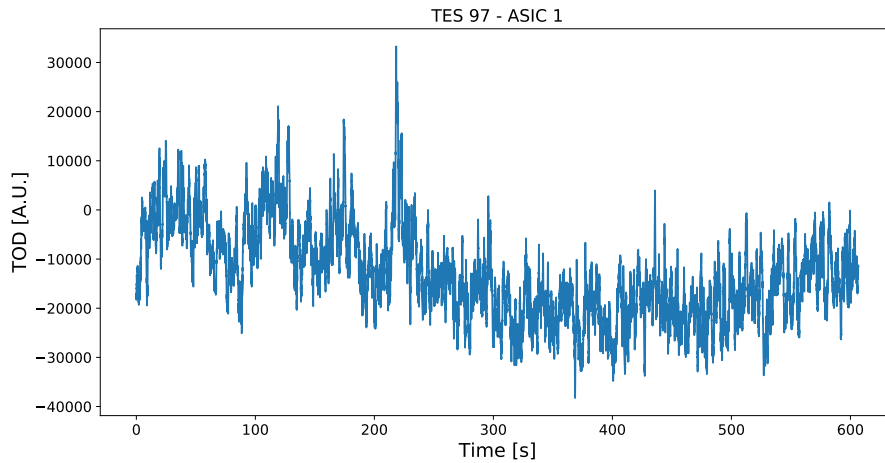


Figure 2.24: Example of a bad TOD signal from 2020-10-27 data set, baseline [18-22].

folded signal of each TES by a step function smoothed by a Gaussian kernel in order to mimic the response time of the detectors. Eight parameters are fit: the time constant of the detector, a global time shift and the six step amplitudes. An example is shown in Figure 2.25. Then, detectors are ordered from the best to the worst as a function of the fit residuals. The best detector becomes the

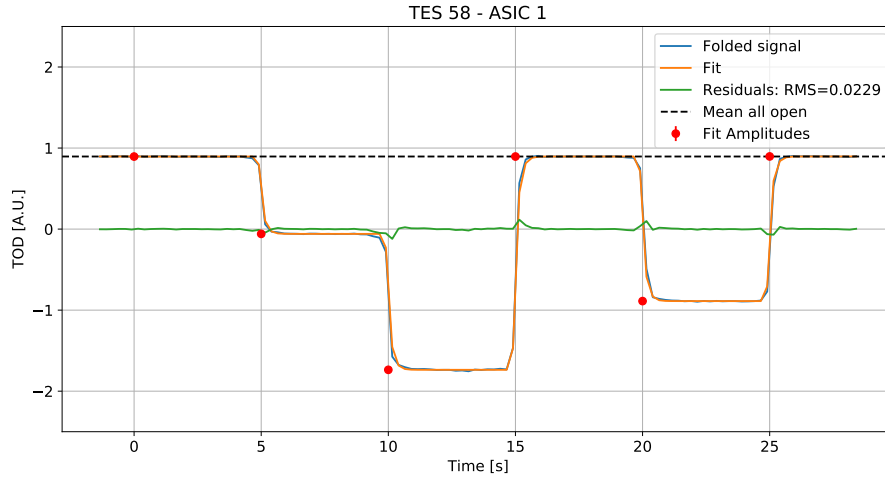


Figure 2.25: Result of the fit for the same TES as in Figure 2.23 after folding.

reference for the analysis I will describe in section 2.5.4. I make a mask for the detector array where the 25% worst detectors are set to a NAN value. This process is repeated for each image in the data set and a detector is considered to be bad only if it is NAN in at least N images. In Figure 2.26, I show the number of TES found to be bad as a function of N . By looking at the signal of the TES

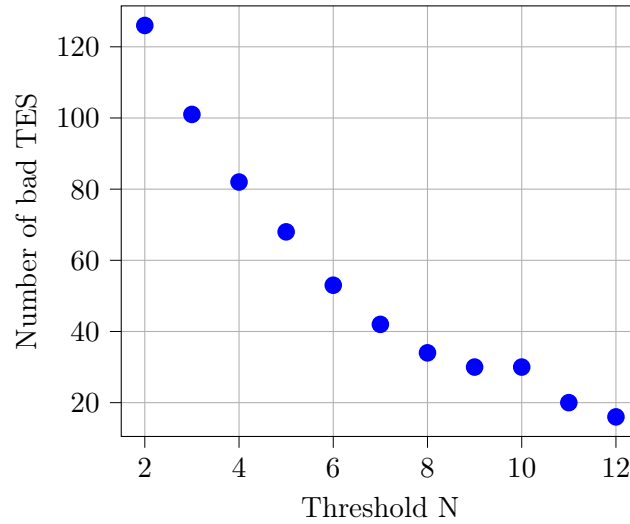


Figure 2.26: Number of detectors found to be bad as a function of the number N of images where the TES was set to NAN.

found to be bad, I concluded that $N \sim 9$ is a good threshold. For example, after this treatment on data set from 2020-10-27, 24 detectors are found to be bad. This is also a good method to eliminate the thermometers which are treated as detectors during data taking. They are four thermometers on each ASIC with indices 4, 36, 68 and 100.

This work could be pursued in several ways:

- Compare this technique with others, for example using the detector Intensity-Voltage $I(V)$ curves.
- Develop a method to detect bad detectors during data taking.
- Another possibility would be to use Machine Learning classification on the TOD signals. A first step could be to implement the DBSCAN clustering algorithm from the `scikit-learn` python library [216].

2.5.4 Data analysis process

The first image with visible fringes was obtained by Michel Piat with the 2019-06-07 data set and I did the corresponding simulation. This is shown in Figure 2.27. This measurement was obtained with

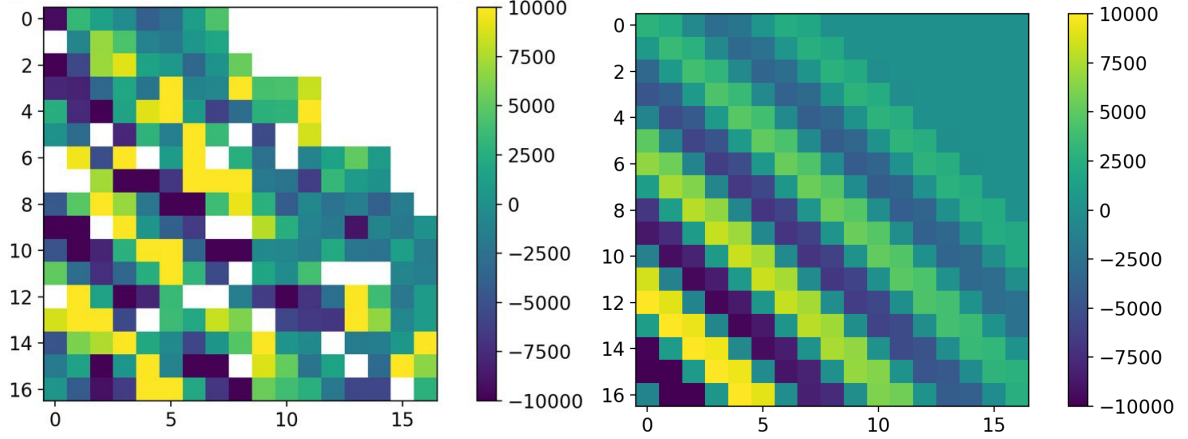


Figure 2.27: First observation of the fringes. The measurement is shown on the left and the corresponding simulation on the right. Each square is a single bolometer. Produced for [8].

a basic analysis. The TOD signal is folded in order to superimpose the cycles before doing the linear combination using the six steps S_i :

$$S_{ij} \sim S_{-ij} - C_{-i} - C_{-j} + \frac{1}{3}(S_{\text{tot}1} + S_{\text{tot}4} + S_{\text{tot}6}). \quad (2.44)$$

Since the first measurement, the data analysis algorithm has been improved a lot, especially regarding the estimation of the errors. I present here the main steps of the analysis. The cycle duration (or period) and the start time t_0 are adjusted on the reference TES which is the best detector found by the method described in section 2.5.3. As shown in Figure 2.28, t_0 is determined by computing the derivative of the average cycle. The beginning of each step corresponds to high derivatives and t_0 is the median of the six beginning times modulo the waiting time. The code also includes an option to fix the period and the start time at given values.

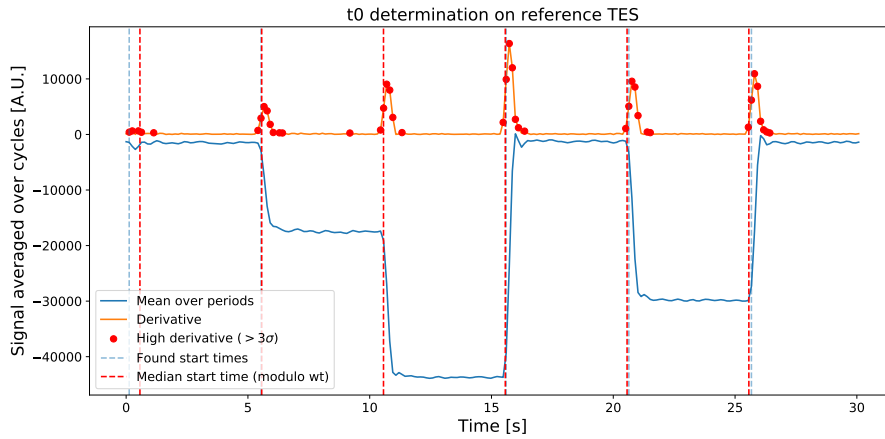


Figure 2.28: Start time determination on the reference TES, for baseline [17-49], 2020-10-27 data set.

Then, for each detector signal we do:

1. Determine a **skip_rise** and **skip_fall** time to eliminate the data at the beginning and at the end of each step when the signal is not stabilized, mainly due to time constants of the switches (detectors are faster). This is visible in Figure 2.28, the steep transition from one step to another needs some time to be stabilized.

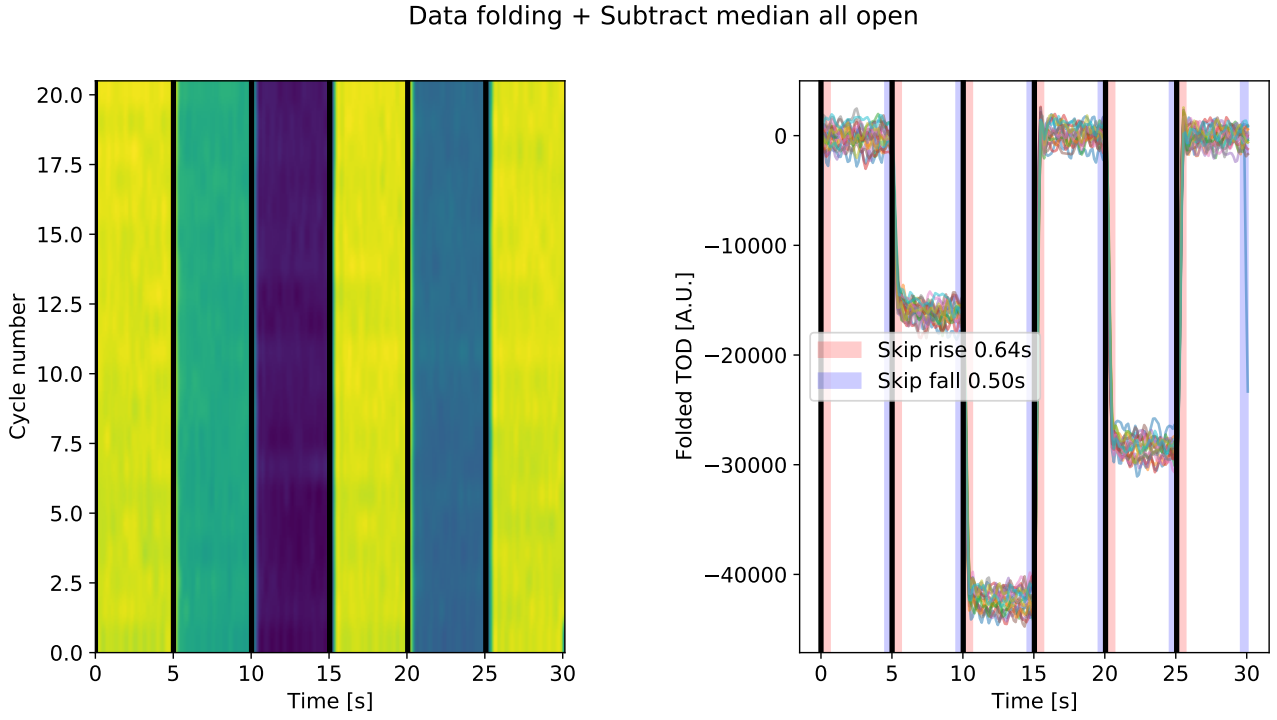


Figure 2.29: Illustration of data folding for the reference TES, baseline [17-49], 2020-10-27 data set. *Left:* The color corresponds to the value of the signal on each cycle. We expect the color to be uniform on each step separated by black vertical lines. *Right:* Superimposition of all the cycles. The skip times where signal rises and falls from one step to another are shown in red and blue.

2. Data filtering: a band-pass filter is applied to remove low frequency drift and high frequency noise. Here the high frequency cut is anyway removed by re-sampling the data in the next step. A notch filter can potentially be applied to remove particular frequency bands, especially the pulse-tube vibration detected around 1.7 Hz.
3. Crop the data in order to have an integer number of periods.
4. Re-sample the signal to have identical number of samples in each cycle.
5. Fold the signal: separate the cycles and make a 2 dimension array with shape (Number of cycles \times Number of samples per cycle).
6. Roll the signal: shift the folded data in order to have $t_0 = 0$.
7. Option: subtract the median when all horns are open so that the corresponding steps are centered on zero.

The result of this process is shown in Figure 2.29. Once this is done, to obtain the fringes, we average the samples on each step, and then we average over the cycles. We can choose between computing the mean or the median. In both cases, we perform a clipped average for which values above 3 sigma are removed. Errors are evaluated by taking the standard deviation. One example is shown in Figure 2.30.

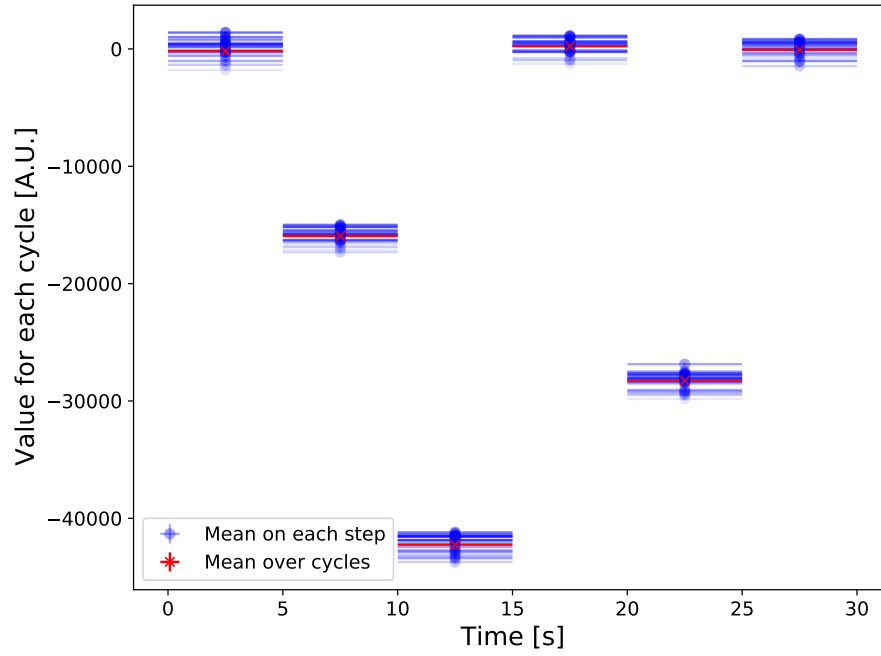


Figure 2.30: The average of the samples on each step is shown in blue. In red, we show the average of the blue values over the cycles. Example for the reference TES, baseline [17-49], 2020-10-27 data set.

The linear combination of the average/median values gives the fringe image together with the corresponding errors. The result is shown in Figure 2.31, for three baselines with different orientations and spacing from 2020-10-27 data set. I also show a simulation using the analytical model described in section 2.4.2 for a focal length of 32.7 cm, as we found in section 2.3.3. The apparent shift between the simulated fringes and the data may be due to a shift of the calibration source with respect to the QUBIC optical axis. In section 2.6, we will try to fit the off-axis angle of the source. This averaging

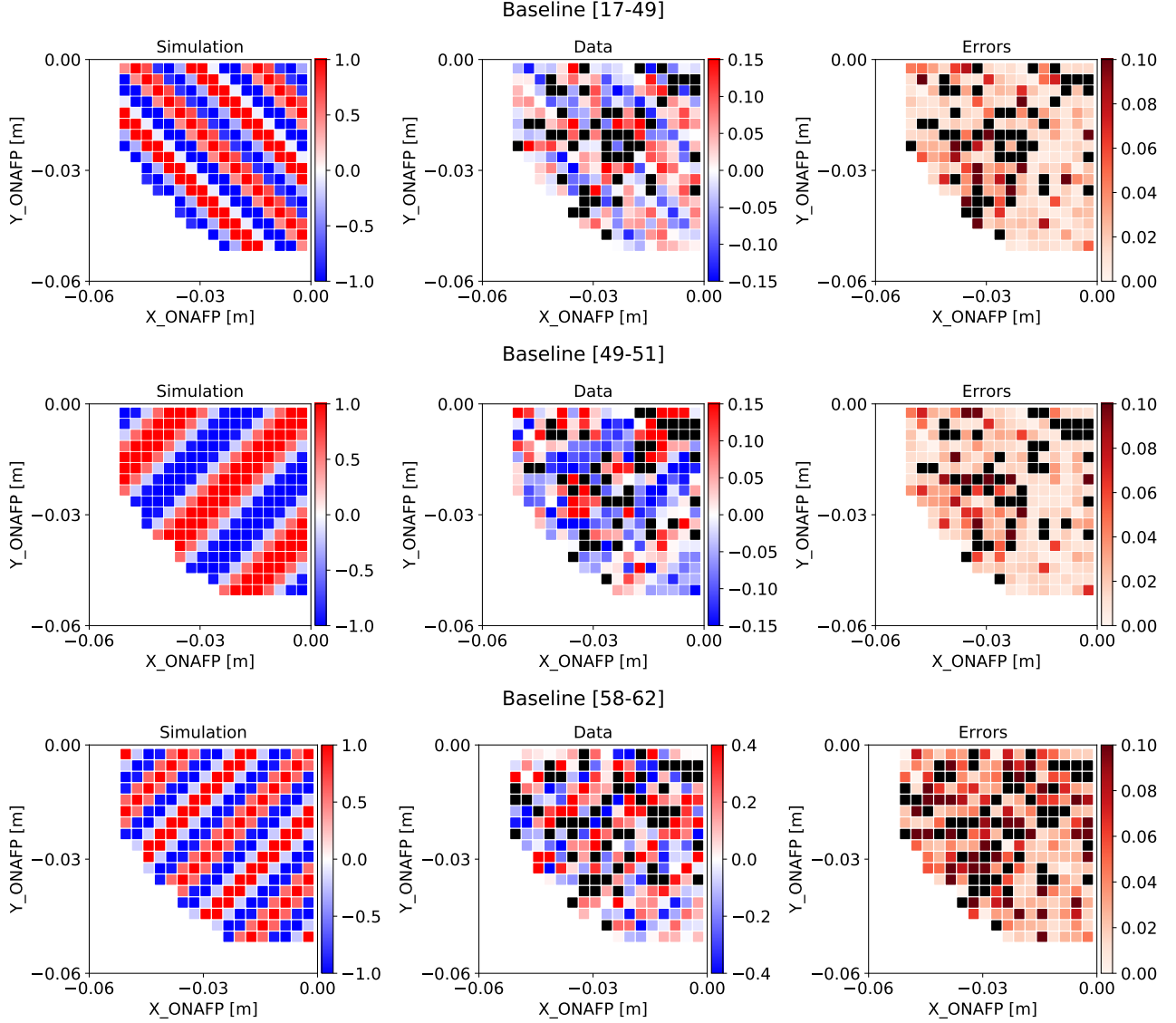


Figure 2.31: Result of the analysis, for three baselines with different orientations and spacing from 2020-10-27 data set. A simulation using the analytical model described in section 2.4.2 is shown on the left. The measurement is shown on the middle with the corresponding errors on the right. The color scale for the errors is fixed from 0 to 0.1. Black detectors are the ones found to be “bad”, they are common to the three images. I also added a personalized mask to each image in order to mask detectors which have a very high signal compared to the median (see section 2.6.3).

process is compared with a second one. Instead of averaging the cycles, which leads to six values, one for each step, we compute the linear combination for each cycle so we get one fringe image for each cycle. This is shown in Figure 2.32. The result fluctuates along the cycles. The histogram on the right compares the two methods:

- First average the cycles and then make the combination to get one mean fringe value called F_1 with error σ_1 .
- Make the fringe combination on each cycle and then average the result over the cycles to get a

mean F_2 with error σ_2 .

The histogram shows the distribution of $(F_2 - F_1) / \sqrt{\sigma_1^2 + \sigma_2^2}$ over detectors. As expected the difference is centered on zero which shows that the two methods give similar results. So both methods are equivalent but with the second one we can look at the stability of the fringe image along the cycles.

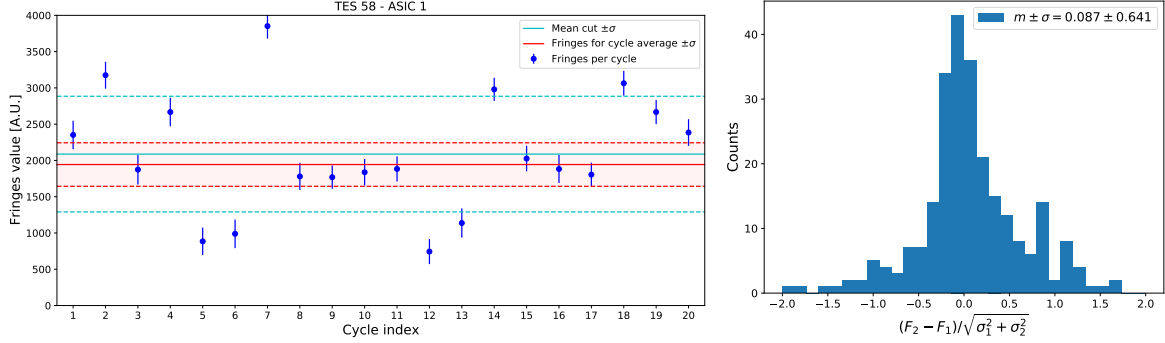


Figure 2.32: *Left:* Result of the fringe combination for each cycle (blue dots) on the reference TES, baseline [17-49], 2020-10-27 data set. Error bars correspond to the standard deviation on each step. In red I show F_1 , the measurement obtained with the first method. Errors σ_1 are shown with red dashed lines. In cyan, I plot F_2 , the mean of the blue dots, clipped at 3 sigma with its error σ_2 . *Right:* Histogram showing the distribution of $(F_2 - F_1) / \sqrt{\sigma_1^2 + \sigma_2^2}$ over detectors.

Prospective for this work

This analysis will be applied on future data taking with many more baselines. For now, we actually have only few images where the fringes are clearly visible by eyes after the treatment described above. This is likely due to a saturation of the detectors because the calibration source was too high. This is why we need more data but with lower signal-to-noise ratio by decreasing the source output power or by using the HWP to attenuate the signal. Moreover, the data analysis process could probably be improved and new data would be a good opportunity for that.

2.5.5 Verification of the horn-array orientation with fringe measurements

This section is one of my contributions to Torchinsky et al. [8], section 6.2. This is again a small step toward self-calibration. We describe the use of the fringe measurement at different baselines to confirm the mechanical orientation of the horn cluster. These measurements also confirm the correct functionality of the horn switch electronics. The detected fringe pattern corresponds to the expected result for the measurement of a given horn-pair. That is, there is no confusion regarding the physical location of the horn in the focal plane which is commanded by the electronics.

The fringe pattern was measured for the baseline formed by horns 25-57 (see Figure 2.27). The position of the horn cluster at that time was verified using pictures taken when it was mounted (see Figure 2.33). Figure 2.34 shows the reference frames used on the instrument. Colors in the horns

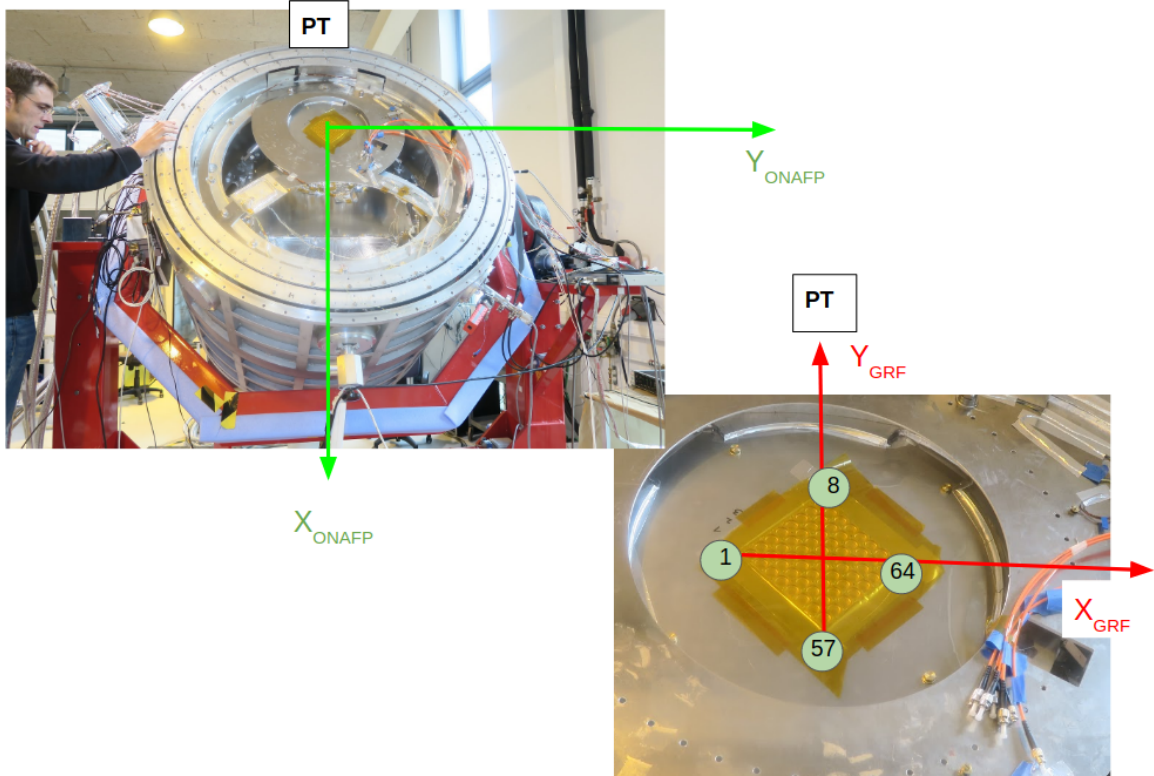


Figure 2.33: Pictures showing the horn cluster orientation. PT gives the location of the pulse-tubes. *Left:* The On Axis Focal Plane (ONAFP) reference frame projected onto the face of the horn cluster. *Right:* The Global Reference Frame (GRF) is co-planar to the face of the horn cluster.

correspond to the switch behavior tested at room temperature for which I participated. Switch shutters were activated one by one several times. By putting a light on one side of the horn array, we could check by eyes if the horn was correctly closed or not.

Finally, the optics simulations can be used to confirm the physical horn orientation in the optical path. The orientation between all the simulations and the measurement agree. A $\pi/2$ rotation difference between measured results and simulations would be easily detected. However, it is not straightforward to detect a π rotation because the differences would be very small (see Figure 2.35). Such a rotation might be detectable by fitting the measurement with the simulations.

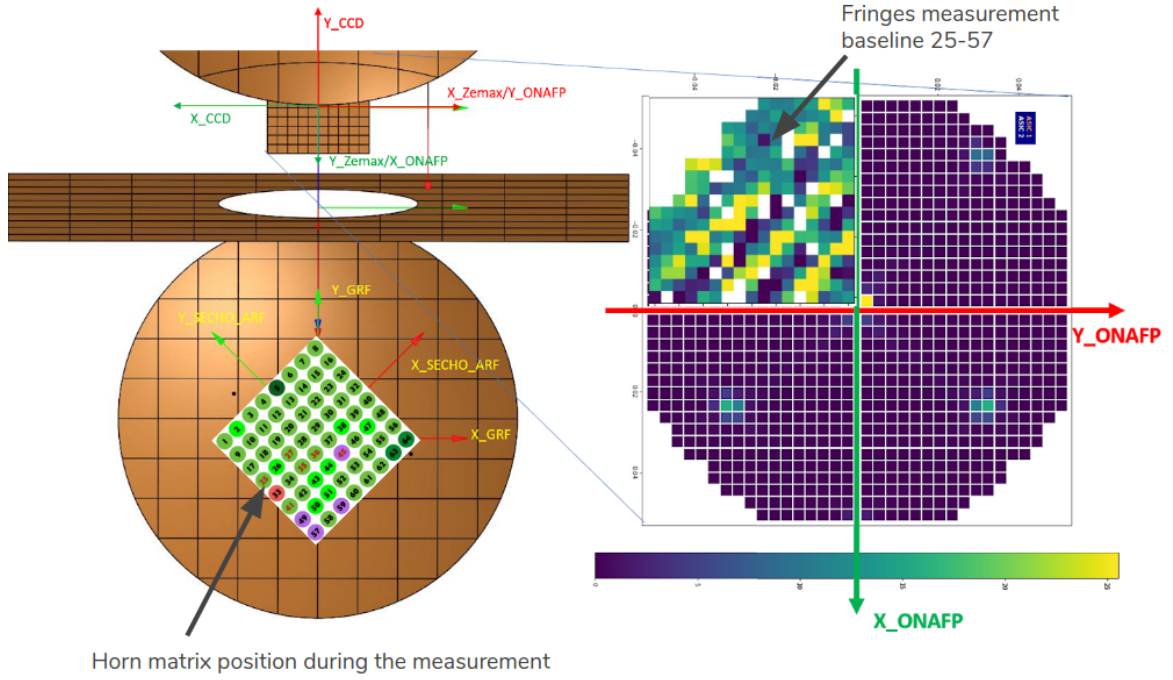


Figure 2.34: QUBIC reference frames. *Left*: The face of the horn cluster is overlaid on the optics schematic. Colors in the horns correspond to the switch behavior tested at room temperature for which I participated. *Right*: The fringe measurement in the negative- x and negative- y quadrant (quadrant 3).

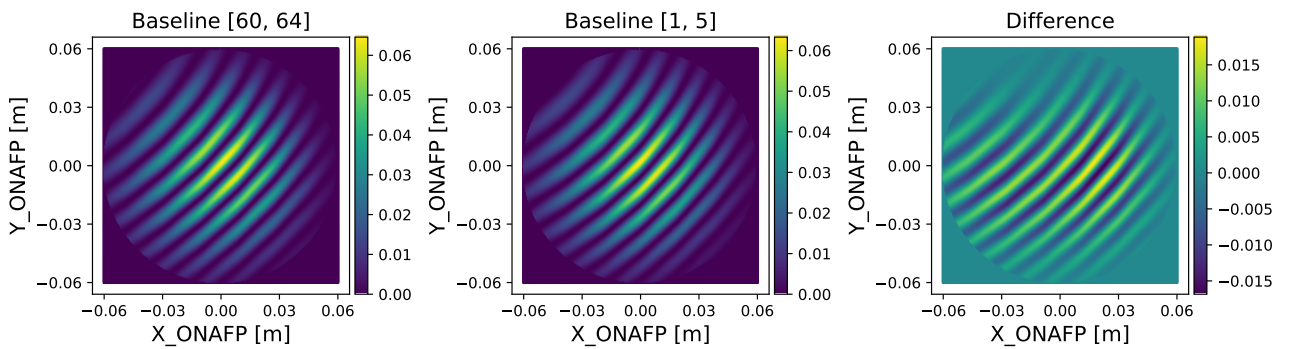


Figure 2.35: Simulated fringes obtained on the focal plane for 2 baselines, symmetric under a π rotation. The simulation was done using our in-house developed python-based software called `qubicsoft` described in section 2.4.1, using MODAL optical modeling results.

2.6 Bolometer inter-calibration using the fringes

I introduced numerical models that allow to simulate fringes on the focal plane and I presented the procedure to acquire calibration data. Here I propose to combine both in order to inter-calibrate the gains of the bolometers of the focal plane by fitting a series of fringe images. I will first present the method theoretically. Then I will illustrate it on simulated data. Finally I will show a first trial on real laboratory data.

2.6.1 Theoretical principle

We consider N_b fringe measurements for different baselines. The rough TOD have been analyzed to obtain the fringe images, indexed by k . Thus, at this stage the data consist of vectors \mathbf{D}_k with dimension the number of detectors N_d . We build a model with parameters

$$\mathbf{p} = \{f, \theta, \mathbf{A}, \mathbf{P}\} \quad (2.45)$$

where f is the focal length and θ the angle between the optical axis of the instrument and the calibration source. \mathbf{A} is a vector with dimension N_d containing the detector gains A_d . \mathbf{P} is a vector with dimension N_b containing the global powers P_k multiplying each image. The number of parameters is $2 + N_d + N_b$. The fringe model for image k is

$$\mathbf{M}_k(\mathbf{p}) = P_k \Phi_k(f, \theta) \cdot \mathbf{A} \quad (2.46)$$

where $\Phi_k(f, \theta)$ is a diagonal matrix with dimension $N_d \times N_d$ which gives the theoretical fringe image for a given f and θ . $\Phi_k(f, \theta)$ is determined by one of the simulations described in section 2.4.

To estimate the parameters, we minimize the χ^2 given by

$$\chi^2 = \sum_{k=1}^{N_b} [\mathbf{M}_k(\mathbf{p}) - \mathbf{D}_k]^T C_k^{-1} [\mathbf{M}_k(\mathbf{p}) - \mathbf{D}_k] \quad (2.47)$$

where C_k is the detector noise covariance matrix, with dimension $N_d \times N_d$, associated with image k .

Written in the form of equation 2.46, the model is linear in \mathbf{A} . This is why \mathbf{A} can be calculated analytically by

$$\frac{\partial \chi^2}{\partial \mathbf{A}} = 0 \iff \sum_k 2P_k \Phi_k^T(f, \theta) C_k^{-1} (P_k \Phi_k(f, \theta) \cdot \mathbf{A} - \mathbf{D}_k) = 0 \quad (2.48)$$

$$\iff \mathbf{A} = \text{Cov}(\mathbf{A}) \cdot \left[\sum_k P_k \Phi_k^T(f, \theta) C_k^{-1} \mathbf{D}_k \right] \quad (2.49)$$

where

$$\text{Cov}(\mathbf{A}) = \left[\sum_k P_k \Phi_k^T(f, \theta) C_k^{-1} P_k \Phi_k(f, \theta) \right]^{-1} \quad (2.50)$$

is the covariance matrix of \mathbf{A} . Finally, we impose

$$\langle \mathbf{A} \rangle = \frac{1}{N_d} \sum_{d=1}^{N_d} A_d = 1 \quad (2.51)$$

so that \mathbf{A} only contains relative fluctuations between detector gains. The mean amplitude is contained in P_k . Indeed, we have

$$\langle P_k \mathbf{A} \rangle = P_k \langle \mathbf{A} \rangle = P_k. \quad (2.52)$$

By doing that, the number of parameters becomes $2 + (N_d - 1) + N_b$.

This is very powerful because \mathbf{A} contains N_d gain parameters, typically 248 for the TD and 992 for the FI so it would be tricky to estimate so many parameters by Monte-Carlo Markov Chain (MCMC) or with any other minimizer.

Of course, the model is also linear with P_k so we could have done the same as we did for \mathbf{A} . However, it is less interesting as the number of images is much less than the number of detectors and it is not possible to do it for P_k and \mathbf{A} at the same time.

2.6.2 Illustration on a simulation

I first illustrate the technique described above on simulated data.

Simulated input data

We consider three baselines [17-49], [49-51] and [58-62] shown in Figure 2.31. We make simulated data following equation 2.46 and adding Gaussian noise with ($\mu = 0, \sigma = 0.08$). For the pure fringe model $\Phi_k(f, \theta)$, we use the analytical model described in section 2.4.2. I chose this model among the three presented in section 2.4 because it is the simplest one so it is good for starting. The input parameters are:

- focal length: $f = 29$ cm,
- source angle: $\theta = 0.5^\circ$,
- three P_k taken randomly between 0 and 1 (uniform distribution),
- detector gains A_d , between 0 and 2, (uniform distribution), with mean forced to be 1.

Minimizing the χ^2

The covariance matrix C_k is diagonal with noise variance $\sigma^2 = 0.0064$ on the diagonal. We start by exploring the χ^2 , looping over f and θ and at each step, we minimize a temporary χ^2 over the three P_k parameters. This provides a χ^2 map shown in Figure 2.36. We do this to have a first look at the χ^2

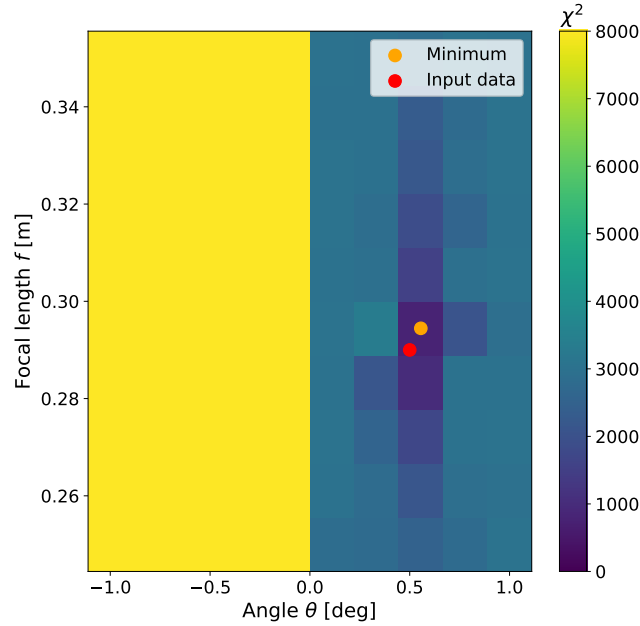


Figure 2.36: χ^2 map obtained by looping over f and θ . The χ^2 is minimized over the three global powers P_k at each step.

evolution in the parameter space. The minimum of the map is taken as a guess for the minimization done with the `iminuit` python package [213], [214]. For this particular example, the reduced χ^2 is 1.04 and the result is shown in Table 2.1. The detector gains are then computed analytically using the result of the minimization. The gains are shown in Figure 2.37 with respect to the input ones (left) and I also show the histogram of the residuals defined as the difference between the output and the input gains (right).

Parameters	Input	Output	Ratio
f [m]	0.29	0.2899	1.0019
θ [deg]	0.5	0.5021	0.9958
P_1	0.1704	0.1747	0.9750
P_2	0.8633	0.8714	0.9907
P_3	0.2568	0.2598	0.9882

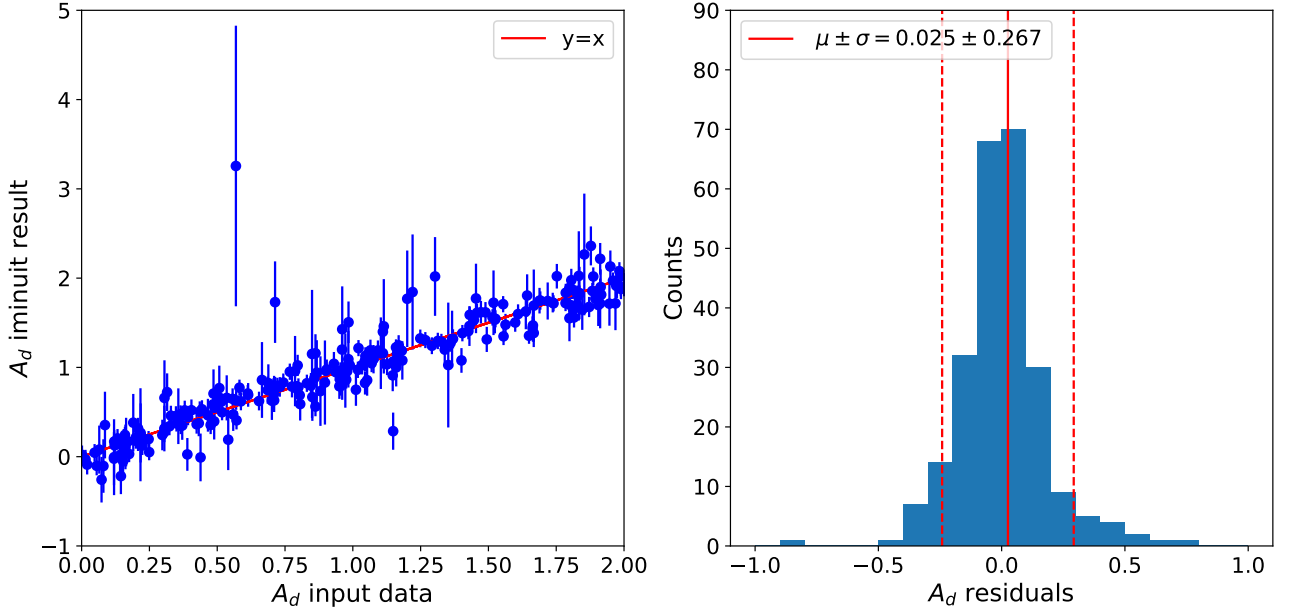
Table 2.1: Estimation of the five parameters using the `iminuit` minimizer.

Figure 2.37: Estimation of the detector gains using `iminuit`. *Left*: Detector gains A_d obtained by minimizing the χ^2 with respect to the input ones. Error bars are given by the square root of the covariance matrix diagonal defined in equation 2.50. *Right*: Histogram of the residuals: $A_d^{\text{iminuit}} - A_d^{\text{input}}$.

I implemented a MCMC in parallel with the `iminuit` minimization. I used the `emcee` python package [217]. The `iminuit` result is taken as the initial point for the MCMC sampling. One difficulty is to determine if the chain has converged or not. For that purpose, I use the Gelman Rubin convergence test [218], [219], based on multiple chain sampling. We considered that the chain has converged if $R < 1.03$ as shown in Figure 2.38. The acceptance rate along the iterations of the MCMC is also shown in this plot.

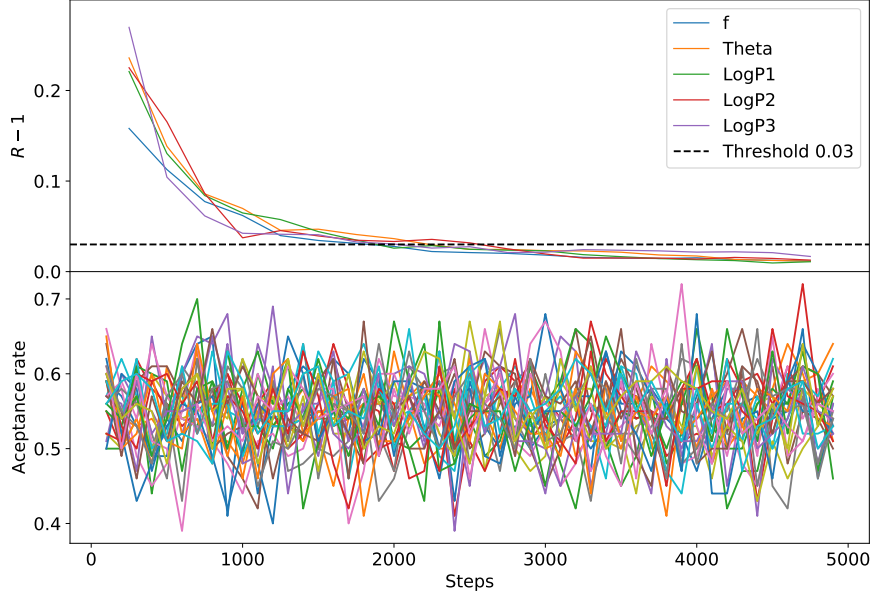


Figure 2.38: *Top*: Gelman Rubin convergence test for the five parameters (focal length f , source angle θ and the three powers P_k). We consider that the chain has converged when $R < 1.03$, shown with the black dashed line. *Bottom*: Acceptance rate along the iterations of the MCMC. Each color corresponds to a chain.

At the end of the MCMC, the reduced χ^2 is 1.06 and the probability distributions of the five parameters are presented in the corner plot, Figure 2.39. Light gray dashed lines show the input parameter values.

Detector gains are computed along the MCMC iterations and stored. The mean and the standard deviation of the distribution of each gain along the MCMC is shown in Figure 2.40. As before for the `iminuit` minimization, I plot the mean detector gains with respect to the input ones as well as an histogram of the residuals.

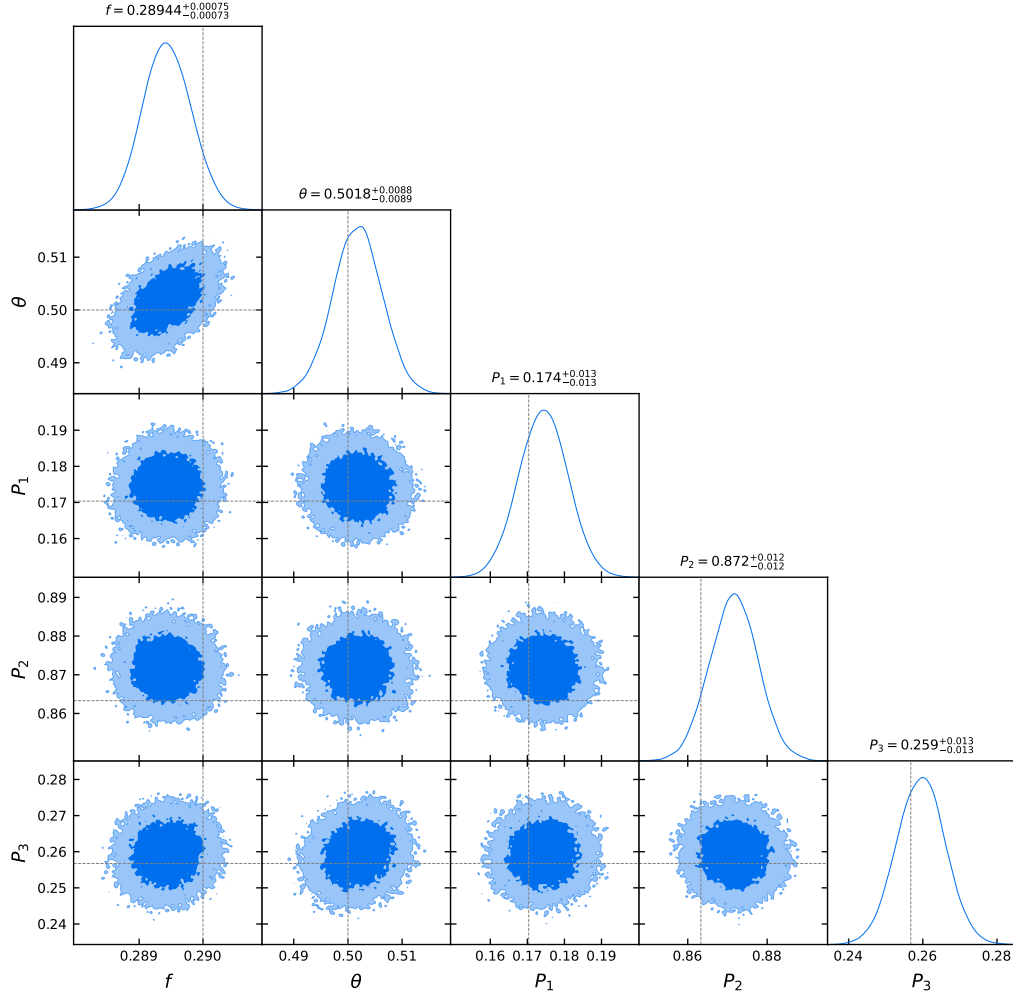


Figure 2.39: Corner plot showing the probability distribution of the five parameters f, θ, P_1, P_2 and P_3 obtained with the MCMC. Light gray dashed lines show the input parameter values.

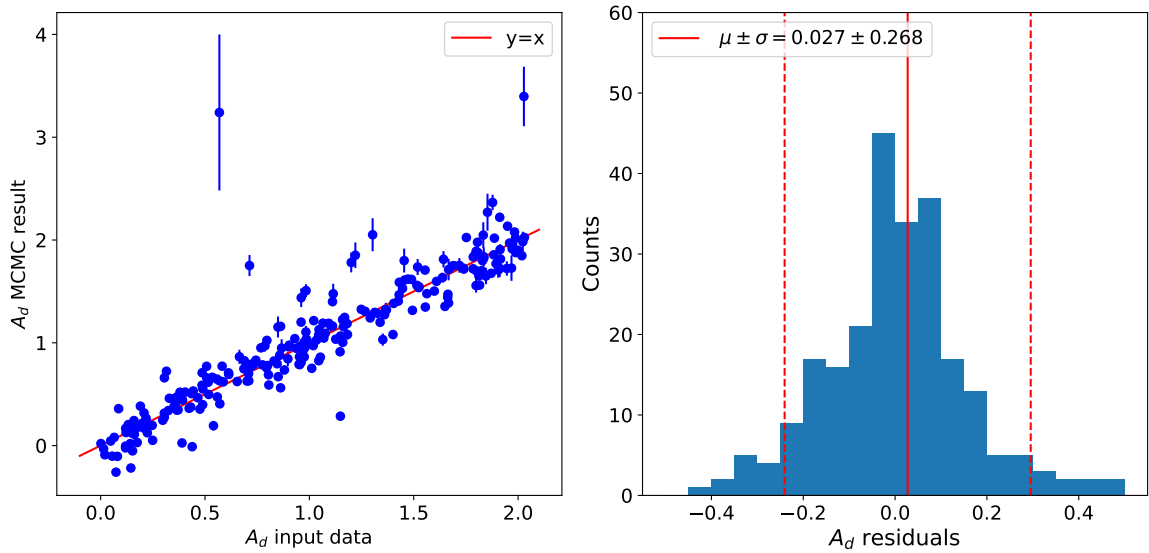


Figure 2.40: Estimation of the detector gains by the MCMC. *Left*: Output gain as a function of the input one. The blue dots and error bars correspond to the mean and the standard deviation of each detector gain computed along the MCMC iteration. *Right*: Histogram of the residuals: $A_d^{\text{MCMC}} - A_d^{\text{input}}$.

Correcting data by the detector gains

Once we have estimated the gains of each detector, we can correct the input fringe images by dividing by the gains. In others words, we get an image with inter-calibrated pixels. This is shown in Figure 2.41 for the three baselines. We also show the residuals on the third row, defined as the difference between the corrected image and the fit model:

$$R_k = \frac{D_k}{A} - P_k \Phi_k(f, \theta). \quad (2.53)$$

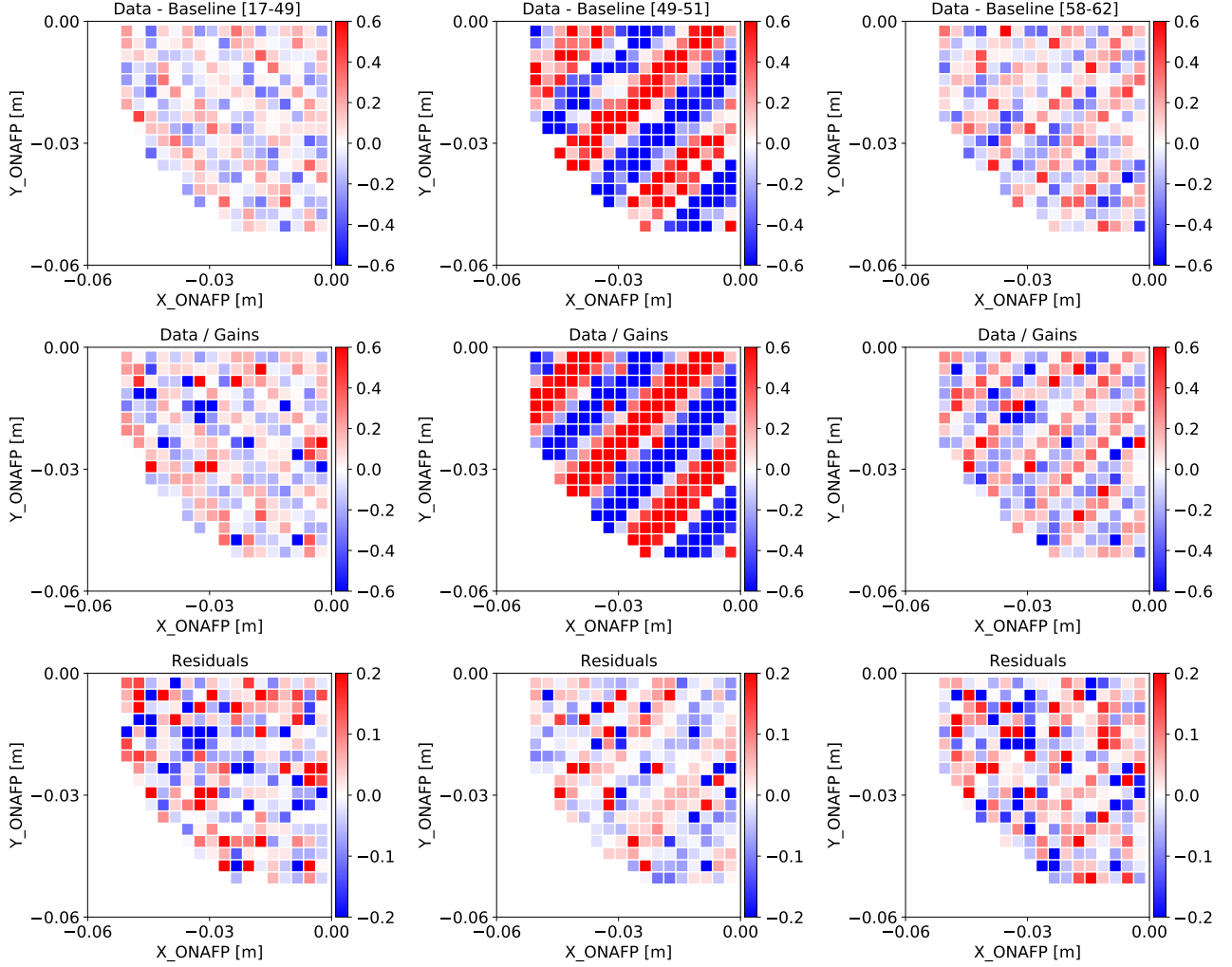


Figure 2.41: The first row contains the three simulated input images. The middle row is the input image divided by the detector gains and the third row shows the map of the residuals of the fit defined by equation 2.53. The color scale amplitude is fixed from -0.6 to 0.6 for the data and the corrected data and from -0.2 to 0.2 for the residuals.

Finally, Figure 2.42 presents the pull distributions of the three baselines defined as

$$\text{Pull}_k = \frac{R_k}{E_k/A}. \quad (2.54)$$

where E_k is the error on the input image k . In case of a simulation, it is the standard deviation of the noise: $E_k = \sigma$. If the errors σ_k are correctly estimated, we expect the pull distribution to be centered on 0 with a standard deviation equal to 1.

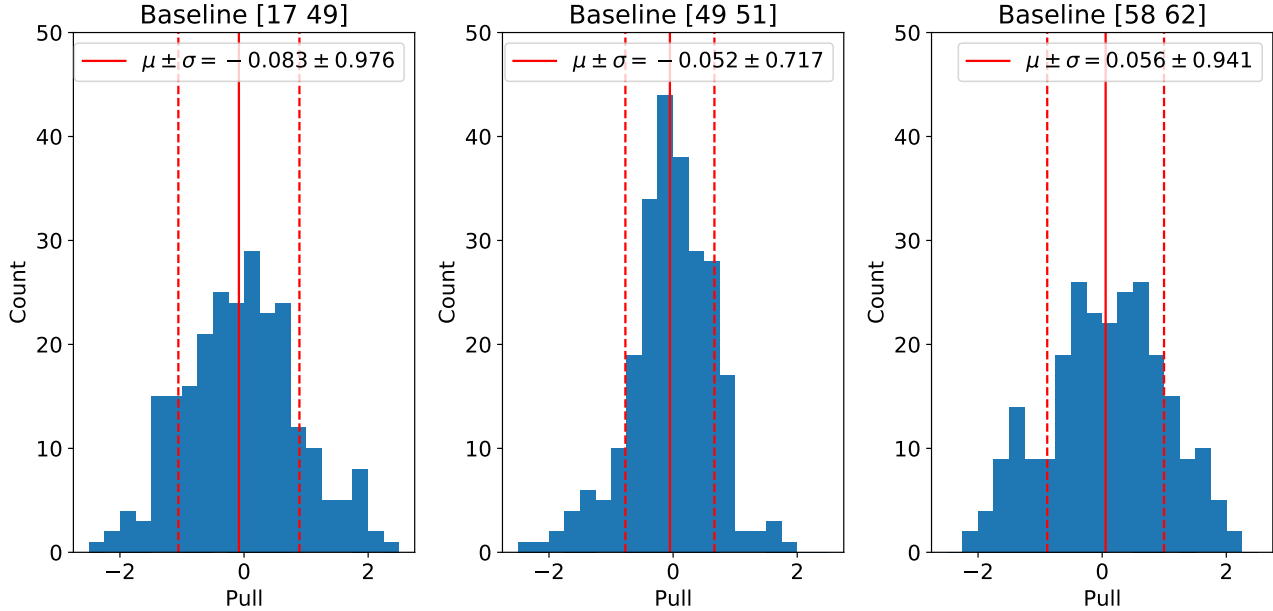


Figure 2.42: Pull distributions of the three baselines obtained after a MCMC on simulated data.

To conclude this part, the method works as expected with simulated data. Using linear algebra to compute the detector gains analytically is a real advantage. The possibility of using either the `iminuit` minimization or a MCMC is an advantage. The MCMC samples the distribution and can for example reveal secondary minima in which `iminuit` could have fallen. Moreover, `iminuit` makes the approximation that the probability distributions of the parameters are Gaussian which may be wrong while the MCMC does not. So the estimation of the errors is more correct with a MCMC. The next step is to apply this method on real data!

2.6.3 First trial on real data

I made a first trial on real data using the data set from 2020-10-27. This work is very preliminary, it must not be taken as a serious measurement of the focal length and of the detector gains. However, it shows that the method I put in place is promising for future data sets. I consider the same three baselines [17-49], [49-51] and [58, 62].

In order to avoid bad detectors determined with the method described in section 2.5.3, we set the corresponding terms on the diagonal of the covariance matrix C_k to a very high value. By doing that, they have very low weight in the fit. Moreover, I chose to make a personalized mask for each image in order to discard some “hot” detectors. Indeed, outlier detectors are quite problematic for the minimization. I noted that by removing them, the minimum χ^2 was decreasing a lot. To detect them, I used the Median Absolute Deviation (MAD) which is a measure of dispersion similar to the standard deviation but more robust to outliers. It is defined as

$$MAD = \text{median}(|X_i - \text{median}(X)|) \quad (2.55)$$

for X a random variable. For each fringe image, detectors with signal higher than $4 \times MAD$ in absolute value were masked.

The same procedure that I presented for simulated data was applied on real images: exploring the χ^2 grid, `iminuit` minimization and MCMC. I present here the result of the MCMC. In this example, I considered the following prior: parameters were limited such as $0.25 < f < 0.35$ m, $-2^\circ < \theta < 2^\circ$ and $10^{-5} < P_k < 10$. Probability contours of the five parameters are shown in the corner plot, Figure 2.43. The reduced χ^2 is 17.5 at minimum, which is not very satisfying. But we must remember that the

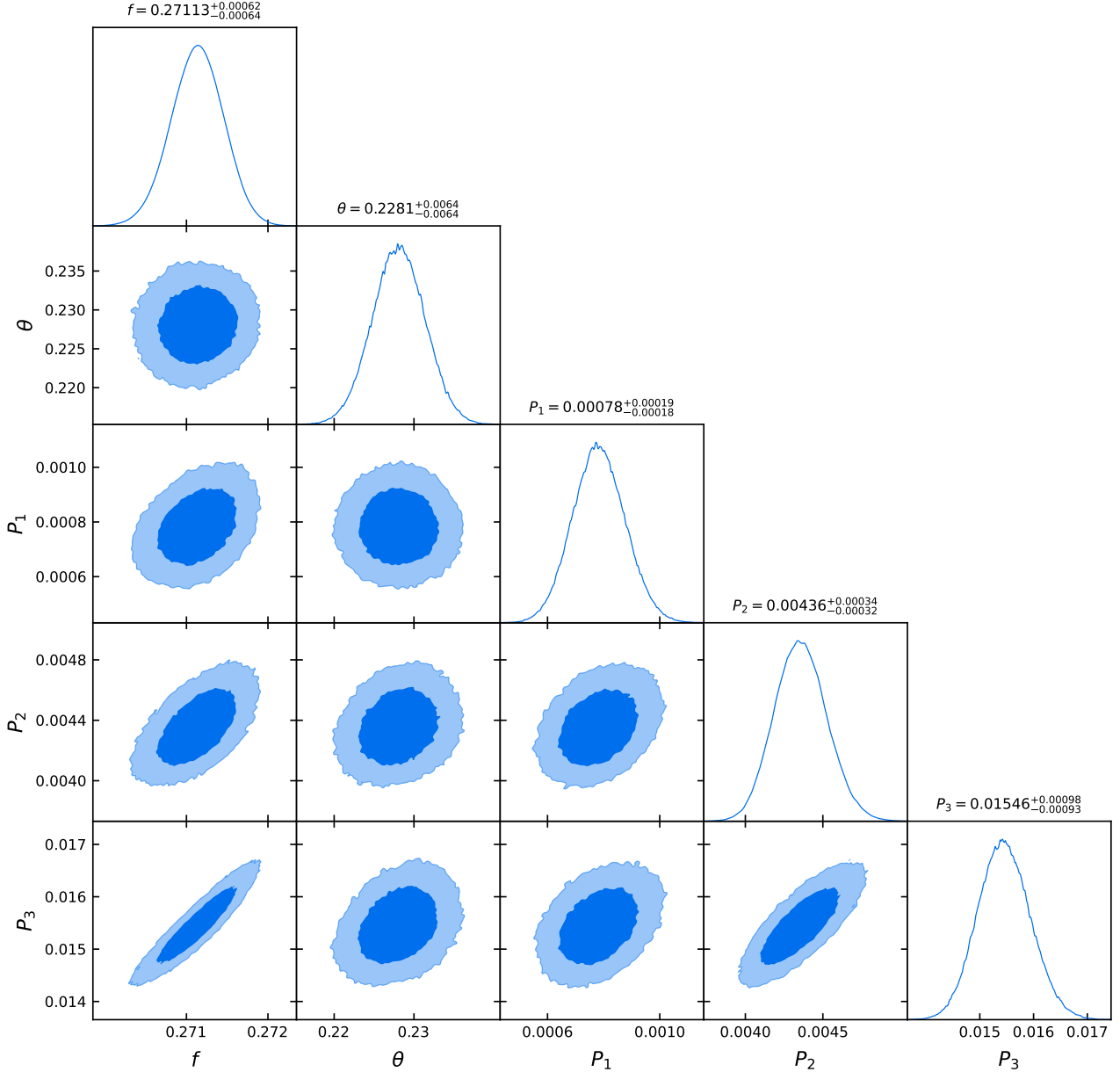


Figure 2.43: Corner plot showing the probability distributions obtained on the five parameters with a MCMC.

model is very simple and not realistic so we do not expect to match the data very well. As I said, this is only a first trial and the model will be improved in the future. For example, it would certainly be better to consider the Maynooth model than the analytical one which is much more realist.

The estimated detector gains with the associated errors are visible on Figure 2.44. As for simulated data, the detector gains are computed analytically along the MCMC iteration and stored. The found gains and the errors correspond to the mean and the standard deviation of the distribution associated with each detector. Gain are mainly included between -40 and 40 with errors mainly around 0 and 15 . Firstly, we can note that errors are large, especially on ASIC 1. This may explain the gains found

to be negative which is clearly non physical, except if for some detectors, the sign of the signal is reversed. We had some hints about that when looking at the raw TODs. So it may be the case for a small number of detectors but for sure not in this proportion. This is part of the things that need to be understood. Finally, the input data corrected by the detector gains are shown in Figure 2.45. I

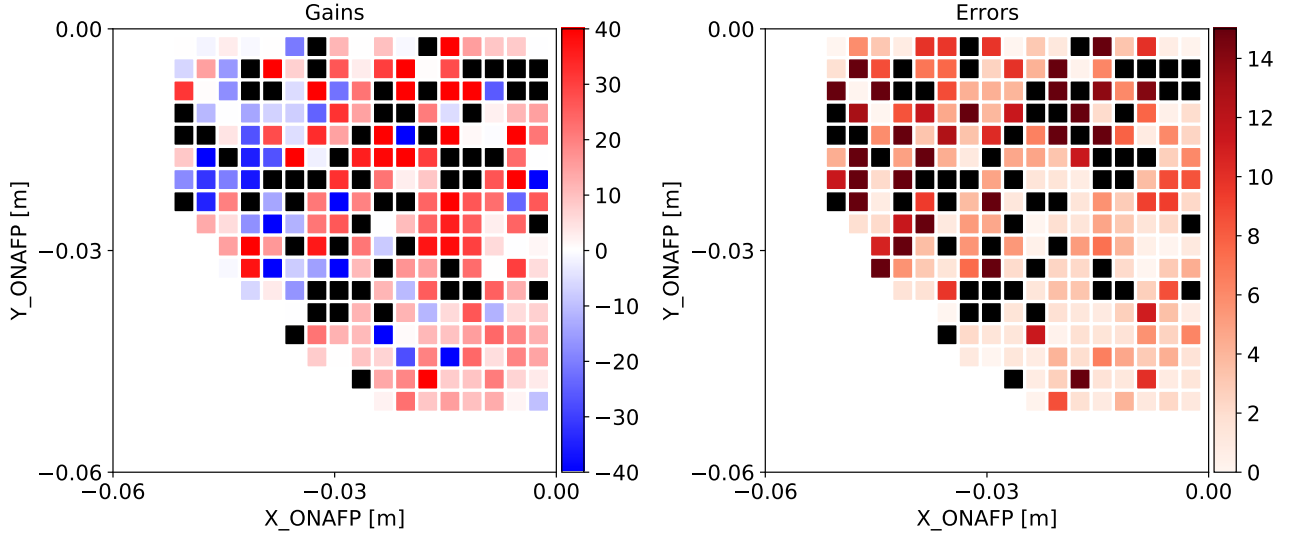


Figure 2.44: Map of the detector gains determined on real data by a MCMC with the corresponding errors.

think baseline [49-51] and [58-62] are improved. However it is less clear on baseline [17-49]. But again, this is a first test and it would be interesting to test this method on more images.

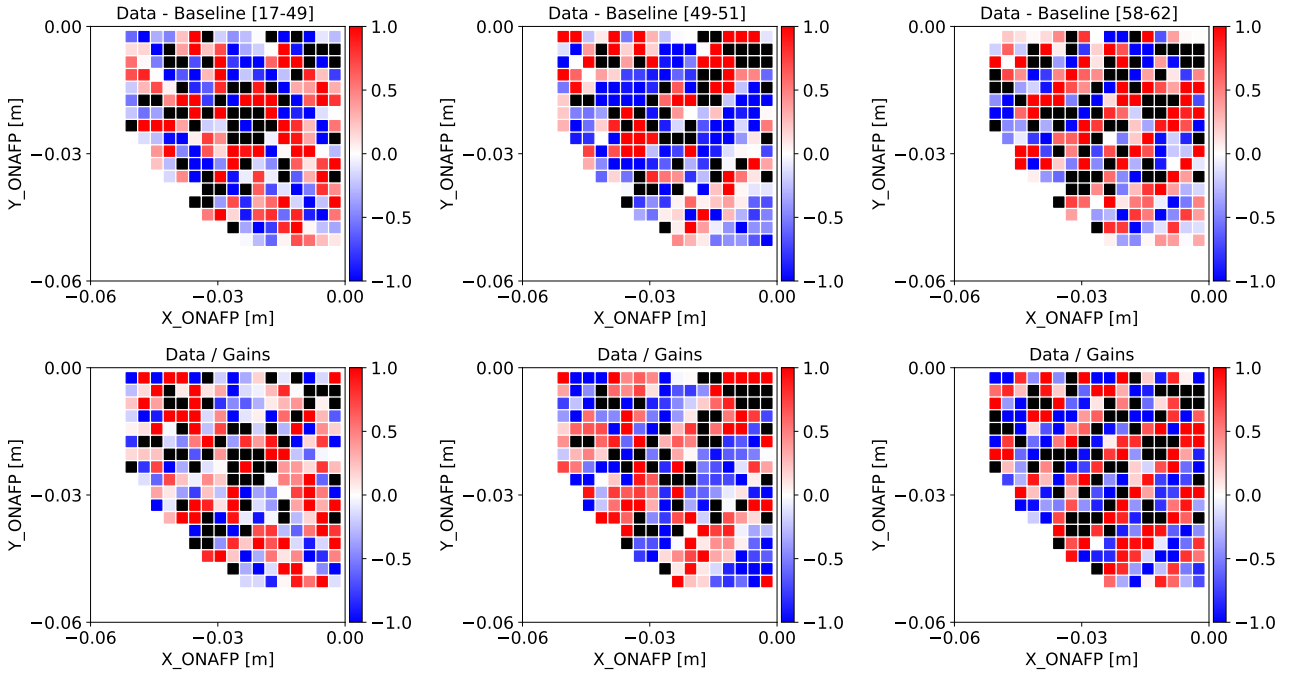


Figure 2.45: The first row show the three input images and the second row contains the same images divided by the detector gains.

2.6.4 Prospective for this work

This work could be pursued in many different ways. I list here some ideas:

- Apply this analysis on new data sets. In the future, we expect to have data sets with a much larger number of images which should help to constrain the parameters. We plan to estimate the detector gains on different image sub-sets and to compare them. The gains should also be compared from one data set to another in order to study the stability in time of the detector behavior which is a major question.
- The model could be more realistic by using the Maynooth simulations instead of the analytical model.
- We only fit one gain parameter for each detector. It would be interesting to add a saturation parameter to each detector. However, those parameters could not be calculated analytically as they will not be linear in the model. So this makes the fit much more complex as it implies fitting a much larger number of parameters. We have reasons to believe this problem exists, but it could also be avoided by having the source less powerful and by integrating the signal a longer time.
- Finally, instead of working with the fringe images, we could directly fit the TOD cycles associated with the image. Since the analysis of the TOD to build the fringe image is quite complex, it may be more accurate.

In conclusion, the method based on linear algebra to derive analytically the detector gains is clearly powerful and will certainly be used in the future. This work is a first step toward full self-calibration of the instrument which has to be developed in the near future. This will have to include much more parameters, for example the horn and detectors positions and possibly detector saturation.

Conclusion In this chapter I reported my work related to the calibration of the instrument. I started by justifying the choice of the polarimeter design made to limit the cross-polarization and the leakage from intensity to polarization. For that purpose, I updated the formalism, introduced by Marie-Anne Bigot-Sazy to model the systematic effects of each optical element, to the current instrument design. This led me to introduce the principle of self-calibration which is based on the horn baseline redundancy.

In a third part, I presented a recent analysis I developed to identify in an absolute way the multiple peaks of the synthesized beam of each detector. For that purpose, I developed optical simulations for comparison with real data. This allowed me to fit the focal length of the optical combiner using the positions of the peaks. This work is very important for map-making with real data that requires an accurate knowledge of the peak positions.

In the three last sections, I presented a complete procedure to measure and analyze interference fringes on the focal plane, which is of course fundamental for self-calibration. This is challenging as we can at maximum close two horns at the same time which means that we have to make a linear combination of four images to get the fringes. By building an optical model of the fringe pattern, I developed a fit which includes the detector gains. This has been successfully tested on simulation and first apply on real data. The advantage is that the gains are computed analytically using linear algebra during the χ^2 minimization. This is a main step because the inter-calibration of the detectors is a major issue for any data analysis.

In summary, all this work is closely related to self-calibration and it can be seen as a first step toward the full procedure. This chapter terminates the presentation of the QUBIC instrument, its working principle and parts of its calibration for which I worked on. In the next chapter, we will move to Cosmology, focusing on the Cosmic Microwave Background physics and how it is part of the Hot Big Bang model.

Chapter 3

The Cosmic Microwave Background

Contents

3.1	Our vision of the universe before 1920	88
3.1.1	Few words about general relativity	88
3.1.2	A static and perpetual universe	88
3.2	From a perpetual universe to an expanding universe	89
3.2.1	Questioning the vision of the universe	89
3.2.2	The Hubble-Lemaître law	90
3.2.3	The standard model of cosmology	91
3.2.4	Proper and comoving distances	92
3.2.5	Relation between the scale factor and the redshift	93
3.2.6	Measurable distances in cosmology	94
3.2.7	The Hot Big Bang model	95
3.3	Thermal history of the Universe	95
3.3.1	Prediction and first observation of the CMB	95
3.3.2	Big Bang nucleosynthesis	97
3.3.3	Recombination	97
3.4	The CMB black-body spectrum	100
3.4.1	A black-body at 2.7 K today	100
3.4.2	Sunyaev Zel’dovich (SZ) effect	101
3.4.3	The CMB dipole	102
3.4.4	CMB thermodynamic units	103

This chapter is an introduction to the Hot Big Bang model and to one of its main consequence: the Cosmic Microwave Background (CMB). The Hot Big Bang model was built in the 1920’ to answer experimental observations and was a revolution of our vision of the Universe at that time. I start by giving the historical context and the scientific motivation for this model before presenting it with its major implications. The last section presents some important physical properties of the CMB radiation. This chapter is mainly based on the books by Scott Dodelson [109] and James Rich [49]. I also enjoyed the physical discussions presented in simple terms in the book by Steven Weinberg who just passed [20].

3.1 Our vision of the universe before 1920

3.1.1 Few words about general relativity

The theory of general relativity was invented by Einstein in the years 1910' [21]. In general relativity, gravity is no longer understood as a force but is replaced by the property of space-time to be curved by the presence of mass.

We consider a particle in a gravitational field \mathbf{g} . The gravitational force writes $\mathbf{F}_g = m_G \mathbf{g}$ where m_G is the gravitational mass of the particle and the Newton's law of motion in a Galilean reference frame writes

$$m_I \frac{d^2 \mathbf{x}}{dt^2} = m_G \mathbf{g} \quad (3.1)$$

where m_I is the inertial mass and \mathbf{x} the coordinates of the mass. Experimentally, m_I and m_G are measured to be equal with a precision of 10^{-15} [50]. General relativity is based on the equality $m_I = m_G$ which is called the equivalence principle. It means that locally, the effect of a gravitational force in a Galilean reference frame is identical to the effect of no gravitational force in an accelerated reference frame. Indeed, in the reference frame (not Galilean) accelerated with the observer so that $\mathbf{x}' = \mathbf{x} - \frac{1}{2} \mathbf{g} t^2$ and $t' = t$, we have:

$$m \frac{d^2 \mathbf{x}'}{dt'^2} = 0. \quad (3.2)$$

The metric of the universe $g_{\mu\nu}$ defines the space time interval ds^2 :

$$ds^2 = g_{\mu\nu} dx^\mu dx^\nu \quad (3.3)$$

where the sum is done using the Einstein convention on the indices μ and ν that go from 0 to 3 for the time and the three space coordinates. Einstein equation is a generalization of Poisson equation which links the Newtonian gravitational potential $\phi(\mathbf{x})$ to the mass density ρ_m :

$$\Delta \phi = 4\pi \mathcal{G} \rho_m \quad (3.4)$$

where \mathcal{G} is the Newtonian gravitational constant. Einstein equation links the content of the universe with the curvature of the metric:

$$G_{\mu\nu} = \frac{8\pi \mathcal{G}}{c^4} T_{\mu\nu}. \quad (3.5)$$

In this equation, $G_{\mu\nu}$ is the Einstein tensor. It is defined as $G_{\mu\nu} = R_{\mu\nu} - \frac{1}{2} R g_{\mu\nu}$ with $R_{\mu\nu}$ the Ricci tensor and $R = g^{\mu\nu} R_{\mu\nu}$ the Ricci scalar. R is the local curvature of space. All these quantities describe the space-time geometry. The content of the universe is described by the stress-energy tensor $T_{\mu\nu}$. For a fluid with pressure p and density ρ , in the proper reference frame of the fluid $T^{\mu\nu}$ is diagonal and it is equal to:

$$T^{\mu\nu} = \begin{pmatrix} \rho c^2 & & & \\ & p & & \\ & & p & \\ & & & p \end{pmatrix}. \quad (3.6)$$

The factor $\frac{8\pi \mathcal{G}}{c^4}$ in the Einstein equation is here to correspond to the Poisson equation in the Newtonian limit.

3.1.2 A static and perpetual universe

In 1917, when Einstein finalizes the theory of general relativity, the universe is considered as static and eternal. To satisfy this conception, Einstein proposes a generalization of its equation:

$$G_{\mu\nu} - \Lambda g_{\mu\nu} = \frac{8\pi \mathcal{G}}{c^4} T_{\mu\nu} \quad (3.7)$$

where Λ is the cosmological constant. A specific value of $\Lambda = 4\pi\mathcal{G}\rho/c^2$ leads to a static but also spherical universe (see section 3.2.3 for a justification).

If we put the term $\Lambda g_{\mu\nu}$ in the right hand-side, we see that it can be interpreted as an effective stress-energy tensor:

$$G_{\mu\nu} = \frac{8\pi\mathcal{G}}{c^4} T_{\mu\nu} + \Lambda g_{\mu\nu} = \frac{8\pi\mathcal{G}}{c^4} (T_{\mu\nu} + T_{\mu\nu}^{\Lambda}) \quad (3.8)$$

where $T_{\mu\nu}^{\Lambda} = \frac{c^2}{8\pi\mathcal{G}} \Lambda g_{\mu\nu}$ is a tensor of the form of equation 3.6 with $\rho_{\Lambda} = \Lambda c^2/8\pi\mathcal{G} = \text{cst}$ and $p_{\Lambda} = -\rho_{\Lambda}$. In this way, this constant can be interpreted as an exotic component with negative pressure and which does not dilute when the volume increases as the density remains constant.

3.2 From a perpetual universe to an expanding universe

A nice overview of the birth of the Big Bang model is presented in the book by P. Luminet [22].

3.2.1 Questioning the vision of the universe

In 1917, our own galaxy is seen as the whole universe but in 1920, the limit of the universe and the nature of the spiral nebulae start to be debated. Spectroscopic observations, carried by Vesto Slipher, lead to the discovery of galaxy redshift [23].

The redshift z is defined as the relative difference between the observed and emitted wavelengths of an object:

$$z = \frac{\lambda_o - \lambda_e}{\lambda_e}. \quad (3.9)$$

This period, opposed astronomers like Heber D. Curtis who argued that nebulae were outside the galaxy mainly against Harlow Shapley. A public debate was organized on 26 April 1920 between the two astronomers but they could not conclude mainly because experimental evidence was missing. It is known as The Great Debate [51].

In 1923, Edwin Hubble established the distance of Cepheids in the Andromeda galaxy [24]. Cepheids are stars that pulse radially with a well defined period. There is a strong relation between the period and the intrinsic luminosity of the star that was discovered by Henrietta Swan Leavitt in 1908 [25], [26]. By comparing the absolute luminosity with the observed one, it is possible to get the distance. Using 40 Cepheids, Hubble claimed: “we find the distance of M31 to be 275 000 parsecs”, much further than the limit of the Milky Way.

Moreover, the idea of an expanding universe was introduced in the same period, first in 1922 by the Russian mathematician and cosmologist Alexandre Friedmann [27]. The evolution of the universe is governed by Einstein equations. Friedmann found a particular solution under the hypothesis of an homogeneous and isotropic universe. Within this frame, the expansion of the universe naturally comes out from equations. This completely changed the way of understanding the universe as it suggests a history for the universe with a beginning. It is also the first time the Universe as a whole is put in equations.

Independently, in 1927, Georges Lemaître, a Belgian catholic priest, mathematician and astronomer, introduced the idea of an expanding universe in an article published in the *Annales de la Société Scientifique de Bruxelles: Un Univers homogène de masse constante et de rayon croissant rendant compte de la vitesse radiale des nébuleuses extra-galactiques* [28].

At that time, Einstein was in favor of a static Universe, he could not admit expansion. At the Solvay congress, in 1927, A. Einstein completely disagreed with G. Lemaître concerning his physical interpretation. He would have said: “from the point of view of Physics this seems to me abominable.” However, he quickly changed his mind, abandoning the cosmological constant that he added previously and making significant contributions to the development of the expanding model [29].

Cosmological principle: The homogeneity and isotropy hypotheses are a generalization of the Copernican principle which states that humans on Earth are not privileged observers in the universe. These two hypotheses form the frame of modern cosmology. Homogeneity means that the universe is

equivalent at any place while isotropic implies equivalence of all directions. Of course we know that on small scales, the universe is not homogeneous, there are very dense regions and empty places but it is valid at cosmological scales. It is impressive to remark how a purely mathematical simplifying assumption changed our vision of the Universe and became a rather well observationnally supported argument. However, the validity of these hypothesis and the scale of transition to homogeneity are still discussed [52], [53].

3.2.2 The Hubble-Lemaître law

Lemaître was interested in the applications in astronomy and he was able to explain the galaxy redshift observed at that time [28]. He found what is called today the “Hubble-Lemaître law” saying that at a given time t , the velocity v of the far galaxies (called at that time nebulae) is proportional to their distance d :

$$v(t) = H(t)d(t) \quad (3.10)$$

where the constant of proportionality $H(t)$ is the expansion rate of the universe (with dimension T^{-1}) which may change during the history of the universe, so it is a function of the proper time t . The value today, noted H_0 , is known as the “Hubble-Lemaître constant”. Using observations made by Edwin Hubble and Gustaf Strömberg, he gave for the first time an estimation of the constant: $H_0 = 625 \text{ km s}^{-1} \text{ Mpc}^{-1}$.

Hubble published his measurements, made at the Mount Wilson Observatory two years later [30] with the famous plot shown in Figure 3.1.

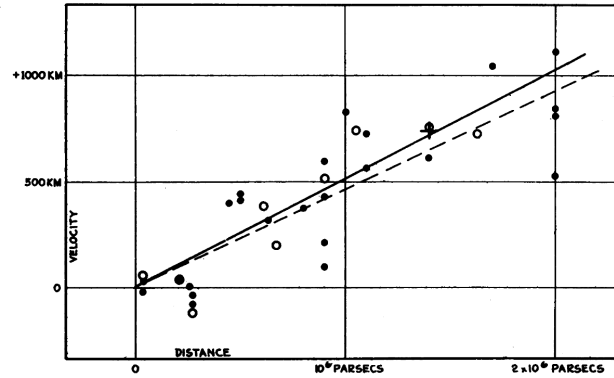


FIGURE 1
Velocity-Distance Relation among Extra-Galactic Nebulae.

Figure 3.1: Measurement of galaxy velocities as a function of their distance obtained by E. Hubble. Taken from [30].

This discovery was exclusively attributed to Hubble during many time. It may be because of the translation from French to English of the Lemaître paper in which the part referring to the H constant was deleted for unclear reasons [31].

The scale factor: To parameterize the expansion of the universe, it is useful to define a time-dependent function $a(t)$, called the scale factor, that is proportional to the distances between galaxies. Hubble law tells us that:

$$H(t) = \frac{\dot{a}}{a}$$

where for simplicity, we note $a = a(t)$ and \dot{a} is the time derivative of a . The scale factor a is unitless. This is a convention, a is sometime defined with dimension of a length.

3.2.3 The standard model of cosmology

The Einstein equation, under the hypothesis of a homogeneous and isotropic universe determines the metric of the universe. In spherical coordinates, it is

$$ds^2 = c^2 dt^2 - a(t)^2 \left(\frac{dr^2}{1 - kr^2} + r^2(d\theta^2 + \sin^2 \theta d\varphi^2) \right) \quad (3.11)$$

known as the Friedmann-Lemaître-Robertson-Walker (FLRW) metric. The space coordinates (r, θ, ϕ) are the comoving coordinates which are time independent, meaning that they are on a grid which dilates with expansion. Note that following the convention where a is unitless, r has the dimension of a length and k is a curvature, homogeneous to L^{-2} . The value of k corresponds to positive, zero or negative curvature of space:

$$k = \begin{cases} > 0 \rightarrow \text{close,} \\ = 0 \rightarrow \text{flat,} \\ < 0 \rightarrow \text{open.} \end{cases} \quad (3.12)$$

Under the hypothesis of homogeneity and isotropy, the Einstein equation becomes the two Friedmann-Lemaître equations:

$$\left(\frac{\dot{a}}{a} \right)^2 = \frac{8\pi\mathcal{G}}{3}\rho - \frac{k}{a^2} + \frac{\Lambda}{3} \quad (3.13)$$

$$\frac{\ddot{a}}{a} = -\frac{4\pi\mathcal{G}}{3}(\rho + 3p) + \frac{\Lambda}{3} \quad (3.14)$$

where we took the convention $c = 1$. By combining these two equations, we can obtain the conservation of energy in an expanding universe:

$$\dot{\rho} + 3\frac{\dot{a}}{a}(\rho + p) = 0. \quad (3.15)$$

p and ρ are the sum of the pressures and densities of the different components in the universe. The equation of state is $p = \omega\rho$ where ω differs for each component. Let us take three simple examples:

- **Universe dominated by radiation:** Radiation and relativistic matter like neutrinos are characterized by a pressure $p_r = \rho_r/3$ (so $\omega_r = 1/3$). The equation 3.15 of energy conservation gives $\rho_r \propto a^{-4}$ and the first Friedmann equation 3.13, if we neglect the curvature term and the cosmological constant term, give an evolution of the scale factor as $a(t) \propto t^{1/2}$. So the expansion is decelerating meaning that energy gravitates and opposes to expansion.
- **Universe dominated by matter:** Non relativistic matter has a zero pressure ($\omega_m = 0$). This leads to $\rho_m \propto a^{-3}$ and $a(t) \propto t^{2/3}$. As expected, the expansion decelerates because gravity opposes to it.
- **Universe dominated by the cosmological constant:** The equation of state for the cosmological constant is $p_\Lambda = -\rho_\Lambda$ (so $\omega_\Lambda = -1$). This leads to $\rho_\Lambda = \text{cst}$ and $a(t) = \exp\left(\sqrt{\frac{\Lambda}{3}}t\right)$. In this case, the expansion is exponentially accelerated.

This is summarized in Figure 3.2 which sketches the evolution of densities as a function of the scale factor. The equality between matter and radiation corresponds to the recombination epoch. In any scenario, the cosmological constant eventually dominates the Universe. As we did for Λ in equation 3.8, we can define an effective density associated with the variable k :

$$\rho_k(t) = -\frac{3k}{8\pi\mathcal{G}a(t)^2} \quad (3.16)$$

which is called the curvature energy density. We also define the critical density ρ_c as the particular value of ρ for which the universe is flat ($k = 0$) assuming no cosmological constant ($\Lambda = 0$). According to the Friedmann equation 3.13, we have:

$$\rho_c(t) = \frac{3H(t)^2}{8\pi\mathcal{G}} \quad (3.17)$$

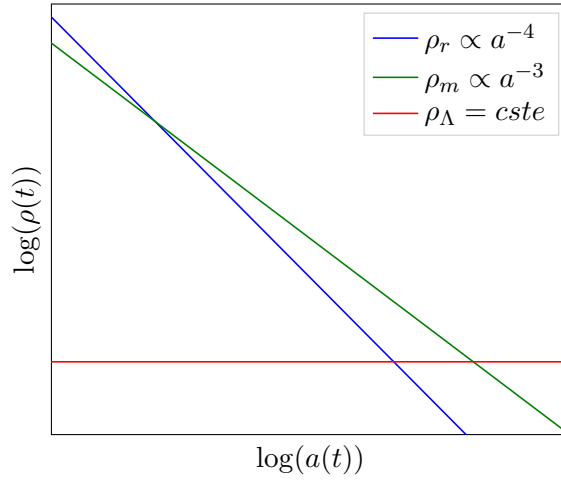


Figure 3.2: Sketch of the evolution of the three densities (radiation, matter and cosmological constant) as a function of the scale factor $a(t)$ in logarithmic scale.

and its present value $\rho_c^0 = \frac{3H_0^2}{8\pi\mathcal{G}}$. And finally, we introduce the dimensionless density parameters $\Omega_i(t) = \frac{\rho_i(t)}{\rho_c(t)}$ where i stands for radiation, matter, cosmological constant or curvature. Using these notations, the first Friedmann equation with $\rho = \rho_m + \rho_r$ simply writes:

$$1 = \Omega_m(t) + \Omega_r(t) + \Omega_k(t) + \Omega_\Lambda(t). \quad (3.18)$$

It is common to express this equation with the present values of the parameters. According to the time evolution of each energy density, we have:

$$\frac{H^2(t)}{H_0^2} = \Omega_m^0 \left(\frac{a(t)}{a_0} \right)^{-3} + \Omega_r^0 \left(\frac{a(t)}{a_0} \right)^{-4} + \Omega_k^0 \left(\frac{a(t)}{a_0} \right)^{-2} + \Omega_\Lambda^0. \quad (3.19)$$

This model describes the expansion of the universe according to its content composed of matter, radiation and the cosmological constant. It is called the Λ -Cold Dark Matter (Λ CDM) model and it is the standard model for cosmology today. We will see in section 7.6.1 that this model is able to constrain the observations accurately with only six parameters.

Can we have a static Universe with a cosmological constant? I mentioned in section 3.1.2 that a particular value of Λ leads to a static universe ($\ddot{a} = \dot{a} = 0$). Indeed, if we consider a matter dominated universe ($p = 0$), imposing $\ddot{a} = 0$ in the second Friedmann-Lemaître equation 3.14 leads to $\Lambda = 4\pi\mathcal{G}\rho$. Moreover, the condition $\dot{a} = 0$ in the first equation 3.13 gives $k = 4\pi\mathcal{G}\rho a^2 = \Lambda a^2 > 0$ which corresponds to a spherical universe. Thus, the universe can be static even with a non-zero cosmological constant equal to $4\pi\mathcal{G}\rho$ but it must also be spherical.

3.2.4 Proper and comoving distances

The definition of a distance in a curved and expanding universe is not trivial. We can refer to paper [54] for details.

In the FLRW metric (t, r, θ, φ) , we consider a luminous object at comoving coordinates $(t_e, r_e, \theta_e, \varphi_e)$. Those coordinates follow the expansion of the universe. The observer is located at $(t_0, 0, 0, 0)$. The proper distance is the length that can be measured at a fixed time (for example today at t_0) between the observer and r_e . Due to the expansion, the proper distance changes over time. We have

$$d_p(t_0, r_e) = \int_0^{r_e} \sqrt{g_{rr}} dr' = \int_0^{r_e} \frac{a_0 dr'}{\sqrt{1 - kr'^2}} \equiv a_0 \chi(r_e). \quad (3.20)$$

where $a_0 = a(t_0)$ and $\chi(r_e)$ is the comoving distance defined as:

$$\chi(r_e) = \int_0^{r_e} \frac{dr'}{\sqrt{1 - kr'^2}} = \begin{cases} \arcsin(r_e) & \text{if } k > 0, \\ r_e & \text{if } k = 0, \\ \text{arcsh}(r_e) & \text{if } k < 0. \end{cases} \quad (3.21)$$

The comoving distance is the proper distance where the expansion effect is removed. For a flat universe, it is equal to the comoving coordinate r_e . Regarding the units, the proper distance is a physical distance expressed in meters. So the comoving coordinate r and the comoving distance $\chi(r)$ have a unit of $m/a(t)$ (the scale factor is dimensionless).

In the same way, we can define a comoving time η such that:

$$dt = a(t)d\eta. \quad (3.22)$$

3.2.5 Relation between the scale factor and the redshift

So far, we have expressed Friedmann-Lemaître equation 3.19 as a function of the scale factor but we will see that $a(t)$ can be related to the redshift z . We consider an electromagnetic wave emitted at $t_e + T_e$ and received at $t_0 + T_0$ where T_e and T_0 are the wave period at emission and reception. The comoving distance for the wave emitted at $t_e + T_e$ is:

$$\chi(t_e + T_e) = \int_{t_e + T_e}^{t_0 + T_0} \frac{cdt}{a(t)} = \int_{t_e}^{t_0} \frac{cdt}{a(t)} + \int_{t_0}^{t_0 + T_0} \frac{cdt}{a(t)} - \int_{t_e}^{t_e + T_e} \frac{cdt}{a(t)} \quad (3.23)$$

By definition, the comoving distance is invariant with time so

$$\chi(t_e + T_e) = \chi(t_e) \Rightarrow \int_{t_0}^{t_0 + T_0} \frac{cdt}{a(t)} = \int_{t_e}^{t_e + T_e} \frac{cdt}{a(t)}. \quad (3.24)$$

Under the hypothesis that $a(t)$ does not vary during a period of the electromagnetic wave, we have

$$\frac{cT_0}{a_0} = \frac{cT_e}{a(t_e)} \Rightarrow \frac{\lambda_0}{a_0} = \frac{\lambda_e}{a(t_e)}. \quad (3.25)$$

So finally, we can link the redshift and the scale factor as

$$1 + z = \frac{\lambda_0}{\lambda_e} = \frac{a_0}{a(t_e)}. \quad (3.26)$$

This definition is very important, it links the theoretical scale factor $a(t)$ which encodes the expansion of the universe with an observable quantity, the redshift z . This allows to rewrite the first Friedmann equation as a function of redshift:

$$\frac{H^2(z)}{H_0^2} = \Omega_m^0(1+z)^3 + \Omega_r^0(1+z)^4 + \Omega_k^0(1+z)^2 + \Omega_\Lambda^0. \quad (3.27)$$

In addition, it is possible to express the comoving distance as a function of redshift z . Light travels in straight line following geodesics so $d\theta = d\phi = 0$ and we have

$$ds^2 = 0 = c^2 dt^2 - \frac{a^2(t)}{1 - kr^2} dr^2. \quad (3.28)$$

Thus, $dr/\sqrt{1 - kr^2} = -cdt/a(t)$. The minus sign means that light travels along the $-r$ direction ($dr < 0$). So the comoving distance becomes:

$$\chi(r_e) = \int_{t_0}^{t_e} \frac{-cdt}{a(t)} = \int_{t_e}^{t_0} \frac{cdt}{a(t)} = \chi(t_e). \quad (3.29)$$

By using

$$H = \frac{1}{a} \frac{da}{dt} \Rightarrow dt = \frac{da}{aH} \quad (3.30)$$

and

$$\frac{a}{a_0} = \frac{1}{1+z} \Rightarrow da = -a_0 \frac{dz}{(1+z)^2} \Rightarrow \frac{da}{a} = \frac{-dz}{(1+z)}, \quad (3.31)$$

it becomes

$$\chi(t_e) = \int_{a_e}^{a_0} \frac{cda}{a^2 H(a)} = \int_{z_e}^{z=0} \frac{-cdz}{(1+z)H(z)} \frac{(1+z)}{a_0} = \int_0^{z_e} \frac{cdz}{a_0 H(z)} = \chi(z). \quad (3.32)$$

And the proper distance as a function of redshift is:

$$d_p(z) = a_0 \chi(z) = \int_0^{z_e} \frac{cdz}{H(z)}. \quad (3.33)$$

3.2.6 Measurable distances in cosmology

Proper and comoving distances are not measurable, you can not fix the time and get it. In this section, we will define two others distances which are experimentally measurable [49], [54].

Luminosity distance

We consider a source, for example a galaxy, at comoving coordinates $(t_e, r_e, \theta_e, \varphi_e)$ emitting N photons at time t_e during a time interval dt_e of mean frequency ν_e . The luminosity of the galaxy at time t_e is:

$$L = \frac{Nh\nu_e}{dt_e} \quad (3.34)$$

where h is the Planck constant. The photons reaching an observer today at $t_0, r = 0$ are located on a sphere of surface $4\pi a_0^2 r_e^2$ (this expression is valid in a curved spacetime). We have the following relation for redshift:

$$1+z = \frac{\nu_e}{\nu_0} = \frac{a_0}{a_e} \quad (3.35)$$

So the energy of the photons today is $h\nu_0 = h\nu_e a_e/a_0$. Photons emitted during dt_e reach the observer during a longer time $dt_0 = dt_e a_0/a_e$. The physical reason is that, because of expansion, each photon must cross a larger distance than the previous one. Thus, the luminous flux today is:

$$\Phi_0 = \frac{Nh\nu_0}{4\pi a_0^2 r_e^2 dt_0} = \frac{Nh\nu_e}{4\pi r_e^2 a_0^2 dt_e (1+z)^2} = \frac{L}{4\pi a_0^2 r_e^2 (1+z)^2} \quad (3.36)$$

Two physical effects contributes to the redshift z dependence in Φ_0 . The first one is the expansion of space between the source and the observer. The second is the shift in wavelength that decreases the energy of the photons while they are traveling.

In a flat and static universe, the observed flux received from a source located at a distance D_L is $L/4\pi D_L^2$. Thus, the luminosity distance $D_L(z)$ of the source is defined as:

$$\Phi_0 = \frac{L}{4\pi D_L^2(z)} \Rightarrow D_L(z) = a_0 r_e (1+z). \quad (3.37)$$

Angular distance

We consider again a bright source at comoving coordinates $(t_e, r_e, \theta_e, \varphi_e)$. At the emission time t_e , the source has a transverse size l . Its angular size on the sky at t_e considering a flat geometry is:

$$d\theta_e = \frac{l}{a(t_e)r_e} \quad (3.38)$$

under the small angle approximation. Photons travel in straight line with $(\theta, \phi = \text{cst})$ so an observer at $r = 0$ and $t = t_0$, sees the source with the same angular size ($d\theta_0 = d\theta_e = d\theta$). The angular distance is the physical distance at which the galaxy would be to be seen under the angle $d\theta$ in a flat and static (Euclidian) geometry:

$$d\theta = \frac{l}{D_A(z)}. \quad (3.39)$$

Thus, the angular distance can be linked to the luminosity distance by:

$$D_A(z) = a(t_e)r_e = \frac{D_L(z)}{(1+z)^2}. \quad (3.40)$$

These two distances are expressed in meters.

3.2.7 The Hot Big Bang model

If the universe is expanding, it seems that by going back in time, density and temperature will increase to infinity and this rises the question of a starting point. In 1931, G. Lemaître, in a short paper in *Nature* proposed that all the matter in the Universe today came from a primeval atom. This was the germ of the Big Bang theory developed in 20th century. Later, in 1946, he published a complete description of his model: *L'hypothèse de l'atome primitif : essai de cosmogonie* which is a compilation of articles and of conferences that he gave from 1929 to 1945, recently reedited [32].

The term Big Bang was introduced for the first time on 28 March 1949, at the BBC radio by Fred Hoyle: “These theories were based on the hypothesis that all the matter in the universe was created in one big bang at a particular time in the remote past.”. He was comparing to the Steady State theory he was defending at that time. Contrary to what is commonly said, F. Hoyle did not introduce the term in a pejorative way in a hotly debate with G. Gamow [33].

The measurement of the expansion rate of the universe is the first major argument in favor with the Big Bang model but it is not the only one as we will see in the next section.

3.3 Thermal history of the Universe

3.3.1 Prediction and first observation of the CMB

In the late 1940s George Gamow, Ralph Alpher and Robert Herman transformed Lemaître’s hypothesis into a sophisticated model of the early universe. They assumed the initial state to consist of a very hot, compressed mixture of nucleons and photons. The theory of nucleosynthesis which describes the formation of the first nuclei, was originally presented in a paper *The Origin of Chemical Elements* [34] known as the $\alpha\beta\gamma$ paper for the three authors R. Alpher, H. Bethe, G. Gamow. At that time, A. Alpher was the PhD student of G. Gamow and H. Bethe was added for humoristic reason ($\alpha\beta\gamma$). The theory was then elaborated in a series of papers in 1948 on the origin of elements [18], [35]–[37]. Figure 3.3 represents the formation of deuteron (association of one neutron and one proton) in the first minutes of the Universe.

In the same papers, they also anticipated the emission of the Cosmic Microwave Background (CMB). The creation of a photon gas was estimated at the time where the mass density of radiation became comparable with the density of matter, called “the condensation time”. In paper [37], they give an estimation for the temperature of the CMB today: “The temperature of the gas at the time of condensation was 600 K., and the temperature in the universe at the present time is found to be about 5 K.” A detailed review of what happened during the year 1948, where actually 11 articles were published on the subject, can be found in [38].

However, those results were forgotten and the prediction of the CMB was redone in the early 1960s independently by Yakov Zel’dovich, Robert Dicke and James Peebles.

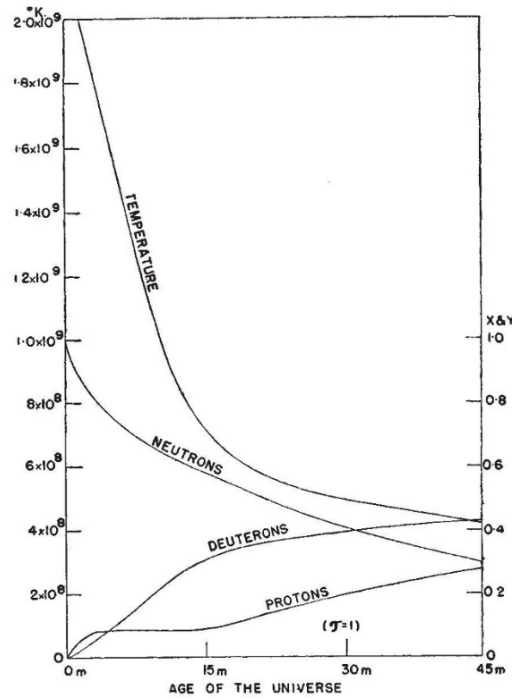


Figure 3.3: The formation of deuterium in the first minutes of the Universe. With X for the concentration of neutrons (with $X(0) = 1$), and Y for the concentration of protons (with $Y(0)=0$). Taken from [18].

An impromptu observation

In 1964, Arno Penzias and Robert Woodrow Wilson at the Bell Telephone Laboratories in New Jersey were working on a Dicke radiometer that they intended to use for radio astronomy and satellite communication experiments (see Figure 3.4). They had measured a noise excess with unexplained origin “about 3.5 K higher than expected. This excess temperature is, within the limits of our observations, isotropic, unpolarized, and free from seasonal variations” [107]. The origin was unexplained until they made the connection with the recent work by Peebles, Dicke, and others. Penzias and Wilson received the 1978 Nobel Prize in Physics for the discovery of the CMB radiation.

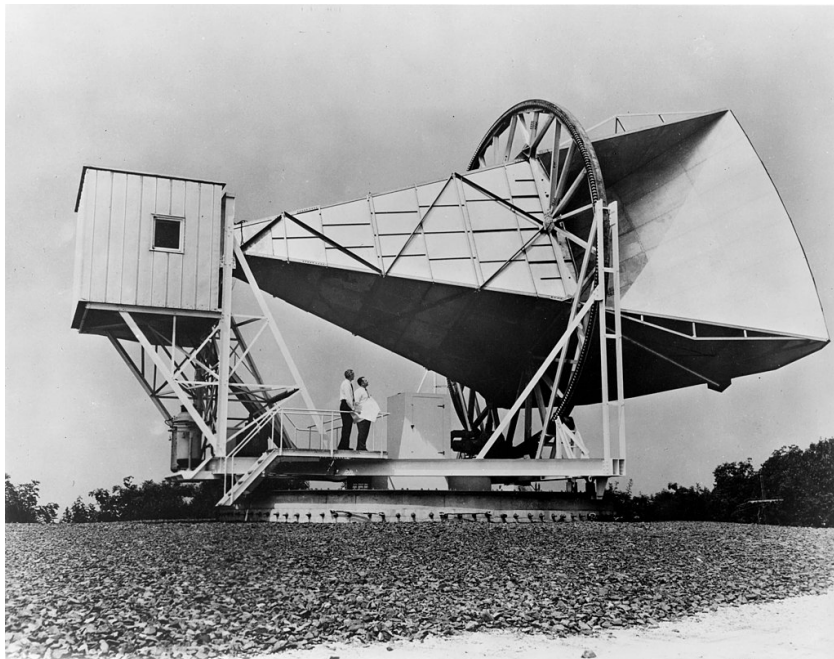
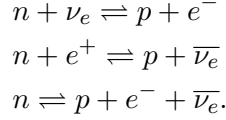


Figure 3.4: Famous picture of Penzias and Wilson in front of their radio antenna.

3.3.2 Big Bang nucleosynthesis

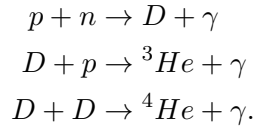
The synthesis of the light elements occurs at the epoch from approximately 10 s to 20 min in the history of the Universe, and is called the Big Bang nucleosynthesis (BBN) [55]. In this phase, the majority of deuterium and helium nuclei are produced and a small fraction of lithium, beryllium and boron too. The remaining and heavier elements will be produced in stellar nucleosynthesis much later. In primordial BBN, the only free parameter is the very small baryon-to-photon ratio $\eta_B = \frac{n_b}{n_\gamma} \sim 6 \times 10^{-10}$. Neutrons and protons can interconvert via weak interactions when the temperature is sufficiently low, so that all the baryons are concentrated in nucleons rather than in free quarks, but high enough so that there are only protons and neutrons rather than bound nuclei. Reactions are



There is a competition between the expansion rate of the Universe and the rate of the reactions. The proton/neutron ratio follows the Maxwell-Boltzmann statistic:

$$\frac{n}{p} = e^{-Q/(kT)} \quad (3.41)$$

where k is the Boltzmann constant and $Q = (m_n - m_p)c^2 \simeq 1.3$ MeV is the Q-value of the reaction which is the amount of energy absorbed or released during the nuclear reaction. Because of the expansion, the temperature decreases and at some point, around $\sim 10^{10}$ K, when the reaction rate becomes lower than the expansion rate, the reactions are frozen. At that time, the ratio $\frac{n}{p}$ is about 6. The only reactions that will continue are neutron β -decay so the ratio $\frac{n}{p}$ increases slowly. Deuterium nuclei, with a binding energy of 2.22 MeV, may form but they are not stable because of very energetic photons¹. When the temperature reaches $\sim 10^9$ K (at $\frac{n}{p} \sim 7$), the deuterium nuclei become stable and the BBN can start with reactions of type:



The BBN eventually stops when the temperature and density become too small for allowing fusion. At this point, the universe is a plasma composed of photons, electrons, light nuclei and dark matter² at thermodynamic equilibrium. The neutrinos have decoupled much before (i.e. roughly 1 second after the Big Bang, at $T \sim 1$ MeV), and no longer play a role. Electrons and photons are highly coupled by Compton scattering making the universe opaque to radiation because the mean free path for photons is small. Any hydrogen produced is quickly ionized by energetic photons. The Universe is radiation dominated.

Today, the observation of the abundance of chemical elements in the universe is another strong evidence for the Big Bang model (see for example Table 2 in [56]).

3.3.3 Recombination

At a redshift of $z \sim 1100$ (around 380 000 years after the Big Bang) and at a temperature of $T \sim 3000$ K, photons were cool enough to allow electrons to recombine with nuclei and form atoms. The Universe becomes neutral. This epoch is known as recombination³. As soon as they decouple from baryons, the photons propagate freely in the universe until now and they form the CMB radiation today. The decoupling takes some time, the ionization rate of the universe corresponding to the fraction of free electrons does not fall to zero instantaneously. Recombination extends over $\Delta z \sim 90$ [110]. This is illustrated in Figure 3.5. To reach the Earth today, CMB photons have traveled since decoupling

¹The mean energy of photons is not enough to dissociate deuterium nuclei but they are many more than protons and neutrons so there is always a photon with enough energy to break new nuclei.

²See section 7.1.1 for an introduction of what dark matter is.

³The term recombination is not very well chosen as electrons and nuclei were never combined before.

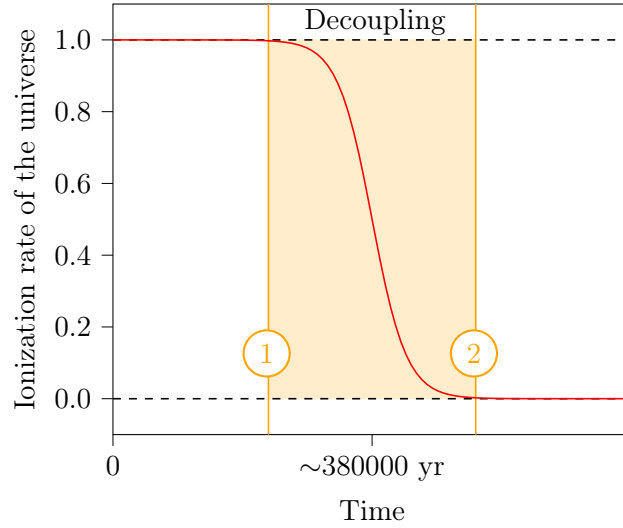


Figure 3.5: Sketch of the ionization rate of the universe during recombination. The recombination phase is highlighted in orange, starting at 1 and ending at 2.

which corresponds to approximately 13.8 billion years (the age of the universe). The ones we observe all come from a spherical shell centered on the Earth, with a radius such that they have traveled this amount of time. This sphere is called the Last Scattering Surface (LSS) and each point in the Universe has its own.

If the Universe was static, assuming no expansion, this sphere would be located at ~ 13.8 billion light years. However, because of the expansion of the universe, at the time of decoupling, the radius (proper distance) of the sphere centered on the point where the Earth will form, was approximately 40 million light years. It means that because of expansion, photons have traveled ~ 13.8 billion years to reach a distance of only 40 million light years because the distance increases as they travel. From the CMB emission, the radius of the sphere has expanded and today it is approximately 47 billion light years. As decoupling is not instantaneous, the LSS is not infinitely thin but has a finite width corresponding to the duration of recombination. All photons that we received today have crossed the same sphere at the same time. However, some photons may have started to propagate freely before others, during recombination phase. This is summarized in Figure 3.6 either on a sketch in space (left) or on a space-time diagram (right).

In summary, measuring the CMB today gives us a picture of the universe at thermodynamic equilibrium around 380 000 years after the Big Bang. Its observation is one of the best arguments in favor of the Big Bang scenario.

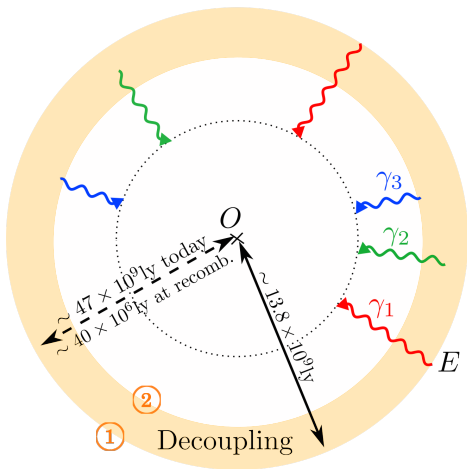


Figure 3.6: Sketch representing the last scattering surface with CMB photons propagating up to the observer O (the Earth). Three types of photons arriving today but emitted at different times during recombination are shown with different colors. Decoupling starts at 1 and ends at 2 similarly to Figure 3.5. *Left*: the continuous black arrow gives the distance in a static universe while the dashed black arrow gives the distance for an expanding universe at the recombination time and today. *Right*: space-time diagram, three CMB are shown considering a flat and static universe so that photons follow light cones with $\pi/4$ inclination. E is the position when the photon was emitted and E' the same position today. In dashed lines, we sketch an example of an expanding universe.

3.4 The CMB black-body spectrum

3.4.1 A black-body at 2.7 K today

As the primordial plasma is at thermodynamic equilibrium, the spectrum of the radiation must follow the black-body Planck law:

$$B_\nu(T) = \frac{2h\nu^3}{c^2} \frac{1}{e^{\frac{h\nu}{kT}} - 1} \quad (3.42)$$

where h is the Planck constant, k the Boltzmann constant, c the speed of light, T the black body temperature and ν the frequency of the radiation. $B_\nu(T)$ (intensity or brightness) is the power emitted by a black body at temperature T , per unit solid angle, per unit surface orthogonal to the propagation and per unit frequency. $B_\nu(T)$ is expressed in $[\text{W m}^{-2} \text{Hz}^{-1} \text{sr}^{-1}]$ or in Jy sr^{-1} where $1 \text{ Jy} = 10^{-26} \text{ W m}^{-2} \text{Hz}^{-1}$. For low frequencies, $h\nu \ll kT$, the Planck law becomes:

$$B_\nu(T) = \frac{2k\nu^2 T}{c^2}, \quad (3.43)$$

known as the Rayleigh-Jeans approximation. It means that in the low frequency regime, the spectral radiance is proportional to the temperature. Equation 3.43 can be expressed in terms of wavelength λ . We require that the integral of $B_\nu(T)$ over a frequency interval is equal to the integral of $B_\lambda(T)$ over the corresponding wavelength interval:

$$\int_{\nu_1}^{\nu_2} B_\nu(T) d\nu = \int_{c/\lambda_2}^{c/\lambda_1} B_\nu(T) \frac{cd\lambda}{\lambda^2} \equiv \int_{\lambda_2}^{\lambda_1} B_\lambda(T) d\lambda. \quad (3.44)$$

This leads to

$$B_\lambda(T) = B_\nu(T) \frac{c}{\lambda^2} = \frac{2ckT}{\lambda^4}. \quad (3.45)$$

The CMB black body spectrum was very well measured by FIRAS [154]–[156], an instrument on the COBE satellite, shown in Figure 3.7. Let us one more time emphasize that this observation is a strong

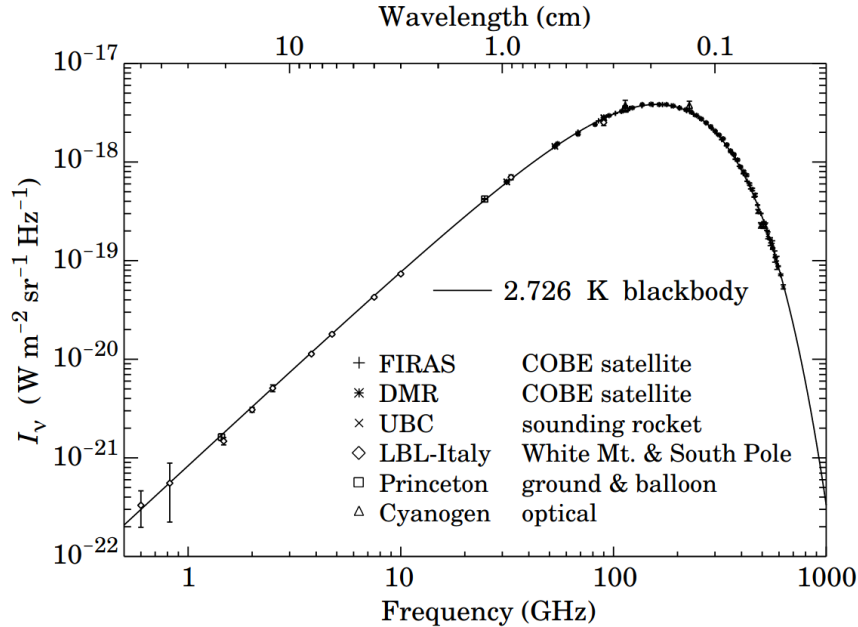


Figure 3.7: CMB black body spectrum measured by COBE. Taken from [111].

argument in favor of the Big Bang model as it is very hard to imagine local astrophysical processes that would lead to such a black-body spectrum.

We have seen that for a relativistic radiation with energy density ρ_r , we have:

$$\rho_r(a)a^4 = \text{cst} \quad (3.46)$$

and at thermodynamic equilibrium, the Stefan law gives $\rho_r \propto T^4$. So the CMB black-body temperature evolves as:

$$T(a)a = \text{cste} \quad \Rightarrow \quad T(z) = T_0(1+z) \quad (3.47)$$

with $T_0 = 2.72548 \pm 0.00057$ K the temperature today [112] measured by FIRAS. This is sketched in Figure 3.8 where we see CMB photons losing energy as they propagate to the observer located in O .

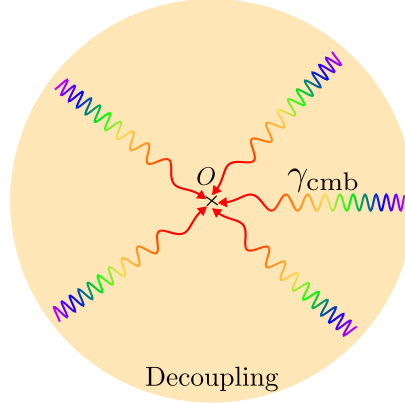


Figure 3.8: Sketch showing CMB photons losing energy so their wavelength increases as they propagate in the universe.

3.4.2 Sunyaev Zel'dovich (SZ) effect

When the CMB photons cross galactic clusters, they can be scattered and converted to higher energies by the electrons in the intergalactic medium through inverse Compton scattering. This process involves the scattering of low energy photons to high energies by ultrarelativistic electrons so that the photons gain energy while the electrons lose energy. It is called inverse because it is the opposite of the standard Compton effect where very energetic photons scatters on electrons so the photons lose energy. Rashid Sunyaev and Yakov Zel'dovich predicted this effect in 1969 [113], [114]. They have shown that it will induce a distortion of the CMB black-body spectrum, see in Figure 3.9. A complete review of this effect can be found for example in [115].

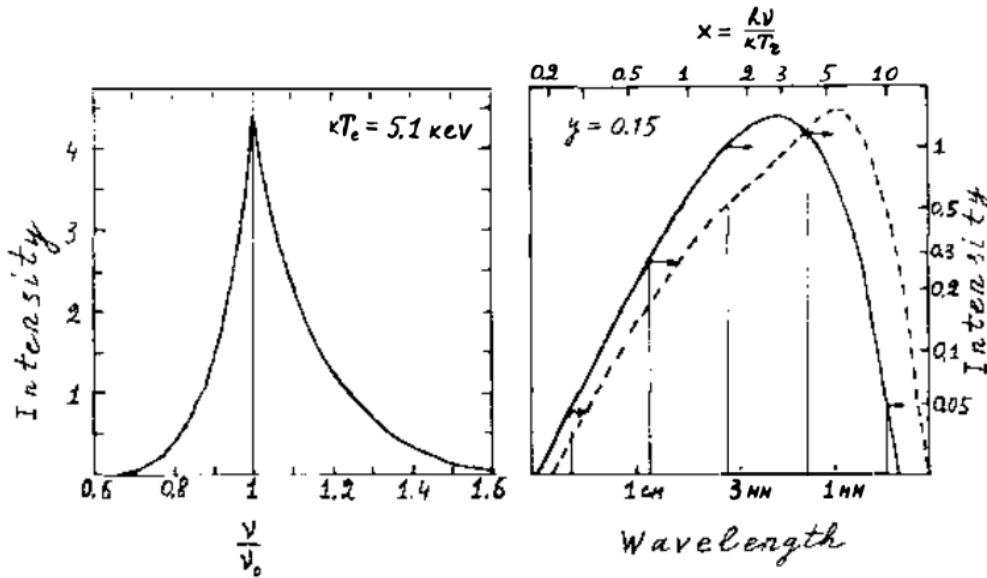


Figure 3.9: *Left:* The monochromatic spectral line profile after one scattering by hot electrons. *Right:* The spectrum of blackbody radiation (solid line) after multiple Compton scattering (broken line). Taken from [114].

There are actually three different SZ effects:

- Thermal: electrons have high energy due to their temperature ($T_e \sim 10^7 - 10^8$ K).
- Kinematic: electrons have high energy due to the bulk motion with respect to the CMB rest frame.
- Non-thermal: many galaxy clusters contain a population of relativistic electrons which produce a diffuse radio emission via synchrotron radiation in a magnetized medium [116].

SZ effect is seen in the direction of galaxy clusters so they are localized. This is why it can be used to detect clusters. Using Planck data, a catalog with 439 clusters was established [117] and this is also a powerful probe to constrain cosmological parameters as we will see in section 7.6.2.

3.4.3 The CMB dipole

The CMB is an isotropic radiation and “our” last scattering surface defines a rest frame. The Earth is moving relatively to this frame. Due to the transverse relativistic Doppler effect, motion with velocity $\beta = v/c$ through an isotropic radiation field yields to an observation of a temperature $T(\theta)$ in the observer’s frame [118], [157]:

$$\frac{T(\theta)}{T_0} = \frac{\sqrt{1-\beta^2}}{1-\beta \cos \theta} \simeq 1 + \beta \cos \theta + \frac{1}{2}\beta^2 \cos(2\theta) + \mathcal{O}(\beta^3) \quad (3.48)$$

where θ is the angle between β and the direction of observation as measured in the observer’s frame and T_0 the mean field temperature. The approximation at second order being valid for $v \ll c$. Thus, to first order in β , the observer measures a black body radiation of temperature $T_0(1 + \beta \cos \theta)$ when observing in the θ direction. The second term is a dipole leading to a higher observed temperature and so a maximum intensity detection toward the direction of motion. The dipole amplitude is about 10^{-3} smaller than the mean temperature.

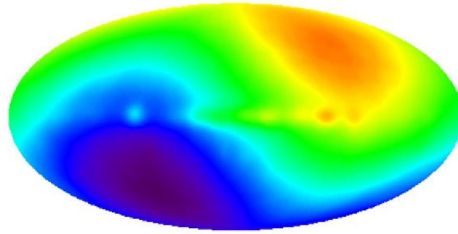


Figure 3.10: CMB dipole obtained by the COBE Differential Microwave Radiometers (DMR).

Using the Planck law, we can predict the spectrum of the CMB dipole:

$$I_\nu(\theta) = B_\nu(T(\theta)) = B_\nu(T_0) + T_0 \left. \frac{\partial B_\nu}{\partial T} \right|_{T_0} \beta \cos \theta + \mathcal{O}(\beta^2) \quad (3.49)$$

where the first term is the monopole and the second one is the dipole. We can calculate the first derivative, that we note b'_ν :

$$b'_\nu = \left. \frac{\partial B_\nu(T)}{\partial T} \right|_{T_0} = \frac{2h\nu^3}{c^2} \frac{e^x}{(e^x - 1)^2} \frac{h\nu}{kT^2} \Big|_{T_0} \quad \text{with} \quad x = \frac{h\nu}{kT}. \quad (3.50)$$

Thus, the observation of the CMB dipole allows to measure our velocity with respect to the CMB rest frame. This was recognized as soon as the CMB was discovered. The first claimed detection was by Edward Conklin [119], using a ground-based differential radiometer working at 8 GHz, followed by the first measurement of the dipole peak declination by Paul Henry [120]. It was later measured by G. Smoot at 33 GHz using a twin-antenna Dicke radiometer [158]. In 1993, the COBE Differential Microwave Radiometers (DMR) [121] measured a temperature of $\Delta T = 3.365 \pm 0.027$ mK toward direction $(l, b) = (264.4^\circ \pm 0.3^\circ, 48.4^\circ \pm 0.5^\circ)$ and a velocity of the local group of $v_{LG} = 627 \pm 22$ km s⁻¹ toward $(l, b) = (276^\circ \pm 3^\circ, 30^\circ \pm 3^\circ)$. The CMB dipole map obtained by DMR is presented in Figure 3.10.

3.4.4 CMB thermodynamic units

The Planck law associates a temperature to a known spectral radiance. This is why it is common in CMB field or in radio astronomy to express the measurements in brightness temperature and not in power.

In this section, we define the CMB and the Rayleigh-Jeans (RJ) brightness temperatures T_{CMB} and T_{RJ} both commonly used in CMB field. The differentiation of equation 3.49, gives

$$dI_\nu = b'_\nu dT_{\text{CMB}} \quad (3.51)$$

and in the same way, with the RJ approximation 3.43, we have

$$dI_\nu = b'_{\text{RJ}} dT_{\text{RJ}} \quad (3.52)$$

where we defined $b'_{\text{RJ}} = 2k\nu^2/c^2$. From those expressions, the conversion from a map expressed in $[\text{W m}^{-2} \text{Hz}^{-1} \text{sr}^{-1}]$ to a map in CMB-Kelvin or RJ-Kelvin could seem obvious. However, as explained in [159], the conversion factor is a function of the frequency ν so it depends on the detector band-pass and this makes the conversion not trivial.

A possibility is to calibrate the conversion factor using the CMB dipole. We consider a sky map M_{CMB} measured by a detector, expressed in CMB-Kelvin:

$$M_{\text{CMB}} = G \int d\nu \tau(\nu) A \Omega dI_\nu \quad (3.53)$$

with A the detector area, Ω the solid angle, $\tau(\nu)$ the spectral band-pass and G a calibration factor. We note $K_{\text{CMB}} = GA\Omega$ with unit $[\text{K}_{\text{CMB}} \text{W}^{-1} \text{m}^2 \text{sr}]$ and we will calibrate it on the CMB dipole for which we have

$$M_{\text{CMB}} = dT_{\text{CMB}} = K_{\text{CMB}} \int d\nu \tau(\nu) dI_\nu = K_{\text{CMB}} \int d\nu \tau(\nu) b'_\nu dT_{\text{CMB}} \quad (3.54)$$

$$\Rightarrow K_{\text{CMB}} = \left[\int d\nu \tau(\nu) b'_\nu \right]^{-1}. \quad (3.55)$$

In the same manner, the map in RJ-Kelvin will be

$$M_{\text{RJ}} = dT_{\text{RJ}} = K_{\text{RJ}} \int d\nu \tau(\nu) dI_\nu \quad \text{with} \quad K_{\text{RJ}} = \left[\int d\nu \tau(\nu) \frac{2k\nu^2}{c^2} \right]^{-1}. \quad (3.56)$$

Conclusion In this chapter, we have seen that the modern understanding of our universe takes its origin around 1920. Basically, thinking about “physical cosmology” was impossible before General Relativity, just because the whole Universe could not be considered as a physical object and be in equations. So, as many people also say, Cosmology really started with General Relativity. This period is also marked by the awareness that the Universe was much bigger than what we thought and had its own dynamic. The discovery of the expansion of the universe quickly led to the Hot Big Bang model for which the CMB is a direct consequence. It is remarkable that the evolution of the universe in a global manner can be treated with simple physics based on equilibrium and reaction rates between existing species. The CMB radiation is a fantastic source for studying the primordial universe.

In this chapter, we have presented the CMB black-body spectrum. In the next chapter, we will see that the CMB temperature and polarization have tiny spatial fluctuations which are of a great interest.

Chapter 4

Spatial anisotropies in the CMB map

Contents

4.1	Temperature anisotropies	105
4.1.1	Sound waves in the primordial plasma	106
4.1.2	Physical processes that create temperature anisotropies	107
4.1.3	Processes that attenuate the anisotropies	108
4.1.4	Angular power spectrum	110
4.1.5	Observed power spectrum	113
4.2	Polarization anisotropies	115
4.2.1	Thomson scattering	115
4.2.2	Thomson scattering as a source of linear polarization in the CMB	116
4.2.3	E and B -mode introduction	117
4.2.4	Origin of quadrupole anisotropies	119
4.2.5	Polarization statistics	122
4.2.6	Perturbations on the way	123

Soon after the first observation of CMB, deviations from the blackbody shape and the isotropy became the next targets for theorists and observers. This chapter is dedicated to the presentation of spatial anisotropies in the CMB radiation, in temperature and polarization. Both originate from processes happening in the primordial plasma but also along the path of the CMB photons. I describe those processes in a not too formal manner, focusing on physical arguments more than on equations. As it is convenient to look at the anisotropies in the Fourier domain, I introduce the angular power spectra. Something remarkable is that temperature and polarization anisotropies and the power spectrum shapes were predicted before the first observation [108].

This chapter is mainly inspired by the well known papers by W. Hu et al. [122]–[125], as well as their tutorials¹, a paper by N. Sugiyama [126] and the books by J. Rich [49] and S. Dodelson [109]. A more analytical description can be found in the paper by W. Hu et al. [127].

4.1 Temperature anisotropies

Once the dipole is removed from the CMB map, very small spatial anisotropies remain, of the order of 30 μK which is 10^5 smaller than the mean CMB temperature. Temperature anisotropies have been observed on the full sky by the COBE, WMAP and Planck satellites, each time improving the angular resolution, as shown in Figure 4.1. In this section, I will describe the physical origins of those tiny fluctuations.

¹<http://background.uchicago.edu/index.html>

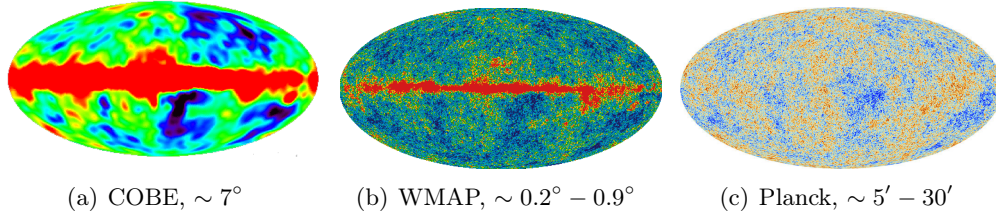


Figure 4.1: CMB temperature anisotropies measured by the COBE (launched in 1989), WMAP (launched in 2001) and Planck (launched in 2009) satellites. The angular resolution (FWHM) is written below each map.

4.1.1 Sound waves in the primordial plasma

Relativistic sound waves raced through the hot plasma that filled the universe throughout its first 380 000 years. That sound left an imprint that is still discernible in the CMB and also in the large-scale distribution of galaxies. CMB anisotropies are essentially a frozen image seen from here and now of the sound-wave pattern at decoupling. A pedagogical description can be found in [57].

Before recombination, the photons are tightly coupled to the electrons and protons. This can be modeled as a single fluid named the baryon-photon fluid described by its pressure and energy density.

The primordial plasma contains perturbations of different natures (scalar, vectorial or tensorial). As we will see in chapter 7, they are thought to be generated by the cosmic inflation phase. Gravity attracts and compresses the fluid into the potential wells more rapidly than the expansion can carry it away. So the contrast between overdense and underdense regions increases. But, compression in the fluid is accompanied with an increase of the temperature leading to an increase of the radiation pressure in the over-dense regions which resists to gravity. This generates an oscillating process which produces sound waves that propagate in the fluid.

What is the sound speed c_s in the plasma? We propose a short demonstration based on [49]. We consider a volume V of fluid made with photons and non-relativistic baryons with energy density $\rho = \rho_\gamma + \rho_b$ and pressure $p = p_\gamma + p_b$. The sound speed is given by:

$$c_s^2 = \frac{dp}{d\rho} \quad (4.1)$$

As seen in section 3.2.3, photons are such that $p_\gamma = c^2 \rho_\gamma / 3$ and $p_b = 0$ for baryons. Thus,

$$c_s^2 = \frac{c^2}{3 \left(1 + \frac{d\rho_b}{d\rho_\gamma} \right)}. \quad (4.2)$$

The fluid is considered as perfect so compression is isentropic ($dS = 0$) so we have $d(\rho V) = -pdV$. For the baryons and respectively for the photons, this translates into

$$d\rho_b = -\rho_b \frac{dV}{V} \quad \text{and} \quad d\rho_\gamma = -\frac{4}{3}\rho_\gamma \frac{dV}{V}. \quad (4.3)$$

Finally,

$$c_s^2 = \frac{c^2}{3 \left(1 + \frac{3\rho_b}{4\rho_\gamma} \right)}. \quad (4.4)$$

The density ratio is given by

$$\frac{\rho_b}{\rho_\gamma} = \frac{\Omega_b}{\Omega_\gamma} = \frac{\Omega_b^0}{\Omega_\gamma^0} \frac{a}{a_0} = \frac{\Omega_b^0}{\Omega_\gamma^0} \frac{1}{1+z} \quad (4.5)$$

with $\Omega_b^0 h^2 = 2.242 \times 10^{-2}$ and $\Omega_\gamma^0 h^2 = 2.47 \times 10^{-5}$ [48]. Thus, up to $z \sim 1000$, we have $\frac{\rho_b}{\rho_\gamma} \ll 1$, which leads to a relativistic sound speed

$$c_s \sim \frac{c}{\sqrt{3}}. \quad (4.6)$$

Acoustic scale

The sound speed defines the sound horizon $s_* = s(t_{\text{rec}}) = \int_0^{t_{\text{rec}}} c_s dt$ which is the maximum distance sound wave can travel from the beginning of the universe to the time of recombination t_{rec} . We have $s_* \simeq 150$ Mpc in comoving coordinates. This proper distance can be converted in comoving angular scale on the CMB anisotropy map:

$$\theta_a = \frac{s_*}{D_A(z_*)} \quad (4.7)$$

where $D_A(z_*)$ is the angular distance at the decoupling transition. θ_a is called the acoustic scale.

What about neutrinos and dark matter?

For a pedagogical explanation, one can refer to [57]. We consider a density perturbation in the primordial plasma which generates sound waves in the baryon-photon fluid. For neutrinos, decoupling with baryons happened much before so they simply stream freely away with a relativistic speed.

Regarding dark matter, it is not coupled to photons so nothing opposes to collapse by gravity (except the expansion) into the over-density. So dark matter reinforce compression without being impacted by the photon pressure. After baryon-photon decoupling, photons propagate freely while matter forms a shell surrounding the initial over density spot. Baryons and dark-matter mutually attract so dark-matter tends to go out from the initial over-density while baryons are attracted back. This phenomenon leads to a Baryon Acoustic Oscillation (BAO) peak in the 2-points correlation function of galaxies that I will briefly describe in section 7.6.3.

4.1.2 Physical processes that create temperature anisotropies

Several processes can create or modify temperature anisotropies. Previously, we have presented the SZ effect (section 3.4.2) which leads to a distortion of the black-body spectrum. On the contrary, the physical processes presented here do not affect the black-body spectrum because they equivalently impact all frequencies. Sometime a distinction is made between primary and secondary anisotropies. The former refers to anisotropies created by processes occurring before recombination while the latter are generated after recombination, due to processes occurring along the path of the CMB photons.

The Sachs–Wolfe effect

The first process that creates anisotropies is known as the Sachs–Wolfe effect as it was predicted first by Rainer Kurt Sachs and Arthur Michael Wolfe in 1967 [128]. It includes intrinsic photon temperature perturbation and gravitational redshift due to density fluctuations. Here I will give a pedagogical demonstration based on [129] which is much more simple than the original proof made by Sachs and Wolfe. We consider photons propagating in a metric perturbed by a gravitational potential Φ . The frequency shift induced by gravitation corresponds to a temperature perturbation:

$$\left. \frac{\Delta T}{T} \right|_f = \left. \frac{\Delta T}{T} \right|_i - \Phi \quad (4.8)$$

where i and f refer to initial and final states. This is simply the expression of energy conservation. The first term on the right hand side is the intrinsic temperature perturbation (an over-density corresponds to a hot spot). The second one is the energy lost when the photon climbs out of a potential well. The gravitational potential affects the time that a stationary observer will measure. Clocks are slowed down in a region of curved space. We have:

$$ds = \sqrt{1 - 2\Phi} dt \simeq (1 - \Phi) dt \quad (4.9)$$

where ds is the space-time interval and we set $c = 1$. Considering small perturbations $ds = (1 + \frac{\delta t}{t}) dt$, we have

$$\frac{\delta t}{t} = -\Phi. \quad (4.10)$$

So the gravitational potential is essentially a perturbation to the time coordinate. The CMB temperature is redshifted with $T \propto a^{-1}$ so:

$$aT = \text{cst} \quad \Rightarrow \quad adT + Tda = 0 \Rightarrow \quad \left. \frac{\Delta T}{T} \right|_i = -\frac{\delta a}{a}. \quad (4.11)$$

Considering a matter dominated universe so $p = 0$ and $a = t^{2/3}$ we obtain:

$$\left. \frac{\Delta T}{T} \right|_i = -\frac{2}{3} \frac{\delta t}{t} = \frac{2}{3} \Phi \quad (4.12)$$

and finally,

$$\left. \frac{\Delta T}{T} \right|_f = -\frac{1}{3} \Phi. \quad (4.13)$$

So this means that an over-density (corresponding to $\Phi > 0$) is associated with a cold spot in the temperature CMB map.

Doppler shift

The second process is due to the motion of the fluid along the line of sight which induces a Doppler shift of the frequency associated with a temperature shift:

$$\left(\frac{\Delta T}{T} \right)_{\text{Doppler}} = \mathbf{v} \cdot \mathbf{n} \quad (4.14)$$

which is the projection of the peculiar velocity of the fluid \mathbf{v} on the direction of observation \mathbf{n} .

Integrated Sachs-Wolfe (ISW) effect

As CMB photons left the LSS and travel up to an observer today, they must pass through clusters of matter which have formed since. As we have seen with the SW effect, the presence of a potential well in the path of a photon can induce a change in the temperature of the photon. We can write [130]:

$$\frac{\Delta T}{T}(\mathbf{n}) = \left. \frac{\Delta T}{T}(\mathbf{n}) \right|_{\text{rec}} + \int_{\eta_{\text{rec}}}^{\eta_0} 2\dot{\Phi} d\eta \quad (4.15)$$

where η_{rec} is the conformal time at recombination and η_0 the conformal time today, as defined in equation 3.22. $\left. \frac{\Delta T}{T}(\mathbf{n}) \right|_{\text{rec}}$ includes the SW effect and the Doppler shift at recombination. In the second term on the right hand side, the integral is taken along the line of sight. It is the Integrated Sachs-Wolfe (ISW) contribution. It depends on the time derivative (with respect to the conformal time η) of the gravitational potential Φ along the line of sight. The nonlinear part of the ISW effect, is sometimes known as the Rees–Sciama effect [131]. To change the temperature of the photon, the energy gained during the fall into the potential must not be balanced by the energy lost as the photon climbs out the well. To have this condition, $\dot{\Phi}$ must not be zero and this is only possible in a universe with accelerated expansion. Thus, the detection of this effect is an evidence for accelerated expansion. It is measured by cross-correlating the CMB anisotropies with a tracer of the Large Scale Structure. It was first reported by [132] and latter by many groups such as [117], providing evidence for accelerated expansion independently from Type-Ia supernovae. Note that for the ISW effect, an over-density along the line of sight, caused by a galaxy cluster for example, will increase the photon energy and thus the apparent temperature in that direction.

4.1.3 Processes that attenuate the anisotropies

There are several processes that tend to attenuate the temperature anisotropies.

Silk damping

The first one is known as Silk damping because it was first pointed out by Joseph Silk in 1968 [133]. It is due to diffusion of the photons from hot regions to cold regions during recombination epoch. Photons push electrons along by Compton diffusion and electrons pull protons by the Coulomb attraction reducing anisotropies. Very small scale inhomogeneities ($\theta_a \lesssim 0.2^\circ$) are smoothed out. In the limit of an instantaneous recombination, the damping factor is:

$$F(k) = e^{-\left(\frac{k}{k_D}\right)^2} \quad (4.16)$$

where k is the wave number of acoustic oscillations and $k_D = \frac{2\pi}{\lambda_D}$ the damping scale with λ_D the diffusion length at recombination [134].

Averaged over the LSS width

The damping is also reinforced by the fact that the LSS has a width ($\Delta z \sim 90$ [110]) so for each line of sight, the temperature is averaged over the width. Figure 3.6 is a good illustration. Consider three photons γ_1, γ_2 and γ_3 coming from the same direction and arriving to the observer at the same time. The three have been emitted at the decoupling temperature but at different times. For the observer, the three photons have different temperatures and he will detect an average. The angular scales impacted by the average are only the ones included in the LSS width. This corresponds to scales below $\sim 0.1^\circ$ or $\ell \gtrsim 2000$ where ℓ is the multipole that we will define in the next section.

Reionization

The Lyman series corresponds to the series of energies required for the transition of the hydrogen atom from the fundamental state to an higher energy state. The transition to the first excited state is called Lyman- α and corresponds to the absorption of a photon with wavelength $\lambda \simeq 121.5$ nm (ultraviolet range).

In cosmology, spectroscopic observations of very bright objects can tell us a lot about the presence of structures with hydrogen atoms on the line of sight. Quasars are galaxies with an active nucleus, their emission comes from a massive black hole accreting matter.

In 1965, Gunn and Peterson observed the spectra of high redshift quasars and galaxies [135]. As expected, after recombination and until $z \sim 6$, the universe is neutral and the Lyman- α ray is absorbed by the intergalactic medium. However this absorption does not occur for light coming from quasars closer to us. This is because around $z \sim 6$ first stars form and start emitting high energetic photons which re-ionize hydrogen atoms. This is called the reionization period.

A small part of the CMB photons scatters on free electrons released at reionization. The optical depth τ is defined such that the number of CMB photons today $N(t_0)$ that have not been scattered from t_i is:

$$\frac{N(t_0)}{N(t_i)} = e^{-\tau}. \quad (4.17)$$

So the probability of a Thomson scattering in the time interval from t_i to present time t_0 is $1 - e^{-\tau}$ [136]. The optical depth writes:

$$\tau = \int_{t_i}^{t_0} \sigma_T n_e(t) dt \quad (4.18)$$

where σ_T is the Thomson cross-section and $n_e(t)$ is the density of free electrons.

If the CMB radiation was isotropic, this scattering would not have any impact. However, because CMB has spatial temperature anisotropies, we will show that small scales are damped. We consider a single line of sight on which the temperature before reionization epoch is $T_0 + \Delta T$. Today, the observed temperature is the initial one minus the contribution of the photons diffused to others line of sight plus the photons scattered in from other lines of sights:

$$T_0 + \Delta T \rightarrow (T_0 + \Delta T) - (T_0 + \Delta T)(1 - e^{-\tau}) + \langle T_0 + \Delta T_i \rangle (1 - e^{-\tau}) \quad (4.19)$$

where $\langle \rangle$ refers to an average over photons coming from directions i . At small angular scales, we can make the approximation that the average is the mean temperature T_0 . This leads to:

$$T_0 + \Delta T \rightarrow T_0 + \Delta T e^{-\tau} \quad (4.20)$$

for small angular scales. So reionization, similarly to Silk damping, translates in an exponential damping of small scales temperature anisotropies. As we will see in section 4.2.6, reionization has also a strong impact on polarization anisotropies on large angular scales.

Gravitational lensing

Finally, as CMB photons propagate from the last scattering surface to the observation point they are deflected by gravity when passing through inhomogeneous mass distributions. This is called gravitational lensing. This results in distortions in the temperature anisotropy map. This was studied for example in [137] and for a complete review of the weak gravitational lensing of the CMB, one can refer to [138]. Mathematically, this can be described in the following way, the effective temperature observed in direction \mathbf{n} is actually deflected from direction $\mathbf{n} + d(\mathbf{n})$ [189]:

$$T_{\text{len}}(\mathbf{n}) = T_{\text{unl}}(\mathbf{n} + d(\mathbf{n})) \quad (4.21)$$

where T_{len} and T_{unl} are the lensed and unlensed temperatures and $d(\mathbf{n})$ is the deflection field. It is the gradient of a scalar lensing potential $\phi(\mathbf{n})$:

$$d(\mathbf{n}) = \nabla \phi(\mathbf{n}), \quad \phi(\mathbf{n}) = -2 \int_0^{z_{\text{rec}}} \frac{dz}{H(z)} \Psi(z, \chi(z)\mathbf{n}) \left(\frac{1}{\chi(z)} - \frac{1}{\chi(z_{\text{rec}})} \right) \quad (4.22)$$

where $\Psi(z, \mathbf{x})$ is the Newtonian potential, $\chi(z)$ the comoving distance at redshift z and $H(z)$ the Hubble constant. The integral is done on the line of sight from today to recombination.

The structures in the universe are not strongly correlated at large scales so lensing has only an effect at small angular scales. In the angular power spectrum (see section 4.1.5), the result is that the acoustic peaks are smoothed at small angular scales. Note that $H(z)$ and $\chi(z)$ depend upon cosmological parameters (see section 3.2). As a result, lensing provides extra constraints on Cosmology.

4.1.4 Angular power spectrum

We note T_0 the mean CMB temperature, and $T(\mathbf{n})$ the temperature in direction $\mathbf{n} = (\theta, \phi)$ where (θ, ϕ) are the usual spherical coordinates. The temperature anisotropies will be written:

$$\frac{T(\mathbf{n}) - T_0}{T_0} = \frac{\Delta T}{T_0}(\mathbf{n}). \quad (4.23)$$

Decomposition on spherical harmonics basis

For quantitative analysis, it is useful to decompose the anisotropy patterns on spherical harmonics which is similar to a 2D Fourier transform on a sphere. As any spherical scalar field, the temperature fluctuations can be decomposed as:

$$\frac{\Delta T}{T_0}(\mathbf{n}) = \sum_{\ell=0}^{\infty} \sum_{m=-\ell}^{\ell} a_{\ell m} Y_{\ell m}(\mathbf{n}) \quad (4.24)$$

where ℓ is the multipole, each ℓ is associated with an angular scale on the sphere (we have $\ell \sim \frac{\pi}{\theta}$). Y_{00} is a constant, corresponding to the mean CMB temperature so $a_{00} = 0$. The coefficient a_{10} gives the temperature of the dipole ($\ell = 1$). It is not possible to separate the dipole due to the Earth motion from the cosmological dipole induced by temperature fluctuations so this is why we will only consider $\ell \geq 2$ in the following. Thus, the $a_{\ell m}$ coefficients are another representation of the temperature field. The spherical harmonics form an orthogonal basis,

$$\int_{4\pi} Y_{\ell m}(\mathbf{n}) Y_{\ell' m'}^*(\mathbf{n}) d\Omega = \delta_{\ell \ell'} \delta_{m m'} \quad (4.25)$$

where $d\Omega = \sin\theta d\theta d\phi$ is the elementary solid angle. Using this orthogonality relation, the $a_{\ell m}$ can be calculated by multiplying equation 4.24 by $Y_{\ell' m'}^*(\mathbf{n})$ on each side and integrating on the sphere. It gives:

$$a_{\ell m} = \int_{4\pi} \frac{\Delta T(\mathbf{n})}{T_0} Y_{\ell m}^*(\mathbf{n}) d\Omega. \quad (4.26)$$

We will see in chapter 7 that temperature anisotropies $\frac{\Delta T}{T_0}$ approximately follow a normal distribution with zero mean. So each $a_{\ell m}$ is also a random variable with normal distribution centered on zero ($\langle a_{\ell m} \rangle = 0$) as illustrated in Figure 4.2. According to the Isserlis' theorem also called the Wick's probability theorem, all the statistical information present in the $a_{\ell m}$ coefficients is contained in their covariance matrix. This is why we are interested in the variance of the coefficients $\text{Var}(a_{\ell m}) = \langle a_{\ell m} a_{\ell' m'}^* \rangle$.

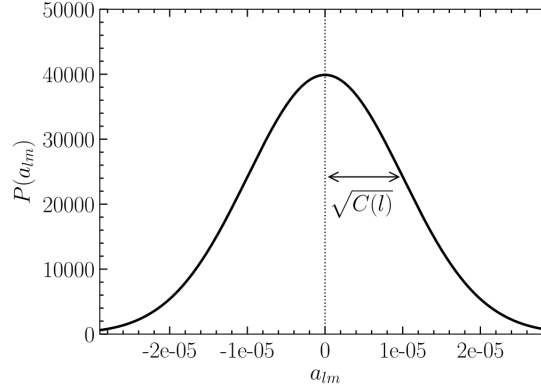


Figure 4.2: Gaussian distribution of the $a_{\ell m}$ coefficients with mean 0 and variance C_ℓ , see below for the definition and the calculation of C_ℓ . Taken from [109].

Characterizing the variance

As the universe is isotropic, we expect that the variance does not depend on m . We define the correlation function $C(\mathbf{n}_1, \mathbf{n}_2)$ of temperature fluctuations taken in two directions \mathbf{n}_1 and \mathbf{n}_2 .

$$C(\mathbf{n}_1, \mathbf{n}_2) = \left\langle \frac{\Delta T}{T_0}(\mathbf{n}_1) \frac{\Delta T}{T_0}(\mathbf{n}_2) \right\rangle. \quad (4.27)$$

The correlation function is invariant under rotation. In other terms, what is important is not the exact direction but the angle between \mathbf{n}_1 and \mathbf{n}_2 that we will note θ . So $C(\mathbf{n}_1, \mathbf{n}_2) = C(\cos\theta)$ and we can decompose it on the basis of the Legendre polynomials P_ℓ with coefficients $(2\ell + 1)C_\ell/4\pi$:

$$C(\cos\theta) = \sum_l \frac{2\ell + 1}{4\pi} C_\ell P_\ell(\cos\theta). \quad (4.28)$$

Also, the Legendre polynomials of a scalar product of unit vectors ($\mathbf{n}_1 \cdot \mathbf{n}_2 = \cos\theta$) can be expanded with spherical harmonics such as

$$P_\ell(\cos\theta) = \frac{4\pi}{2\ell + 1} \sum_{m=-\ell}^{\ell} Y_{\ell m}(\mathbf{n}_1) Y_{\ell m}^*(\mathbf{n}_2). \quad (4.29)$$

So finally, we have

$$C(\mathbf{n}_1, \mathbf{n}_2) = \sum_{\ell=0}^{\infty} \sum_{m=-\ell}^{\ell} C_\ell Y_{\ell m}(\mathbf{n}_1) Y_{\ell m}^*(\mathbf{n}_2). \quad (4.30)$$

We go back to the calculation of the variance of the $a_{\ell m}$:

$$\langle a_{\ell m} a_{\ell' m'}^* \rangle = \left\langle \int d\Omega_1 \frac{\Delta T(\mathbf{n}_1)}{T_0} Y_{\ell m}^*(\mathbf{n}_1) \int d\Omega_2 \frac{\Delta T(\mathbf{n}_2)}{T_0} Y_{\ell m}(\mathbf{n}_2) \right\rangle \quad (4.31)$$

$$= \int \int d\Omega_1 d\Omega_2 Y_{\ell m}^*(\mathbf{n}_1) Y_{\ell m}(\mathbf{n}_2) C(\mathbf{n}_1, \mathbf{n}_2) \quad (4.32)$$

$$= \int \int d\Omega_1 d\Omega_2 Y_{\ell m}^*(\mathbf{n}_1) Y_{\ell m}(\mathbf{n}_2) \sum_{\ell''=0}^{\infty} \sum_{m=-\ell''}^{\ell''} C_{\ell''} Y_{\ell'' m''}(\mathbf{n}_1) Y_{\ell'' m''}^*(\mathbf{n}_2) \quad (4.33)$$

$$= C_{\ell} \delta_{\ell\ell'} \delta_{mm'} \quad (4.34)$$

where we have used the orthogonality of spherical harmonics defined in equation 4.25.

Thus, the variance of the $a_{\ell m}$ does not depend on m and it is equal to the coefficients C_{ℓ} of the decomposition on Legendre polynomials of the two-points correlation function of temperature fluctuations. We define the angular power spectrum as,

$$C_{\ell} = \langle a_{\ell m} a_{\ell m}^* \rangle = \langle |a_{\ell m}|^2 \rangle. \quad (4.35)$$

Finally, this definition is a consequence of invariance under rotation of the correlation function defined in equation 4.27.

How can we measure the angular power spectrum?

So far, averages were supposed to be done on many realizations of the universe which, of course, is not experimentally feasible. This is why we need an estimator of the variance. The temperature field on the sky is a real field so we have $a_{\ell m} = (-1)^m a_{\ell -m}^*$ and it means that for each ℓ , there are $2\ell + 1$ independent m . Thus, a simple way to get an estimator of the variance of the $a_{\ell m}$ is to replace the average over universe realizations by an average over harmonic modes m at given ℓ . We define the observable power spectrum as:

$$\hat{C}_{\ell} = \langle |a_{\ell m}|^2 \rangle_m = \frac{1}{2\ell + 1} \sum_{m=-\ell}^{\ell} |a_{\ell m}|^2. \quad (4.36)$$

Link between the power spectrum and temperature anisotropies

The power spectrum is directly linked to the variance on the sky of the temperature anisotropies. Indeed we have

$$\left\langle \left(\frac{\Delta T}{T_0} \right)^2 \right\rangle = \frac{1}{4\pi} \int \left(\frac{\Delta T}{T_0} \right)^2 d\Omega \quad (4.37)$$

$$= \frac{1}{4\pi} \sum_{\ell \geq 2} \sum_{m=-\ell}^{\ell} a_{\ell m} a_{\ell m}^* \int Y_{\ell m}(\mathbf{n}) Y_{\ell m}^*(\mathbf{n}) d\Omega \quad (4.38)$$

$$= \frac{1}{4\pi} \sum_{\ell=2}^{\infty} \sum_{m=-\ell}^{\ell} |a_{\ell m}|^2 \quad (4.39)$$

$$= \frac{1}{4\pi} \sum_{\ell=2}^{\infty} (2\ell + 1) \hat{C}_{\ell}. \quad (4.40)$$

For small angular scales, we can replace the sum by an integral [49]:

$$\left\langle \left(\frac{\Delta T}{T_0} \right)^2 \right\rangle \simeq \frac{1}{4\pi} \int_2^{\infty} \ell(2\ell + 1) \hat{C}_{\ell} \frac{d\ell}{\ell}. \quad (4.41)$$

Thus, the term $\ell(2\ell + 1) \hat{C}_{\ell} / 4\pi$ gives the contribution per interval of logarithmic multipole $\ln(\ell)$ to the power of temperature fluctuations. Figure 4.3 is an illustration showing temperature maps corresponding to single mode power spectra at $\ell = 3, 10$ and 60 .

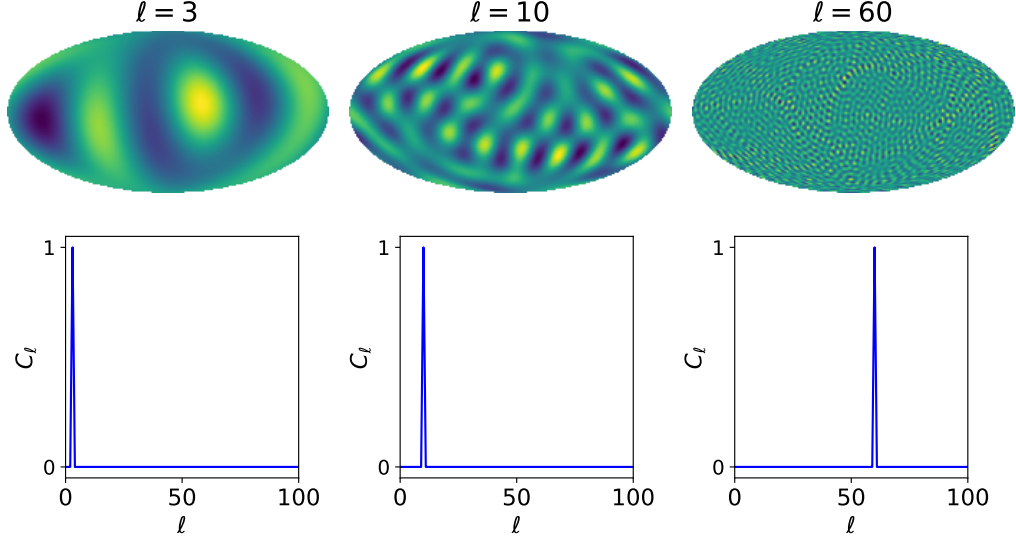


Figure 4.3: Temperature maps associated with single mode power spectrum C_ℓ (a Dirac at $\ell = 3, 10$ and 60).

Cosmic variance

What accuracy can we reach on the power spectrum? For a given ℓ , by measuring the $(2\ell + 1)$ $a_{\ell m}$ coefficients, we are sampling the distribution. Thus, there is a fundamental uncertainty on the estimate of the variance C_ℓ and this uncertainty is most pronounced at low ℓ where the number of samples is small. It is called the cosmic variance and it scales as the inverse of the square root of $(2\ell + 1)$:

$$\left(\frac{\Delta C_\ell}{C_\ell} \right)_{\text{cosmic}} = \sqrt{\frac{2}{2\ell + 1}}. \quad (4.42)$$

where ΔC_ℓ is the standard deviation of C_ℓ . A demonstration of this formula is done in annex A.2.

4.1.5 Observed power spectrum

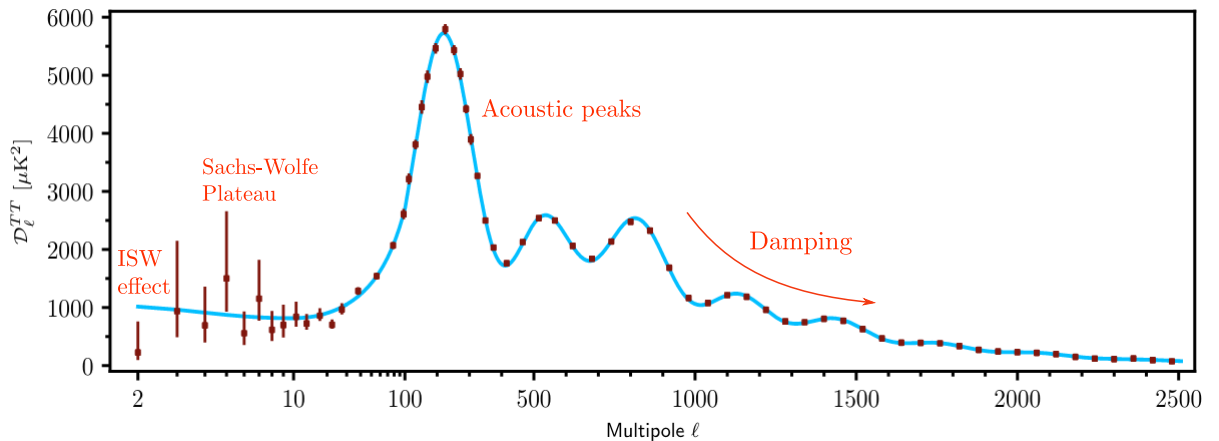


Figure 4.4: CMB temperature (TT) angular power spectrum measured by the Planck mission. Taken from [160] and adapted.

Actually, to represent the angular power spectrum, as will be justified below, it is convenient to use

$$D_\ell = \frac{\ell(\ell + 1)}{2\pi} C_\ell. \quad (4.43)$$

Figure 4.4 shows the CMB temperature power spectrum D_ℓ^{TT} measured by the Planck mission. We clearly see in this plot the effect of cosmic variance, leading to large error bars at large angular scales ($\ell \lesssim 10$).

The shape of the angular power spectrum can be explained with the physical processes occurring in the primordial plasma or along the travel of photons described in section 4.1.2. It can roughly be divided in three main zones:

The Sachs-Wolfe plateau $\ell \lesssim 100$: At large angular scales, when $\theta > \theta_a$, where θ_a is the acoustic scale defined in section 4.1.1, non-homogeneities only evolve by gravitation. The pressure of the photon-baryon plasma does not play any role, acoustic oscillations did not have time to propagate on those scales. So the dominant phenomenon is the Sachs-Wolfe effect and large angular scales reflect the initial spectrum of density perturbations that was laid down at early times. On the angular power spectrum, we observe a plateau known as the Sachs-Wolfe plateau: $\ell(\ell+1)C_\ell \simeq \text{cste}$. This is a strong argument to say that gravitational primordial fluctuations are scale invariant. We will come back on this point in chapter 7. This explains why we represent D_ℓ instead of C_ℓ .

We can also notice that for the largest angular scales ($\ell \lesssim 10$) the power spectrum rises and this is due to the ISW effect [124]. However, it is hard to measure because of the cosmic variance.

The acoustic peaks $100 \lesssim \ell \lesssim 1000$: The more characteristic pattern of the spectrum is the series of acoustic peaks. They correspond to the acoustic oscillations in the primordial plasma. These fluctuations can be roughly written as standing waves confined by the sound horizon s_* :

$$\frac{\Delta T}{T} \propto \cos(k_n s_*) \quad \text{with} \quad k_n = \frac{n\pi}{s_*} \quad (n = 1, 2, 3, \dots). \quad (4.44)$$

The first peak corresponds to the mode that is caught in its first compression (1/4 of the wavelength) by recombination, the second peak to the mode that went through a full cycle of compression (1/2 of the wavelength)... This is illustrated in Figure 4.5. The acoustic scale defined previously in equation 4.7

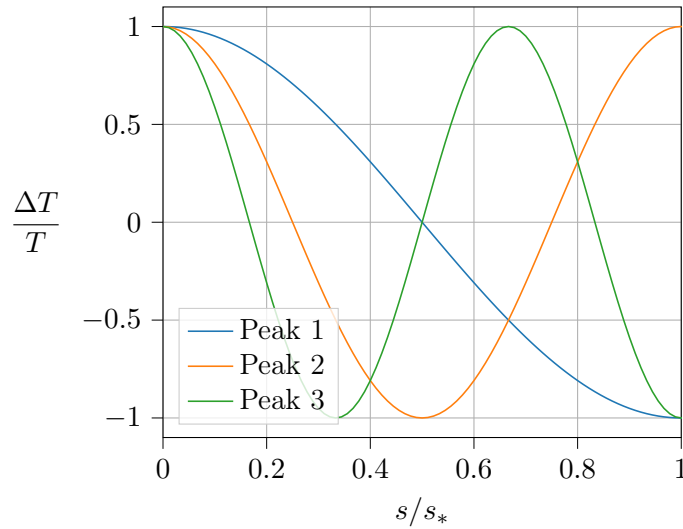


Figure 4.5: Acoustic oscillations in the primordial plasma, standing waves leading to the acoustic peaks in the angular power spectrum. s is the sound horizon which evolves in time until s_* at recombination.

can be converted in multipole:

$$\ell_a \simeq \frac{\pi}{\theta_a} = \frac{\pi D_A(z_*)}{s_*}. \quad (4.45)$$

So the peaks are located at $\ell_n = n\ell_a$. The first peak is at $\ell_1 \simeq 200 \Leftrightarrow \theta_1 \simeq 0.9^\circ$.

The damping tail $\ell \gtrsim 1000$: At small angular scales the exponential damping of the peaks, described previously, is clearly visible.

4.2 Polarization anisotropies

The CMB radiation is linearly polarized [139], [140]. In this section, we describe the physical processes leading to a polarized radiation field and we introduce the mathematical tools commonly used in the CMB field to describe polarization.

4.2.1 Thomson scattering

The polarization of the CMB radiation originates from Thomson scattering of photons onto electrons in the primordial plasma.

In Compton scattering, the electric field of the incident electromagnetic wave, always orthogonal to the incoming direction, induces an oscillation of the target electron orthogonal to the incoming direction. The electron re-emits an electromagnetic wave polarized in the direction of its vibration. The polarization of the outgoing electromagnetic wave is orthogonal to both the incoming and the outgoing directions, and therefore to the scattering plane. Such a process in which the photon energy remains unchanged is called Thomson scattering.

We consider an unpolarized incident radiation with direction of propagation \mathbf{k} . This radiation scatters on an electron with mass m and charge e and an observer looks at the diffusion of the radiation in direction \mathbf{n} . The angle between the incident and the scattered directions is θ . The differential cross section $d\sigma/d\Omega$ is given by [232]:

$$\frac{d\sigma}{d\Omega} = \frac{3\sigma_T}{8\pi} \frac{1}{2} (1 + \cos^2 \theta) \quad (4.46)$$

with $d\Omega$ the differential solid angle in the direction of the incoming radiation and $\sigma_T = \frac{8\pi}{3} \left(\frac{e^2}{mc^2} \right)^2$ the Thomson cross section. This means that an observer looking at the diffusion with a right angle from the incident direction ($\theta = \frac{\pi}{2}$) will get half of the intensity compared to a on-axis observer ($\theta = 0$). This is illustrated in Figure 4.6. We can also write

$$\frac{d\sigma}{d\Omega} = \frac{3\sigma_T}{8\pi} |\boldsymbol{\epsilon} \cdot \boldsymbol{\epsilon}'|^2 \quad (4.47)$$

where $\boldsymbol{\epsilon}, \boldsymbol{\epsilon}'$ are the incident and scattered polarization directions.

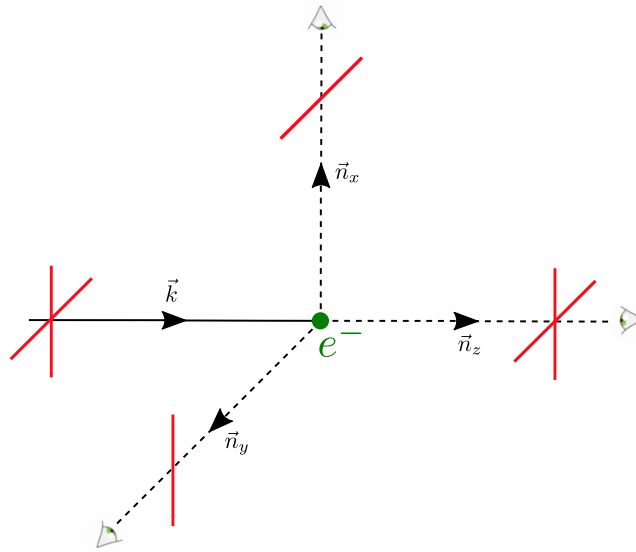


Figure 4.6: Thomson scattering of an unpolarized electromagnetic field with incident direction \mathbf{k} on an electron. Three observers in directions \mathbf{n}_x , \mathbf{n}_y and \mathbf{n}_z are represented. Observers looking at $\pi/2$ from the incident direction receive a linear polarization.

4.2.2 Thomson scattering as a source of linear polarization in the CMB

For the CMB, the situation is different. We consider a single observer in direction z with incident radiations from all directions on an electron. We work in the rest frame of the electron.

If the incoming radiation is unpolarized and isotropic (monopole) the scattered radiation will be unpolarized too. However an anisotropic incoming radiation (in the rest frame of the electron), meaning that there is hotter and colder radiation compared to the mean temperature coming from different directions, can generate polarization. The incident radiation field should actually have a quadrupole variation in temperature to produce outgoing linear polarization. This happens when the average incoming radiation is hotter than the one coming from an orthogonal direction. An incoming dipole radiation will not produce polarized light. Figure 4.7 illustrates the three cases (monopole, dipole and quadrupole).

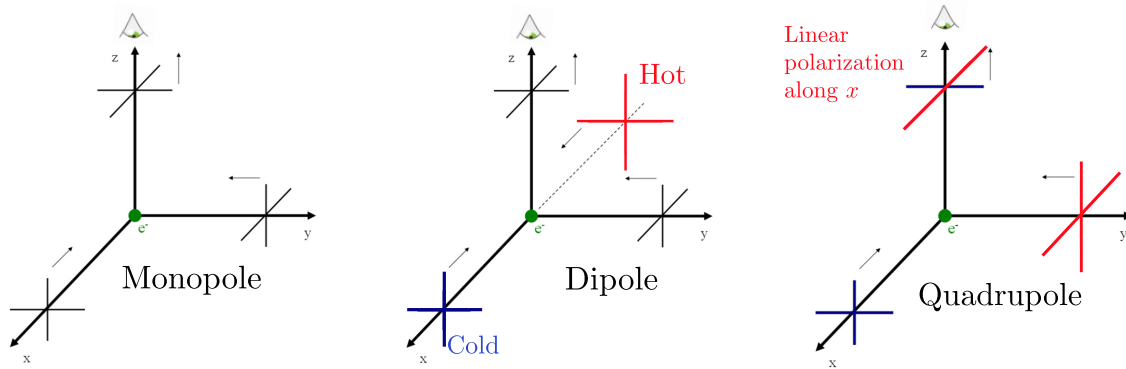


Figure 4.7: Thomson scattering of incoming unpolarized radiation in case of a monopole (isotropic radiation), a dipole and a quadrupole temperature anisotropy in the rest frame of the electron. The observer looks in the z direction. Black lines denote radiation with average intensity. Blue/red lines show incoming radiation that is colder/hotter than the average. The only case that can produce a linear outgoing polarization is the quadrupole.

Also, note that any polarization gets averaged out by successive rescatterings, therefore we only observe polarization from the last one, at the end of recombination.

Let us mathematically demonstrate why quadrupole anisotropy is required. We will refer to Figure 4.8 for notations. The incident radiation is unpolarized so it is fully characterized by its intensity

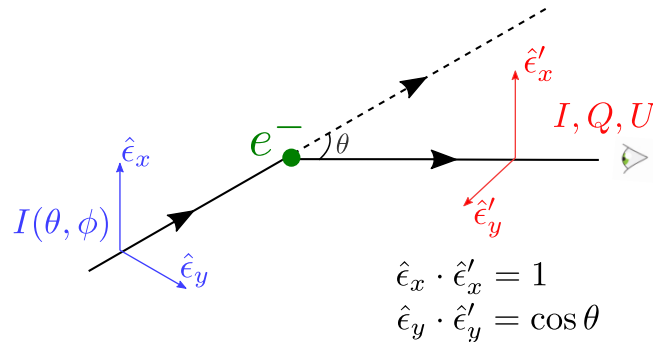


Figure 4.8: Thomson scattering of an incoming unpolarized radiation on an electron.

$I(\theta, \phi)$. The scattered radiation may be polarized so it is characterized by the four Stokes parameters (I', Q', U', V') . We can equivalently use the two intensities along x and y : $I'_x = (I' + Q')/2$ and $I'_y = (I' - Q')/2$. For the incident radiation, as it is unpolarized, we have $I_x = I_y = I/2$. Using equation 4.47, we can compute the scattered intensities, for incident radiations in $d\Omega$:

$$I'_x = \frac{3\sigma_T}{8\pi} I |\boldsymbol{\epsilon} \cdot \boldsymbol{\epsilon}'_x|^2 = \frac{3\sigma_T}{8\pi} [I_x(\boldsymbol{\epsilon}_x \cdot \boldsymbol{\epsilon}'_x)^2 + I_y(\boldsymbol{\epsilon}_y \cdot \boldsymbol{\epsilon}'_x)^2] = \frac{3\sigma_T}{16\pi} I \quad (4.48)$$

$$I'_y = \frac{3\sigma_T}{8\pi} I |\boldsymbol{\epsilon} \cdot \boldsymbol{\epsilon}'_y|^2 = \frac{3\sigma_T}{8\pi} [I_x(\boldsymbol{\epsilon}_x \cdot \boldsymbol{\epsilon}'_y)^2 + I_y(\boldsymbol{\epsilon}_y \cdot \boldsymbol{\epsilon}'_y)^2] = \frac{3\sigma_T}{16\pi} I \cos^2 \theta \quad (4.49)$$

where we used $I\boldsymbol{\epsilon} = I_x\boldsymbol{\epsilon}_x + I_y\boldsymbol{\epsilon}_y$. In terms of the Stokes parameters, it gives

$$I' = \frac{3\sigma_T}{16\pi} I (1 + \cos^2 \theta) \quad (4.50)$$

$$Q' = \frac{3\sigma_T}{16\pi} I \sin^2 \theta. \quad (4.51)$$

By doing the computation in a frame rotated by 45° with respect to (x, y) , we can show that $U' = 0$ (it is equal to Q'_{45° in the rotated frame).

To compute the signal received by an observer looking at a single line of sight, we need to integrate over all incident directions. In order to have $Q', U' \neq 0$ in the same frame, we make a rotation by an angle ϕ such that $Q' \cos(2\phi) \rightarrow Q'$ and $-Q' \sin(2\phi) \rightarrow U'$ (see equation 1.64):

$$I'_{\text{obs}} = \frac{3\sigma_T}{16\pi} \int I(\theta, \phi) (1 + \cos^2 \theta) d\Omega, \quad (4.52)$$

$$Q'_{\text{obs}} = \frac{3\sigma_T}{16\pi} \int I(\theta, \phi) \sin^2 \theta \cos(2\phi) d\Omega, \quad (4.53)$$

$$U'_{\text{obs}} = -\frac{3\sigma_T}{16\pi} \int I(\theta, \phi) \sin^2 \theta \sin(2\phi) d\Omega. \quad (4.54)$$

The signal $I(\theta, \phi)$ can be decomposed on the spherical harmonics: $I(\theta, \phi) = \sum_{\ell, m} Y_{\ell m}(\theta, \phi)$. By using the orthogonality relation of the harmonics given by equation 4.25 and with the expressions of Y_{00}, Y_{02} and Y_{22} , we obtain:

$$I'_{\text{obs}} = \frac{3\sigma_T}{16\pi} \left[\frac{8}{3} \sqrt{\pi} a_{00} + \frac{4}{3} \sqrt{\frac{\pi}{5}} a_{20} \right], \quad (4.55)$$

$$Q'_{\text{obs}} = \frac{3\sigma_T}{4\pi} \sqrt{\frac{2\pi}{15}} \text{Re}(a_{22}), \quad (4.56)$$

$$U'_{\text{obs}} = -\frac{3\sigma_T}{4\pi} \sqrt{\frac{2\pi}{15}} \text{Im}(a_{22}). \quad (4.57)$$

Thus, this demonstrates that only a quadrupole anisotropy (a_{22}) can generate linear polarization by Thomson scattering from unpolarized incident radiation.

What about circular polarization? To get circular polarization, a phase shift must be introduced between the two directions of polarization and this is not possible by Thomson scattering. This is why circular polarization in the CMB is negligible and the V Stokes parameter is usually not considered [141].

4.2.3 E and B -mode introduction

As seen in section 1.3.1, the Stokes Q and U parameters are defined with respect to a fixed coordinate system in the sky and we have seen how they transform under rotation. They are not scalar fields. In 1997, two decompositions of the CMB polarization field have been independently developed in order to get rid of the frame dependence. The first one by M. Zaldarriaga and U. Seljak [142] based on a decomposition on a sphere into spin ± 2 spherical harmonics and a second one by M. Kamionkowski, A. Kosowsky and A. Stebbins [143] using tensor spherical harmonics. In this section, we will introduce the first one which is the one commonly used today in the CMB field.

The pattern of polarization on the sky can be characterized in terms of a scalar, $E(\theta, \phi)$, and a pseudo-scalar field, $B(\theta, \phi)$ which are, by construction, non local quantities. Here, I give an intuitive

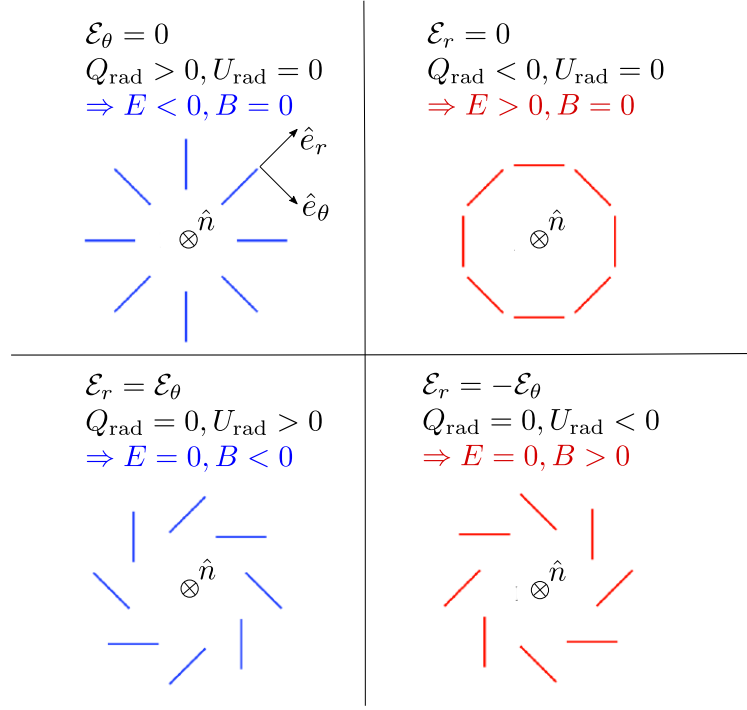


Figure 4.9: Definition of E and B -modes. In this figure, the four patterns correspond to the direction of the electric field around a line of sight \hat{n} where E and B -modes are computed. \mathcal{E}_r and \mathcal{E}_θ are the electric field components in the radial reference frame $(\hat{e}_r, \hat{e}_\theta)$. E and B are weighted average of the Q_{rad} and U_{rad} Stokes parameters along circles centered on \hat{n} .

definition of E and B -modes based on [144]. A more canonical definition will be given in section 4.2.5. Figure 4.9 illustrates how E and B are built from Q and U Stokes parameters. \hat{n} is the line of sight which gives the point on the sphere where E and B -modes are computed. In this figure, the four patterns correspond to the direction of the electric field around \hat{n} . \mathcal{E}_r and \mathcal{E}_θ are the electric field components in the radial reference frame $(\hat{e}_r, \hat{e}_\theta)$. E and B -modes are defined from the Stokes parameters, Q_{rad} and U_{rad} , computed in the radial reference frame, on a circle centered on \hat{n} . Locally, we can define E and B -modes as:

$$E(\hat{n}) = \int w(\hat{n} \cdot \hat{n}') Q_{\text{rad}}(\hat{n}') d^2 \hat{n}' \quad (4.58)$$

$$B(\hat{n}) = \int w(\hat{n} \cdot \hat{n}') U_{\text{rad}}(\hat{n}') d^2 \hat{n}'. \quad (4.59)$$

$w(\hat{n} \cdot \hat{n}')$ is a weighted function which only depends on the radius of the circles on which the integration is made. It must be constant along a given circle. The canonical definition for E and B -modes from spin-2 field analysis, that I will give in section 4.2.5, corresponds to the choice $w(\theta) = -1/\theta^2$ with $\theta = (\hat{n}, \hat{n}')$. E and B -modes are the weighted averages of Q_{rad} and U_{rad} on circles centered on \hat{n} and weighted by $w(\hat{n} \cdot \hat{n}')$.

Thus, thanks to the integration, and to the rotational invariance of the scalar product, E and B -modes do not depend on the reference frame, contrary to Q_{rad} and U_{rad} . By construction, they are non-local quantities, meaning that they can not be calculated from the measurement of Q and U at a single point. In the Figure 4.9, the four patterns are the ones that lead to positive or negative pure E -modes (with $B = 0$) and positive or negative pure B -modes (with $E = 0$).

Contrary to Q and U , E and B are invariant by rotation around the direction \hat{n} . However, E and B differ in their behavior under reflection (parity transformation), B changes sign while E does not. E is a scalar while B is a pseudo-scalar. The name E and B were chosen by analogy with the electric and magnetic fields which have similar behavior under symmetry as they are respectively vectorial and pseudo-vectorial fields.

4.2.4 Origin of quadrupole anisotropies

As seen before, quadrupole anisotropies are needed to get polarization with Thomson scattering but how can they be produced in the primordial plasma? There are two mechanisms: density fluctuations (scalar perturbations) and gravitational waves (tensor perturbations). We will see that the first can only lead to E -modes while the second can produce E and B -modes. This is a major advantage of this decomposition as in this way, B -modes become a direct observable of gravitational waves passing through the primordial plasma. Today, these waves, if any, form a contribution to the stochastic gravitational wave background [58].

Density fluctuations

Velocity gradient in the photon-baryon fluid around density fluctuations can produce quadrupole anisotropies in the radiation. This is illustrated in Figure 4.10. We consider a primordial over-density, which, as seen in section 4.1.2, is associated with a cold spot in the CMB map. Acoustic oscillations propagate in the fluid. The photon-baryon fluid can either fall by gravity into the potential well with acceleration or climb up the well with deceleration because of radiation pressure. Thus, the velocity field of the fluid can either converge toward the cold spot or diverge from it.

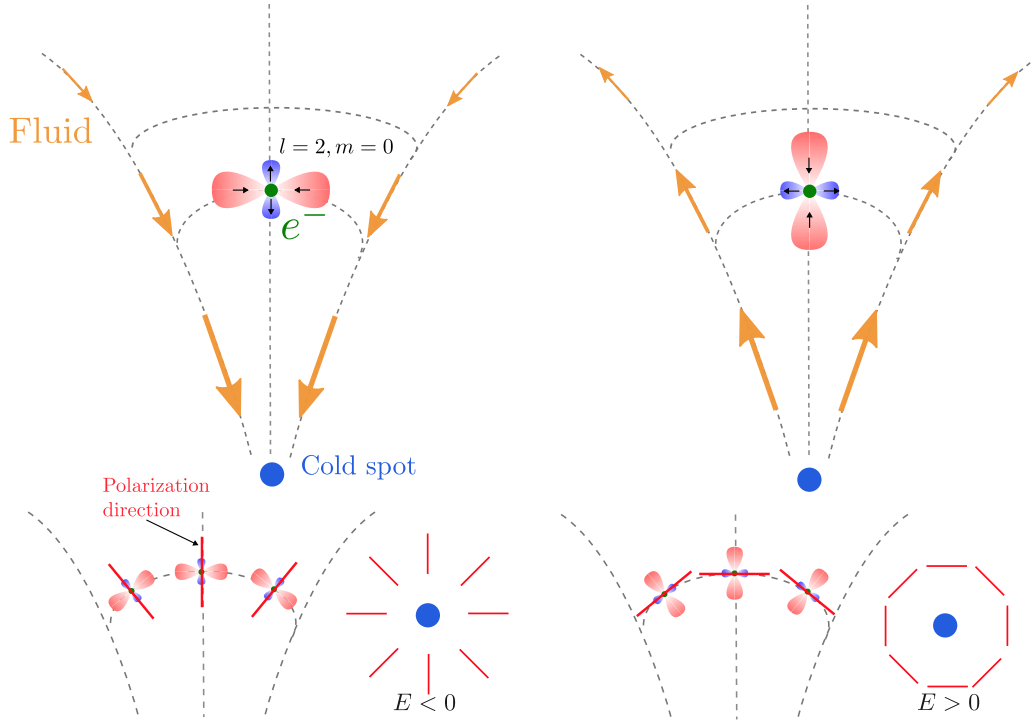


Figure 4.10: Generation of E -modes from velocity gradients in the photon-baryon fluid around an over-density (cold spot). The fluid can either fall into the potential well with acceleration or climb up the well with deceleration (yellow arrow drawn in the observer frame). This creates quadrupole anisotropy of the radiation in the rest frame of electrons. Small black arrows show the motion of the fluid in the rest frame of the electron. Red lines show the electric field direction of the radiation scattered by Thomson scattering on the electrons. This results in positive or negative E -mode polarization patterns.

We consider Thomson scattering on an electron in the fluid falling or climbing the well. In the first case the electron, in its own rest frame, sees the fluid behind him and in front of him moving away. However, the fluid on its side (on the same isocurve of the well) gets closer to him. By Doppler effect, the electron sees the photon energy (so their frequency) going up or down, which shifts the black-body spectrum temperature. This results in a temperature quadrupole anisotropy in the rest frame of the electron. In the second case, it is the opposite, the electron sees the fluid behind him and in front of him coming closer while the fluid on its side is moving away. This also results in a quadrupole radiation, $\pi/2$ rotated compared to the first case.

As seen before, the outgoing polarization after Thomson scattering is orthogonal to the hot quadrupole lobes (see Figure 4.7). We represent several electrons on the same potential isocurve and we look at the well from above. The first case where electrons are falling down creates a radial polarization pattern centered on the over-density while the second case where the electrons are climbing up creates a tangential polarization pattern surrounding the over-density.

We clearly recognize the patterns associated with positive and negative E -modes. So in summary, a cold spot can generate alternatively positive and negative E -modes at the frequency of the acoustic oscillation. However it can not generate B -modes.

Gravitational waves

By distorting space when they propagate, gravitational waves generate E and B -modes. In Figure 4.11, we consider a gravitational wave with a wave vector \mathbf{k} propagating along the z direction. The metric is modified in the transverse plane (\hat{e}_x, \hat{e}_y) with two polarization modes h_+ and h_\times . The dashed lines represent particles placed on a circle which is periodically deformed following the frequency of the gravitational wave. By Doppler effect, similarly to density perturbations, this creates temperature quadrupoles ($\ell = 2, m = 2$) around the electron, in its own rest frame.

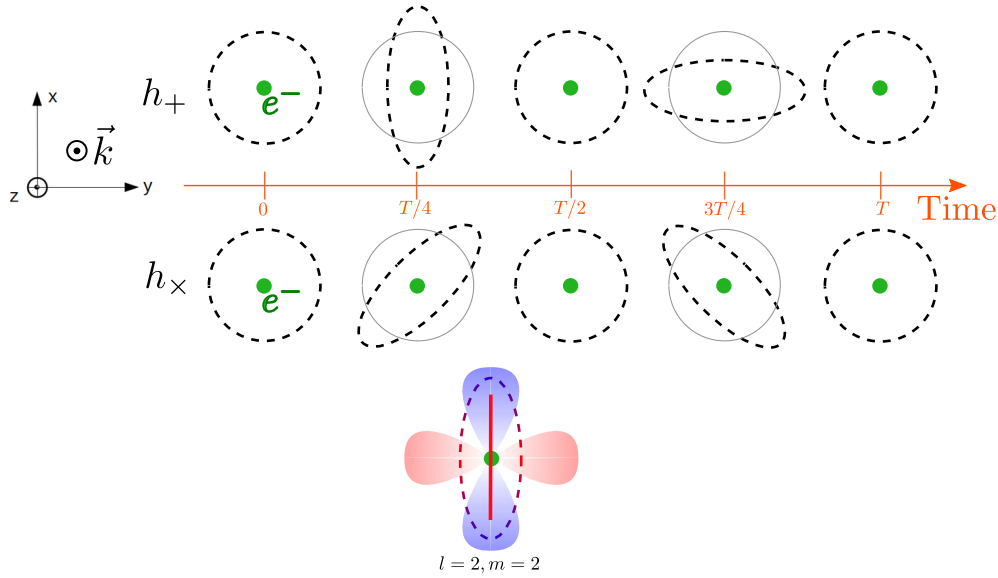


Figure 4.11: Propagation of a gravitational wave with wave vector \mathbf{k} along z direction. The dashed lines represent particles placed on a circle periodically deformed according to the period T of the gravitational wave. There are two polarization modes h_+ and h_\times . This creates a temperature quadrupole ($\ell = 2, m = 2$) around the electron, in its own rest frame. The red line is the polarization direction of a photon emitted by Thomson scattering along z , which is orthogonal to the hot lobes.

We consider a small portion of the LSS that locally can be approximated by a plane. Observers on Earth see photons emitted orthogonally from the LSS plane. Figure 4.12 illustrates how a gravitational

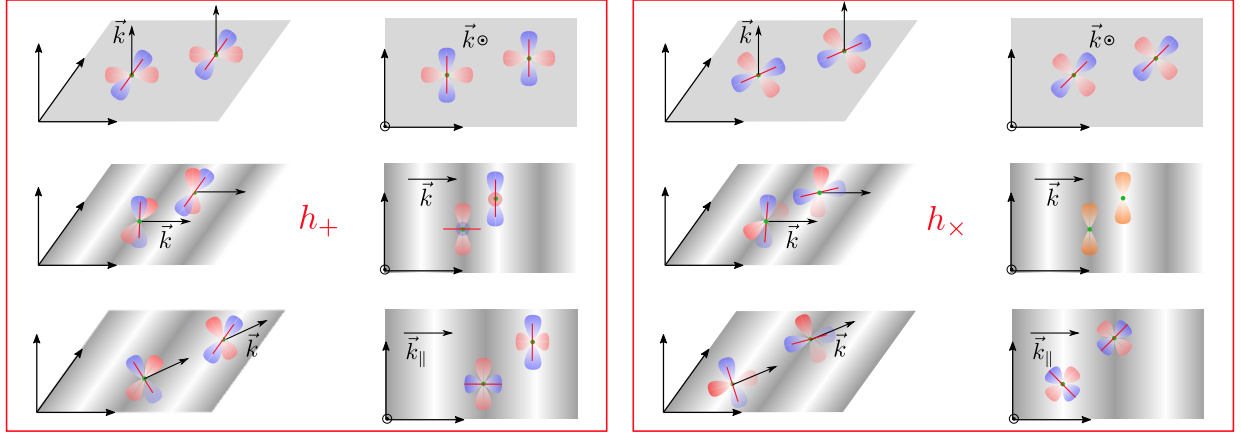


Figure 4.12: *Left*: Polarization generated by gravitational wave with direction \mathbf{k} and polarization h_+ . The gray rectangle is a part of the LSS locally approximated by a plane. On the right, it is a projection on the LSS as seen by an observer on Earth while on the left it is a 3D representation. The gray degrade represents the phase of the gravitational wave as seen by the observer. The polarization of the emitted photon is always parallel or perpendicular to the projection of \mathbf{k} . *Right*: Similar to the left panel but for a gravitational wave with h_\times polarization. Here, the emitted photon polarization is oriented at 45° from the projection of \mathbf{k} . Contrary to h_+ , when \mathbf{k} is tangential to the LSS, the scattering photon is unpolarized because the projection of the quadrupole on the LSS superimposes hot and cold lobes (drawn in orange).

wave h_+ or h_\times , depending on its direction of propagation \mathbf{k} with respect to the LSS, produces polarized light. We consider three cases (one on each row): \mathbf{k} orthogonal to the LSS plane, \mathbf{k} tangential to the LSS plane and \mathbf{k} with a random inclination. In the right column, we represent the projection on the LSS which corresponds to what the observer sees. We can point out four facts:

- When \mathbf{k} is orthogonal, the LSS plane is a wavefront of the gravitational wave so all the quadrupoles surrounding electrons sitting on the LSS are oriented in the same direction. This means that all photons, scattered through Thomson scattering share a common direction of polarization (red bare). This results in zero E and B -modes because the integral of Q_{rad} and U_{rad} on a circle will be zero for a constant polarization direction. This is true for h_+ and h_\times .
- For h_+ , with \mathbf{k} tangential or inclined but not orthogonal to the LSS, the resulting polarization is always parallel or perpendicular to the projection \mathbf{k}_\parallel of \mathbf{k} on the LSS.
- For h_\times , when \mathbf{k} is tangential, it does not create polarization light because on the projection, a hot lobe superimposes with a cold one so the quadrupole disappears (sketched in orange).
- For h_\times , when \mathbf{k} is out of the LSS plane but not orthogonal, it creates linear polarization at 45° to the projection \mathbf{k}_\parallel .

Now, the question is whether it produces E or B -mode polarization. On Figure 4.13, we consider a single point on the LSS, sketched by a blue spot. Red bars represent the direction of polarization, given by the electric field surrounding the point. Four cases are represented: positive and negative E -modes, positive and negative B -modes. The projection on the LSS of the gravitational wave vector \mathbf{k}_\parallel pointing on the blue spot is shown with a black arrow. When the polarization direction is parallel or perpendicular to \mathbf{k}_\parallel , it corresponds to E -mode patterns. On the contrary, when the polarization is oriented at 45° from \mathbf{k}_\parallel it corresponds to B -mode patterns.

So, let us summarize. If \mathbf{k} is orthogonal to the LSS, as we already say, neither h_+ or h_\times can generate E or B -modes. If \mathbf{k} is tangential or inclined with respect to the LSS plane, h_+ will generate E -modes because \mathbf{k}_\parallel is parallel or perpendicular to the polarization direction. B -modes are only produced with

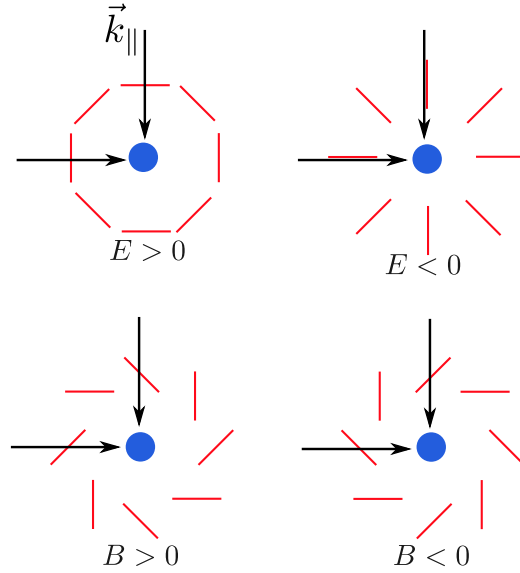


Figure 4.13: we consider a single point on the LSS, blue spot. Red bars represent the direction of polarization, given by the electric field surrounding the point. Four cases are represented with pure E positive and negative, pure B positive and negative. The projection of the gravitational wave vector \mathbf{k}_{\parallel} pointing on the blue spot is shown. When the polarization direction is parallel or perpendicular to \mathbf{k}_{\parallel} , it corresponds to E -mode patterns. On the contrary, when the polarization is oriented at 45° to \mathbf{k}_{\parallel} , it corresponds to B -mode patterns.

h_{\times} when \mathbf{k} is inclined with respect to the LSS plane because in this case, \mathbf{k}_{\parallel} is at 45° with respect to the polarization direction.

4.2.5 Polarization statistics

As we did for temperature in section 4.1.4, we can decompose E and B fields on the spherical harmonics basis:

$$E(\mathbf{n}) = \sum_{\ell m} a_{\ell m}^E Y_{\ell m}(\mathbf{n}) \quad \text{and} \quad B(\mathbf{n}) = \sum_{\ell m} a_{\ell m}^B Y_{\ell m}(\mathbf{n}), \quad (4.60)$$

and we can define the angular power spectra:

$$C_{\ell}^{EE} = \langle |a_{\ell m}^E|^2 \rangle \quad \text{and} \quad C_{\ell}^{BB} = \langle |a_{\ell m}^B|^2 \rangle. \quad (4.61)$$

As temperature anisotropies are related to polarization, it is interesting to look at the correlations. We define the cross power spectra:

$$C_{\ell}^{TE} = \langle a_{\ell m}^T a_{\ell m}^{E*} \rangle, \quad C_{\ell}^{TB} = \langle a_{\ell m}^T a_{\ell m}^{B*} \rangle \quad \text{and} \quad C_{\ell}^{EB} = \langle a_{\ell m}^E a_{\ell m}^{B*} \rangle. \quad (4.62)$$

However, because of the difference of behavior under reflection between T, E and B, the two last one are zero. B has no correlations with T or E . Thus, only four angular power spectra are needed to characterize the temperature and polarization of the CMB: TT , EE , BB and TE .

Canonical definition of E and B -modes

I give here the canonical definition for E and B -modes as originally presented in [142]. Indeed, from equation 1.65, we see that the two quantities $(Q \pm iU)$ have a ± 2 spin. Thus, we can expand it on the appropriated spin-weighted spherical harmonics basis:

$$(Q \pm iU)(\mathbf{n}) = \sum_{\ell=2}^{\infty} \sum_{m=-\ell}^{\ell} a_{\pm 2, \ell m} \pm 2 Y_{\ell m}(\mathbf{n}). \quad (4.63)$$

By linear combination of the coefficients of this decomposition, we can form two scalar quantities,

$$a_{\ell m}^E = \frac{-(a_{2,\ell m} + a_{-2,\ell m})}{2} \quad \text{and} \quad a_{\ell m}^B = \frac{i(a_{2,\ell m} - a_{-2,\ell m})}{2}, \quad (4.64)$$

which correspond to the coefficients of the spherical harmonics decomposition E and B fields defined on the sphere. This definition and definition from section 4.2.3 give expressions for E and B that are non local, invariant by translation and rotation of the coordinate system and with the correct parity properties. The choice of the weight function $w(\theta) = -1/\theta^2$ defined in section 4.2.3 ensures that the two definitions have the same expressions in the Fourier domain [144], [145].

4.2.6 Perturbations on the way

Different mechanisms can modify the CMB polarization between recombination epoch and today.

Gravitational lensing

As we said in section 4.1.2, gravitational lensing has an effect on temperature anisotropies but it also modifies the polarization [146], [147]. By deforming the polarization patterns on the sky, lensing mixes E and B modes. As E mode signal is much more intense than B mode signal², lensing B -modes can dominate the primordial B -mode signal at small angular scales. Because gravitational lensing is independent on the frequency ν , the two signals have the same electromagnetic spectrum so they are not easily distinguishable. Moreover, lensing introduces correlations between T , E and B fields such that EB and TB correlations can be non zero.

Similarly to temperature, we have

$$Q_{\text{len}}(\mathbf{n}) = Q_{\text{unl}}(\mathbf{n} + d(\mathbf{n})) \quad \text{and} \quad U_{\text{len}}(\mathbf{n}) = U_{\text{unl}}(\mathbf{n} + d(\mathbf{n})) \quad (4.65)$$

and from equation 4.22, we can compute the power spectrum of the lensed B -modes [189]:

$$C_{\ell_1, \text{len}}^{BB} = \frac{1}{2\ell_1 + 1} \sum_{\ell_2 \ell} |f_{\ell_1 \ell_2 \ell}^{EB}|^2 C_{\ell_2}^{EE} C_{\ell}^{\phi\phi}. \quad (4.66)$$

$C_{\ell}^{\phi\phi}$ is the angular power spectrum of the lensing potential ϕ and $f_{\ell_1 \ell_2 \ell}^{EB}$ is a coupling coefficient. To get rid of the lensing B -modes, there are methods called delensing and it is a wide research field. Given the above expression, it is clear that delensing requires two ingredients: the measurement of E -modes and a measurement of the gravitational field ϕ .

Reionization bump

As seen in section 4.1.3, Thomson scattering between CMB photons and free electrons released at reionization attenuates temperature anisotropies. However, it also creates additional polarization because electrons see quadrupoles anisotropies in the CMB radiation. This time, the quadrupole comes from the CMB temperature itself, it is the same quadrupole we observe today. So it is different from what happens at recombination. This induces a peak, called the reionization bump, in the polarization EE and BB angular power spectra at:

$$\ell_p \simeq 2(\sqrt{z_{\text{ion}} + 1} - 1) \quad (4.67)$$

where $z_{\text{ion}} \sim 6$ is the redshift at reionization [136]. The amplitude of the peak is proportional to the optical depth τ [148]. Thus, measuring the position and the amplitude of the peak in the power spectra gives information about reionization period. It was first presented by Zaldarriaga in [142].

² E -modes are produced by density fluctuations and gravitational waves while B -modes can only be produced by gravitational waves.

Conclusion In this chapter I have presented the temperature and polarization anisotropies in the CMB, focusing on their physical origin in the primordial plasma.

To conclude this chapter, Figure 4.14 shows the recent measurements of the CMB temperature and polarization power spectra (TT , EE , BB and TE). The BB signal detected today corresponds to the lensing B -modes. The expected primordial BB signal is shown for $r = 0.1$. We will define this parameter called the tensor-to-scalar ratio in chapter 7. To end this chapter, I wish to emphasize once more something I find remarkable: spatial CMB anisotropies and the power spectrum shapes were predicted before the first observation [108].

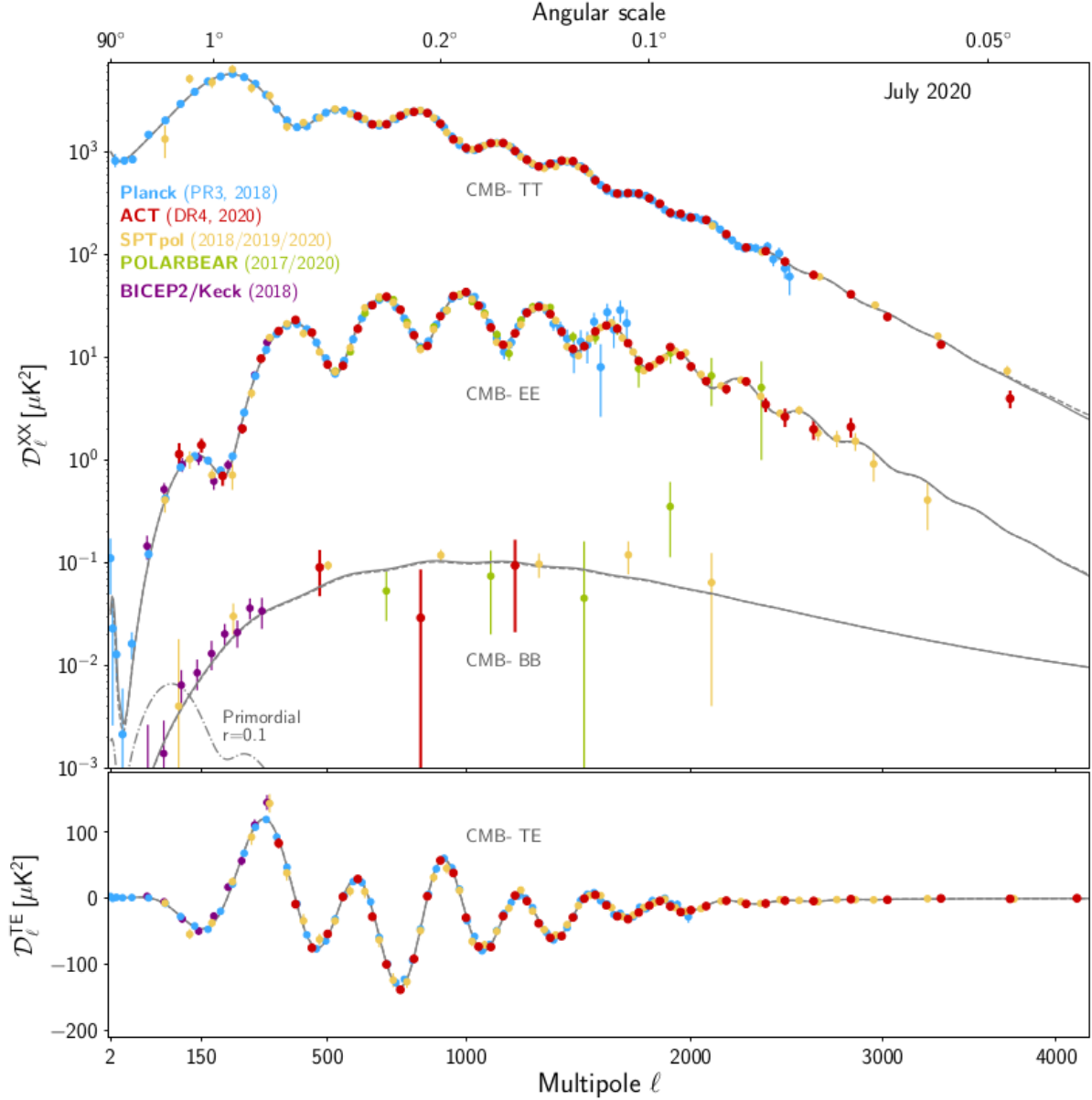


Figure 4.14: Recent measurements of the CMB temperature and polarization power spectra (TT , EE , BB and TE). The expected primordial BB signal is shown for $r = 0.1$. Taken from [161].

In the next chapter I will present the main observational techniques for CMB experiments.

Chapter 5

Observing and measuring the CMB

Contents

5.1	Projects targeting B-modes	126
5.1.1	Ground based telescopes	126
5.1.2	Balloons	127
5.1.3	LiteBIRD space mission	127
5.1.4	Summary and discussion	127
5.2	Making sky maps	129
5.2.1	Why scanning?	129
5.2.2	Data model	130
5.2.3	Map-making solution	130
5.2.4	Numerical implementation	131
5.2.5	QUBIC monochromatic map-making	132
5.2.6	HWP angle spacing	135
5.2.7	Spatial correlations	138
5.3	Power spectrum estimation with real data	139
5.3.1	Interest of doing cross spectra	139
5.3.2	Pixel and beam window correction	140
5.3.3	Partial coverage and pseudo spectra	141
5.3.4	E and B leakage and pure decomposition	141
5.3.5	Theoretical error bars on the reconstructed power spectrum	142
5.3.6	Namaster	142
5.3.7	Maximum likelihood solution	143
5.4	Foreground contamination of the CMB signal	144
5.4.1	Astrophysical foregrounds	144
5.4.2	Atmospheric opacity	145
5.5	QUBIC on a TOAST	147

This chapter treats the CMB from the point of view of observers. I first review the main current projects targeting CMB polarization. Then I focus on data analysis methods: map-making and power spectrum estimation. A pedagogical review can be found in [190]. Some concepts are illustrated using the QUBIC data analysis and simulation pipeline and I also emphasize some specificities of bolometric interferometry. People doing data analysis have to face a major issue: the CMB signal is contaminated by foregrounds emissions, for example Galactic dust thermal emission or atmospheric opacity in the case of ground experiments. Finally, I terminate with an idea that would allow to adapt typical CMB data analysis software developed for classical imagers to the case of bolometric interferometers.

Personal contributions: I did the implementation of the **Namaster** package in the QUBIC soft pipeline in collaboration with Claudia Scóccola and Suzana Landau. I contributed in many aspects to the QUBIC soft pipeline. With Martin Gamboa and James Murphy, we made tutorials so that it is easier to learn how to use the software. Finally, the study concerning HWP angle spacing presented in section 5.2.6, is my personal work.

5.1 Projects targeting B -modes

Since the first detection in 1964, the CMB has been widely observed¹. Here we give a brief overview of the current and planned experiments aiming at measuring B -mode polarization. The list does not attempt to be exhaustive.

CMB experiments can be separated in three types: ground based telescopes, balloons and satellites, each with their own advantages. Moreover, generally speaking, the Large Aperture Telescopes (LAT) target small angular scales temperature and polarization power spectra, focusing on lensing B -modes. On the contrary, the Small Aperture Telescopes (SAT), with lower resolution, aim at constraining the tensor-to-scalar ratio accessible on large angular scales.

5.1.1 Ground based telescopes

BICEP2/Keck Array: operating since 2010 at the South Pole in Antarctica, observing at 95, 150 and 220 GHz [149], [162]. They reported a first detection of primordial B -modes in 2014 [152] but it was quickly shown through a joint analysis using the Planck data that the observed B -modes were due to polarized emission from galactic dust [153]. BICEP Array is the next stage instrument, replacing the Keck Array, with additional receivers at 30 and 40 GHz [163].

POLARBEAR: installed in 2012 at the Atacama plateau in Chile, observing at 150 GHz [164]. A continuous rotating half-wave plate was installed in 2014. They have access to angular scales between $50 \leq \ell \leq 600$. POLARBEAR-2 and Simons Array [165] are extensions of POLARBEAR, adding receivers at 95 and 220 GHz and improving the sensitivity.

South Pole Telescope (S-PT): a 10 m diameter telescope (LAT) located at South pole. The SPTpol polarization sensitive receiver was installed on the telescope in January 2012 [166]. It has two arrays of polarization sensitive bolometers observing at 95 and 150 GHz. SPT-3G is the third generation camera on the SPT, installed in 2017 [167] with $\sim 16\,000$ multichroic detectors observing at 95, 150 and 220 GHz.

ACTpol: a large aperture telescope (6 m diameter receiver), located at the Atacama plateau in the Cerro Toco site [161], [168]. First observations started in 2007 in two frequency bands at 97 and 148 GHz. A third band at 220 GHz was added later. Advanced ACTpol is an upgrade with new frequency bands and better sensitivity through adding receivers [169], [170].

CLASS: a telescope array observing from the Atacama desert, at frequency bands around 40, 90, 150, and 220 GHz [171]. CLASS measures the large angular scale ($1^\circ \leq \theta \leq 90^\circ$), targetting primordial B -modes. The 40 GHz CLASS telescope has been observing since 2016 and other channels were deployed later. The polarization-sensitive dichroic 150/220 GHz detector array was for instance delivered in June 2019 [172].

¹One may have a look to this NASA page with a very long list of past, current and planned CMB experiments <https://lambda.gsfc.nasa.gov/product/expt/>.

Simons Observatory (SO): currently under construction at the Atacama plateau, in the Cerro Toco site, it will share the site with ACTpol, POLARBEAR, CLASS and CMB-S4 [173]. It will consist in 60 000 detectors distributed over one large aperture telescope (6 m diameter primary reflector), observing in six frequency bands from 27 to 280 GHz, and three small aperture telescopes (50 cm diameter) similar to BICEP3 receivers with continuous rotating HWP.

CMB-S4: a single experiment with 21 instruments mixing large (5 and 6 meter diameter) and small aperture telescopes (~ 50 cm diameter) [174], [175]. It will be deployed both at the South Pole and in Chile at the Cerro Toco site. In total, more than 500 000 detectors distributed on the telescopes will observe the sky. The telescope design is very similar to that of Simons Observatory. It will observe in 11 frequency bands distributed between 20 and 270 GHz.

LSPE-STRIP: a telescope based in Tenerife coupled with the LSPE-SWIPE balloon [176]. It is among the few CMB experiments dedicated to the observation of the Northern Hemisphere. First observations should start next year with two frequency channels at 43 and 95 GHz.

5.1.2 Balloons

SPIDER: a balloon experiment, launched in Antarctica in January 2015 for a duration of 16.5 days [177], [178]. It consists in six refracting telescopes (two-lens refractor) housed in a single cryostat. It has two frequency channels at 95 and 150 GHz. The polarization of the signal is modulated with step rotating half-wave plates mounted on each telescope. A second flight with upgrades is planned for December 2021 [179].

LSPE-SWIPE: a balloon, associated with the LSPE-Strip ground telescope [176]. It will observe at 145, 220 and 240 GHz in a stratospheric flight in Arctic, scheduled for winter 2021-2022.

PIPER: a balloon-borne instrument with twin cryogenic telescopes, observing in four bands from 200 to 600 GHz [180]. The polarization sensitivity is achieved with a variable-delay polarization modulator. This allows Piper to instantaneously measure the full Stokes vector (I, Q, U, V) for each pointing. The first flight for astrophysical observations occurred in October 2019. Unfortunately, failure of an observation hatch to open prevented observations [181].

5.1.3 LiteBIRD space mission

LiteBIRD [182], [183], the Lite (Light) satellite for the study of B-mode polarization and Inflation from cosmic background Radiation Detection, is a space mission, led by JAXA with a strong European support, designed to measure the CMB polarization with unprecedented precision. It will be launched in the late 2020s and it will perform a complete survey of the sky during three years. LiteBIRD can be considered as a fourth generation CMB space mission, successor of the Planck satellite. The focal planes are made with more than 4600 bolometers (Transition-Edges Sensors) and the satellite will observe from 34 to 448 GHz split in 15 sub-bands with three telescopes. The polarization of the sky will be modulated using half-wave-plates located at the entrance of each telescope. The expected sensitivity is $2.16 \mu\text{K-arcmin}$ with an angular resolution around 0.5 degree at 100 GHz.

5.1.4 Summary and discussion

The main characteristics of the experiments listed above are summarized in Table 5.1.

Project	Type	Location	Start	ℓ range	Frequency [GHz]	$\sigma(r)$
BICEP2/Keck	Ground	Antarctica	2010	35 – 300	30, 40, 95, 150, 220, 270	3×10^{-3}
POLARBEAR + SA	Ground	Chile	2012	50 – 600	95, 150, 220	0.006
CLASS	Ground	Chile	2016	2 – 200	40, 90, 150, 220	0.01
SPIDER	Balloon	Antarctica	2015	10 – 300	90, 150, 280	0.01
SO	Ground	Chile	Future	30 – 8000	27, 39, 90, 150, 220, 270	0.003
QUBIC TD + FI	Ground	Argentina	2022	40 – 400	150, 220	0.01
LSPE	Ground + Balloon	Canaries + Arctic	Future	2 – 100	43, 90, 95, 145, 245	0.01
PIPER	Balloon		Future	2 – 300	200, 270, 350, 600	0.003
CMB-S4	Ground	Chile + Antarctica	Future		11 bands from 20 to 270	5×10^{-4}
LiteBIRD	Satellite		Future	2 – 200	15 bands from 34 to 448	1×10^{-3}
SPT + SPT-3G	Ground	Antarctica	2012	50 – 2300	95, 150, 220	
ACTpol	Ground	Chile	2007	225 – 8725	30, 40, 98, 150, 220	

Table 5.1: Summary of the CMB experiments presented above. The cyan color indicates the project dedicated to small angular scales only. The last column gives the expected uncertainty on the tensor-to-scalar ratio r , a parameter related to cosmic inflation that I will introduce in chapter 7.

Ground based telescopes have the advantage to be easily upgraded compared to satellites but they have to deal with atmosphere opacity as we will see in section 5.4.2. Balloons are a nice compromise between space and ground based experiments but they are limited by the duration of flight. All those projects are really complementary as they slightly differ regarding the frequency channels, the angular resolution, the detectors... Moreover, redundancy between experiments, for example regarding the same sky region is a good point if we want to compare the results. I think that a detection of a non zero tensor-to-scalar ratio, a parameter related to cosmic inflation that I will introduce in chapter 7, will have to be confirmed by several instruments.

To conclude this short overview, I think it is nevertheless important to note that all projects are variations of the same design: classical imaging with TES arrays at focal plane. The control of systematic effects relies on the scanning strategy coupled with a modulation of the signal by an HWP. From this point of view, the QUBIC design is very original. An alternative design will have different instrumental systematic effects and could provide a novel manner to approach the problem. For instance, QUBIC provides higher spectral resolution thanks to the spectral imaging technique that will be presented in chapter 6.

5.2 Making sky maps

5.2.1 Why scanning?

As briefly mentioned in section 1.1.3, CMB experiments acquire data by continuously scanning the sky, producing Time-Ordered Data (TOD). TOD consist in a large array:

$$TOD = \{d_i(t), RA(t), DEC(t), \text{Housekeeping}(t)\} \quad (5.1)$$

where $d_i(t)$ is the signal received by bolometer i at time t and (RA, DEC) are the pointing coordinates. Housekeeping data contain diverse information, for example the temperatures at different places in the instrument or the bias voltage of the TES. CMB telescopes do not integrate during a long time period in a fixed position with respect to the sky. This technique is not specific to CMB data and was also called raster scan, see for example [191]. Historically, the small number of bolometers was certainly the reason for that: if one wants to get an image of the sky with only one or a small number of detectors, it is necessary to scan. However, scanning has another interesting feature regarding the noise and especially the $1/f$ component which can originate from electronic, cryogenic fluctuations, atmospheric variations. Indeed, it modulates the sky signal in a controlled manner.

As shown in Figure 5.1, contrary to white noise, $1/f$ noise includes low frequency drifts which results in a non flat frequency power spectrum $P(f)$, also called power spectral density, defined as

$$\langle \tilde{n}(f) \tilde{n}(f') \rangle = P(f) \delta(f - f') \quad (5.2)$$

where $\tilde{n}(f)$ is the Fourier transform of the noise. The power spectrum can actually be split in two

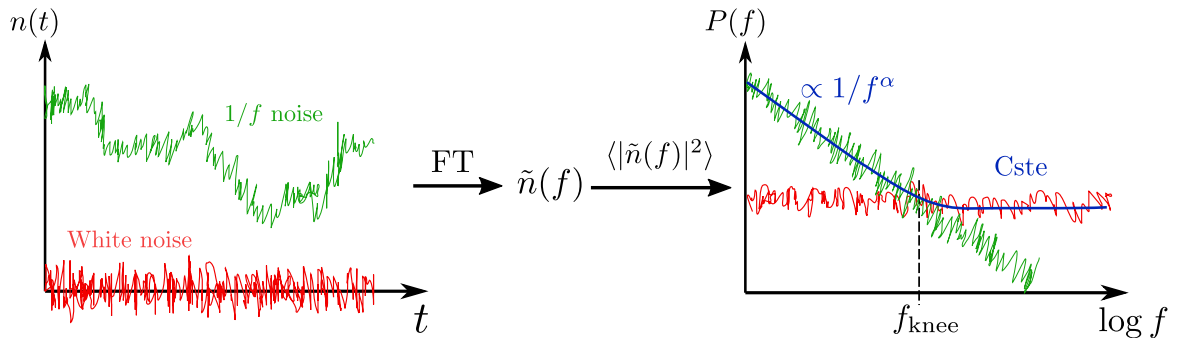


Figure 5.1: Illustration of $1/f$ noise in green compared to white noise in red. A typical evolution as a function of time is shown on the left with the corresponding frequency power spectrum on the right.

parts separated by the knee frequency f_{knee} . The low frequency part has a dependence in $1/f^\alpha$ where

α is the slope coefficient, while in the high frequency part white noise dominates. The power spectrum can be written as [192], [193]

$$P(f) = P_{\text{white}} \left(1 + \left(\frac{f_{\text{knee}}}{f} \right)^\alpha \right). \quad (5.3)$$

Here α is positive and close to one, which explains the name $1/f$ noise². As an example, for the Planck low frequency instrument, in the 44 GHz channel, we have $f_{\text{knee}} = 53.0$ mHz and $\alpha = 0.88$ [184]. From Figure 5.1, it is clear that integrating the signal over a long period would significantly increase the noise variance.

The idea of making differential measurements was first mentioned by Dicke in 1946 [39]. For example, the COBE DMR instrument was based on a differential measurement between two antennas implemented in the hardware [185]. Instead, the current CMB experiments modulate the signal, at a frequency above f_{knee} , thanks to a continuous scan. Knowing the scanning strategy, TOD can then be rearranged in order to build a sky map. Differential measurement is done in post-processing, the idea is to require that all measurements of a single point on the sky share the same sky temperature. This was for example proposed in 1998 for temperature in the context of the Planck mission [193] and soon extended to polarization [194]. The case of polarization is more complicated because the angle of the polarimeter may be different from one scan to another.

5.2.2 Data model

As seen in section 1.2.5, a detector observes the sky temperature through an instrumental beam. It is equivalent to say that the sky is convolved with the instrumental beam and that a detector measures the temperature in a single direction, corresponding to a given sky pixel. The convolved pixelised sky \mathbf{T} is a N_p dimension vector. The TOD of a given detector are written as a vector noted \mathbf{d} which contains the N_t time sample data. We can write [195]

$$\mathbf{d} = A \cdot \mathbf{T} + \mathbf{n} \quad (5.4)$$

where A , called the pointing matrix, is a 2-dimensional matrix: number of time samples \times number of sky pixels. A is an operator that describes the convolution by the synthesized beam as well as the pointing at the different directions of the sky according to the scanning strategy. For standard imagers, A is such that each line (corresponding to sky pixels contributing to one time sample) only contains a single 1 value [195].

\mathbf{n} is the noise, it is a vector with dimension N_t . The noise has two contributions: photon noise and detector noise. Photon noise is the Poisson fluctuations from the temperature of the CMB ($T_{\text{CMB}} \simeq 2.7$ K), the atmosphere, and the internal optical components. Detector noise is given by the Noise Equivalent Power (NEP) measured in each detector. So far, in the QUBIC pipeline, the atmosphere emissivity is assumed to be stable, we did not consider the effect of fluctuations in the atmospheric load.

The noise is assumed to be Gaussian so that all the information is contained in its covariance matrix

$$N = \langle \mathbf{n} \cdot \mathbf{n}^T \rangle. \quad (5.5)$$

The probability distribution of the noise is

$$P(\mathbf{n}) = \frac{1}{|(2\pi)^{N_t} N|^{1/2}} \exp \left[-\frac{1}{2} \mathbf{n}^T \cdot N^{-1} \cdot \mathbf{n} \right]. \quad (5.6)$$

5.2.3 Map-making solution

Map-making consists in finding the best estimator $\hat{\mathbf{T}}$ for the sky temperature convolved at the beam resolution, knowing \mathbf{d} and A . The noise \mathbf{n} is unknown but the covariance matrix N can for instance be estimated by Monte-Carlo simulations. The general solution for map-making is given by maximizing

²Sometime the definition is chosen as the opposite, for example in [184], with a negative slope.

the likelihood function assuming a given noise model [195], [196]. The likelihood function is the probability of getting data \mathbf{d} given a theoretical sky \mathbf{T} ,

$$\mathcal{L} \equiv P(\mathbf{d}|\mathbf{T}). \quad (5.7)$$

The Bayes theorem relates the likelihood to the posterior probability which is the probability of having a sky \mathbf{T} given the data, $P(\mathbf{T}|\mathbf{d})$.

$$P(\mathbf{d}|\mathbf{T}) = \frac{P(\mathbf{T}|\mathbf{d})P(\mathbf{d})}{P(\mathbf{T})}. \quad (5.8)$$

$P(\mathbf{T})$ is the prior on the theoretical model, for example a constrain coming from a previous experiment. Assuming a uniform prior, i.e. $P(\mathbf{T}) = \text{cst}$, we have

$$\mathcal{L} \equiv P(\mathbf{d}|\mathbf{T}) \propto P(\mathbf{T}|\mathbf{d}). \quad (5.9)$$

We expect that the data deviate from the sky by the Gaussian noise so the posterior probability is proportional to the noise probability distribution. Thus,

$$\mathcal{L} \propto P(\mathbf{n}) \propto \frac{1}{|(2\pi)^{N_t} N|^{1/2}} \exp \left[-\frac{1}{2} (\mathbf{d} - A\mathbf{T})^T \cdot N^{-1} \cdot (\mathbf{d} - A\mathbf{T}) \right] \quad (5.10)$$

where we have used equations 5.4 and 5.6. The most likely values of \mathbf{T} are those which maximize the likelihood function. This is equivalent to minimizing the χ^2 ,

$$\chi^2 = -2 \ln \mathcal{L} = (\mathbf{d} - A\mathbf{T})^T \cdot N^{-1} \cdot (\mathbf{d} - A\mathbf{T}). \quad (5.11)$$

This leads to solve the linear equation [14]

$$(A^T N^{-1} A) \mathbf{T} = A^T N^{-1} \mathbf{d} \quad (5.12)$$

with solution

$$\hat{\mathbf{T}} = (A^T N^{-1} A)^{-1} A^T N^{-1} \mathbf{d}. \quad (5.13)$$

where $\hat{\mathbf{T}}$ is the sky convolved at the instrument resolution.

White noise: If the noise is white, N is diagonal so equation 5.13 reduces to

$$\hat{\mathbf{T}} = (A^T A)^{-1} A^T \mathbf{d}. \quad (5.14)$$

This is the simplest map-making, data are averaged in each sky pixel³. This is equivalent to have a long integration time. As discussed in section 5.2.1, this is only optimal, in the sense that it maximizes the likelihood, for pure white noise.

By adding N^{-1} in the map-making, we take into account the noise correlations. N^{-1} appears as a high pass filter with frequency cut f_{knee} . It removes the low frequency drifts in the noise through optimal noise weighting [192].

5.2.4 Numerical implementation

We have written the general map-making solution for an arbitrary noise. However, the numerical implementation is not trivial because timeline data are usually very large and large matrix system inversion is required. Brute inversion, as proposed in 1999 with the MADCAP software [197], has become very difficult as the number of samples increased. Iterative solution became the standard technique. This was first proposed in 2000 by using a Jacobi iterator [198]. It was soon replaced by conjugate gradient descent which accelerates the convergence, for example in the Mirage software [199] or MADmap [200]. A review of map-making techniques can be found in [201] and a discussion about iterative techniques in [202].

³ $(A^T A)$ counts hits in pixels and $A^T \mathbf{d}$ projects data in pixels. So this is an empirical average.

As this is what we used in the QUBIC map-making software, let us summarize what a Conjugate Gradient (CG) descent is. A pedagogical tutorial can be found in [220]. A CG is a method that solves iteratively linear systems with the form

$$A\mathbf{x} = \mathbf{b} \quad (5.15)$$

where \mathbf{x} is an unknown vector, \mathbf{b} a known vector and A a known, square, symmetric and positive-definite matrix. This is precisely equivalent to the map-making equation 5.12 where T is the unknown vector, $(A^T N^{-1} A)$ the matrix and $(A^T N^{-1})\mathbf{d}$ the known vector. Solving $A\mathbf{x} = \mathbf{b}$ is equivalent to minimize the quadratic form

$$f(\mathbf{x}) = \frac{1}{2}\mathbf{x}^T A \mathbf{x} - \mathbf{b}^T \mathbf{x} + c \quad (5.16)$$

where c is a scalar constant. Indeed, the gradient of f is

$$f'(\mathbf{x}) = \frac{1}{2}A^T \mathbf{x} \frac{1}{2}A \mathbf{x} - \mathbf{b} \quad (5.17)$$

which reduces to $A\mathbf{x} - \mathbf{b}$ if A is symmetric. Different algorithms can find the minimum by converging iteratively. Here I detail the Preconditioned Conjugate Gradient (PCG). A preconditioning can be applied to accelerate the convergence. Instead of solving $A\mathbf{x} = \mathbf{b}$, we solve $M^{-1}A\mathbf{x} = M^{-1}\mathbf{b}$ where M is a symmetric, positive-definite matrix that approximates A . Intuitively, the preconditioning stretches the quadratic form to make it more spherical. The steps of the algorithm are:

- Choose an initial point \mathbf{x}_0 .
- Compute the residuals $\mathbf{r}_0 = \mathbf{b} - A\mathbf{x}_0$ which must be 0 at the minimum.
- The direction of the first descent is given by $\mathbf{d}_0 = M^{-1}\mathbf{r}_0$.
- Then, for each i -th step,
 1. Compute the step size $\alpha_i = \frac{\mathbf{r}_i^T M^{-1} \mathbf{r}_i}{\mathbf{d}_i^T A \mathbf{d}_i}$.
 2. Go to the next position $\mathbf{x}_{i+1} = \mathbf{x}_i + \alpha_i \mathbf{d}_i$.
 3. Compute the new residuals $\mathbf{r}_{i+1} = \mathbf{r}_i - \alpha_i A \mathbf{d}_i$.
 4. The next direction is chosen to be M^{-1} -orthogonal to the previous one, i.e. they would be orthogonal if the quadratic form was stretched to be a circle. To do that, we use the conjugate Gram-Schmidt process [220]: $\mathbf{d}_{i+1} = M^{-1}\mathbf{r}_{i+1} + \beta_{i+1}$ with $\beta_{i+1} = \frac{\mathbf{r}_{i+1}^T M^{-1} \mathbf{r}_{i+1}}{\mathbf{r}_i^T M^{-1} \mathbf{r}_i}$.

The difficulty of this method is to determine an efficient preconditioning.

5.2.5 QUBIC monochromatic map-making

As shown in chapter 1, the QUBIC instrument is essentially equivalent to a standard imager, scanning the sky with the synthesized beam, producing TOD that can be projected onto sky maps. The map-making will therefore be very similar to that of a standard imager. TOD can be written as equation 5.4.

For standard imagers, the A operator is such that each line (corresponding to sky pixels contributing to one time sample) only contains a single non-zero value, meaning that \mathbf{T} is actually the sky map convolved at the instrument's resolution and that the instrument samples the convolved sky with a single peak [195], [197].

In the case of a bolometric interferometer, this assumption is not valid due to the multiple peaked shape of the synthesized beam (see Figure 1.20) which makes it impossible to use the map-making algorithms usually developed for direct imagers. We use instead an “inverse problem” approach based on an algorithm that starts from an initial guess and then simulates iterative maps \mathbf{T}_i , where i is the iterative index⁴. For each of these maps, we apply the bolometric interferometer acquisition model, taking into account the scanning strategy of the sky, and we construct TOD $\mathbf{d}_i = A\mathbf{T}_i$ that are then

⁴The software uses the massively parallel libraries [221] developed by P. Chianial: pyoperators (<https://pchanial.github.io/pyoperators/>) and pysimulators (<https://pchanial.github.io/pysimulators/>).

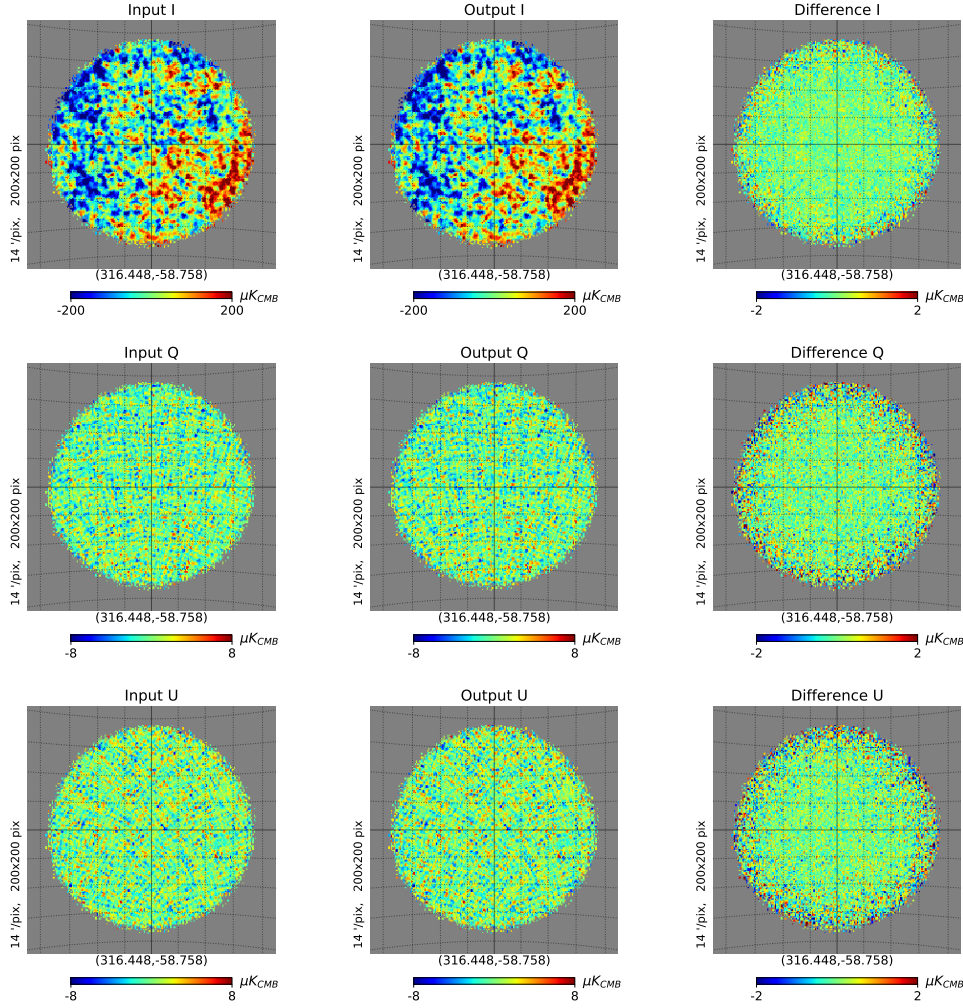


Figure 5.2: Result of the map-making for IQU Stokes parameters for a bolometric interferometer pointing in a 15 degree radius sky patch containing only CMB. The first column is the input sky convolved at the resolution of the instrument using a Gaussian with a FWHM equal to 0.4 degrees. The second column is the sky reconstructed by map-making. The last column is the difference between both. The grid lines are equally spaced every 5° . This simulation was obtained with the QUBIC full pipeline in the 220 GHz band. The noise was scaled to 4 years of observations. This simulation required 127 iterations to converge. Produced for [9].

compared to the data TOD \mathbf{d} using a merit function that accounts for the noise in the TOD domain. In the case of stationary and Gaussian distributed noise, the maximum likelihood solution is reached by minimizing the χ^2

$$\chi^2(\mathbf{d}_i) = (\mathbf{d} - \mathbf{d}_i)^T \cdot \mathbf{N}^{-1} \cdot (\mathbf{d} - \mathbf{d}_i). \quad (5.18)$$

The QUBIC software uses a preconditioned conjugate gradient method. The map-making is jointly done for all detectors and for the *IQU* Stokes parameters and results in unbiased estimates of the maps as shown in Figure 5.2. The synthesized beam used for the instrument model during map-making is actually just a set of Dirac functions with the relevant amplitude at the location of the peaks of the synthesized beam (ideal, including optical aberrations or resulting from self-calibration). In such a way, and similarly as with an imager, the map-making does not attempt to deconvolve from the resolution of the peaks, but only from the multiple peaks.

Allocated memory

The multiple peak QUBIC map-making requires high memory resources. The dimension of the operator which needs to be stored is $N_{\text{ptg}} \times N_d \times N_p$ where N_{ptg} is the number of pointings on the sky, N_d the

number of detectors and N_p the number of peaks considered for the synthesized beam. Note that it is independent on the number of sky pixels given by N_{side} for **Healpix** maps. This is because we do not store the entire A operator which is in the map space but only the synthesized beam peak locations (sky pixel number) for each time sample and each detector. For example, with 1000 pointings, 992 detectors (FI), and 25 peaks (up to second diffraction order), the memory stored is

$$1000 \times 992 \times 25 \times 16 = 396800000 \text{ bits} \simeq 378 \text{ Mib.} \quad (5.19)$$

As we will see in chapter 6 dedicated to spectral imagery, we actually decompose the signal in frequency sub-bands so that the allocated memory is multiplied by the number of sub-bands.

In the QUBIC map-making software, the number of peaks is determined by two parameters:

- k_{max} which is the diffraction order taken into account for the synthetic beam. The number of peaks is given by $N_p = (2 \times k_{\text{max}} + 1)^2$.
- The synthesized beam fraction SB_{frac} which is the fraction of the total integral of the synthesized beam (over all the peaks). This fixes the number of peaks to keep. Let us consider an example: for 9 peaks corresponding to $k_{\text{max}} = 1$, with the following partition: 50% of the power in the central peak integral, 10% in the 4 peaks forming the nearest cross and 2.5% in each of the 4 furthest peaks. Then for $SB_{\text{frac}} = 0.9$, the 4 furthest peaks are eliminated.

Decreasing the number of peaks reduces the required memory but it also has an impact on map-making performance. We performed simulations changing those parameters and we concluded that $k_{\text{max}} = 8$ with $SB_{\text{frac}} = 0.99$ which corresponds to keep 32 peaks is the minimum required not to lose accuracy.

5.2.6 HWP angle spacing

As seen in section 1.3.2, by measuring the signal in direction z in at least three different HWP positions, we are able to deduce the I, Q, U Stokes parameters in this direction. According to paper [203], in order to minimize the error on the reconstruction of I, Q, U and to avoid any correlations, the HWP rotating steps must be regularly spaced between 0 and $\frac{\pi}{2}$ such as:

$$\alpha_p = \alpha_1 + (p - 1) \frac{\pi}{2n} \quad (5.20)$$

with $p = 1, \dots, n$ ($n \geq 3$) and usually, we choose $\alpha_1 = 0$.

I have checked this result using the `qubicsoft` map-making pipeline, considering a noiseless simulation, and a TD instrument observing a 4° sky patch. The scan is performed with a not realistic random strategy, the same scan (1000 pointings) is repeated p times with the HWP in a fix position (see Figure 5.3). Residuals are defined as the difference between the input sky and the reconstructed

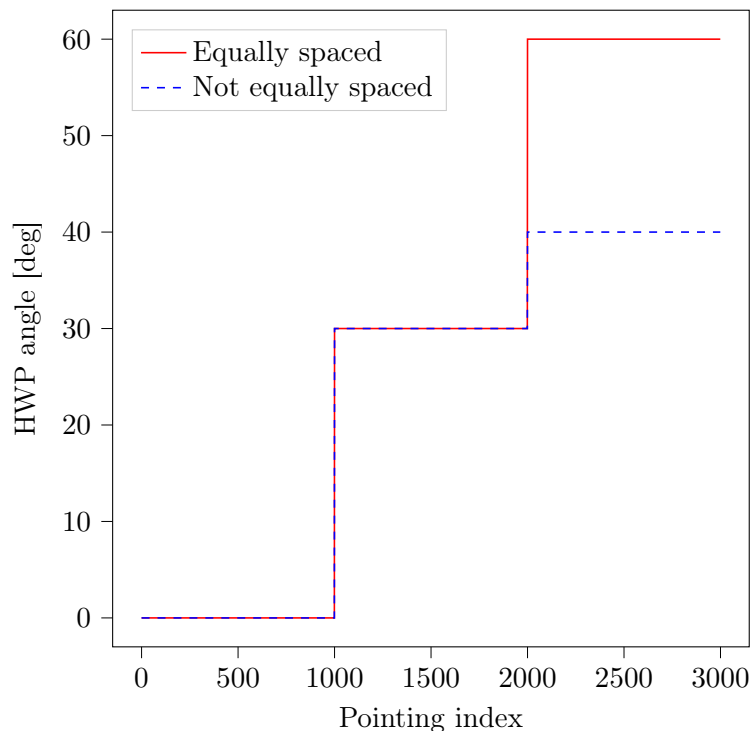


Figure 5.3: HWP angles during the scan for $p = 3$. The same 1000 pointings are repeated 3 times with a different HWP angle: 0° , 30° , 40° (blue) or 0° , 30° , 60° (red).

sky after the map-making process. As expected, the residuals are much higher when the HWP angles are not regularly spaced. This is shown in Figure 5.4 in the case of $p = 3$ angles. The same effect is observed for a higher number of angles. This “repeat” strategy was implemented, as an option, in the `qubicsoft` package. The goal is to mimic a random scanning with a much higher number of pointings, that would assure a sufficient coverage of each sky pixel with various HWP positions.

Figure 5.5 compares the two strategies. I consider 3000 pointings in a 4° sky patch. The HWP moves randomly on three equally spaced positions between 0 and $\pi/2$. The “repeat” strategy is compared to the random one in the Q and U residual polarization maps. The standard deviation of the residual maps differs approximately by a factor 20 between the two strategies. The residuals in intensity (not shown) are comparable for both. This confirms that what imports is the coverage of each sky pixel by the three HWP angles, which is forced to be optimal in case of the “repeat” strategy.

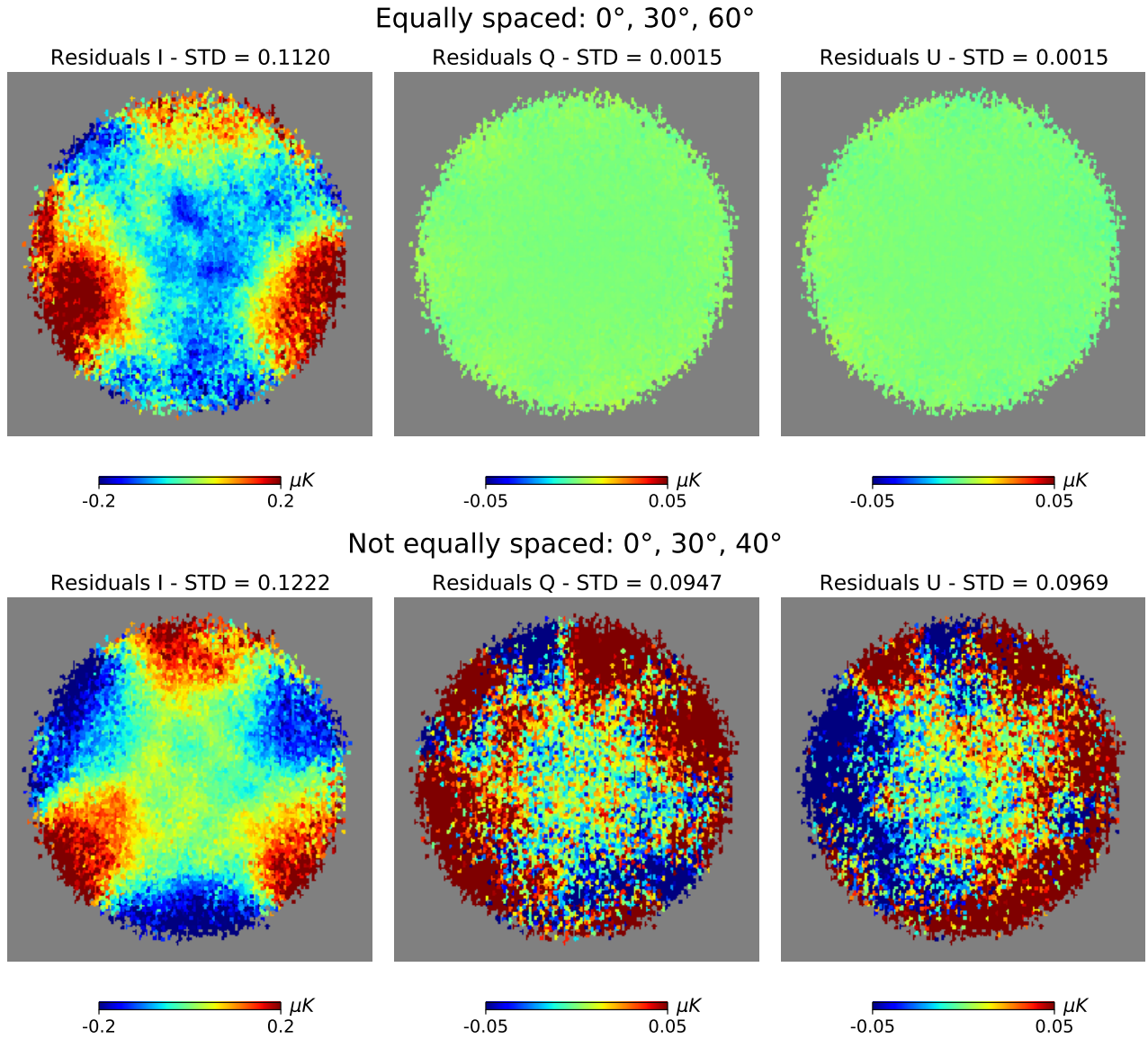


Figure 5.4: Residual maps for the I, Q, U Stokes parameters in case of three HWP angles regularly spaced at $0^\circ, 30^\circ, 60^\circ$ (top) and not regularly spaced at $0^\circ, 30^\circ, 40^\circ$ (bottom). The color scale is fixed in order to better see the difference and the standard deviation (STD) is written on the top of each map.

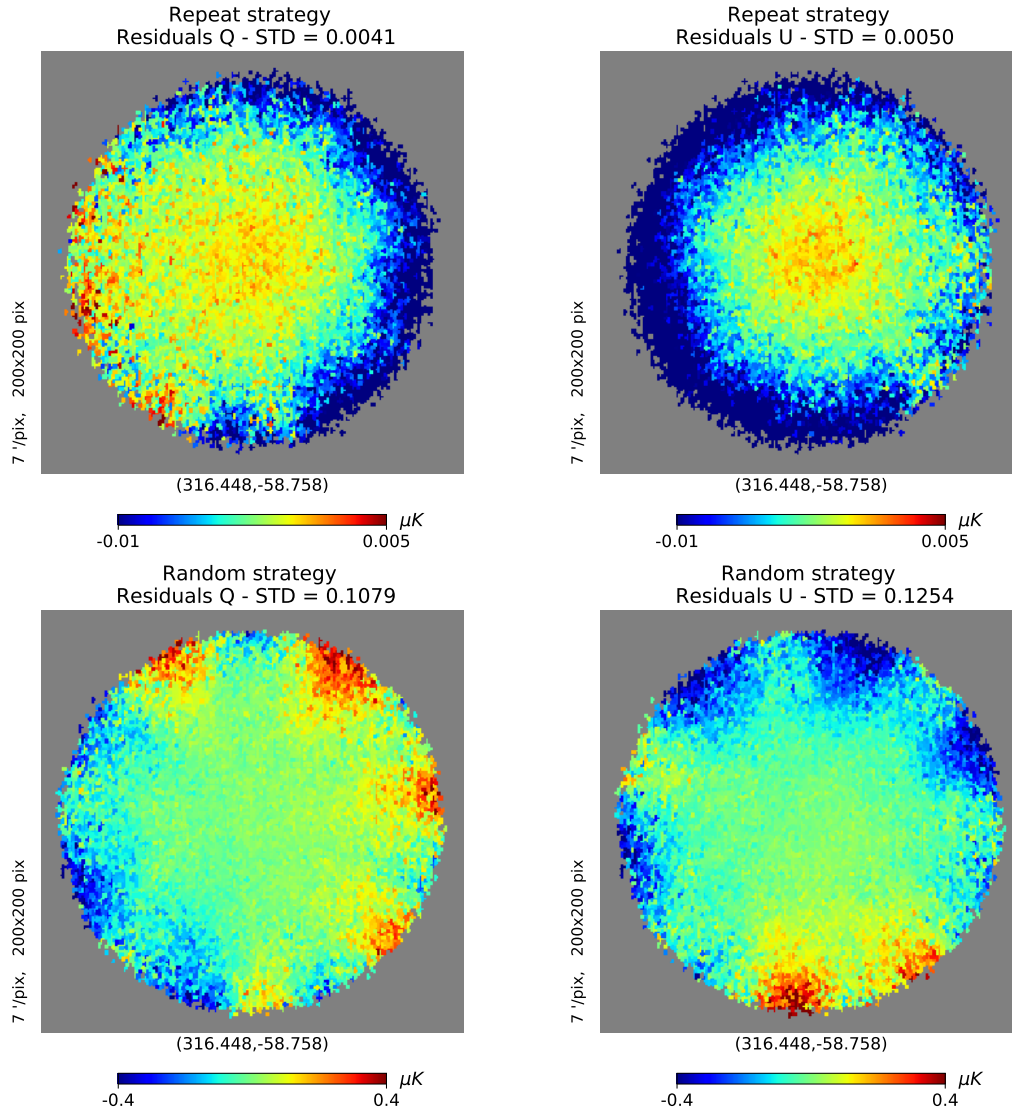


Figure 5.5: Comparison between the “repeat” (first row) and the random strategy (second row) in the residual polarization Q and U maps. The color scale is fixed differently for the two strategies in order to better see the difference and the standard deviation (STD) is written on the top of each map.

5.2.7 Spatial correlations

A specific feature of the QUBIC map-making is spatial correlations. This was already mentioned in the thesis by Marie-Anne Bigot-Sazy defended in 2013 [11] (Figure 6.3.3). Map-making with a multiple-peaked synthesized beam involves partial deconvolution because a given time sample in a detector's TOD receives power from distinct pixels in the sky with weights given by the shape of the synthesized beam. As a result, we expect significant spatial noise correlations in our maps. This is confirmed by end-to-end simulations as shown in the left panel of Figure 5.6. Anti-correlation peaks, are expected, at an angle corresponding to the angular separation between the peaks in the synthesized beam ($\theta_{\text{peaks}} = 8.8^\circ$ at 150 GHz and 6° at 220 GHz). A similar 2pt-correlation function is found at 220 GHz, but with even higher correlation amplitude because the secondary peaks are higher due to the top-hat shape of the primary beam resulting from multimode optics at 220 GHz (see Figure 4 in [6]).

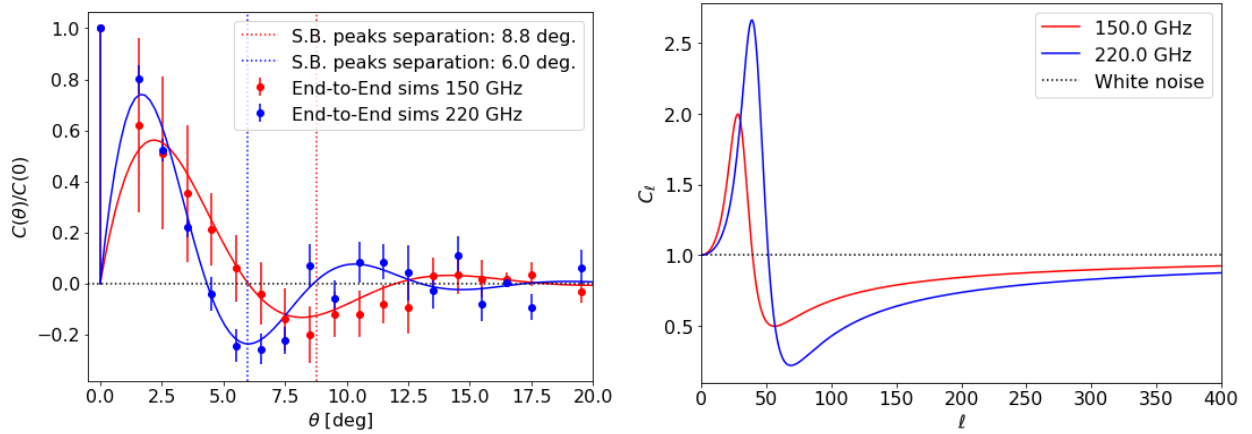


Figure 5.6: *Left*: QUBIC spatial noise 2pt-correlation function obtained from end-to-end simulations normalized by the variance in the maps $C(\theta = 0)$. The solid lines show an adjustment by a sine-wave modulated by an exponential with a Dirac function at $\theta = 0$ (the noise variance in the maps). The maximum anti-correlation is found as expected at the scale of the angular distance between two peaks of the synthesized beam. The amplitude of the correlation is higher at 220 GHz than at 150 GHz because of the top-hat shape of the primary beam at 220 GHz. *Right*: Spatial noise correlation converted to multipole space. The straight-line at $C_\ell = 1$ shows the expected shape for white noise. The noise correlation results in a reduction of the noise for multipoles larger than $\sim 40 - 50$, that is for angular scales $\lesssim \theta_{\text{peaks}}$ (angular separation between the synthesized beam peaks). At lower multipoles (larger angular scales), we observe an increase of the noise. This is an advantage for measuring the recombination peak around $\ell = 100$ as discussed in section 7.7.2. Taken from [1].

In the right panel of Figure 5.6 we display the spherical harmonics transform of the 2pt-correlation function:

$$C_\ell = 2\pi \int_{-1}^1 C(x) P_\ell(x) dx \quad (5.21)$$

where $x = \cos \theta$ and P_ℓ are the Legendre polynomials. This is our noise angular power spectrum which corresponds to the equivalent for QUBIC of typical white noise for a classical imager. The shape of this noise in Harmonic Space exhibits an excess with respect to white noise at very large scales (small multipoles, below $\ell = 40$ at 150 GHz and $\ell = 50$ at 220 GHz) and a significant reduction at smaller angular scales (larger multipoles). The scale of this transition is determined by the angular distance between peaks in the synthesized beam⁵. Angular scales $\gtrsim \theta_{\text{peaks}}$ are not well constrained due to the presence of the multiple peaks that are effectively deconvolved during the map-making. Conversely, angular scales smaller than this angular separation see their noise significantly reduced thanks to the positive correlation of the noise at these angles. Because these angular scales correspond to those of the

⁵It is however not strictly equal to $\pi/\theta_{\text{peaks}}$ because of the shape of the 2pt-correlation function and the non-trivial correspondence between angles and multipoles.

recombination peak in the B-mode spectrum, this specific noise feature for Bolometric Interferometry turns out to be a significant advantage for detecting primordial B-modes. This is discussed with more details from Monte-Carlo simulations in section 7.7.2 and visible in Figure 7.10. Also, because our noise is not white, the RMS in the maps does not have direct meaning. In our case, it is more meaningful to measure the noise level in the angular power-spectrum as we will detail in section 7.7.2.

5.3 Power spectrum estimation with real data

Cosmological parameters are usually determined with the angular power spectrum computed from the maps. We already defined the power spectrum in section 4.1.4. The problem becomes much more complex when one wants to estimate it from real data.

5.3.1 Interest of doing cross spectra

In this section, I show the interest of making cross-correlations between two observations, for instance, by splitting the data set in two parts. We recall that the empirical angular power spectrum is defined as

$$C_\ell = \langle a_{\ell m} a_{\ell m}^* \rangle_m \quad (5.22)$$

where the average is taken over the $2\ell + 1$ value of m (see section 4.1.4). The $a_{\ell m}$ coefficients contain the CMB signal and the noise, $a_{\ell m} = a_{\ell m}^S + a_{\ell m}^N$. For simplicity we write $a \equiv a_{\ell m}$. One can do the auto-spectrum of each observation. To study the statistics of this, I produce N_r realizations with independent noise. The ensemble average over the N_r realizations is noted $\langle \cdot \rangle_r$. The averaged auto-spectrum is given by

$$\langle C_\ell^{\text{auto}} \rangle_r = \langle \langle (a^S + a^N)(a^{S*} + a^{N*}) \rangle_m \rangle_r \quad (5.23)$$

$$= \langle \langle a^S a^{S*} \rangle_m + \langle a^N a^{N*} \rangle_m + \langle a^S a^{N*} \rangle_m + \langle a^N a^{S*} \rangle_m \rangle_r. \quad (5.24)$$

The signal is not correlated with the noise so the two last terms disappear when N_r tends to infinity and we get

$$\langle C_\ell^{\text{auto}} \rangle_r \simeq \langle \langle a^S a^{S*} \rangle_m + \langle a^N a^{N*} \rangle_m \rangle_r. \quad (5.25)$$

The noise bias appears clearly in the term $\langle \langle a^N a^{N*} \rangle_m \rangle_r$, which has a non zero mean. We will see that it can easily be removed by doing cross-spectra between two observations. The averaged cross-spectrum over N_r noise realizations is

$$\langle C_\ell^{\text{cross}} \rangle_r = \langle \langle a_1 a_2^* \rangle_m \rangle_r \quad (5.26)$$

$$= \langle \langle (a_1^S + a_1^N)(a_2^{S*} + a_2^{N*}) \rangle_m \rangle_r \quad (5.27)$$

$$= \langle \langle a_1^S a_2^{S*} \rangle_m + \langle a_1^N a_2^{N*} \rangle_m + \langle a_1^S a_2^{N*} \rangle_m + \langle a_1^N a_2^{S*} \rangle_m \rangle_r. \quad (5.28)$$

The noise bias vanishes because the two observations have independent noises so the mean is zero for $N_r \rightarrow \infty$: $\langle \langle a_1^N a_2^{N*} \rangle_m \rangle_r \rightarrow 0$. Assuming that the signal is the same in the two data sets, i.e. $a_1^S = a_2^S = a^S$, it remains

$$\langle C_\ell^{\text{cross}} \rangle_r \simeq \langle \langle a^S a^{S*} \rangle_m \rangle_r. \quad (5.29)$$

So the noise bias is removed.

Figure 5.7 shows an example using the QUBIC software implementation of the **Namaster** python package (see section 5.3.6 below). I consider 100 noise realizations of the same CMB sky. I compute the auto-spectrum of each realization and I plot the average over the 100 realizations (red points). The noise bias is, as expected, clearly visible on the auto-spectra. In addition, I compute 50 cross-spectra with independent pairs of realizations and I plot the average (blue points). The averaged auto-spectrum is biased compared to the input simulated D_ℓ spectrum while the averaged cross-spectrum in blue is unbiased and superimposed with the input spectrum.

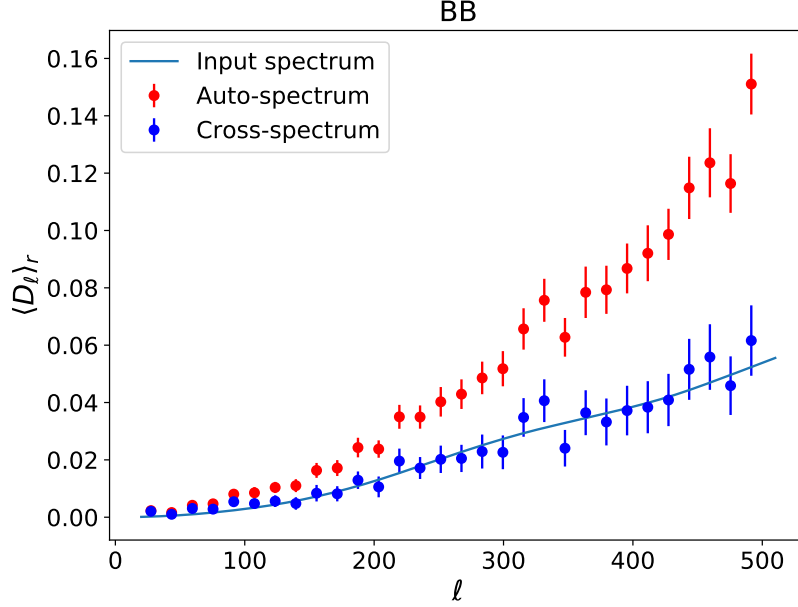


Figure 5.7: Auto and cross BB angular power spectra averaged over 100 independent noise realizations. The averaged auto-spectrum in red is biased compared to the input simulated D_ℓ spectrum (blue line) while the averaged cross-spectrum in blue is unbiased. Error bars show the standard deviation over realizations. Error bars of the cross-spectra are multiplied by $\sqrt{2}$ to assure the same time of observation for auto and cross-spectra.

5.3.2 Pixel and beam window correction

The measured map contains noise and the map is limited by the instrument beam and the sky pixellisation. The observed temperature in direction \mathbf{k} is $T(\mathbf{k}) + n(\mathbf{k})$ where as before $T(\mathbf{k})$ is the convolved pixellised sky and $n(\mathbf{k})$ is the noise. In the harmonic space, the temperature can be written as [199]

$$T(\mathbf{k}) = \sum_{\ell=0}^{\infty} \sum_{m=-\ell}^{\ell} a_{\ell m} p_\ell B_\ell Y_{\ell m} \quad (5.30)$$

where p_ℓ and B_ℓ are the pixel and beam window functions. This approximation is only valid if the beam is axisymmetric and the pixels smaller than the beam resolution. In the case of QUBIC, the multipole synthesized beam is not axisymmetric. However, the computation of the power spectrum occurs after map-making which deconvolves from the effect of secondary peaks. Thus, after map-making, the beam is well approximated by a Gaussian.

Similarly to equation 4.27, we define the correlation function in two directions \mathbf{k}_1 and \mathbf{k}_2 . Under the assumption that the temperature is not correlated with the noise, we have

$$\langle (T(\mathbf{k}_1) + n(\mathbf{k}_1))(T(\mathbf{k}_2) + n(\mathbf{k}_2))^T \rangle = \langle T(\mathbf{k}_1)T(\mathbf{k}_2)^T \rangle + \langle n(\mathbf{k}_1)n(\mathbf{k}_2)^T \rangle \quad (5.31)$$

$$= \sum_{\ell} \frac{2\ell+1}{4\pi} C_\ell (p_\ell B_\ell)^2 P_\ell(\mathbf{k}_1, \mathbf{k}_2) + N \quad (5.32)$$

where N is the covariance matrix of the noise and $P_\ell(\mathbf{k}_1, \mathbf{k}_2)$ is the Legendre polynomials.

Thus the measured power spectrum is

$$C_\ell^{\text{meas}} = (p_\ell B_\ell)^2 C_\ell + N_\ell \quad (5.33)$$

but the pixel and beam window functions are known so we can correct for them. For a Gaussian beam, the beam function is well approximated by [204]

$$B_\ell = \exp \left\{ -\frac{1}{2} \ell(\ell+1) \sigma^2 \right\} \quad (5.34)$$

where σ is the width of the beam. For the definition of the pixel window function, one can have a look to <https://healpix.jpl.nasa.gov/html/intrnode14.htm>. It is approximated as an average over all pixels.

5.3.3 Partial coverage and pseudo spectra

Ground-based CMB experiments observe only a fraction of the sky and even for space experiments the coverage of the sky is usually not uniform. We define the instrument window function [204] such that the observed sky is $\tilde{T}(\mathbf{n}) = W(\mathbf{n})T(\mathbf{n})$. The window function gives a weight to the sky pixels according to the number of hits. The pseudo- $a_{\ell m}^{TT}$ coefficients are defined as

$$\tilde{a}_{\ell m}^{TT} = \int \tilde{T}(\mathbf{n}) Y_{\ell m}(\mathbf{n}) d\mathbf{n}. \quad (5.35)$$

In the following, we write $a_{\ell m} = a_{\ell m}^{TT}$ for simplicity.

The pseudo-spectrum can be defined as

$$\tilde{C}_\ell = \frac{1}{2\ell+1} \sum_{m=-\ell}^{\ell} |\tilde{a}_{\ell m}|^2. \quad (5.36)$$

The pseudo-spectrum is clearly different from the full sky power spectrum but they can be related by their ensemble averages

$$\langle \tilde{C}_\ell \rangle = \sum_{\ell'} M_{\ell\ell'} \langle C_{\ell'} \rangle \quad (5.37)$$

where $M_{\ell\ell'}$ describes the coupling between modes resulting from the partial coverage. This mixing is due to the fact that spherical harmonics are not orthogonal on a cut sky. For a complete derivation of this expression, one can refer to appendix A in [199]. Note that, as expected, a simple product becomes a convolution product in Fourier space.

Taking into account the noise, the pixel and beam functions defined in section 5.3.2, the pseudo-spectrum is finally given by

$$\langle \tilde{C}_\ell \rangle = \sum_{\ell'} M_{\ell\ell'} (p_{\ell'} B_{\ell'})^2 \langle C_{\ell'} \rangle + \langle \tilde{N}_\ell \rangle \quad (5.38)$$

where $\langle \tilde{N}_\ell \rangle$ is the averaged noise power spectrum.

Equation 5.38 can be written

$$\langle \tilde{C}_\ell \rangle = K_{\ell\ell'} \langle C_{\ell'} \rangle + \langle \tilde{N}_\ell \rangle. \quad (5.39)$$

We can not compute the ensemble average. This is why we define unbiased estimators \hat{C}_ℓ and \hat{N}_ℓ such that

$$\tilde{C}_\ell = K_{\ell\ell'} \hat{C}_{\ell'} + \hat{N}_\ell. \quad (5.40)$$

5.3.4 E and B leakage and pure decomposition

In the case of polarization, it can be shown that the pseudo-spectra are given by [205]

$$\begin{pmatrix} \langle \tilde{C}_\ell^{EE} \rangle \\ \langle \tilde{C}_\ell^{BB} \rangle \end{pmatrix} = \sum_{\ell'} \begin{pmatrix} K_{\ell\ell'}^+ & K_{\ell\ell'}^- \\ K_{\ell\ell'}^- & K_{\ell\ell'}^+ \end{pmatrix} \begin{pmatrix} \hat{C}_{\ell'}^{EE} \\ \hat{C}_{\ell'}^{BB} \end{pmatrix} + \begin{pmatrix} \hat{N}_\ell^{EE} \\ \hat{N}_\ell^{BB} \end{pmatrix} \quad (5.41)$$

where the mixture kernels K^+, K^- are related to the expansion of the cut-sky over the spin-2 spherical harmonics. Thus the pseudo-spectra are a mixture of the true EE and BB power spectra. However if the kernels K^+, K^- are known, this expression can be inverted to retrieve the real EE and BB power spectra, avoiding any leakage between EE and BB . The real problem is the leakage of EE variance into that of BB variance:

$$\text{Var}(\hat{C}_{\ell'}^{BB}) = \text{Var}(\tilde{C}_\ell^{BB}) + \text{Var}(\hat{C}_{\ell'}^{EE \rightarrow BB}) + \text{Var}(\tilde{N}_\ell^{BB}) \quad (5.42)$$

where \hat{C}_ℓ is the estimator of C_ℓ . This is known as the leakage problem. Since the E signal is much stronger than the B signal, the E to B leakage is a major issue while B to E is negligible. A formalism has been developed in order to build new power spectrum estimator to avoid this leakage. They are known as “pure” estimators [205], [206]. This means that the BB (EE) power spectrum estimator is zero in any noiseless realization of the CMB which contains only E (B) modes. This formalism was soon extended to cross power spectra [207].

5.3.5 Theoretical error bars on the reconstructed power spectrum

We already defined the cosmic variance in chapter 4, see equation 4.42. This theoretical estimation of the errors can be extended to the realistic case, taking into account the pixel and beam window function, the noise power spectrum and the partial sky observation. The error on the C_ℓ power spectrum is then given by [195], [97]

$$\frac{\Delta C_\ell}{C_\ell} = \sqrt{\frac{2}{(2\ell+1)f_{\text{sky}}\Delta\ell}} \times \frac{1}{B_\ell^2} \times \frac{1}{W_\ell^2} \times N_\ell \quad (5.43)$$

where f_{sky} is the fraction of the sky used for analysis, $\Delta\ell$ is the width of the ℓ -space binning. B_ℓ is the beam transfer function and W_ℓ is the pixel window of the Healpix pixellisation. N_ℓ is the expected shape for the noise power spectrum that can be either a constant in the case of white noise or a constant multiplying the shape from Figure 5.6 (right) in the case of QUBIC.

5.3.6 Namaster

Namaster is a public software package to compute pseudo-spectra [208], [209]. It is not exclusive to CMB, it can be used for any spin-0 or spin-2 field, as large scale structures for example. I implemented **Namaster** in the QUBIC data analysis software.

The implementation of the beam and pixel window corrections have been tested. Figure 5.8 shows the reconstructed TT power spectrum with and without the beam correction. Before computing the spectrum, the map is previously smoothed with a Gaussian at the QUBIC beam resolution. This simulation is noiseless. In order to test the pixel window correction, the map is previously pixellized

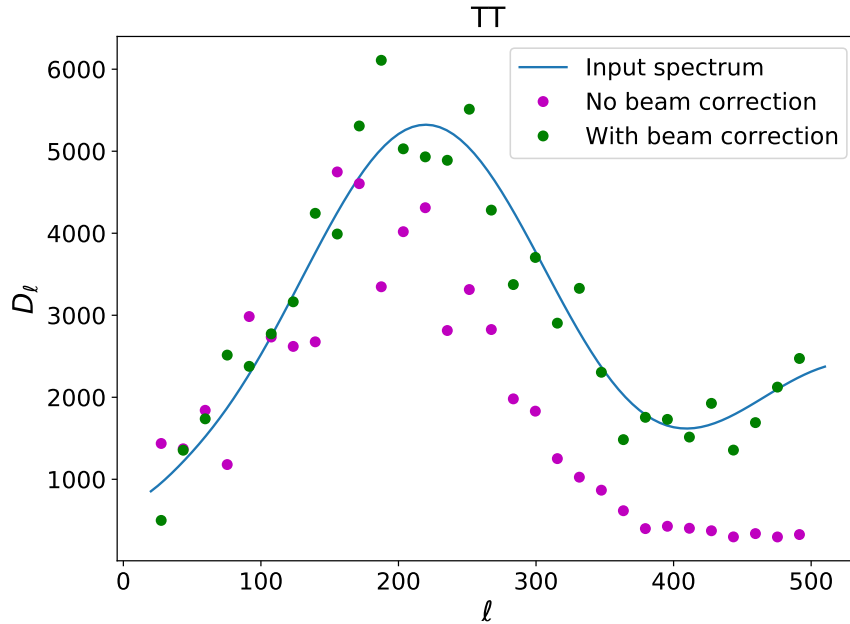


Figure 5.8: TT power spectrum reconstructed with **Namaster** implemented in the QUBIC software with and without the beam correction. The blue line shows the input spectrum.

using the pixel window function from **Healpix**. The TT power spectrum with or without the correction is shown in Figure 5.9.

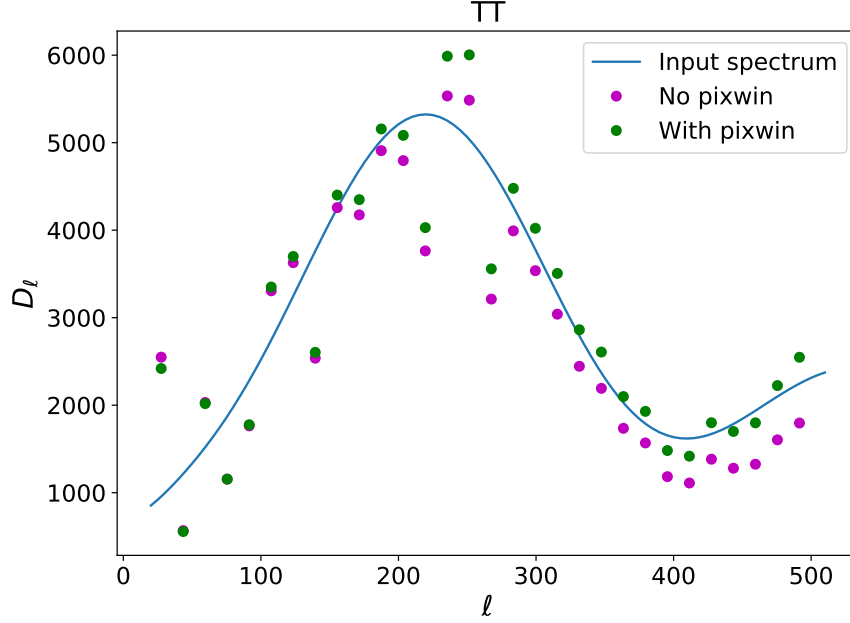


Figure 5.9: TT power spectrum computed with and without the pixel window correction. The blue line shows the input spectrum.

5.3.7 Maximum likelihood solution

Besides the pseudo- C_ℓ method, there is an optimal method for power spectrum estimation from a map, based on a maximum likelihood estimate. This method avoids any leakage between E and B -modes but requires a huge number of large matrix operations. Details can be found in [195], [210]. Here I present the general concept for temperature only for the sake of simplicity. The extension to polarization is straightforward but implies a number of complicated terms. The sky map of temperature fluctuations is composed with signal and noise, $\mathbf{T} = \mathbf{s} + \mathbf{n}$. The covariance matrix of the map is

$$M = \langle \mathbf{T} \cdot \mathbf{T}^T \rangle = \langle \mathbf{s} \cdot \mathbf{s}^T \rangle + \langle \mathbf{n} \cdot \mathbf{n}^T \rangle = S + N. \quad (5.44)$$

The signal part $S = \langle \mathbf{s} \cdot \mathbf{s}^T \rangle$ is a matrix in which element $S_{pp'}$ is the 2-point correlation function in pixel space between two pixels p and p' . As seen in section 4.1.4, equation 4.28, it can be decomposed on the Legendre polynomial basis

$$S_{pp'} = \sum_{\ell} \frac{2\ell+1}{4\pi} C_\ell B_\ell P_\ell(\cos \theta) \quad (5.45)$$

where θ is the angle subtended by the two pixels p and p' . So M is a function of C_ℓ .

The map \mathbf{T} is a random realization of the power spectrum C_ℓ . Assuming Gaussian statistics and $\langle \mathbf{T} \rangle = 0$, the probability density to get the map \mathbf{T} , given its covariance matrix M , is

$$P(\mathbf{T}|C_\ell) = (2\pi)^{-N_p/2} \exp \left\{ -\frac{1}{2} [(\mathbf{T}^T \cdot M^{-1} \cdot \mathbf{T}) + \text{Tr}(\ln M)] \right\}. \quad (5.46)$$

The trace appears from the normalization of the Gaussian with the determinant of M :

$$\frac{1}{|M|} = \exp [-\text{Tr}(\ln M)]. \quad (5.47)$$

The Bayes theorem gives $P(C_\ell|\mathbf{T}) \propto P(\mathbf{T}|C_\ell)$ so one has to maximize equation 5.46 to get the most probable C_ℓ function given the data map \mathbf{T} . This can be done through a gradient descent on the C_ℓ values (which are contained in M), usually using the Newton-Raphson iterative algorithm. This method was implemented in the MADCAP software [197]. This leads to an optimal estimation of the power spectrum but it requires huge computer resources. This is why this method is only applicable on small data sets with a reduced number of pixels in the map.

5.4 Foreground contamination of the CMB signal

5.4.1 Astrophysical foregrounds

The signal from the primordial universe is contaminated by astrophysical foregrounds. This is a major issue for the measurement of the CMB signal, especially for polarization. Note that, they are contaminants if one wants to measure the CMB but they are incredible sources of information for studying the interstellar medium and the physics of the Milky Way.

Only two astrophysical foregrounds are significantly polarized:

Thermal dust: It dominates the CMB polarization at high frequencies, above approximately 100 GHz. It is the thermal emission of galactic dust grains. Grains tend to perpendicularly align with the magnetic field lines and they emit (or absorb) photons most efficiently along the longest axis. This results in a partially polarized radiation [40].

The emission spectrum is well described by a modified black body,

$$I_\nu \propto \nu^\beta B_\nu(T) \quad (5.48)$$

where β is the dust spectral index, typically around 1.5 and $B_\nu(T)$ the Planck spectrum for a temperature about 20 K [224]. This model is a raw approximation, first it can vary with the sky direction as well as along a given line of sight because astrophysical conditions differ. A better approximation is to vary β on the sky, see for example [224], where Planck has mapped the spectral index on the sky.

Synchrotron: At low frequency, the CMB polarization is dominated by the synchrotron emission emitted by relativistic cosmic ray electrons which are accelerated by the galactic magnetic field. Photons are polarized perpendicularly to the magnetic field lines. The synchrotron emission is well approximated by a power law

$$T \propto \nu^{\beta_s} \quad (5.49)$$

where β_s is the synchrotron spectral index, typically around $\beta_s \simeq -2.7$ [225]. Similarly to galactic dust, there is no reason to have an homogeneous emission on the sky.

Regarding the temperature, additional foregrounds which are not or very little ($< 1\%$) polarized, must be considered. Typically, we have

- free-free radiation, also called thermal bremsstrahlung, emitted by free electrons-ions scattering;
- spinning dust, electric dipole radiation coming from the smallest dust grains or molecules ($\sim 10^{-9}$ m) which can rotate at GHz frequencies;
- carbon monoxide (CO) emission lines due to rotational transitions of the molecule, localized in frequency.

In temperature, foregrounds are more complex but they are often below the CMB signal. On the contrary, for polarization they are only two foregrounds but they are well above the CMB signal. For a short review of CMB foregrounds, one can refer for example to [226], [227].

Thus, foregrounds behave differently as a function of frequency and this is how we can disentangle them from the CMB. In Figure 5.10, we show the typical spectra of unpolarized (left) and polarized (right) foregrounds. Using component separation techniques, foregrounds can be isolated from the CMB signal. It is a wide field in CMB data analysis. Future sensitive surveys require foreground modeling with a much higher accuracy than what was done in the past. The key point for component separation is to have measurements in several frequency bands and this is why today experiments always have several frequency channels. For example, the LiteBIRD satellite will have 15 frequency bands which have been optimized for the treatment of foregrounds [182]. This also motivates the next chapter which is dedicated to spectral imaging with QUBIC.

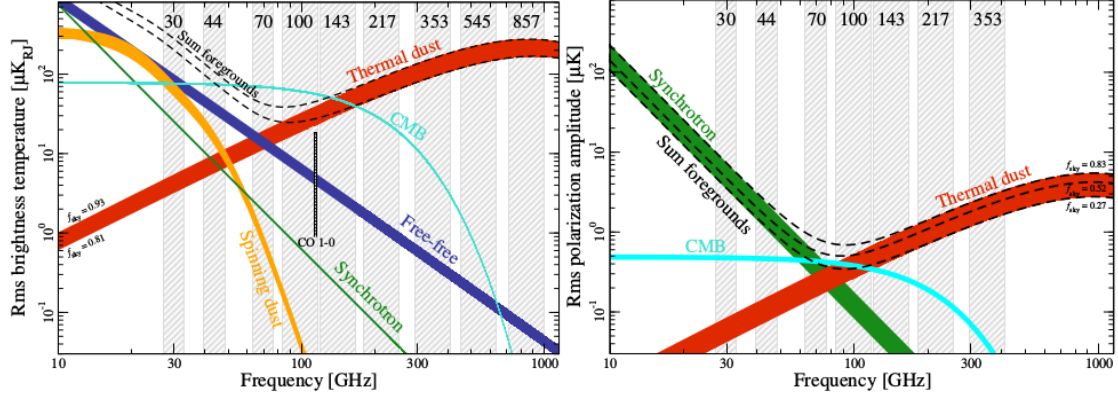


Figure 5.10: Major astrophysical foregrounds for CMB in temperature and polarization. Vertical gray lines correspond to the Planck frequency channels. Taken from [160].

5.4.2 Atmospheric opacity

A disadvantage for ground experiments is the partial opacity of the atmosphere in the millimeter wavelength. A modeling of atmospheric emission for CMB ground based experiments was proposed in [228].

Water vapor is the primary cause of atmospheric opacity. The atmospheric transmission from the Atacama plateau at the zenith for different amounts of precipitable water vapor (depth of water in a column of the atmosphere) is shown in Figure 5.11. This explains why CMB experiments are

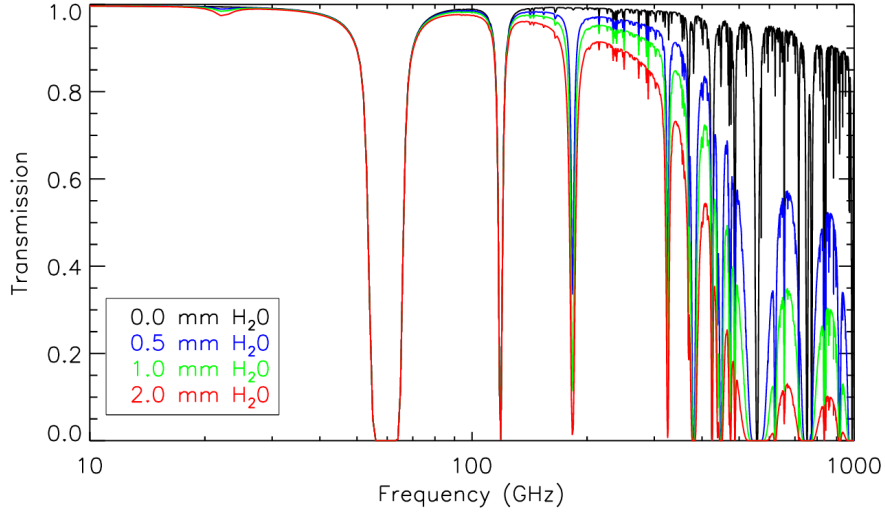


Figure 5.11: Atmospheric transmission from the Atacama plateau at the zenith for different amounts of precipitable water vapor. Taken from [228].

always installed in very dry regions and at high altitude like the Atacama plateau or Antarctica. The observation is only possible in the transmission bands below 50 GHz and around 95, 150 and 250 GHz.

Atmosphere shines brightly at millimeter wavelengths. So the first impact is to increase the background loading on the detectors. For example, the total background emission at 150 GHz is ~ 20 K on the ground while it is only ~ 1 K in space. This is not only due to atmosphere but also because the telescope temperature is much higher so its emissivity is higher and the ground itself radiates too.

Moreover, the atmosphere varies both in time and space. These fluctuations combined with the scanning strategy induce correlated noise which contributes to the total $1/f$ noise.

Despite those facts, ground-based experiments have others advantages. First they are much easy to deploy than a space mission and they can be fixed and upgraded. Moreover, they are not limited in size and integration time so they can easily achieve a high angular resolution by deploying large

reflectors.

QUBIC specificity

A specificity of the QUBIC map-making is that the presence of multiple peaks separated by 8.8 degrees on the sky at 150 GHz (6 degrees at 220 GHz) makes QUBIC insensitive to modes larger than this separation [1]. This occurs because the deconvolution from the multiple peaks relies on the measured signal difference between observations from different directions where the peaks capture different amounts of power. This naturally filters-out large-scale information, larger than the angular distance between peaks in the synthesized beam, be it from the sky itself, or from atmospheric gradients.

To understand the impact of fluctuations on smaller scales we need to run simulations based on dedicated atmosphere measurements taken on the observation site. This is work in progress. However, in appendix A of paper [1], we briefly discuss this issue and show how we expect a significant impact only from turbulence cells in a restricted range of scales. The study is based on meteorological data taken at sites similar to that of QUBIC. In a study conducted in the framework of the POLARBEAR experiment Errard et al. [228] studied the distribution of various atmosphere parameters at Atacama. They showed that the coherence length L_0 of atmospheric turbulence are distributed in the interval $L_0 \in [200 \text{ m}, 800 \text{ m}]$ with a peak around 300 m. By comparing the synthesized beam cutoff scales with the coherence length L_0 , we conclude that the effect from turbulent cells larger than 300 m will be increasingly negligible. However we may expect some impact from cells in the range $[200 \text{ m}, 300 \text{ m}]$.

5.5 QUBIC on a TOAST

Despite the specificity of bolometric interferometry, could we use typical map-making software for imagers? TOAST is a public software for simulating and processing timestream data collected by telescopes⁶. It is developed under the objective of being adaptable for any CMB experiment. As it is developed by a large community, it is more advanced than the QUBIC software, especially in terms of the study of systematic effects and simulation of realistic atmospheres based on meteorological data. However, this is only adapted to classical imagers and not for a bolometric interferometer such as QUBIC.

Here I would like to present an idea I had during a Workshop on TOAST to tune this software for QUBIC. However I did not have time to go deep in this study so I will just give the concept. I think it would be great in the sense that QUBIC could benefit from the efforts of the TOAST community to develop realistic simulations and powerful tools for data analysis.

In the case of QUBIC, because of the multi-peak synthesized beam, each bolometer observes the sky in several directions at the same time. For simplicity, let us consider that the synthesized beam only has 9 peaks. In order to mimic the QUBIC synthesized beam with TOAST we could build a fake focal plane. One QUBIC bolometer will be replaced by several virtual detectors placed at the nine positions corresponding to the synthesized beam peaks. Each TOAST detector would have a single peak Gaussian beam. This is sketched in Figure 5.12. The TOD simulation could then be performed

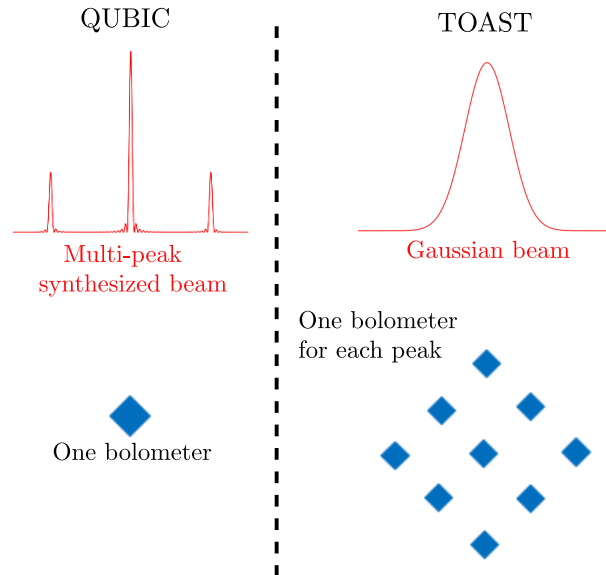


Figure 5.12: Sketch explaining how to mimic the QUBIC synthesized beam with TOAST software.

with this very complex focal plane. To compare with the QUBIC TOD, we will have to sum the TOD from the nine TOAST detectors with appropriated coefficients corresponding to the amplitudes of the synthesized beam peaks.

⁶<https://toast-cmb.readthedocs.io/en/docs/intro.html>

Conclusion In this chapter I started by reviewing the current and planned experiments aiming at measuring B -mode polarization in order to give the scientific context of the QUBIC project.

Then, I have presented the typical data analysis methods used in the CMB community. Observations rely on scanning strategies that imply map-making techniques from the TODs. I have presented the principle of those methods, including illustrations with the QUBIC simulation pipeline. I have also shown a specificity of bolometric interferometry caused by the multiple peak synthesized beam: spatial noise correlations in the maps. I also presented how to estimate the power spectrum from real data.

Finally, we have seen that the CMB signal is contaminated by emissions from astrophysical foregrounds. The two main one in polarization are the thermal emission from the galactic dust and the synchrotron emission. Moreover, for ground experiments, the atmosphere opacity is an important issue.

I concluded this chapter by presenting a possible way to adapt the TOAST software to bolometric interferometers.

Chapter 6

Spectral imaging

Contents

6.1	Spectral dependence	150
6.1.1	The polychromatic synthesized beam	150
6.1.2	Spectral imaging capabilities	152
6.2	Testing spectral imaging on simple cases	153
6.2.1	Extended source reconstruction	153
6.2.2	Angular resolution	154
6.2.3	Frequency Point Spread Function (FPSF) characterization	155
6.2.4	Galactic dust	158
6.3	Noise characterization	163
6.3.1	Noise behavior in the sub-bands at map level	163
6.3.2	Fast noise simulator	163
6.3.3	Noise analysis using the power spectrum	166
6.4	Spectral imaging on real data	168

Bolometric interferometers have the ability to perform spectral imaging. QUBIC detectors are mono-band, they integrate the signal over a wide frequency band. However it is possible to reconstruct sky maps in several sub-bands within the physical band in post-processing of the data. This provides a powerful spectral method to discriminate between the CMB and astrophysical foregrounds. In this chapter, the methodology is illustrated with examples based on QUBIC. We consider the specific cases of point source reconstruction and Galactic dust mapping and we characterize the point spread function as a function of frequency. We study the noise properties of spectral imaging, especially the correlations between sub-bands, using end-to-end simulations together with a fast noise simulator.

Personal contributions: This work is the heart of my thesis, it was done in collaboration with Martín Gamboa and it led to paper [9]. The large majority of this chapter is taken from this article, entirely reproduced in annex A.5. Additional details are given: a pedagogical introduction in the first section with visible light, a discussion about frequency sub-band spacing in section 6.1.2, details on the frequency point spread function in section 6.2.3 and a description of the fast noise simulator in section 6.3.2.

6.1 Spectral dependence

6.1.1 The polychromatic synthesized beam

By illuminating with white light a double axis diffracting grid (same child glasses as in Figure 1.16), we immediately see the frequency dependence of the synthesized beam. Figure 6.1 shows the setup that I made in order to mimic QUBIC in the visible domain. The first element is a white lamp with a small aperture placed at the focal plane of a lens. This makes a point source at infinity. The double diffracting axis grid mimics the horn array and a second lens combines the light similarly to the two QUBIC mirrors. The white screen is placed at the focal plane of the lens, similarly to the QUBIC detector focal plane. The polychromatic point spread function observed on the white screen is shown on the right.

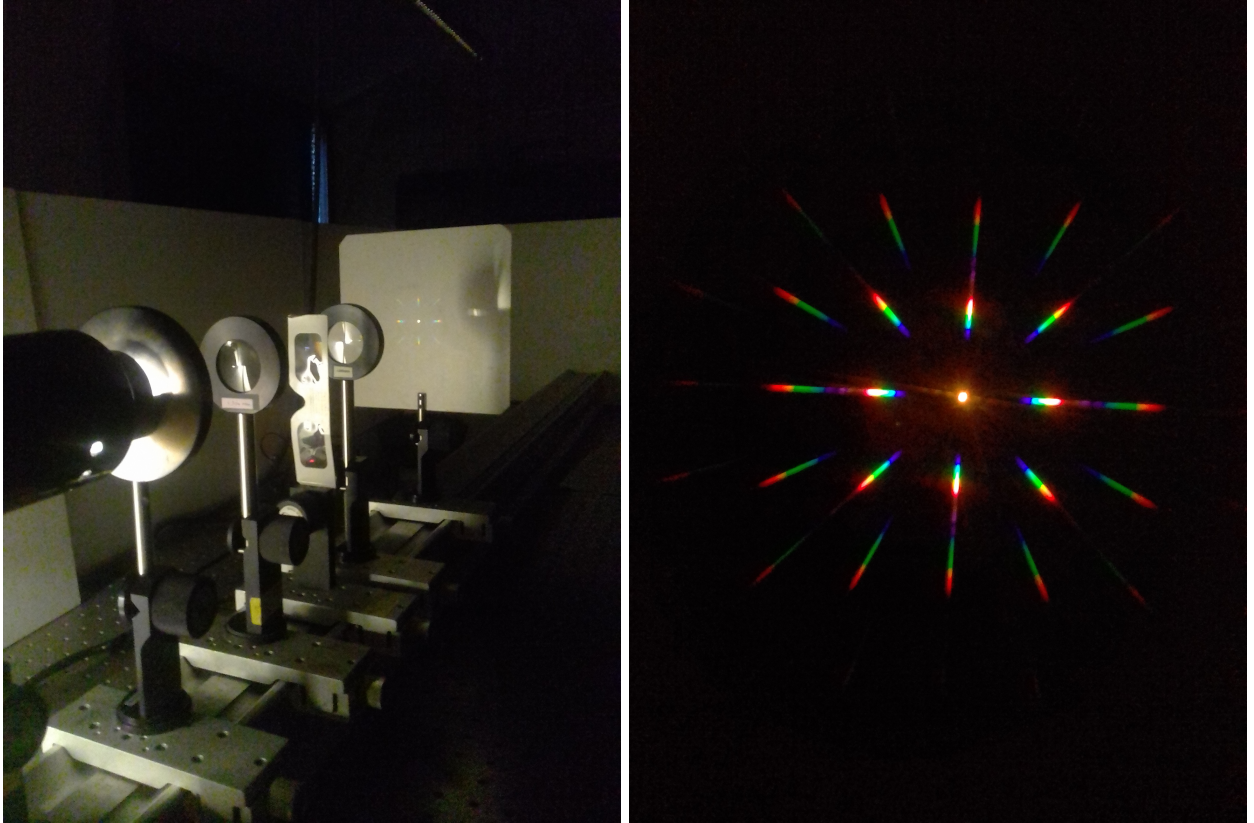


Figure 6.1: *Left:* Setup that I made in order to mimic QUBIC in the visible domain: white lamp with a small aperture placed at the focal plane of a lens, double axis diffracting grid (child glasses), a second lens and a white screen in the focal plane of the lens. *Right:* Polychromatic point spread function observed on the white screen.

The frequency dependence is visible in the expression of the Point Spread Function (equation 1.45) reproduced here:

$$\text{PSF}_{\mathbf{k}}(\mathbf{r}, \lambda) = \text{PSF}_{\mathbf{k}}^{\text{horn}} \frac{\sin^2(P \frac{\pi}{\lambda} \Delta_h (\frac{x}{f} - \alpha_0))}{\sin^2(\frac{\pi}{\lambda} \Delta_h (\frac{x}{f} - \alpha_0))} \times \frac{\sin^2(P \frac{\pi}{\lambda} \Delta_h (\frac{y}{f} - \beta_0))}{\sin^2(\frac{\pi}{\lambda} \Delta_h (\frac{y}{f} - \beta_0))} \quad (6.1)$$

The off-axis angle (given by the primary beam of the pupils), the FWHM of the peaks (hence the resolution of the maps), and the angle on the sky between two peaks all depend linearly on wavelength λ . Figure 6.2 shows a multichroic representation of the synthesized beam maps measured in the lab. Each frequency is assigned a color, 130 GHz (red), 150 GHz (green), and 170 GHz (blue). A cross cut of the synthesized beams modeled according to equation 6.1 for 131 and 169 GHz is also shown on the right.

This dependence on wavelength can be exploited to achieve spectral imaging capabilities. Within a wide band, the synthesized beam will be the integral of the synthesized beam of all the monochromatic

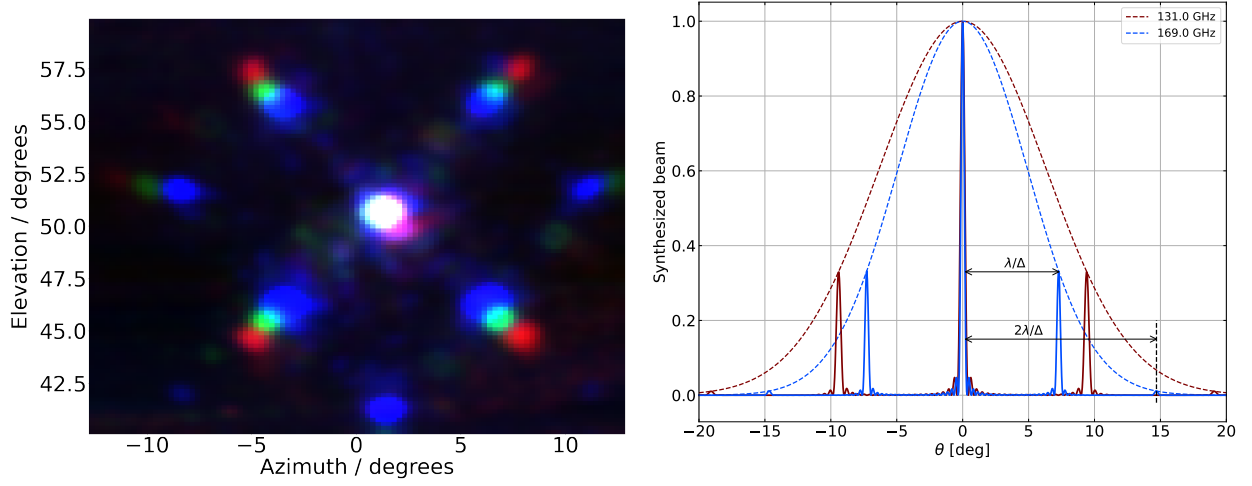


Figure 6.2: *Left*: Multichroic representation of the synthesized beam maps measured in the lab. Each frequency is assigned a color, 130 GHz (red), 150 GHz (green), and 170 GHz (blue). The central lobes of the three frequencies coincide while the secondary lobes are closer to center as frequency increases. Produced for [8]. *Right*: Monochromatic synthesized beam at 131 and 169 GHz for a detector placed at the center of the focal plane. Each synthesized beam is modeled according to equation 6.1 for a square array of 20×20 pupils separated 14 mm apart at 131 and 169 GHz. The primary beam at each frequency is shown by a dashed line. Produced for [9].

contributions within the band resulting in a polychromatic synthesized beam. Figure 6.3 shows a polychromatic synthesized beam using 9 monochromatic synthesized beams.

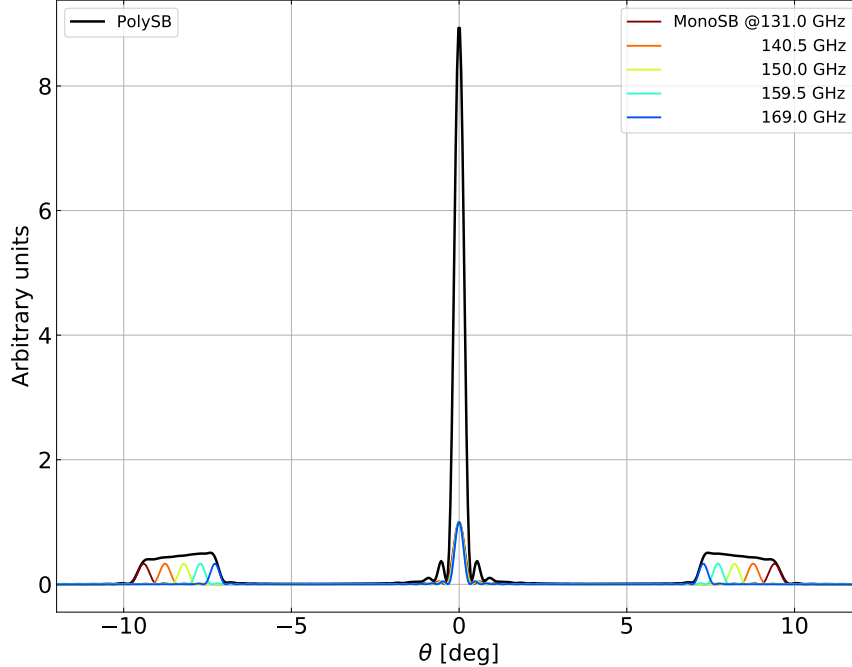


Figure 6.3: Polychromatic beam (*PolySB*, black line) as result of the addition of 9 monochromatic synthesized beams (*MonoSB*). Five of them are shown in colored lines) spanning our 150 GHz band (131 to 169 GHz). We sample the continuous frequency band with discrete frequencies.

With a bolometric interferometer operating over a large bandwidth, for each pointing towards a given direction in the sky, one gets contributions from all the multiple peaks in the synthesized beam at all frequencies. As a result, we have both spatial and spectral information in the TOD. Precise

knowledge of the synthesized beam along the frequency will then allow one to reconstruct the position and amplitude of the sky in multiple frequency sub-bands. Note that spectral imaging is fully done in post-processing of the data, bolometers are monoband detectors, they integrate the signal in a wide frequency band between 130 and 170 GHz (190 and 250 GHz for the second focal plane).

6.1.2 Spectral imaging capabilities

We need to sample the continuous frequency band with a finite number of frequencies. The question is how many sub-bands can we reconstruct inside the large band and how should we space them in order to sample the beam uniformly. This was already studied in the thesis by M. Stolpovskiy [14] (section 5.0.1.1).

Frequency sub-band spacing

It was chosen to require that the distance between the peaks of two synthesized beams of two next to next frequency sub-bands must be some fraction k of the sum of their widths.

As seen in chapter 1, section 1.2.5, the angular resolution is given by the FWHM of the peaks λ/D where D is the aperture diameter. Considering a $P \times P$ square array of horns spaced by Δ_h we have $D = P\Delta_h$. As shown in Figure 6.2, the distance between the central peak and the n -th order peak is $n\lambda/\Delta_h$.

Therefore, the requirement is

$$\frac{n(\lambda_2 - \lambda_1)}{\Delta_h} = k \left(\frac{\lambda_1}{P\Delta_h} + \frac{\lambda_2}{P\Delta_h} \right) \Rightarrow \lambda_2 = \lambda_1 \frac{nP + k}{nP - k}. \quad (6.2)$$

This means that we can recursively define λ_{i+1} as λ_i multiplied by a constant factor $q = (nP+k)/(nP-k)$. Thus, the correct way for sampling the frequency band is the logarithmic scale

$$\lambda_{i+1} = \lambda_i \times q \Rightarrow \log(\lambda_{i+1}) - \log(\lambda_i) = \log(q) = \text{cst}. \quad (6.3)$$

How many sub-bands?

The synthesized beam at two different frequencies ν_1 and ν_2 will be distinguishable from one another as long as their peaks are sufficiently separated. The angular separation between the two peaks $\Delta\theta = \frac{c\Delta\nu}{\nu^2\Delta_h}$ (where $\Delta\nu = \nu_2 - \nu_1$ and $\nu = \sqrt{\nu_1\nu_2}$) must be large enough to unambiguously distinguish the two peaks. In order to have an order of magnitude of the possible width for each sub-band we consider a square array of pupils and we apply the Rayleigh criterion [236]:

$$\frac{c\Delta\nu}{\nu^2\Delta_h} \gtrsim \frac{c}{\nu(P-1)\Delta_h} \Leftrightarrow \Delta\nu \gtrsim \frac{\nu}{(P-1)} \quad (6.4)$$

where P is the number of pupils on a side of the square-packed pupil-array. A bolometric interferometer therefore not only has a resolution on the sky $\text{FWHM}_\theta \simeq \frac{c}{\nu(P-1)\Delta_h}$, but also in electromagnetic frequency space $\frac{\Delta\nu}{\nu} \simeq \frac{1}{P-1}$.

The map-making presented in section 5.2.5 can be extended in order to build, simultaneously with the same TOD, maps at a number of different frequencies as long as they comply with the frequency separation given above. The iterative TOD \mathbf{d}_i can be written as:

$$\mathbf{d}_i = \sum_{j=0}^{N_{\text{rec}}-1} A_j \hat{\mathbf{T}}_{ij} + \mathbf{n} \quad (6.5)$$

where A_j describes the acquisition (convolution+pointing) operator with the synthesized beam at frequency ν_j , $\hat{\mathbf{T}}_{ij}$ is the sky signal estimator at iteration i for the frequency ν_j and N_{rec} is the number of reconstructed sub-bands. Similarly, as in the map at a single frequency (Figure 5.2), one can recover

Parameter	Details
N_{in}	Number of input or true maps (in μK) used to simulate a broadband observation (TOD). Each map represents a sky at a specific frequency ν_j for the IQU Stokes parameters ^{a b} . Possible values: 15, 16, 18, 21 or 48.
N_{rec}	Number of sub-bands reconstructed from a single broadband observation, from 1 to 8. In all simulations N_{rec} is a divisor of N_{in} .
N_{conv}	Number of convolved maps equal to N_{rec} . Each of these maps is obtained convolving the N_{in} input maps at the QUBIC spatial resolution corresponding to that input frequency and then averaging within the reconstructed sub-band.
θ	Radius of sky patch observed in simulations. Value: 15 degrees.
Pointings	Number of times that the instrument observes in a given sky direction aligned with the optical axis. Values $> 10^4$.
NEP_{det}	Detector noise equivalent power (NEP) added as white noise. Value: $4.7 \times 10^{-17} \text{ W}/\sqrt{\text{Hz}}$.
NEP_{γ}	Photon NEP added as white noise in time-domain, calculated from the atmospheric emissivity measured in our site, as well as emissivities from all components in the optical chain. The atmospheric load is assumed to be stable. The value is different for each detector because of their different illumination by the secondary beam B_{sec} . The average value at 150 GHz is $4.55 \times 10^{-17} \text{ W}/\sqrt{\text{Hz}}$ and $1.72 \times 10^{-16} \text{ W}/\sqrt{\text{Hz}}$ at 220 GHz.

^aSkies are generated using PySM: Python Sky Model [222].

^bMaps are projected using HEALPix: Hierarchical Equal Area Isolatitude Pixellization of sphere [223].

Table 6.1: Typical parameters used in acquisition, instrument and map-making to do an end-to-end simulation. A preconditionned conjugate gradient method is used for map-making.

the maps \mathbf{T}_j by solving equation 6.5 using a preconditioned conjugate-gradient method (see section 6.2 for corresponding simulations). Thus, the instrument acquires data in a single wide frequency band and spectral imaging technique applies during map-making, in the post-processing of the data.

The QUBIC FI has two wide-bands centered at 150 and 220 GHz with $\Delta\nu/\nu = 0.25$ and a 400-feedhorn array packed on a square grid within a circular area (see Figure 1.5). We approximate it with a square grid 20×20 so $\frac{1}{(P-1)} \sim 0.05$. It is thus possible to reconstruct approximately 5 sub-bands in each of the initial bands of QUBIC. Note that this number should just be taken as an order of magnitude for the achievable number of sub-bands but we will see in Figure 6.7 that it is a good approximation. In section 6.3 we will show that reconstructing up to 8 sub-bands is feasible but with a significant degradation of the signal-to-noise ratio.

6.2 Testing spectral imaging on simple cases

We can use the QUBIC simulation pipeline to test the spectral imaging capabilities of bolometric interferometry in a simple way. Some concepts and parameters used in simulations are defined in Table 6.1.

6.2.1 Extended source reconstruction

This section is a result obtained by Martín Gamboa. The input map used for this example to simulate

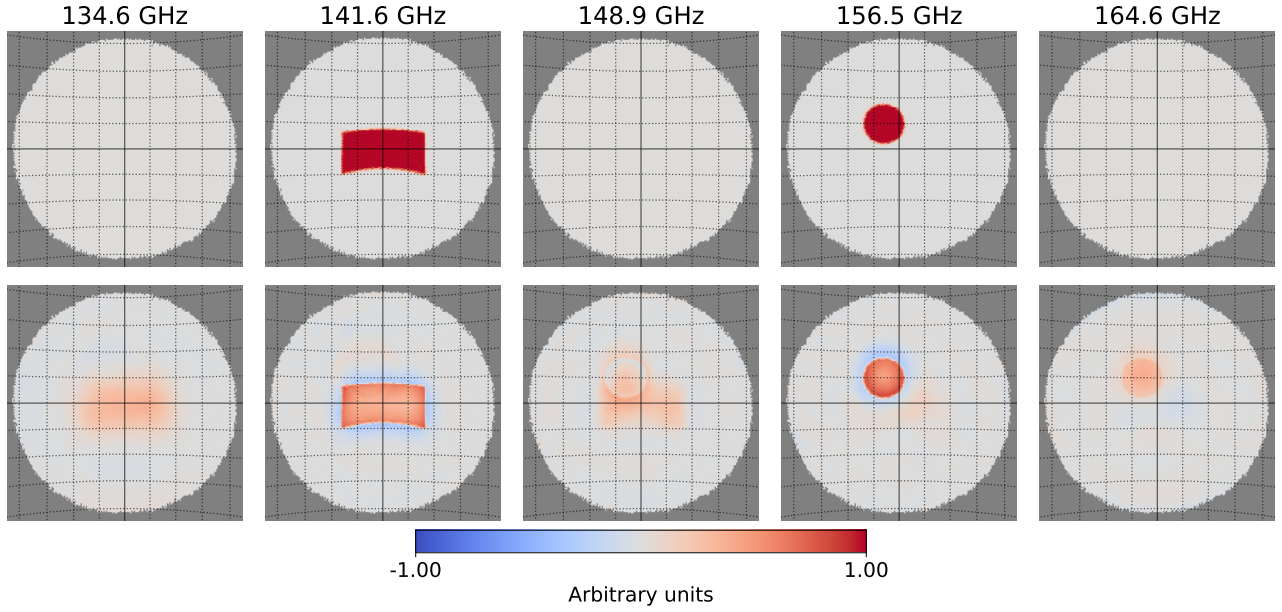


Figure 6.4: Map-making for a sky full of zeros with two extended, monochromatic regions centered at 141.6 (square) and 156.5 GHz (disk). Each column corresponds to one sub-band. The first row shows the input sky maps spatially convolved at the QUBIC resolution. The reconstructed maps using the QUBIC pipeline are shown in the second row. The units are arbitrary.

TOD is composed of zeros in each pixel of its 15 input frequencies, N_{in} , and for the three Stokes components. Two monochromatic extended regions with a high signal-to-noise ratio are added: a square centered at 141.6 GHz and a disk centered at 156.5 GHz. Map-making is done for 5 sub-bands centered at 134.6, 141.6, 148.9, 156.5 and 164.6 GHz, with a bandwidth of 6.8, 7.1, 7.5, 7.9 and 8.3 GHz respectively. The scan is performed with 8500 points randomly placed over a 150 square degrees sky patch. Noise is included in the TOD.

The first row in Figure 6.4 shows the input sky maps spatially convolved at the QUBIC resolution. The second row shows the reconstructed maps after map-making onto five sub-bands. The maps are normalized by the maximum value in the convolved maps. In the first, third and fifth sub-bands, where originally the signal is zero, structures corresponding to the signals of neighboring sub-bands appear. The median of the signal on such sub-bands are 0.27, 0.19, 0.31 respectively. The medians are calculated within a region defined by the shape of the signal in the adjacent sub-band, i.e. rectangle (1st sub-band), rectangle + disk (3rd) and disk (5th). The leakage occurs during the map-making process. It comes from neighboring sub-bands due to the Frequency Point Spread Function (FPSF) that will be studied in section 6.2.3.

6.2.2 Angular resolution

This is also a result obtained by Martín Gamboa. As an example, we used the end-to-end pipeline to simulate the reconstruction onto 4 sub-bands of a point source emitting with a flat spectrum in the 150 GHz wide band. Figure 6.5 shows the measured (red stars) and theoretical (blue dots) values of the FWHM at the central frequency of each sub-band. Theoretical values are obtained from a quasi-optical simulation [6] at 150 GHz and scaled proportionally to frequency. Measurements were made on HEALPix maps and corrected by pixel size and resolution [15]. The difference between measured and theoretical values are up to 0.5% which makes it acceptable. The real angular resolution will be determined once QUBIC is installed on the site using far-field observations (astronomical objects and/or calibration tower). This analysis was done for a flat spectrum over the wide frequency band but this hypothesis is not required. In the code, it is only assumed to be flat in small frequency sub-bands with bandwidths around 1/20 of the total bandwidth. The result would be similar in case of a non flat spectrum.

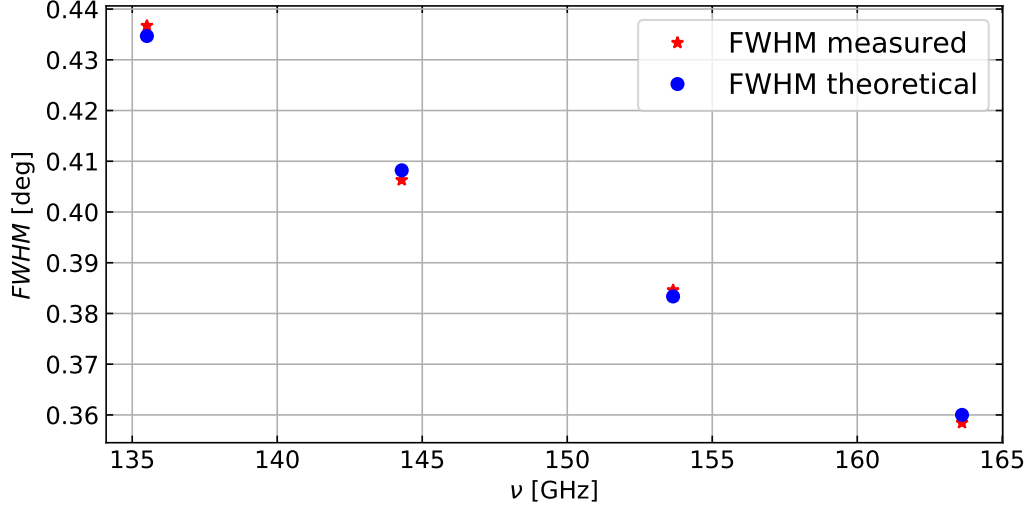


Figure 6.5: Red stars represent the angular resolution measured for a single point source emitting in the broad band after map-making onto 4 sub-bands. Blue dots are the theoretical values expected for each central frequency of the sub-bands.

6.2.3 Frequency Point Spread Function (FPSF) characterization

The simulations presented in this section were realized by Martin Gamboa but we work together on the interpretation of the results. In section 6.2.1 it was shown that the reconstructed map for a sub-band has a fraction of signal coming from neighboring bands (see Figure 6.4). In order to study this effect, we simulate monochromatic point source reconstruction to characterize the FPSF.

If we consider a monochromatic input signal with a spectral energy density $S_{\text{in}}(\nu) = I_0 \delta(\nu - \nu_{\text{in}})$ [W/Hz], and considering ideal map-making, then the intensity of the output map $I_{\text{out}}(\nu)$ [W] will be given by the convolution of the input signal with the FPSF [unitless]:

$$I_{\text{out}}(\nu) = [S_{\text{in}} \otimes \text{FPSF}](\nu) \equiv \int S_{\text{in}}(\nu') \text{FPSF}(\nu - \nu') d\nu' = I_0 \text{FPSF}(\nu - \nu_{\text{in}}). \quad (6.6)$$

Thus, we can obtain the FPSF by measuring the intensity in the reconstructed sub-bands.

In order to investigate the FPSF of the instrument, we simulate a scan in frequency by moving ν_{in} in a high-resolution frequency grid. We use a grid with $N_{\text{in}} = 48$ which gives us a resolution of ~ 0.78 GHz for the 150 GHz wide band (it would be ~ 1.15 GHz for the 220 GHz band). This grid allows to improve the map within the spectral range and thus obtain more precise information on how the signal is reconstructed at the center and edge of each sub-band. We performed 22 independent simulations of monochromatic point sources with high signal-to-noise ratio. We kept the spatial location of the point source unchanged and we varied its frequency ν_{in} , covering a spectral range from 133 to 162.25 GHz.

We present results for map-making onto 4 sub-bands with central frequencies at $\nu_c = 135.5, 144.3, 153.6, 163.6$ GHz and bandwidths of $\Delta\nu_c = 8.5, 9.1, 9.7, 10.3$ GHz respectively. The FPSF depends on the number of sub-bands so this result is specific to 4 sub-bands. For each simulation, we measure the intensity, normalized to the input one, of the central pixel of the point source in each reconstructed sub-band. Figure 6.6 shows the intensity measured in each sub-band considering four different point source input frequencies ν_{in} among the 22 simulations. As expected, the reconstructed intensity is maximal in the reconstructed sub-band that contains the input frequency. In the hypothesis that the FPSF does not depend on the input frequency, we can superimpose all the results. This is done in Figure 6.7 (blue dots) by subtracting ν_{in} in order to center all the measurements on 0. All the points are well superimposed on a continuous line that we will call the synthetic FPSF of the instrument with 4 sub-bands. A spline fitting is shown in Figure 6.7 (red line) to get a model for the synthetic FPSF. We also plot a Gaussian (blue line) with $\text{FWHM} = \frac{\nu_0}{P-1}$, $P = 20$ and $\nu_0 = 150$ GHz, showing an order

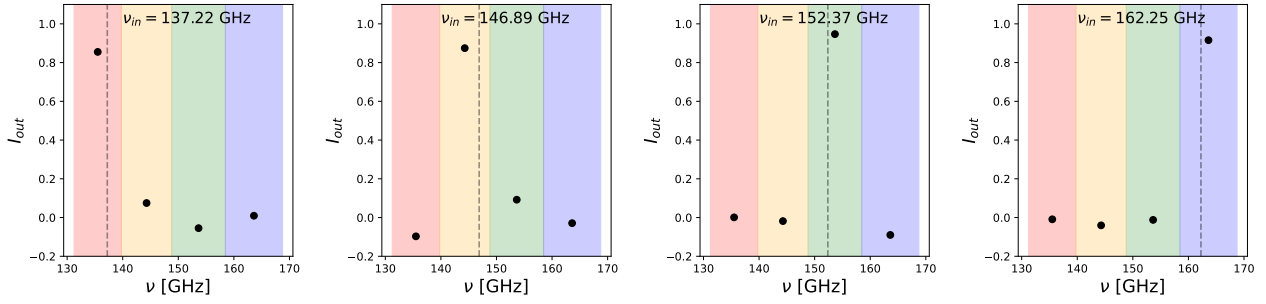


Figure 6.6: Reconstructed sub-bands are delimited with color bands. Black dots show the intensity of the central pixel of the point source, normalized to the input one, measured in each reconstructed sub-band. The point source input frequency is written on each plot and shown with the vertical dashed line.

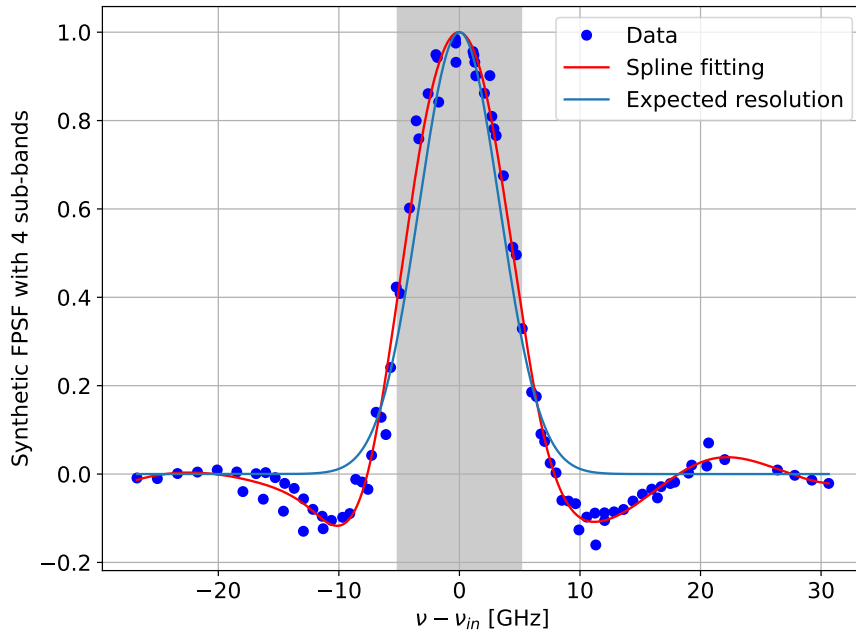


Figure 6.7: Synthetic FPSF when reconstructing in 4 sub-bands. Blue dots are the intensity of the central pixel of the point source in each sub-band and each simulation superimposed (see text for detailed explanation). Red line is a spline fit. Blue line is a Gaussian with $\text{FWHM} = \frac{\nu_0}{P-1}$, $P = 20$ and $\nu_0 = 150$ GHz, showing an order of magnitude of the expected frequency resolution (see section 6.1.2). Strong-gray band represent a typical width of a sub-band when reconstruction is performed for 4 sub-bands.

of magnitude of the expected frequency resolution as explained in section 6.1.2. As expected from Figure 6.4, we observe that the FPSF extends beyond a single sub-frequency and should be accounted for in the data analysis. This means that our reconstructed sub-bands are not independent from each other and we should expect noise correlation between sub-bands. Because the FPSF is negative in the nearest band we should expect the noise correlations to be negative between neighboring sub-bands. This will be studied in section 6.3.1.

To terminate this section, I show an other way of plotting the same data. This is presented in Figure 6.8. The four reconstructed sub-bands are again delimited with color bands. For each sub-band, I plot the reconstructed intensity in the central point source pixel as a function of the input point source frequency ν_{in} . It is similar to make a swipe in frequency and see the response of each sub-band separately. This is different from the FPSF which is the response of the instrument to a monochromatic pulse.

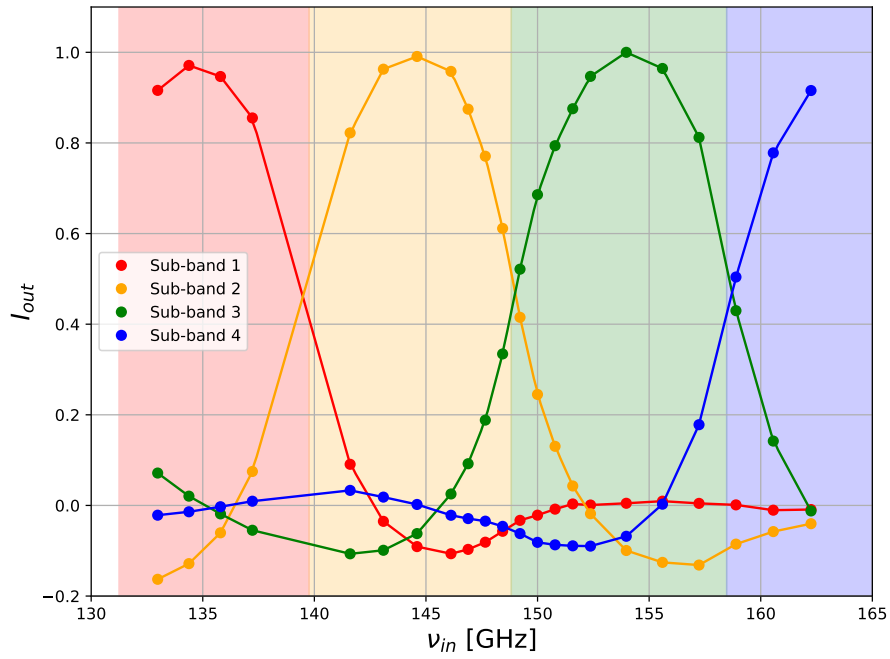


Figure 6.8: The four reconstructed sub-bands are again delimited with color bands. For each sub-band, the reconstructed intensity in the central point source pixel (colored dots) is shown as a function of the input point source frequency ν_{in} . Point measurements are interpolated by a line just for improving the visualization.

6.2.4 Galactic dust

We demonstrate spectral imaging capabilities by trying to recover the frequency dependence of the dust emission with simulated observations towards the Galactic center.

Map reconstruction

The sky maps contain IQU Stokes parameter components and the dust model is the one provided by PySM3, named d1 [222]. We simulate an observation in a sky patch of 15 degree radius. This choice was made in order to minimize the number of pointings required to get a sufficient coverage and so to reduce computational resources needed for simulations. However, a bigger patch would give similar results, even better as border effects would be reduced.

We have used a simplified sky coverage obtained using random pointings on the sky from one time sample to another, reproducing the same sky fraction as the anticipated sky coverage. While this allows obtaining a fast and efficient coverage of the QUBIC observed sky, it prevents one from simulating actual $1/f$ noise from atmospheric or any time-domain instrumental fluctuations as successive time samples do not correspond to nearby pointings as in a more realistic scanning strategy. Moreover, we have used the “repeat” pointing strategy described in section 5.2.6 in order to cover all pixels with a sufficient number of pointing with different HWP angles.

The parameters of the pipeline are set in such a way that the simulated instrument has a single focal plane operating either at 150 GHz or at 220 GHz with a 25% bandwidth each. The wide band TOD are formed through the sum of a number of monochromatic TOD throughout the wide bandwidth as shown in equation 6.5. For this simulation we have used N_{in} (see Table 6.1) input maps covering the ranges from 137 to 162 GHz and from 192 to 247 GHz. From these wide-band TOD, we are able to reconstruct several numbers of sub-bands using spectral imaging. We have performed simulations with $N_{\text{rec}} = 1, 2, \dots, 8$ reconstructed sub-bands. NEP, including photon noise and detector noise (see Table 6.1) are added as white noise for each TOD. In each case, we perform a Monte-Carlo analysis to get several independent noise realizations and also a noiseless reconstruction that will be the reference. Those end-to-end simulations require high memory usage and need to be parallelized on several machines¹. The result of this procedure at the map level for the I and Q components, for a given realization, is shown in Figures 6.9 and 6.10. The two figures display a sky reconstructed in 5 sub-bands within the 220 GHz wide band. The residual map is the difference between a reconstruction and the noiseless reference.

We can see that the Galactic dust is efficiently reconstructed in the 5 sub-bands as the residuals are compatible with pure noise. Note that the noise is not white but has spatial correlations due to the deconvolution with the multi-peak synthesized beam (see section 5.2.7). We also note that the residuals are higher on the edges than in the center of the sky patch. This is due to the higher coverage of the sky in the center due to the scanning strategy.

¹For instance, with 10 000 pointings, 992 detectors (FI), considering the main 14 peaks in the synthesized beam, the size of the pointing matrix for each input sub-band is: $\sim 10000 \times 992 \times 14 \times 16/1024^3 \sim 2$ GiB and typically, there are $N_{\text{in}} \sim 20$ sub-bands. Regarding the convergence of the map-making, the number of iterations needed will vary, especially with the level of noise and with the number of sub-bands. For a typical end-to-end simulation with $N_{\text{rec}} = 6$, it is around 320 iterations.

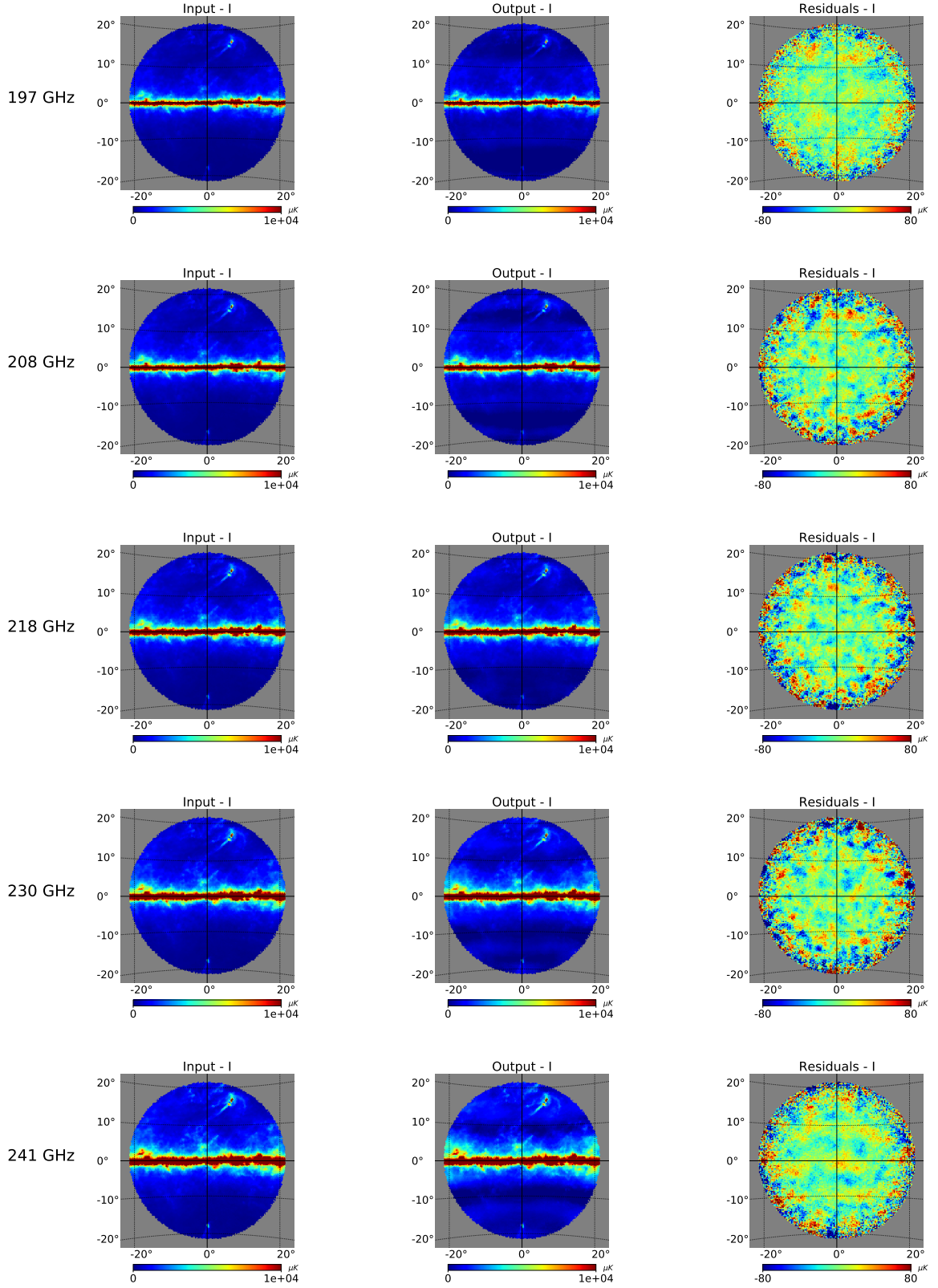


Figure 6.9: Map-making of the galaxy dust in $N_{\text{rec}} = 5$ frequency sub-bands from 192 to 247 GHz for I component. The map unit is μK CMB. The first column is the input sky convolved to the resolution of the instrument in that sub-band. The second column is the reconstructed map after the map-making process. Residuals, defined by the difference between the simulation including noise and a noiseless one, are shown in the last column. The noise is not white but has spatial correlations due to the deconvolution with the multi-peak synthesized beam, it is clearly visible in the 241 GHz sub-band.

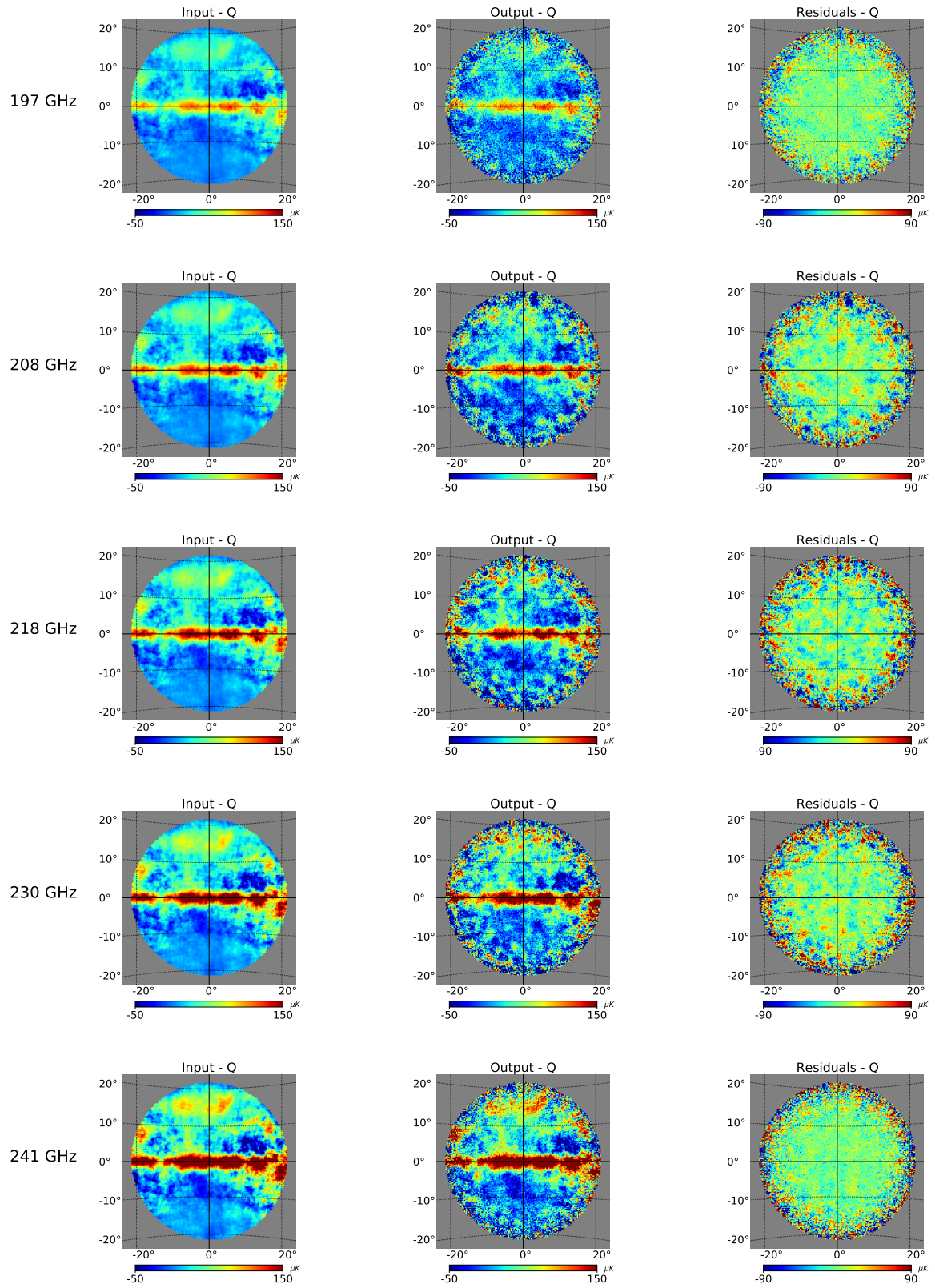


Figure 6.10: Map-making of the galaxy dust in 5 frequency sub-bands from 192 to 247 GHz. Same as Figure 6.9 but for Q component.

Pixel Spectral Energy Distribution (SED)

Instead of looking at the full map, one can look at the reconstructed intensity as a function of frequency in a given sky pixel.

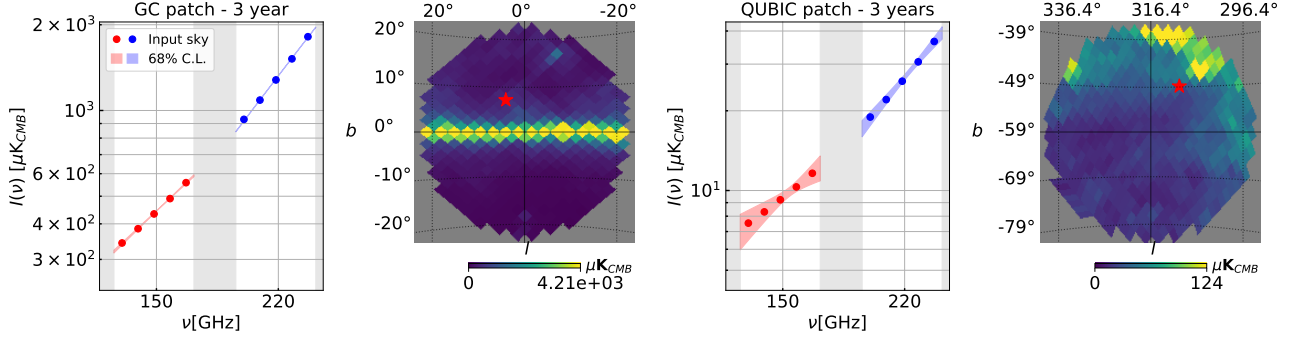


Figure 6.11: Intensity as a function of the frequency for $N_{\text{rec}} = 5$ sub-bands in each wide band at 150 (red) and 220 (blue) GHz for a given pixel. The gray regions correspond to the unobserved frequencies outside our physical bands. Two sky pixels are shown as red stars, one in a patch centered at the Galactic center and one in the patch that QUBIC plans to observe centered in $[0, -57 \text{ deg}]$. Red and blue dots: Input sky convolved with the instrument beam. In both cases are shown in light color the 68% CL regions for a modified black-body spectrum reconstructed with a MCMC from our simulated measurements and sub-band covariance matrices (see Figure 6.13 for the case of 3 sub-bands). Maps are in $\mu\text{K CMB}$ and $N_{\text{side}} = 32$.

Figure 6.11 shows the intensity of the input sky convolved with the instrument beam, and the reconstructed intensity for a given pixel, considering 5 sub-bands in each wide band at 150 (red) and 220 (blue) GHz. Instead, we have performed a Monte-Carlo-Markov-Chain (MCMC) exploration of the amplitude and spectral-index of a typical dust model (modified black-body, see [229]) accounting for the sub-bands covariance matrix that will be presented in section 6.3.1. The fit is done separately for our two physical bands at 150 and 220 GHz. The 68% confidence level (CL) is shown in light colors in each case and represents the QUBIC measurements within this band using spectral imaging.

Simulation procedure: First we have calculated 100 realizations of the reconstructed maps of the observed sky patch using the fast simulation pipeline described in section 6.3.2 with $N_{\text{side}} = 256$ and degrading the pixel resolution to $N_{\text{side}} = 64$ for total intensity maps and $N_{\text{side}} = 8$ for polarization maps. Then, for each pixel we have computed the average $I(\nu_j)$, with its 68% confidence interval for each sub-band frequency ν_j . We do not display the measured points and error-bars which are not good indicators of our uncertainties due to the highly anti-correlated nature of the covariance matrix (see Figure 6.13 in the case of 3 sub-bands). Instead, we calculated the confidence interval by modelling the SED as a modified black-body:

$$I(\nu) = a \times B_\nu(T_{\text{dust}} = 19.6 \text{ K}) \times \left(\frac{\nu}{353 \text{ GHz}} \right)^\beta, \quad (6.7)$$

then we performed a Monte-Carlo-Markov-Chain exploration of the posterior likelihood of this model given our full band-band covariance matrix (see Figure 6.13). This provides us with a chain of (a, β) parameters that sample the likelihood. From these samples, we then calculate the 68% confidence interval for the model at each frequency in the band, obtaining the light red areas represented in Figure 6.11.

We verified that the shape of the confidence interval does not depend on the model we assumed for the MCMC exploration. Indeed, we obtain almost identical regions with a second order polynomial instead of the modified power law. It is worth noting that the angular resolution of our reconstructed maps in each sub-band is not constant and improves with frequency (see section 6.2.2). As a result, fitting a modified power law without accounting for this change of resolution does not lead to a β parameter that can be compared with the usual β dust spectral index that needs to be corrected for varying angular resolution [229]. This is not a problem here as this analysis is just intended to show our ability to measure SED with spectral imaging.

For detail, one can refer to [1], where we presented the expected SED reconstruction both for the FI and the TD in intensity and polarization. We have shown that with one year sky integration with the QUBIC TD it is possible to reconstruct the SED of the dust emission on angular scales of the order of $\sim 1^\circ$ and frequency resolution of ~ 4 GHz in total intensity. We can also detect the dust emission SED in polarization on larger scales ($\sim 7^\circ$) close to the Galactic plane, where the signal intensity is larger.

Dust angular power spectrum

The dust reconstruction is also studied in the angular power spectrum using the public code NaMaster [209] which computes TT , EE , BB and TE spectra where T is the temperature and E , B are the two polarization modes. Spectra are computed from a multipole moment $\ell = 40$ to $\ell = 2 \times N_{\text{side}} - 1$ with $N_{\text{side}} = 256$ the pixel resolution parameter for HEALPix maps. We compute inter-band cross spectra (IBCS), meaning that from N_{rec} sub-band maps, one can compute $N_{\text{rec}}(N_{\text{rec}} + 1)/2$ IBCS. Having independent noise realizations allows us to make IBCS crossing two realizations, so we eliminate the noise bias. BB IBCS for 3 sub-bands in each of the 150 and 220 GHz wide bands are shown in Figure 6.12. We plot $D_\ell = \frac{\ell(\ell+1)}{2\pi} C_\ell$, C_ℓ being the B -mode angular power spectrum. In this Figure, the input theoretical dust spectra coming from the PySM model d1 are superposed to the reconstructed ones.

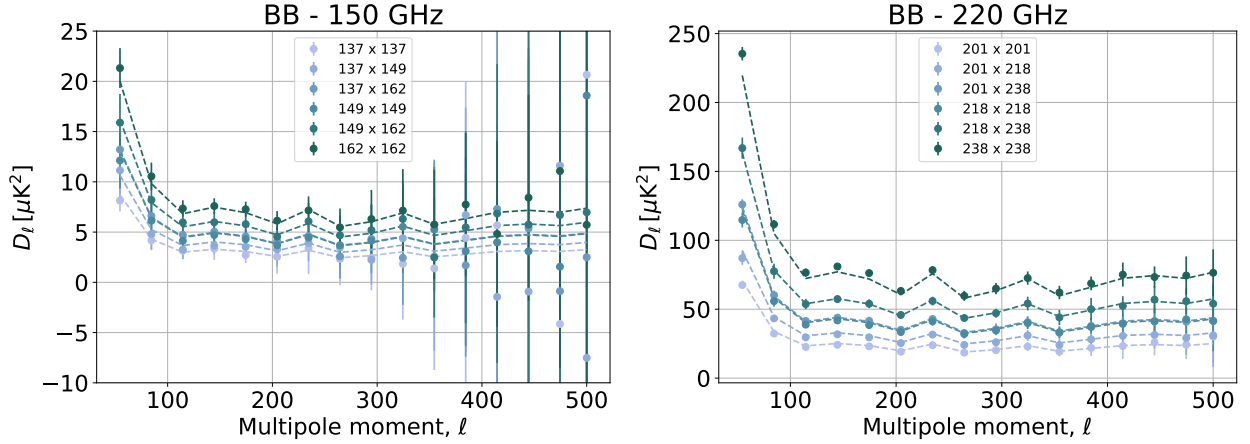


Figure 6.12: BB IBCS at 150 GHz (left) and 220 GHz (right) computed from reconstructed maps in 3 sub-bands (137, 149 and 162 GHz and 201, 218 and 238 GHz respectively), obtained with end-to-end simulations. For each IBCS, we cross-correlate 2 sub-bands with central frequencies in GHz shown in the legend of each plot. Dashed lines are the IBCS of the input sky that contains only Galactic dust. The dots with error bars show the mean and the standard deviation over 20 IBCS. Each IBCS is made with 2 maps with independent noise realizations to eliminate the noise bias.

6.3 Noise characterization

For the map-making described in section 5.2.5, we added noise to the TOD which was composed of the detector NEP ($4.7 \times 10^{-17} W/\sqrt{Hz}$) and photon NEP (see Table 6.1). As before, the atmospheric load is assumed to be stable. The goal here is to study how close to optimal (in the statistical sense) is our spectral imaging map-making. We will study the noise behavior as a function of the number of reconstructed sub-bands N_{rec} . This is done at two different levels: on the reconstructed maps and on the power spectra computed from the maps.

6.3.1 Noise behavior in the sub-bands at map level

We performed simulations with 40 independent noise realizations and a noiseless simulation as a reference. After map-making, residual maps are computed by taking the difference between each simulation and the noiseless reference. For each pixel, we compute the covariance matrix, over all the noise realizations, between the sub-bands and the Stokes parameters.

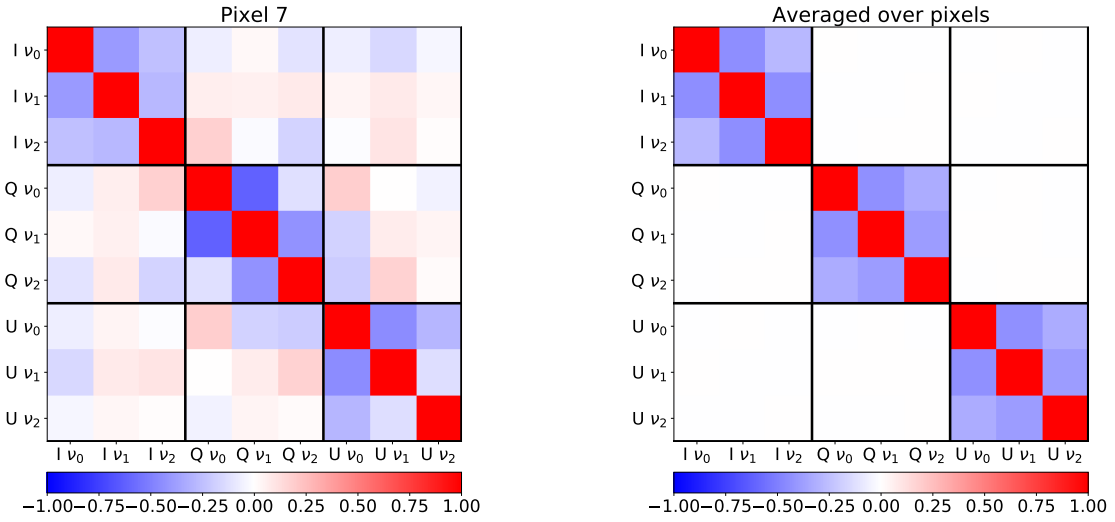


Figure 6.13: Correlation matrices between frequency sub-bands $\nu_0 = 137$ GHz, $\nu_1 = 149$ GHz and $\nu_2 = 162$ GHz and I, Q, U Stokes components obtained from 40 end-to-end simulations. *Left*: example for a given pixel. *Right*: The average over pixels. Blue means anti-correlations while red is for positive correlations.

The reason why we treat the pixels separately, not computing covariance over them, is that the noise level varies with the position in the sky. This is due to the coverage of the sky by the instrument beam which is not uniform. Note that the QUBIC coverage is not trivial because of the multiple peaked synthesized beam.

A correlation matrix for a given pixel, considering 3 sub-bands, is shown in Figure 6.13 and we also show the average over pixels. It can be seen that for each Stokes parameter, residual sub-bands next to one another are anticorrelated and this is seen on every pixel. However, cross-correlations between Stokes parameters are negligible. This is why we can consider the 3 correlation matrices C_{Ip} , C_{Qp} and C_{Up} separately.

6.3.2 Fast noise simulator

The peculiar noise structure of the QUBIC maps has been studied in detail using 40 end-to-end simulations for each of the considered configurations. Simulations run on supercomputers as they have large memory requirements². We extract from these simulations the main features of the noise

²With a 156.25 Hz sampling rate, QUBIC produces $156.25 \times 3600 \times 24 \times 1024 \times 2 \times 8/1e9 \simeq 220$ GB/day.

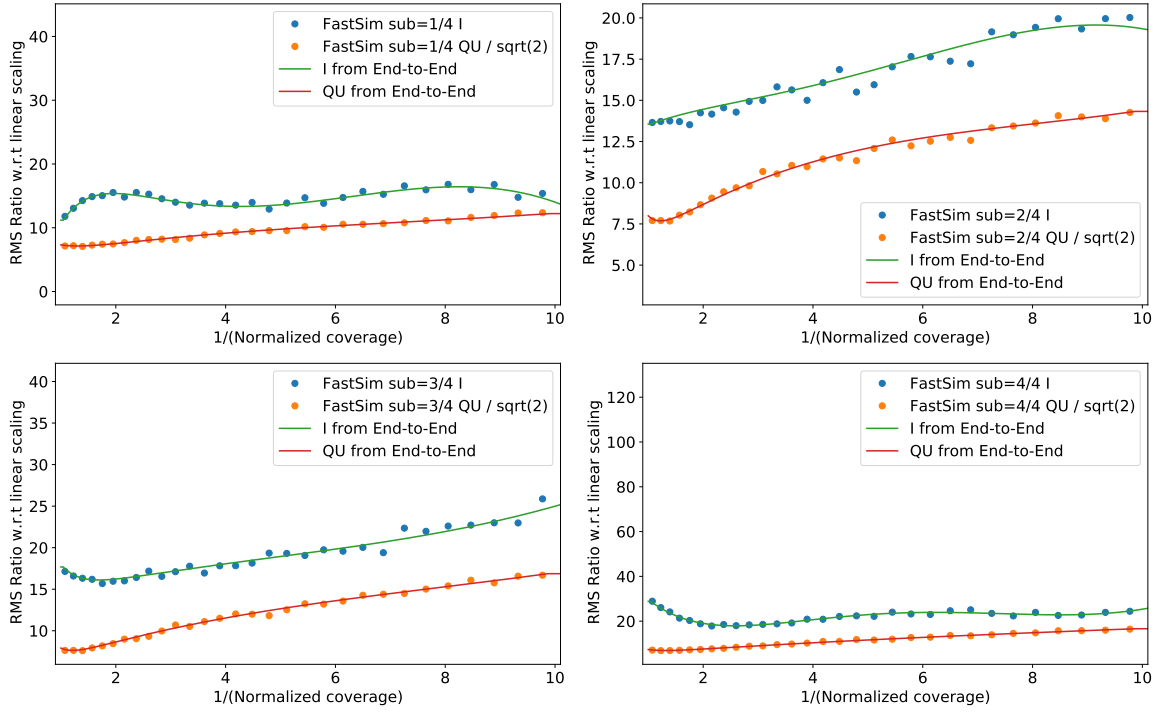


Figure 6.14: Root Mean Square (RMS) of the noise in the sky pixels as a function of the inverse sky coverage. In this case we considered 4 sub-bands and each plot corresponds to one of them. Intensity I and polarization Q, U are treated separately because they behave differently in the end-to-end simulations.

discussed above:

- noise scaling as a function of normalized coverage;
- anti-correlations in neighboring bands for each Stokes parameter (see section 6.3.1);
- spatial (pixel-pixel) structure of noise that was presented in section 5.2.7;

The two last properties are specific to polychromatic interferometers. We have built a “Fast Simulator” that directly produces maps with these features:

1. we start by creating (in harmonic space) noise maps with the observed spatial correlation (see Figure 5.6),
2. we then make linear combinations of these noise maps in order to have I , Q and U maps for each sub-band with the appropriate correlation matrix (see Figure 6.13),
3. finally, we scale the noise in the maps according to the scaling with respect to coverage.

The overall noise normalization is adjusted to match that of the end-to-end simulations with the same integration time. We have checked in detail the accuracy of the Fast Simulator by performing the same noise structure analysis on the output maps and verifying that they lead to the same noise modeling as with the end-to-end simulations. In the next plots, we compare the Fast Simulator noise properties with the end-to-end simulations. We have considered 4 reconstructed sub-bands in the wide band centered on 220 GHz and 10000 pointings.

Figure 6.14 shows the Root Mean Square (RMS) of the noise in the sky pixels as a function of the inverse sky coverage. Intensity I and polarization Q, U are treated separately because they behave differently in the end-to-end simulations.

In Figure 6.15, we compare the covariance matrices between sub-bands computed from end-to-end simulated maps and from maps produced by the Fast Simulator. We only consider correlations between

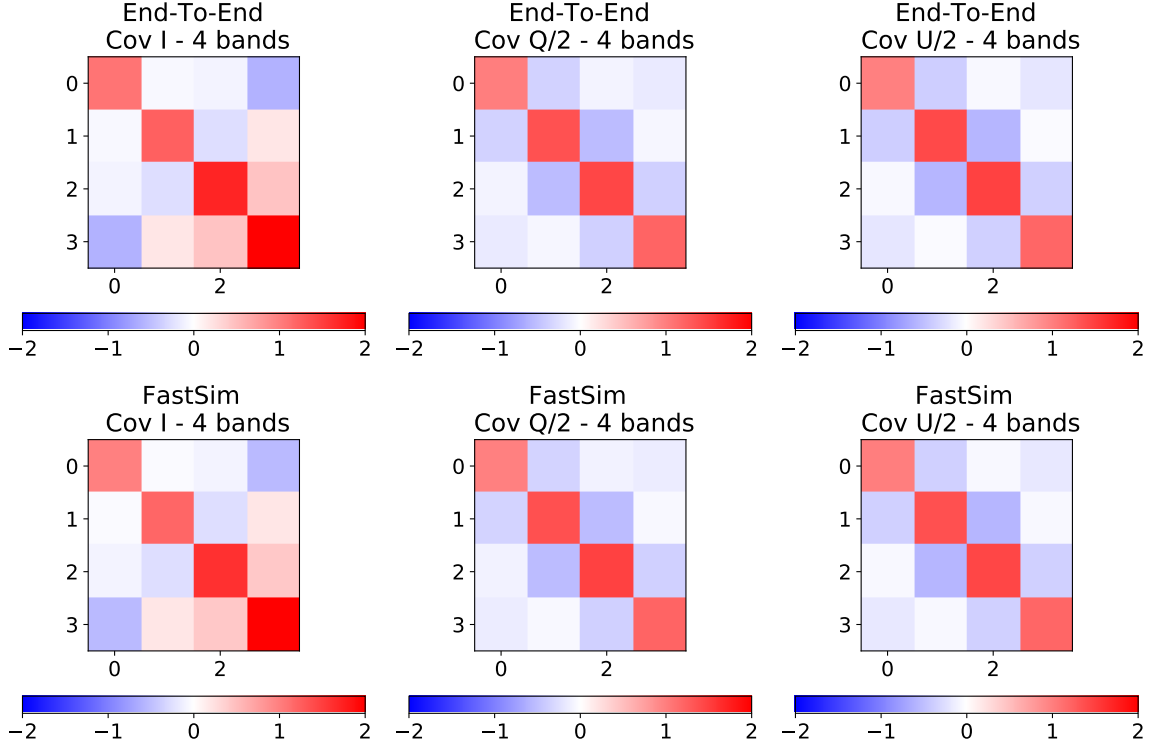


Figure 6.15: Covariance matrices between sub-bands computed from end-to-end simulated maps (first row) and from maps produced by the Fast Simulator (second row) for I, Q, U components.

sub-bands within the same Stokes parameter and not between two different Stokes parameters because, as seen in section 6.3.1, they are negligible.

Finally, in Figure 6.16, we show the spatial noise 2pt-correlation function obtained from maps produced with the Fast Simulator. Each color corresponds to a given sub-band. So far, we made the approximation that the 2pt-correlation function does not depend on the number of reconstructed sub-bands nor the Stokes component. Thus, all sub-band maps produced by the Fast Simulator have the same spatial noise correlation: the one shown in Figure 5.6 from end-to-end simulations with only one reconstructed sub-band. This will be refined in the future to make the Fast Simulator more realistic.

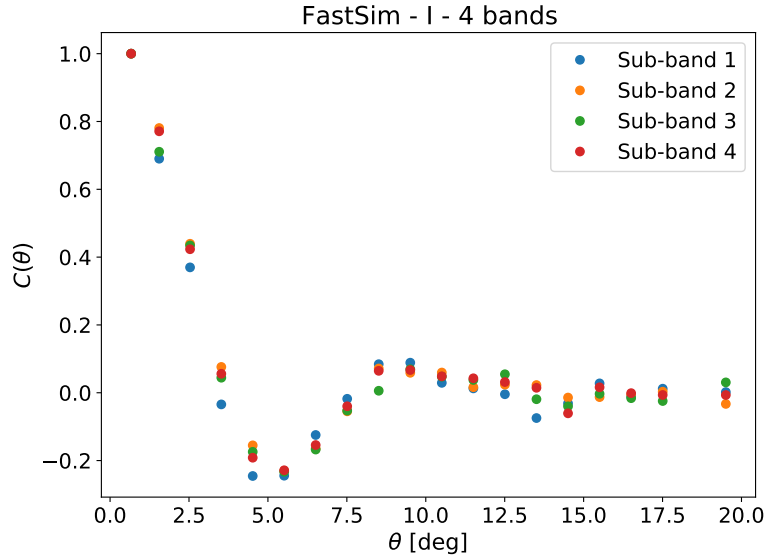


Figure 6.16: Spatial noise 2pt-correlation function obtained from intensity maps produced with the Fast Simulator. Each color corresponds to one sub-band.

Thus, the Fast Simulator allows for fast production of maps with large-number statistics (thousands of realizations) and has been used extensively for forecasts presented in [1]. In the following, it is used in parallel with end-to-end simulations.

6.3.3 Noise analysis using the power spectrum

In this section, we characterize the noise behavior of spectral imaging using the power spectrum. As shown in the last part of section 6.2.4, from the maps we can compute power spectra using the public code NaMaster. From N_{rec} bands, we compute the Inter-Band Cross-Spectra (IBCS) for each TT , EE , BB and TE power spectra. As we are interested in the noise, we compute the power spectra of the residual maps containing only noise. Figure 6.17 shows the IBCS computed for each noise realization in the case of 3 sub-bands at 150 GHz. As we plot D_ℓ the noise bias goes as $\ell(\ell+1)$. We find that the IBCS within the same band ($\nu_0\nu_0$, $\nu_1\nu_1$ and $\nu_2\nu_2$) are positively correlated. However the IBCS crossing 2 different bands ($\nu_0\nu_1$, $\nu_0\nu_2$ and $\nu_1\nu_2$) are anti-correlated.

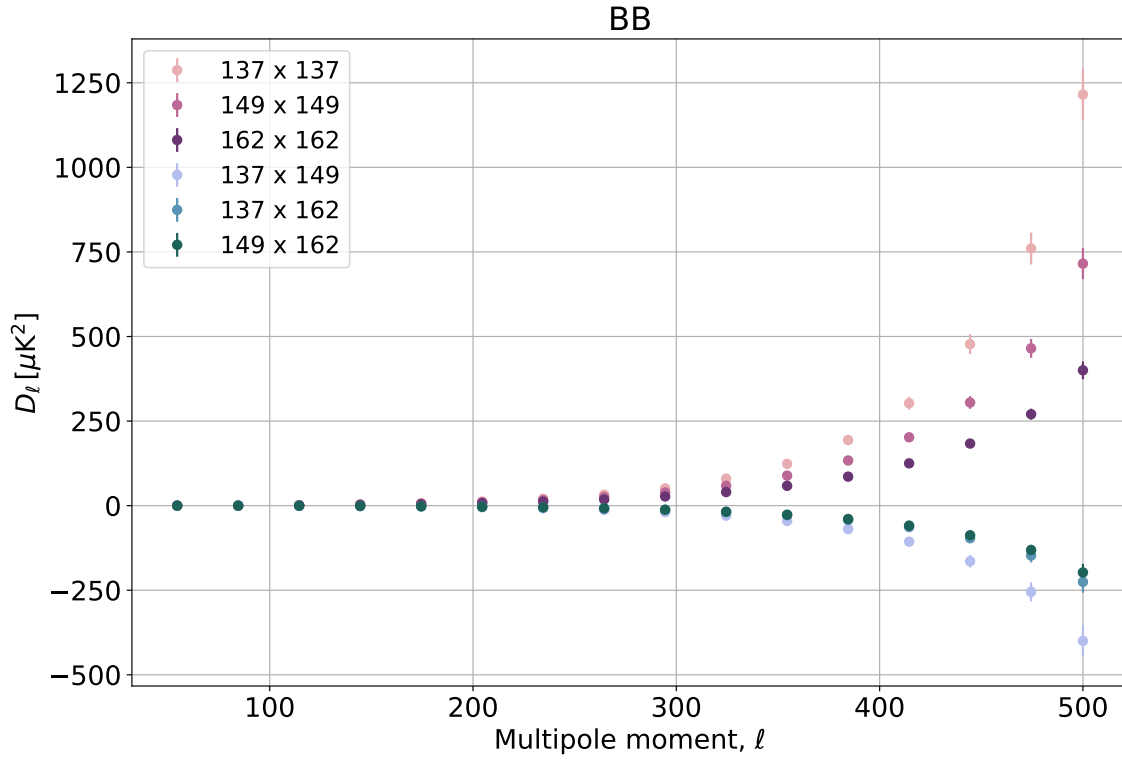


Figure 6.17: BB Inter Band Cross Spectra on the residual maps containing only noise for 3 sub-bands in the wide 150 GHz band, centered at 137, 149 and 162 GHz. Dots and error bars show average and standard deviation over 1000 independent noise realization IBCS computed with the fast noise simulator.

The correlations are observed in greater detail by computing the correlation matrices. In Figure 6.18, we show the correlation matrix between ℓ -bins and IBCS for BB angular power spectrum considering $N_{\text{rec}} = 3$ sub-bands in the 150 GHz wide band. In this matrix, we see that anti-correlations, in blue in the matrix, only appear between the IBCS crossing 2 different bands ($\nu_0\nu_1$, $\nu_0\nu_2$ and $\nu_1\nu_2$ in the case of 3 sub-bands) and that the correlations between bins are negligible. The same behavior is observed for TT , EE and TE spectra.

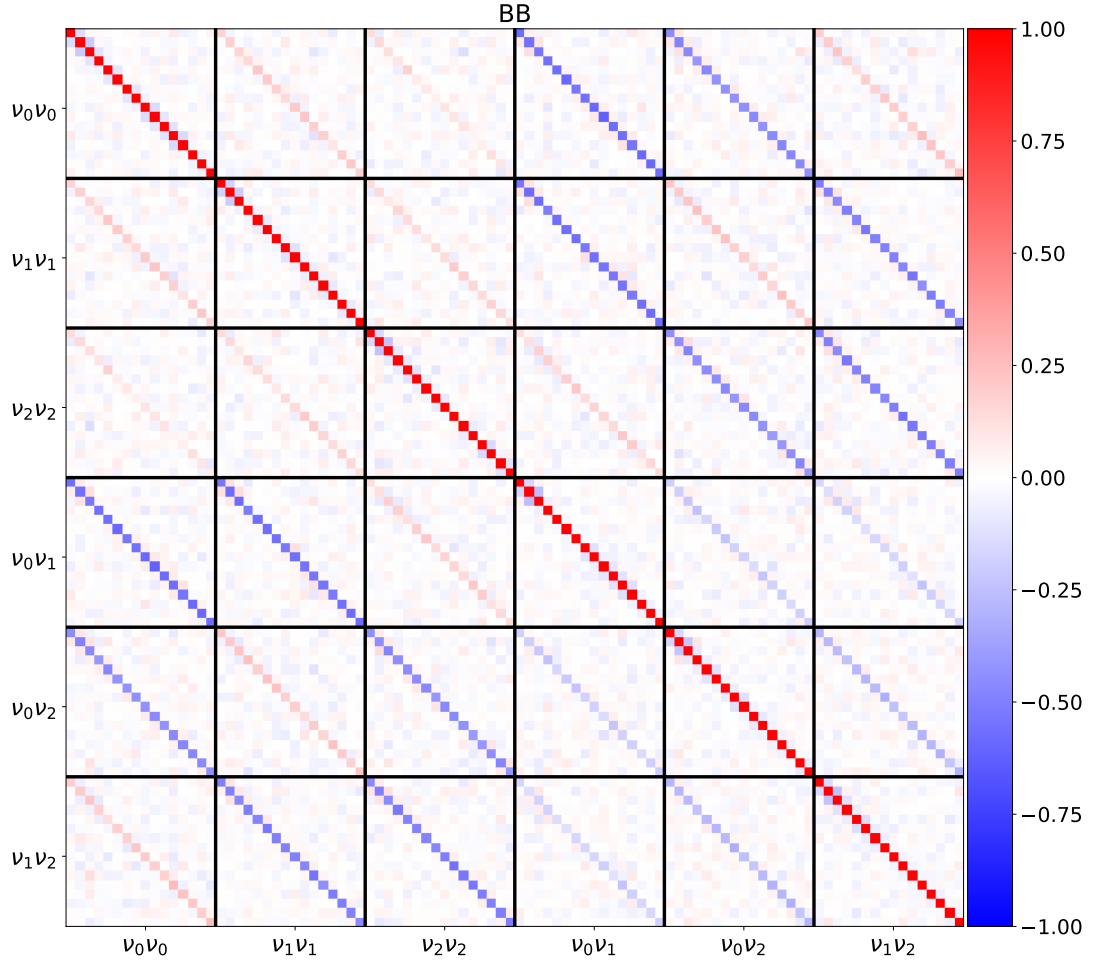


Figure 6.18: Correlation matrix between ℓ -bins and IBCS for BB angular power spectrum considering 3 sub-bands at $\nu_0 = 137$, $\nu_1 = 149$ and $\nu_2 = 162$ GHz. For example, $\nu_0\nu_1$ is the IBCS between frequencies ν_0 and ν_1 . In each black square we show the correlations between the 16 ℓ -bins used to compute the IBCS as in Figure 6.17.

6.4 Spectral imaging on real data

Spectral imaging has been applied on real data for the first time during the calibration campaign at the APC laboratory. The QUBIC instrument was placed on an alt-azimuth mount in order to scan a calibration source tuned at 150 GHz (with 144 Hz bandwidth) and placed in the far field. The corresponding analysis is presented in [8]. We then perform a scan in azimuth and elevation with the instrument, obtaining a TOD for each bolometer. We then apply our spectral imaging map-making algorithm with five sub-bands to a selection of 26 bolometers that do not exhibit saturation. The synthesized beam for each bolometer is realistically modeled in our map-making through a series of Gaussian whose amplitude, width and locations are fit from a measured map of the synthesized beam for each bolometer (see Figure 20 from [8] for an example). The frequency evolution of this synthesized beam only assumes linear scaling with wavelength. We were able to reconstruct a map of the point-like artificial calibration source as well as its location in frequency space. In Figure 6.19, we show the reconstruction onto 5 sub-bands. The expected point-source shape is clearly visible in the central frequency sub-band containing the emission frequency of the source at 150 GHz.

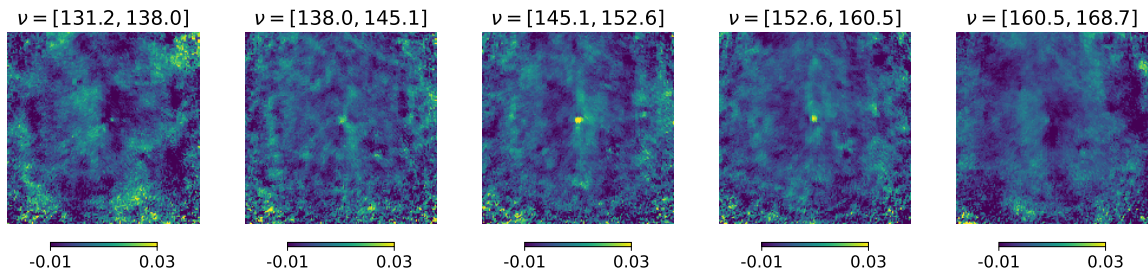


Figure 6.19: Calibration data with the source at 150 GHz projected on the sky using our map-making software to deconvolve from the multiple peaked synthesized beam and split the physical band of the instrument into 5 sub-bands.

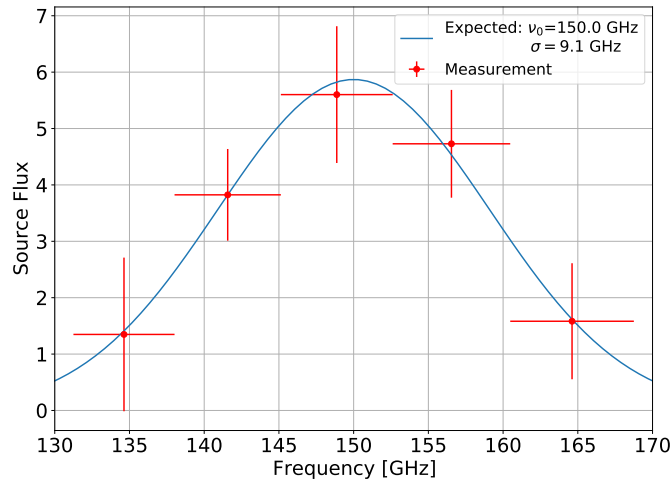


Figure 6.20: Measurement of the flux of the source in reconstructed sub-bands. The measurement (simple aperture photometry) in red is compared to the expected value spectrum in blue. The expected shape is a Gaussian centered on $\nu = 150$ GHz and a FWHM equal to $\frac{\nu}{(P-1)}$ with $P = 8$ for the TD instrument. A global offset and the amplitude of the Gaussian are adjusted to the data.

The calibration source is fainter in adjacent bands, and not visible in the furthest bands. In Figure 6.20, we show the detected amplitude in the central pixel as a function of the frequency. The measurement in red is compared to the expected value spectrum in blue. The expected shape is a Gaussian centered on $\nu = 150$ GHz and a FWHM equal to $\frac{\nu}{(P-1)}$ as explained in section 6.1.2.

Those data were acquired with the TD instrument that has a square 8×8 feedhorn array so $P = 8$. The global offset and the amplitude of the Gaussian are adjusted to the data. Error bars are computed in a very conservative manner.

Conclusion In this chapter, we have shown how the new technique of bolometric interferometry offers the possibility to also perform spectral imaging. This makes it possible to split, in post processing, the wide-band observations into multiple sub-bands achieving spectral resolution. After having presented the spectral imaging technique we have illustrated it on simple cases: monochromatic point sources, spatially extended sources, and sky maps with frequency-dependent emission such as Galactic dust. We have shown our ability to increase spectral resolution with respect to the physical bandwidth, considering a full sky patch but also at the level of individual pixels. Finally, we studied the signal and noise behavior using Monte-Carlo simulations for an instrument like QUBIC which shows spatial and spectral correlations.

The precise measurement of foreground contaminants is essential for the detection of primordial B-modes. Foregrounds have spectral properties distinct from the CMB which leads to the conclusion that only a multichroic approach enables the measurement and subtraction of foreground contamination. This is usually done in classical imagers through detectors operating at distinct frequencies, each of them being wide-band in order to maximize signal-to-noise ratio. However, constraining foregrounds with such data relies on extrapolation between distant frequency bands, which may miss non-trivial variations of the spectral behavior of complex foregrounds such as multiple dust clouds in the line of sight. In particular, scenarios where dust exhibits a certain level of decorrelation between widely separated bands, or with non constant spectral indices would be impossible to be identified with a usual wide-band analysis. Spectral imaging could put significant constraints on such scenarios. This is being studied in detail by the QUBIC collaboration.

An order of magnitude for the number of sub-bands we expect to reconstruct was given at the beginning of this chapter, in section 6.1.2. However, we will come back to that point in section 7.7.3 using end-to-end simulations for a more accurate estimation.

Chapter 7

Constraining Cosmology from CMB observation

Contents

7.1	First doubts and questions	172
7.1.1	Missing matter	172
7.1.2	Horizon problem	173
7.1.3	Flatness problem	173
7.1.4	Absence of magnetic monopoles	174
7.2	Saving the Big Bang model with cosmic inflation	174
7.2.1	Hubble radius	174
7.2.2	Definition of inflation	174
7.2.3	A scalar field: the inflaton	176
7.2.4	The slow-roll approximation	177
7.2.5	How inflation ends?	177
7.3	Primordial perturbations from inflation	178
7.3.1	From microscopic physics to macroscopic observables	178
7.3.2	Connection with CMB observations	180
7.4	Experimental evidences for inflation	181
7.4.1	Scale invariance	181
7.4.2	Tensor modes	182
7.4.3	Coherence	183
7.4.4	Gaussian	183
7.4.5	Adiabatic	183
7.4.6	Discussion	183
7.5	New surprise, the expansion is accelerating	184
7.6	Constraints on the cosmological parameters	184
7.6.1	The success of the Λ CDM model	184
7.6.2	From CMB observation to cosmological parameters	186
7.6.3	Others cosmological probes	189
7.7	Constraining r with QUBIC	190
7.7.1	Description of the simulations	190
7.7.2	QUBIC Full Instrument expected performance	191
7.7.3	Spectral imaging and constraints on r	192
7.7.4	Ability to recognize the presence of dust residuals	194

Up to now in this manuscript, we only discussed observations that perfectly corroborate the Big Bang model. The observation of the CMB may even be seen as the triumph of the Hot Big Bang theory. However, different observations, especially in the second part of the 20 century, have raised new doubts and questions. As we will see in this chapter, the Hot Big Bang model was not abandoned but it was needed to add new unknown ingredients, the “dark part” of the model, as well as a new phase in the universe history called inflation.

In this chapter, the motivations for this inflation phase, a brief review of this theory and the experimental evidences are presented. New parameters, derived from inflation theory, are needed in order to fully describe the observations. This leads me to present the standard cosmological model commonly used today as well as the current constraints on it. I also explain how CMB observations have the ability to constrain it.

The tensor-to-scalar ratio r is a crucial parameter, derived from inflation theory, which characterizes the ratio between E and B -mode amplitude. This is why it is so important for current CMB experiments which aim at measuring it or, at least, putting an upper limit on its value.

Personal contributions: Section 7.7 is my personal work, realized in collaboration with Jean-Christophe and Martín. It first contains the QUBIC forecasts on the measurement of the tensor-to-scalar ratio. The achieved constraint on r is then studied as a function of the number of reconstructed sub-bands, showing that spectral imaging performance are nearly optimal up to five sub-bands in the case of QUBIC. Finally we show how spectral imaging gives the ability to detect the presence of dust residuals. This is part of paper [1] that gives an overview of the QUBIC project, and paper [9] related to spectral imaging for which I am the second and first author respectively.

7.1 First doubts and questions

7.1.1 Missing matter

In 1934, Hubble made the first measurement of the matter density of the universe by counting the number of galaxies. He found $\rho_m = (1.3 - 1.6) \times 10^{-30} \text{ g cm}^{-3}$ [41].

The need of additional matter, for coherence with observations, was first mentioned in 1933 by Zwicky [42]. He looked at the radial velocities of galaxies in the Coma cluster: “In order to obtain the observed value of an average Doppler effect of 1000 km s^{-1} or more, the average density in the Coma system would have to be at least 400 times larger than that derived on the grounds of observations of luminous matter. If this would be confirmed we would get the surprising result that dark matter is present in much greater amount than luminous matter.” Zwicky, was a very innovative physicist, also known for the discovery of supernovae [43] and the prediction of strong gravitational lensing [44]. Similar observations were done in the 1930’ by Smith in the Virgo cluster [45] and by Babcock [46] in the Andromeda galaxy.

However, those works were forgotten until 1970’ when Vera Rubin measured the rotation velocity of stars in the Andromeda galaxy as a function of their distance to the center [59]. Contrary to what was expected, the velocity stays constant when the distance increases. This can be explained by an halo of invisible matter, called dark matter, surrounding the galaxy and that would constitute around 90% of the galaxy mass. The lack of matter to explain velocity measurements was latter observed in many others galaxies.

Since that time, a huge number of tentatives to detect a candidate for dark matter particles over a wide energy range, were carried out, so far with no success. Another possibility is that the theory of gravitation is incomplete and need to be modified. This idea was first presented by Milgrom in 1983 [60], it is known as the Modified Newtonian Dynamics (MOND). However, an observation in the Bullet cluster, which is the result of a collision of two galaxy clusters, showed that the apparent center of mass is far displaced from the baryonic center of mass [61]. Since, this observation was repeated

on a couple of other clusters in collision. This almost ruled out the modified gravity theories for dark matter because it is independent on the nature of the gravitational force law.

7.1.2 Horizon problem

At the recombination era, the universe has lived $\sim 380\,000$ years. The finiteness of light speed induces an horizon which is the maximum distance light can have traveled since the “birth of the universe”. The horizon at decoupling corresponds to $\sim 1^\circ$ on the celestial sphere today¹. Thus, the CMB map is composed of many causally disconnected regions. This is illustrated on Figure 7.1. Then, why is the

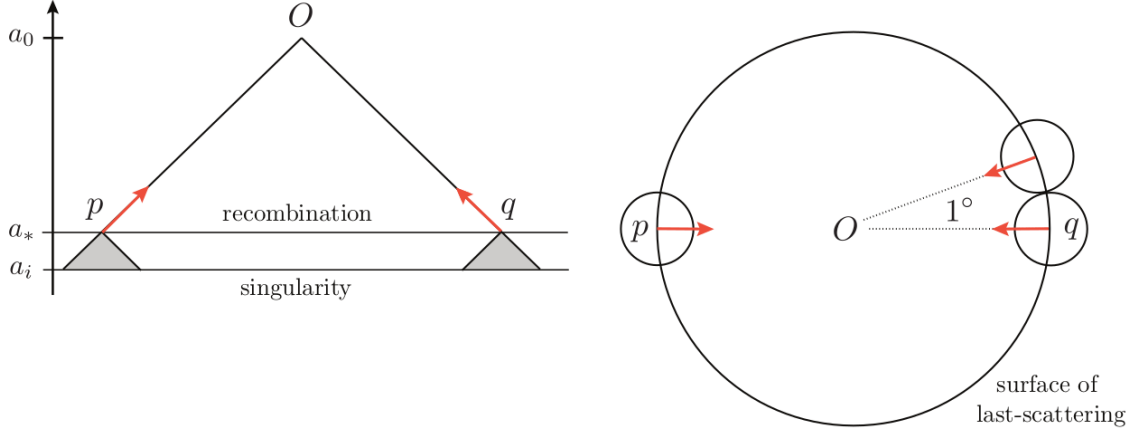


Figure 7.1: Illustration of the horizon problem. *Left:* The events that we currently observe in O are on our light cone. p and q could not have been in causal contact between the Big Bang singularity and the recombination (shown in gray). *Right:* p and q are opposite points on the LSS. Little circles show the horizon of one point at recombination which corresponds to 1° on the sky. Taken from [62].

CMB temperature so homogeneous over the sphere, within 10^{-5} ? At the time where this question was raised, the temperature anisotropies were not yet observed but the measurement of the temperature angular power spectrum raises another point, even more intriguing: why are the CMB fluctuations correlated at larger scales than the decoupling horizon as shown by the Sach-Wolfe plateau?

7.1.3 Flatness problem

After the discovery of the expansion of the universe, the cosmological constant Λ was removed from the Friedmann equation². We note $\rho = \rho_m + \rho_r$ and $\Omega = \Omega_m + \Omega_r$ so from equation 3.18, without the cosmological constant, we have $\Omega_k = 1 - \Omega$. The first Friedmann equation can be written as [63]:

$$\left(\frac{1}{\Omega(t)} - 1\right) \rho(t) a^2(t) = -\frac{3k}{8\pi\mathcal{G}}. \quad (7.1)$$

The right term is constant over time and the universe today appears to be flat, we have $k \simeq 0$, $\Omega_k^0 \simeq 0$ and so $\Omega^0 \simeq 1$, within 1%³. This implies that the left term must be zero today but also at any time. When radiation dominates the universe, a characteristic time scale is the Planck time:

$$t_p = \sqrt{\frac{h\mathcal{G}}{2\pi c^5}} \sim 10^{-43} \text{ s}. \quad (7.2)$$

¹This angle can easily be derived from the BAO scale (see section 7.6.3) and the angular distance at recombination

$$\theta \simeq \frac{150 \text{ Mpc}}{D_A(z=1100)} \simeq \frac{150 \text{ Mpc}}{12800 \text{ Mpc}} \sim 0.67^\circ.$$

²but reappeared later as we will see in section 7.5.

³In 1980, when this was discussed, the constraint was $0.01 < \Omega^0 < 10$ [98]!

When the universe was t_p old, the term $\rho(t_p)a^2(t_p)$ was 10^{60} times higher than today. This means that $\Omega(t_p)$ must have been equal to 1 within 10^{-60} (i.e. $|1 - \Omega(t_p)|$ less than 10^{-60}). The condition $\Omega = 1$ is unstable in the sense that a tiny deviation from 1 at any time would lead to a non zero curvature today. The flatness problem states that such finely tuned initial conditions seem extremely unlikely.

7.1.4 Absence of magnetic monopoles

Grand Unified Theories (GUT), which unify electroweak and strong interactions, predict the existence of topological defects produced by the symmetry breaking at the phase transition (Higgs mechanism), such as magnetic monopoles. The fact that they have never been observed suggests that they are very distant from each others compared to the Hubble radius [64].

7.2 Saving the Big Bang model with cosmic inflation

The horizon and flatness puzzles require very specific initial conditions in the universe. At this point, either one can consider that those initial conditions are the requirements and do not need to be justified, or one can try to find a mechanism to explain them. In 1981, Guth and others proposed to add a phase of cosmic inflation in the early universe, typically around 10^{-34} s, above GUT scale, after the Big Bang which precisely leads to the required initial conditions [98]. This model does not replace the Hot Big Bang model, but rather completes it without disturbing any of its success.

This section is mainly inspired by [145], [62], [99], [100].

7.2.1 Hubble radius

Let us recall that the expansion rate of the universe is given by the Hubble-Lemaître parameter $H = \dot{a}/a$ with dimension T^{-1} . Thus, we can define the Hubble time H^{-1} and the Hubble length cH^{-1} . Note that with the choice of unit $c = 1$, the two are equal. The Hubble time is the characteristic timescale of evolution of the scale factor a . It is also a good estimate of the age of the universe:

$$\text{Age} = \int_{\text{Big Bang}}^{\text{Now}} dt = \int_{a=0}^{a=a_0=1} \frac{da}{aH(a)} \sim H_0^{-1}. \quad (7.3)$$

The Hubble length, also called the Hubble radius, defines a sphere around us beyond which objects recede faster than the speed of light [65]. We can define a comoving Hubble length \mathcal{X}_H :

$$H^{-1} = a\mathcal{X}_H \quad \Rightarrow \quad \mathcal{X}_H = \frac{1}{aH} \quad (7.4)$$

where we set $c = 1$. This comoving Hubble radius is a very important scale, especially for inflation considerations.

7.2.2 Definition of inflation

To solve the horizon and flatness problems, we need an inflation phase during which the Hubble rate increases so the comoving Hubble radius decreases:

$$\frac{d}{dt} \left(\frac{1}{aH} \right) = \frac{d}{dt} \left(\frac{1}{\dot{a}} \right) = -\frac{\ddot{a}}{\dot{a}^2} < 0. \quad (7.5)$$

This condition implies an accelerated expansion

$$\ddot{a} > 0. \quad (7.6)$$

This means that the observable universe becomes smaller during inflation. This condition can also be written as:

$$\frac{d}{dt} \left(\frac{1}{aH} \right) = -\frac{1}{a} \left(1 + \frac{\dot{H}}{H^2} \right) < 0 \quad (7.7)$$

and we usually define $\varepsilon \equiv -\dot{H}/H^2$ so the condition for a decreasing Hubble radius becomes $\varepsilon < 1$. Another consequence is that the pressure must be negative. Indeed, if $\ddot{a} > 0$, the second Friedmann equation 3.14 with no cosmological constant implies that:

$$\rho + 3p < 0. \quad (7.8)$$

The energy density ρ is always positive so the pressure p must be negative and the equation of state parameter w must be lower than $-1/3$.

How does inflation solve the horizon and flatness problems? The horizon problem is automatically solved by saying that the Hubble radius at the beginning of inflation was bigger than the Hubble radius today. Thus, the whole observable universe today has already been in causal contact during inflation. At the end of inflation the Hubble radius was much smaller than today and it slowly increased during the radiation and matter domination epochs. This is illustrated in a space-time diagram in Figure 7.2.

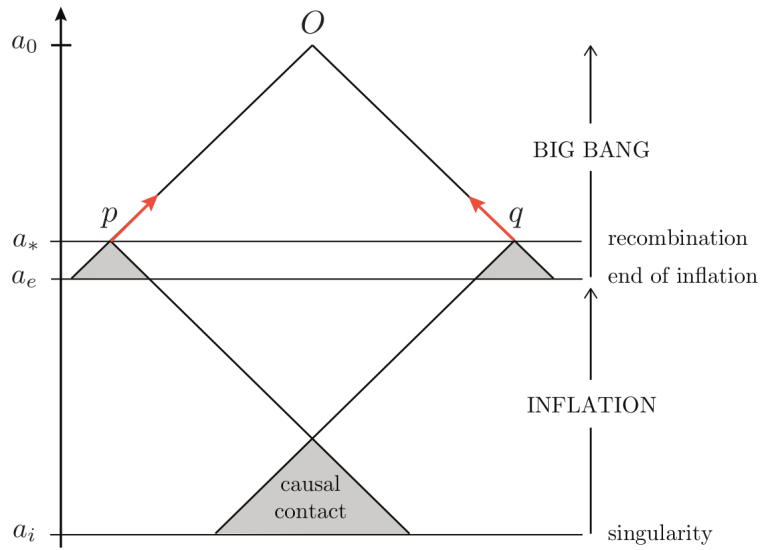


Figure 7.2: Illustration of the horizon problem solved with inflation on a space-time diagram. The two light cones in gray intersect at an earlier time during inflation so the two points p and q have been in causal contact. Taken from [62].

Regarding the flatness problem, we can rewrite equation 7.1 dividing by the critical density $\rho_c(t) = 3H^2/8\pi\mathcal{G}$:

$$1 - \Omega(t) = \frac{-k}{a^2(t)H^2(t)}. \quad (7.9)$$

During inflation, the comoving Hubble radius $1/aH$ decreases so the right term tends to zero and hence $\Omega(t)$ tends to one. If inflation lasts long enough, the universe can be sufficiently flat at the end of inflation in order to solve the flatness problem.

How big is inflation? The amount of inflation is characterized by the ratio of the scale factor at the end of inflation to its value at some initial time t_i . Because the increasing is huge, the exponential is well appropriated. We define the number of e-folds N such that

$$a(t_{\text{end}}) = e^{N(t_i)} a(t_i) \quad \Leftrightarrow \quad N(t_i) = \ln \left(\frac{a(t_{\text{end}})}{a(t_i)} \right). \quad (7.10)$$

To solve the horizon and flatness problems, the number of e-folds must be at least 60 [99]. An order of magnitude for this limit can be derived easily. In order to solve the horizon problem, the increase

of the Hubble radius during radiation phase needs to be approximately equal to its decrease during inflation. During radiation era, we have

$$\rho \propto a^{-4} \quad \text{and} \quad H^2 \propto \rho \quad \Rightarrow \quad \mathcal{X}_H = \frac{1}{aH} \propto a. \quad (7.11)$$

On the contrary, during inflation phase we have

$$H = \text{cst} \quad \Rightarrow \quad \mathcal{X}_H \propto a^{-1}. \quad (7.12)$$

Thus, the number of e-folds is typically

$$N(t_i) = \ln \frac{a(t_{\text{end}})}{a(t_i)} \simeq \ln \frac{a(t_{\text{today}})}{a(t_{\text{end}})} = \ln \frac{T(t_{\text{end}})}{T(t_{\text{today}})} \simeq \ln 10^{29} \simeq 66. \quad (7.13)$$

7.2.3 A scalar field: the inflaton

The unusual property of negative pressure required for inflation can be satisfied by a scalar field describing scalar particles with spin-0. The scalar field responsible for inflation is called the inflaton ϕ . It is described by a Lagrangian with general form [237]:

$$\mathcal{L} = \frac{1}{2}(\partial_\mu \phi \partial^\mu \phi) - V(\phi) \quad (7.14)$$

which is the difference between a kinetic term and a potential. The potential usually contains a mass term $\frac{1}{2}m^2\phi^2$ and possibly others terms. It represents the self-interaction of the field. From the Lagrangian we can compute the energy momentum tensor $T^{\mu\nu}$ defined as

$$T^{\mu\nu} = \frac{2}{\sqrt{-g}} \frac{\delta(\sqrt{-g}\mathcal{L})}{\delta g_{\mu\nu}} \quad (7.15)$$

where $g_{\mu\nu}$ is the FLRW metric. Thus we derive the energy density and the pressure. For an homogeneous scalar field (which does not depend on the position \mathbf{x} but can vary in time), we obtain [99]

$$\rho_\phi = \frac{1}{2}\dot{\phi}^2 + V(\phi) \quad (7.16)$$

$$p_\phi = \frac{1}{2}\dot{\phi}^2 - V(\phi). \quad (7.17)$$

The stress-energy tensor of the scalar field is diagonal, there is no term mixing ρ_ϕ and p_ϕ , so the scalar field can be seen as a perfect fluid (see equation 3.6).

We can write the equations of motion of the scalar field. The first Friedmann equation 3.13, without the cosmological constant and for a zero curvature⁴, gives the evolution of the universe during inflation:

$$H^2 = \frac{8\pi\mathcal{G}}{3} \left(\frac{1}{2}\dot{\phi}^2 + V(\phi) \right), \quad (7.18)$$

and the equation of energy conservation 3.15 gives the evolution of the scalar field:

$$\ddot{\phi} + 3H\dot{\phi} = -\frac{dV}{d\phi} = -V'(\phi). \quad (7.19)$$

We see that the expansion acts as a friction term proportional to the Hubble constant H .

Let us express ε as a function of ϕ . We can differentiate the Friedmann equation 7.18 with respect to time obtaining

$$2H\dot{H} = \frac{8\pi\mathcal{G}}{3}\dot{\phi} \left(\ddot{\phi} + V'(\phi) \right), \quad (7.20)$$

and using the second equation of motion 7.19, we get $2\dot{H} = -8\pi\mathcal{G}\dot{\phi}^2$. This allows to write ε as:

$$\varepsilon \equiv -\frac{\dot{H}}{H^2} = \frac{3}{2} \frac{\dot{\phi}^2}{\dot{\phi}^2 + V(\phi)}. \quad (7.21)$$

⁴Inflation makes the universe flat. The curvature is assumed to be negligible from the start, if it is not, the beginning of inflation will render it negligible [99].

7.2.4 The slow-roll approximation

To get a negative pressure, it is clear from equation 7.17 that the potential energy must dominate the kinetic energy, i.e. the scalar field must roll slowly. This is the first slow-roll condition:

$$\dot{\phi}^2 \ll V. \quad (7.22)$$

Inflation will end when this condition is violated. We must also require that inflation lasts long enough to solve the horizon problem, so we require the acceleration of the field to be small. This is the second slow-roll condition:

$$\ddot{\phi} \ll 3H\dot{\phi}. \quad (7.23)$$

Under those two conditions, equations of motion 7.18 and 7.19 become:

$$H^2 = \frac{1}{3M_p^2}V \quad \text{and} \quad 3H\dot{\phi} = -V'. \quad (7.24)$$

where $M_p = 1/\sqrt{8\pi\mathcal{G}}$ is the reduced Planck mass. From equation 7.16 we see that the first condition implies that $\rho \simeq V$ and V must vary slowly. So, from the equation of motion 7.24 we see that H must also vary slowly and we can assume it to be constant, at least over a Hubble time. This implies an exponential expansion:

$$H \equiv \frac{\dot{a}}{a} = \text{cst} \quad \Rightarrow \quad a \propto e^{Ht}. \quad (7.25)$$

Let us write the two conditions in a different form. We first define a second parameter

$$\eta \equiv -\frac{\ddot{\phi}}{H\dot{\phi}}. \quad (7.26)$$

Using the two equations of motion, conditions 7.22 and 7.23 lead to

$$\frac{M_p^2}{3} \left(\frac{V'}{V} \right)^2 \ll 1 \quad \text{and} \quad M_p^2 \frac{V''}{V} \ll 1. \quad (7.27)$$

We define the slow-roll parameters

$$\varepsilon_v \equiv \frac{M_p^2}{2} \left(\frac{V'}{V} \right)^2 \quad \text{and} \quad \eta_v \equiv M_p^2 \frac{V''}{V}, \quad (7.28)$$

which coincide with ε and η in the slow-roll approximation. Thus, the two conditions become:

$$\varepsilon \simeq \varepsilon_v \ll 1 \quad \text{and} \quad \eta \simeq \eta_v \ll 1. \quad (7.29)$$

Thus, any scalar field which satisfies the slow-roll conditions will lead to a phase of inflation. An example of a slow-roll potential is shown in Figure 7.3. Inflation occurs in the gray zones when the scalar field ϕ falls slowly in the potential well. It ends when ϕ starts to fall too fast. It is clear that a huge quantity of models is allowed, see for example the paper about inflation from the Particle Data Group [48].

In the slow-roll regime, the number of e-folds can be written as a function of the potential V . We have $dN = -d \ln a = -da/a = -H/dt = -Hd\phi/\dot{\phi}$. This leads to

$$N = \int_{\phi_{\text{start}}}^{\phi_{\text{end}}} \frac{V}{M_p^2 V'} d\phi \quad \text{where we used} \quad \frac{H}{\dot{\phi}} = \frac{V}{M_p^2 V'}. \quad (7.30)$$

7.2.5 How inflation ends?

First of all, it is not the most well understood aspect of inflation. At the end of inflation the universe is typically, in a very cold and non-thermal state. A period of *reheating* follows to catch up with the Hot Big Bang model. During this period, the inflaton decays into the fermionic and bosonic particles that we know today. Reheating starts with a phase where the scalar field oscillates around the minimum of the potential. Oscillations can last a considerable time because the particle decay time can be much larger than the Hubble time (the age of the universe). After the decay, there is a thermalization phase during which the decay products interact and may decay again into new particles. One can refer to the review [101] for details.

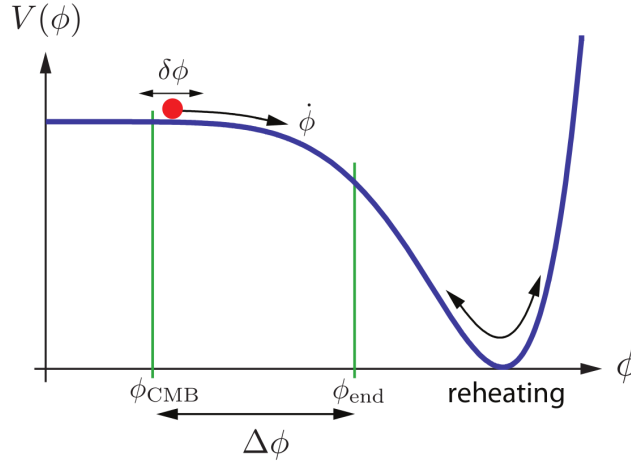


Figure 7.3: Illustration of the inflaton ϕ rolling in a potential $V(\phi)$. Inflation occurs in the slow-roll regime between the two green lines. Taken from [100].

7.3 Primordial perturbations from inflation

As we have seen in the previous section, adding a cosmic inflation phase at the beginning of the Big Bang model solves the horizon and flatness problems in an elegant manner. Moreover, it was rapidly realized that inflation also offers a mechanism to generate the fluctuations in the primordial plasma required for the formation of large-scale structure.

7.3.1 From microscopic physics to macroscopic observables

Quantum fluctuations generate small spatial perturbations of the scalar field

$$\phi(t, \mathbf{x}) = \phi(t) + \delta\phi(t, \mathbf{x}), \quad (7.31)$$

that can also be described in Fourier space by

$$\delta\phi_{\mathbf{k}} = \int d^3x \delta\phi(t, \mathbf{x}) e^{i\mathbf{k} \cdot \mathbf{x}}. \quad (7.32)$$

We can have scalar, vector or tensor perturbations depending on the behavior of $\delta\phi_{\mathbf{k}}$ under a rotation around a single Fourier wavevector \mathbf{k} by an angle ψ :

$$\delta\phi_{\mathbf{k}} \rightarrow e^{im\psi} \delta\phi_{\mathbf{k}} \quad \text{with} \quad m = \begin{cases} 0 & \text{scalar} \\ \pm 1 & \text{vector} \\ \pm 2 & \text{tensor} \end{cases} \quad (7.33)$$

We can treat the three types of perturbations separately because they independently evolve during inflation. Actually, the vector perturbations decay with the expansion so we can neglect them and we will only consider scalar and tensor perturbations.

The inflaton is connected with the metric by the Einstein equation. This is why the fluctuations of the inflaton generate perturbations of the metric. Scalar and tensor perturbations respectively correspond to density perturbations and gravitational waves. Both are identified by their comoving wavenumber k arising from the Fourier decomposition.

Scalar perturbations

We note \mathcal{R} the curvature perturbation generated by scalar fluctuations. A powerful tool to statistically describe the primordial scalar fluctuations is the power spectrum of \mathcal{R} ,

$$\langle \mathcal{R}_{\mathbf{k}} \mathcal{R}_{\mathbf{k}'} \rangle = (2\pi)^3 \delta(\mathbf{k} - \mathbf{k}') P_{\mathcal{R}}(k). \quad (7.34)$$

In order to get rid of the volume dependence of $P_{\mathcal{R}}(k)$, we define the scalar power spectrum as

$$\Delta_s^2 \equiv \Delta_{\mathcal{R}}^2 = \frac{k^3}{2\pi^2} P_{\mathcal{R}}(k). \quad (7.35)$$

The power spectrum is often approximated by a power law with amplitude A_s ,

$$\Delta_s^2(k) = A_s(k_*) \left(\frac{k}{k_*} \right)^{n_s(k_*)-1} \quad (7.36)$$

where k_* is an arbitrary reference scale, called the pivot scale. Thus, the scale dependence of the power spectrum is given by the scalar spectral index:

$$n_s - 1 \equiv \frac{d \ln \Delta_s^2}{d \ln k}. \quad (7.37)$$

Tensor perturbations

Regarding gravitational waves, the power spectrum for the two polarization modes $h \equiv h_+, h_\times$ is

$$\langle h_{\mathbf{k}} h_{\mathbf{k}'} \rangle = (2\pi)^3 \delta(\mathbf{k} - \mathbf{k}') P_h(k) \quad \text{and} \quad \Delta_h^2 = \frac{k^3}{2\pi^2} P_h(k). \quad (7.38)$$

The power spectrum for tensor perturbations is the sum of the power spectra of the two polarization modes:

$$\Delta_t^2 \equiv 2\Delta_h^2 \quad (7.39)$$

and it is approximated by a power law

$$\Delta_t^2(k) = A_t(k_*) \left(\frac{k}{k_*} \right)^{n_t(k_*)}. \quad (7.40)$$

This time, the scale dependence is given by the tensor spectral index

$$n_t \equiv \frac{d \ln \Delta_t^2}{d \ln k}. \quad (7.41)$$

Basically, inflation relates microscopic physics and macroscopic observables. A microscopic perturbation with a comoving wavenumber k , will reach cosmic scales during inflation. At the same time, the Hubble radius decreases, so when $k = aH$, the perturbation exits the horizon. Later, in the radiation or matter dominated epoch, the Hubble radius increases so the same perturbation can re-enter the horizon. This is precisely the solution to the horizon problem.

After a mode exits the horizon, it is frozen so it can be described by the power spectrum evaluated at horizon crossing. After a quantization of the perturbations, one can find

$$\Delta_s^2(k) = \frac{1}{8\pi^2} \frac{H^2}{M_p^2} \frac{1}{\varepsilon} \Big|_{k=aH} \quad \text{and} \quad \Delta_t^2(k) = \frac{2}{\pi^2} \frac{H^2}{M_p^2} \Big|_{k=aH}. \quad (7.42)$$

The relative amplitude between the scalar and tensor perturbations is given by the tensor-to-scalar ratio r

$$r \equiv \frac{\Delta_t^2}{\Delta_s^2} = 16\varepsilon_* \quad (7.43)$$

where ε_* is evaluated at the time where the fluctuation exits the horizon.

Slow-roll regime

In the slow-roll regime, the power spectra defined in equation 7.42 become

$$\Delta_s^2(k) \simeq \frac{1}{24\pi^2} \frac{V}{M_p^4} \frac{1}{\varepsilon_v} \Big|_{k=aH} \quad \text{and} \quad \Delta_t^2(k) \simeq \frac{2}{3\pi^2} \frac{V}{M_p^4} \Big|_{k=aH}. \quad (7.44)$$

From those expressions and using definitions 7.37, 7.41 and 7.43, the three observables can be expressed as functions of the slow-roll parameters ε_v and η_v :

$$n_s - 1 = 2\eta_v - 6\varepsilon_v, \quad n_t = -2\varepsilon_v, \quad r = 16\varepsilon_v = -8n_t. \quad (7.45)$$

7.3.2 Connection with CMB observations

Inflation offers a mechanism to produce density perturbations and gravitational waves in the primordial plasma which are precisely the sources for temperature and polarization anisotropies in the CMB (see chapter 4). But how can we relate the primordial power spectrum $P(k)$ to the CMB anisotropies?

Let us first focus on the scalar perturbations. We want to connect the primordial scalar power spectrum $P_{\mathcal{R}}(k)$ to the observed temperature angular power spectrum C_{ℓ}^{TT} . Of course, from inflation, the primordial perturbations have evolved through different physical processes. This can be modeled by a transfer function Δ_r , which may be complicated, but which can be computed numerically assuming a cosmological model, for example with CAMB. Let us write $\mathcal{R}' = \mathcal{R}\Delta_r$ the perturbations at the time where we measure the CMB.

Firstly, as we have seen, it is natural to decompose the temperature anisotropies on the spherical harmonics to get the $a_{\ell m}$ (analogue to a 2D-Fourier transform on a sphere). Then, the angular power spectrum is the variance of the $a_{\ell m}$ defined in equation 4.36.

Secondly, $\mathcal{R}_{\mathbf{k}}$ is the Fourier transform of \mathcal{R} in the Cartesian space (x, y, z) and the power spectrum is the variance of $\mathcal{R}_{\mathbf{k}}$. Therefore, it seems to be possible to relate $P_{\mathcal{R}}(k)$ with C_{ℓ}^{TT} knowing the transfer function and the geometry transform from ℓ -space to k -space. Indeed it is possible to show that [109]:

$$a_{\ell m} = 4\pi(-i)^{\ell} \int \frac{d^3k}{(2\pi)^3} \Delta_{T\ell}(k) \mathcal{R}_{\mathbf{k}} Y_{\ell m}(\hat{\mathbf{k}}) \quad (7.46)$$

where $\Delta_{T\ell}(k)$ is the transfer function which contains physical processes and geometric projection factors. The geometric mapping between k -space and ℓ -space is done with a combination of Bessel functions. We can now substitute this expression in the angular power spectrum. Using the identity

$$\sum_{m=-\ell}^{\ell} Y_{\ell m}(\hat{\mathbf{k}}) Y_{\ell m}(\hat{\mathbf{k}}') = \frac{2\ell+1}{4\pi} P_{\ell}(\hat{\mathbf{k}} \cdot \hat{\mathbf{k}}') \quad (7.47)$$

where P_{ℓ} is a Legendre Polynomial and knowing that $P_{\ell}(1) = 1$, we obtain

$$C_{\ell}^{TT} = \frac{1}{2\ell+1} \sum_{m=-\ell}^{\ell} \langle a_{\ell m}^* a_{\ell m} \rangle = \frac{2}{\pi} \int k^2 dk P_{\mathcal{R}}(k) \Delta_{T\ell}(k) \Delta_{T\ell}(k). \quad (7.48)$$

The conversion between $P(k)$ and C_{ℓ} is summarized in Figure 7.4.

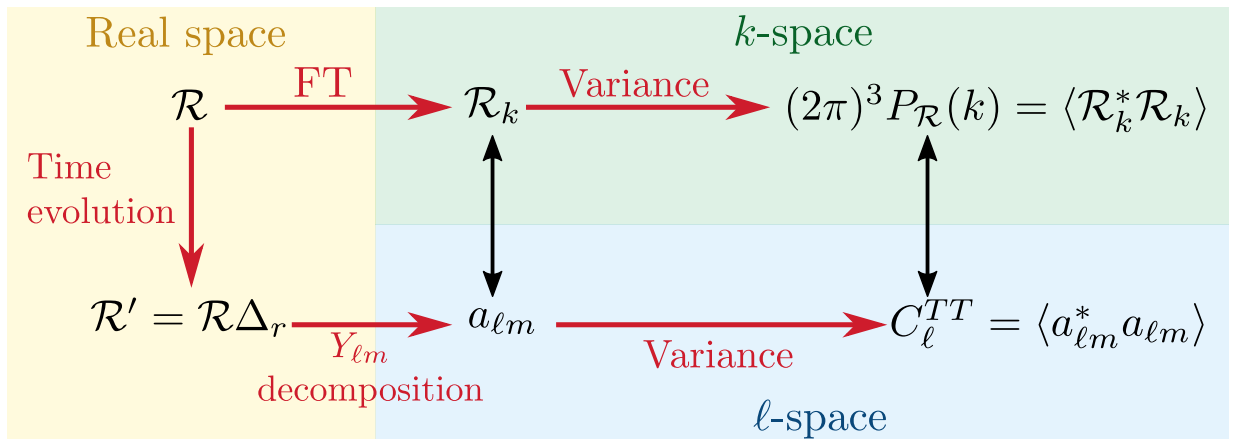


Figure 7.4: Summary of the conversion between the primordial power spectrum $P(k)$ and the CMB angular power spectrum C_{ℓ} .

More generally, we have

$$C_{\ell}^{XY} = \frac{2}{\pi} \int k^2 dk P(k) \Delta_{X\ell}(k) \Delta_{Y\ell}(k) \quad (7.49)$$

where X, Y refer to temperature T and E, B polarization modes. For TT, EE and TE power spectra, we have $P(k) = P_{\mathcal{R}}(k)$ while for BB , we have $P(k) = P_h(k)$. Thus, the CMB angular power spectra

provide a fascinating probe for the scalar and tensor primordial power spectra. To obtain it, one needs to deconvolve the C_ℓ with the appropriate transfer function assuming a cosmological model⁵. Note that, in a very similar manner, the primordial power spectrum can be measured from the distribution of galaxies [66].

Instead of the power spectrum, we could have worked with the 2-point correlation function in the real space $\xi(\mathbf{r}) = \langle \delta(\mathbf{x})\delta(\mathbf{x} + \mathbf{r}) \rangle$ where δ is a perturbation of an arbitrary field. This would be equivalent because the 2-point correlation function is the inverse Fourier transform of the power spectrum. The Fourier transform $\delta(\mathbf{k})$ of the perturbation is defined as

$$\delta(\mathbf{k}) = \int \delta(\mathbf{r}) e^{i\mathbf{k}\cdot\mathbf{r}} d^3r \quad \text{and} \quad \delta(\mathbf{r}) = \frac{1}{(2\pi)^3} \int \delta(\mathbf{k}) e^{-i\mathbf{k}\cdot\mathbf{r}} d^3k \quad (7.50)$$

and the power spectrum as $\langle \delta^*(\mathbf{k})\delta(\mathbf{k}') \rangle = (2\pi)^3 P(k) \delta(\mathbf{k} - \mathbf{k}')$. Therefore, for a real field, we obtain

$$\xi(\mathbf{r}) = \langle \delta^*(\mathbf{x})\delta(\mathbf{x} + \mathbf{r}) \rangle = \frac{1}{(2\pi)^3} \int P(k) e^{-i\mathbf{k}\cdot\mathbf{r}} d^3k. \quad (7.51)$$

The primordial power spectrum inferred from various cosmological probes, CMB and Large Scale Structure is shown in Figure 7.5.

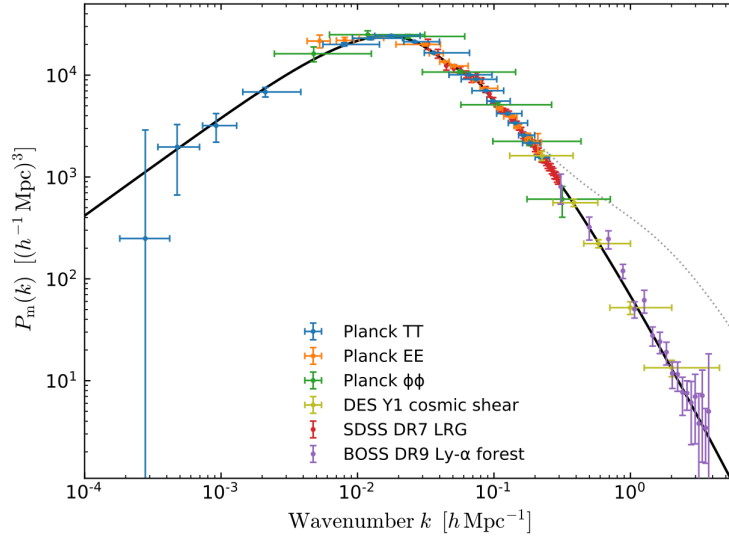


Figure 7.5: Primordial power spectrum $P(k)$ inferred from various cosmological probes, CMB and Large Scale Structure. Taken from [160].

7.4 Experimental evidences for inflation

Inflation was designed to solve the horizon and flatness problems so it would be strange to consider those facts as evidences for inflation. Primordial fluctuations, tensor and scalar can already be seen as a consequence of inflation. However, inflation has others consequences which have been or which are currently being experimentally investigated [97].

7.4.1 Scale invariance

In cosmology, the primordial power spectrum is considered scale-invariant if it is flat, i.e. when the scalar index n_s is one. The physics is generally not scale-invariant, see the discussion by Feynman in [238] (Chapter 52 related to symmetries). However, scale invariance occurs in some cases, for example in electromagnetism, Maxwell equations with no sources (no charge and no current) are invariant under a space dilatation. Similarly, the field equation of general relativity, without cosmological constant, is

⁵Usually done all at once fitting transfer function and primordial cosmological parameters.

scale invariant for empty space. Actually, since there is nothing to define a scale in an empty space, this seems quite obvious [102]. Another scale invariant is a massless scalar field. Indeed, the mass term in the Lagrangian breaks the invariance under a dilatation transformation [237].

Regarding inflation, in the slow-roll regime, we have seen in equation 7.45 that $n_s - 1 = 2\eta_v - 6\varepsilon_v$ with $\varepsilon_v, \eta_v \ll 1$ so $n_s \simeq 1$ which leads to a nearly scale-invariant power spectrum. From the definition of the slow-roll parameters 7.28, we see that the slow-roll approximation restricts the form of the potential. The first and second derivatives, V' and V'' must be small compared to the potential V itself. However, in order inflation to end, we must require n_s slightly different from 1.

How does scale invariance translate in the angular power spectrum? In the Sachs-Wolfe regime, modes were still outside the horizon at recombination so they are not affected by the physical processes occurring in the primordial plasma. Therefore, the transfer function is only the geometric projection from k -space to ℓ -space, i.e. a Bessel function. For a scale-invariant input spectrum ($n_s = 1$), one can show that the quantity

$$D_\ell^{TT} = \frac{\ell(\ell+1)}{2\pi} C_\ell^{TT} \quad (7.52)$$

is independent on ℓ [100]. Hence, the Sachs-Wolfe plateau at large scales reflects the prediction of a scale invariant spectrum. This prediction is a major success for inflation.

Detecting deviations from scale invariance The variation of the spectral index with scale, also called the running of the spectral index is defined as:

$$\alpha_s \equiv \frac{dn_s}{d\ln k}, \quad \Delta_s^2(k) = A_s(k_\star) \left(\frac{k}{k_\star} \right)^{n_s(k_\star)-1+\frac{1}{2}\alpha_s(k_\star)\ln(k/k_\star)}. \quad (7.53)$$

α_s is expected to be small, so a detection of a large variation would imply to reconsider the simplest models for inflation. The Planck 2020 limit is $\alpha_s = 0.013 \pm 0.012$ [103].

Measuring the scale dependence of tensor fluctuations is quite optimistic from the observational point of view, but from relations 7.45 we see that the slow-roll regime implies

$$r = -8n_t. \quad (7.54)$$

The verification of this relation would be a strong argument for slow-roll inflation models and basically an amazing consistency test for inflation!

7.4.2 Tensor modes

The detection of B -modes and the measurement of the C_ℓ^{BB} primordial angular power spectrum would be a direct measurement of primordial gravitational waves which are hard to produce without a period of inflation.

Moreover, the energy scale of inflation is directly linked to the tensor amplitude so that such a measurement would constraint inflation models very strictly. It is possible to show that [100]

$$A_t = \frac{2}{\pi^2} \frac{H_\star^2}{M_p^2} \quad (7.55)$$

which shows that A_t is a direct measurement of the expansion rate during inflation. One can also derive the following relation with the tensor-to-scalar ratio r

$$V^{1/4} \sim \left(\frac{r}{0.01} \right)^{1/4} 10^{16} \text{ GeV}. \quad (7.56)$$

Thus r is a direct measurement of the energy scale during inflation.

7.4.3 Coherence

In section 4.1.5, we claimed that the acoustic peaks in the CMB angular power spectrum originate from stationary waves in the primordial plasma, such as harmonics produced by a guitar string tied down at its ends. However, there are no tied conditions in the primordial universe. So how are frequencies selected? To get a series of peaks in the CMB power spectrum, all Fourier modes of a given wavelength must have the same phase in order to interfere coherently. If not, the CMB power spectrum would simply be white noise so it would be flat [100].

Inflation precisely proposes a mechanism to coordinate the phases of all Fourier modes. During inflation, the perturbations oscillate quantum mechanically. When the wavelength of a mode becomes greater than the Hubble radius, the mode leaves horizon and its amplitude is frozen. This happens before inflation ends. The mode only re-enters horizon much later, typically 100 000 years after. After re-entry, its amplitude starts to oscillate again, under the competing influences of pressure and gravity. The crucial point is that all perturbations associated with this mode oscillate now in phase. If we think of each Fourier mode as a linear combination of a sine and a cosine modes, inflation excites only the cosine modes [104]. As an analogy, one can think of a collection of pendulums that oscillate with random phases and amplitudes. Now, imagine that all pendulums are frozen at the same time and that they are released at a posterior time without initial speed. In this case, they will all oscillate with different amplitudes but in phase, driven by a cosine mode.

One could argue that it is possible to find a mechanism to coordinate the phases in the primordial plasma but the TE angular power spectrum has a feature that almost kills this argument. It has a negative peak around $100 < \ell < 200$ which implies a clear anti-correlated signal at scales that were still outside the horizon at recombination. Therefore, any model that generates perturbations in the primordial plasma inside the horizon can not explain the negative peak in the C_ℓ^{TE} power spectrum on those scales. On the contrary, inflation gives a natural explanation by synchronizing the phases, as described just before [109].

7.4.4 Gaussian

Simple models of inflation predict that the scalar perturbations should be Gaussian to a very high degree. In this case, the primordial power spectrum $P_{\mathcal{R}}(k)$, or equivalently, as seen in section 7.3.2, the 2-point correlation function, contains all the statistical information. Non-Gaussianities are a measure of interactions of the inflaton field. However, in the slow-roll regime, the potential is very flat so inflaton has to be very weakly interacting. Therefore, a detection of a non Gaussian contribution to the correlations of cosmological fluctuations would be very interesting. In this case, the 2-point correlation function would not be sufficient to entirely describe the statistic of the perturbations. To detect non-Gaussianities, one has to compute the bispectrum which is defined as the 3-point correlation function in real space.

7.4.5 Adiabatic

Single field inflation models generate purely adiabatic primordial density perturbations described by a single curvature perturbation \mathcal{R} [67]. This means that all perturbations (baryon, dark matter, radiation) originate from \mathcal{R} and that the ratio between non-relativistic and relativistic species is constant⁶: $\delta(n_{NR}/n_R) = 0$. For example, an over-density in terms of photons by a factor two also corresponds to an over density in terms of electrons in the same proportion.

Non adiabaticity would generate isocurvature perturbations detectable in the shape of the angular power spectrum and would be a clear signature for multifield models or for a cosmology without inflation.

7.4.6 Discussion

In summary, inflation is a powerful model to solve the horizon and flatness problems and its predictions are so far well verified. This may be why it is the favorite model in the cosmology community today.

⁶The definition of adiabaticity in cosmology is not the one commonly used in thermodynamics.

Personally, I find the argument of phase coherence described in section 7.4.3 very convincing.

However, one could argue that inflation actually replaces some questions by others. Classical problems raised by inflation are for example discussed in [105]. The authors present three main problems for inflation:

- Fine-tuning problem: to get the observed amplitude of the primordial density fluctuations ($\delta\rho/\rho \sim 10^{-5}$), the inflation potential must be fine tuned by orders of magnitude.
- Initial condition problem: the probability to have a region with the right initial conditions to have a number of inflation e-folds at least equal to 60 is exponentially small.
- Multiverse or measure problem: large quantum fluctuations of the inflaton field should prevent inflation for end, yielding to eternal inflation.

Therefore I think it is important to keep in mind those questions in order not to “believe in inflation” as the theory that solves all cosmological questions. Interesting alternatives have been studied, see for example [106].

7.5 New surprise, the expansion is accelerating

As we already said, after the discovery of the expansion of the universe, the cosmological constant was abandoned. The main goal was to measure the expansion rate, i.e. the Hubble constant H_0 . At the end of the 1980', physicists were quite confident on the fact that expansion should decelerate because of gravitational attraction between galaxies. To quantify the deceleration rate, the measurement of matter density was required. At the beginning of 1990', different measurements lead to the conclusion that $\Omega_m^0 \sim 0.3$ [68], [69]. This was not compatible with a flat universe without cosmological constant in which, the matter density must be equal to the critical density so $\Omega_m^0 = 1$. The reintroduction of the cosmological constant starts to be considered. One can have a look to this amazing paper by Efstathiou et al. [70].

In 1998, two different teams were aiming at measuring the decelerating parameter using type-Ia supernova in order to characterize the expansion. The result was very surprising, the expansion is not decelerating but is accelerating [71], [72]! In FLRW, this can only come from the cosmological constant so Λ was definitely reintroduced (at least until today). As Λ can be associated with an energy density, it is also called the dark energy component. By combining data from type-Ia supernova and from the CMB, they obtained $\Omega_\Lambda^0 \simeq 0.7$. Thus, in order to compensate the gravitational attraction, dark energy must fill the universe at 70%! A pedagogical presentation of the cosmological constant measurement with supernovae can be found in [73].

Since 1998, many others observations, CMB lensing, Integrated Sachs Wolfe effect, Baryon Acoustic Oscillations (BAO), conclude in an accelerated expansion, without relying on type-Ia supernova. More details about the historical context and the observational evidence of the accelerated expansion can be found in [74].

7.6 Constraints on the cosmological parameters

At this point, we have introduced all the cosmological parameters considered in the Λ CDM model. Let us review them and discuss their measured values.

7.6.1 The success of the Λ CDM model

The Λ CDM model is able to predict a wide range of observations with only six independent parameters, in this sens it is a very successful phenomenological model. Its weakness is however to rely on mysterious ingredients: dark matter and dark energy which are so far unexplained by the standard model of particle physics⁷. By convention, the Hubble constant today is written as $H_0 = 100h \text{ km s}^{-1} \text{ Mpc}^{-1}$ with h

⁷not quite true, for Dark Matter, the Suzy neutralino is perfect but does not seem to exist... [75]

Parameter	Planck alone	Planck + BAO
$\Omega_b h^2$	0.02237 ± 0.00015	0.02242 ± 0.00014
$\Omega_c h^2$	0.1200 ± 0.0012	0.11933 ± 0.00091
$100\theta_{\text{MC}}$	1.04092 ± 0.00031	1.04101 ± 0.00029
τ	0.0544 ± 0.0073	0.0561 ± 0.0071
$\ln(10^{10} A_s)$	3.044 ± 0.014	3.047 ± 0.014
n_s	0.9649 ± 0.0042	0.9665 ± 0.0038

Table 7.1: Λ CDM parameters that best fit to data from Planck (temperature and polarization), with and without BAO data, taken from [160]. θ_{MC} is an approximation of θ_a used in the code CosmoMC (see [76]).

the dimensionless Hubble constant. The six parameters are, for some of them, a combination with h . They are:

- $\Omega_b h^2$ the density of baryons,
- $\Omega_c h^2$ the density of Cold Dark Matter (CDM),
- $\theta_a(z_*)$ the angular acoustic scale at recombination defined in section 4.1.1,
- τ the optical depth to Thomson scattering from reionization defined in section 4.1.3,
- A_s the amplitude and
- n_s the spectral index of the scalar primordial power-law spectrum introduced in section 7.3.1.

A major result of the Planck mission [76] is to have obtained sub-percent precision on the Λ CDM parameters (except for the optical depth). This is shown in Table 7.1. In the fit, they assume that the radiation is made of photons (a black-body with $T = 2.7260$ K [112]) and neutrinos. As explained in [109], the energy density of neutrinos in the universe is given by

$$\rho_\nu = N_{\text{eff}} \frac{7}{8} \left(\frac{4}{11} \right)^{4/3} \rho_\gamma \quad (7.57)$$

with the so-called effective number of neutrinos $N_{\text{eff}} = 3.046$, as derived in [77]. They also assume that neutrinos have very low mass, $m_\nu = 0.06$ eV which corresponds to the minimum mass given by experiments on neutrino oscillations [78], [79].

In order to describe the content of the universe, it is useful to consider additional parameters which can be derived from the previous ones. Here are four examples:

The Hubble constant H_0 : The Hubble constant, is a key parameter for the standard model of cosmology. The last result derived from Planck is found to be

$$H_0 = 67.66 \pm 0.42 \text{ km s}^{-1} \text{ Mpc}^{-1} \quad (68\% \text{CL}). \quad (7.58)$$

Let us also give the recent SPT-3G result [186]: $H_0 = 68.8 \pm 1.5 \text{ km s}^{-1} \text{ Mpc}^{-1}$. The value of H_0 is very debated today because an other type of measurements, based on the evaluation on type-IA supernova distances, finds a different result. The most recent result using cepheids in order to calibrate type-IA supernova distances with GAIA and Hubble Space Telescope data is $H_0 = 73.2 \pm 1.3 \text{ km s}^{-1} \text{ Mpc}^{-1}$ [80]. This results in a tension of about 4σ with the Planck value. In case it is not due to systematic errors, it could be a sign for a failure of the Λ CDM model. For a recent and complete review of the topic, one can refer to [81].

Matter density Ω_m : Using the Planck measurement, associated with BAO, the matter density $\Omega_m = \Omega_b + \Omega_c$ is found to be [160]:

$$\Omega_m = 0.3111 \pm 0.0056 \quad (68\% \text{CL}). \quad (7.59)$$

Cosmological constant Ω_Λ : The radiation density is given by the Stefan-Boltzmann law ($\rho_\gamma \propto T^4$). Since, today, the black-body temperature of CMB photons is very low, the contribution of radiation in the total density is negligible, we have $\Omega_\gamma \simeq 5.38 \times 10^{-5}$ (see the CMB chapter in [48]). In addition, the curvature today is very small ($\Omega_k \ll 1$). Thus, the cosmological constant is given by $\Omega_\Lambda = 1 - \Omega_m$. The Planck measurement, associated with BAO [160] is

$$\Omega_\Lambda = 0.6889 \pm 0.0056 \quad (68\% \text{CL}). \quad (7.60)$$

Matter power spectrum amplitude: The amplitude of the primordial power spectrum is characterized by A_s . However, for large scale structure studies, it is common to use σ_8 which is the RMS fluctuation in total matter mass density in $8h^{-1}$ Mpc spheres at $z = 0$. It is related to the matter power spectrum \mathcal{P}_m in linear theory by

$$\sigma_R^2 = \int \frac{dk}{k} \mathcal{P}_m(k) \left(\frac{3j_1(kR)}{kR} \right)^2, \quad (7.61)$$

where $R = 8h^{-1}$ Mpc and j_1 is the spherical Bessel function of order 1 [76]. It is found to be

$$\sigma_8 = 0.8102 \pm 0.0060 \quad (68\% \text{CL}). \quad (7.62)$$

7.6.2 From CMB observation to cosmological parameters

We will give some clues about how the CMB angular power spectrum evolves depending on the cosmological parameter values. Parameters are partially degenerated, meaning that the effect of varying one can be reproduced by varying others in a specific way. Those degeneracies can be broken by using large scale structure probes. The following description is mainly based on [109].

Shift of the peaks: Ω_k and Ω_Λ

Those two quantities are late time geometrical effects that change the way we see the acoustic scale on the sky. As shown on Figure 7.6 (left), an object of a given size is not seen under the same angle for a flat, closed or open universe. A fixed physical scale gets projected on smaller angle in case of a negative curvature and larger for a positive curvature. Considering this effect for the acoustic peaks, they will be shift to lower or higher multipoles ℓ . This is illustrated on Figure 7.6 (right).

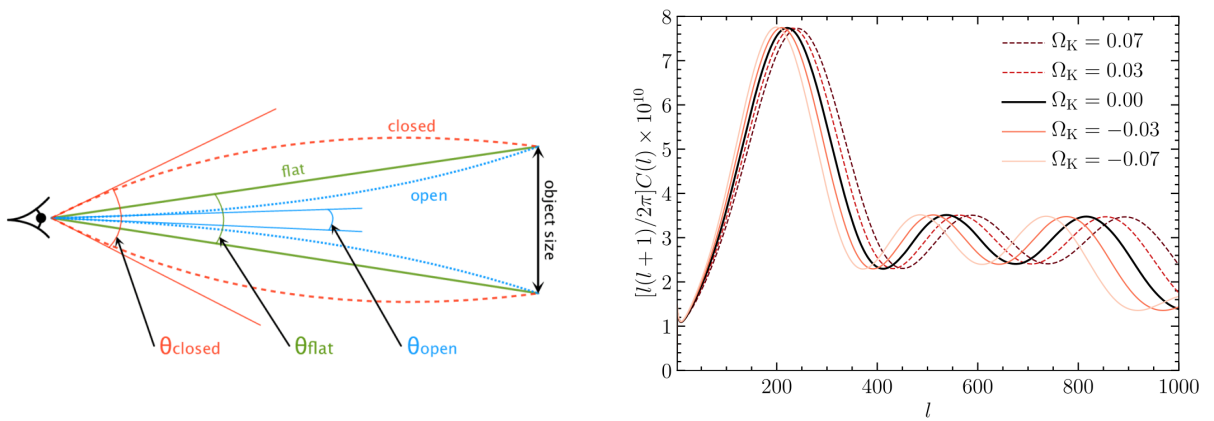


Figure 7.6: *Left:* Sketch showing the apparent angle subtending an object of a given transverse size in a flat, closed and open universe (taken from [82]). *Right:* Effect on the temperature angular power spectrum when varying the curvature (taken from [109]).

Similarly to Ω_k , the cosmological constant changes the angular diameter distance to the last scattering surface $D_a(z_*)$. Its effect on the power spectrum is to shift the peaks too. Varying Ω_Λ , while knowing $\Omega_m h^2$ via direct fit on the power spectrum (see Table 7.1), is equivalent to varying H_0 (see the first Friedmann equation 3.27).

In the Planck analysis, the peak positions are used to determine the acoustic scale θ_a at recombination, assuming a flat universe. It is the best constrained parameter because the positions of the peaks are precisely known and the measurement obtained from temperature and polarization power spectra separately are highly consistent [160].

Change in the peak amplitudes: A_s, n_s and τ

From equations 7.36 and 7.49, the effect on the C_ℓ of changing the primordial power spectrum $P(k)$ is quite easy to see. If the amplitude A_s is multiplied by a factor, the C_ℓ are multiplied by the same factor. Regarding the spectral index, if n_s varies by a small amount ($n_s + \alpha$), the small-scales C_ℓ change by a factor $(\ell/\ell_\star)^\alpha$ where ℓ_\star is the multipole associated with the pivot scale [109].

Unfortunately, this effect is degenerated with that of optical depth due to reionization. As we have seen in section 4.1.3, reionization leads to an attenuation of the small scale anisotropies, the ones within the horizon at reionization ($\ell \gtrsim 100$). This is why the effect of increasing τ can be equivalent to a change of A_s and n_s . This is shown in Figure 7.7 (left).

This degeneracy can be broken with polarization measurements because the optical depth can also be constrained with the reionization bump at large scale in the polarization power spectrum, described in section 4.2.6. This is shown in Figure 7.7 (right) for the EE spectrum. Note that detecting the

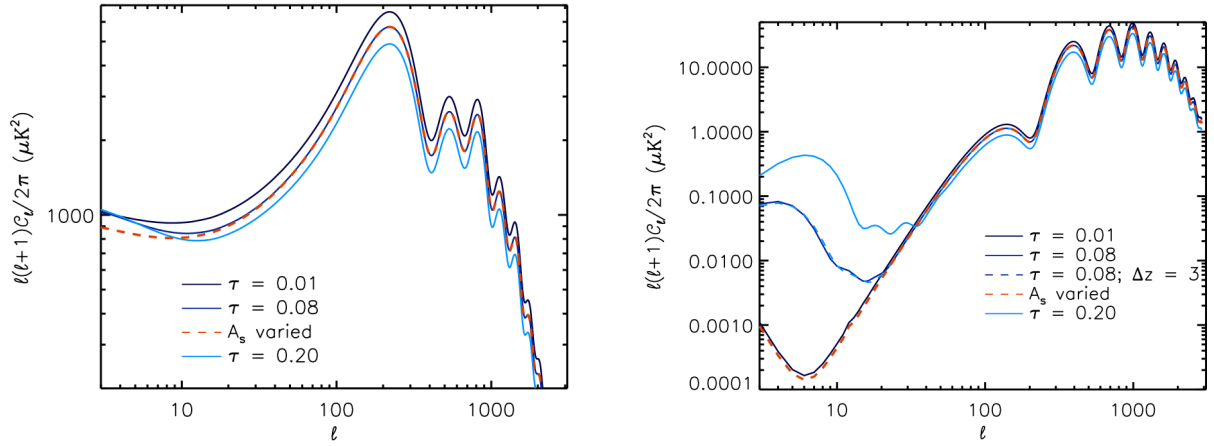


Figure 7.7: *Left*: Effect of the reionization optical depth on the temperature angular power spectrum, degenerated with A_s as shown in red. *Right*: Effect on the EE polarization power spectrum, causing a bump at low ℓ . Taken from [148].

reionization bump requires full sky observation in order to have access to large angular scales ($\theta \sim 7^\circ$).

Richer variations: $\Omega_b h^2$ and $\Omega_c h^2$

The variation of these two densities are considered keeping an Euclidean space by compensating the change of the matter density through the cosmological constant. We first consider the variation of the baryon density $\Omega_b h^2$, shown in Figure 7.8 (left). The most visible effect is the increase of the ratio between odd and even peak heights when $\Omega_b h^2$ is large. A second effect is that when $\Omega_b h^2$ is large, the diffusion length λ_D , defined in equation 4.16, decreases (or k_D increases) and this moves damping to smaller angular scales. Finally, changing the CDM density $\Omega_c h^2$ has a similar effect as changing the baryon density. It is shown in Figure 7.8 (right) where the Planck results with error bars (blue points) are also added. The rich variation induced by $\Omega_b h^2$ and $\Omega_c h^2$ allows to constraint these two parameters with a high significance.

BB angular power spectrum

Following equations 7.43 and 7.49, we see that the primordial angular BB power spectrum is directly proportional to the tensor-to-scalar ratio r (for A_s fixed). This is shown in Figure 7.9 where the total BB spectrum (lensing and primordial) is represented for different values of r . The line for $r = 0$

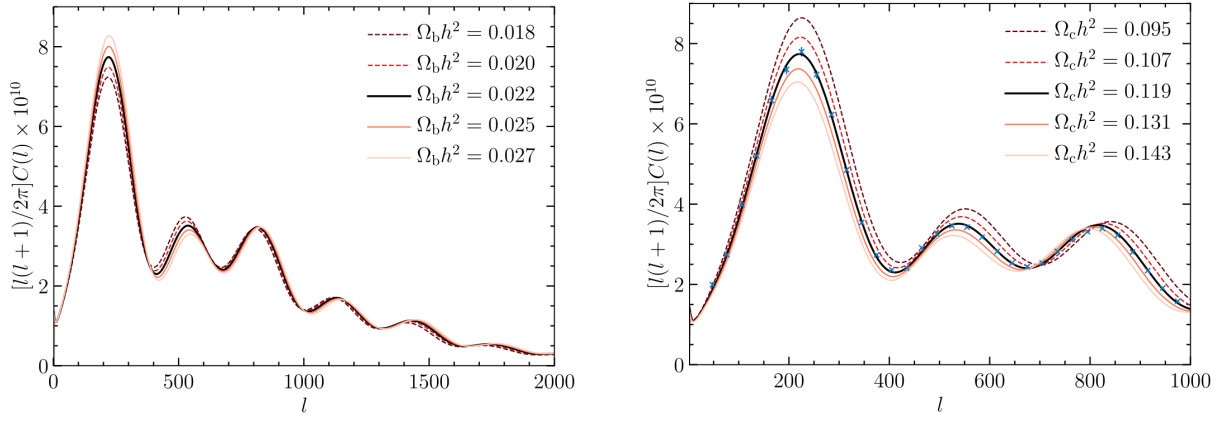


Figure 7.8: *Left*: Effect of varying the baryon density Ω_b on the TT power spectrum. *Right*: Effect of varying the CDM density Ω_c . The Planck result is represented in blue for illustration purpose. Taken from [109].

corresponds to the lensing signal only. It is clear that the primordial signal is accessible at large scales (low ℓ) and this is even more true when r decreases. Lensing B -modes have first been detected by

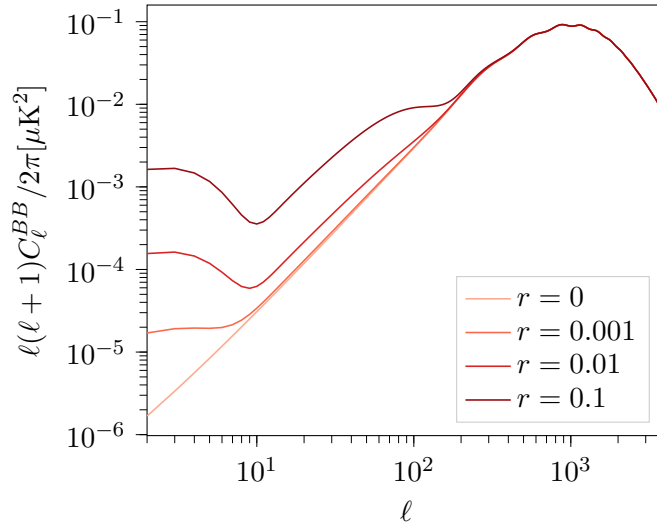


Figure 7.9: Total BB power spectrum (primordial + lensing) for r between 0 and 0.1. The case where $r = 0$ shows the lensing B -mode signal. The bump at low ℓ from reionization is clearly visible (plot done with CAMB).

the South Pole Telescope [187] in 2013. Since then, many experiments have measured it, as shown in Figure 4.14. However, primordial B -modes have not been detected yet. In 2018, BICEP2/Keck experiment set an upper limit at $r_{0.05} < 0.07$ at 95% confidence, including the data up to 2015 [149] where the index on r is the pivot scale $k_* = 0.05 \text{ Mpc}^{-1}$ considered in the analysis. Very recently, they published a new limit, including the 2018 observing season: $r_{0.05} < 0.036$ at 95% confidence. This is the current best upper limit [162]. In addition, we can mention an analysis that obtained $r_{0.05} < 0.044$ at 95% confidence by combining Planck with BICEP2-Keck 2015 data [150]. The complete results of Planck to constrain inflation parameters are presented in [103].

Cosmological constraints with the SZ effect

Let us finally mention that the detection of galaxy clusters thanks to the SZ effect allows to constrain cosmological parameters such as Ω_m , σ_8 , the equation of state of dark energy with w , the sum of the neutrino masses and H_0 [151].

7.6.3 Others cosmological probes

CMB is a powerful probe for cosmology but it is far from being the only one! Here we give four examples of observations which are currently used to test the Λ CDM model. The number of probes, so far in agreement with the Λ CDM model, is actually impressive. So the list is of course not exhaustive.

Baryon Acoustic Oscillation (BAO)

The acoustic oscillations occurring in the primordial plasma are imprinted in the CMB but also in the matter distribution. The acoustic scale at recombination, around 150 Mpc today, translates in a preferred scale for distances between galaxies. This leads to the so-called BAO peak in the 2-point correlation function which is the excess probability of finding one galaxy at a particular distance from another. The physics of BAO is introduced in a very pedagogical manner in [57] and one can refer to [83] for precision. The measurement of the BAO peak requires large galaxy surveys such as the Sloan Digital Sky Surveys (SDSS) [84] or the Dark Energy Spectroscopic Instrument (DESI) [85].

BAO are a major probe for cosmology, especially to constrain the dark energy equation of state. Indeed, the BAO acoustic peak defines a standard ruler and contrary to the CMB, galaxies can be observed at different redshifts, so it allows to constrain the dark energy along the time. It is also amazing to realize that we do find in the galaxy distribution ($z \sim 0.5$) the very same acoustic peaks we see in the CMB at $z \simeq 1100$!

Type-Ia supernovae

Distance measurement in cosmology is a tricky point. In section 3.2.1, we already mentioned Cepheid stars which can be used to measure distances. They are standard candles in the sense that we know their intrinsic luminosity so we can have their distances. A second type of objects that can be used as standard candles is type-Ia supernovae. Cepheid stars are visible in our galaxy and nearby ones up to few Mpc while type-Ia supernovae are visible up to $z \sim 1$.

Type-Ia supernovae occur in binary systems where one of the stars is a white dwarf. The white dwarf accretes mass from its companion until it reaches the critical Chandrasekhar mass [47] (about 1.44 solar masses) and explodes [86]. Thanks to this trigger mass, type-Ia supernovae are expected to be very similar to each other. They have a characteristic light curve, i.e. evolution of the luminosity as a function of time. This was first recognized by Phillips in 1993 [87]. The advantage compared to cepheids is that they give access to higher redshifts thanks to their very bright luminosity. This is essential for constraining matter density Ω_m and the dark energy equation of state w [88]. Knowing that type-Ia supernovae only occur about one per century per galaxy, large deep field surveys are needed. For instance, the Vera Rubin Observatory plans to detect around ten thousand type-Ia supernovae with well measured light curves [89]. As mentioned in section 7.6.1, nearby type-Ia supernovae can also be used to constrain the Hubble constant [80].

Lyman- α forest

As we have seen in section 4.1.3, light emitted by quasars gives information about the ionization rate of the intergalactic medium and about the reionization period. This is because photon absorption requires neutral hydrogen. By observing the emission spectrum of quasars, we see numerous absorption lines called the Lyman- α forest. This is due to the expansion of the universe: photons emitted with wavelength λ_e get redshifted to $\lambda_e(1+z)$ and are absorbed when they reach 121.5 nm. It was first detected in 1971 [90].

This measurement allows to constrain the matter distribution, especially the baryon density Ω_b and σ_8 . Note that the BAO peak is also detected in the spatial correlation of the Lyman- α spectra. For detail, one can refer to the reviews [91], [92].

Gravitational waves

The first direct detection of gravitational waves in 2015 by the LIGO interferometer [93] opened a new era: multimessenger astronomy and cosmology. Combining electromagnetic observations with

gravitational waves is clearly a major step for the field. Adding one day the observation of the neutrino counterpart would be great!

Regarding the Λ CDM model, gravitational waves can also constrain its parameters. In 2017, the merge of a binary neutron stars was detected, and for the first time with its electromagnetic counterpart too [94]. This measurement allowed to constrain the Hubble constant to $H_0 = 69_{-8}^{+16} \text{ km s}^{-1} \text{ Mpc}^{-1}$ [95]. Of course this is the very beginning and the accumulation of events in the next future will reduce error bars.

Finally, as discussed earlier, inflation generates gravitational waves in the primordial plasma. This waves are still present and contribute to the stochastic gravitational wave background that the LISA space-based interferometer may detect in the future [96].

7.7 Constraining r with QUBIC

We have seen how the CMB can provide fundamental probes on the primordial universe and we have introduced all the theoretical concepts which drive the QUBIC project. In this section, we will see how QUBIC should help to constrain cosmic inflation models. Indeed, QUBIC was designed to put constraints on the tensor-to-scalar ratio r , trying to detect the tiny B -mode polarization signal. This section presents the forecasts of the experiment that were produced for paper [1] and [9]. This is my personal work, realized in collaboration, mainly with Martín Gamboa and Jean-Christophe Hamilton.

7.7.1 Description of the simulations

We have performed simulations for a three-year observation of the sky using the QUBIC Full Instrument (FI) with realistic instrumental noise [7], [8] and with atmospheric background noise, assumed to be stable. We have used the “Fast Simulator” described in section 6.3.2 to produce thousands of realizations of the noise in the maps incorporating the peculiar noise structure: spatial variations of the noise as a function of coverage as well as spatial and sub-band correlations. The parameters of our simulations are summarized in Table 7.2.

Parameter	Value TD	Value FI
Detector noise $[\text{W}/\sqrt{\text{Hz}}]$	2.05×10^{-16}	4.7×10^{-17}
Atmosphere ¹ temperature [K]	270	270
Atmosphere emissivity ¹ at 150 GHz	0.081	0.081
Photon noise $[\text{W}/\sqrt{\text{Hz}}]$	2.6×10^{-17} (150 GHz)	3.1×10^{-17} (150 GHz), 1.17×10^{-16} (220 GHz)
Total noise $[\text{W}/\sqrt{\text{Hz}}]$	2.06×10^{-16} (150 GHz)	5.7×10^{-17} (150 GHz), 1.26×10^{-16} (220 GHz)
Cumulated observation time [years]	1	3
r upper-limit (68% C.L., No FG)	-	0.021 (150 GHz), 0.023 (220 GHz), 0.015 (Combined)

¹The atmosphere is considered perfectly stable.

Table 7.2: Main instrumental and simulation parameters used in our computations. The noise value for TD is measured from the TES calibration data [8] while that for the FI is the intrinsic TES noise and assumes reduction of the noise aliasing in the readout chain found in the TD. We have used average atmospheric parameters at 50 degrees elevation accounting for maximal seasonal and diurnal variations. This corresponds to negligible change for the total noise for the TD, 5% and 20% for the FI at 150 and 220 GHz respectively.

For each realization, we have used NaMaster⁸ [209] to compute pure TT , EE , TE and BB power spectra on the residual maps (therefore noise-only maps) in order to compute the expected noise on

⁸<https://github.com/LSSTDESC/NaMaster>

the power spectra. Exploring various values for the minimum multipole ℓ_{\min} , the size of the multipole bins Δ_ℓ and minimum value of the relative coverage (normalized to 1 at maximum) of the sky that defines the region of the sky we keep for analysis, Cov_c , we have found the best configuration to be $\ell_{\min} = 40$, $\Delta_\ell = 30$ and $\text{Cov}_c = 0.1$ (keeping all pixels with relative coverage above 0.1) at 150 GHz. We have kept the same configuration for the 220 GHz for the sake of simplicity.

Comment about the atmospheric noise model

The atmospheric background noise has been obtained from measurements performed over 3 years at the QUBIC site in Argentina from a tipper at 210 GHz used for the LLAMA radiotelescope⁹ to be installed near QUBIC. Atmospheric background is averaged over the 9 best months of the year and corresponds to an atmospheric temperature of 270 K and emissivities 0.081 and 0.138 at 150 and 220 GHz respectively for an average observation elevation of 50 degrees.

Changing the atmospheric parameters according to maximal diurnal and seasonal variations induces 15 and 25% change in the photon noise at 150 and 220 GHz respectively (with respect to the numbers given in Table 7.2). This corresponds to a negligible change of sensitivity for the TD because our noise is dominated by that of the detectors. For the FI, the change in the total noise is 5% at 150 GHz and 20% at 220 GHz.

7.7.2 QUBIC Full Instrument expected performance

We present the expected sensitivity on the “effective” tensor-to-scalar ratio r of the sky. Forecasts are made by simulating a sky without any foregrounds. We call it “effective” in the sense that our simulations are done without any component separation assumption, so, in the presence of foregrounds, r would include the non primordial B -modes produced by astrophysical foregrounds.

As remarked in section 5.2.7, measuring the RMS of a map in the case of non-white noise is meaningless, and the actual measurement of the effective depth of our maps is done in ℓ -space. The resulting uncertainties from the Monte-Carlo on the BB polarization power spectrum (ΔD_ℓ) are shown in the left panel of Figure 7.10.

We have also displayed theoretical B -mode power spectra D_ℓ (including lensing) for $r = 0, 0.01$, and 0.044 (current best upper limit [150]). Besides the QUBIC Monte Carlo error bars, we also plot the expected shape for white noise (dotted lines) and for the QUBIC noise (dashed lines) from Figure 5.6. In both cases the theoretical error-bars are obtained through the formula 5.43. In this case, the fraction of the sky used for analysis is $f_{\text{sky}} = 0.015$, the width of the ℓ -space binning is $\Delta\ell = 30$. We performed a fit of the above noise normalization for QUBIC to our Monte-Carlo error-bars leading to 2.7 and 3.7 $\mu\text{K.arcmin}$ at 150 and 220 GHz respectively. This is shown as dashed lines in Figure 7.10. However these numbers are hardly comparable with the case of a standard imager for which the noise is white: for each frequency we overplot the expected shape for white noise with the same normalization. The significant noise reduction with respect to the white noise case is particularly visible at the scales of the recombination peak near $\ell = 100$, giving QUBIC an enhanced sensitivity at those scales. At scales larger than the separation between peaks in the synthesized beam however, the error-bars increase sharply. The first bin at 220 GHz exhibits significantly larger error-bars for all spectra. This is not surprising as we have kept the same $\ell_{\min} = 40$ for both channels. In reality, the multiple-peaked shape of our synthesized beam is such that we have little sensitivity to multipoles corresponding to angular scales larger than the distance between the peaks (8.8 and 6 degrees at 150 and 220 GHz respectively). As a result, the optimal ℓ_{\min} at 150 GHz is slightly too low for 220 GHz, resulting in larger error-bars for the first bin. This will be optimized when analyzing real data.

The right panel of Figure 7.10 shows the posterior on the tensor-to-scalar ratio which, in the absence of foregrounds, was the only free-parameter for this power-spectrum-based likelihood (simple χ^2 accounting for sample variance [211]) with all parameters except r fixed to their fiducial values¹⁰. We calculate the likelihood at 150 and 220 GHz separately as well as jointly. These simulations show

⁹<https://www.llamaobservatory.org/>

¹⁰We have used a fiducial cosmology with parameters [$h = 0.675$, $\Omega_b h^2 = 0.022$, $\Omega_c h^2 = 0.122$, $\Omega_k = 0$, $\tau = 0.06$, $A_s = 2e - 9$, $n_s = 0.965$].

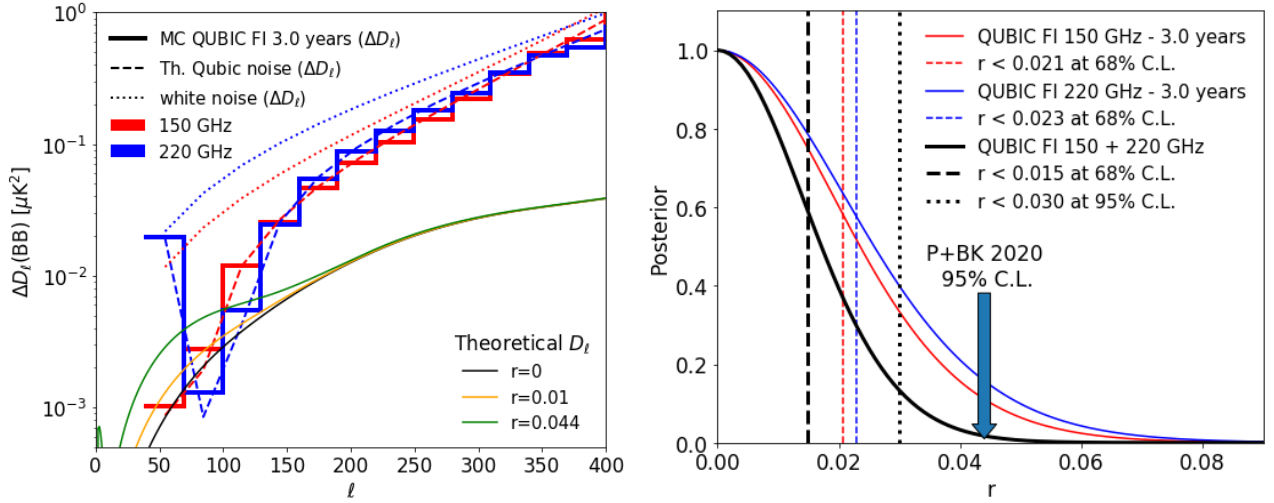


Figure 7.10: *Left:* BB power spectrum error-bars ΔD_ℓ on $D_\ell = \ell(\ell + 1)C_\ell/2\pi$ on residual maps from the Fast-Simulator Monte-Carlo in the absence of foregrounds, atmospheric fluctuations and instrument systematic effects for an integration time on the sky of three years from the site in San Antonio de los Cobres, Argentina. As these are calculated on residual maps, they do not incorporate sample variance and only refer to the instrumental noise. The reduction at low- ℓ of our error-bars with respect to theoretical white-noise (dotted lines) is clearly visible and in agreement with the expected shape from the 2pt correlation function in Figure 5.6 (dashed lines). The difference in the first bin is discussed in the text. *Right:* Posterior likelihood on the r (assuming no foregrounds) using QUBIC FI (two bands) with three years integration on the sky (including both noise and sample variance). The Planck+Bicep/Keck constraint from [150] is shown with the blue arrow.

that QUBIC has the statistical power (without foregrounds, atmospheric fluctuations and systematics) to constrain the B -modes down to a tensor-to-scalar ratio $r < 0.015$ at 68% C.L. ($r < 0.03$ at 95% C.L.) with three years integration on the sky from our site in Argentina.

In the presence of foregrounds, the numbers above are to be understood as our statistical sensitivity to effective B -modes including the contribution from primordial tensors as well as dust polarization. Component separation has not been included in the current forecasts and will be investigated in details in the next future.

7.7.3 Spectral imaging and constraints on r

We now come back to the spectral imaging technique studied in chapter 6. The division of the wide band into a number of sub-bands for spectral imaging could have a detrimental effect on the estimate of the tensor-to-scalar ratio r and this is what we want to quantify in this section. On the one hand, we would certainly like to make as many sub-bands as possible in order to constrain the foreground spectra in a very precise manner. However, on the other hand, there is an upper-limit to the achievable number of sub-bands, when the angular distance between peaks in the synthesized beams at different frequencies becomes smaller than the peak width (angular resolution), as explained in section 6.1.2. We therefore expect the performance of spectral imaging to degrade when projecting data onto too many sub-bands. In fact, even for a small number of sub-bands, spectral imaging cannot be strictly optimal because the synthesized beams at different sub-frequencies do not form an orthogonal basis. We therefore expect a certain loss in signal-to-noise ratio when performing spectral imaging. The higher the number of reconstructed sub-bands is, the more overlap there is between the synthesized beams at each sub-frequency. This results in stronger degeneracy between sub-bands, hence a higher noise in the reconstruction. This is the price to pay for improved spectral resolution. As a result, one needs to find the best balance between performance and spectral resolution for a given scientific objective.

Thus, we study how the tensor-to-scalar ratio r is constrained as a function of the number of

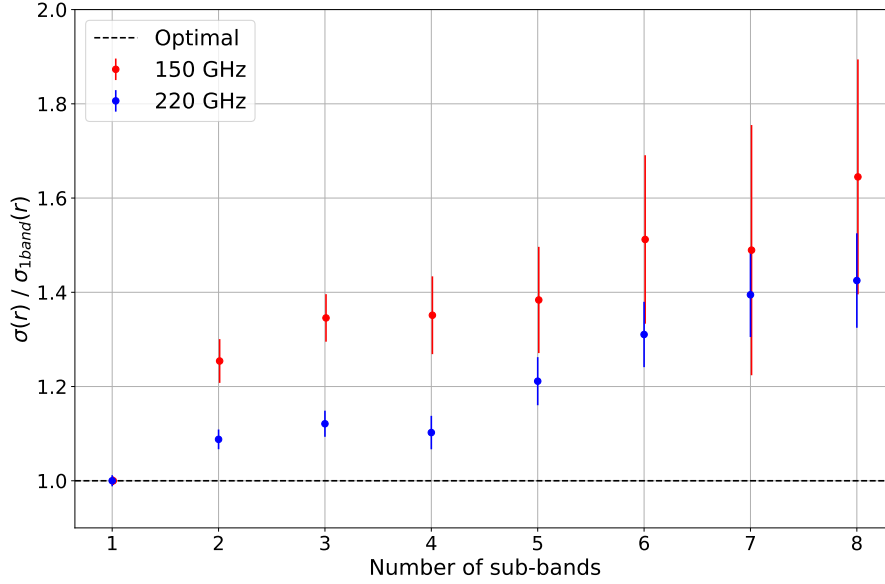


Figure 7.11: Uncertainties (68% CL upper limits) on the tensor-to-scalar ratio r obtained by combining an increasing number of sub-bands, normalized to that of one band, for a pure $r = 0$ CMB (with lensing). The slow increase of the uncertainty on r with the number of sub-bands illustrates the moderate sub-optimality of spectral imaging and shows that we can use up to 5 sub-bands with only 40% degradation at 150 GHz (and only 20% degradation at 220 GHz). It is possible to achieve 8 sub-bands but with more significant degradation.

sub-bands N_{rec} . The sky model is a pure CMB sky, including lensing but no Galactic foregrounds, with $r = 0$. For that purpose, we project simulated data onto an increasing number of sub-bands N_{rec} , calculate the corresponding IBCS and in each case we compute a likelihood to estimate the tensor-to-scalar ratio r combining all sub-bands accounting for their cross-correlations. From this method, we get the error on r at 68% confidence level for each number of sub-bands. This is presented in figure 7.11. We normalize by the case of “spectral imaging” with just one band. Error bars are obtained from Monte-Carlo simulations, varying the data in the likelihood according to their diagonal uncertainties. As expected, we observe a moderate degradation due to spectral imaging in the sense that the constraints on r become less stringent when the number of sub-bands is greater than one. This degradation slowly evolves from 25% to 40% at 150 GHz and from 10% to 20% at 220 GHz when the number of sub-bands evolves from 2 to 5. The better performance at 220 GHz is not a surprise as our horns are slightly multimoded at 220 GHz (see [6] for details) resulting in a flatter primary beam, which, in turn, favours spectral imaging because multiple peaks of the synthesized are higher in amplitude. It is possible to project onto as many as 8 sub-bands with a corresponding performance reduction due to the fact that synthesized beam peaks become too close with respect to their width, as explained in section 6.1.2.

This study demonstrates that, although not strictly optimal from the noise point of view, spectral imaging performance remains close to optimal for up to 5 bands providing extra spectral resolution. This can be key for constraining foreground contamination with realistic models for which the spectrum might not be a simple power law. The appropriate balance between spectral resolution and noise performance can be adjusted for each specific analysis thanks to the fact that spectral imaging is done entirely in post-processing.

7.7.4 Ability to recognize the presence of dust residuals

In this section, we assume that the component separation has already been done and we show that spectral imaging gives the ability to detect the presence of dust residuals at the tensor-to-scalar ratio likelihood level. Here, we have considered the FI after 3 years of sky integration in the 220 GHz wide band split into 2 sub-bands.

Using the library PySM3 [222], we simulate 2 sub-band maps containing dust residuals made with a fraction f_{dust} of a dust map (d1 PySM model) added to a pure CMB sky with $r = 0$. From those 2 maps, we compute the 3 *BB* Inter-Band Cross Spectra (IBCS) at effective frequencies $\nu_{\text{eff}} = \sqrt{\nu_i \nu_j}$ where ν_i and ν_j are the central frequencies of the 2 sub-bands. Then, we perform a likelihood to estimate the tensor-to-scalar ratio r assuming a pure CMB model (no component separation). The error included in the likelihood estimation is the full multipole-space covariance matrix between the 3 *BB* IBCS and the bins in ℓ of the spectra obtained with Monte-Carlo simulations. As the sky also contains dust residuals, the likelihood is biased leading to a detection of non-zero tensor-modes which we called r_{dust} . Figure 7.12 shows the detected r_{dust} value as a function of the dust residual fraction.

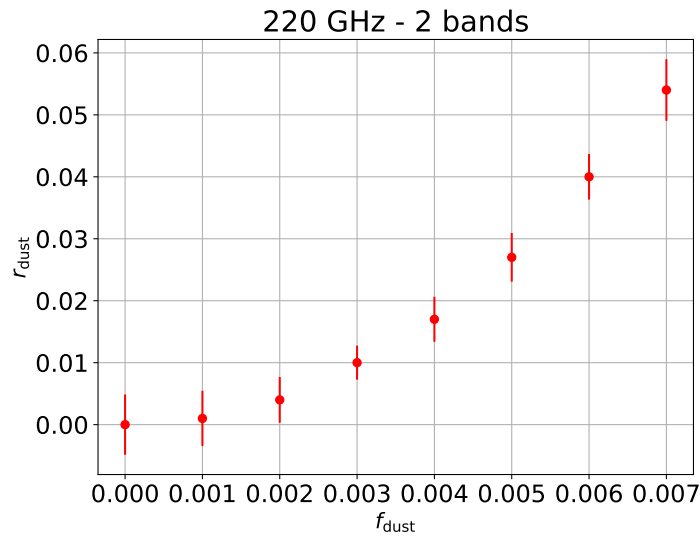


Figure 7.12: Detected r_{dust} value as a function of the dust residual fraction f_{dust} . Dots corresponds to the positions of the maximum of each likelihood and error bars are the sigma at 68%CL.

Instead of having a global estimation of r_{dust} over all IBCSs, we can compute a likelihood for each IBCS separately. This gives an estimate of r_{dust} for each effective frequency. As the dust emits like a modified black body spectrum, increasing with frequency, the r_{dust} estimate increases with frequency. On the contrary, for pure primordial B-modes, the estimated tensor-to-scalar ratio does not depend on frequency. Measuring the evolution of the estimated r_{dust} as a function of frequency within the band using spectro-imaging is therefore a powerful tool to estimate our dust contamination independently of any dust modeling.

In Figure 7.13, we show an example where we are able to distinguish the case of pure primordial tensor modes with $r = 0.05$ from a sky with no primordial tensor-modes ($r = 0$) but 0.7 % dust residuals. Indeed, in the first case, the measurement of r_{dust} is constant with the frequency while the presence of dust leads to a slope that is detected at the 2.9σ level. We want to underline here that the value 0.7 % does not have any particular meaning, it is simply the small fraction of dust residual that leads to the detection of a spurious r of the order of 0.05. This test shows that QUBIC is able to detect it in the data thanks to spectral imaging.

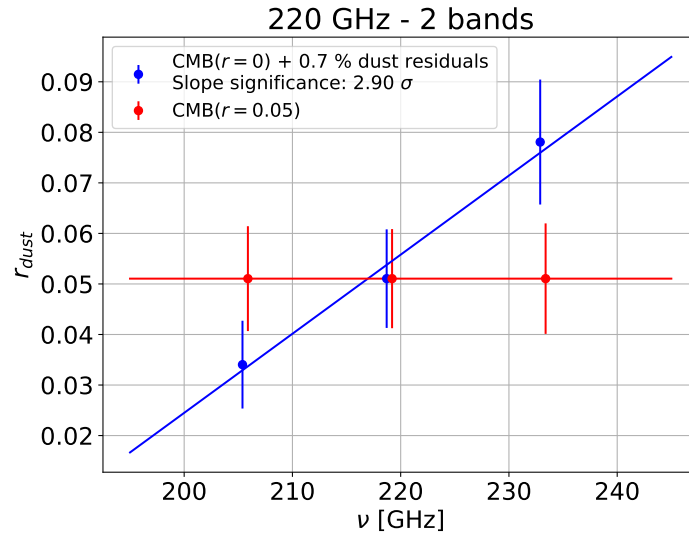


Figure 7.13: Constraints on the tensor-to-scalar ratio r , from a Likelihood analysis, for a sky containing CMB and dust residuals. We consider the 220 GHz wide band split into two sub-bands. This leads to three Inter-Band Cross Spectra (IBCS) at effective frequencies $\nu_{\text{eff}} = \sqrt{\nu_i \nu_j}$ where ν_i and ν_j are the central frequencies of the two sub-bands. We can distinguish between a pure CMB sky with $r = 0.05$ and a sky with CMB ($r = 0$) but having 0.7 % dust residuals. In the first case (red), the measurement of r_{dust} is constant with the frequency while the presence of dust leads to a slope (blue) which we detect at the 2.9σ level. In that case, the likelihood estimation was performed on each IBCS separately using the full multipole-space covariance matrix (in contrast with Figure 7.10 where we have only used the diagonal in order to remain conservative).

Conclusion In this chapter I first presented cosmic inflation: description, motivations for it and experimental evidences. I also made the link between the CMB angular power spectrum that we observe and the primordial power spectrum from inflation. This allowed me to introduced the tensor-to-scalar ratio, directly connected to the energy scale of inflation, and which is the quantity that QUBIC aims at constraining.

In the last section, I presented forecasts on r for the QUBIC instrument. We have shown that QUBIC has the statistical power (without foregrounds, atmospheric fluctuations and systematic effects) to constrain the B -modes down to a tensor-to-scalar ratio $r < 0.015$ at 68% C.L. ($r < 0.03$ at 95% C.L.) with three years integration on the sky from our site in Argentina.

We have also quantified the loss of statistical performance for the measurement of the tensor-to-scalar ratio when increasing the number of sub-bands and have shown it to be moderate up to 5 sub-bands. In summary, spectral imaging improves spectral resolution within a wide physical band, while nearly preserving the optimal performance of the analysis. It may therefore become a key technique for detecting the elusive B -mode polarization of the CMB. In addition we have shown that spectral imaging provides a way to detect the presence of dust residuals.

General conclusion

QUBIC is part of the global effort made in the scientific community to detect the B -mode signature from cosmic inflation imprinted in the CMB polarization. In order to target primordial B -modes, QUBIC will focus on large angular scales from 0.5° to 8° , roughly corresponding to multipoles from $\ell \simeq 40$ to 400. The tensor-to-scalar ratio is a direct measurement of the energy scale during inflation. Measuring it or at least decreasing the current upper limit $r < 0.044$ [150], would tightly constrain the inflation models.

The QUBIC collaboration made the choice to build an instrument with a non standard design. The concept of bolometric interferometry offers new capabilities that need to be explored and understood. In this manuscript, I report the work I have carried out between September 2018 and August 2021. Along those three years, we considerably improved our understanding of bolometric interferometry, both thanks to the calibration measurements and to the development of the full simulation pipeline. My contributions include calibration data taking and data analysis as well as pure simulations up to the estimation of cosmological parameters.

Review of the main results

In chapter 1, I presented the working principle of the QUBIC instrument. I introduced the concept of bolometric interferometry in a pedagogical way, focusing on the optical part. I chose to describe the instrument as a classical imager having a very specific point spread function caused by the horn-array placed at the entrance of the telescope. It is also possible to consider QUBIC as an interferometer, in the same way that any imager is actually an interferometer because each point of the aperture can be seen as a source re-emitting the radiation, equivalent to the horns. In this way, the formation of an image on the focal plane can be seen as the result of constructive interference between all re-emitted radiation.

I ended the first chapter with the optical verification of the mirror alignment for which I was responsible. This technique developed on the TD instrument will be soon re-used for the upgrade. The FI has much more reflective mirrors in the visible light domain than the TD which will make the optical alignment more accurate.

An important part of my thesis is dedicated to calibration data taking and data analysis, and this is presented in chapter 2. This must be seen as a first step toward a full self-calibration of the instrument.

I first updated the formalism developed by Marie-Anne Bigot-Sazy to the current instrument design. This led me to justify the choice of the polarimeter design made to limit the cross-polarization and the leakage from intensity to polarization.

Regarding the calibration in the laboratory, I worked on two main measurements: the synthesized beams of each detector by scanning a calibration point source and the interference fringes on the focal plane observed by closing at maximum two horns simultaneously. In both cases, I developed optical simulations in order to compare with real data. Thanks to those simulations, I was able to identify with an absolute numbering the peaks of the synthesized beam of each detector. This is a major step for the map-making of real data which requires an accurate knowledge of the synthesized beam peak positions. Regarding the fringes, I developed a complete procedure for data taking and data analysis. The observation of interference fringes is crucial for self-calibration which relies on the comparison of equivalent baselines. Thanks to an optical model, I was able to develop a fit of the fringe images that computes analytically the inter-calibrations of the detector gains.

The heart of my thesis work was to characterize the technique of spectral imaging offered by bolometric interferometry. This work was realized in close collaboration with Martín Gamboa but I led most of the developments. Spectral imaging makes possible to split, in post processing, the wide-band observations into multiple sub-bands achieving spectral resolution. I have studied carefully the characteristics of the noise, especially the spatial correlations in the maps and the correlation between sub-bands. We have also introduced the concept of Frequency Point Spread Function (FPSF) in the particular context of bolometric interferometry. I have quantified the loss of statistical performance for the measurement of the tensor-to-scalar ratio when increasing the number of sub-bands and have shown it to be moderate up to 5 sub-bands. It may therefore become a key technique to mitigate astrophysical foreground contamination. Moreover, I have shown that spectral imaging offers the possibility to detect the presence of dust residuals in the signal.

I have also worked on end-to-end simulations in order to assess the capability that QUBIC has for constraining r . I have shown that QUBIC has the statistical power (without foregrounds, atmospheric fluctuations and systematic effects) to constrain the B -modes down to a tensor-to-scalar ratio $r < 0.015$ at 68% C.L. with three years integration on the sky from our site in Argentina.

Data analysis perspectives

Regarding data analysis and simulations, several points on which I worked during my PhD need to be pursued. I give some of them in the following.

In order to fully characterize the potential of spectral imaging, the first thing to do is to develop component separation techniques. Those methods need to be specifically tuned for QUBIC which has two wide frequency bands centered on 150 and 220 GHz, split in small sub-bands. The main difference from others experiments, is that the noise is correlated between sub-bands as they are built in post processing thanks to spectral imaging. The integration of component separation techniques in the QUBIC pipeline will also help to refine forecasts on the measurement of r .

Still focusing on spectral imaging potential, I plan to run simulations considering a single focal plane that would integrate the signal from 130 to 250 GHz. This fits in the perspective of upgrading the instrument. Indeed, simulations suggest that it is possible to replace the two FI focal planes by a single focal plane, eliminating the need for a dichroic and reducing the overall complexity of the instrument.

Also, this thesis has highlighted concepts specific to bolometric interferometers that could be studied in a more detailed way. I am thinking of the FPSF and to the spatial correlations of the noise due to the multiple peak synthesized beam. In particular, it would be interesting to see how those properties evolve with the number of reconstructed sub-bands.

Regarding my work on calibration data, we will soon need to apply map-making on real data. The analysis I did with the synthesized beam maps must be pushed forward. Moreover, this could also be used to inter-calibrate the detectors which is a major issue for data analysis. This will also be an important step toward a full self-calibration procedure that needs to be designed. The analysis of the interference fringes should also be pursued. In particular, it would be very helpful to apply it on a more complete data set with a large number of baselines.

Finally, I think it would make a lot of sense to include the inter-calibration of the detectors directly in the map-making algorithm. As they are obtained analytically using linear algebra, it should be possible to fit everything at the same time.

Concerning data analysis, I would like to end on a general thought. Firstly seen as an interferometer, QUBIC is now treated like a standard imager. It is convenient to copy the concepts and data analysis tools developed for imagers: map-making, power spectrum estimation, component separation... Adapting those tools to QUBIC is already a challenge but it is for sure much easier than developing everything from scratch. However, designing specific tools for bolometric interferometry will be more efficient. One idea that will be pursued in the collaboration is to develop a component based map-making. Indeed, all the spectral information is present in the TOD, so we should be able to use it during the map-making and produce one map for each sky component. At the end, this seems much more straightforward than what we currently do: spectral map-making in frequency sub-bands before applying imager component separation techniques, either on the frequency maps or on the power

spectra. That would fully exploit the capabilities of bolometric interferometry.

Next steps for the QUBIC instrument

The instrument has been sent to Argentina and will be installed on the observation site after a short calibration campaign in the laboratory which has already started. The first light from the sky is expected in 2022. We will continue to use the technical demonstrator as a proof of concept. In particular, testing spectral imaging on bright galactic regions, will be very decisive regarding the potential of this method. The full self-calibration will also be developed and tested on the TD instrument. The upgrade to the FI should happen after one year of data taking with the TD. It will mainly consist in increasing the mirror size, the horn-array size and to complete the focal plane. FI mirrors and horns are already delivered and the detectors are currently being built.

Annexes

A.1 Demonstration of the Huygens-Fresnel principle

We will demonstrate the Huygens-Fresnel principle in the case of paraxial optics. We start from equation 1.11, reproduced below where $f_0(x, y)$ is the amplitude of a monochromatic wave in the plane $z = 0$, expanded in a Fourier series (see section 1.2.1 for the notations). It can be any type of wave, not especially a plane wave.

$$f_0(x, y) = \int_{-\infty}^{\infty} \int_{-\infty}^{\infty} \frac{1}{\lambda^2} \hat{f}_0\left(\frac{\alpha}{\lambda}, \frac{\beta}{\lambda}\right) e^{\frac{2i\pi}{\lambda}(\alpha x + \beta y)} d\alpha d\beta \quad (63)$$

Equation 63 is a continue sum of plane waves. So when it propagates, we have to multiply each plane wave by a phase shift $\exp\left\{\frac{2i\pi}{\lambda}\gamma z\right\}$ so the amplitude in the plane z is given by

$$f_z(x, y) = \int_{-\infty}^{\infty} \int_{-\infty}^{\infty} \frac{1}{\lambda^2} \hat{f}_0\left(\frac{\alpha}{\lambda}, \frac{\beta}{\lambda}\right) e^{\frac{2i\pi}{\lambda}(\alpha x + \beta y + \gamma z)} d\alpha d\beta. \quad (64)$$

We consider a small angle between the wave vector and the optical axis z (i.e. $\theta_x, \theta_y \ll 1$). Under this hypothesis, we have $\alpha \simeq \theta_x$, $\beta \simeq \theta_y$ and $\gamma = 1 - \frac{\alpha^2 + \beta^2}{2}$. So we can write

$$f_z(x, y) = e^{\frac{2i\pi z}{\lambda}} \int_{-\infty}^{\infty} \int_{-\infty}^{\infty} \frac{1}{\lambda^2} \hat{f}_0(u, v) e^{-i\pi\lambda z(u^2 + v^2)} e^{2i\pi(ux + vy)} d\alpha d\beta \quad (65)$$

with the substitution $\alpha = \lambda u$, $\beta = \lambda v$. This is the expression of an inverse Fourier transform:

$$f_z(x, y) = e^{\frac{2i\pi z}{\lambda}} \mathcal{F}^{-1} \left[\hat{f}_0(u, v) \hat{g}(u, v) \right] \quad (66)$$

where we defined $\hat{g}(u, v) = e^{-i\pi\lambda z(u^2 + v^2)}$. Finally, we see that this can be written using a convolution product:

$$f_z(x, y) = e^{\frac{2i\pi z}{\lambda}} f_0(x, y) \otimes g(x, y) \quad (67)$$

with $g(x, y) = \mathcal{F}^{-1}[\hat{g}(u, v)]$. This calculation can be done using the theorem of the residus and it gives

$$g(x, y) = \frac{1}{i\lambda z} e^{\frac{i\pi}{\lambda z}(x^2 + y^2)}. \quad (68)$$

A.2 Cosmic variance and some statistics for a normal distribution

We will start with some statistics results and then we will apply it to the case of the cosmic variance. We consider a random variable x which follows a normal distribution with mean μ and standard deviation σ . By definition, we have

$$\langle x \rangle = \mu \quad \text{and} \quad \text{Var}(x) = \langle [x - \langle x \rangle]^2 \rangle = \langle x^2 \rangle - \langle x \rangle^2 = \sigma^2 \quad (69)$$

where $\text{Var}()$ stands for the variance.

The cosmic variance is the variance of the power spectrum C_ℓ which is itself the variance of the $a_{\ell m}$ coefficients that follow a normal distribution. This is why we will give a non biased estimator of the variance σ^2 and we will compute its own variance. But first, let us start with an estimator of the mean μ .

The sample mean m : Considering N samples x_i , the sample mean m is defined as

$$m = \frac{1}{N} \sum_{i=1}^N x_i. \quad (70)$$

It is straightforward to show that the mean of m is μ :

$$\langle m \rangle = \left\langle \frac{1}{N} \sum_i x_i \right\rangle = \frac{1}{N} \sum_i \langle x_i \rangle = \frac{1}{N} \sum_i \mu = \mu. \quad (71)$$

So the sample mean m is a non biased estimator of μ .

What is the standard deviation of m ? We first recall some properties. For two independent random variables X and Y , we have $\text{Var}(X + Y) = \text{Var}(X) + \text{Var}(Y)$ and for a linear combination, $\text{Var}(aX + b) = a^2 \text{Var}(X)$. So let us compute the variance of m :

$$\text{Var}(m) = \text{Var} \left(\sum_i \frac{x_i}{N} \right) = \sum_i \text{Var} \left(\frac{x_i}{N} \right) = \sum_i \frac{1}{N^2} \text{Var}(x_i) = \sum_i \frac{\sigma^2}{N^2} = \frac{\sigma^2}{N}. \quad (72)$$

This is a classical result, the standard deviation of the mean of a normal distribution evolves with the square root of the number of samples:

$$\sigma(m) = \sqrt{\text{Var}(m)} = \frac{\sigma}{\sqrt{N}}. \quad (73)$$

The sample variance s^2 : By definition,

$$s^2 = m(x^2) - m(x)^2 \quad (74)$$

where m stands for the sample mean defined above. We make the change of variable $X_i = x_i - \mu$ so that the variance is unchanged but the mean $m(X)$ is 0. So, the mean of s^2 is:

$$\langle s^2 \rangle = \langle m(X^2) - m(X)^2 \rangle = \left\langle \frac{1}{N} \sum_i X_i^2 \right\rangle = \frac{1}{N} \sum_i \langle X_i^2 \rangle = \frac{1}{N} \sum_i \sigma^2 = \sigma^2 \quad (75)$$

So, the sample variance is a non biased estimator of the variance σ^2 of a normal distribution. What is the standard deviation of s^2 ?

$$\text{Var}(s^2) = \text{Var} (m(X^2) - m(X)^2) \quad (76)$$

$$= \text{Var} \left(\frac{1}{N} \sum_i X_i^2 \right) = \sum_i \text{Var} \left(\frac{X_i^2}{N} \right) \quad (77)$$

$$= \frac{1}{N^2} \sum_i \text{Var}(X_i^2) = \frac{1}{N} \text{Var}(X^2) \quad (78)$$

$$= \frac{1}{N} [\langle X^4 \rangle - \langle X^2 \rangle^2] \quad (79)$$

We will use the Isserlis's theorem,

$$\langle abcd \rangle = \langle ab \rangle \langle cd \rangle + \langle ac \rangle \langle bd \rangle + \langle ad \rangle \langle bc \rangle \quad (80)$$

where a, b, c, d are Gaussian random variables. Thus,

$$\text{Var}(s^2) = \frac{1}{N} [3\langle X^2 \rangle^2 - \langle X^2 \rangle^2] = \frac{2}{N} \langle X^2 \rangle^2 = \frac{2}{N} \sigma^4 \quad (81)$$

We can now apply it to the cosmic variance. We have $C_\ell = \text{Var}(a_{\ell m})$ where the $a_{\ell m}$ follow a normal distribution centered on 0. For each ℓ , there are $N = 2\ell + 1$ samples. Thus, we find the formula of the cosmic variance:

$$\text{Var}(C_\ell) = \frac{2}{2\ell + 1} C_\ell^2. \quad (82)$$

Figure 14 is a numerical illustration for $\mu = 10$, $\sigma = 2$ and $N = 100$.

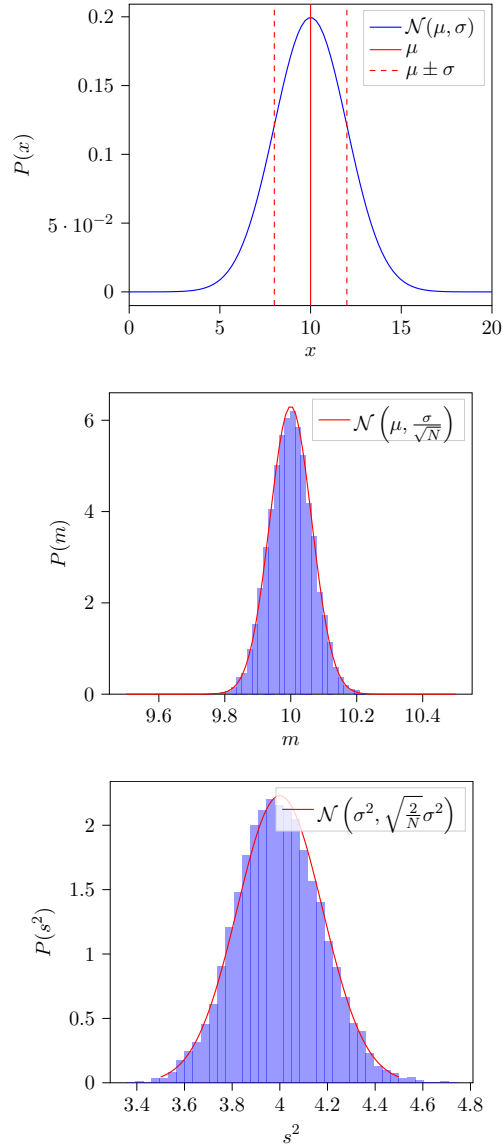


Figure 14: Numerical illustration for $\mu = 10$, $\sigma = 2$ and $N = 100$. m and s^2 are computed over 10 000 realizations.

A.3 Fringe data taking

Date	ELOG	Calibration source			Cycles		TES		Baselines
		Frequency [GHz]	DC offset [V]	Echosorb	# of cycles	Stable time [ms]	Vbias [V]	I (FLL)	
2019-05	245	150	4		10, 20	1000, 3000	9	200	12-39, 13-40, 13-22, 13-34
2019-05-24	258	150	2.5		1000		9	200	13-40
2019-05-25	260	150	DC off		20, 1000		9	200	13-40
2019-06-04	277	150	5		20		5	300	14-40, 14-35
2019-06-14	281	150	2, 4		20, 100		4, 5	200, 300	14-35
2019-06-17	282	150	2, 3, 4, 5		20		5	200	14-35
2019-06-07	285	150	1.5, 4		20		2, 5	300	1-25, 1-17, 25-49, 25, 57
2019-06-12	288	150	2, 3, 4, 5, 6, 7		20	1000	5	300	See caption
2019-06-13	290	150	6		20, 200	1000	5	300	25-57
2019-12-19	350	150	2.5						
2020-01-13	373	150	4	NO	100	3000	1.2	150	See caption
2020-06-24	451	150	5, 10	YES	20	1000, 3000	2, 3		49-25, 57-25
2020-06-25	454	150	10	YES	20	1000, 3000	2		49-25, 57-25
2020-07-27	505	150	4	YES		1000	2.5	150	9-49, 49-57
2020-07-28	509	150	3			1000	2.5	200	49-57, 49-53
2020-07-28	510	150	3			1000	2.5	200	49-57, 49-53
2020-10-27	558	150	4	YES	20	5000	5		
2020-10-28	559	150		YES, NO	20, 50	5000	3.5, 4		

Table 3: List of data taking for fringe measurements during the calibration phase at APC. ELOG is the numerical laboratory notebook entry. Baselines for 2019-06-12: 25-57, 24-56, 24-40, 57-64, 49-52, 40-64, 20-25, 16-40. Baselines for 2020-01-13: 49-25, 57-25, 52-28, 60-28, 25-28, 25-29, 1-5, 1-4, 1-28, 1-37, 10-28, 10-37, 49-28, 49-21, 57-29, 57-43, 60-63, 60-64, 40-64, 40-63, 39-64, 39-63.

A.4 Rigorous expression of the focal length

The idea is to determine the focal length of the optical combiner by the displacement of the synthesized beam from one detector to another. We consider two TES placed in A and B on the focal plane. If one of the two TES is placed at the center of the focal plane, we have

$$\alpha \simeq \tan \alpha = \frac{AB}{f} \quad (83)$$

where f is the focal length and α is the angle subtended by the two detectors defined in Figure 1.17. If we consider a given peak in the synthesized beam, α is the angle between the peak of TES A and the peak of TES B . Thus, α is easily measurable on the synthesized beam maps by looking at the peak displacements. Then, from α one can determine the focal length f .

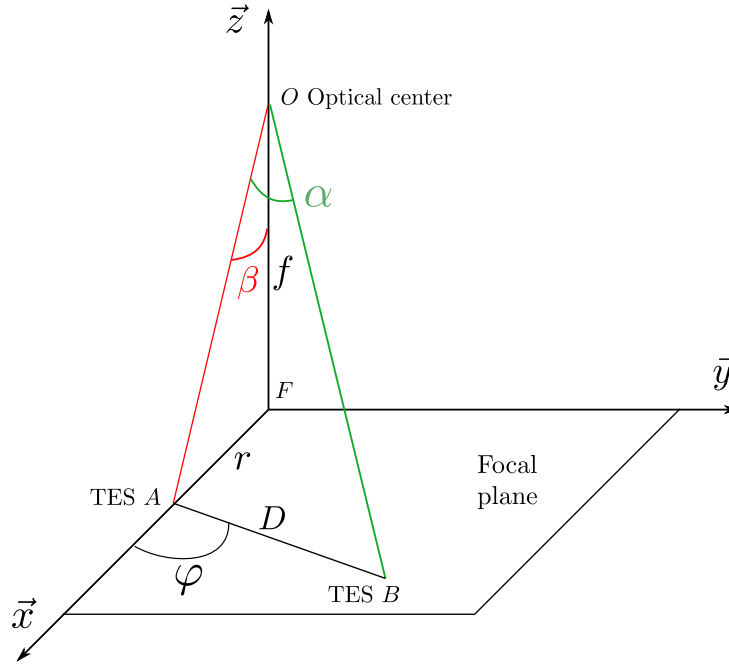


Figure 15: Sketch showing the notations used in the calculation. The optical center O is at the top of the figure. Line (OF) is the optical axis and the focal length is $f = OF$. The x and y axis are on the focal plane. We consider 2 TES on the focal plane at A and B separated by a distance D . r is the radial distance of the TES located in A .

However, for two TES arbitrary placed, expression 83 is only an approximation. In the following we will show that it is still possible to find a rigorous expression of the focal length f as a function of known quantities: α , the distance $D = AB$ between the two TES, the radial distance $r = FA$ of the first TES and the angle φ which is the angle between \overrightarrow{AB} and the x axis. The notations are defined in Figure 15. This calculation was done in collaboration with Jean Kaplan.

The TES coordinates (x_A, y_A) and (x_B, y_B) are assumed to be known. So we have $r = FA = \sqrt{x_A^2 + y_A^2}$ and

$$\overrightarrow{AB} \cdot \overrightarrow{FA} = Dr \cos \varphi = (x_B - x_A)x_A + (y_B - y_A)y_A. \quad (84)$$

Expression of the α angle

First, we want to evaluate the angle α under which length D between the two TES is seen from the optical center O . For that purpose, we evaluate

$$\tan^2 \alpha = \frac{1}{\cos^2 \alpha} - 1 = \frac{OA^2 OB^2}{(\overrightarrow{OA} \cdot \overrightarrow{OB})^2} - 1. \quad (85)$$

We have

$$\overrightarrow{OA} = \begin{pmatrix} f \tan \beta \\ 0 \\ -f \end{pmatrix} \quad \text{and} \quad \overrightarrow{AB} = \begin{pmatrix} D \cos \varphi \\ D \sin \varphi \\ 0 \end{pmatrix} \quad (86)$$

so we can compute

$$\overrightarrow{OA} \cdot \overrightarrow{OB} = OA^2 + \overrightarrow{OA} \cdot \overrightarrow{AB} = \frac{f^2}{\cos^2 \beta} + f D \tan \beta \cos \varphi \quad (87)$$

$$= \frac{f^2}{\cos^2 \beta} \left(1 + \frac{D}{f} \cos \beta \sin \beta \cos \varphi \right) \quad (88)$$

and

$$OB^2 = OA^2 + AC^2 + 2\overrightarrow{OA} \cdot \overrightarrow{AB} \quad (89)$$

$$= \frac{f^2}{\cos^2 \beta} + D^2 + 2f D \tan \beta \cos \varphi \quad (90)$$

$$= \frac{f^2}{\cos^2 \beta} \left(1 + \frac{D^2}{f^2} \cos^2 \beta + 2\frac{D}{f} \cos \beta \sin \beta \cos \varphi \right). \quad (91)$$

After some simplifications, we obtain

$$\tan^2 \alpha = \frac{D^2 \cos^2 \beta (1 - \sin^2 \beta \cos^2 \varphi)}{f^2 \left(1 + \frac{D}{f} \cos \beta \sin \beta \cos \varphi \right)^2}. \quad (92)$$

β can easily be replaced by r and f variables using

$$\sin^2 \beta = \frac{r^2}{OA^2} = \frac{r^2}{r^2 + f^2} \quad \text{and} \quad \cos^2 \beta = \frac{f^2}{r^2 + f^2}. \quad (93)$$

Writing the problem as a polynomial equation

Let us introduce $X = r^2 + f^2$ and $k = Dr \cos \varphi$. After some simplifications, expression 92 becomes

$$\tan^2 \alpha = \frac{D^2 X - k^2}{X^2 + k^2 + 2kX}. \quad (94)$$

This can be written as a second order polynomial equation in X :

$$\mathcal{P}(X) = X^2 \tan^2 \alpha + X(2k \tan^2 \alpha - D^2) + \frac{k^2}{\cos^2 \alpha} = 0. \quad (95)$$

$\mathcal{P}(X)$ has real roots if

$$\Delta = D^4 - 4 \tan^2 \alpha k (k + D^2) > 0 \iff \tan^2 \alpha < \frac{D}{4r \cos \varphi (1 + \frac{r}{D} \cos \varphi)}. \quad (96)$$

Calling X_+, X_- the two roots, their product is

$$X_+ \times X_- = (1 + \tan^2 \alpha) / \tan^2 \alpha \quad (97)$$

so it is positive. This means that the two roots have the same sign. Their sum is

$$X_+ + X_- = (D^2 - 2k \tan^2 \alpha) / \tan^2 \alpha \quad (98)$$

Thus, both roots are positive if:

$$X_+, X_- > 0 \iff \tan^2 \alpha < D/2r \cos \varphi. \quad (99)$$

This condition is automatically satisfied when condition 96 is verified.

Can we choose between the two roots?

A way to select between X_+ and X_- is to impose that the focal length must be positive, $f^2 = X - r^2 > 0 \iff r^2 < X$. This root selection only works if r^2 lies between the roots, i.e. $X_- < r^2 < X_+$. If this is the case the polynomial $\mathcal{P}(X)$ should be negative when $X = r^2$. Using equation 95, one can obtain

$$\mathcal{P}(r^2) < 0 \iff \tan^2 \alpha < \frac{r^2 D^2 - k^2}{(r^2 + k)^2}. \quad (100)$$

The right term is the value of $\tan^2 \alpha$ when $X = r^2$ given by relation 94. To verify whether condition 100 is satisfied, let us look at the variation of $\tan^2 \alpha$ with X . Using equation 94, we obtain

$$\frac{d}{dX} (\tan^2 \alpha) = \frac{-XD^2 + D^2 k + 2k^2}{(X + k)^3}. \quad (101)$$

Therefore $\tan^2 \alpha$ decreases when $X + k > 0$ and

$$X > k + 2\frac{k^2}{D^2} \iff r^2 + f^2 > r \cos \varphi (D + 2r \cos \varphi). \quad (102)$$

As f seems to be significantly larger than r and D , $\tan^2 \alpha$ decreases with X and, as $X > r^2$, $\tan^2 \alpha$ obeys condition 100. Thus the root selection by imposing that the focal length must be positive is valid and X_+ is the solution.

Final expression of the focal length

Once we have X_+ , we actually have the focal length:

$$f^2 = X_+ - r^2 = \frac{-2k \tan^2 \alpha + D^2 + \sqrt{\Delta}}{2 \tan^2 \alpha} - r^2 \quad \text{with} \quad k = Dr \cos \varphi. \quad (103)$$

As planned at the beginning, the expression we obtained depends on known quantities: α , D , r and φ . Note that all of this requires to know the position of the focus point on the focal plane and the TES coordinates from that point.

Verification of the expression we derived

The expression we obtained can be verified in simple cases:

- Case $\varphi = \pi/2$: $k = 0$, $\Delta = D^4$ so

$$X_+ = r^2 + f^2 = \frac{D^2}{\tan^2 \alpha} \quad (104)$$

- Case $\varphi = 0$: $k = Dr$ so

$$\Delta = D^4 \left(1 - 4 \tan^2 \alpha \left(\frac{r^2}{D^2} + \frac{D}{r} \right) \right) \quad (105)$$

and

$$X_+ = r^2 + f^2 = -Dr + \frac{1}{2 \tan^2 \alpha} (D^2 + \sqrt{\Delta}) \quad (106)$$

A.5 Spectral imaging paper

Paper concerning spectral imaging published in the context of this thesis is reproduced below.

**QUBIC — Q & U BOLOMETRIC INTERFEROMETER FOR COSMOLOGY:
INSTRUMENT, CURRENT STATUS AND FORECAST**

QUBIC II: Spectral polarimetry with bolometric interferometry



The QUBIC collaboration

L. Mousset,^{1,a} M.M. Gamboa Lerena,^{2,3,a} E.S. Battistelli,^{4,5}
P. de Bernardis,^{4,5} P. Chanial,¹ G. D'Alessandro,^{4,5} G. Dashyan,⁶
M. De Petris,^{4,5} L. Grandsire,¹ J.-Ch. Hamilton,¹ F. Incardona,^{7,8}
S. Landau,⁹ S. Marnieros,¹⁰ S. Masi,^{4,5} A. Mennella,^{7,8}
C. O'Sullivan,¹¹ M. Piat,¹ G. Ricciardi,⁷ C.G. Scóccola,^{2,3}
M. Stolpovskiy,¹ A. Tartari,¹² J.-P. Thermeau,¹ S.A. Torchinsky,^{1,13}
F. Voisin,¹ M. Zannoni,^{14,15} P. Ade,¹⁶ J.G. Alberro,¹⁷ A. Almela,¹⁸
G. Amico,⁴ L.H. Arnaldi,¹⁹ D. Auguste,¹⁰ J. Aumont,²⁰ S. Azzoni,²¹
S. Banfi,^{14,15} B. Bélier,²² A. Baù,^{14,15} D. Bennett,¹¹ L. Bergé,¹⁰
J.-Ph. Bernard,²⁰ M. Bersanelli,^{7,8} M.-A. Bigot-Sazy,¹
J. Bonaparte,²³ J. Bonis,¹⁰ E. Bunn,²⁴ D. Burke,¹¹ D. Buzi,⁴
F. Cavaliere,^{7,8} C. Chapron,¹ R. Charlassier,¹ A.C. Cobos Cerutti,¹⁸
F. Columbro,^{4,5} A. Coppolecchia,^{4,5} G. De Gasperis,^{25,26}
M. De Leo,^{4,27} S. Dheilly,¹ C. Duca,¹⁸ L. Dumoulin,¹⁰
A. Etchegoyen,¹⁸ A. Fasciszewski,²³ L.P. Ferreyro,¹⁸ D. Fracchia,¹⁸
C. Franceschet,^{7,8} K.M. Ganga,¹ B. García,¹⁸ M.E. García
Redondo,¹⁸ M. Gaspard,¹⁰ D. Gayer,¹¹ M. Gervasi,^{14,15} M. Giard,²⁰
V. Gilles,^{4,28} Y. Giraud-Heraud,¹ M. Gómez Berisso,¹⁹
M. González,¹⁹ M. Gradziel,¹¹ M.R. Hampel,¹⁸ D. Harari,¹⁹
S. Henrot-Versillé,¹⁰ E. Jules,¹⁰ J. Kaplan,¹ C. Kristukat,²⁹
L. Lamagna,^{4,5} S. Loucatos,^{1,30} T. Louis,¹⁰ B. Maffei,⁶ W. Marty,²⁰
A. Mattei,⁵ A. May,²⁸ M. McCulloch,²⁸ L. Mele,^{4,5} D. Melo,¹⁸

¹Main author.

**L. Montier,²⁰ L.M. Mundo,¹⁷ J.A. Murphy,¹¹ J.D. Murphy,¹¹
**F. Nati,^{14,15} E. Olivieri,¹⁰ C. Oriol,¹⁰ A. Paiella,^{4,5} F. Pajot,²⁰
**A. Passerini,^{14,15} H. Pastoriza,¹⁹ A. Pelosi,⁵ C. Perbost,¹
**M. Perciballi,⁵ F. Pezzotta,^{7,8} F. Piacentini,^{4,5} L. Piccirillo,²⁸
**G. Pisano,¹⁶ M. Platino,¹⁸ G. Polenta,^{4,31} D. Prêle,¹ R. Puddu,³²
**D. Rambaud,²⁰ E. Rasztocky,³³ P. Ringegni,¹⁷ G.E. Romero,³³
**J.M. Salum,¹⁸ A. Schillaci,^{4,34} S. Scully,^{11,35} S. Spinelli,¹⁴
**G. Stankowiak,¹ A.D. Supanitsky,¹⁸ P. Timbie,³⁶ M. Tomasi,^{7,8}
**G. Tucker,³⁷ C. Tucker,¹⁶ D. Viganò,^{7,8} N. Vittorio,²⁵ F. Wicek,¹⁰
M. Wright²⁸ and A. Zullo⁵******************

¹Université de Paris, CNRS, Astroparticule et Cosmologie, F-75006 Paris, France

²Facultad de Ciencias Astronómicas y Geofísicas (Universidad Nacional de La Plata), Argentina

³CONICET, Argentina

⁴Università di Roma — La Sapienza, Roma, Italy

⁵INFN sezione di Roma, 00185 Roma, Italy

⁶Institut d'Astrophysique Spatiale, Orsay (CNRS-INSU), France

⁷Università degli studi di Milano, Milano, Italy

⁸INFN sezione di Milano, 20133 Milano, Italy

⁹Departamento de Física and IFIBA, Facultad de Ciencias Exactas y Naturales, Universidad de Buenos Aires, Argentina

¹⁰Laboratoire de Physique des 2 Infinis Irène Joliot-Curie (CNRS-IN2P3, Université Paris-Saclay), France

¹¹National University of Ireland, Maynooth, Ireland

¹²INFN sezione di Pisa, 56127 Pisa, Italy

¹³Observatoire de Paris, Université Paris Science et Lettres, F-75014 Paris, France

¹⁴Università di Milano — Bicocca, Milano, Italy

¹⁵INFN sezione di Milano — Bicocca, 20216 Milano, Italy

¹⁶Cardiff University, U.K.

¹⁷GEMA (Universidad Nacional de La Plata), Argentina

¹⁸Instituto de Tecnologías en Detección y Astropartículas (CNEA, CONICET, UNSAM), Argentina

¹⁹Centro Atómico Bariloche and Instituto Balseiro (CNEA), Argentina

²⁰Institut de Recherche en Astrophysique et Planétologie, Toulouse (CNRS-INSU), France

²¹Department of Physics, University of Oxford, U.K.

²²Centre de Nanosciences et de Nanotechnologies, Orsay, France

²³Centro Atómico Constituyentes (CNEA), Argentina

²⁴University of Richmond, Richmond, U.S.A.

²⁵Università di Roma “Tor Vergata”, Roma, Italy

²⁶INFN sezione di Roma2, 00133 Roma, Italy

²⁷University of Surrey, U.K.

²⁸University of Manchester, U.K.

²⁹Escuela de Ciencia y Tecnología (UNSAM) and Centro Atómico Constituyentes (CNEA), Argentina

³⁰IRFU, CEA, Université Paris-Saclay, F-91191 Gif-sur-Yvette, France

³¹Italian Space Agency, Roma, Italy

³²Pontificia Universidad Católica de Chile, Chile

³³Instituto Argentino de Radioastronomía (CONICET, CIC, UNLP), Argentina

³⁴California Institute of Technology, U.S.A.

³⁵Institute of Technology, Carlow, Ireland

³⁶University of Wisconsin, Madison, U.S.A.

³⁷Brown University, Providence, U.S.A.

E-mail: mousset@apc.in2p3.fr, mgamboa@fcaglp.unlp.edu.ar

Received November 24, 2020

Revised May 12, 2021

Accepted July 6, 2021

Published ???, 2021

Abstract. Bolometric interferometry is a novel technique that has the ability to perform spectral imaging. A bolometric interferometer observes the sky in a wide frequency band and can reconstruct sky maps in several sub-bands within the physical band in post-processing of the data. This provides a powerful spectral method to discriminate between the cosmic microwave background (CMB) and astrophysical foregrounds. In this paper, the methodology is illustrated with examples based on the Q & U Bolometric Interferometer for Cosmology (QUBIC) which is a ground-based instrument designed to measure the B-mode polarization of the sky at millimeter wavelengths. We consider the specific cases of point source reconstruction and Galactic dust mapping and we characterize the point spread function as a function of frequency. We study the noise properties of spectral imaging, especially the correlations between sub-bands, using end-to-end simulations together with a fast noise simulator. We conclude showing that spectral imaging performance are nearly optimal up to five sub-bands in the case of QUBIC.

Keywords: CMBR experiments, CMBR theory, cosmological parameters from CMBR, gravitational waves and CMBR polarization

ArXiv ePrint: [2010.15119](https://arxiv.org/abs/2010.15119)

Contents

1	Introduction	1
2	Bolometric interferometry as synthesized imaging	3
2.1	Synthesized imaging	3
2.2	Realistic case	6
2.3	The monochromatic synthesized beam	6
2.4	Monochromatic map-making	6
3	Spectral dependence	9
3.1	The polychromatic synthesized beam	9
3.2	Spectral imaging capabilities	10
4	Testing spectral imaging on simple cases	10
4.1	Extended source reconstruction	11
4.2	Angular resolution	12
4.3	Frequency point spread function characterization	12
4.4	Galactic dust	14
5	Noise characterization	19
5.1	Noise behaviour in the sub-bands at map level	19
5.2	Noise analysis using the power spectrum	19
5.3	Nearly optimal performance of spectral imaging	20
6	Spectral imaging on real data	23
7	Conclusion	24

1 Introduction

This article is the second in a series of eight on the Q & U Bolometric Interferometer for Cosmology (QUBIC), and it introduces the spectroscopic imaging capability made possible by bolometric interferometry. QUBIC will observe the sky at millimeter wavelengths, looking at the cosmic microwave background (CMB).

The CMB, detected by Penzias and Wilson [1], has a thermal distribution with a temperature of 2.7255 ± 0.0006 K [2]. It is a partially polarized photon field released 380,000 years after the Big Bang when neutral hydrogen was formed. The polarization can be fully described by a scalar and a pseudo-scalar fields: E and B-modes respectively. B-mode polarization anisotropies are generated by primordial gravitational waves occurring at the inflation era. The indirect detection of these waves would represent a major step towards understanding the inflationary epoch that is believed to have occurred in the early Universe. Tensor modes in the metric perturbations are a specific prediction of inflation. The measurement of the corresponding B-mode polarization anisotropies would reveal the inflationary energy scale, which is directly related to the amplitude of this signal. This amplitude, relative to the scalar mode, is parametrized by the so called tensor-to-scalar ratio r .

Currently, there are several instruments aiming at measuring the primordial B modes. These include SPTPol [3], SPT-3G [4], POLARBEAR [5], ACTPol [6, 7], CLASS [8], and BICEP2/Keck Array [9]. Some of them are planned to be upgraded: CLASS [10], POLARBEAR 2 + Simons Array [11], AdvACT [12], and BICEP3/BICEP array [13]. Planned experiments include Simons Observatory [14], PIPER [15], LSPE [16], CMB-S4 [17] and LiteBIRD [18].

The main foreground contaminant at high frequencies is the polarized thermal emission from elongated dust grains in the Galaxy [19]. At lower frequencies, emission from synchrotron [20] is expected to be significant, even in a so-called clean CMB field, if r is below 10^{-2} . Current estimates depend strongly on the assumption that synchrotron is well described by a simple power law with a steep spectral index (but spectral curvature might well be there). While free-free is not expected to be a major contaminant due to its vanishingly small degree of polarization [21], spinning dust, whose impact is addressed by Remazeilles et al. [22], should not be neglected. Since 2014, large advances in understanding the galactic foregrounds and developing mitigation techniques have been made but a lot of work remains to be done in this field and it is among the main challenges for CMB experiments today.

The control of contamination from foregrounds can only be achieved with a number of frequencies around the maximum emission of the CMB relying on the fact that the spectral distribution of the CMB polarization is significantly different from that of the foregrounds so that low and high frequencies can be used as templates to remove the contamination in the CMB frequencies.

A bolometric interferometer such as QUBIC acquires data in a focal plane containing bolometers operating over a single wide frequency band. However, this type of instrument has the ability to split, in post-processing of the data, the wide band into multiple frequency sub-bands, achieving spectral resolution. In the following, this technique will be called spectral imaging. This idea was already mentioned in earlier work by Malu et al. [23]. It is possible thanks to the very particular instrument beam pattern, given by the geometric distribution of an array of apertures operating as pupils of the interferometer. The synthesized beam contains multiple peaks whose angular separation is linearly dependent on the wavelength.

This paper does not attempt to make realistic simulations and forecasts for the QUBIC project, this is addressed in the companion paper Hamilton et al. [24]. The goal is to demonstrate spectral imaging technique on simple cases, with very basic foreground models, not accounting for any systematic effect. The expected spectral imaging performance for a real instrument will be treated in detail in the near future.

This article is organized as follows. In section 2 we describe the working principle of a bolometric interferometer taking the example and characteristics of QUBIC. In section 3 we describe the spectral dependence of the synthesized beam and show under which conditions the spectral information can be recovered at the map making level. In section 4 we test spectral imaging on simple cases using the QUBIC data analysis and simulation pipeline. Finally, in section 5 we present the performance of the spectral reconstruction. We compare a simulated sky to the reconstructed one using the QUBIC data analysis pipeline. Tests with a real point source were carried out in the lab and results are presented by Torchinsky et al. [25].

Detailed information about QUBIC can be found in the companion papers: scientific overview and expected performance of QUBIC [24], characterization of the technological demonstrator (TD) [25], transition-edge sensors and readout characterization [26], cryogenic system performance [27], half-wave plate (HWP) rotator design and performance [28], feed-

Parameter	Full instrument value
Frequency channels	150 GHz & 220 GHz
Frequency range 150 GHz	[131–169] GHz
Frequency range 220 GHz	[192.5–247.5] GHz
Window Aperture [m]	0.56
Focal plane temp. [mK]	300
Sky Coverage	1.5%
FWHM [degrees]	0.39 (150 GHz), 0.27 (220 GHz)

Table 1. QUBIC main parameters (from Hamilton et al. [24]).

horn-switches system of the TD [29], and optical design and performance [30].

2 Bolometric interferometry as synthesized imaging

A bolometric interferometer is an instrument observing in the millimeter and submillimeter frequency range based on the Fizeau interferometer [31]. A set of pupils are used at the front of the instrument to select baselines. The resulting interference pattern is then imaged on a focal plane populated with an array of bolometers. With the addition of a polarizing grid and a rotating HWP before the pupil array, the instrument becomes a polarimeter, such as QUBIC. A schematic of the QUBIC instrument optical chain is shown in figure 1 (left) with a sectional cut of the cryostat (right). The main parameters are summarized in table 1.

Each pair of pupils, called a baseline, contributes with an interference fringe in the focal plane. The whole set of pupils produces a complex interference pattern that we call the synthesized image (or dirty image) of the source. For a multiplying interferometer, the observables are the visibilities associated with each baseline. In bolometric interferometry, the observable is the synthesized image, which can be seen as the image of the inverse Fourier transform of the visibilities.

The left panel of figure 2 shows the array of back-to-back feedhorns of the full instrument (FI). The feedhorn array is made of 400 pupils arranged on a rectangular grid 22×22 within a circle. More details on measurements and realistic simulations are presented in Cavaliere et al. [29] and O’Sullivan et al. [30], especially about cross-polarization. However, in this paper, we consider an ideal instrument. The beam looking at the sky is called the primary beam, and secondary beam is the one looking toward the focal plane. In the right panel, we can see the synthesized image obtained on the focal plane of the FI, composed by 992 bolometers, when the instrument is looking at a point source located on the optical axis in the far field.

2.1 Synthesized imaging

A bolometer is a total power detector. The signal $S_\eta(\mathbf{r}, \lambda)$ on a point $\mathbf{r} = (x, y)$ of the focal plane¹ is the square modulus of the electric field $E_\eta(t, \mathbf{n}, \lambda)$ averaged over time t and integrated over all sky directions \mathbf{n} . The signal with polarization η from each direction is re-emitted by each of the pupils resulting in a path difference in the optical combiner. The signal on the focal plane depends on the location of each pupil \mathbf{h}_j , its primary beam $B_{\text{prim}}(\mathbf{n}, \lambda)$, the focal length of the combiner f , the secondary beam of the pupil on the focal plane $B_{\text{sec}}(\mathbf{r}, \lambda)$,

¹ $\mathbf{r} = 0$ at the optical center of the focal plane.

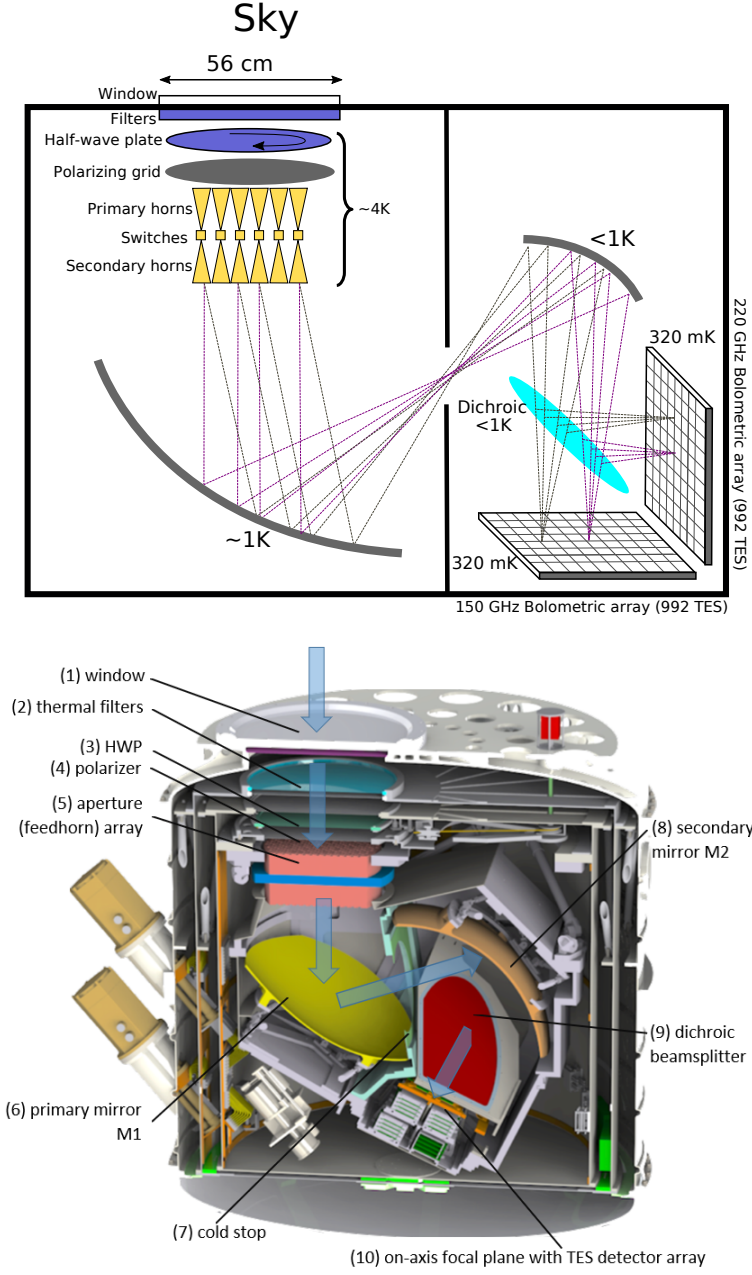


Figure 1. Schematic of the QUBIC instrument and sectional cut of the cryostat showing the same sub-systems in their real configuration.

and the wavelength λ :

$$\begin{aligned}
 S_{\eta}(\mathbf{r}, \lambda) = \int B_{\text{prim}}(\mathbf{n}, \lambda) B_{\text{sec}}(\mathbf{r}, \lambda) \left\langle \left| \sum_j E_{\eta}(t, \mathbf{n}, \lambda) \right. \right. \\
 \left. \left. \times \exp \left[i 2 \pi \frac{\mathbf{h}_j}{\lambda} \cdot \left(\frac{\mathbf{r}}{\sqrt{f^2 + r^2}} - \mathbf{n} \right) \right] \right|^2 \right\rangle d\mathbf{n}, \quad (2.1)
 \end{aligned}$$

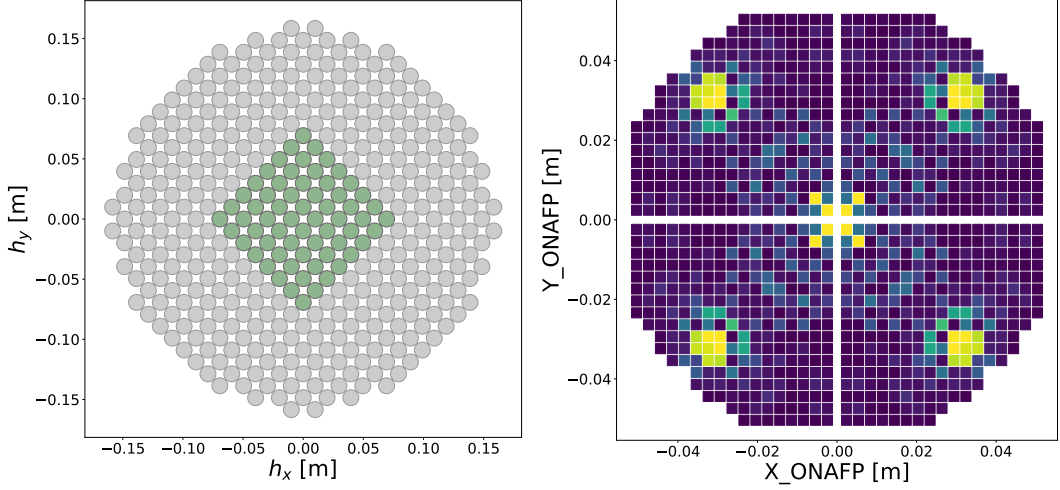


Figure 2. *Left:* Feedhorn array of the FI made of 400 pupils arranged on a rectangular grid 22×22 within a circle. The TD horn array is highlighted in green. *Right:* intensity pattern on the focal plane of the FI composed by 992 bolometers for an on-axis point source in the far field emitting at 150 GHz with all horns open. The color scale in intensity is arbitrary.

where r is the norm of \mathbf{r} . We use the concept of the point spread function (PSF) of the synthesized beam,

$$PSF(\mathbf{n}, \mathbf{r}, \lambda) = B_{\text{prim}}(\mathbf{n}, \lambda) B_{\text{sec}}(\mathbf{r}, \lambda) \times \left| \sum_j \exp \left[i2\pi \frac{\mathbf{h}_j}{\lambda} \cdot \left(\frac{\mathbf{r}}{\sqrt{f^2 + r^2}} - \mathbf{n} \right) \right] \right|^2, \quad (2.2)$$

to rewrite equation (2.1) as

$$S_\eta(\mathbf{r}, \lambda) = \int \langle |E_\eta(t, \mathbf{n}, \lambda)|^2 \rangle \times PSF(\mathbf{n}, \mathbf{r}, \lambda) \, d\mathbf{n}. \quad (2.3)$$

The rotating HWP modulates the polarized signal, with a varying angle ϕ , so we can write equation (2.3) in terms of the synthesized images of the Stokes parameters:

$$S(\mathbf{r}, \lambda) = S_I(\mathbf{r}, \lambda) + \cos(4\phi) S_Q(\mathbf{r}, \lambda) + \sin(4\phi) S_U(\mathbf{r}, \lambda) \quad (2.4)$$

where the synthesized images are the convolution of the sky through the synthesized beam:

$$S_X(\mathbf{r}, \lambda) = \int X(\mathbf{n}, \lambda) \times PSF(\mathbf{n}, \mathbf{r}, \lambda) \, d\mathbf{n}, \quad (2.5)$$

X standing for the Stokes parameters I, Q or U. The signal received in the detectors with a bolometric interferometer is therefore exactly similar to that of a standard imager: the sky convolved with a beam. The only difference being that this beam is not that of the primary aperture system (telescope in the case of an ordinary imager) but is given by the geometry of the input pupil array and the beam of the pupils (see equation (2.2)). With such an instrument, one can scan the sky in the usual manner with the synthesized beam, gathering time-ordered-data (TOD) for each sky direction (and orientation of the instrument) and reproject this data onto a map at the data analysis stage (see section 2.4).

2.2 Realistic case

Note that in a real detector the signal is integrated over the wavelength range defined by filters and also over the surface of the detectors [32]. If one assumes that the sky signal does not vary within the wavelength range,² the expression for the signal, equation (2.4), is unchanged and one just needs to redefine the synthesized beam as

$$PSF(\mathbf{n}, \mathbf{r}_d, \lambda_k) = \int \int PSF(\mathbf{n}, \mathbf{r}, \lambda) J_{\lambda_k}(\lambda) \Theta(\mathbf{r} - \mathbf{r}_d) d\lambda d\mathbf{r} \quad (2.6)$$

where $J_{\lambda_k}(\lambda)$ is the shape of the filter for the band centered in λ_k and $\Theta(\mathbf{r})$ represents the top-hat function for integrating over the detector whose center is at \mathbf{r}_d .

2.3 The monochromatic synthesized beam

If the pupil array is a regular square grid of P pupils on a side spaced by a distance Δh , the sum in equation (2.2) can be analytically calculated (see O’Sullivan et al. [30] for more detail) and the monochromatic point-like synthesized beam, assuming f is large enough to use the small-angle approximation, becomes

$$PSF(\mathbf{n}, \mathbf{r}, \lambda) = B_{\text{prim}}(\mathbf{n}, \lambda) B_{\text{sec}}(\mathbf{r}, \lambda) \times \frac{\sin^2 \left[P \pi \frac{\Delta h}{\lambda} \left(\frac{x}{f} - n_x \right) \right]}{\sin^2 \left[\pi \frac{\Delta h}{\lambda} \left(\frac{x}{f} - n_x \right) \right]} \frac{\sin^2 \left[P \pi \frac{\Delta h}{\lambda} \left(\frac{y}{f} - n_y \right) \right]}{\sin^2 \left[\pi \frac{\Delta h}{\lambda} \left(\frac{y}{f} - n_y \right) \right]}, \quad (2.7)$$

where $\mathbf{n} = (n_x, n_y)$ is the off-axis angle of the source. In such a case, the synthesized beam of the monochromatic point-like detectors has the shape of a series of large peaks with ripples in between, modulated by the primary beam of the pupils. For illustrative purpose, a cut of the synthesized beam is shown in figure 3 for such a square 20×20 array of horns. The realistic synthesized beam corresponding to our circular array (see figure 2) is shown by O’Sullivan et al. [30] (figure 11) and shows minor differences. Figure 3 shows this approximate synthesized beam for two different detectors emphasizing the fact that the location of the peaks moves with the detector location in the focal plane. Moreover, the intensity received by the detector changes inversely with r so the two Gaussian envelopes also differ. From the expression in equation (2.7) it is straightforward to see that the full width at half maximum (FWHM) of the large peaks is roughly given by $\text{FWHM} = \frac{\lambda}{(P-1)\Delta h}$ while their separation is $\theta = \frac{\lambda}{\Delta h}$ as illustrated in figure 3.

The real synthesized beam of the QUBIC TD has been measured in the lab using a monochromatic calibration source and is presented by Torchinsky et al. [25]. For the TD, the horn array is an 8×8 square array. The measured synthesized beam is in overall good agreement with the approximate analytical expression in equation (2.7) and figure 3 although excursions from this perfect case are expected due to optical defects and diffraction in the optical chain. It was shown by Bigot-Sazy et al. [33] that the shape of the synthesized beam for each detector can be precisely recovered through the “self-calibration” technique that is heavily inspired from synthesis imaging techniques [34].

2.4 Monochromatic map-making

Before discussing spectral imaging, we first describe the map-making with a bolometric interferometer in the monochromatic case. As shown in section 2.1, the instrument is essentially

²This clarification is only made so that we can write the integral analytically. In the code, the integration is done numerically over small sub-bands (around 16 sub-bands into the wide band.)

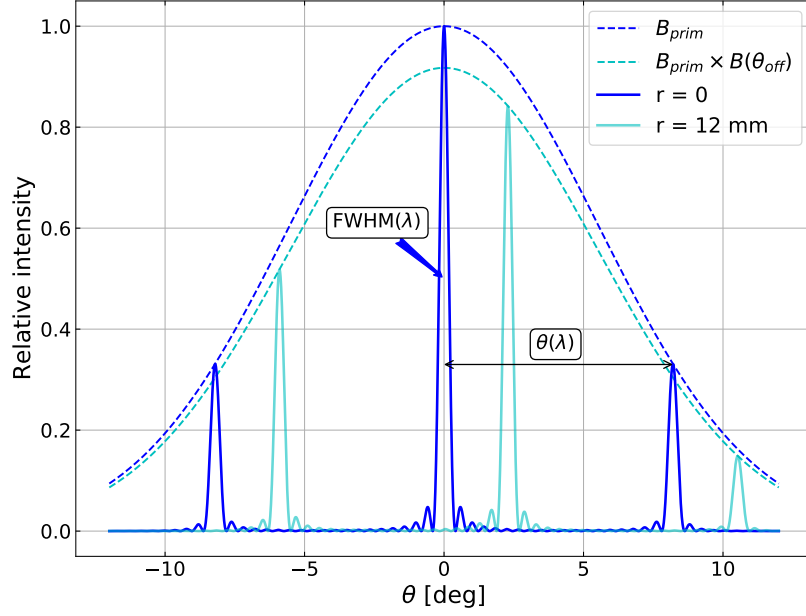


Figure 3. Cut of the synthesized beam as a function of θ (angle between \mathbf{n} and the optical axis) given by equation (2.7) for a square array of 20×20 pupils separated by $\Delta h = 14$ mm at 150 GHz frequency (2 mm wavelength) for a detector located at the center of the optical axis in blue and 12 mm apart in cyan. Dashed lines represent the primary beam of the pupils (here Gaussian). Resolution and peak separation depend linearly on the wavelength λ .

equivalent to a standard imager, scanning the sky with the synthesized beam, producing TOD that can be projected onto sky maps. The map-making will therefore be very similar to that of a standard imager. In the monochromatic case, if the sky signal is \vec{s} , the TOD \vec{y} can be written as:

$$\vec{y} = H \cdot \vec{s} + \vec{n} \quad (2.8)$$

where \vec{n} is the noise and H is an operator that describes the convolution by the synthesized beam in equation (2.5) as well as the pointing at the different directions of the sky. H is a 2-dimensional matrix: number of time samples (scaling with the number of detectors) \times number of sky pixels. The noise has two contributions: photon noise and detector noise. Photon noise is the Poisson fluctuations from the temperature of the CMB ($T_{\text{CMB}} \simeq 2.7$ K), the atmosphere, and the internal optical components. Detector noise is given by the noise equivalent power (NEP) measured in each detector. The atmosphere emissivity is assumed to be stable, we did not consider the effect of fluctuations in the atmospheric load, this requires a significant step forward in our pipeline that we are currently carrying out. Equation (2.8) will be generalized to the case of several frequency sub-bands in section 3.2.

For standard imagers, the H operator is such that each line (corresponding to sky pixels contributing to one time sample) only contains a single non-zero value, meaning that \vec{s} is actually the sky map convolved to the instrument's resolution and that the instrument samples the convolved sky with a single peak [35, 36].

In the case of a bolometric interferometer, this assumption is not valid due to the multiple peaked shape of the synthesized beam (see figure 3) which makes it impossible to use the map-making algorithms usually developed for direct imagers. We use instead an algorithm that starts from an initial guess and then simulates iterative maps \vec{s}_i , where i is the

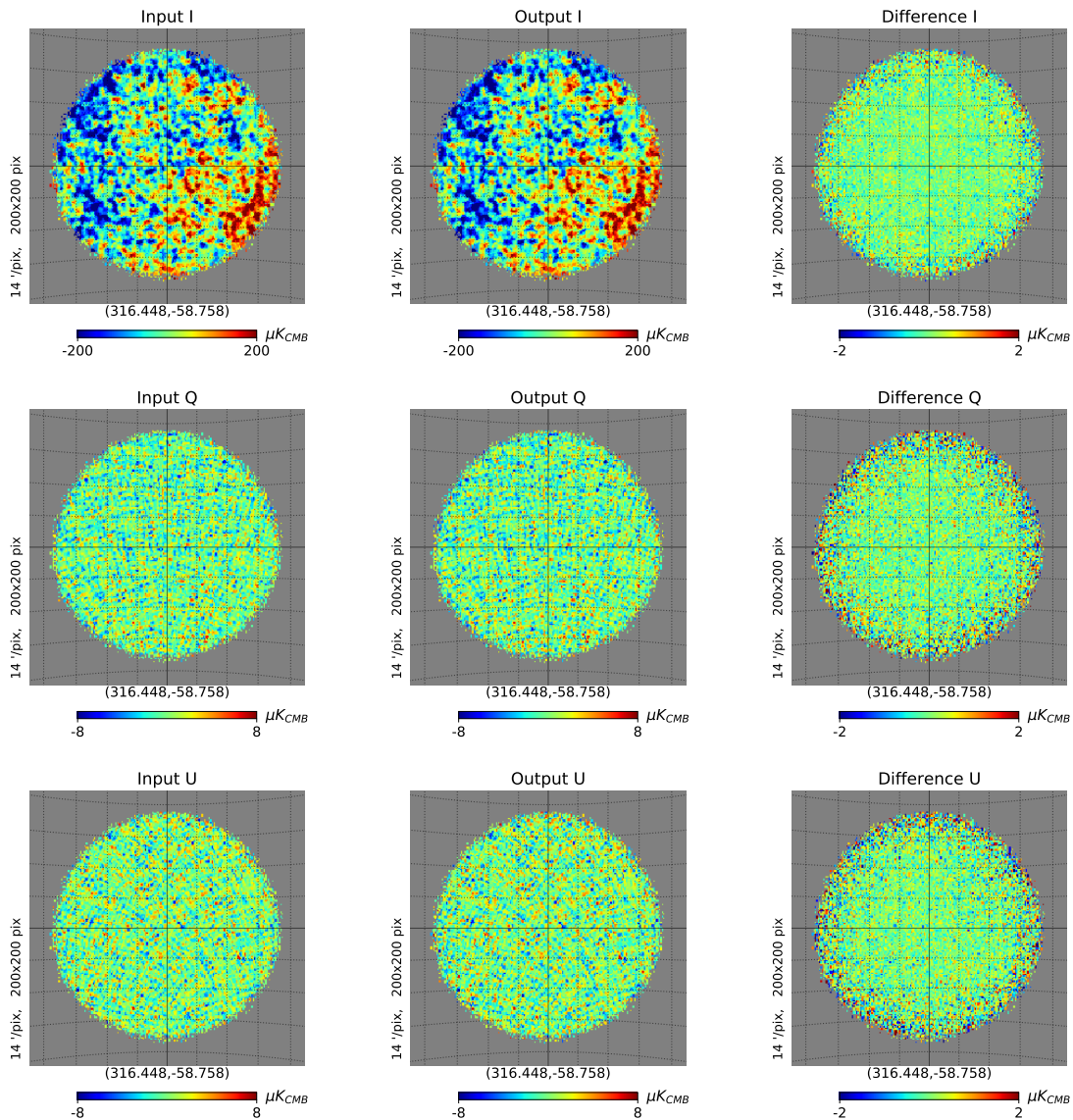


Figure 4. Result of the map-making for IQU Stokes parameters for a bolometric interferometer pointing in a 15 degree radius sky patch containing only CMB. The first column is the input sky convolved at the resolution of the instrument using a Gaussian with a FWHM equal to 0.4 degrees. The second column is the sky reconstructed by map-making. The last column is the difference between both. The grid lines are equally spaced every 5° . This simulation was obtained with the QUBIC full pipeline in the 220 GHz band. The noise was scaled to 4 years of observations. This simulation required 127 iterations to converge.

iterative index.³ For each of these maps, we apply the bolometric interferometer acquisition model, taking into account the scanning strategy of the sky, and we construct TOD \vec{y}_i that are then compared to the data TOD \vec{y} using a merit function that accounts for the noise in the TOD domain. In the case of stationary and Gaussian distributed noise, the maximum

³The software uses the massively parallel libraries [37] developed by P. Chianial pyoperators (<https://pchanial.github.io/pyoperators/>) and pysimulators (<https://pchanial.github.io/pysimulators/>).

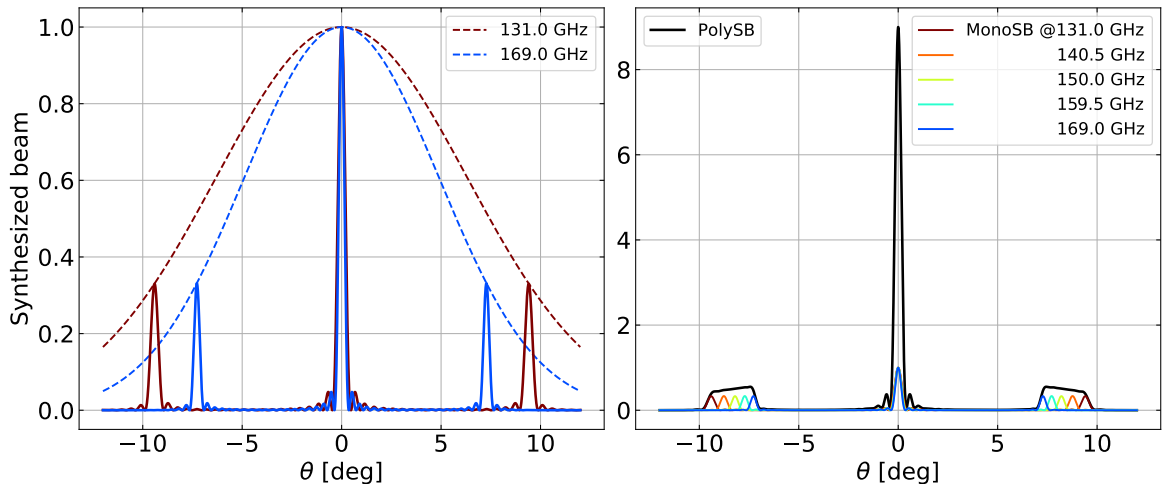


Figure 5. *Left:* monochromatic synthesized beam (*MonoSB*) for 131 and 169 GHz. Each synthesized beam is modeled according to equation (2.7) for a square array of 20×20 pupils separated 14 mm apart at 131 and 169 GHz. The primary beam at each frequency is shown by a dashed line. *Right:* polychromatic beam (*PolySB*, black line) as result of the addition of 9 monochromatic synthesized beams (5 of them are shown in colored lines) spanning our 150 GHz band (131 to 169 GHz). We sample the continuous frequency band with discrete frequencies.

likelihood solution is reached by minimizing the χ^2 :

$$\chi^2(\vec{s}_i) = (\vec{y} - \vec{y}_i)^T \cdot N^{-1} \cdot (\vec{y} - \vec{y}_i) \quad (2.9)$$

where N is the covariance matrix of the noise. We minimize equation (2.9) to find the best simulated sky map, $\hat{\vec{s}}$, using a preconditioned conjugate gradient method [38, 39]. This is jointly done for the IQU Stokes parameters and results in unbiased estimates of the maps as shown in figure 4.

3 Spectral dependence

3.1 The polychromatic synthesized beam

As can be seen in equation (2.7), the synthesized beam is directly dependent on wavelength and this is shown in figure 3.

The off-axis angle (given by the primary beam of the pupils), the FWHM of the peaks (hence the resolution of the maps), and the angle on the sky between two peaks all depend linearly on λ . This dependence on wavelength can be exploited to achieve spectral imaging capabilities. Within a wide band, the synthesized beam will be the integral of the synthesized beam of all the monochromatic contributions within the band resulting in a polychromatic synthesized beam. Figure 5 shows the cross cut of the synthesized beams modeled according to equation (2.7). The left panel shows the monochromatic synthesized beam for 131 and 169 GHz while the right panel shows a polychromatic synthesized beam using 9 monochromatic synthesized beams.

With a bolometric interferometer operating over a large bandwidth, for each pointing towards a given direction in the sky, one gets contributions from all the multiple peaks in the synthesized beam at all frequencies. As a result, we have both spatial and spectral

information in the TOD. Precise knowledge of the synthesized beam along the frequency will then allow one to reconstruct the position and amplitude of the sky in multiple frequency sub-bands.

3.2 Spectral imaging capabilities

The synthesized beam at two different frequencies ν_1 and ν_2 will be distinguishable from one another as long as their peaks are sufficiently separated. The angular separation between the two peaks $\Delta\theta = \frac{c\Delta\nu}{\nu^2\Delta h}$ (where $\Delta\nu = \nu_2 - \nu_1$ and $\nu = \sqrt{\nu_1\nu_2}$) must be large enough to unambiguously distinguish the two peaks. In order to have an order of magnitude of the possible width for each sub-band we consider a square array of pupils and we apply the Rayleigh criterion [40]:

$$\frac{c\Delta\nu}{\nu^2\Delta h} \gtrsim \frac{c}{\nu(P-1)\Delta h} \Leftrightarrow \Delta\nu \gtrsim \frac{\nu}{(P-1)} \quad (3.1)$$

where P is the number of pupils on a side of the square-packed pupil-array. A bolometric interferometer therefore not only has a resolution on the sky $\text{FWHM}_\theta \simeq \frac{c}{\nu(P-1)\Delta h}$, but also in electromagnetic frequency space $\frac{\Delta\nu}{\nu} \simeq \frac{1}{P-1}$.

The map-making presented in section 2.4 can be extended in order to build, simultaneously, with the same TOD, maps at a number of different frequencies as long as they comply with the frequency separation given above. The iterative TOD \vec{y}_i can be written as:

$$\vec{y}_i = \sum_{j=0}^{N_{rec}-1} H_j \hat{s}_{ij} + \vec{n} \quad (3.2)$$

where H_j describes the acquisition (convolution+pointing) operator with the synthesized beam at frequency ν_j , \hat{s}_{ij} is the sky signal estimator at iteration i for the frequency ν_j and N_{rec} is the number of reconstructed sub-bands. Similarly, as in the map at a single frequency (figure 4), one can recover the maps \vec{s}_j by solving equation (3.2) using a preconditioned conjugate-gradient method (see section 4 for corresponding simulations). Thus, the instrument acquires data in a single wide frequency band and spectral imaging technique applies during map-making, in the post-processing of the data.

The QUBIC FI has two wide-bands centered at 150 and 220 GHz with $\Delta\nu/\nu = 0.25$ and a 400-feedhorn array packed on a square grid within a circular area (see figure 2). We approximate it with a square grid 20×20 so $\frac{1}{(P-1)} \sim 0.05$. It is thus possible to reconstruct approximately 5 sub-bands in each of the initial bands of QUBIC. Note that this number should just be taken as an order of magnitude for the achievable number of sub-bands but we will see in figure 8 that it is a good approximation. In section 5 we will show that reconstructing up to 8 sub-bands is feasible but with a significant degradation of the signal-to-noise ratio.

4 Testing spectral imaging on simple cases

We can use the QUBIC simulation pipeline to test the spectral imaging capabilities of bolometric interferometry in a simple way. Some concepts and parameters used in simulations are defined in table 2.

Parameter	Details
N_{in}	Number of input or true maps (in μK) used to simulate a broadband observation (TOD). Each map represents a sky at a specific frequency ν_j for the IQU Stokes parameters. ^{a,b} Possible values: 15, 16, 18, 21 or 48.
N_{rec}	Number of sub-bands reconstructed from a single broadband observation, from 1 to 8. In all simulations N_{rec} is a divisor of N_{in} .
N_{conv}	Number of convolved maps equal to N_{rec} . Each of these maps is obtained convolving the N_{in} input maps at the QUBIC spatial resolution corresponding to that input frequency and then averaging within the reconstructed sub-band.
θ	Radius of sky patch observed in simulations. Value: 15 degrees.
Pointings	Number of times that the instrument observes in a given sky direction aligned with the optical axis. Values $> 10^4$.
NEP_{det}	Detector noise equivalent power (NEP) added as white noise. Value: $4.7 \times 10^{-17} \text{ W}/\sqrt{\text{Hz}}$.
NEP_{γ}	Photon NEP added as white noise in time-domain, calculated from the atmospheric emissivity measured in our site, as well as emissivities from all components in the optical chain. The atmospheric load is assumed to be stable. The value is different for each detector because of their different illumination by the secondary beam B_{sec} . The average value at 150 GHz is $4.55 \times 10^{-17} \text{ W}/\sqrt{\text{Hz}}$ and $1.72 \times 10^{-16} \text{ W}/\sqrt{\text{Hz}}$ at 220 GHz.

^aSkies are generated using PySM: Python Sky Model [41].

^bMaps are projected using HEALPix: Hierarchical Equal Area Isolatitude Pixellization of sphere [42].

Table 2. Typical parameters used in acquisition, instrument and map-making to do an end-to-end simulation. A preconditionned conjugate gradient method is used for map-making.

4.1 Extended source reconstruction

The input map used for this example to simulate TOD is composed of zeros in each pixel of its 15 input frequencies, N_{in} , and for the three Stokes components. Two monochromatic extended regions with a high signal-to-noise ratio are added: a square centered at 141.6 GHz and a disk centered at 156.5 GHz. Map-making is done for 5 sub-bands centered at 134.6, 141.6, 148.9, 156.5 and 164.6 GHz, with a bandwidth of 6.8, 7.1, 7.5, 7.9 and 8.3 GHz respectively. The scan is performed with 8500 points randomly placed over a 150 square degrees sky patch. Noise is included in the TOD.

The first row in figure 6 shows the input sky maps spatially convolved at the QUBIC resolution. The second row shows the reconstructed maps after map-making onto five sub-bands. The maps are normalized by the maximum value in the convolved maps. In the first, third and fifth sub-bands, where originally the signal is zero, structures corresponding to the signals of neighboring sub-bands appear. The median of the signal on such sub-bands are 0.27, 0.19, 0.31 respectively. The medians are calculated within a region defined by the shape of the signal in the adjacent sub-band, i.e. rectangle (1st sub-band), rectangle + disk (3rd) and disk (5th). The leakage is due to the fact that during the map-making process, it occurs from the frequencies where the monochromatic signal was located towards the neighboring sub-bands due to the frequency point spread function (FPSF) that will be studied in section 4.3.

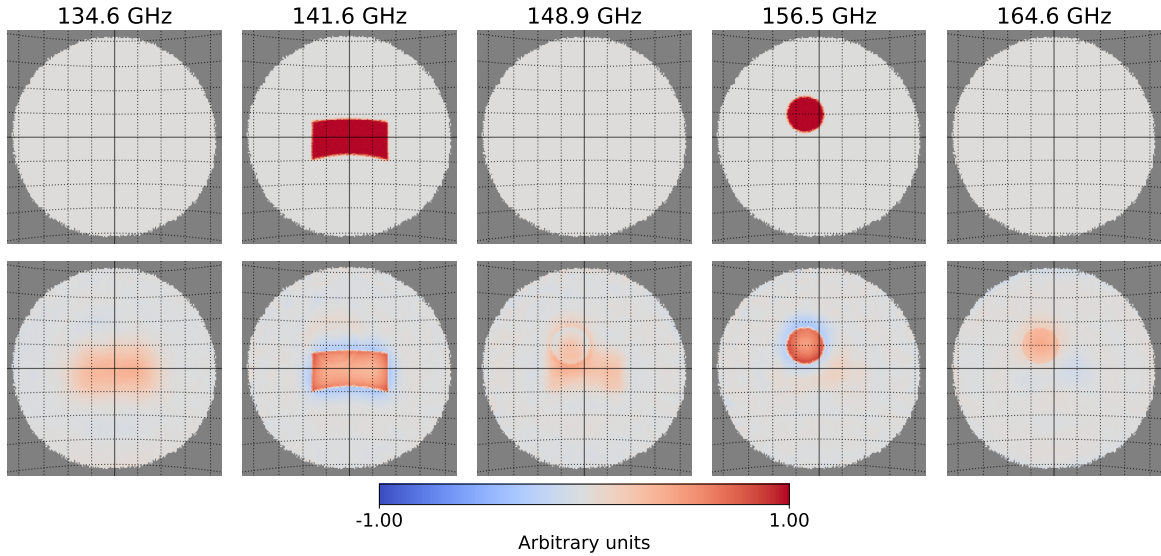


Figure 6. Map-making for a sky full of zeros with two extended, monochromatic regions centered at 141.6 (square) and 156.5 GHz (disk). Each column corresponds to one sub-band. The first row shows the input sky maps spatially convolved at the QUBIC resolution. The reconstructed maps using the QUBIC pipeline are shown in the second row. The units are arbitrary.

4.2 Angular resolution

As an example, we used the end-to-end pipeline to simulate the reconstruction onto 4 sub-bands of a point source emitting with a flat spectrum in the 150 GHz wide band. Figure 7 shows the measured (red stars) and theoretical (blue dots) values of the FWHM at the central frequency of each sub-band. Theoretical values are obtained from a quasi-optical simulation [30] at 150 GHz and scaled proportionally to frequency. Measurements were made on HEALPix maps and corrected by pixel size and resolution [43]. The difference between measured and theoretical values are up to 0.5% which makes it acceptable. The real angular resolution will be determined once QUBIC is installed on the site using far-field observations (astronomical objects and/or calibration tower). This analysis was done for a flat spectrum over the wide frequency band but this hypothesis is not required. In the code, it is only assumed to be flat in small frequency sub-bands with bandwidths around 1/20 of the total bandwidth. The result would be similar in case of a non flat spectrum.

4.3 Frequency point spread function characterization

In section 4.1 it was shown that the reconstructed map for a sub-band has a fraction of signal coming from neighboring bands (see figure 6). In order to study this effect, we simulate monochromatic point source reconstruction to characterize the FPSF.

If we consider a monochromatic input signal with a spectral energy density $S_{\text{in}}(\nu)$ [W/Hz], and considering ideal map-making, then the intensity of the output map $I_{\text{out}}(\nu)$ [W] will be given by the convolution of the input signal with the FPSF [unitless]:

$$I_{\text{out}}(\nu) = [S_{\text{in}} \otimes \text{FPSF}](\nu). \quad (4.1)$$

Thus, for a monochromatic source at ν_{in} with spectral energy density $S_{\text{in}}(\nu) = I_0 \delta(\nu - \nu_{\text{in}})$, we can obtain the FPSF by measuring the intensity in the reconstructed sub-bands.

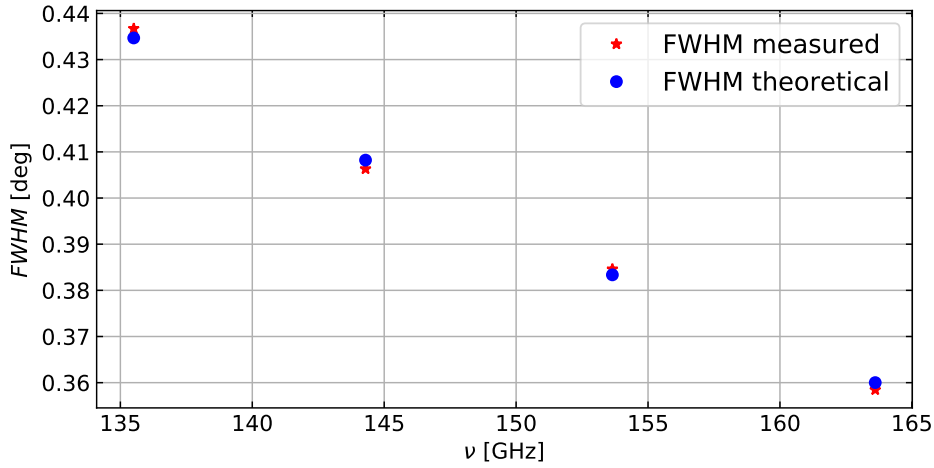


Figure 7. Red stars represent the angular resolution measured for a single point source emitting in the broad band after map-making onto 4 sub-bands. Blue dots are the theoretical values expected for each central frequency of the sub-bands.

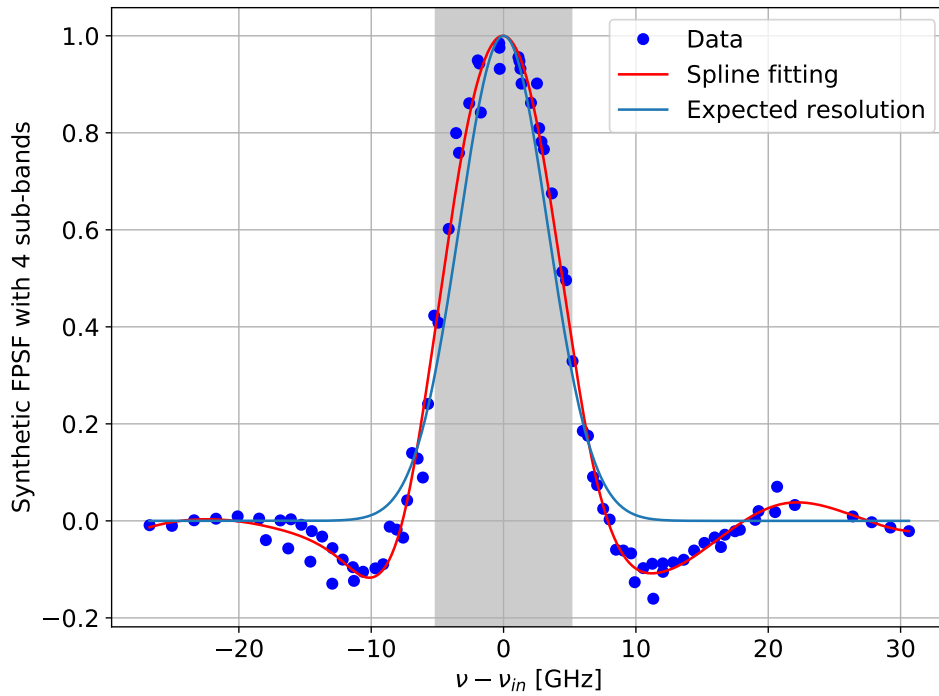


Figure 8. Synthetic FPSF when reconstructing in 4 sub-bands. Blue dots are the intensity of the central pixel of the point source in each sub-band and each simulation superimposed (see text for detailed explanation). Red line is a spline fit. Blue line is a Gaussian with $\text{FWHM} = \frac{\nu_0}{P-1}$, $P = 20$ and $\nu_0 = 150$ GHz, showing an order of magnitude of the expected frequency resolution (see section 3.2). Strong-grey band represent a typical width of a sub-band when reconstruction is performed for 4 sub-bands.

In order to investigate the FPSF of the instrument, we simulate a scan in frequency by moving ν_{in} in a high-resolution frequency grid. We use a grid with $N_{\text{in}} = 48$ which gives us a resolution of ~ 0.78 GHz for the 150 GHz wide band (it would be ~ 1.15 GHz for the 220 GHz band). This grid allows to improve the map within the spectral range and thus obtain more precise information on how the signal is reconstructed at the center and edge of each sub-band. We performed 22 independent simulations of monochromatic point sources with high signal-to-noise ratio. We kept the spatial location of the point source unchanged and we varied its frequency ν_{in} , covering a spectral range from 133 to 162.25 GHz.

We present results for map-making onto 4 sub-bands with central frequencies at $\nu_c = 135.5, 144.3, 153.6, 163.6$ GHz and bandwidths of $\Delta\nu_c = 8.5, 9.1, 9.7, 10.3$ GHz respectively. The FPSF depends on the number of sub-bands so this result is specific to 4 sub-bands. For each simulation, we measure the intensity, normalized to the input one, of the central pixel of the point source in each reconstructed sub-band. In the hypothesis that the FPSF does not depend on the input frequency, we can superimpose all the results. This is done in figure 8 (blue dots) by subtracting ν_{in} to center all the measurements on 0. All the points are well superimposed on a continuous line that we will call the synthetic FPSF of the instrument with 4 sub-bands. A spline fitting is shown in figure 8 (red line) to get a model for the synthetic FPSF. We also plot a Gaussian (blue line) with $\text{FWHM} = \frac{\nu_0}{P-1}$, $P = 20$ and $\nu_0 = 150$ GHz, showing an order of magnitude of the expected frequency resolution as explained in section 3.2. As expected from figure 6, we observe that the FPSF extends beyond a single sub-frequency and should be accounted for in the data analysis. This means that our reconstructed sub-bands are not independent from each other and we should expect noise correlation between sub-bands. Because the FPSF is negative in the nearest band we should expect the noise correlations to be negative between neighbouring sub-bands. This will be studied in section 5.1.

4.4 Galactic dust

We demonstrate spectral imaging capabilities by trying to recover the frequency dependence of the dust emission with simulated observations towards the Galactic center. The sky maps contain IQU Stokes parameter components and the dust model is the one provided by PySM3, named d1 [41]. We simulate an observation in a sky patch of 15 degree radius. This choice was made in order to minimize the number of pointings required to get a sufficient coverage and so to reduce computational resources needed for simulations. However, a bigger patch would give similar results, even better as border effects would be reduced. The parameters of the pipeline are set in such a way that the simulated instrument has a single focal plane operating either at 150 GHz or at 220 GHz with a 25% bandwidth each. The wide band TOD are formed through the sum of a number of monochromatic TOD throughout the wide bandwidth as shown in equation (3.2). For this simulation we have used N_{in} (see table 2) input maps covering the ranges from 137 to 162 GHz and from 192 to 247 GHz. From these wide-band TOD, we are able to reconstruct several numbers of sub-bands using spectral imaging. We have performed simulations with $N_{\text{rec}} = 1, 2, \dots, 8$ reconstructed sub-bands. NEP, including photon noise and detector noise (see table 2) are added as white noise for each TOD. In each case, we perform a Monte-Carlo analysis to get several independent noise realizations and also a noiseless reconstruction that will be the reference. Those end-to-end

simulations require high memory usage and need to be parallelized on several machines.⁴ The result of this procedure at the map level for the I and Q components, for a given realization, is shown in figures 9 and 10. The two figures display a sky reconstructed in 5 sub-bands within the 220 GHz wide band. The residual map is the difference between a reconstruction and the noiseless reference.

We can see that the Galactic dust is efficiently reconstructed in the 5 sub-bands as the residuals are compatible with pure noise. Note that the noise is not white but has spatial correlations due to the deconvolution with the multi-peak synthesized beam (see section 3.1.1 in Hamilton et al. [24]). We also note that the residuals are higher on the edges than in the center of the sky patch. This is due to the higher coverage of the sky in the center due to the scanning strategy.

Instead of looking at the full map, the reconstructed intensity as a function of frequency can also be studied pixel by pixel. Figure 11 shows the intensity of the input sky convolved with the instrument beam, and the reconstructed intensity for a given pixel, considering 5 sub-bands in each wide band at 150 (red) and 220 (blue) GHz. We do not display the measured points and error-bars which are not good indicators of our uncertainties due to the highly anti-correlated nature of the covariance matrix (see figure 13 in the case of 3 sub-bands). Instead, we have performed a Monte-Carlo-Markov-Chain (MCMC) exploration of the amplitude and spectral-index of a typical dust model (modified black-body, see Irfan et al. [44]) accounting for the sub-bands covariance matrix. The fit is done separately for our two physical bands at 150 and 220 GHz. The 68% confidence level (CL) is shown in light colors in each case and represents the QUBIC measurements within this band using spectral imaging. Note that the angular resolution of the maps improves with frequency (see section 4.2) and is not accounted for. As a result this simple analysis cannot be interpreted as a measurement of the dust spectral index which would require a more detailed analysis including the beam profile to properly infer the dust property in each sky pixel (such as [44]). This study is being carried out for a future article.

The dust reconstruction is also studied in the angular power spectrum using the public code NaMaster [45] which computes TT, EE, BB and TE spectra where T is the temperature and E, B are the two polarization modes. Spectra are computed from a multipole moment $l = 40$ to $l = 2 \times N_{\text{side}} - 1$ with $N_{\text{side}} = 256$ the pixel resolution parameter for HEALPix maps. We compute inter-band cross spectra (IBCS), meaning that from N_{rec} sub-band maps, one can compute $N_{\text{rec}}(N_{\text{rec}} + 1)/2$ IBCS. Having independent noise realizations allows us to make IBCS crossing two realizations, so we eliminate the noise bias. BB IBCS for 3 sub-bands in each of the 150 and 220 GHz wide bands are shown in figure 12. We plot $D_l = \frac{l(l+1)}{2\pi} C_l$, C_l being the B-mode angular power spectrum. In this figure, the input theoretical dust spectra coming from the PySM model d1 are superposed to the reconstructed ones.

⁴For instance, with 10000 pointings, 992 detectors (FI), considering the main 14 peaks in the synthesized beam, the size of the pointing matrix for each input sub-band is: $\sim 10000 \times 992 \times 14 \times 16/1024^3 \sim 2$ GiB and typically, there are $N_{\text{in}} \sim 20$ sub-bands. Regarding the convergence of the map-making, the number of iterations needed will vary, especially with the level of noise and with the number of sub-bands. For a typical end-to-end simulation with $N_{\text{rec}} = 6$, it is around 320 iterations.

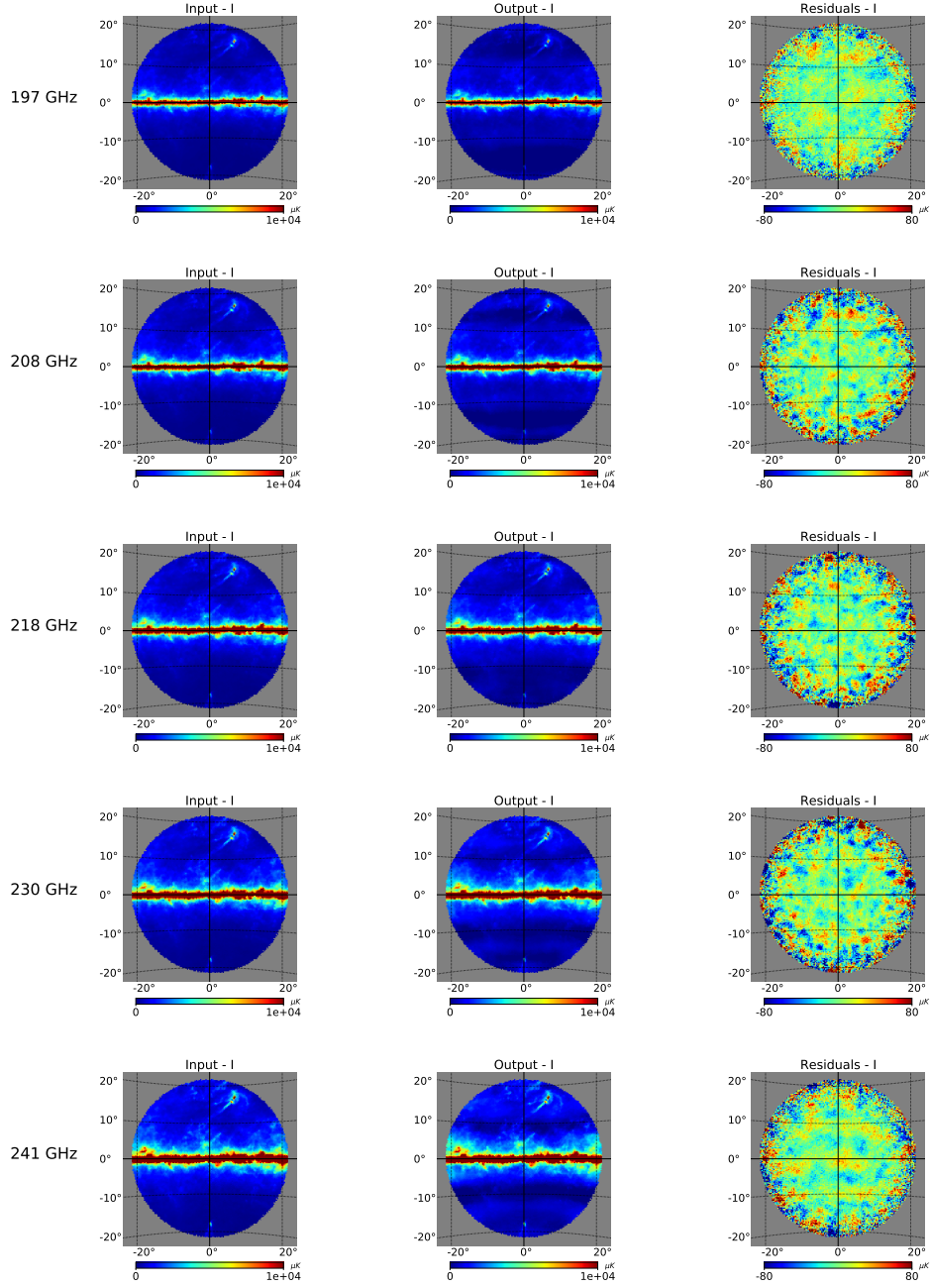


Figure 9. Map-making of the galaxy dust in $N_{\text{rec}} = 5$ frequency sub-bands from 192 to 247 GHz for I component. The map unit is $\mu\text{K CMB}$. The first column is the input sky convolved to the resolution of the instrument in that sub-band. The second column is the reconstructed map after the map-making process. Residuals, defined by the difference between the simulation including noise and a noiseless one, are shown in the last column. The noise is not white but has spatial correlations due to the deconvolution with the multi-peak synthesized beam, it is clearly visible in the 241 GHz sub-band.

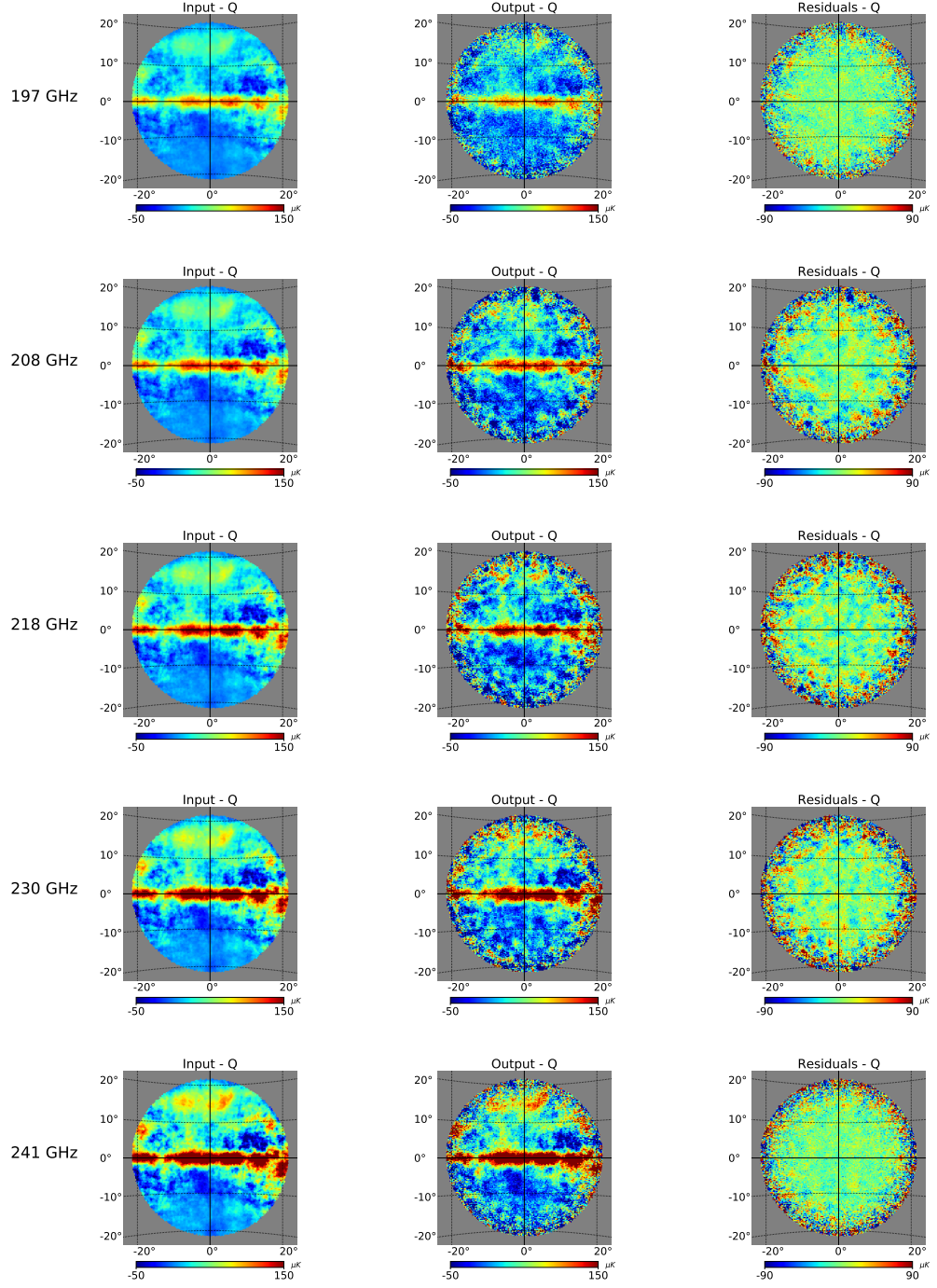


Figure 10. Map-making of the galaxy dust in 5 frequency sub-bands from 192 to 247 GHz. Same as figure 9 but for Q component.

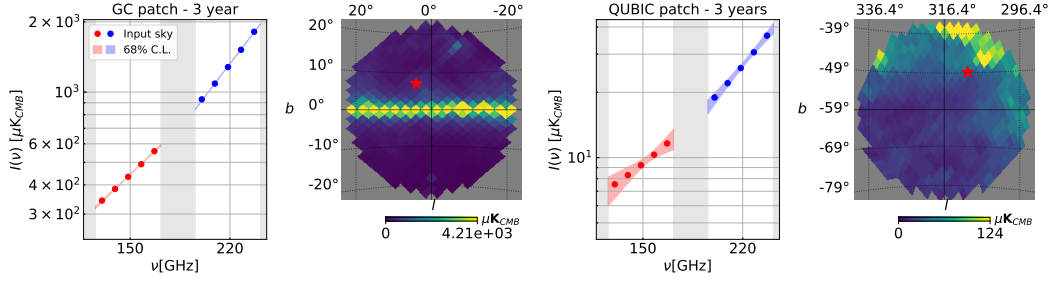


Figure 11. Intensity as a function of the frequency for $N_{\text{rec}} = 5$ sub-bands in each wide band at 150 (red) and 220 (blue) GHz for a given pixel. The grey regions correspond to the unobserved frequencies outside our physical bands. Two sky pixels are shown as red stars, one in a patch centered at the Galactic center and one in the patch that QUBIC plans to observe centered in $[0, -57 \text{ deg}]$. Red and blue dots: input sky convolved with the instrument beam. In both cases are shown in light color the 68% CL regions for a modified black-body spectrum reconstructed with a MCMC from our simulated measurements and sub-band covariance matrices (see figure 13 for the case of 3 sub-bands). Maps are in $\mu\text{K CMB}$ and $N_{\text{side}} = 32$.

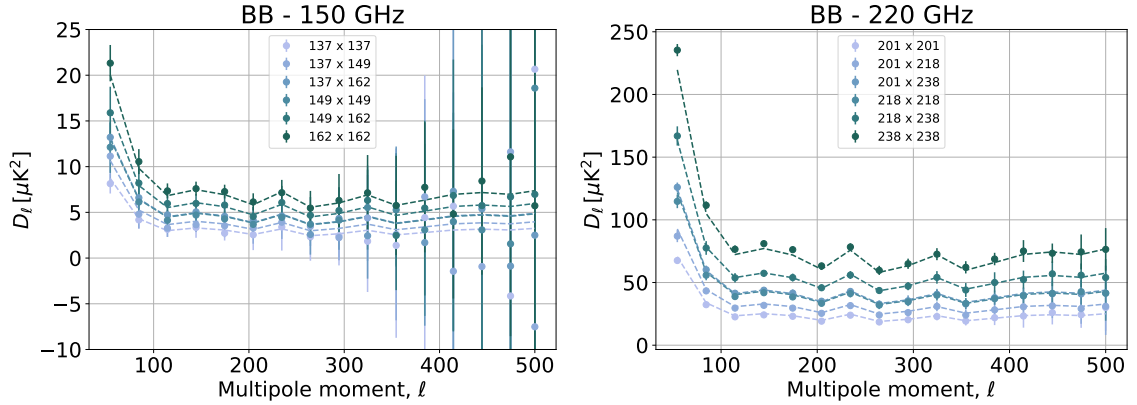


Figure 12. BB IBCS at 150 GHz (left) and 220 GHz (right) computed from reconstructed maps in 3 sub-bands (137, 149 and 162 GHz and 201, 218 and 238 GHz respectively), obtained with end-to-end simulations. For each IBCS, we cross-correlate 2 sub-bands with central frequencies in GHz shown in the legend of each plot. Dashed lines are the IBCS of the input sky that contains only Galactic dust. The dots with error bars show the mean and the standard deviation over 20 IBCS. Each IBCS is made with 2 maps with independent noise realizations to eliminate the noise bias.

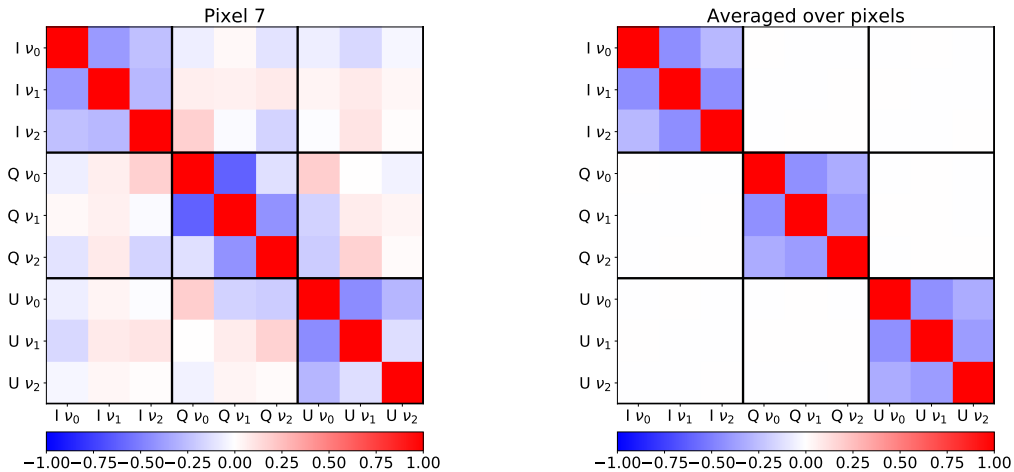


Figure 13. Correlation matrices between frequency sub-bands $\nu_0 = 137$ GHz, $\nu_1 = 149$ GHz and $\nu_2 = 162$ GHz and I, Q, U Stokes components obtained from 40 end-to-end simulations. *Left:* example for a given pixel. *Right:* the average over pixels. Blue means anti-correlations while red is for positive correlations.

5 Noise characterization

For the map-making described in section 2.4, we added noise to the TOD which was composed of the detector NEP ($4.7 \times 10^{-17} \text{W}/\sqrt{\text{Hz}}$) and photon NEP (see table 2). As before, the atmospheric load is assumed to be stable. The goal here is to study how close to optimal (in the statistical sense) is our spectral imaging map-making. We will study the noise behaviour as a function of the number of reconstructed sub-bands N_{rec} . This is done at three different levels: on the reconstructed maps, on the power spectra computed from the maps, and on a likelihood estimation for the tensor-to-scalar ratio r .

5.1 Noise behaviour in the sub-bands at map level

We performed simulations with 40 independent noise realizations and a noiseless simulation as a reference. After map-making, residual maps are computed by taking the difference between each simulation and the noiseless reference. For each pixel, we compute the covariance matrix, over all the noise realizations, between the sub-bands and the Stokes parameters.

The reason why we treat the pixels separately, not computing covariance over them, is that the noise level varies with the position in the sky. This is due to the coverage of the sky by the instrument beam which is not uniform. Note that the QUBIC coverage is not trivial because of the multi-peak synthesized beam.

A correlation matrix for a given pixel, considering 3 sub-bands, is shown in figure 13 and we also show the average over pixels. It can be seen that for each Stokes parameter, residual sub-bands next to one another are anticorrelated and this is seen on every pixel. However, cross-correlations between Stokes parameters are negligible. This is why we can consider the 3 correlation matrices C_{I_p} , C_{Q_p} and C_{U_p} separately.

5.2 Noise analysis using the power spectrum

In section 5.1 it was shown that a polychromatic interferometer has anti-correlations in neighbouring bands for each Stokes parameter. Furthermore, the spatial structure of noise is

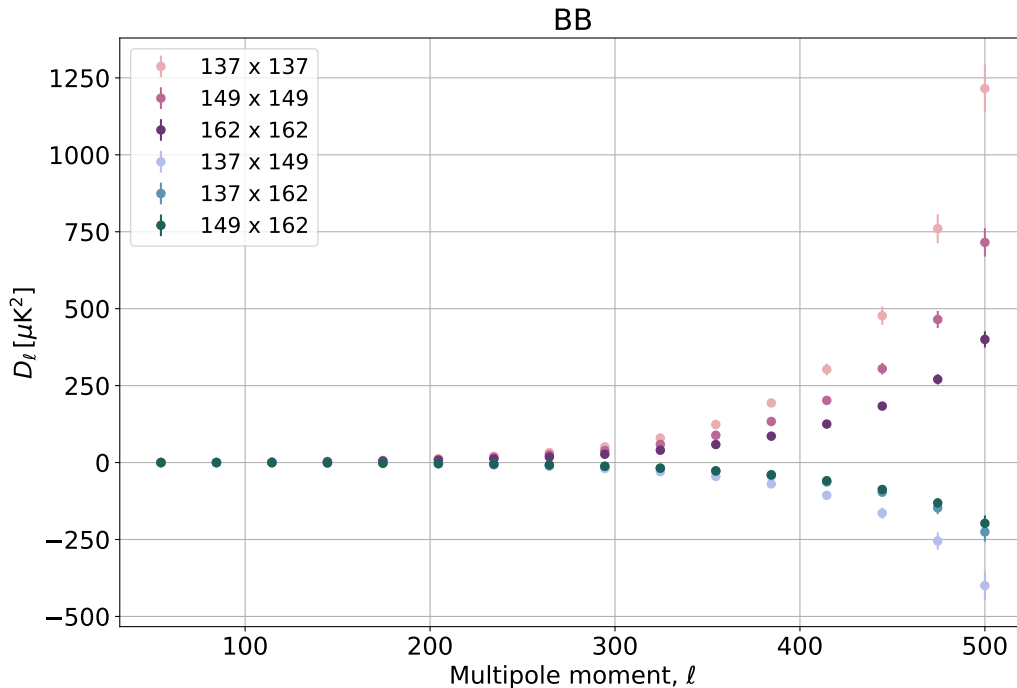


Figure 14. BB Inter Band Cross Spectra on the residual maps containing only noise for 3 sub-bands in the wide 150 GHz band, centered at 137, 149 and 162 GHz. Dots and error bars show average and standard deviation over 1000 independent noise realisation IBCS computed with the fast noise simulator.

studied in detail in Hamilton et al. [24] using end-to-end simulations. This allows us to build a fast noise simulator that reproduces efficiently the noise behaviour in the reconstructed maps. In the following, the fast noise simulator will be used in parallel with end-to-end simulations as it allows us to improve the statistics while consuming much less computing time.

We characterize the noise behaviour of spectral imaging using the power spectrum. As shown in section 4.4, from the maps we can compute power spectra using the public code NaMaster. From N_{rec} bands, we compute the IBCS for each TT, EE, BB and TE power spectra. As we are interested in the noise, we compute the power spectra of the residual maps containing only noise. Figure 14 shows the IBCS computed for each noise realization in the case of 3 sub-bands at 150 GHz. As we plot D_l the noise bias goes as $l(l+1)$. We find that the IBCS within the same band ($\nu_0\nu_0, \nu_1\nu_1$ and $\nu_2\nu_2$) are positively correlated. However the IBCS crossing 2 different bands ($\nu_0\nu_1, \nu_0\nu_2$ and $\nu_1\nu_2$) are anti-correlated.

The correlations are observed in greater detail by computing the correlation matrices. In figure 15, we show the correlation matrix between ℓ -bins and IBCS for BB angular power spectrum considering $N_{\text{rec}} = 3$ sub-bands in the 150 GHz wide band. In this matrix, we see that anti-correlations, in blue in the matrix, only appear between the IBCS crossing 2 different bands ($\nu_0\nu_1, \nu_0\nu_2$ and $\nu_1\nu_2$ in the case of 3 sub-bands) and that the correlations between bins are negligible. The same behaviour is observed for TT, EE and TE spectra.

5.3 Nearly optimal performance of spectral imaging

In order to assess, in a manner easy to interpret, how far from optimal is spectral imaging, we study how the tensor-to-scalar ratio r is constrained as a function of the number of sub-

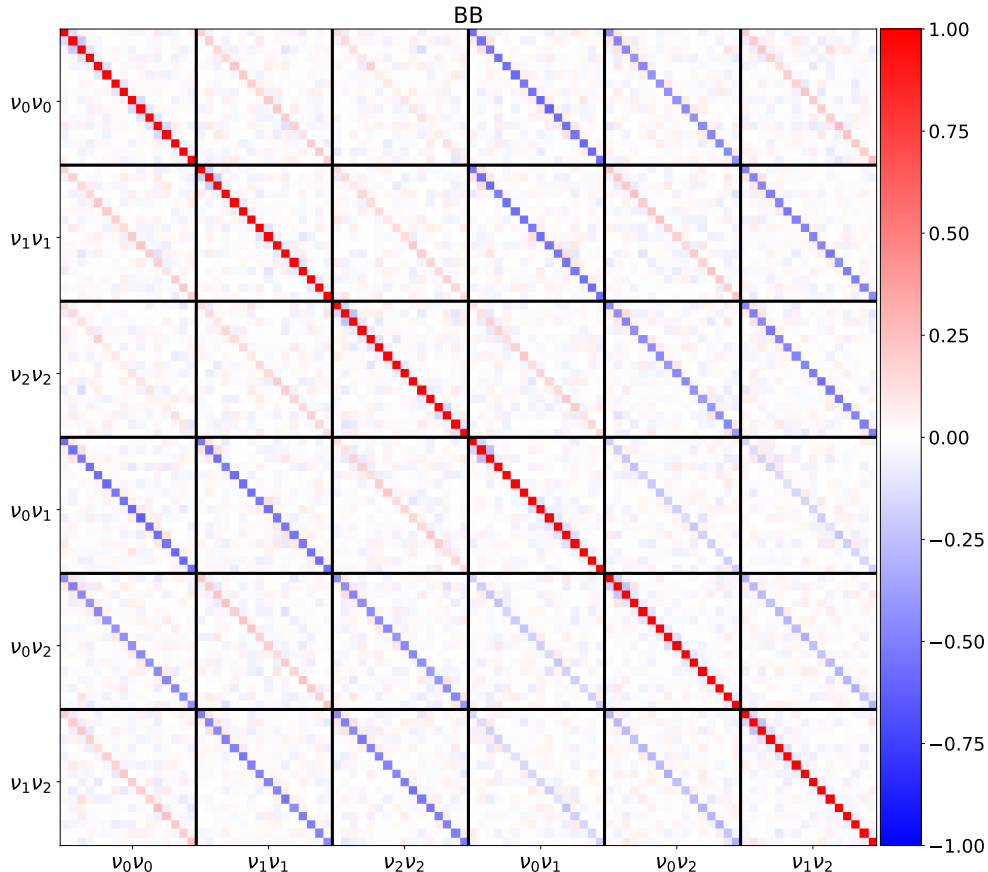


Figure 15. Correlation matrix between ℓ -bins and IBCS for BB angular power spectrum considering 3 sub-bands at $\nu_0 = 137$, $\nu_1 = 149$ and $\nu_2 = 162$ GHz. For example, $\nu_0\nu_1$ is the IBCS between frequencies ν_0 and ν_1 . In each black square we show the correlations between the 16 ℓ -bins used to compute the IBCS as in figure 14.

bands N_{rec} . The sky model is a pure CMB sky, including lensing but no Galactic foregrounds, with $r = 0$. The aim of this section is not to make precise forecasts on the sensitivity on r . This is addressed in the companion paper Hamilton et al. [24] and we expect to reach a sensitivity to B-modes corresponding to a 68% CL upper-limit on the effective tensor-to-scalar ratio (primordial tensors + galactic dust) $\sigma(r) = 0.015$ with three years of observations.

The division of the wide band into a number of sub-bands for spectral imaging could have a detrimental effect on the estimate of the tensor-to-scalar ratio r and this is what we want to quantify in this section. On the one hand, we would certainly like to make as many sub-bands as possible in order to constrain the foreground spectra in a very precise manner. However, on the other hand, there is an upper-limit to the achievable number of sub-bands, when the angular distance between peaks in the synthesized beams at different frequencies becomes smaller than the peak width (angular resolution), as explained in section 3.2. We therefore expect the performance of spectral imaging to degrade when projecting data onto too many sub-bands. In fact, even for a small number of sub-bands, spectral imaging cannot be strictly optimal because the synthesized beams at different sub-frequencies do not form an orthogonal basis. We therefore expect a certain loss in signal-to-noise ratio when performing spectral imaging. The higher the number of reconstructed sub-bands, the more overlap there

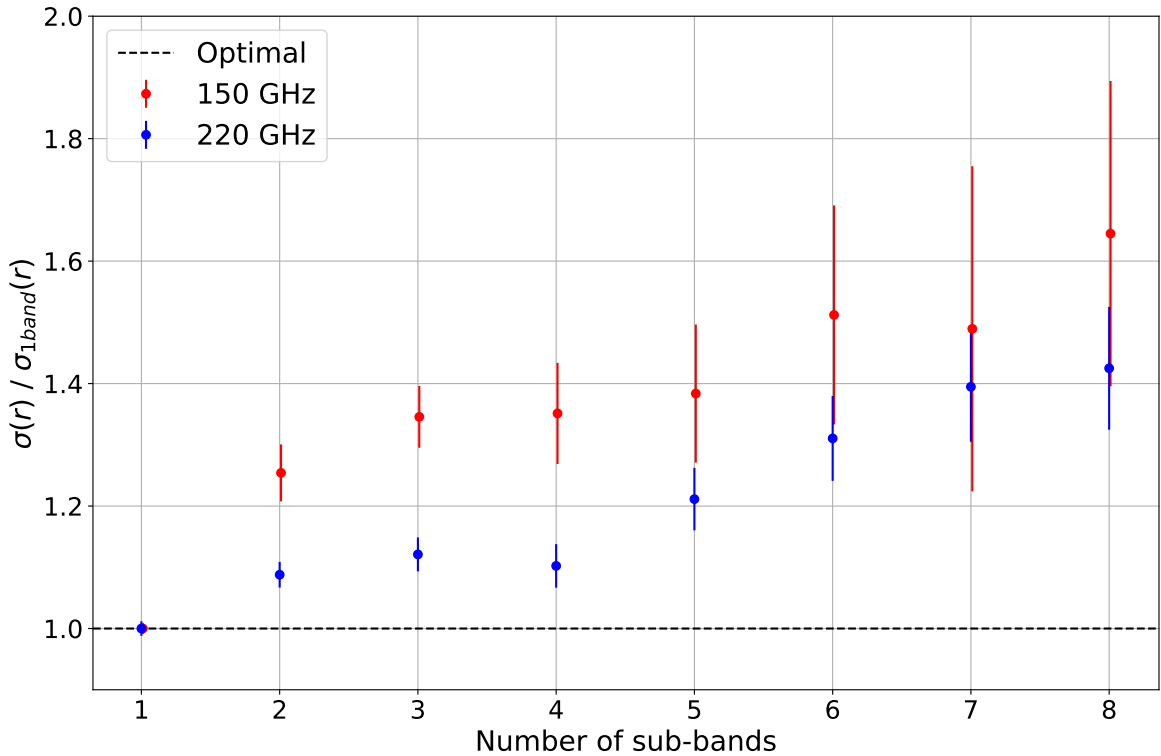


Figure 16. Uncertainties (68% CL upper limits) on the tensor-to-scalar ratio r obtained by combining an increasing number of sub-bands, normalized to that of one band, for a pure $r = 0$ CMB (with lensing). The slow increase of the uncertainty on r with the number of sub-bands illustrates the moderate sub-optimality of spectral imaging and shows that we can use up to 5 sub-bands with only 40% degradation at 150 GHz (and only 20% degradation at 220 GHz). It is possible to achieve 8 sub-bands but with more significant degradation.

is between the synthesized beam at each sub-frequency. This results in stronger degeneracy between sub-bands, hence a higher noise in the reconstruction. This is the price to pay for improved spectral resolution. As a result, one needs to find the best balance between performance and spectral resolution for a given scientific objective.

For that purpose, we project simulated data onto an increasing number of sub-bands N_{rec} , calculate the corresponding IBCS and in each case we compute a likelihood to estimate the tensor-to-scalar ratio r combining all sub-bands accounting for their cross-correlations. From this method, we get the error on r at 68% confidence level for each number of sub-bands. This is presented in figure 16. We normalize by the case of “spectral imaging” with just one band. Error bars are obtained from a Monte-Carlo analysis, varying the data in the likelihood according to their diagonal uncertainties. As expected, we observe a moderate degradation due to spectral imaging in the sense that the constraints on r become less stringent when the number of sub-bands is greater than one. This degradation slowly evolves from 25% to 40% at 150 GHz and from 10% to 20% at 220 GHz when the number of sub-bands evolves from 2 to 5. The better performance at 220 GHz is not a surprise as our horns are slightly multimoded at 220 GHz (see O’Sullivan et al. [30] for details) resulting in a flatter primary beam, which, in turn, favours spectral imaging because multiple peaks of the synthesized are higher in amplitude. It is possible to project onto as many as 8 sub-bands with a

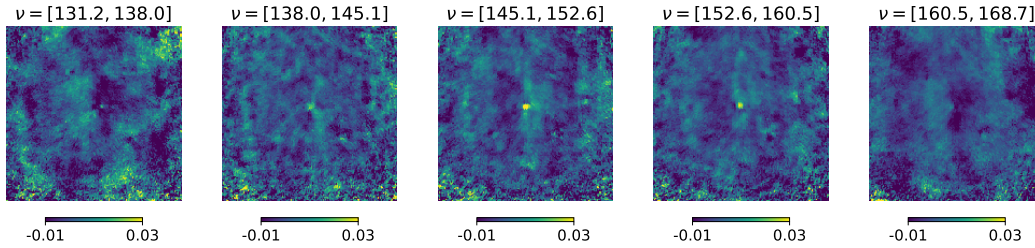


Figure 17. Calibration data with the source at 150 GHz projected on the sky using our map-making software to deconvolve from the multiple peaked synthesized beam and split the physical band of the instrument into 5 sub-bands.

corresponding performance reduction due to the fact that synthesized beam peaks become too close with respect to their width, as explained in section 3.2.

This study demonstrates that, although not optimal from the noise point of view, spectral imaging performance remains close to optimal for up to 5 bands, providing extra spectral resolution that can be key for constraining foreground contamination with realistic models for which the spectrum might not be a simple power law, work being in progress on this. The appropriate balance between spectral resolution and noise performance can be adjusted for each specific analysis thanks to the fact that spectral imaging is done entirely in post-processing.

This work is a first step to characterize the potential of spectral imaging. In order to place the technique in context, we need to include spectral imaging into a proper component separation step. This will be addressed in future work.

6 Spectral imaging on real data

Spectral imaging has been applied on real data for the first time during the calibration campaign at the APC laboratory. The QUBIC instrument was placed on an alt-azimuth mount in order to scan a calibration source tuned at 150 GHz (with 144 Hz bandwidth) and placed in the far field. The corresponding analysis presented in the companion paper Torchinsky et al. [25]. We then perform a scan in azimuth and elevation with the instrument, obtaining a TOD for each bolometer. We then apply our spectral imaging map-making algorithm with five sub-bands to a selection of 26 bolometers that do not exhibit saturation. The synthesized beam for each bolometer is realistically modeled in our map-making through a series of Gaussian whose amplitude, width and locations are fit from a measured map of the synthesized beam for each bolometer (see figure 20 from Torchinsky et al. [25] for an example). The frequency evolution of this synthesized beam only assumes linear scaling with wavelength. We were able to reconstruct a map of the point-like artificial calibration source as well as its location in frequency space. In figure 17, we show the reconstruction onto 5 sub-bands. The expected point-source shape is clearly visible in the central frequency sub-band containing the emission frequency of the source at 150 GHz.

The calibration source is fainter in adjacent bands, and not visible in the furthest bands. In figure 18, we show the detected amplitude in the central pixel as a function of the frequency. The measurement in red is compared to the expected value spectrum in blue. The expected shape is a Gaussian centered on $\nu = 150$ GHz and a FWHM equaled to $\frac{\nu}{(P-1)}$ as explained in section 3.2. Those data were acquired with the TD instrument that has a square 8×8

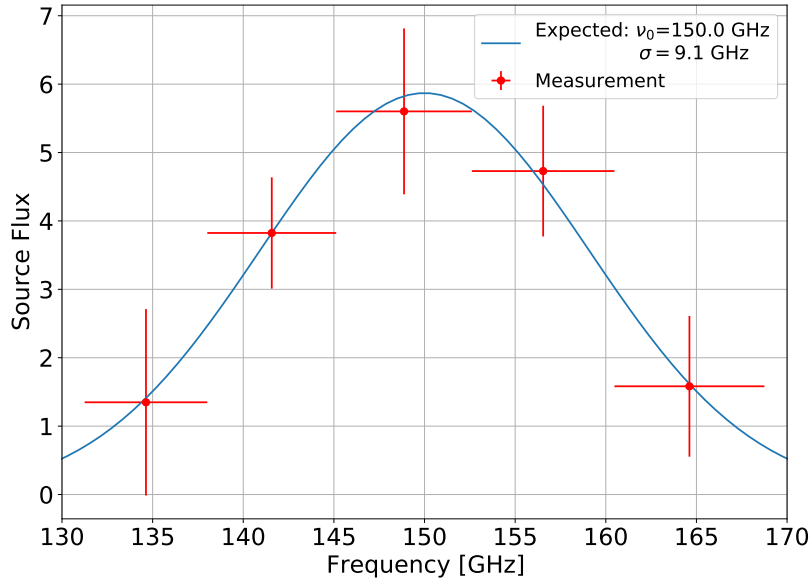


Figure 18. Measurement of the flux of the source in reconstructed sub-bands. The measurement (simple aperture photometry) in red is compared to the expected value spectrum in blue. The expected shape is a Gaussian centered on $\nu = 150$ GHz and a FWHM equal to $\frac{\nu}{(P-1)}$ with $P = 8$ for the TD instrument. A global offset and the amplitude of the Gaussian are adjusted to the data.

feedhorn array so $P = 8$. The global offset and the amplitude of the Gaussian are adjusted to the data. Error bars are computed in a very conservative manner.

7 Conclusion

In this article, we have shown how the new technique of bolometric interferometry offers the possibility to also perform spectral imaging. This makes it possible to split, in post processing, the wide-band observations into multiple sub-bands achieving spectral resolution. To illustrate this method, we apply it to the case of the QUBIC instrument soon to be installed at its observation site in Argentina.

After having presented the design, concept, and mathematical aspects of the instrument and the spectral imaging technique we have illustrated it on simple cases: monochromatic point sources, spatially extended sources, and sky maps with frequency-dependent emission such as Galactic dust. We have shown our ability to have increased spectral resolution with respect to the physical bandwidth, considering a full sky patch but also at the level of individual pixels. We studied the signal and noise behavior using Monte-Carlo simulations for an instrument like QUBIC which shows spatial and spectral correlations. We have quantified the loss of statistical performance for the measurement of the tensor-to-scalar ratio when increasing the number of sub-bands and have shown it to be moderate up to 5 sub-bands.

The precise measurement of foreground contaminants is essential for the detection of primordial B-modes. Foregrounds have spectral properties distinct from the CMB which leads to the conclusion that only a multichroic approach enables the measurement and subtraction of foreground contamination. This is usually done in classical imagers through detectors operating at distinct frequencies, each of them being wide-band in order to maximize signal-to-noise ratio. However, constraining foregrounds with such data relies on extrapolation between dis-

tant frequency bands, which may miss non-trivial variations of the spectral behaviour of complex foregrounds such as multiple dust clouds in the line of sight. In particular, scenarios where dust exhibits a certain level of decorrelation between widely separated bands, or with non constant spectral indices would be impossible to be identified with a usual wide-band analysis. Spectral imaging could put significant constraints on such scenarios. This is being studied in detail by the QUBIC collaboration and will be presented in the near future.

In summary, spectral imaging improves spectral resolution within a wide physical band, while nearly preserving the optimal performance of the analysis. It may therefore become a key technique for detecting the elusive B-mode polarization of the CMB.

Acknowledgments

We thank the anonymous referees as well as the editor for insightful reviews that greatly improved this work. QUBIC is funded by the following agencies. France: ANR (Agence Nationale de la Recherche) 2012 and 2014, DIM-ACAV (Domaine d'Interet Majeur-Astronomie et Conditions d'Apparition de la Vie), Labex UnivEarthS (Université de Paris), CNRS/IN2P3 (Centre National de la Recherche Scientifique/Institut National de Physique Nucléaire et de Physique des Particules), CNRS/INSU (Centre National de la Recherche Scientifique/Institut National des Sciences de l'Univers). Italy: CNR/PNRA (Consiglio Nazionale delle Ricerche/Programma Nazionale Ricerche in Antartide) until 2016, INFN (Istituto Nazionale di Fisica Nucleare) since 2017. Argentina: MINCyT (Ministerio de Ciencia, Tecnología e Innovación), CNEA (Comisión Nacional de Energía Atómica), CONICET (Consejo Nacional de Investigaciones Científicas y Técnicas).

References

- [1] A.A. Penzias and R.W. Wilson, *A measurement of excess antenna temperature at 4080-Mc/s*, *Astrophys. J.* **142** (1965) 419 [[INSPIRE](#)].
- [2] D.J. Fixsen, *The Temperature of the Cosmic Microwave Background*, *Astrophys. J.* **707** (2009) 916 [[arXiv:0911.1955](#)] [[INSPIRE](#)].
- [3] SPT collaboration, *Measurements of B-mode Polarization of the Cosmic Microwave Background from 500 Square Degrees of SPTpol Data*, *Phys. Rev. D* **101** (2020) 122003 [[arXiv:1910.05748](#)] [[INSPIRE](#)].
- [4] SPT-3G collaboration, *Detection of Galactic and Extragalactic Millimeter-Wavelength Transient Sources with SPT-3G*, [arXiv:2103.06166](#) [[INSPIRE](#)].
- [5] POLARBEAR collaboration, *A Measurement of the Degree Scale CMB B-mode Angular Power Spectrum with POLARBEAR*, *Astrophys. J.* **897** (2020) 55 [[arXiv:1910.02608](#)] [[INSPIRE](#)].
- [6] ACT collaboration, *The Atacama Cosmology Telescope: a measurement of the Cosmic Microwave Background power spectra at 98 and 150 GHz*, *JCAP* **12** (2020) 045 [[arXiv:2007.07289](#)] [[INSPIRE](#)].
- [7] ACT collaboration, *The Atacama Cosmology Telescope: DR4 Maps and Cosmological Parameters*, *JCAP* **12** (2020) 047 [[arXiv:2007.07288](#)] [[INSPIRE](#)].
- [8] Z. Xu et al., *Two-year Cosmology Large Angular Scale Surveyor (CLASS) Observations: 40 GHz Telescope Pointing, Beam Profile, Window Function, and Polarization Performance*, *Astrophys. J.* **891** (2019) 134 [[arXiv:1911.04499](#)] [[INSPIRE](#)].

- [9] BICEP2 and KECK ARRAY collaborations, *Constraints on Primordial Gravitational Waves using Planck, WMAP, and New BICEP2/Keck Observations through the 2015 Season*, *Phys. Rev. Lett.* **121** (2018) 221301 [[arXiv:1810.05216](#)] [[INSPIRE](#)].
- [10] S. Dahal et al., *The CLASS 150/220 GHz Polarimeter Array: Design, Assembly, and Characterization*, *J. Low Temp. Phys.* **199** (2020) 289 [[arXiv:1908.00480](#)] [[INSPIRE](#)].
- [11] POLARBEAR collaboration, *The POLARBEAR-2 and the Simons Array Experiment*, *J. Low Temp. Phys.* **184** (2016) 805 [[arXiv:1512.07299](#)] [[INSPIRE](#)].
- [12] S.W. Henderson et al., *Advanced ACTPol Cryogenic Detector Arrays and Readout*, *J. Low Temp. Phys.* **184** (2016) 772 [[arXiv:1510.02809](#)] [[INSPIRE](#)].
- [13] A. Schillaci et al., *Design and Performance of the First BICEP Array Receiver*, *J. Low Temp. Phys.* **199** (2020) 976 [[arXiv:2002.05228](#)] [[INSPIRE](#)].
- [14] SIMONS OBSERVATORY collaboration, *The Simons Observatory: Science goals and forecasts*, *JCAP* **02** (2019) 056 [[arXiv:1808.07445](#)] [[INSPIRE](#)].
- [15] R. Datta et al., *Anti-reflection coated vacuum window for the Primordial Inflation Polarization ExploreR (PIPER) balloon-borne instrument*, *Rev. Sci. Instrum.* **92** (2021) 035111 [[arXiv:2103.07936](#)] [[INSPIRE](#)].
- [16] LSPE collaboration, *The large scale polarization explorer (LSPE) for CMB measurements: performance forecast*, [arXiv:2008.11049](#) [[INSPIRE](#)].
- [17] K. Abazajian et al., *CMB-S4 Science Case, Reference Design, and Project Plan*, [arXiv:1907.04473](#) [[INSPIRE](#)].
- [18] H. Sugai et al., *Updated Design of the CMB Polarization Experiment Satellite LiteBIRD*, *J. Low Temp. Phys.* **199** (2020) 1107 [[arXiv:2001.01724](#)] [[INSPIRE](#)].
- [19] PLANCK collaboration, *Planck 2018 results. XI. Polarized dust foregrounds*, *Astron. Astrophys.* **641** (2020) A11 [[arXiv:1801.04945](#)] [[INSPIRE](#)].
- [20] U. Fuskeland, I.K. Wehus, H.K. Eriksen and S.K. Næss, *Spatial variations in the spectral index of polarized synchrotron emission in the 9-yr WMAP sky maps*, *Astrophys. J.* **790** (2014) 104 [[arXiv:1404.5323](#)] [[INSPIRE](#)].
- [21] N. Macellari, E. Pierpaoli, C. Dickinson and J. Vaillancourt, *Galactic foreground contributions to the WMAP5 maps*, *Mon. Not. Roy. Astron. Soc.* **418** (2011) 888 [[arXiv:1108.0205](#)] [[INSPIRE](#)].
- [22] M. Remazeilles, C. Dickinson, H.K.K. Eriksen and I.K. Wehus, *Sensitivity and foreground modelling for large-scale cosmic microwave background B-mode polarization satellite missions*, *Mon. Not. Roy. Astron. Soc.* **458** (2016) 2032 [[arXiv:1509.04714](#)] [[INSPIRE](#)].
- [23] S.S. Malu and P.T. Timbie, *Broadband Fizeau Interferometers for Astrophysics*, [arXiv:1006.5936](#) [[INSPIRE](#)].
- [24] QUBIC collaboration, *QUBIC I: Overview and Science Program*, [arXiv:2011.02213](#) [[INSPIRE](#)].
- [25] QUBIC collaboration, *QUBIC III: Laboratory Characterization*, [arXiv:2008.10056](#).
- [26] QUBIC collaboration, *QUBIC IV: Performance of TES Bolometers and Readout Electronics*, [arXiv:2101.06787](#) [[INSPIRE](#)].
- [27] QUBIC collaboration, *QUBIC V: Cryogenic system design and performance*, [arXiv:2008.10659](#) [[INSPIRE](#)].
- [28] QUBIC collaboration, *QUBIC VI: cryogenic half wave plate rotator, design and performances*, [arXiv:2008.10667](#) [[INSPIRE](#)].
- [29] F. Cavaliere et al., *QUBIC VII: The feedhorn-switch system of the technological demonstrator*, [arXiv:2008.12721](#) [[INSPIRE](#)].

- [30] QUBIC collaboration, *QUBIC VIII: Optical design and performance*, [arXiv:2008.10119](#) [[INSPIRE](#)].
- [31] H. Fizeau, *Sur les hypothèses relatives à l'éther lumineux et sur une expérience qui paraît démontrer que le mouvement de corps change la vitesse avec laquelle la lumière se propage dans leur intérieur*, *Compte Rendu des Séances de l'Académie des Sciences* (1851) 349.
- [32] QUBIC collaboration, *QUBIC: The QU Bolometric Interferometer for Cosmology*, *Astropart. Phys.* **34** (2011) 705 [[arXiv:1010.0645](#)] [[INSPIRE](#)].
- [33] M.A. Bigot-Sazy, R. Charlassier, J.C. Hamilton, J. Kaplan and G. Zahariade, *Self-calibration: an efficient method to control systematic effects in bolometric interferometry*, *Astron. Astrophys.* **550** (2013) A59 [[arXiv:1209.4905](#)] [[INSPIRE](#)].
- [34] T. Cornwell and P. Wilkinson, *A new method for making maps with unstable radio interferometers*, *Mon. Not. Roy. Astron. Soc.* **196** (1981) 1067.
- [35] M. Tegmark, *CMB mapping experiments: A Designer's guide*, *Phys. Rev. D* **56** (1997) 4514 [[astro-ph/9705188](#)] [[INSPIRE](#)].
- [36] J. Borrill, *Madcap — the microwave anisotropy dataset computational analysis package*, [astro-ph/9911389](#) [[INSPIRE](#)].
- [37] P. Chanial and N. Barbey, *PyOperators: Operators and solvers for high-performance computing*, *SF2A* (2012) 513.
- [38] M. Hestenes and E. Stiefel, *Methods of conjugate gradients for solving linear systems*, *J. Res. Natl. Bur. Stand.* **49** (1952) 409.
- [39] J.R. Shewchuk et al., *An introduction to the conjugate gradient method without the agonizing pain*, Carnegie Mellon University, U.S.A. (1994).
- [40] L. Rayleigh, *XXXI. Investigations in optics, with special reference to the spectroscope*, *Philos. Mag.* **8** (1879) 261.
- [41] B. Thorne, J. Dunkley, D. Alonso and S. Naess, *The Python Sky Model: software for simulating the Galactic microwave sky*, *Mon. Not. Roy. Astron. Soc.* **469** (2017) 2821 [[arXiv:1608.02841](#)] [[INSPIRE](#)].
- [42] K.M. Gorski et al., *HEALPix — A Framework for high resolution discretization, and fast analysis of data distributed on the sphere*, *Astrophys. J.* **622** (2005) 759 [[astro-ph/0409513](#)] [[INSPIRE](#)].
- [43] M.M. Gamboa Lerena et al., *Angular resolution at map level in the QUBIC instrument*, *Bol. A. A. Astron. La Plata Argentina* **B 61** (2020) 155.
- [44] M.O. Irfan, J. Bobin, M.-A. Miville-Deschênes and I. Grenier, *Determining thermal dust emission from Planck HFI data using a sparse, parametric technique*, *Astron. Astrophys.* **623** (2019) A21 [[arXiv:1901.01713](#)] [[INSPIRE](#)].
- [45] C. García-García, D. Alonso and E. Bellini, *Disconnected pseudo- C_ℓ covariances for projected large-scale structure data*, *JCAP* **11** (2019) 043 [[arXiv:1906.11765](#)] [[INSPIRE](#)].

Résumé en français

B.1 Introduction

Ce résumé substantiel en français présente le contexte scientifique et reprend les principaux points de mon travail de thèse.

L’interféromètre bolométrique QUBIC est un instrument dédié à la mesure de la polarisation du fond diffus cosmologique (CMB pour *Cosmic Microwave Background*), et plus précisément à la détection des modes B primordiaux. L’assemblage et la caractérisation de l’instrument ont commencé à l’APC en 2018 lorsque je débuteais mon doctorat. Le télescope a maintenant rejoint l’Argentine pour une dernière phase de calibration avant d’être installé sur son site d’observation. Pendant ma thèse, j’ai travaillé sur divers aspects du projet, combinant instrumentation, analyse de données de calibration, simulations et développement d’algorithmes de reconstruction des cartes du ciel.

B.2 Contexte scientifique

Le CMB, détecté pour la première fois par Penzias et Wilson [107], est un rayonnement de corps noir, aujourd’hui à 2.7255 ± 0.0006 K [112]. Il a été émis 380 000 ans après le Big Bang au moment de la formation des premiers atomes d’hydrogène. Ce rayonnement isotrope dans lequel baigne l’univers est en fait une conséquence directe du modèle du Big Bang et c’est dans ce cadre qu’il a pu être prédit dès 1948, bien avant la première observation [37].

Ce rayonnement est isotrope mais possède néanmoins de faibles anisotropies en température, environ 10^5 fois plus faibles que la température moyenne. Ces anisotropies sont l’empreinte de fluctuations de densité au sein du plasma primordial. Le CMB peut être vu comme une image figée de la physique se déroulant dans le plasma au moment de son émission. Il constitue donc une précieuse source d’information sur l’enfance de l’univers.

Aussi, le CMB est linéairement polarisé et cela est dû à de la diffusion Thomson entre électrons et photons du plasma primordial en présence d’anisotropies quadripolaires. Ces anisotropies quadripolaires ont pu être créées par des ondes gravitationnelles se propageant dans le plasma. La polarisation du CMB se décompose généralement en deux champs appelés modes E et B , respectivement scalaires et pseudo-scalaires. L’un des intérêts de cette décomposition est que ces modes sont directement associables à des processus physiques prédits par l’inflation cosmique. L’inflation est une phase d’expansion accélérée de l’univers qui aurait eu lieu juste après le Big Bang. Elle offre un moyen naturel d’expliquer la génération des fluctuations de densité et prédit la propagation d’ondes gravitationnelles. La quête des modes B de polarisation du CMB fait aujourd’hui partie des enjeux majeurs de la cosmologie observationnelle. Leur détection permettrait de valider ou non, et surtout de contraindre, les théories d’inflation, et aurait des conséquences importantes en physique des particules.

L’amplitude prédite du signal que l’on cherche à détecter est très faible et c’est pourquoi des détecteurs extrêmement sensibles alliés à un contrôle rigoureux des effets systématiques sont nécessaires. Hélas, les avant-plans astrophysiques, comme l’émission thermique des grains de poussière galactiques, produisent également des modes B de polarisation venant s’ajouter aux modes B primordiaux. Il s’agit donc d’avoir un instrument capable de séparer finement cette émission du signal cosmologique, avec des effets systématiques maîtrisés.

B.3 L'interféromètre bolométrique QUBIC

QUBIC a précisément été conçu pour répondre à ces problématiques [1]. C'est un télescope entièrement incluí dans un cryostat. L'originalité de cet instrument réside dans son design optique qui fait le choix de l'interférométrie au lieu de l'imagerie classique. La Figure B.1 présente une photo ainsi qu'un schéma de l'instrument. Le signal venu du ciel entre dans le cryostat par une fenêtre de 56 cm de diamètre suivie d'une série de filtres permettant de supprimer le rayonnement de haute fréquence qui augmenterait la puissance de fond dans le cryostat [3]. La polarization du signal est immédiatement modulée par une lame demi-onde rotative maintenue à 4 K [4]. Un polariseur, placé juste après la lame transmet une unique direction de polarisation vers la matrice de 400 cornets [5] qui illumine le combineur optique fait de deux miroirs refroidis à 1 K. Ce système optique, à l'aide d'un filtre dichroïque, focalise la lumière sur deux plans focaux, centrés respectivement autour de 150 et 220 GHz, assurant une observation à l'infini. Les rayonnements provenant de chaque cornet se superposent sur les plans focaux pour former des figures d'interférence. Ces images sont échantillonnées par une matrice de 1024 bolomètres (*Transition-Edge-Sensors*) sur chaque plan focal [7].

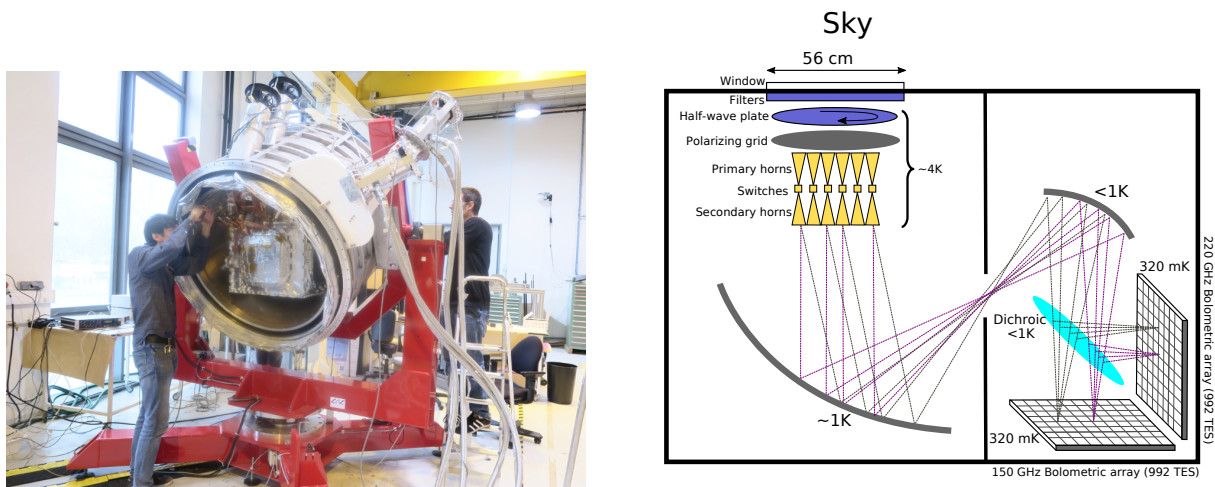


Figure B.1: *Gauche* : Photo de l'instrument QUBIC au laboratoire APC pendant son assemblage. *Droite* : Schéma du design optique de l'instrument.

Souvent présenté sous l'angle de l'interférométrie, QUBIC peut aussi être vu comme un imageur classique possédant une ouverture bien particulière. Ce qui le distingue des imageurs classiques est sa fonction d'étalement du point (PSF pour *Point Spread Function*), c'est-à-dire la réponse de l'instrument sur le plan focal pour une source lumineuse ponctuelle dans une direction donnée, émettant à une fréquence donnée. En effet, la PSF de QUBIC présente un pic central, placé à l'image géométrique de la source, entouré de pics secondaires. De façon équivalente, on pourrait parler du lobe de l'instrument, qui est sa réponse en fonction de la direction sur le ciel, à une fréquence donnée. Le lobe est donc propre à chaque bolomètre puisqu'il dépend de la position sur le plan focal. Le lobe mesuré en laboratoire et la simulation correspondante sont présentés Figure B.2. En résumé sur le plan focal on observe une image qui est le résultat d'interférences constructives entre les rayonnements émis par chaque cornet. Ceci est finalement en tout point similaire à un imageur classique pour lequel chaque point fictif de l'ouverture peut être vu comme une source secondaire à l'image des cornets de QUBIC. Sous cet angle, n'importe quel imageur est un interféromètre.

B.4 Vérification de l'alignement des miroirs

Les miroirs sont placés sur des hexapodes permettant d'ajuster leur position. Ils ont d'abord été alignés à l'aide d'un bras mécanique permettant de mesurer la position de leur surface en trois dimensions. En comparant les positions mesurées à un modèle mécanique nous étions alors capables d'ajuster les hexapodes pour corriger l'alignement.

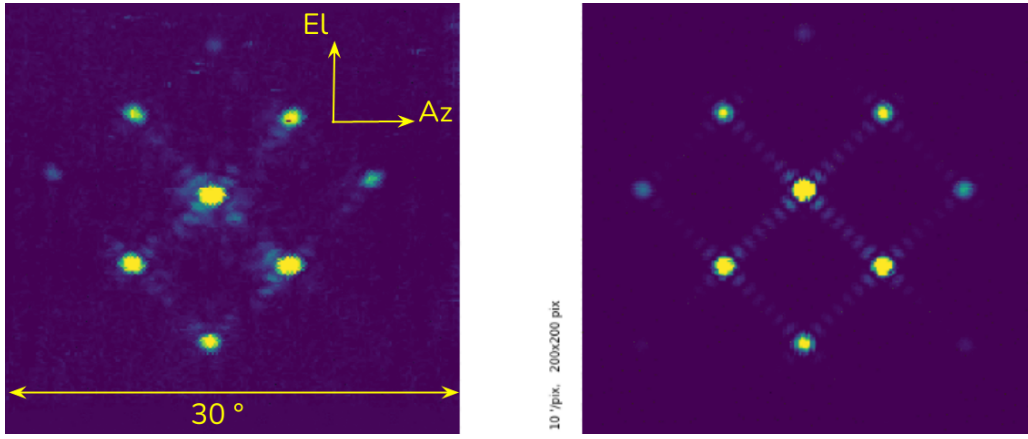


Figure B.2: Lobe de l'un des détecteurs à 150 GHz. Comparaison entre la mesure (gauche) et la simulation (droite). Tirée de [8].

Cet alignement a également été contrôlé optiquement à l'aide d'un laser comme décrit dans [6]. Ce travail a été réalisé en mai 2018 et j'étais responsable de l'alignement optique en collaboration avec des collègues de Rome. Le laser était positionné à l'emplacement futur de la matrice de cornets. Comme le montre la Figure B.3 (gauche), il pouvait être translaté selon deux directions orthogonales et également incliné d'un petit angle autour de ces deux directions. La méthode consistait à vérifier qu'en translatant le laser selon les deux axes, la tâche sur le plan focal restait fixe. Une photo du plan focal fictif est montrée Figure B.3 (droite). J'ai développé deux analyses indépendantes et une troisième a été développée à Rome. Les trois analyses ont donné des résultats consistants. En revanche, la réflectivité des miroirs du *Technological Demonstrator* dans le domaine visible s'est avérée insuffisante pour satisfaire à la précision requise. L'alignement a donc finalement été fait à l'aide du bras mécanique. En revanche, cette méthode sera réutilisée lors de l'alignement des miroirs de l'instrument complet qui auront une surface bien plus réfléchissante dans le domaine visible.

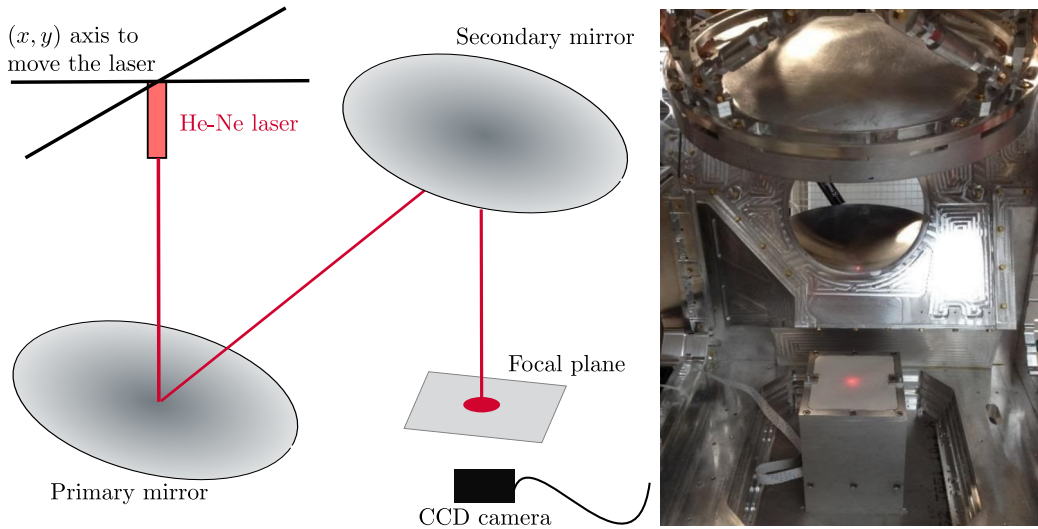


Figure B.3: *Gauche* : Schéma du dispositif expérimental. *Droite* : Photo du plan focal fictif utilisé pour la mesure avec la tâche rouge du laser.

B.5 Premiers pas vers la self-calibration

Tout d'abord, le design du polarimètre de QUBIC a été choisi pour limiter au maximum les effets systématiques. Premièrement, puisque les bolomètres détectent l'intensité du champ électromagnétique et non sa polarisation, le fait de placer la lame demi-onde et le polariseur en entrée rend l'instrument

insensible à toute cross-polarisation qui se produirait en aval, c'est-à-dire dans les cornets, sur les miroirs ou suite à n'importe quelle réflexion dans l'instrument. De plus, le choix de la lame demi-onde et du polariseur pour moduler la polarisation n'est pas anodin, il permet de limiter la fuite d'intensité vers la polarisation. En me basant sur le formalisme développé par Marie-Anne Bigot-Sazy, j'ai pu montrer cela analytiquement en le comparant à deux designs alternatifs. Cette étude a été réalisée dans le cadre d'un stage pour deux étudiants de Licence 3 que j'encadrais.

Si la collaboration QUBIC a opté pour un interféromètre bolométrique, c'est avant tout pour contrôler avec une grande précision les effets systématiques de l'instrument. Ceci est possible grâce à une technique bien connue en radioastronomie, appelée *self-calibration*. Quelques précisions sur les cornets: chaque cornet peut être ouvert ou fermé au moyen d'un interrupteur placé dans son guide d'onde. On appelle "ligne de base" une paire de cornets et deux lignes de base sont dites équivalentes (ou redondantes) si elles ont même écartement et même direction. En ouvrant une unique ligne de base, on observe sur le plan focal des franges d'interférence, comme dans l'expérience des trous d'Young. La *self-calibration* repose sur la comparaison des franges obtenues sur le plan focal pour des lignes de base équivalentes. En effet, puisque, dans le cas d'un instrument idéal, les franges sont strictement identiques, les comparer permet de mesurer les systématiques de l'instrument. Cela a été étudié en détail durant la thèse de Marie-Anne [11], [13].

Pour ma part, j'ai travaillé sur la mesure des franges d'interférence pendant la calibration de l'instrument. Cette mesure m'a amenée à développer un code d'analyse permettant notamment d'inter-calibrer les bolomètres entre eux. J'ai aussi développé le code qui permet de simuler l'instrument complet et les figures d'interférences observées. L'intercalibration se fait au moyen d'un ajustement des données par un modèle. L'avantage est que les gains des bolomètres sont des paramètres linéaires du modèle ce qui permet de les obtenir analytiquement et non numériquement pendant la minimisation du χ^2 . Il va sans dire que l'observation des franges est cruciale pour la *self-calibration* et l'intercalibration des bolomètres est requise pour toute analyse.

Enfin, j'ai travaillé sur la mesure et la caractérisation des lobes des détecteurs. J'ai notamment développé une analyse permettant d'identifier sans ambiguïté les pics multiples d'un détecteur à l'autre. En déterminant la position des pics de chaque lobe, j'ai pu remonter à la distance focale du télescope en ajustant un modèle optique aux données. Cette étude n'est qu'une étape préliminaire, la mesure de la distance focale n'est pas une fin en soi mais plutôt un premier exercice pour vérifier que l'on comprend bien les données. Toutefois, la reconstruction des cartes du ciel à partir des données temporelles obtenues après un scan du ciel ne pourra se faire que si l'on connaît précisément le lobe de chaque détecteur, c'est-à-dire son champ de vue. C'est pourquoi, ce travail est extrêmement important et sera poursuivi, la classification rigoureuse des pics ayant permis de débloquer une difficulté majeure.

B.6 Imagerie spectrale

Le lobe de l'instrument, déterminé par la géométrie de la matrice de cornets placée à l'entrée du télescope, contient des pics secondaires dont la séparation est proportionnelle à la longueur d'onde.

L'équivalent de la matrice de cornets dans le domaine visible des longueurs d'onde serait un réseau dispersif selon deux directions orthogonales (une grille). La Figure B.4 montre un dispositif sur banc optique que j'ai construit pour illustrer le principe de fonctionnement de QUBIC dans le domaine visible. Sur la photo de droite on voit la décomposition des couleurs sur les pics secondaires de la PSF. Grâce à l'interférométrie, l'information spectrale est donc bien présente dans les données. C'est pourquoi QUBIC a la capacité de faire de l'imagerie spectrale, c'est-à-dire de reconstruire des cartes du ciel dans des sous-bandes de fréquence au sein de la bande large dans laquelle les bolomètres intègrent le signal.

L'imagerie spectrale est réalisée lors de l'analyse des données, en post-processing. La démonstration de cette technique et la caractérisation de ses performances est une partie importante de ma thèse et cela m'a conduit à être première auteure de l'article de collaboration [9]. Au travers de simulations *end-to-end*, nous avons montré qu'il est possible de reconstruire cinq sous-bandes au sein de chaque large bande (130 à 170 GHz et 200 à 240 GHz environ) avec une dégradation modérée de la qualité du signal vis à vis d'une situation "optimale". Nous avons aussi montré qu'il est possible de mesurer la

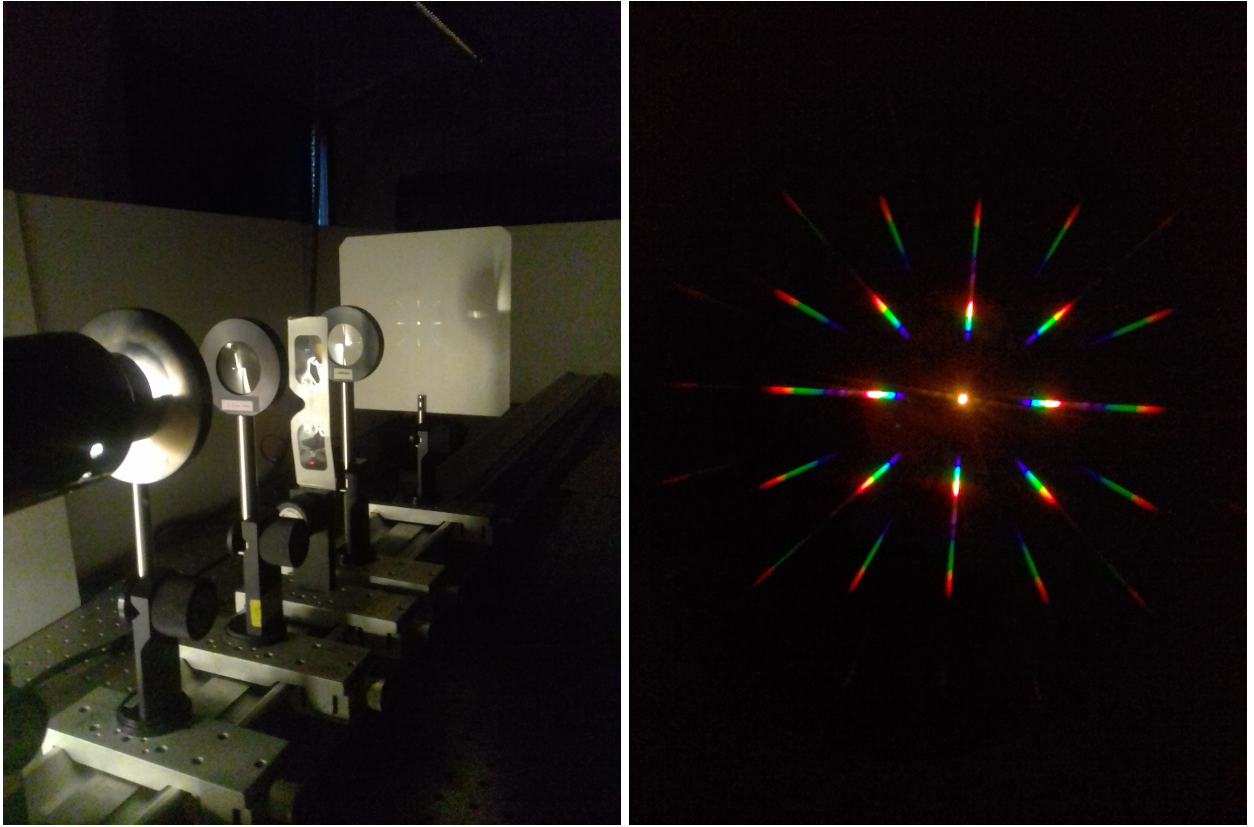


Figure B.4: *Gauche*: Dispositif optique qui serait l'analogue de QUBIC dans le domaine visible: lampe blanche suivie d'un diaphragme placée au foyer objet d'une lentille pour avoir un point source à l'infini, réseau dispersif selon deux directions orthogonales (lunettes), une seconde lentille et un écran placé dans le plan focal image pour assurer une observation à l'infini. *Droite*: PSF polychromatique observée sur l'écran.

distribution spectrale d'énergie localement sur le ciel, voir Figure B.5. Cela est très prometteur pour l'étude des avant-plans astrophysiques comme la poussière galactique.

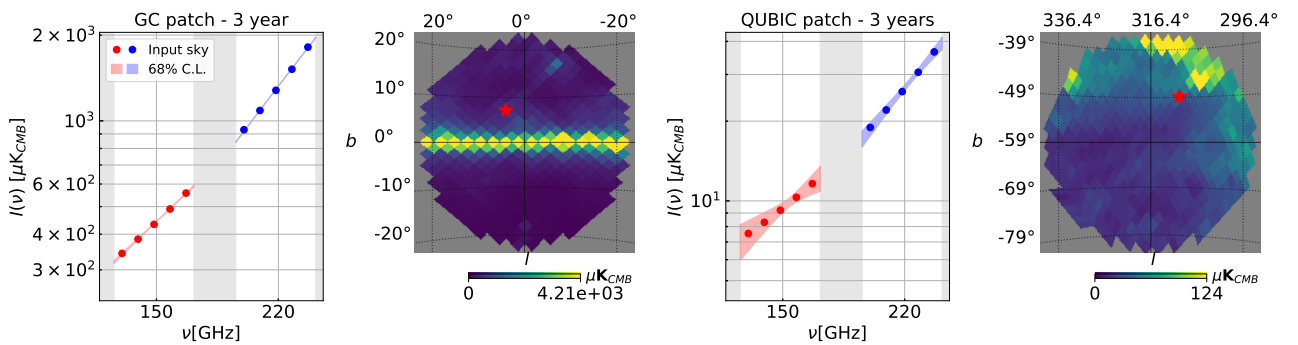


Figure B.5: Intensité en fonction de la fréquence pour 5 sous-bandes reconstruites dans chaque large bande autour de 150 (rouge) et 220 (bleu) GHz dans un pixel donné du ciel. Les régions grisées correspondent aux fréquences en dehors des bandes observées par QUBIC. Le résultat est montré pour deux pixels (étoile rouge), l'un dans un patch centré sur le centre galactique et l'autre dans le patch que QUBIC observera centré en $[0, -57 \text{ deg}]$. Points rouges et bleus: ciel d'entrée convolué par le lobe de l'instrument. Les zones rouge et bleu clair représentent les régions à 68% C.L. pour un corps noir modifié reconstruit à l'aide d'un Monte-Carlo par chaînes de Markov à partir des données simulées et des matrices de covariance entre sous-bandes. Les cartes sont en $\mu\text{K CMB}$ et $N_{\text{side}} = 32$.

Aussi, l'imagerie spectrale donne la capacité de détecter la présence résiduelle d'avant-plans dans les données. En effet, au contraire du CMB, les avant-plans émettent différemment en fonction de la

fréquence¹¹. Ainsi, la mesure du rapport tenseur-sur-scalaire va varier d'une sous-bande à l'autre dans le cas où il reste du signal autre que celui du CMB.

Nous avons également étudié en détail la structure du bruit qui est tout à fait particulière à l'interférométrie bolométrique. Nous avons notamment mis en lumière la corrélation spatiale du bruit au niveau des cartes qui est due à la présence des pics secondaires dans le lobe. Nous avons aussi montré que les sous-bandes accolées sont anti-corrélées entre elles.

Enfin, nous avons pour la première fois appliqué cette technique à des données de calibration en parvenant à reconstruire l'image d'une source ponctuelle de calibration émettant à 150 GHz dans cinq sous-bandes.

B.7 Conclusion

La détection des modes B primordiaux dans la polarisation du fond diffus cosmologique est un enjeu majeur pour la cosmologie observationnelle, notamment parce que cela permettrait de contraindre les modèles d'inflation cosmique. La collaboration QUBIC a fait le choix original de l'interférométrie bolométrique et a développé ce concept tout à fait nouveau. Ce type d'instrument permet une mesure précise des effets systématiques grâce à la *self-calibration* et offre aussi la possibilité de faire de l'imagerie spectrale.

Pendant ma thèse j'ai travaillé sur ces deux aspects. Mon travail autour de la calibration de l'instrument, en particulier la mesure des franges d'interférence, ouvre la voie au développement d'une procédure complète de self-calibration. Aussi, la mesure du lobe du télescope est une étape cruciale pour la fabrication des cartes du ciel et ce travail doit être poursuivi. La démonstration et la caractérisation de l'imagerie spectrale est fondamentale et montre tout le potentiel de cet instrument. L'étape suivante est d'inclure la séparation de composantes, c'est-à-dire la discrimination entre CMB et avant-plans astrophysiques, dans notre pipeline d'analyse. Enfin, les premières observations du ciel vont notamment permettre de tester l'imagerie spectrale sur des sources astrophysiques.

¹¹à condition de travailler en Kelvin CMB.

Bibliography

QUBIC

- [1] J.-C. Hamilton, L. Mousset, *et al.*, “QUBIC I: Overview and Science Program,” May 2021 (cit. on pp. [9](#), [138](#), [146](#), [162](#), [166](#), [172](#), [190](#), [240](#)).
- [2] R. Charlassier, “Mesure des anisotropies de polarisation du fond diffus cosmologique avec l’interféromètre bolométrique QUBIC,” Paris 7, 2010, 1 vol. (244 p.) (Cit. on pp. [13](#), [34](#), [50](#)).
- [3] S. Masi, E. Battistelli, *et al.*, “QUBIC V: Cryogenic system design and performance,” Sep. 2020 (cit. on pp. [14](#), [19](#), [240](#)).
- [4] G. D’Alessandro, L. Mele, *et al.*, “QUBIC VI: Cryogenic half wave plate rotator, design and performances,” Sep. 2020 (cit. on pp. [14–16](#), [44](#), [240](#)).
- [5] F. Cavaliere, A. Mennella, *et al.*, “QUBIC VII: The feedhorn-switch system of the technological demonstrator,” Sep. 2020 (cit. on pp. [14](#), [17](#), [64](#), [240](#)).
- [6] C. O’Sullivan, M. De Petris, *et al.*, “QUBIC VIII: Optical design and performance,” Sep. 2020 (cit. on pp. [14](#), [17](#), [30](#), [37](#), [62](#), [63](#), [138](#), [154](#), [193](#), [241](#)).
- [7] M. Piat, G. Stankowiak, *et al.*, “QUBIC IV: Performance of TES Bolometers and Readout Electronics,” Apr. 2021 (cit. on pp. [15](#), [18](#), [19](#), [190](#), [240](#)).
- [8] S. A. Torchinsky, J.-C. Hamilton, *et al.*, “QUBIC III: Laboratory Characterization,” Nov. 2020 (cit. on pp. [29](#), [30](#), [37](#), [44](#), [45](#), [63](#), [69](#), [74](#), [151](#), [168](#), [190](#), [241](#)).
- [9] L. Mousset, M. Gamboa Lerena, *et al.*, “QUBIC II: Spectro-Polarimetry with Bolometric Interferometry,” Nov. 2020 (cit. on pp. [31](#), [133](#), [149](#), [151](#), [172](#), [190](#), [242](#)).
- [10] R. Charlassier, J.-C. Hamilton, *et al.*, “An efficient phase-shifting scheme for bolometric additive interferometry,” *Astronomy & Astrophysics*, vol. 497, no. 3, pp. 963–971, Apr. 2009. DOI: [10.1051/0004-6361/200810306](#) (cit. on pp. [34](#), [50](#)).
- [11] M.-A. Bigot-Sazy, “Mesure des anisotropies de polarisation du fond diffus cosmologique avec l’interféromètre bolométrique QUBIC,” These de doctorat, Paris 7, Jan. 1, 2013 (cit. on pp. [43](#), [46](#), [47](#), [138](#), [242](#)).
- [12] T. Q. collaboration, E. Battistelli, *et al.*, “QUBIC: The QU Bolometric Interferometer for Cosmology,” *Astroparticle Physics*, vol. 34, no. 9, pp. 705–716, Apr. 2011. DOI: [10.1016/j.astropartphys.2011.01.012](#). arXiv: [1010.0645](#) (cit. on p. [44](#)).
- [13] M.-A. Bigot-Sazy, R. Charlassier, *et al.*, “Self-calibration: An efficient method to control systematic effects in bolometric interferometry,” *Astronomy & Astrophysics*, vol. 550, A59, Feb. 2013. DOI: [10.1051/0004-6361/201220429](#). arXiv: [1209.4905](#) (cit. on pp. [46](#), [50](#), [64](#), [242](#)).
- [14] M. Stolpovskiy, “Development of the B-mode measurements pipeline for QUBIC experiment,” These de doctorat, Sorbonne Paris Cité, Nov. 25, 2016 (cit. on pp. [131](#), [152](#)).
- [15] M. M. Gamboa Lerena, C. G. Scóccola, *et al.*, “Angular resolution at map level in the QUBIC instrument,” *Boletín de la Asociacion Argentina de Astronomia La Plata Argentina*, vol. 61B, pp. 155–158, Jul. 1, 2020 (cit. on p. [154](#)).

Instrumentation

- [16] J. Choi, H. Ishitsuka, *et al.*, “Radio-transparent multi-layer insulation for radiowave receivers,” *Review of Scientific Instruments*, vol. 84, no. 11, p. 114502, Nov. 1, 2013. DOI: [10.1063/1.4827081](https://doi.org/10.1063/1.4827081) (cit. on p. 15).
- [17] A. T. Lee, P. L. Richards, *et al.*, “A superconducting bolometer with strong electrothermal feedback,” *Applied Physics Letters*, vol. 69, no. 12, pp. 1801–1803, Sep. 16, 1996. DOI: [10.1063/1.117491](https://doi.org/10.1063/1.117491) (cit. on p. 18).

Historical cosmology

- [18] G. Gamow, “The Evolution of the Universe,” *Nature*, vol. 162, no. 4122, pp. 680–682, Oct. 1948. DOI: [10.1038/162680a0](https://doi.org/10.1038/162680a0) (cit. on pp. 10, 95, 96).
- [19] S. Chandrasekhar, *Radiative Transfer*. New York: Dover Publications, 1960, 393 pp. (cit. on p. 34).
- [20] S. Weinberg and J.-B. Yelnik, *Les trois premières minutes de l’univers*, Nouv. éd, ser. Points 20. Paris: Éd. du Seuil, 1988 (cit. on p. 87).
- [21] A. Einstein, “Kosmologische Betrachtungen zur allgemeinen Relativitätstheorie,” *Sitzungsberichte der Königlich Preussischen Akademie der Wissenschaften (Berlin)*, Seite 142-152., 1917 (cit. on p. 88).
- [22] J.-P. Luminet, *L’invention du big bang*. 2014 (cit. on p. 89).
- [23] V. M. Slipher, “Radial velocity observations of spiral nebulae,” *The Observatory*, vol. 40, pp. 304–306, Aug. 1, 1917 (cit. on p. 89).
- [24] E. P. Hubble, “A spiral nebula as a stellar system, Messier 31.,” *The Astrophysical Journal*, vol. 69, p. 103, Mar. 1929. DOI: [10.1086/143167](https://doi.org/10.1086/143167) (cit. on p. 89).
- [25] H. S. Leavitt, “1777 variables in the Magellanic Clouds,” *Annals of Harvard College Observatory*, vol. 60, pp. 87–108.3, 1908 (cit. on p. 89).
- [26] H. S. Leavitt and E. C. Pickering, “Periods of 25 Variable Stars in the Small Magellanic Cloud.,” *Harvard College Observatory Circular*, vol. 173, pp. 1–3, Mar. 1, 1912 (cit. on p. 89).
- [27] A. Friedman, “Über die Krümmung des Raumes,” *Zeitschrift für Physik*, vol. 10, no. 1, pp. 377–386, Dec. 1, 1922. DOI: [10.1007/BF01332580](https://doi.org/10.1007/BF01332580) (cit. on p. 89).
- [28] G. Lemaître, “Un Univers homogène de masse constante et de rayon croissant rendant compte de la vitesse radiale des nébuleuses extra-galactiques,” *Annales de la Société Scientifique de Bruxelles*, vol. 47, pp. 49–59, 1927 (cit. on pp. 89, 90).
- [29] A. Einstein and W. de Sitter, “On the Relation between the Expansion and the Mean Density of the Universe,” *Proceedings of the National Academy of Sciences*, vol. 18, no. 3, pp. 213–214, Mar. 1, 1932. DOI: [10.1073/pnas.18.3.213](https://doi.org/10.1073/pnas.18.3.213). pmid: [16587663](https://pubmed.ncbi.nlm.nih.gov/16587663/) (cit. on p. 89).
- [30] E. Hubble, “A relation between distance and radial velocity among extra-galactic nebulae,” *Proceedings of the National Academy of Sciences*, vol. 15, no. 3, pp. 168–173, Mar. 15, 1929. DOI: [10.1073/pnas.15.3.168](https://doi.org/10.1073/pnas.15.3.168) (cit. on p. 90).
- [31] S. van den Bergh, “The Curious Case of Lemaître’s Equation No. 24,” *Journal of the Royal Astronomical Society of Canada*, vol. 105, no. 4, p. 151, Aug. 2011 (cit. on p. 90).
- [32] G. Lemaître, *La Naissance Du Big Bang*. Presses de l’Université Laval, Oct. 28, 2020. DOI: [10.2307/j.ctv1h0p17b](https://doi.org/10.2307/j.ctv1h0p17b). JSTOR: [10.2307/j.ctv1h0p17b](https://www.jstor.org/stable/10.2307/j.ctv1h0p17b) (cit. on p. 95).
- [33] H. Kragh, “Big Bang: The etymology of a name,” *Astronomy & Geophysics*, vol. 54, no. 2, pp. 2.28–2.30, Apr. 1, 2013. DOI: [10.1093/astrophys/att035](https://doi.org/10.1093/astrophys/att035) (cit. on p. 95).
- [34] R. A. Alpher, H. Bethe, *et al.*, “The Origin of Chemical Elements,” *Physical Review*, vol. 73, no. 7, pp. 803–804, Apr. 1, 1948. DOI: [10.1103/PhysRev.73.803](https://doi.org/10.1103/PhysRev.73.803) (cit. on p. 95).

- [35] R. A. Alpher and R. C. Herman, “On the Relative Abundance of the Elements,” *Physical Review*, vol. 74, no. 12, pp. 1737–1742, Dec. 15, 1948. DOI: [10.1103/PhysRev.74.1737](https://doi.org/10.1103/PhysRev.74.1737) (cit. on p. 95).
- [36] G. Gamow, “The Origin of Elements and the Separation of Galaxies,” *Physical Review*, vol. 74, no. 4, pp. 505–506, Aug. 15, 1948. DOI: [10.1103/PhysRev.74.505.2](https://doi.org/10.1103/PhysRev.74.505.2) (cit. on p. 95).
- [37] R. A. Alpher and R. Herman, “Evolution of the Universe,” *Nature*, vol. 162, no. 4124, pp. 774–775, Nov. 1948. DOI: [10.1038/162774b0](https://doi.org/10.1038/162774b0) (cit. on pp. 95, 239).
- [38] P. J. E. Peebles, “Discovery of the Hot Big Bang: What happened in 1948,” *The European Physical Journal H*, vol. 39, no. 2, pp. 205–223, Apr. 2014. DOI: [10.1140/epjh/e2014-50002-y](https://doi.org/10.1140/epjh/e2014-50002-y). arXiv: [1310.2146](https://arxiv.org/abs/1310.2146) (cit. on p. 95).
- [39] R. H. Dicke, “The Measurement of Thermal Radiation at Microwave Frequencies,” *Review of Scientific Instruments*, vol. 17, no. 7, pp. 268–275, Jul. 1, 1946. DOI: [10.1063/1.1770483](https://doi.org/10.1063/1.1770483) (cit. on p. 130).
- [40] L. Davis Jr. and J. L. Greenstein, “The Polarization of Starlight by Aligned Dust Grains,” *The Astrophysical Journal*, vol. 114, p. 206, Sep. 1, 1951. DOI: [10.1086/145464](https://doi.org/10.1086/145464) (cit. on p. 144).
- [41] E. Hubble, “The Distribution of Extra-Galactic Nebulae,” *The Astrophysical Journal*, vol. 79, p. 8, Jan. 1934. DOI: [10.1086/143517](https://doi.org/10.1086/143517) (cit. on p. 172).
- [42] F. Zwicky, “Republication of: The redshift of extragalactic nebulae,” *General Relativity and Gravitation*, vol. 41, pp. 207–224, Jan. 1, 2009. DOI: [10.1007/s10714-008-0707-4](https://doi.org/10.1007/s10714-008-0707-4) (cit. on p. 172).
- [43] F. Zwicky, “On the Masses of Nebulae and of Clusters of Nebulae,” *The Astrophysical Journal*, vol. 86, p. 217, Oct. 1937. DOI: [10.1086/143864](https://doi.org/10.1086/143864) (cit. on p. 172).
- [44] F. Zwicky, “Nebulae as Gravitational Lenses,” *Physical Review*, vol. 51, no. 4, pp. 290–290, Feb. 15, 1937. DOI: [10.1103/PhysRev.51.290](https://doi.org/10.1103/PhysRev.51.290) (cit. on p. 172).
- [45] S. Smith, “The Mass of the Virgo Cluster,” *The Astrophysical Journal*, vol. 83, p. 23, Jan. 1936. DOI: [10.1086/143697](https://doi.org/10.1086/143697) (cit. on p. 172).
- [46] H. W. Babcock, “The rotation of the Andromeda Nebula,” *Lick Observatory Bulletin*, vol. 498, pp. 41–51, 1939. DOI: [10.5479/ADS/bib/1939LicOB.19.41B](https://doi.org/10.5479/ADS/bib/1939LicOB.19.41B) (cit. on p. 172).
- [47] S. Chandrasekhar, “The Maximum Mass of Ideal White Dwarfs,” *The Astrophysical Journal*, vol. 74, p. 81, Jul. 1, 1931. DOI: [10.1086/143324](https://doi.org/10.1086/143324) (cit. on p. 189).

no

General cosmology

- [48] M. Tanabashi, K. Hagiwara, *et al.*, “Review of Particle Physics,” *Phys.Rev.D*, vol. 98, no. 3, p. 030 001, 2018. DOI: [10.1103/PhysRevD.98.030001](https://doi.org/10.1103/PhysRevD.98.030001) (cit. on pp. 56, 106, 177, 186).
- [49] J. Rich and J.-L. Basdevant, *Principes de la cosmologie*. 2001 (cit. on pp. 87, 94, 105, 106, 112).
- [50] G. Métris, M. Rodrigues, *et al.*, “MICROSCOPE Mission: First Results of a Space Test of the Equivalence Principle,” *Physical Review Letters*, vol. 119, no. 23, p. 231 101, Dec. 4, 2017. DOI: [10.1103/PhysRevLett.119.231101](https://doi.org/10.1103/PhysRevLett.119.231101) (cit. on p. 88).
- [51] D. H. Clark and M. D. H. Clark, *Measuring the Cosmos: How Scientists Discovered the Dimensions of the Universe*. New Brunswick, N.J: Rutgers University Press, 2004, 202 pp. (cit. on p. 89).
- [52] J. K. Yadav, J. S. Bagla, *et al.*, “Fractal dimension as a measure of the scale of homogeneity: The scale of homogeneity,” *Monthly Notices of the Royal Astronomical Society*, no–no, Apr. 2010. DOI: [10.1111/j.1365-2966.2010.16612.x](https://doi.org/10.1111/j.1365-2966.2010.16612.x) (cit. on p. 90).

- [53] R. G. Clowes, K. A. Harris, *et al.*, “A structure in the early Universe at $z \approx 1.3$ that exceeds the homogeneity scale of the R-W concordance cosmology,” *Monthly Notices of the Royal Astronomical Society*, vol. 429, no. 4, pp. 2910–2916, Mar. 11, 2013. DOI: [10.1093/mnras/sts497](https://doi.org/10.1093/mnras/sts497) (cit. on p. 90).
- [54] D. W. Hogg, “Distance measures in cosmology,” *arXiv e-prints*, astro-ph/9905116, May 1, 1999 (cit. on pp. 92, 94).
- [55] T. P. Walker, G. Steigman, *et al.*, “Primordial nucleosynthesis redux,” *The Astrophysical Journal*, vol. 376, p. 51, Jul. 1991. DOI: [10.1086/170255](https://doi.org/10.1086/170255) (cit. on p. 97).
- [56] C. Pitrou, A. Coc, *et al.*, “A new tension in the cosmological model from primordial deuterium?” *Monthly Notices of the Royal Astronomical Society*, vol. 502, no. 2, pp. 2474–2481, Feb. 10, 2021. DOI: [10.1093/mnras/stab135](https://doi.org/10.1093/mnras/stab135) (cit. on p. 97).
- [57] D. J. Eisenstein and C. L. Bennett, “Cosmic sound waves rule,” *Physics Today*, vol. 61, no. 4, pp. 44–50, Apr. 2008. DOI: [10.1063/1.2911177](https://doi.org/10.1063/1.2911177) (cit. on pp. 106, 107, 189).
- [58] N. Christensen, “Stochastic gravitational wave backgrounds,” *Reports on Progress in Physics*, vol. 82, no. 1, p. 016 903, Jan. 1, 2019. DOI: [10.1088/1361-6633/aae6b5](https://doi.org/10.1088/1361-6633/aae6b5) (cit. on p. 119).
- [59] V. C. Rubin and W. K. Ford Jr., “Rotation of the Andromeda Nebula from a Spectroscopic Survey of Emission Regions,” *The Astrophysical Journal*, vol. 159, p. 379, Feb. 1, 1970. DOI: [10.1086/150317](https://doi.org/10.1086/150317) (cit. on p. 172).
- [60] M. Milgrom, “A modification of the Newtonian dynamics as a possible alternative to the hidden mass hypothesis,” *The Astrophysical Journal*, vol. 270, pp. 365–370, Jul. 1983. DOI: [10.1086/161130](https://doi.org/10.1086/161130) (cit. on p. 172).
- [61] D. Clowe, M. Bradač, *et al.*, “A Direct Empirical Proof of the Existence of Dark Matter*,” *The Astrophysical Journal*, vol. 648, no. 2, p. L109, Aug. 30, 2006. DOI: [10.1086/508162](https://doi.org/10.1086/508162) (cit. on p. 172).
- [62] D. Baumann. (Jul. 9, 2018). TASI Lectures on Primordial Cosmology. arXiv: [1807.03098](https://arxiv.org/abs/1807.03098) [astro-ph, physics:hep-ph, physics:hep-th], [Online]. Available: <http://arxiv.org/abs/1807.03098> (cit. on pp. 173–175).
- [63] P. Coles and F. Lucchin, *Cosmology: The Origin and Evolution of Cosmic Structure*. Chichester ; New York: John Wiley, 1995, 449 pp. (cit. on p. 173).
- [64] J. P. Preskill, “Cosmological Production of Superheavy Magnetic Monopoles,” *Physical Review Letters*, vol. 43, no. 19, pp. 1365–1368, Nov. 5, 1979. DOI: [10.1103/PhysRevLett.43.1365](https://doi.org/10.1103/PhysRevLett.43.1365) (cit. on p. 174).
- [65] T. M. Davis and C. H. Lineweaver, “Expanding Confusion: Common misconceptions of cosmological horizons and the superluminal expansion of the Universe,” *Publications of the Astronomical Society of Australia*, vol. 21, no. 1, pp. 97–109, 2004. DOI: [10.1071/AS03040](https://doi.org/10.1071/AS03040). arXiv: [astro-ph/0310808](https://arxiv.org/abs/astro-ph/0310808) (cit. on p. 174).
- [66] N. E. Chisari, D. Alonso, *et al.*, “Core Cosmology Library: Precision Cosmological Predictions for LSST,” *The Astrophysical Journal Supplement Series*, vol. 242, no. 1, p. 2, May 1, 2019. DOI: [10.3847/1538-4365/ab1658](https://doi.org/10.3847/1538-4365/ab1658) (cit. on p. 181).
- [67] S. Weinberg, “Adiabatic modes in cosmology,” *Physical Review D*, vol. 67, no. 12, p. 123 504, Jun. 6, 2003. DOI: [10.1103/PhysRevD.67.123504](https://doi.org/10.1103/PhysRevD.67.123504) (cit. on p. 183).
- [68] S. J. Maddox, G. Efstathiou, *et al.*, “Galaxy correlations on large scales,” *Monthly Notices of the Royal Astronomical Society*, vol. 242, no. 1, pp. 43P–47P, Feb. 1, 1990. DOI: [10.1093/mnras/242.1.43P](https://doi.org/10.1093/mnras/242.1.43P) (cit. on p. 184).
- [69] S. D. M. White, J. F. Navarro, *et al.*, “The baryon content of galaxy clusters: A challenge to cosmological orthodoxy,” *Nature*, vol. 366, no. 6454, pp. 429–433, Dec. 1993. DOI: [10.1038/366429a0](https://doi.org/10.1038/366429a0) (cit. on p. 184).
- [70] G. Efstathiou, W. J. Sutherland, *et al.*, “The cosmological constant and cold dark matter,” *Nature*, vol. 348, no. 6303, pp. 705–707, Dec. 1990. DOI: [10.1038/348705a0](https://doi.org/10.1038/348705a0) (cit. on p. 184).

- [71] S. Perlmutter, G. Aldering, *et al.*, “Measurements of ω and λ from 42 High-Redshift Supernovae,” *The Astrophysical Journal*, vol. 517, no. 2, pp. 565–586, Jun. 1999. DOI: [10.1086/307221](#) (cit. on p. 184).
- [72] A. G. Riess, A. V. Filippenko, *et al.*, “Observational Evidence from Supernovae for an Accelerating Universe and a Cosmological Constant,” *The Astronomical Journal*, vol. 116, no. 3, pp. 1009–1038, Sep. 1998. DOI: [10.1086/300499](#) (cit. on p. 184).
- [73] S. Perlmutter, “Supernovae, Dark Energy, and the Accelerating Universe,” *Physics Today*, vol. 56, no. 4, pp. 53–60, Apr. 2003. DOI: [10.1063/1.1580050](#) (cit. on p. 184).
- [74] P. Astier and R. Pain, “Observational evidence of the accelerated expansion of the universe,” *Comptes Rendus Physique*, vol. 13, no. 6-7, pp. 521–538, Jul. 2012. DOI: [10.1016/j.crhy.2012.04.009](#) (cit. on p. 184).
- [75] J. Ellis and K. A. Olive, “Supersymmetric dark matter candidates,” in *Particle Dark Matter*, Cambridge University Press, Jan. 1, 2010, pp. 142–163. DOI: [10.1017/CB09780511770739.009](#) (cit. on p. 184).
- [76] Planck Collaboration, P. A. R. Ade, *et al.*, “Planck 2013 results. XVI. Cosmological parameters,” *Astronomy and Astrophysics*, vol. 571, A16, Nov. 1, 2014. DOI: [10.1051/0004-6361/201321591](#) (cit. on pp. 185, 186).
- [77] G. Mangano, G. Miele, *et al.*, “A precision calculation of the effective number of cosmological neutrinos,” *Physics Letters B*, vol. 534, no. 1-4, pp. 8–16, May 2002. DOI: [10.1016/S0370-2693\(02\)01622-2](#) (cit. on p. 185).
- [78] M. Maltoni, T. Schwetz, *et al.*, “Status of global fits to neutrino oscillations,” *New Journal of Physics*, vol. 6, pp. 122–122, Sep. 29, 2004. DOI: [10.1088/1367-2630/6/1/122](#) (cit. on p. 185).
- [79] G. Fogli, E. Lisi, *et al.*, “Global analysis of three-flavor neutrino masses and mixings,” *Progress in Particle and Nuclear Physics*, vol. 57, no. 2, pp. 742–795, Oct. 2006. DOI: [10.1016/j.pnpnp.2005.08.002](#) (cit. on p. 185).
- [80] A. G. Riess, S. Casertano, *et al.*, “Cosmic Distances Calibrated to 1% Precision with Gaia EDR3 Parallaxes and Hubble Space Telescope Photometry of 75 Milky Way Cepheids Confirm Tension with LambdaCDM,” *The Astrophysical Journal*, vol. 908, no. 1, p. L6, Feb. 9, 2021. DOI: [10.3847/2041-8213/abdbaf](#). arXiv: [2012.08534](#) (cit. on pp. 185, 189).
- [81] E. Di Valentino, O. Mena, *et al.*, “In the Realm of the Hubble tension - a Review of Solutions,” *Classical and Quantum Gravity*, Jun. 4, 2021. DOI: [10.1088/1361-6382/ac086d](#). arXiv: [2103.01183](#) (cit. on p. 185).
- [82] A. Boucaud, “Large Imaging Surveys For Cosmology: Cosmic Magnification And Photometric Calibration,” in collab. with J. G. Bartlett, Sep. 27, 2013. DOI: [10.5281/ZENODO.48950](#) (cit. on p. 186).
- [83] B. A. Bassett and R. Hlozek. (Oct. 27, 2009). Baryon Acoustic Oscillations. arXiv: [0910.5224](#) [[astro-ph](#), [physics:gr-qc](#), [physics:hep-ex](#), [physics:hep-ph](#)], [Online]. Available: <http://arxiv.org/abs/0910.5224> (cit. on p. 189).
- [84] S. Alam, M. Aubert, *et al.*, “Completed SDSS-IV extended Baryon Oscillation Spectroscopic Survey: Cosmological implications from two decades of spectroscopic surveys at the Apache Point Observatory,” *Physical Review D*, vol. 103, p. 083533, Apr. 1, 2021. DOI: [10.1103/PhysRevD.103.083533](#) (cit. on p. 189).
- [85] P. Zarrouk, M. Rezaie, *et al.*, “Baryon acoustic oscillations in the projected cross-correlation function between the eBOSS DR16 quasars and photometric galaxies from the DESI Legacy Imaging Surveys,” *Monthly Notices of the Royal Astronomical Society*, vol. 503, no. 2, pp. 2562–2582, Mar. 26, 2021. DOI: [10.1093/mnras/stab298](#) (cit. on p. 189).
- [86] P. A. Mazzali, F. K. Röpké, *et al.*, “A Common Explosion Mechanism for Type Ia Supernovae,” *Science*, vol. 315, no. 5813, pp. 825–828, Feb. 9, 2007. DOI: [10.1126/science.1136259](#). pmid: [17289993](#) (cit. on p. 189).

- [87] M. M. Phillips, “The Absolute Magnitudes of Type IA Supernovae,” *The Astrophysical Journal*, vol. 413, p. L105, Aug. 1, 1993. DOI: [10.1086/186970](https://doi.org/10.1086/186970) (cit. on p. 189).
- [88] M. Betoule, R. Kessler, *et al.*, “Improved cosmological constraints from a joint analysis of the SDSS-II and SNLS supernova samples,” *Astronomy and Astrophysics*, vol. 568, A22, Aug. 2014. DOI: [10.1051/0004-6361/201423413](https://doi.org/10.1051/0004-6361/201423413) (cit. on p. 189).
- [89] H. Zhan and J. A. Tyson, “Cosmology with the Large Synoptic Survey Telescope: An overview,” *Reports on Progress in Physics*, vol. 81, p. 066 901, Jun. 1, 2018. DOI: [10.1088/1361-6633/aab1bd](https://doi.org/10.1088/1361-6633/aab1bd) (cit. on p. 189).
- [90] R. Lynds, “The Absorption-Line Spectrum of 4c 05.34,” *The Astrophysical Journal*, vol. 164, p. L73, Mar. 1, 1971. DOI: [10.1086/180695](https://doi.org/10.1086/180695) (cit. on p. 189).
- [91] D. H. Weinberg, R. Davé, *et al.*, “The Lyman- α Forest as a Cosmological Tool,” vol. 666, pp. 157–169, May 1, 2003. DOI: [10.1063/1.1581786](https://doi.org/10.1063/1.1581786) (cit. on p. 189).
- [92] M. Viel, “The Lyman- α Forest As a Cosmological Probe,” vol. 352, pp. 191–205, Sep. 1, 2006 (cit. on p. 189).
- [93] LIGO Scientific Collaboration and Virgo Collaboration, B. P. Abbott, *et al.*, “Observation of Gravitational Waves from a Binary Black Hole Merger,” *Physical Review Letters*, vol. 116, no. 6, p. 061 102, Feb. 11, 2016. DOI: [10.1103/PhysRevLett.116.061102](https://doi.org/10.1103/PhysRevLett.116.061102) (cit. on p. 189).
- [94] LIGO Scientific Collaboration and Virgo Collaboration, B. P. Abbott, *et al.*, “GW170817: Observation of Gravitational Waves from a Binary Neutron Star Inspiral,” *Physical Review Letters*, vol. 119, no. 16, p. 161 101, Oct. 16, 2017. DOI: [10.1103/PhysRevLett.119.161101](https://doi.org/10.1103/PhysRevLett.119.161101) (cit. on p. 190).
- [95] B. P. Abbott, R. Abbott, *et al.*, “A Gravitational-wave Measurement of the Hubble Constant Following the Second Observing Run of Advanced LIGO and Virgo,” *The Astrophysical Journal*, vol. 909, no. 2, p. 218, Mar. 2021. DOI: [10.3847/1538-4357/abdc7](https://doi.org/10.3847/1538-4357/abdc7) (cit. on p. 190).
- [96] N. Bartolo, C. Caprini, *et al.*, “Science with the space-based interferometer LISA. IV: Probing inflation with gravitational waves,” *Journal of Cosmology and Astroparticle Physics*, vol. 2016, p. 026, Dec. 1, 2016. DOI: [10.1088/1475-7516/2016/12/026](https://doi.org/10.1088/1475-7516/2016/12/026) (cit. on p. 190).

Cosmic inflation

- [97] L. Knox, “Determination of inflationary observables by cosmic microwave background anisotropy experiments,” *Physical Review D*, vol. 52, no. 8, pp. 4307–4318, Oct. 15, 1995. DOI: [10.1103/PhysRevD.52.4307](https://doi.org/10.1103/PhysRevD.52.4307) (cit. on pp. 142, 181).
- [98] A. H. Guth, “Inflationary universe: A possible solution to the horizon and flatness problems,” *Physical Review D*, vol. 23, no. 2, pp. 347–356, Jan. 15, 1981. DOI: [10.1103/PhysRevD.23.347](https://doi.org/10.1103/PhysRevD.23.347) (cit. on pp. 173, 174).
- [99] A. R. Liddle and D. H. Lyth, *Cosmological Inflation and Large-Scale Structure*. Cambridge, U.K. ; New York: Cambridge University Press, 2000, 400 pp. (cit. on pp. 174–176).
- [100] D. Baumann. (Nov. 30, 2012). TASI Lectures on Inflation. arXiv: [0907.5424](https://arxiv.org/abs/0907.5424) [[astro-ph](#), [physics:gr-qc](#), [physics:hep-ph](#), [physics:hep-th](#)], [Online]. Available: <http://arxiv.org/abs/0907.5424> (cit. on pp. 174, 178, 182, 183).
- [101] B. A. Bassett, S. Tsujikawa, *et al.*, “Inflation dynamics and reheating,” *Reviews of Modern Physics*, vol. 78, no. 2, pp. 537–589, May 24, 2006. DOI: [10.1103/RevModPhys.78.537](https://doi.org/10.1103/RevModPhys.78.537) (cit. on p. 177).
- [102] A. Maeder and V. Gueorguiev, “Scale Invariance, Horizons, and Inflation,” 2021. DOI: [10.1093/mnras/stab1102](https://doi.org/10.1093/mnras/stab1102) (cit. on p. 182).
- [103] P. Collaboration, Y. Akrami, *et al.*, “Planck 2018 results. X. Constraints on inflation,” *Astronomy and Astrophysics*, vol. 641, A10, Sep. 2020. DOI: [10.1051/0004-6361/201833887](https://doi.org/10.1051/0004-6361/201833887) (cit. on pp. 182, 188).

- [104] S. Dodelson, “Coherent Phase Argument for Inflation,” in *AIP Conference Proceedings*, vol. 689, Cairns, Queensland (AUSTRALIA): AIP, 2003, pp. 184–196. DOI: [10.1063/1.1627736](https://doi.org/10.1063/1.1627736) (cit. on p. 183).
- [105] A. Ijjas and P. J. Steinhardt, “Implications of Planck2015 for inflationary, ekpyrotic and anamorphic bouncing cosmologies,” *Classical and Quantum Gravity*, vol. 33, no. 4, p. 044001, Jan. 2016. DOI: [10.1088/0264-9381/33/4/044001](https://doi.org/10.1088/0264-9381/33/4/044001) (cit. on p. 184).
- [106] R. H. Brandenberger, “Alternatives to the inflationary paradigm of structure formation,” *Int. J. Mod. Phys. Conf. Ser.*, vol. 01, S. P. Kim, Ed., pp. 67–79, 2011. DOI: [10.1142/S2010194511000109](https://doi.org/10.1142/S2010194511000109) (cit. on p. 184).

Physics of the CMB

- [107] A. A. Penzias and R. W. Wilson, “A Measurement of Excess Antenna Temperature at 4080 Mc/s,” *The Astrophysical Journal*, vol. 142, p. 419, Jul. 1965. DOI: [10.1086/148307](https://doi.org/10.1086/148307) (cit. on pp. 10, 96, 239).
- [108] J. R. Bond and G. Efstathiou, “The statistics of cosmic background radiation fluctuations,” *Monthly Notices of the Royal Astronomical Society*, vol. 226, no. 3, pp. 655–687, Jun. 1, 1987. DOI: [10.1093/mnras/226.3.655](https://doi.org/10.1093/mnras/226.3.655) (cit. on pp. 10, 105, 124).
- [109] S. Dodelson and F. Schmidt, *Modern Cosmology*, 2nd ed. Philadelphia: Elsevier Inc, 2020 (cit. on pp. 87, 105, 111, 180, 183, 185–188).
- [110] B. Hadzhiyska and D. Spergel, “Measuring the duration of last scattering,” *Physical Review D*, vol. 99, no. 4, p. 043537, Feb. 25, 2019. DOI: [10.1103/PhysRevD.99.043537](https://doi.org/10.1103/PhysRevD.99.043537) (cit. on pp. 97, 109).
- [111] G. F. Smoot. (May 18, 1997). The Cosmic Microwave Background Spectrum. arXiv: [astro-ph/9705101](https://arxiv.org/abs/astro-ph/9705101), [Online]. Available: <http://arxiv.org/abs/astro-ph/9705101> (cit. on p. 100).
- [112] D. J. Fixsen, “The Temperature of the Cosmic Microwave Background,” *Astrophys. J.*, vol. 707, pp. 916–920, 2009. DOI: [10.1088/0004-637X/707/2/916](https://doi.org/10.1088/0004-637X/707/2/916) (cit. on pp. 101, 185, 239).
- [113] R. A. Sunyaev and Y. B. Zeldovich, “Distortions of the Background Radiation Spectrum,” *Nature*, vol. 223, no. 5207, pp. 721–722, Aug. 1969. DOI: [10.1038/223721a0](https://doi.org/10.1038/223721a0) (cit. on p. 101).
- [114] R. A. Sunyaev and Y. B. Zel’dovich, “Microwave Background Radiation as a Probe of the Contemporary Structure and History of the Universe,” *Annual Review of Astronomy and Astrophysics*, vol. 18, no. 1, pp. 537–560, Sep. 1980. DOI: [10.1146/annurev.aa.18.090180.002541](https://doi.org/10.1146/annurev.aa.18.090180.002541) (cit. on p. 101).
- [115] M. Birkinshaw, “The Sunyaev–Zel’dovich effect,” *Physics Reports*, vol. 310, no. 2-3, pp. 97–195, Mar. 1999. DOI: [10.1016/S0370-1573\(98\)00080-5](https://doi.org/10.1016/S0370-1573(98)00080-5) (cit. on p. 101).
- [116] S. Colafrancesco, P. Marchegiani, *et al.*, “The non-thermal Sunyaev–Zel’dovich effect in clusters of galaxies,” *Astronomy & Astrophysics*, vol. 397, no. 1, pp. 27–52, Jan. 2003. DOI: [10.1051/0004-6361:20021199](https://doi.org/10.1051/0004-6361:20021199) (cit. on p. 102).
- [117] Planck Collaboration, P. A. R. Ade, *et al.*, “Planck 2015 results. XXI. The integrated Sachs–Wolfe effect,” *Astronomy and Astrophysics*, vol. 594, A21, Sep. 1, 2016. DOI: [10.1051/0004-6361/201525831](https://doi.org/10.1051/0004-6361/201525831) (cit. on pp. 102, 108).
- [118] P. J. E. Peebles and D. T. Wilkinson, “Comment on the Anisotropy of the Primeval Fireball,” *Physical Review*, vol. 174, no. 5, pp. 2168–2168, Oct. 25, 1968. DOI: [10.1103/PhysRev.174.2168](https://doi.org/10.1103/PhysRev.174.2168) (cit. on p. 102).
- [119] E. K. Conklin, “Velocity of the Earth with Respect to the Cosmic Background Radiation,” *Nature*, vol. 222, no. 5197, pp. 971–972, Jun. 1969. DOI: [10.1038/222971a0](https://doi.org/10.1038/222971a0) (cit. on p. 102).
- [120] P. S. Henry, “Isotropy of the 3 K Background,” *Nature*, vol. 231, no. 5304, pp. 516–518, Jun. 1971. DOI: [10.1038/231516a0](https://doi.org/10.1038/231516a0) (cit. on p. 102).

- [121] A. Kogut, C. Lineweaver, *et al.*, “Dipole Anisotropy in the COBE Differential Microwave Radiometers First-Year Sky Maps,” *The Astrophysical Journal*, vol. 419, p. 1, Dec. 1993. DOI: [10.1086/173453](https://doi.org/10.1086/173453) (cit. on p. 102).
- [122] W. Hu, N. Sugiyama, *et al.*, “The physics of microwave background anisotropies,” *Nature*, vol. 386, no. 6620, pp. 37–43, 6620 Mar. 1997. DOI: [10.1038/386037a0](https://doi.org/10.1038/386037a0) (cit. on p. 105).
- [123] W. Hu, “CMB Anisotropies: A Decadal Survey,” p. 131, 2001 (cit. on p. 105).
- [124] W. Hu and S. Dodelson, “Cosmic Microwave Background Anisotropies,” *Annual Review of Astronomy and Astrophysics*, vol. 40, no. 1, pp. 171–216, Sep. 2002. DOI: [10.1146/annurev.astro.40.060401.093926](https://doi.org/10.1146/annurev.astro.40.060401.093926) (cit. on pp. 105, 114).
- [125] W. Hu, “CMB Temperature and Polarization Anisotropy Fundamentals,” *Annals of Physics*, vol. 303, no. 1, pp. 203–225, Jan. 2003. DOI: [10.1016/S0003-4916\(02\)00022-2](https://doi.org/10.1016/S0003-4916(02)00022-2). arXiv: [astro-ph/0210696](https://arxiv.org/abs/astro-ph/0210696) (cit. on p. 105).
- [126] N. Sugiyama, “Introduction to temperature anisotropies of Cosmic Microwave Background radiation,” *Progress of Theoretical and Experimental Physics*, vol. 2014, no. 6, 6B101–, Jun. 11, 2014. DOI: [10.1093/ptep/ptu073](https://doi.org/10.1093/ptep/ptu073) (cit. on p. 105).
- [127] W. Hu and N. Sugiyama, “Anisotropies in the cosmic microwave background: An analytic approach,” *The Astrophysical Journal*, vol. 444, pp. 489–506, May 1, 1995. DOI: [10.1086/175624](https://doi.org/10.1086/175624) (cit. on p. 105).
- [128] R. K. Sachs and A. M. Wolfe, “Perturbations of a Cosmological Model and Angular Variations of the Microwave Background,” *The Astrophysical Journal*, vol. 147, p. 73, Jan. 1967. DOI: [10.1086/148982](https://doi.org/10.1086/148982) (cit. on p. 107).
- [129] M. White and W. Hu, “The Sachs-Wolfe effect.,” *Astronomy and Astrophysics*, vol. 321, pp. 8–9, May 1997 (cit. on p. 107).
- [130] U. Seljak, “Rees-Sciama Effect in a Cold Dark Matter Universe,” *The Astrophysical Journal*, vol. 460, p. 549, Apr. 1, 1996. DOI: [10.1086/176991](https://doi.org/10.1086/176991) (cit. on p. 108).
- [131] M. J. Rees and D. W. Sciama, “Large-scale Density Inhomogeneities in the Universe,” *Nature*, vol. 217, pp. 511–516, Feb. 1, 1968. DOI: [10.1038/217511a0](https://doi.org/10.1038/217511a0) (cit. on p. 108).
- [132] S. P. Boughn and R. G. Crittenden, “The cross-correlation between the microwave and X-ray backgrounds: Foregrounds and systematics,” *Monthly Notices of the Royal Astronomical Society*, vol. 360, no. 3, pp. 1013–1021, Jul. 2005. DOI: [10.1111/j.1365-2966.2005.09090.x](https://doi.org/10.1111/j.1365-2966.2005.09090.x) (cit. on p. 108).
- [133] J. Silk, “Cosmic Black-Body Radiation and Galaxy Formation,” *The Astrophysical Journal*, vol. 151, p. 459, Feb. 1, 1968. DOI: [10.1086/149449](https://doi.org/10.1086/149449) (cit. on p. 109).
- [134] W. Hu and M. White, “The Damping Tail of Cosmic Microwave Background Anisotropies,” *The Astrophysical Journal*, vol. 479, no. 2, p. 568, Apr. 20, 1997. DOI: [10.1086/303928](https://doi.org/10.1086/303928) (cit. on p. 109).
- [135] J. E. Gunn and B. A. Peterson, “On the Density of Neutral Hydrogen in Intergalactic Space.,” *The Astrophysical Journal*, vol. 142, pp. 1633–1636, Nov. 1, 1965. DOI: [10.1086/148444](https://doi.org/10.1086/148444) (cit. on p. 109).
- [136] Z. Haiman and L. Knox, “Reionization of the Intergalactic Medium and its Effect on the CMB,” vol. 181, p. 227, 1999 (cit. on pp. 109, 123).
- [137] U. Seljak, “Gravitational Lensing Effect on Cosmic Microwave Background Anisotropies: A Power Spectrum Approach,” *The Astrophysical Journal*, vol. 463, p. 1, May 1, 1996. DOI: [10.1086/177218](https://doi.org/10.1086/177218) (cit. on p. 110).
- [138] A. Lewis and A. Challinor, “Weak Gravitational Lensing of the CMB,” *Physics Reports*, vol. 429, no. 1, pp. 1–65, Jun. 2006. DOI: [10.1016/j.physrep.2006.03.002](https://doi.org/10.1016/j.physrep.2006.03.002). arXiv: [astro-ph/0601594](https://arxiv.org/abs/astro-ph/0601594) (cit. on p. 110).

- [139] W. Hu and M. White, “A CMB Polarization Primer,” *New Astronomy*, vol. 2, no. 4, pp. 323–344, Oct. 1997. DOI: [10.1016/S1384-1076\(97\)00022-5](#). arXiv: [astro-ph/9706147](#) (cit. on p. 115).
- [140] J. Kaplan, J. Delabrouille, *et al.*, “CMB Polarization as complementary information to anisotropies,” *Comptes Rendus Physique*, vol. 4, no. 8, pp. 917–924, Oct. 2003. DOI: [10.1016/j.crhy.2003.10.006](#). arXiv: [astro-ph/0310650](#) (cit. on p. 115).
- [141] P. Montero-Camacho and C. M. Hirata, “Exploring circular polarization in the CMB due to conventional sources of cosmic birefringence,” *Journal of Cosmology and Astroparticle Physics*, vol. 2018, no. 08, pp. 040–040, Aug. 28, 2018. DOI: [10.1088/1475-7516/2018/08/040](#) (cit. on p. 117).
- [142] M. Zaldarriaga and U. Seljak, “All-sky analysis of polarization in the microwave background,” *Physical Review D*, vol. 55, no. 4, pp. 1830–1840, Feb. 15, 1997. DOI: [10.1103/PhysRevD.55.1830](#) (cit. on pp. 117, 122, 123).
- [143] M. Kamionkowski, A. Kosowsky, *et al.*, “Statistics of cosmic microwave background polarization,” *Physical Review D*, vol. 55, no. 12, pp. 7368–7388, Jun. 15, 1997. DOI: [10.1103/PhysRevD.55.7368](#) (cit. on p. 117).
- [144] M. Zaldarriaga, “The nature of the E-B decomposition of CMB polarization,” *Physical Review D*, vol. 64, no. 10, p. 103001, Oct. 3, 2001. DOI: [10.1103/PhysRevD.64.103001](#). arXiv: [astro-ph/0106174](#) (cit. on pp. 118, 123).
- [145] M. Kamionkowski and E. D. Kovetz, “The Quest for B Modes from Inflationary Gravitational Waves,” *Annual Review of Astronomy and Astrophysics*, vol. 54, no. 1, pp. 227–269, Sep. 19, 2016. DOI: [10.1146/annurev-astro-081915-023433](#). arXiv: [1510.06042](#) (cit. on pp. 123, 174).
- [146] M. Zaldarriaga and U. Seljak, “Gravitational lensing effect on cosmic microwave background polarization,” *Physical Review D*, vol. 58, no. 2, p. 023003, Jun. 22, 1998. DOI: [10.1103/PhysRevD.58.023003](#) (cit. on p. 123).
- [147] J. Guzik, U. Seljak, *et al.*, “Lensing effect on polarization in the microwave background: Extracting the convergence power spectrum,” *Physical Review D*, vol. 62, no. 4, p. 043517, Jul. 26, 2000. DOI: [10.1103/PhysRevD.62.043517](#) (cit. on p. 123).
- [148] C. L. Reichardt, “Observing the Epoch of Reionization with the Cosmic Microwave Background,” in *Understanding the Epoch of Cosmic Reionization: Challenges and Progress*, ser. Astrophysics and Space Science Library, A. Mesinger, Ed., Cham: Springer International Publishing, 2016, pp. 227–245. DOI: [10.1007/978-3-319-21957-8_8](#) (cit. on pp. 123, 187).
- [149] Keck Array and bicep2 Collaborations, P. A. R. Ade, *et al.*, “Constraints on Primordial Gravitational Waves Using Planck, WMAP, and New BICEP2/Keck Observations through the 2015 Season,” *Physical Review Letters*, vol. 121, no. 22, p. 221301, Nov. 27, 2018. DOI: [10.1103/PhysRevLett.121.221301](#) (cit. on pp. 126, 188).
- [150] M. Tristram, A. J. Banday, *et al.*, “Planck constraints on the tensor-to-scalar ratio,” *Astronomy & Astrophysics*, vol. 647, A128, Mar. 1, 2021. DOI: [10.1051/0004-6361/202039585](#) (cit. on pp. 188, 191, 192, 197).
- [151] P. Collaboration, P. a. R. Ade, *et al.*, “Planck 2015 results. XXIV. Cosmology from Sunyaev-Zeldovich cluster counts,” *Astronomy and Astrophysics*, vol. 594, A24, Sep. 2016. DOI: [10.1051/0004-6361/201525833](#) (cit. on p. 188).

Projects dedicated to CMB observation

- [152] BICEP2 Collaboration, P. A. R. Ade, *et al.*, “Detection of *B*-Mode Polarization at Degree Angular Scales by BICEP2,” *Physical Review Letters*, vol. 112, no. 24, p. 241101, Jun. 19, 2014. DOI: [10.1103/PhysRevLett.112.241101](#) (cit. on pp. 44, 126).

- [153] BICEP2/Keck and Planck Collaborations, P. A. R. Ade, *et al.*, “Joint Analysis of BICEP2/Keck Array and Planck Data,” *Physical Review Letters*, vol. 114, no. 10, p. 101 301, Mar. 9, 2015. DOI: [10.1103/PhysRevLett.114.101301](https://doi.org/10.1103/PhysRevLett.114.101301) (cit. on pp. 44, 126).
- [154] N. W. Boggess, J. C. Mather, *et al.*, “The COBE mission - Its design and performance two years after launch,” *The Astrophysical Journal*, vol. 397, p. 420, Oct. 1992. DOI: [10.1086/171797](https://doi.org/10.1086/171797) (cit. on p. 100).
- [155] J. C. Mather, E. S. Cheng, *et al.*, “Measurement of the cosmic microwave background spectrum by the COBE FIRAS instrument,” *The Astrophysical Journal*, vol. 420, p. 439, Jan. 1994. DOI: [10.1086/173574](https://doi.org/10.1086/173574) (cit. on p. 100).
- [156] J. C. Mather, E. S. Cheng, *et al.*, “A preliminary measurement of the cosmic microwave background spectrum by the Cosmic Background Explorer (COBE) satellite,” *The Astrophysical Journal*, vol. 354, p. L37, May 1990. DOI: [10.1086/185717](https://doi.org/10.1086/185717) (cit. on p. 100).
- [157] D. J. Fixsen, E. S. Cheng, *et al.*, “Cosmic microwave background dipole spectrum measured by the COBE FIRAS instrument,” *The Astrophysical Journal*, vol. 420, p. 445, Jan. 1994. DOI: [10.1086/173575](https://doi.org/10.1086/173575) (cit. on p. 102).
- [158] G. F. Smoot, M. V. Gorenstein, *et al.*, “Detection of Anisotropy in the Cosmic Blackbody Radiation,” *Physical Review Letters*, vol. 39, no. 14, pp. 898–901, Oct. 3, 1977. DOI: [10.1103/PhysRevLett.39.898](https://doi.org/10.1103/PhysRevLett.39.898) (cit. on p. 102).
- [159] P. Collaboration, P. a. R. Ade, *et al.*, “Planck 2013 results. IX. HFI spectral response,” *Astronomy and Astrophysics*, vol. 571, A9, Nov. 2014. DOI: [10.1051/0004-6361/201321531](https://doi.org/10.1051/0004-6361/201321531) (cit. on p. 103).
- [160] P. Collaboration, N. Aghanim, *et al.*, “Planck 2018 results. I. Overview and the cosmological legacy of Planck,” *Astronomy and Astrophysics*, vol. 641, A1, Sep. 2020. DOI: [10.1051/0004-6361/201833880](https://doi.org/10.1051/0004-6361/201833880) (cit. on pp. 113, 145, 181, 185–187).
- [161] S. K. Choi, M. Hasselfield, *et al.*, “The atacama cosmology telescope: A measurement of the cosmic microwave background power spectra at 98 and 150 GHz,” *Journal of Cosmology and Astroparticle Physics*, vol. 2020, no. 12, p. 045, Dec. 2020. DOI: [10.1088/1475-7516/2020/12/045](https://doi.org/10.1088/1475-7516/2020/12/045) (cit. on pp. 124, 126).
- [162] BICEP/Keck Collaboration, P. A. R. Ade, *et al.*, “Improved Constraints on Primordial Gravitational Waves using Planck, WMAP, and BICEP/Keck Observations through the 2018 Observing Season,” *Physical Review Letters*, vol. 127, no. 15, p. 151 301, Oct. 4, 2021. DOI: [10.1103/PhysRevLett.127.151301](https://doi.org/10.1103/PhysRevLett.127.151301) (cit. on pp. 126, 188).
- [163] A. Schillaci, P. A. R. Ade, *et al.*, “Design and Performance of the First BICEP Array Receiver,” *Journal of Low Temperature Physics*, vol. 199, no. 3, pp. 976–984, May 1, 2020. DOI: [10.1007/s10909-020-02394-6](https://doi.org/10.1007/s10909-020-02394-6) (cit. on p. 126).
- [164] Polarbear Collaboration, S. Adachi, *et al.*, “A Measurement of the Degree-scale CMB B-mode Angular Power Spectrum with POLARBEAR,” *The Astrophysical Journal*, vol. 897, p. 55, Jul. 1, 2020. DOI: [10.3847/1538-4357/ab8f24](https://doi.org/10.3847/1538-4357/ab8f24) (cit. on p. 126).
- [165] A. Suzuki, P. Ade, *et al.*, “The Polarbear-2 and the Simons Array Experiments,” *Journal of Low Temperature Physics*, vol. 184, pp. 805–810, Aug. 1, 2016. DOI: [10.1007/s10909-015-1425-4](https://doi.org/10.1007/s10909-015-1425-4) (cit. on p. 126).
- [166] SPTpol Collaboration, J. T. Sayre, *et al.*, “Measurements of B -mode polarization of the cosmic microwave background from 500 square degrees of SPTpol data,” *Physical Review D*, vol. 101, no. 12, p. 122 003, Jun. 22, 2020. DOI: [10.1103/PhysRevD.101.122003](https://doi.org/10.1103/PhysRevD.101.122003) (cit. on p. 126).
- [167] J. A. Sobrin, A. J. Anderson, *et al.*, “The Design and Integrated Performance of SPT-3G,” *arXiv e-prints*, Jun. 1, 2021 (cit. on p. 126).
- [168] S. Aiola, E. Calabrese, *et al.*, “The Atacama Cosmology Telescope: DR4 maps and cosmological parameters,” *Journal of Cosmology and Astroparticle Physics*, vol. 2020, p. 047, Dec. 1, 2020. DOI: [10.1088/1475-7516/2020/12/047](https://doi.org/10.1088/1475-7516/2020/12/047) (cit. on p. 126).

- [169] S. W. Henderson, R. Allison, *et al.*, “Advanced ACTPol Cryogenic Detector Arrays and Read-out,” *Journal of Low Temperature Physics*, vol. 184, no. 3-4, pp. 772–779, Aug. 1, 2016. DOI: [10.1007/s10909-016-1575-z](https://doi.org/10.1007/s10909-016-1575-z) (cit. on p. 126).
- [170] S. K. Choi, J. Austermann, *et al.*, “Characterization of the Mid-Frequency Arrays for Advanced ACTPol,” *Journal of Low Temperature Physics*, vol. 193, no. 3-4, pp. 267–275, Nov. 2018. DOI: [10.1007/s10909-018-1982-4](https://doi.org/10.1007/s10909-018-1982-4) (cit. on p. 126).
- [171] Z. Xu, M. K. Brewer, *et al.*, “Two-year Cosmology Large Angular Scale Surveyor (CLASS) Observations: 40 GHz Telescope Pointing, Beam Profile, Window Function, and Polarization Performance,” *The Astrophysical Journal*, vol. 891, no. 2, p. 134, Mar. 2020. DOI: [10.3847/1538-4357/ab76c2](https://doi.org/10.3847/1538-4357/ab76c2) (cit. on p. 126).
- [172] S. Dahal, M. Amiri, *et al.*, “The CLASS 150/220 GHz Polarimeter Array: Design, Assembly, and Characterization,” *Journal of Low Temperature Physics*, vol. 199, no. 1, pp. 289–297, Apr. 1, 2020. DOI: [10.1007/s10909-019-02317-0](https://doi.org/10.1007/s10909-019-02317-0) (cit. on p. 126).
- [173] P. Ade, J. Aguirre, *et al.*, “The Simons Observatory: Science goals and forecasts,” *Journal of Cosmology and Astroparticle Physics*, vol. 2019, no. 02, pp. 056–056, Feb. 27, 2019. DOI: [10.1088/1475-7516/2019/02/056](https://doi.org/10.1088/1475-7516/2019/02/056) (cit. on p. 127).
- [174] K. N. Abazajian, P. Adshead, *et al.*, “CMB-S4 Science Book, First Edition,” *arXiv e-prints*, Oct. 1, 2016 (cit. on p. 127).
- [175] K. Abazajian, G. Addison, *et al.*, “CMB-S4 Science Case, Reference Design, and Project Plan,” *arXiv e-prints*, Jul. 1, 2019 (cit. on p. 127).
- [176] G. Addamo, P. A. R. Ade, *et al.*, “The large scale polarization explorer (LSPE) for CMB measurements: Performance forecast,” *Journal of Cosmology and Astroparticle Physics*, vol. 2021, p. 008, Aug. 1, 2021. DOI: [10.1088/1475-7516/2021/08/008](https://doi.org/10.1088/1475-7516/2021/08/008) (cit. on p. 127).
- [177] J. P. Filippini, P. A. R. Ade, *et al.*, “SPIDER: A balloon-borne CMB polarimeter for large angular scales,” vol. 7741, 77411N, Jul. 1, 2010. DOI: [10.1117/12.857720](https://doi.org/10.1117/12.857720) (cit. on p. 127).
- [178] SPIDER Collaboration, P. A. R. Ade, *et al.*, “A Constraint on Primordial B -Modes from the First Flight of the SPIDER Balloon-Borne Telescope,” *arXiv e-prints*, Mar. 1, 2021 (cit. on p. 127).
- [179] E. C. Shaw, P. A. R. Ade, *et al.*, “Design and pre-flight performance of SPIDER 280 GHz receivers,” vol. 11453, 114532F, Dec. 1, 2020. DOI: [10.1117/12.2562941](https://doi.org/10.1117/12.2562941) (cit. on p. 127).
- [180] N. N. Gandilo, P. A. R. Ade, *et al.*, “The Primordial Inflation Polarization Explorer (PIPER),” in *Millimeter, Submillimeter, and Far-Infrared Detectors and Instrumentation for Astronomy VIII*, vol. 9914, International Society for Optics and Photonics, Jul. 19, 2016, 99141J. DOI: [10.1117/12.2231109](https://doi.org/10.1117/12.2231109) (cit. on p. 127).
- [181] T. Essinger-Hileman, P. A. Ade, *et al.*, “The Primordial Inflation Polarization Explorer (PIPER): 2019 Flight and Telescope Performance,” vol. 236, p. 244.01, Jun. 1, 2020 (cit. on p. 127).
- [182] M. Hazumi, P. A. Ade, *et al.*, “LiteBIRD satellite: JAXA’s new strategic L-class mission for all-sky surveys of cosmic microwave background polarization,” in *Space Telescopes and Instrumentation 2020: Optical, Infrared, and Millimeter Wave*, M. Lystrup, N. Batalha, *et al.*, Eds., Online Only, United States: SPIE, Dec. 21, 2020, p. 249. DOI: [10.1117/12.2563050](https://doi.org/10.1117/12.2563050) (cit. on pp. 127, 144).
- [183] H. Sugai, P. A. R. Ade, *et al.*, “Updated design of the CMB polarization experiment satellite LiteBIRD,” *Journal of Low Temperature Physics*, vol. 199, no. 3-4, pp. 1107–1117, May 2020. DOI: [10.1007/s10909-019-02329-w](https://doi.org/10.1007/s10909-019-02329-w). arXiv: [2001.01724](https://arxiv.org/abs/2001.01724) (cit. on p. 127).
- [184] P. Collaboration, Y. Akrami, *et al.*, “Planck 2018 results. II. Low Frequency Instrument data processing,” *Astronomy and Astrophysics*, vol. 641, A2, Sep. 2020. DOI: [10.1051/0004-6361/201833293](https://doi.org/10.1051/0004-6361/201833293) (cit. on p. 130).

- [185] G. Smoot, C. Bennett, *et al.*, “COBE Differential Microwave Radiometers: Instrument Design and Implementation,” *The Astrophysical Journal*, vol. 360, p. 685, Sep. 1, 1990. DOI: [10.1086/169154](https://doi.org/10.1086/169154) (cit. on p. 130).
- [186] D. Dutcher, L. Balkenhol, *et al.*, “Measurements of the E -mode polarization and temperature-E -mode correlation of the CMB from SPT-3G 2018 data,” *Physical Review D*, vol. 104, p. 022 003, Jul. 1, 2021. DOI: [10.1103/PhysRevD.104.022003](https://doi.org/10.1103/PhysRevD.104.022003) (cit. on p. 185).
- [187] SPTpol Collaboration, D. Hanson, *et al.*, “Detection of *B*-Mode Polarization in the Cosmic Microwave Background with Data from the South Pole Telescope,” *Physical Review Letters*, vol. 111, no. 14, p. 141 301, Sep. 30, 2013. DOI: [10.1103/PhysRevLett.111.141301](https://doi.org/10.1103/PhysRevLett.111.141301) (cit. on p. 188).

CMB data analysis: map-making, power spectrum estimation...

- [188] T. J. Cornwell and P. N. Wilkinson, “A new method for making maps with unstable radio interferometers,” *Monthly Notices of the Royal Astronomical Society*, vol. 196, pp. 1067–1086, Sep. 1, 1981. DOI: [10.1093/mnras/196.4.1067](https://doi.org/10.1093/mnras/196.4.1067) (cit. on p. 50).
- [189] K. M. Smith, D. Hanson, *et al.*, “Delensing CMB Polarization with External Datasets,” *Journal of Cosmology and Astroparticle Physics*, vol. 2012, no. 06, pp. 014–014, Jun. 8, 2012. DOI: [10.1088/1475-7516/2012/06/014](https://doi.org/10.1088/1475-7516/2012/06/014). arXiv: [1010.0048](https://arxiv.org/abs/1010.0048) (cit. on pp. 110, 123).
- [190] J.-C. Hamilton, “CMB map-making and power spectrum estimation,” *Comptes Rendus Physique*, vol. 4, no. 8, pp. 871–879, Oct. 2003. DOI: [10.1016/S1631-0705\(03\)00108-7](https://doi.org/10.1016/S1631-0705(03)00108-7) (cit. on p. 125).
- [191] D. T. Emerson and R. Graeve, “The reduction of scanning noise in raster scanned data,” *Astronomy and Astrophysics*, vol. 190, pp. 353–358, Jan. 1988 (cit. on p. 129).
- [192] M. Bucher, “An exact result concerning the $1/f$ noise contribution to the large-angle error in CMB temperature and polarization maps,” *arXiv e-prints*, Feb. 1, 2016 (cit. on pp. 130, 131).
- [193] J. Delabrouille, “Analysis of the accuracy of a destriping method for future cosmic microwave background mapping with the PLANCK SURVEYOR satellite,” *Astronomy and Astrophysics Supplement Series*, vol. 127, no. 3, pp. 555–567, 3 Feb. 1, 1998. DOI: [10.1051/aas:1998119](https://doi.org/10.1051/aas:1998119) (cit. on p. 130).
- [194] B. Revenu, A. Kim, *et al.*, “Destriping of polarized data in a CMB mission with a circular scanning strategy,” *Astronomy and Astrophysics Supplement Series*, vol. 142, no. 3, pp. 499–509, 3 Mar. 1, 2000. DOI: [10.1051/aas:2000308](https://doi.org/10.1051/aas:2000308) (cit. on p. 130).
- [195] M. Tegmark, “CMB mapping experiments: A designer’s guide,” *Physical Review D*, vol. 56, no. 8, pp. 4514–4529, Oct. 15, 1997. DOI: [10.1103/PhysRevD.56.4514](https://doi.org/10.1103/PhysRevD.56.4514). arXiv: [astro-ph/9705188](https://arxiv.org/abs/astro-ph/9705188) (cit. on pp. 130–132, 142, 143).
- [196] E. L. Wright, “Scanning and Mapping Strategies for CMB Experiments,” *arXiv e-prints*, astro-ph/9612006, Nov. 1, 1996 (cit. on p. 131).
- [197] J. Borrill, “MADCAP - The Microwave Anisotropy Dataset Computational Analysis Package,” *arXiv e-prints*, astro-ph/9911389, Nov. 1, 1999 (cit. on pp. 131, 132, 143).
- [198] S. Prunet, C. B. Netterfield, *et al.*, “Iterative map-making for scanning experiments,” *arXiv e-prints*, astro-ph/0006052, Jun. 1, 2000 (cit. on p. 131).
- [199] E. Hivon, K. M. Gorski, *et al.*, “MASTER of the CMB Anisotropy Power Spectrum: A Fast Method for Statistical Analysis of Large and Complex CMB Data Sets,” *The Astrophysical Journal*, vol. 567, no. 1, pp. 2–17, Mar. 2002. DOI: [10.1086/338126](https://doi.org/10.1086/338126). arXiv: [astro-ph/0105302](https://arxiv.org/abs/astro-ph/0105302) (cit. on pp. 131, 140, 141).
- [200] C. M. Cantalupo, J. D. Borrill, *et al.*, “MADmap: A Massively Parallel Maximum Likelihood Cosmic Microwave Background Map-maker,” *Astrophysical Journal Supplement*, vol. 187, p. 212, Mar. 2010. DOI: [10.1088/0067-0049/187/1/212](https://doi.org/10.1088/0067-0049/187/1/212) (cit. on p. 131).

- [201] R. Stompor, A. Balbi, *et al.*, “Making Maps Of The Cosmic Microwave Background: The MAXIMA Example,” *Physical Review D*, vol. 65, no. 2, p. 022003, Dec. 26, 2001. DOI: [10.1103/PhysRevD.65.022003](#). arXiv: [astro-ph/0106451](#) (cit. on p. 131).
- [202] J. Papez, L. Grigori, *et al.*, “Solving linear equations with messenger-field and conjugate gradient techniques: An application to CMB data analysis,” *Astronomy and Astrophysics - A&A*, vol. 620, A59, Nov. 2018. DOI: [10.1051/0004-6361/201832987](#) (cit. on p. 131).
- [203] F. Couchot, J. Delabrouille, *et al.*, “Optimised polarimeter configurations for measuring the Stokes parameters of the Cosmic Microwave Background Radiation,” *Astronomy and Astrophysics Supplement Series*, vol. 135, no. 3, pp. 579–584, Mar. 1999. DOI: [10.1051/aas:1999191](#). arXiv: [astro-ph/9807080](#) (cit. on p. 135).
- [204] M. White and M. Srednicki, “Window Functions for Cosmic Microwave Background Experiments,” *The Astrophysical Journal*, vol. 443, p. 6, Apr. 1, 1995. DOI: [10.1086/175497](#) (cit. on pp. 140, 141).
- [205] K. M. Smith, “Pseudo- C_{ell} estimators which do not mix E and B modes,” *Physical Review D*, vol. 74, no. 8, p. 083002, Oct. 4, 2006. DOI: [10.1103/PhysRevD.74.083002](#). arXiv: [astro-ph/0511629](#) (cit. on pp. 141, 142).
- [206] E. F. Bunn, M. Zaldarriaga, *et al.*, “E/B decomposition of finite pixelized CMB maps,” *Physical Review D*, vol. 67, p. 023501, Jan. 1, 2003. DOI: [10.1103/PhysRevD.67.023501](#) (cit. on p. 142).
- [207] J. Grain, M. Tristram, *et al.*, “Polarized CMB power spectrum estimation using the pure pseudo-cross-spectrum approach,” *Physical Review D*, vol. 79, p. 123515, Jun. 1, 2009. DOI: [10.1103/PhysRevD.79.123515](#) (cit. on p. 142).
- [208] D. Alonso, J. Sanchez, *et al.*, “A unified pseudo- C_{ell} framework,” *Monthly Notices of the Royal Astronomical Society*, vol. 484, no. 3, pp. 4127–4151, Apr. 11, 2019. DOI: [10.1093/mnras/stz093](#). arXiv: [1809.09603](#) (cit. on p. 142).
- [209] C. García-García, D. Alonso, *et al.*, “Disconnected pseudo- C_{ell} covariances for projected large-scale structure data,” *Journal of Cosmology and Astroparticle Physics*, vol. 2019, no. 11, pp. 043–043, Nov. 28, 2019. DOI: [10.1088/1475-7516/2019/11/043](#). arXiv: [1906.11765](#) (cit. on pp. 142, 162, 190).
- [210] J. R. Bond, A. H. Jaffe, *et al.*, “Radical Compression of Cosmic Microwave Background Data,” *The Astrophysical Journal*, vol. 533, pp. 19–37, Apr. 1, 2000. DOI: [10.1086/308625](#) (cit. on p. 143).
- [211] S. Hamimeche and A. Lewis, “Likelihood analysis of CMB temperature and polarization power spectra,” *Physical Review D*, vol. 77, p. 103013, May 1, 2008. DOI: [10.1103/PhysRevD.77.103013](#) (cit. on p. 191).

Algorithms and Python packages for data analysis

- [212] P. Virtanen, R. Gommers, *et al.*, “SciPy 1.0: Fundamental algorithms for scientific computing in Python,” *Nature Methods*, vol. 17, no. 3, pp. 261–272, Mar. 2, 2020. DOI: [10.1038/s41592-019-0686-2](#) (cit. on p. 56).
- [213] F. James and M. Roos, “Minuit - a system for function minimization and analysis of the parameter errors and correlations,” *Computer Physics Communications*, vol. 10, pp. 343–367, Dec. 1, 1975. DOI: [10.1016/0010-4655\(75\)90039-9](#) (cit. on pp. 56, 77).
- [214] H. Dembinski, P. Ongmongkolkul, *et al.*, “Scikit-hep/iminuit: V2.8.0,” Jul. 25, 2021. DOI: [10.5281/zenodo.5136400](#) (cit. on pp. 56, 77).
- [215] N. Metropolis and S. Ulam, “The Monte Carlo Method,” *Journal of the American Statistical Association*, vol. 44, no. 247, pp. 335–341, 1949. DOI: [10.2307/2280232](#). JSTOR: [2280232](#) (cit. on p. 57).

- [216] F. Pedregosa, G. Varoquaux, *et al.*, “Scikit-learn: Machine Learning in Python,” *arXiv e-prints*, Jan. 1, 2012 (cit. on p. 68).
- [217] D. Foreman-Mackey, D. W. Hogg, *et al.*, “Emcee: The MCMC Hammer,” *Publications of the Astronomical Society of the Pacific*, vol. 125, p. 306, Mar. 1, 2013. DOI: [10.1086/670067](https://doi.org/10.1086/670067) (cit. on p. 79).
- [218] A. Gelman and D. B. Rubin, “Inference from Iterative Simulation Using Multiple Sequences,” *Statistical Science*, vol. 7, no. 4, pp. 457–472, Nov. 1992. DOI: [10.1214/ss/1177011136](https://doi.org/10.1214/ss/1177011136) (cit. on p. 79).
- [219] S. P. Brooks and A. Gelman, “General methods for monitoring convergence of iterative simulations,” *Journal of Computational and Graphical Statistics*, vol. 7, pp. 434–455, 1998 (cit. on p. 79).
- [220] J. R. Shewchuk, “An Introduction to the Conjugate Gradient Method Without the Agonizing Pain,” Carnegie Mellon University, USA, Technical Report, 1994 (cit. on p. 132).
- [221] P. Chanial and N. Barbey, “PyOperators: Operators and solvers for high-performance computing,” pp. 513–517, Dec. 1, 2012 (cit. on p. 132).
- [222] B. Thorne, J. Dunkley, *et al.*, “The Python Sky Model: Software for simulating the Galactic microwave sky,” *Monthly Notices of the Royal Astronomical Society*, vol. 469, no. 3, pp. 2821–2833, Aug. 2017. DOI: [10.1093/mnras/stx949](https://doi.org/10.1093/mnras/stx949). arXiv: [1608.02841](https://arxiv.org/abs/1608.02841) (cit. on pp. 153, 158, 194).
- [223] K. M. Górski, E. Hivon, *et al.*, “HEALPix: A Framework for High-Resolution Discretization and Fast Analysis of Data Distributed on the Sphere,” *The Astrophysical Journal*, vol. 622, pp. 759–771, Apr. 1, 2005. DOI: [10.1086/427976](https://doi.org/10.1086/427976) (cit. on p. 153).

Astrophysical foregrounds and atmosphere

- [224] P. Collaboration, A. Abergel, *et al.*, “Planck 2013 results. XI. All-sky model of thermal dust emission,” *Astronomy and Astrophysics*, vol. 571, A11, Nov. 2014. DOI: [10.1051/0004-6361/201323195](https://doi.org/10.1051/0004-6361/201323195) (cit. on p. 144).
- [225] P. Collaboration, Y. Akrami, *et al.*, “Planck 2018 results. IV. Diffuse component separation,” *Astronomy and Astrophysics*, vol. 641, A4, Sep. 2020. DOI: [10.1051/0004-6361/201833881](https://doi.org/10.1051/0004-6361/201833881) (cit. on p. 144).
- [226] K. Ichiki, “CMB foreground: A concise review,” *Progress of Theoretical and Experimental Physics*, vol. 2014, no. 6, Jun. 1, 2014. DOI: [10.1093/ptep/ptu065](https://doi.org/10.1093/ptep/ptu065) (cit. on p. 144).
- [227] C. Dickinson, “CMB foregrounds - A brief review,” *arXiv e-prints*, Jun. 1, 2016 (cit. on p. 144).
- [228] J. Errard *et al.*, “Modeling atmospheric emission for CMB ground-based observations,” *Astrophys. J.*, vol. 809, p. 63, 2015. DOI: [10.1088/0004-637X/809/1/63](https://doi.org/10.1088/0004-637X/809/1/63) (cit. on pp. 145, 146).
- [229] M. O. Irfan, J. Bobin, *et al.*, “Determining thermal dust emission from *Planck* HFI data using a sparse, parametric technique,” *Astronomy & Astrophysics*, vol. 623, A21, Mar. 2019. DOI: [10.1051/0004-6361/201834394](https://doi.org/10.1051/0004-6361/201834394) (cit. on p. 161).

Divers: optics, electromagnetism...

- [230] P. Pellat-Finet, *Optique de Fourier*. Paris: Springer Paris, 2009. DOI: [10.1007/978-2-287-99168-4](https://doi.org/10.1007/978-2-287-99168-4) (cit. on p. 21).
- [231] M. Born and E. Wolf, *Principles of Optics: Electromagnetic Theory of Propagation, Interference and Diffraction of Light*, 6th (corr.) ed. Cambridge, UK ; New York: Cambridge University Press, 1997, 808 pp. (cit. on p. 23).
- [232] J. D. Jackson, C. Jeanmougin, *et al.*, *Electrodynamique classique: cours et exercices d’électromagnétisme*. Paris: Dunod, 2001 (cit. on pp. 23, 115).

- [233] A. R. Thompson, J. M. Moran, *et al.*, *Interferometry and Synthesis in Radio Astronomy*, 3rd ed. 2017, ser. Astronomy and Astrophysics Library. Cham: Springer International Publishing : Imprint: Springer, 2017, 1 p. DOI: [10.1007/978-3-319-44431-4](https://doi.org/10.1007/978-3-319-44431-4) (cit. on p. [34](#)).
- [234] R. C. Jones, “New calculus for the treatment of optical systems. I. Description and discussion of the calculus,” *Journal of the Optical Society of America (1917-1983)*, vol. 31, p. 488, Jul. 1, 1941 (cit. on p. [35](#)).
- [235] R. C. Jones, “A new calculus for the treatment of optical systems. IV,” *Journal of the Optical Society of America (1917-1983)*, vol. 32, p. 486, Aug. 1, 1942 (cit. on p. [35](#)).
- [236] Rayleigh, “XXXI. *Investigations in optics, with special reference to the spectroscope*,” *The London, Edinburgh, and Dublin Philosophical Magazine and Journal of Science*, vol. 8, no. 49, pp. 261–274, Oct. 1879. DOI: [10.1080/14786447908639684](https://doi.org/10.1080/14786447908639684) (cit. on p. [152](#)).
- [237] P. Ramond, *Field Theory: A Modern Primer*, 2nd ed., rev. print, ser. Frontiers in Physics 74. Boulder, Colo: Westview Press, 1990, 329 pp. (cit. on pp. [176](#), [182](#)).
- [238] R. P. Feynman, R. B. Leighton, *et al.*, *Mainly Mechanics, Radiation, and Heat*, Nachdr., ser. The Feynman Lectures on Physics Richard P. Feynman; Robert B. Leighton; Matthew Sands ; 1. Reading/Mass.: Addison-Wesley, 2007 (cit. on p. [181](#)).